Effects of Seismic Soil-Structure Interaction on The Analysis, Design and Behaviour of Structures During Their Entire Life Cycle

A thesis submitted to the Brunel University London, for the degree of Doctor of Philosophy

By

Alaa Alisawi

Doctor of Philosophy

College of Engineering, Design and Physical Sciences

Civil and Environmental Engineering

BRUNEL UNIVERSITY LONDON

2021

Abstract

Dynamic response records of co-seismic pile performance are limited due to complexities and a lack of well-documented soil–pile response case histories. These limitations lead to inadequate provision of a standardised basis for the calibration and validation of the methods developed for seismic soil–pile superstructure interaction (SSPSI) and multi-hazard events problems. To address this, a series of numerical simulations (using finite element analysis (FEA)) for shaking table tests of scaled model piles in soft clay has been developed. The study identifies all numerical simulation aspects and soil constitutive criteria successfully. The shaking table test programme developed by Philip Meymand has been adopted as a physical test case. The study uses dimensional analysis to identify scale modelling criteria and develop a scaled soil and pile-supported structure model correctly. A unique numerical methodology is designed to permit multi-directional shear deformations, minimise boundary effects and replicate the free-field site response. Soil–structure interaction (SSI) effects, including the gap/slap mechanism and the consequences of kinematic and inertial force, are clearly shown.

Full-scale co-seismic physical tests are complicated and even impossible as no fixed reference point is available as a benchmark. Most investigations performed after earthquake events analyse the consequences of the earthquake rather than the system behaviour. Employing a scaled testing technique, using shaking table tests in the one-g environment is a viable alternative. In this research, a calibration method for establishing the relationship between full-scale numerical analysis and scaled laboratory tests in one-g environment is developed. A sophisticated approach of scaling and validating full-scale seismic SSI problem is proposed. This considers the scaling concept of implied prototypes and 'modelling of models' techniques which can ensure a satisfactory level of accuracy.

Pile integrity is commonly assessed during dynamic loading through simplified and uncodified analysis approaches. Two widely used seismic design codes (EC8 and ASCE) are compared, and revisions proposed. The effects of SSI on the seismic response of structures are determined. The findings reveal that structural response may exceed the codes' limitations, making the provisions unsafe. The significance of the connection between the input motion and the site's ground properties is also supported. The number of modes is associated with the response of the SSI model. The findings have important implications for the understanding of pile and pile group effects. Moreover, the definition

of soil class *F* in EC8 and ASCE is ambiguous. The decision of designating class *F* or not for a project mostly depends on the experience of the personnel concerned. To reduce risk and to achieve a clear definition, the minimum thickness of sensitive clay to be considered to meet code condition for soil class *F* and the minimum thickness of sand layer that cuts off the continuity of soft clay layer to be no longer classified as *F* class are defined accurately. Furthermore, relatively little research has taken place into major multi-hazard events such as post-earthquake fire (PEF) and this is poorly covered in design codes. Structures subjected to an earthquake may experience partial damage, with an increased risk of structural failure during a later fire. A multi-hazard approach is developed, and two types of failure mechanisms are detected—global and local failure. The seismic SSI effects have been implicitly considered in the analyses.

Finally, the study provides a robust evidence base for FEA aspect, including employing the correct soil model, in addition to an accurate scaling and validation methodology for co-seismic systems. It can contribute to a better understanding of seismic SSI codes provision including the application of SSI and the definition of soil class *F,* and delivers an effective methodology for multi-hazard analysis.

Publications

The present PhD study has led to a list of journal papers, conference papers and technical presentations, as follows:

Journal Papers

1- **Alisawi A. T**, Collins P.E.F. and Katherine A.Cashell (2019). "Fully Non-Linear Numerical Simulation of a Shaking Table Test of Dynamic Soil-Pile-Structure Interactions in Soft Clay Using ABAQUS". Special issue ASCE Library, https://doi.org/10.1061/9780784482100.026

2- **Alisawi A. T**, Collins P.E.F. and Katherine A.Cashell (2020). "Nonlinear Numerical Simulation of Physical Shaking Table Test, Using Three Different Soil Constitutive Models." (under revision with the *Soil Dynamics and Earthquake Engineering,* Manuscript Number SOILDYN_*2020_532*

Conference Papers

1- **Alisawi A.T**, and Collins P.E.F. "The Effect of Soil-Structure Interaction on the Post-Earthquake Fire Performance of Structures" published in conference proceedings of the *8th International Conference on Case Histories in Geotechnical Engineering,* Geo-Congress 2019, Philadelphia, USA

2- **Alisawi A. T**, Collins P.E. F, and Katherine A.Cashell (2019). "Nonlinear analysis of a steel frame structure exposed to post earthquake fire" published in conference proceedings of the *3rd International Conference on Structural Safety Under Fire and Blast Loading,* Cobfab-2019, London, UK

3- **Alisawi A.T**, Collins P.E.F. "Prediction of the behaviour of a soil-pile foundation system under static vertical load" published in conference proceedings of the *3rd international conference Challenges in Geotechnical Engineering,* Poland, Zielona Gora , (Won the first price in pile test (pile group) competition)

4- **Alisawi A.T**, Collins P.E.F. "Numerical Simulation of a Shaking Table Test: Effects of Dynamic Soil–Pile Structure Interactions in Soft Clay Using Different Soil Constitutive Models" published in conference proceedings of the *3rd*

international conference Challenges in Geotechnical Engineering, Poland , Zielona Gora

5- **Alisawi A.T**, and Collins P.E.F , "Effects of Soil-Structure Interaction on Design and Analysis of High Rise Buildings Resting on Soft Clay: A Comparative Study between EC8 and ASCE" published in conference proceedings of the *international conference on Case Histories & Soil Properties (ICCS2019) , Singapore*

6- **Alisawi A.T**, Collins P.E.F. "A Novel Methodology for the Prediction of Soil–Pile Foundation System Behaviour under Dynamic Loading Conditions" Submitted to the *International Foundations Conference and Equipment Expo* (IFCEE-2021), Texas, USA

Technical Presentations

1. **Alisawi A.T**, "Effect of Soil-Structure-Interaction of Tall-Buildings on System-Stability under Earthquake" Presented a poster at poster conference conducted by Brunel University London 2016, London, UK

2. **Alisawi A.T**, "Effects of soil structure interaction on structure behaviour during and after Seismic Excitation" Presented at *Civil and Environmental Engineering Research Conference* conducted by Brunel University London 2016, London, UK

3. **Alisawi A.T** "Seismic Hazard Analysis–the Effects of Oil Extraction" Presented at *Civil Engineering department,* Azerbaijan Architecture and Construction University (AUAC), Baku 2019, Azerbaijan

Acknowledgement

Table of contents

List of Figures

List of Tables

Notation

The following notation is used in the thesis. All symbols are initially defined within the text as it first appears and in the context in which it is used. Some symbols are followed by subscripts and superscripts referring to certain formulations. Those not defined below are explained in the text.

Symbol	Definition
$A_{E,d}$	Design value of seismic action load
A_{steel}	Area of steel
$A_{concrete}$	Area concrete
$A_{pile\,.model}$	Pile cross sectional area
$acce.$	Acceleration of soil and or structure
a_g	Design ground acceleration EC8
α_M	Mass and stiffness proportional damping coefficients
a	Size of the yield surface parameter
β	Shape modification constant- CC model
$\beta_{l.b}$	Lower bound factor for the horizontal design spectrum –EC8
β_K	Mass and stiffness proportional damping coefficients
c	Soil cohesion
c_0	Initial cohesion yield stress
C_v	Coefficient of consolidation
d	Pile diameter
d_s	Storey drift
D_T	Tangent modulus of soil
δ	Departure angle
EA	Longitudinal rigidity
E	Young's modulus
E_{steel}	Steel Young's modulus
$E_{concrete}$	Concrete Young's modulus
E_{pile}	Pile Young's modulus
E_{soil}	Soil Young's modulus

EI	Flexural rigidity
EI_{steel}	Steel flexural rigidity
$EI_{concrete}$	Concrete flexural rigidity
$EI_{composit}$	Composite concrete/steel flexural rigidity
$EI_{composit}$	Composite concrete/steel flexural rigidity
$EI_{pile.model}$	Pile flexural rigidity
E_r	Soil storage modulus
E_l	Soil loss modulus
e	Void ratio
e_0	Initial void ratio
$e_{dev.}$	Deviatoric eccentricity parameter
ϵ	Meridional eccentricity parameter
ε_1	Main specific strain
ε_v	Volumetric strain
ε_o	Strain of the soil due to creep, temperature, etc.
F	Force
F_c	Cap yield surface DP
F_t	Smooth transition surface component
F_a	Acceleration related soil factor
F_v	Velocity related soil factor
F_A	Axial force
ϕ	Angle of internal friction
G_f	Flow potential-MC model
G	Shear modulus
g	The acceleration of gravity
$G_{k,j}$	Permanent load
G_s	Soil shear modulus
η	Damping correction factor
I	Moment of inertia
$I_{pile.model}$	Pile moment of inertia
γ_I	Importance factor
i	Hydraulic gradient of external water
J^{pl}	Plastic volumetric change

J^e	Elastic volumetric change
J_c	Moment of inertia of the pile cap
K_r	Pile flexibility
K_b	Bulk elastic stiffness
κ	Unloading- Reloading line slope
K_f	Bulk modulus of pore water and/or external water
k	Permeability of soil
K	Stiffness
K_s	Bulk modulus of the solid grains of soil
L	Pile length
LL	Liquid Limit
l	Length
λ	Geometric scaling factor
λ_{NCL}	Normal consolidation line slope
M_p	Pile mass per unit length
M_c	Pile cap mass
μ	Mass
M	Bending moment
n	Porosity of soil
υ	Poisson's ratio
OD	Pile outer diameter
OD_m	Pile outer diameter (model)
PI	Plasticity index
PL	Plastic Limit
p	Equivalent pressure stress
p'	Mean effective stress
p_a	Evolution parameter
p_b	Yield effective stress
p_c'	Preconsolidation pressure
PGA	Peak ground acceleration
P_l	Pre-stressing load
P	Pressure of pore water and/or external water
q_{Mises}	Mises equivalent stress

q	Behaviour factor EC8
Q_d	Design dead load
$Q_{k,i}$	Live load
Q_K	Design live load
R	Epicentre distance
θ	Deviatoric polar angle
θ_{inc}	Inclination angle
R	Return period
RF	Reduction factor
RSN	Record Sequence Number of an earthquake
R_f	Friction ratio
r	Third invariant of deviatoric stress
ρ	Mass density of saturated soil, pile and structure
ρ_b	Mass per unit length
$\rho_{pile\ .m}$	Model pile density
S_p	Pile spacing
S	Deviatoric stress
S_{Ds}	Mapped acceleration parameter (short period, ASCE)
S_{D1}	Mapped acceleration parameter (1 sec period)
S_e	Absolute acceleration elastic design spectrum
S_{De}	Design elastic displacement spectrum
S_{Ms}	Zonation factor (short period, ASCE)
S_{M1}	Zonation factor (I sec period, ASCE)
S_t	Soil sensitivity
S_u	Soil shear strength
$S_{u_{static}}$	Static soil shear strength
$S_{u_{dynamic}}$	Dynamic soil shear strength
S_{shear}	Shear force
S_u/p'	Undrained Strength Ratio
σ	Normal stress
σ'	Effective stress of soil
t_{wall}	Pile wall thickness
t	Shape factor

τ	Shear strength
T_B	Lower and the upper bands of the period of the constant Spectral acceleration
T_D	Period value that specifies the start of the constant displacement response range of the spectrum.
T	Fundamental vibration period
T_t	Time
$t_{wall.p}$	Pile wall thickness (prototype)
$t_{wall.m}$	Pile wall thickness (model)
U	Displacement of soil or structure
V	Specific volume
V_s	Shear wave velocity
W	Average displacement of pore water relative to the soil skeleton
W_f	Rate of pore water flow
w	Moisture content
w_c	Natural Water Content
ω	Frequency
ω_i, ω_j	System modes' frequencies
$\Psi_{2,i}$	Specific reduction factor
ψ	Dilation angle
ξ_i, ξ_j	Damping ratio

Chapter 1: Introduction

1.1. Introduction

In this thesis, a new basis for numerical finite element analysis aspects employing in seismic soil-structure interaction (SSI) studies is provided. This includes employing the most suitable soil constitutive model which can represent the numerical soil model in the seismic SSI system analysis and presents accurate scaling and validation methodology for co-seismic systems. Moreover, one primary aim of this thesis is to critically address the safety problems and provide a deeper understanding of seismic SSI codes standard. This includes the application of SSI in considering the clear definition of the most challenging soil, referred to in ASCE and Eurocode standards as type F, and develops an effective methodology for multi-hazard (post-earthquake fire) analysis.

Deep foundations are typically used in the design of structures built on soft soils to ensure that axial loads are successfully transferred to deep layers with strong bearing capacity. These foundation components may be subject to seismic, dynamic or cyclic lateral load originating from waves, blast, wind, impact, ship or train motions, machine loading and natural disasters such as earthquakes. The coincidence of founding these major pile-supported structures on soft soils in earthquake hazard zones contributes to substantial demands on these deep foundation systems. Potential resonance repercussions between the long period of soft soil deposits, which may lengthen motion wave and amplify ground acceleration, and high-rise structures may intensify the problem. The potential strain softening and/or liquefaction in the soft soil may inflict extra demands on foundation systems.

The effect of piles on the ground motions of a structure has been prevalently ignored or simplified in traditional seismic design practices. This design assumption is commonly accepted as a conservative spectral analysis approach as the flexible embedded piles result in lengthened ground motion period and increased damping. Consequently, the structural base shear forces in flexible embedded piles are reduced compared with those in a fixed base (see Figure 1.1). In extreme circumstances such as the 1985 Mexico City earthquake, period lengthening may result in increased response spectrum values corresponding to the design response spectrum specified by code provisions (Figure 1.2). Owing to the effects of seismic soil–pile–structure interaction, the stiffness of the pile foundation system may

decrease, and that can increase the permanent piles' deformations. Consequently, the displacement and seismic response of the entire structure as can be greatly influenced. High-rise buildings may experience resonance as a result of soil–structure interaction (SSI) during an earthquake (Guin & Banerjee, 1998, Mylonakis & Gazetas, 2000, Malhotra, 2010, Phanikanthl et al., 2015).
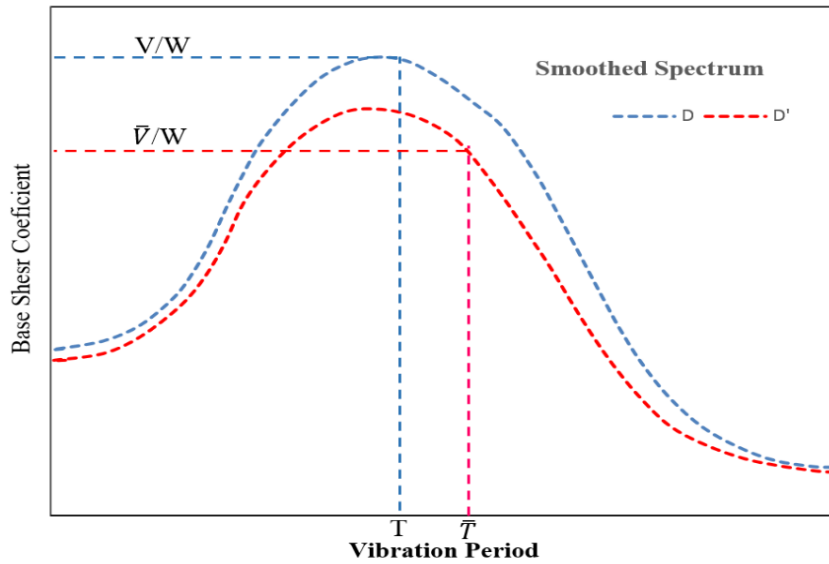
Figure 1-1 Effect of Soil–Structure Interaction on Seismic Coefficient for Base Shear
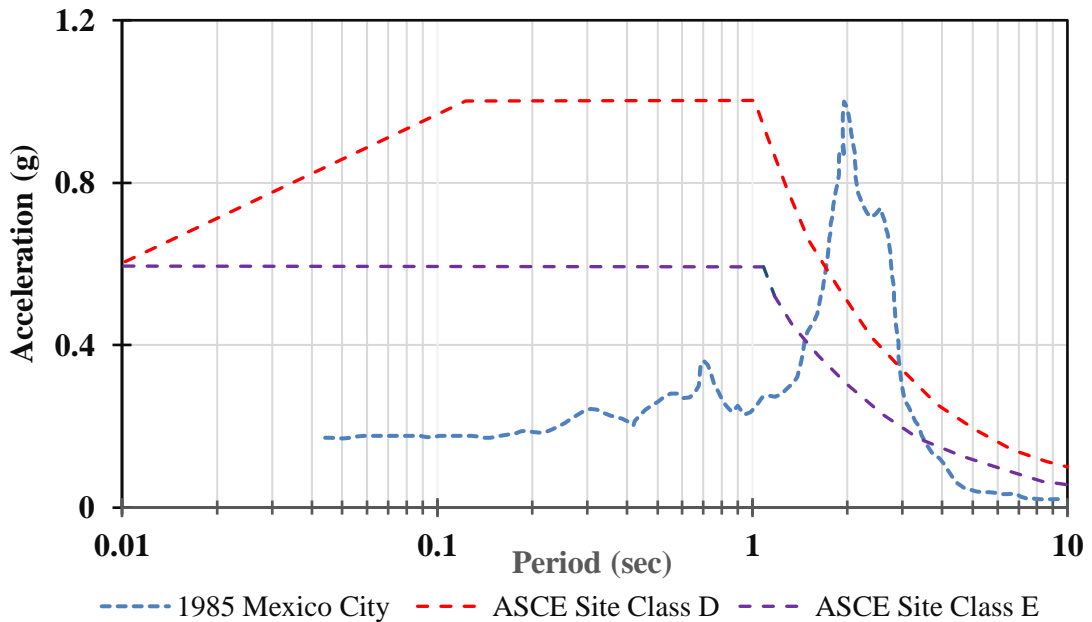
Figure 1-2 Comparison of 1985 Mexico City Earthquake Response Spectra with ASCE Code Design Spectrum.

Assessing pile integrity during seismic loading has become common, and it is achieved with simplified and non-coded analysis practices. Two main aspects related to pile performance must be considered during an earthquake. Firstly, the ground motions imposing the superstructure are influenced by the embedded pile foundation system. Secondly, extreme damage and even failure may occur in the piles during an earthquake due to seismic loading.

The purpose of this thesis is to examine these two aspects of this complicated SSI problem, provide a scaling and validation methodology for researchers who deals with dynamic SSI issues, review the seismic provision by Eurocode 8 and ASCE seismic code and suggest soil class provision and outline the effects of dynamic SSI on the structures subject to multi-hazard analysis such as post-earthquake fire (PEF).Despite the importance of considering SSI aspects in most engineering practices, a paucity remains in well-documented evidence regarding seismic soil–pile response case histories. Only a small number of the existing case studies include piles that record dynamic response using instrumented measurements. Pile performance under earthquake conditions currently has no sound validation and calibration methods or guidelines due to the limited databases available on assessed pile performance. Shaking table and centrifuge model tests are used to develop field case histories with laboratory data obtained under controlled conditions.

The majority of shaking table and centrifuge tests explore the soil–pile seismic response of liquefiable and potentially cohesionless soils. Numerous pile foundation systems supporting important structures are founded on soft clay that can experience cyclic strength degradation under seismic loading condition. A shaking table test study done by Meymand (1998) has been adopted as a reference case study to examine the aforementioned seismic SSI aspects and develop a scaling and validation methodology. This reference case utilise the San Francisco–Oakland Bay Bridge situated on San Francisco Bay mud that represents a crucial example for soft clay sites in a seismic zone. However, physical shaking table tests for clay are expensive in terms of cost, facilities and time. A scaled model must also be developed to perform the studied seismic soil-structure interaction (SSSI) system. A correct scaling method that can define the similarity between the primary properties of the scale model and the prototype model should be designed in addition to a practical method to validate findings. These two important aspects are aimed to be developed correctly in this thesis employing the association between physical and numerical modelling. The current limitations in the seismic soil–pile–superstructure interaction (SSPSI) database can be solved or mitigated by adopting the aforementioned scaling and validation method. Field

case histories can then be validated with the use of associated numerical and physical shaking table model tests. The scaled physical model can be used to validate the numerical results, and the validated numerical analysis results can be utilised to understand the behaviour of the full-scale system.

1.2. Primary Characteristics of SSPSI

The primary characteristics of SSPSI for an individual pile are demonstrated schematically in Figure 1-3. The components of the SSPSI system are the pile(s), pile cap, superstructure, near- and far-field domains of the soil and the energy source of the seismic activity. The interaction modes of an SSPSI system involve kinematic, inertial, physical and radiation damping interaction. These interaction modes are described below.

- Kinematic interaction is the seismic response of the soil profile transmitted to the pile which try to deform according to soil displacement. Consequently, the superstructure experiences diverse ground motion unlike free-field soil.

- Inertial interaction comprises structural inertial forces transferred to the pile. These forces set up lateral loads concentrated close to the pile head and axial loads once the structure is in a rocking mode.

- Physical interaction between the pile and soil arises before and during seismic loading. During pile installation and initial loading, soil displacement, load transfer, and shear forces impose an initial stress in the piles and surrounding soil. Consequently, seismically induced stresses are superimposed. During seismic loading, gaps may occur between the soil and the pile at the top ground surface. In case of cohesionless soils, the gap may refill and be compacted, but in a cohesive soil which is the concern in this study, the gap may remain open, causing a decrease in soil–pile lateral stiffness. In submerged soil, water alternately pulled in and discharged from the gap during each load increment may wash out the soil adjacent to the pile, contributing to an additional reduction in soil–pile lateral stiffness. This situation has been simulated as saturated soft clay with gap/slap mechanism system behaviour.

- Radiation damping arises due to the stiffness difference between the soil and pile. Piles oscillate at frequencies much higher than the soil deposit. However, under the soil–pile contact conditions, the soil demand to oscillate at these high frequencies. Consequently, high-frequency energy are transmitted away from the piles into the soil deposit. Radiation damping is most noticeable at high frequencies and low levels

4

of soil damping. The primary condition for radiation damping is the soil–pile contact. It cannot propagate through 'gaps' between the pile and soil.
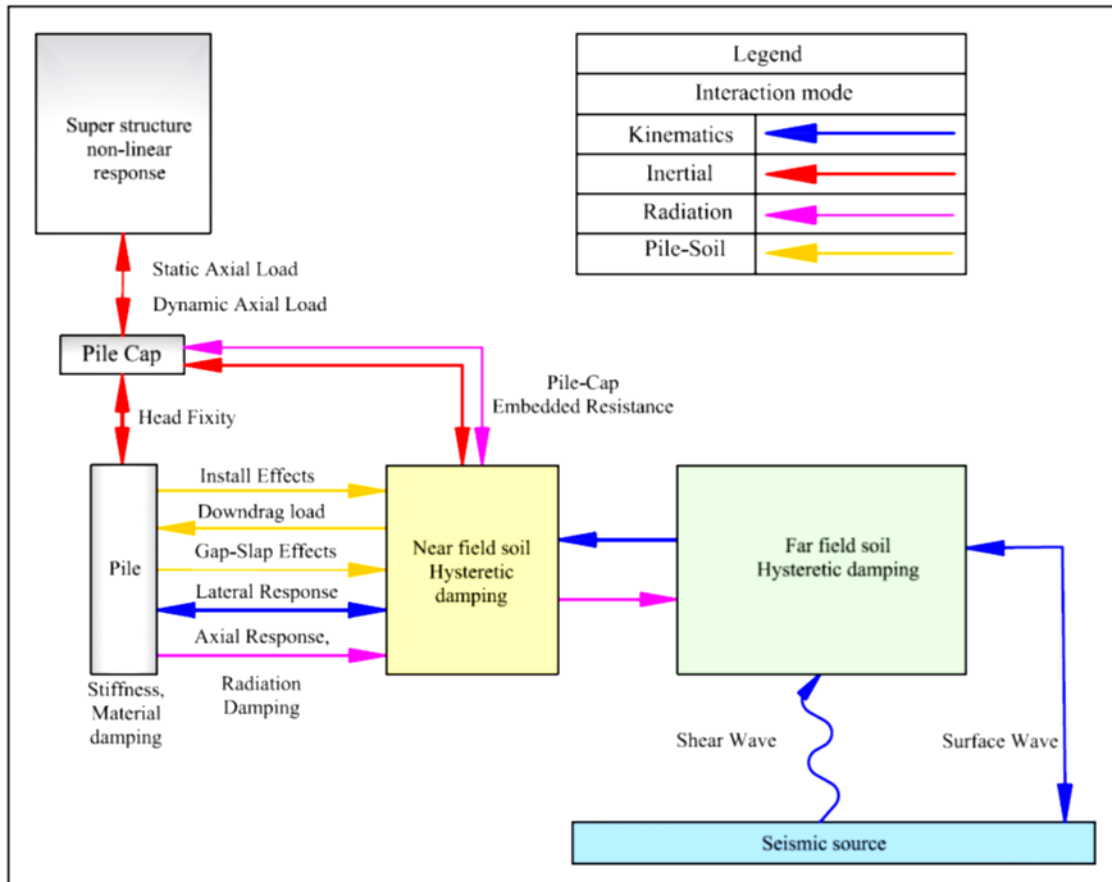
Figure 1-3 Single Pile Seismic Response Modes, (Meymand, 1998)

The complexity of SSPSI is illustrated by the high degree of system coupling between the system components and the interaction modes. Another level of complexity can be added by the seismic response of piles installed in a group system. In systems that have a robust non-linear response, a fully coupled analysis approach may be preferable. Such an analysis technique can evaluate how the development of non-linearity in one component of the system affects the demands on another, which can possibly contribute to a decent and economical design practice. Such design practice is in contrast with the commonly used, so-called dynamic sub-structuring methods. These methods are discussed in detail in Chapters 2 and 3. They can be described as simplified methods to avoid fully coupled analysis of nonlinear SSI. The empirical equation of motion is adopted as the kinematic formula for the interaction analysis of the pile–soil–structure system in simulating all SSI problems addressed in this study.

1.3. Needs and Objectives of the Research

A considerable number of studies are conducted on the failure of pile-supported structures exposed to earthquakes and SSPSI effects. Many of these cases are in liquefiable cohesionless soils, but the potential for detrimental performance of pile-supported structures embedded in soft sensitive clay soils is of major concern as well. The experimental empirical cases in the literature supply meaningful qualitative information concerning SSPSI effects, but the shortage of such data hinders the progress of the practice. To fill this gap and investigate SSPSI problems, researchers have used an arsenal of in-situ and laboratory test processes.

These empirical methods concentrate on separate parts of SSPSI, with variable degrees of accuracy and accomplishment. Likewise, the different analytical approaches developed commonly have uncoupled response from the entire system. These methods that are regarded as sub-structuring tools are created as a result of the limitation of computing capability and artificial impediment between geotechnical and structural analysis. Consequently, phase one of this thesis concerns the transfer from the physical shaking table test to the numerical test. By address the association between physical and numerical tests, a sophisticated methodology of scaling, calibration and validation for SSI problems is developed. Such a methodology can contribute to new reliable and accurate analysis practice. The lack of data in the literature can be filled, enabling researchers to validate their results. To achieve precise transformation results, criteria of three soil constitutive models are applied in addition to the package of proceedings to control the desired output of the analysis process, for instance, the scaling and validation methodology and its scaling factors and parameters. Mohr–Coulomb, Drucker–Prager and Cam–Clay failure criteria are applied in these simulation processes. The Cam–Clay model is adopted in the next two phases of the research given its compatibility with dynamic loading conditions, especially for seismic loading, concurrently with the analysis principles mentioned earlier.

Seismic codes (Eurocode 8 and ASCE in this study) do not specify many significant characteristics of (SSPSI) instead; the researcher has adopted a simplified and non-coding analysis approaches for that purpose. The nonlinearity of the analysis, the degradation of resistance, the effects of choosing the ground motions and their frequency content, the impact of applied dynamic load and the effects of pile group are important aspects that have been ignored or simplified in seismic codes. Identification of sensitive soft clay soil class also include unclear instructions. To reduce the risky consequences of identifying and

applying the aforementioned aspects, coding them is essential, demanded and necessary. The provisions of the seismic codes for nonlinear seismic soil–structure analysis must be reviewed and upgraded to include the characteristics mentioned above in certain analysis conditions and correct approach of application. In addition to the aforementioned problems, many critical problems concerning seismic SSI analysis and design have not sufficiently addressed in Eurocode 8 and ASCE provision. Examples are the coupled nonlinear dynamic response of pile groups and superstructure and the performance, behaviour and integrity of these piles. Codes disregard the essential characteristics of SSPSI listed above, including nonlinearity, degradation of resistance, frequency dependence, dynamic load distribution and pile group effects. Simplified and non-coding analysis methods are used instead. The effect and identification of soil class F in Eurocode 8 and ASCE follow vague instructions. Consequently, the decision mostly depends on the experience and deduction of the personnel concerned. To minimize the hazardous consequences of making the wrong decisions and to obtain a clear vision and a reliable solution for researchers, designers, analysers and people who are not experts in the geotechnical area, these problems should be coded. The following three critical issues are addressed in this thesis.

- The minimum thickness of sensitive clay to meet class F soil class code condition
- The minimum thickness of sand layer that cut off the continuity of sensitive clay layer which meets class F soil class code condition
- The effect of the natural period of structure (frequency dependence)

All these SSPSI aspects are covered in phase two of this study. The probability of extreme events such as an earthquake, fire, blast and floods occurring during the lifetime of a structure is very low as evidenced by the literature. However, these events can cause severe damage to the structures as well as human life. Given the grave consequences regarding occupant and structural safety, accurate analysis of structures exposed to these events is required. Some of these events may occur consequently or subsequently, for instance, a fire may occur after or before the occurrence of an earthquake, that is, PEF and post-fire earthquake. The effect of flood may also take place prior or after the earthquake event. In these instances, the structure is subjected to a multi-hazard loading scenario. The significance of multi-hazard events which are reasonably likely to occur but have been the theme of relatively little research in the available literature is highlighted in phase three of the thesis. The multi-hazard problem aspects of PEF and the influences of the analysis condition of whether to consider or not the effect of SSI on structural behaviour during and after a multi-hazard event are also covered in this phase.

In most design codes, the structures exposed to multi-hazard events such as earthquake and fire are analysed and designed separately. Structures subjected to an event experience partial damage, and the subsequent occurrence of another event may lead to structural collapse. Most available analysis procedures and design codes do not address the association between the two hazards. Thus, the design of structures based on existing standards may develop high risk of structural failure. A suitable method of analysis is required to investigate the behaviour of the structures exposed to a sequential hazard. In this study, PEF multi-hazard analysis approach is developed, and the analysis is performed to study the nonlinear behaviour of a structure with and without considering the effect of SSI.

Traditionally, in the multi-hazard analysis process, the effect of earthquake on structure is studied either using approximate methods or ignoring/disregarding the effect of SSI. Approximate analysis methods, for instance, pushover analysis, may not induce proper plastic damage to the structure. However, in most of the major earthquake events, the structure undergoes plastic deformation. Owing to this unrealistic analysis methodology, many researchers demonstrated that the influence of earthquake on the fire resistance of a structure is either negligible or minimal, and studies that deal with PEF events are lacking. This phase aims to bridge this gap and mitigate the effect of the current risk analysis and design approach. Multi-hazard time history analyses are developed for PEF circumstance which can induce the effect of SSI and the damage due to earthquake motion for subsequent thermal analysis.

With this background and several research needs concerning SSPSI, the following objectives are identified as manageable by time history finite element analysis using Abaqus software. These objectives constitute the focus of the contributions of the thesis. The three phases of this thesis are listed along with their corresponding contribution below.

❖ *Phase I: Numerical analysis of shaking table test*

- Non-linear elastoplastic numerical simulation of a shaking table test of dynamic soil–pile–structure interactions in soft clay during strong shaking: Three soil failure criteria are used to simulate the soil constitutive models, i.e. Mohr–Coulomb model, Drucker–Prager model, Cam–Clay model, with the target of addressing which criteria are appropriate to simulate the soil and develop an accurate seismic SSI model.

- A novel methodology for scaling, calibrating and validating the seismic SSI problems by using the association between scaled physical and full-scale numerical

tests: A correct scale model is developed, and the validation of full-scale numerical results against scaled physical results is accomplished by employing the developed scaling method.

❖ *Phase II: Effect of soil class in Eurocode 8 and ASCE*

- Evaluate the minimum thickness of sensitive clay soil to meet class *F* soil class code condition.
- Evaluate the minimum thickness of sand soil layer that can cut off the continuity of class *F* sensitive clay layer, causing different soil profile classifications.
- Develop the time history ground motion input data for non-linear elastoplastic dynamic analysis as well as examine the effect of the natural period of the system.
- Examine the effect of seismic SSI on the structural behaviour of high-rise buildings founded on soft clay.

❖ *Phase III: Multi-hazard analysis*

- Develop a methodology for multi-hazard analysis that incorporate the degradation of material resistance due to applying the first hazard and SSI effects.
- Conduct PEF multi-hazard analysis for multi-storey buildings, including the impact of the SSI, for soft clay soil.

1.3.1. Numerical Analysis of Shaking Table Test

Many studies on the failure of pile-supported structures exposed to earthquakes are available, but fundamental understanding of the mechanism of the pile response as well as the pile performance during seismic excitation remains lacking. With a flexible wall barrel, shaking table test is a suitable approach for investigating pile behaviour during an earthquake. Cost, time and difficulties in identifying soil properties accurately in physical models, in addition to the effects of test conditions, have led the current research to replace the physical test with numerical simulation. Moreover, many researchers have experienced difficulties validating their numerical models and have found lack of available information in the literature. Thus, developing a practical scaling and validation approach will extend the SSI database and promote the validation opportunities for studies on pile performance at different levels of excitations. This study provides an insight into a set of SSI problems and proposes a procedure for calibration of the advanced SSI analysis. A framework is performed for scaling and validating using the association between the physical shaking

table test and the numerical simulation of the transformed shaking table test of a model pile–foundation superstructure on soft clay to full-scale non-linear numerical test.

A suitable scaling procedure and a variety of soil constitutive models are used to develop an approach that allows observation of the inherent dynamic and non-linear nature of SSI behaviour. Three-dimensional, non-linear dynamic response and elastoplastic analysis are included in the simulation through the development of finite element analysis (FEA) using ABAQUS software. The inertial, kinematic and damping interaction components of the response are also examined. The gap-slap mechanism between soil and pile is a critical aspect of the model. The results are validated using physical test results.

1.3.2. Soil Constitutive Models and Soil Model Parameters

To incorporate a sufficiently precise and accurate transfer of physical test to the numerical model, three soil failure criteria are employed to simulate the soil constitutive models of the numerical shaking table test. Mohr–Coulomb, Drucker–Prager and Cam-Clay models are used for simulating the elastoplastic response and the subsequent constitutive relationship of the clay soil model. To come up with the soil constitutive model that can represent the clay soil model appropriately for simulating non-linear seismic SSI problem, all simulation aspects and relevant soil composition which can be used to address and meet the dynamic characteristics have been described clearly for these three criteria. In doing so, a reasonable decision-making process of selecting the best-applied criteria is achieved.

1.3.3. Development of Scaling and Validation Methodology

Pile performance in clay soil subjected to earthquake loading conditions currently has no sound validation or calibration methods or guidelines of available numerical methods developed for SSPSI problems. Centrifuge and shaking table model tests are used to supplement the field case histories with the data obtained under controlled conditions. Developing a scaling and validation method according to numerical guidelines described in the numerical simulation part and defining a correct link between the full-scale numerical analysis and scaled physical test solve the problem of the limitations in the SSPSI database.

Complicated and multifaceted systems can be simulated within a set of controlled variables and conditions using scale models. Scale modelling allows a user to understand the relationship between the corresponding behaviour of a prototype and the scale model and produce a scale model that can replicate the scaled parameter of the corresponding prototype. Therefore, employing the power of a composite scaling method used for the transformation of the physical shaking table test to numerical analysis, the actual size model

can be analysed. The results of this simulation can be scaled down for comparison to the original physical shaking table for validation. A framework for this methodology is thus developed in this study to show how to use the transformed numerical shaking table to validate the results. The framework can be followed by researchers who intend to validate their SSSI findings.

1.4. SSI and Effect of Soil Type: Examination According to Code Provision

Seismic SSI problem is a complicated area of study. Geotechnical and structural engineers have to be involved in the process of design and analysis. In practice, the majority of the analysis and design team members who deal with the issue are usually structural engineers. In some cases, they try to avoid whenever possible any specific provisions in seismic codes that impose SSI demands with particular analysis or when the available site geotechnical data are insufficient. By simplifying the problems or ignoring the effect of SSI, the decision of choosing the sites class are not always on the safe side. Hidden characteristics in soil and time history motions can drive the output towards a perilous direction if the effects are not detected by anybody who is not expert in these two areas before application. Even experts may be unable to identify the error in the results after implementation.

In this thesis, the effects of SSI on design and analysis procedures and the provisions for pile and structure performance analysis of high-rise building resting on clay soil subjected to a seismic load are examined with respect to Eurocode8 and ASCE. Both codes include simplified approaches to SSI analysis, but they recommend that specific dynamic analysis for structures resting on soft soils subject to intense levels of shaking is essential. In addition to the objective mentioned above, the influence and identification of soil class according to Eurocode 8 and ASCE are addressed.

1.4.1. Analysis of Pile and Structure Performance: According to Seismic Code Provision

Seismic code provisions do not sufficiently address the coupled non-linear dynamic response of pile groups and superstructure. Instead, approximate approaches for extending static and single pile analyses to this complex problem are used. Furthermore, codes disregard essential characteristics of SSPSI, including non-linearity, degradation of resistance, frequency dependence, dynamic load distribution and pile group effects. Nonetheless, pile performance, behaviour, and integrity can be evaluated by simplified and non-coding analysis methods for seismic analysis purposes.

For circumstances wherein the piles' system contribute largely to lateral stiffness (i.e. soft soils), the factors of single-pile stiffness determined by field tests or numerical analysis have

unconservative and insufficient details. Therefore, the provisions recommend computing the stiffness factors to calculate the stiffness of the pile group without reduction factors. The procedure should base on the strain levels expected in the soil response to reduce the effect of non-linearity limitation. Thus, this part covers all these aspects to deliver a clear answer and solution for aforementioned significant issues. Vague instructions leads to irrational and, consequently, hazardous input data and output. Two of the seismic code guidelines, i.e. Eurocode8 and ASCE codes, are examined to determine the effect of SSI on design and analysis procedure and provisions for pile performance analysis approach of the buildings resting on clay soil subjected to a seismic load.

1.4.1.1. Effect of Soil Class According to Eurocode 8 and ASCE

Based on the site soil properties for the analysis and design purposes, codes such as Eurocode 8 and ASCE classify sites as site class A, B, C, D, E or F. Choosing a site class for a particular circumstance depend on several soil criteria, such as shear wave velocity $\bar{V}_s$ (for upper 30 m), averaged SPT resistance or blow counts $(\bar{N} \ or \ \bar{N}_{cb})$ and undrained shear strength $\bar{S}_u$ for fine-grained soil once the measurement of undrained shear strength is available. These site classes that vary from A for hard rock soil type to F for sensitive soft clay soils require site response analysis following Section 21.1 in ASCE code or Section 1.2.3 in Eurocode 8.

Site class F is given to soft clay soils that can strongly amplify long-period ground motions. Codes impose several characteristics and condition to classify the effect of site class F in analysis procedure. Section 20.3.1. ASCE or Section 1.2.3 in Eurocode 8 classify site class of soil as class F if one of the following four conditions is satisfied.

1. Soil vulnerable to potential failure or collapse under seismic loadings, such as liquefiable soils quicksand, *highly sensitive clays* and collapsible weakly cemented soils.
2. Peats and/or highly organic clays $[H > 10 \ ft. (3m)]$ of peats and/or highly organic clays where H is the thickness of the soil layer.
3. Very high plasticity clay $[H > 25 \ ft. (7.6 \ m) \ with \ PI > 75]$, where PI is the soil plasticity index.
4. Very thick, soft/medium stiff clays $[H > 120 \ ft. (37 \ m)]$ with $\bar{S}_u < 1000 \ psf \ (50 \ kPa)$.

The characteristics' definition of the first and fourth conditions has many ambiguities and problems, thus opening the door to personal interpretations that may lead to real mistakes. Therefore, the present study attempts to specify clay soil characteristics concerning these two parts and code these characteristics. Consequently, the decision is based on code specification rather than on the opinion of engineers.

1.4.1.2. Minimum Thickness of Sensitive Clay to Meet Class *F* Code Condition

Codes specify that soils vulnerable to potential failure under seismic loadings, such as highly sensitive clays fall under site class *F* classification (Section 20.3.1, ASCE code). The question is how thick is the layer of this soil type in soil profile? What is the limitation to start considering the effect of site class *F*? No clear and specific answer for this particular circumstance is found in the standards. Codes mention the type of soil that falls on the site class *F* without reference to any thickness limitations, and here lies the confusion. To specify the minimum thickness of sensitive clay that is going to filter the passing ground motions and then meet class F code condition is the objective of this part.

1.4.1.3. Minimum Effective Thickness of Sand Layer for Continuity of Sensitive Clay Layer

One of the (Section 20.3.1) criteria to consider the soil class as *F* addressed in ASCE is soil which has a thick layer of a 37 m of soft, medium or stiff clay and has $S_u < 50$ kPa. This criterion is tricky due to soil profile arrangement conditions, such as the existing tiny layer of sand between several thicker layers of clay. That is, a thin layer of sand may cut the continuity of the clay layer that is supposed to meet the 37 m thickness condition according to code provisions. A much-debated question is whether the accumulative thickness of clay layers but not the individual layer that meet the code condition can be considered to meet the code condition for *F* class? Alternatively, the sand layer slices the profile and changes the code classification condition. This circumstance is examined meticulously in this section with the object of defining the minimum effective thickness of sand layer that may cut off the continuity of sensitive clay layer to be no longer classified as *F* code condition.

1.4.1.4. Earthquake Input Data for Non-Linear Elastoplastic Time History Analysis

Nonlinear elastoplastic time history analysis is one of the most complex problems in seismic interpretation. Many factors lead to this complexity, and most of them are given in phase one of the study. The most critical and tricky issue is how to choose and modify the time history input data to match the target spectrum of the desired analysis. That is, what time history input data of a real earthquake can be used to evaluate the response of the system.

The combined complex seismic SSI system requires a sophisticated methodology to investigate and modify suitable time histories to match the target objective of analysis.

The key objective of this section is to choose and collect real earthquake time histories using the arsenal of earthquake database such as PEER Ground Motion Database website and utilise them as initial seed time histories for scaling, modifying and matching procedures using SeismoSignal and SeismoMatch software to achieve a modified earthquake time history which can represent the potential site design earthquake. The guideline of this method is the design response spectrum approach developed on the basis of analysis condition and code specifications. The evaluation of these input data for use in nonlinear elastic-plastic analysis to fit the objectives and method of analysis remain a challenging concern. These modified or artificial ground motion input data must be developed in such a way that can demonstrate the original ground motion parameters adequately and, consequently, describe the nonlinear inelastic behaviour of the system correctly. The characteristics of delivered input data must be coherent with the target design spectrum parameters.

Conversely, ignoring the significance of some traits, such as frequency content, leads to deviations in parameters of the resulted time history. Most of the current seismic codes necessitate evaluating either the maximum considered earthquake (MCE) or/and the designed earthquake (DE). Buildings are typically designed according to the DE which is usually lower than MCE. In developing this methodology, the MCE is chosen as a critical situation. In this study, a method is developed to select and modify the ground motion for the purpose of nonlinear elastoplastic time history analysis.

1.5. Multi-Hazard Analysis

1.5.1. PEF Multi-Hazard Analysis

The probability of extreme events such as an earthquake, fire and blast occurring during the lifetime of a structure is very low (Miguel & Riera, 2013), but these events can cause serious damage to the structure as well as human life. Owing to the grave consequences regarding occupant and structural safety, an accurate analysis of structures exposed to these events is required. In such a scenario, the structure is subjected to a multi-hazard loading scenario. One of the critical multi-hazard events is PEF which is likely to occur but has been the subject of relatively little research in the available literature. In most design codes, the structures exposed to multi-hazards such as earthquake and then fire and vice versa are analysed and designed separately. Structures subjected to an earthquake or fire experience

partial damage, and the subsequent occurrence of a fire may lead to structural collapse. Most available analysis procedures and design codes do not address the association between the two hazards. Thus, the design of structures based on existing standards may result in high risk of structural failure. A suitable method of analysis is required to investigate the behaviour of the structures exposed to a sequential hazard. Therefore, multi-hazard analysis approach is developed which can infer the damage due to the first event. A methodology for multi-hazard analysis is developed to incorporate the degradation of material resistance due to the first hazard and SSI effects. The model accounts for the nonlinearity of material and structural behaviour.

1.6. Organization of The Thesis

The organization of the thesis chapters are demonstrated schematically in Figure 1-4.
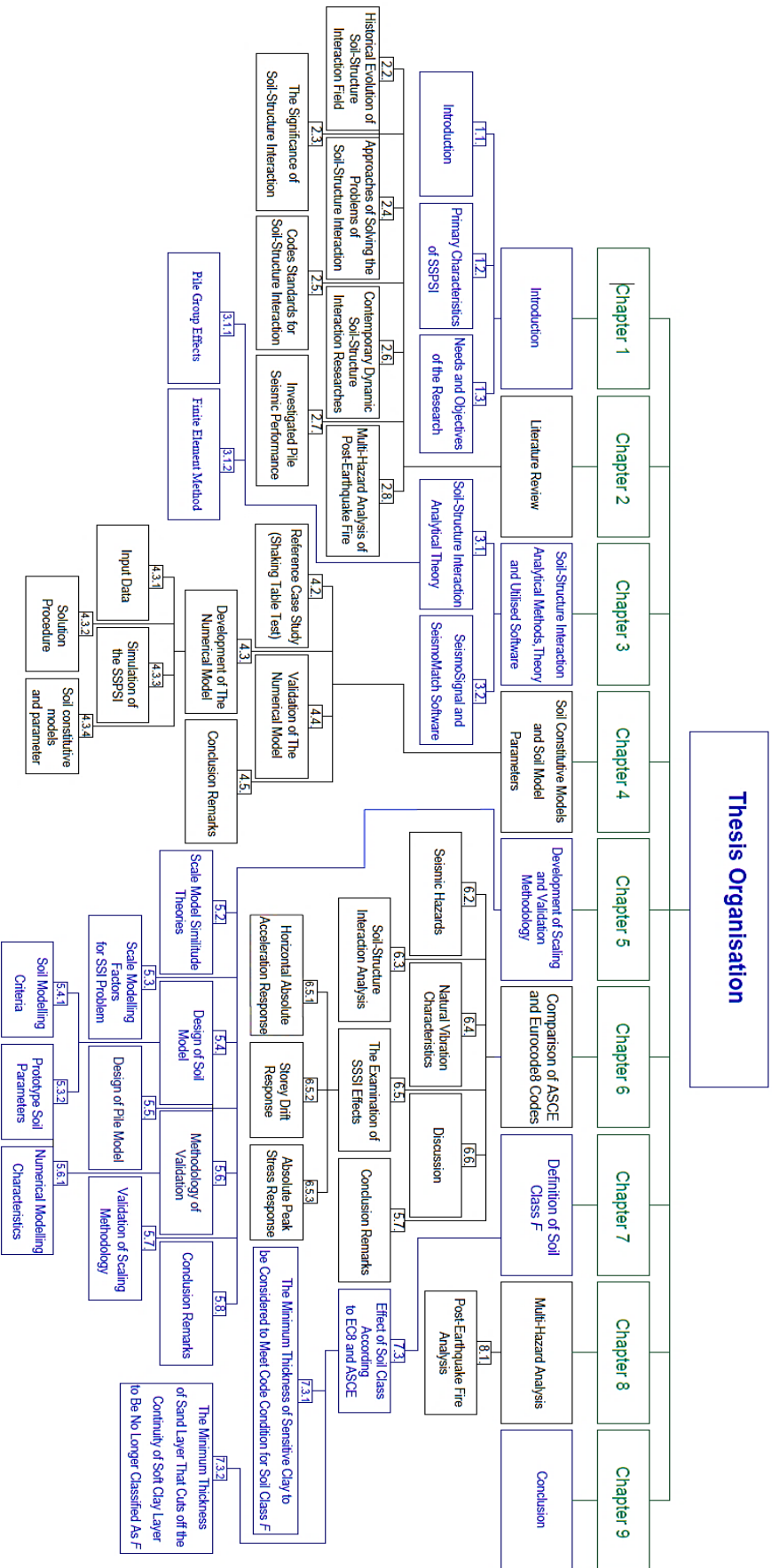
Figure 1-4 Schematic of the organization of the thesis chapters

Chapter 2: Literature Review

2.1. Introduction

Once a foundation system is subjected to the dynamic load, it can be concluded that structural and ground behaviour are dependent of each other and the procedure of dependency of the response of structural and soil has been designated as soil-structure interaction. SSI effects have often been disregarded to facilitate analyses and avoid intricacies (Mylonakis and Gazetas 2000). This practice is generally accepted as a conservative design hypothesis for spectral analysis because a flexible pile foundation lengthens the natural period of the structure and increases damping (Fan *et al.*, 1992). On the other hand, SSI effects are presumed advantageous during earthquake excitation because they increase the structural flexibility and natural period of the structure and consequently decrease structural base shear forces (Stone & Yokel, 1987).

(Kotronis, Tamagnini & Grange, 2013) described SSI as a contact issue wherein the surfaces of a foundation's structural element and surrounding soil's deposit are in contact. The stresses along this interface zone must be identified simultaneously, including the deformation and displacement along the same interface surface. SSI problems are categorised as a coupled contact issue once the interaction forces along the interface zone become functions of each other. However, the domain of SSI can be classified as being either static or dynamic according to the type of loading. Dynamic SSI (DSSI) represents the SSI effect for a foundation system subjected to machine operations or seismic events. According to (Wolf, 1985) and (Jaya & Prasad, 2001), DSSI can be interpreted by identifying and contrasting the three aspects in which soil and structures influence structural dynamic behaviour. The free surface motion of soil layer(s) lying above the base bedrock is distinctive from that at the bedrock. The magnitude of the amplification effect depends on the frequency content the motion passed through the media.

Over the past few decades, severe earthquakes have occurred in densely populated regions, often associated with significant damage even for structures built according to contemporary design codes. In particular, the 1906 San Francisco earthquake, 1964 Niigata earthquake, 1964 Alaska earthquake, 1971 San Fernando earthquake, 1985 Mexico City earthquake, 1989 Loma Prieta earthquake, 1991 Costa Rica earthquake, 1992 Cape Mendocino earthquake, 1994 Northridge earthquakes in California, 1995

Kobe earthquake in Japan, 2009 L'Aquila earthquake, 2011 Lorca earthquake in Spain and 2012 Emilia Romagna earthquake in Italy, caused remarkable destruction on the structures. Such phenomena showed that these buildings were seismically vulnerable due to the deficiency of previous seismic codes and provisions (Rodrigues *et al.*, 2013), weak criteria of construction because of negligence to local detailing and failures in quality control with high deviation in material properties (Sorace, 2012). The effect of DSSI has been diversely researched. (Roesset, 2013) and (Kausel, 2010) provided a summary review of several important developments that paved the way for the current state of the research. (Wolf, 1985), (Wolf & Hall, 1988) and (Wolf, 1995) contributed continuously to the DSSI field. However, researchers lacked consensus on the consequences of the DSSI.

(Gazetas & Mylonakis, 2001) characterised this ambiguous nature of past SSI research by presenting a crucial assessment of the existing vision of structural engineers, as stated in seismic codes. In the codes, the effects of DSSI are always presumed advantageous for the seismic design forces. (Newmark & Hall, 1972) suggested approximate relationships of ductility strength reduction factors by employing equal displacement and energy rules for stiff and flexible structural systems. Based on the relationships mentioned above, the strength reduction factor is decreased due to the DSSI effect lengthening in the time period for a particular ductility. This scenario substantiates the argument that SSI is advantageous. Although conventional, this study could not stand well against similar analysis conducted for structures founded on soft soil by (Miranda & Bertero, 1994). The study revealed that the strength reduction factor is affected mainly by the maximum tolerable demand for ductility displacement, system period and site soil conditions. Expressions of strength reduction factors are simplified to evaluate the inelastic design spectrums according to the principal influence parameters. (Gazetas & Mylonakis, 2001) similarly observed that employing ductility terms is indeed controversial in terms of demand and capacity.

2.2. Historical Evolution of Soil–Structure Interaction Field

The SSI components, i.e. kinematic and inertial interactions, were originally developed by (Seed & Whitman, 1970). (Roesset, 2013) and (Kausel, 2010) reviewed the early-stage development in the SSI field. They reviewed the two main methods of SSI analysis: the direct and substructure approaches. They also reviewed several early studies on dynamic foundation stiffness, effects of stratified deposits and effect of pile embedment

and pile group which are developed by (Reissner and Bycroft; Parmelle; Veletsos and Wei; Luco and Westman; and Novak). (Kausel, 2010) submitted a historical revision of the development of SSI, set up from the fundamental approach which is commonly termed as "Green's function", this approach was developed by mathematicians and scientists in early 19th Century and has been applied to most contemporary approaches of finite element analysis. Another notable early contribution in the DSSI field reported by Kausel were the significant works of Housner (1954, 1957), Bycroft (1956, 1977), Newmark (1969, 1977), Luco, (1971, 1972, 1974, 1986), Prof. Nathan M. Veletsos (1971, 1974, 1975, 1977), Whitman (1973, 1977, 1978), Wong (1976, 1978, 1986) and many others researchers. In addition, Kausel himself initiated the development of the substructure approach to describe the SSI problems.

2.3. Significance of Soil–Structure Interaction

Ignoring the effects of considering the influence of SSI on the seismic structural response of a structure has been prevalent in seismic design practice. According to seismic design codes, a reduction factor of the general seismic coefficient on account of SSI is either accepted or disregarded. The conventional hypothesis is that considering the effects of SSI results in enhancing the flexibility of the structure/pile, lengthening the natural period and increasing the effective damping ratio of the structure/pile. These modifications reduce design base shear force. However, data from studies on several earthquake damaged sites indicated opposite consequences, thus confirming a that different hypothesis is needed (Meymand 1998).

(Badry & Satyam, 2017) developed the seismic SSI analysis for asymmetrical buildings of T, L and C (see Figure 2-1, Figure 2-2 and Figure 2-3) shapes and piled raft-supported buildings which experienced major damage during the Nepal earthquake on 25 April 2015 with 7.8 magnitude. Figure 2-1 show the simulations developed in C++ to model the DSSI system using finite element analysis. The study confirmed that the traditional hypothesis of SSI being always beneficial is not true for many structures and/or soil conditions. The destructive influences of SSI may also be intensified by the asymmetric geometry of the superstructure. This finding supports the idea of revising the past observations stated from previous research. However, numerous parameters may control the significance of considering SSI in structural design and influence their seismic response. Appropriate boundary conditions and other analysis aspects which are compatible to deliver accurate

results that are consistent with the objectives of the analysis must be considered. This point is one of the significant targets in the present study.
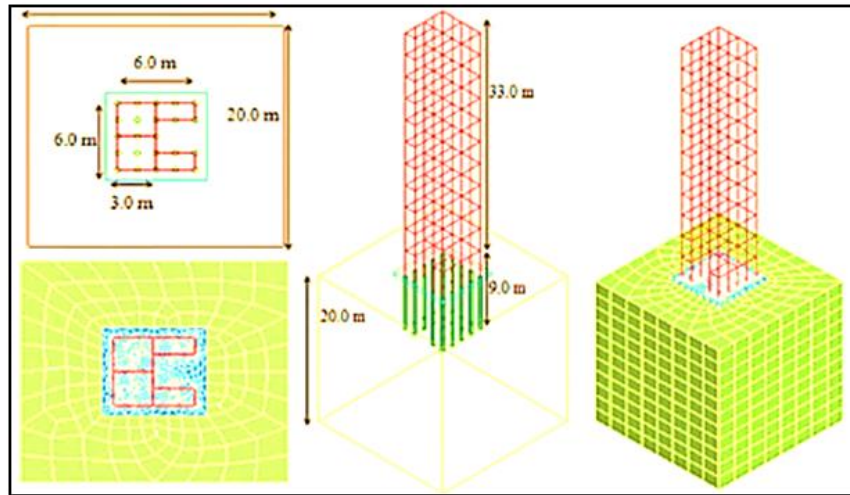
Figure 2-1 Finite Element Model (FEM) of C-shaped 11 Storey Building for DSSI Analysis (Badry & Satyam, 2017)
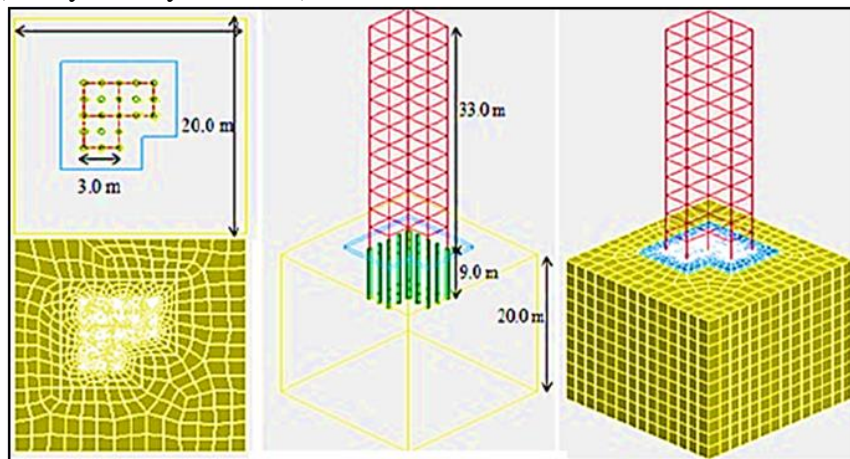
Figure 2-2 FEM of L-shaped 11 Storey Building for DSSI Analysis (Badry & Satyam, 2017)

(Nguyen, Fatahi & Hokmabadi, 2016) and (Van Nguyen, Fatahi & Hokmabadi, 2017) investigated the significance of the types and dimensions of a pile supporting intermediate-rise buildings in high-risk seismic areas (Figure 2-4). The types and dimensions may change the dynamic properties of the soil–pile–foundation system due SSI. Three-dimensional FEMs for a 15-storey moment-resisting frame for various sizes of end-bearing and embedded pile foundations were developed numerically.
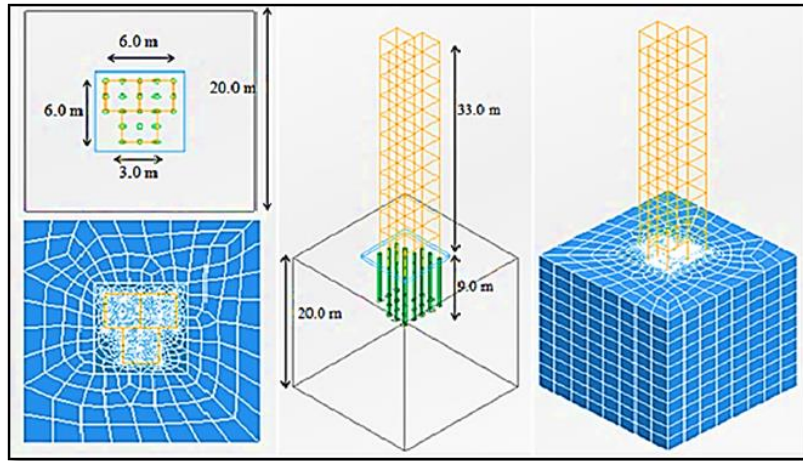
Figure 2-3 FEM of T-shaped 11 Storey Building for DSSI Analysis, (Badry & Satyam, 2017)
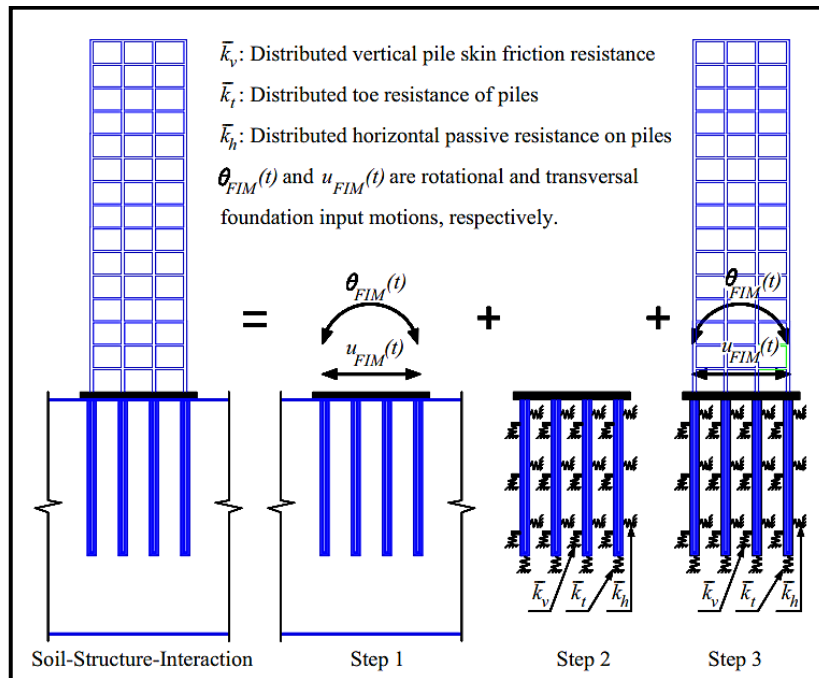
Figure 2-4 Substructure Method for Modelling the Soil–Pile–Structure Interaction (SPSI), (Van Nguyen, Fatahi & Hokmabadi, 2017)

Figure 2.4 and 2.5 show the adopted substructure approach. Step 1 is the evaluation of foundation input motion (FIM) using transfer functions, Step 2 is the evaluation of impedance functions and Step 3 is the analysis of structure on compliant base subjected to FIM. The findings of (Nguyen, Fatahi & Hokmabadi, 2016) support engineers' selection of the appropriate size and type of pile in which the structural seismic performance of buildings resting on soft soil is considered. The findings also help in optimizing the design of such buildings.

21

(Ciampolp & Pinto, 1995) stated that considering SSI in the inelastic response of bridge piers induces a reduction in structural ductility and results in a small increase in the displacement of the top structure. They identified two input parameters, namely, wave motion properties and structure slenderness. The former signifies the soil-to-structure stiffness contrast, whereas the latter is merely a geometrical property of the structure.
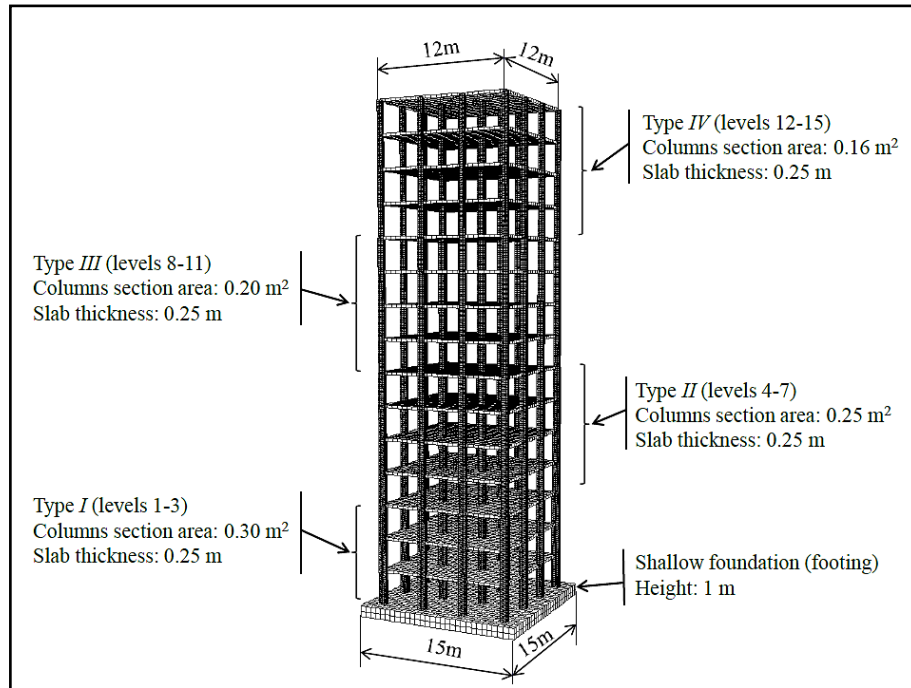
Figure 2-5 Designed Sections of 15 Storey MR Building Implemented in the Numerical Model, (Van Nguyen, Fatahi & Hokmabadi, 2017)

(Ghalibafian, Ventura & Foschi, 2008) also reached a similar conclusion by examining the effects of nonlinear SSI on the inelastic response of pile-supported bridge piers. Like other studies, the two aforementioned examples supported the conventional conviction of SSI being advantageous to the seismic response of structures. However, adopting a study with a precise condition of modelling reveals a different picture seeing that many studies already obtained more than halfway toward achieving a correct solution to the problem of SSSI . (De Carlo, Dolce & Liberatore, 2000) examined the effects of SSI on the seismic response of bridge piers subjected to EC8 response spectrum and other five artificial motions (Figure 2-6). The study concluded that ignoring the effects of SSI, particularly in situations of stiffer superstructures, may produce a substantial underestimation of curvature ductility requirements and lateral displacements. Moreover, the behaviour of flexible and slender structures can be substantially influenced by the rotational component at the base due to inertial forces interaction (Figure 2-7).

22
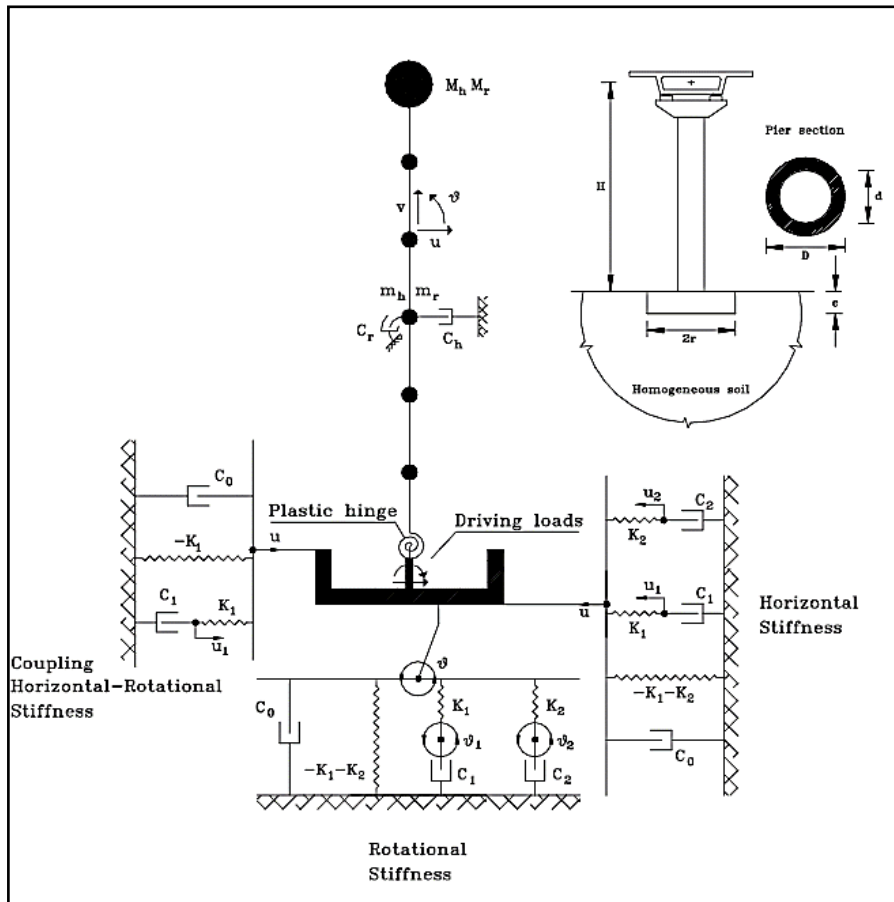
Figure 2-6 Model of Pier on a Cylindrical Foundation Embedded in Soil, (De Carlo, Dolce & Liberatore, 2000)
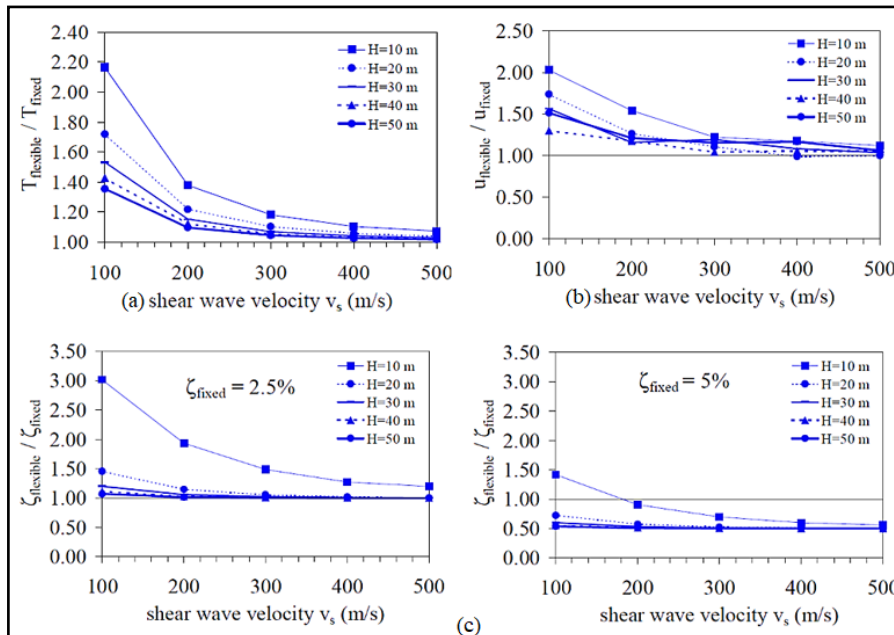
Figure 2-7 (a) Period Ratio, (b) Top Displacement Ratio, (c) Equivalent Damping Ratio, 2.5% and 5%, (Structure with Interaction or Fixed Base Structure), (De Carlo, Dolce & Liberatore, 2000)

(Mylonakis and Gazetas 2000) observed that this situation may cause displacement of a bridge deck from bearings situated at the pier top. The risk of differential settlement evolving due to soil flexibility (Figure 2-8) was observed by (Raychowdhury, 2011) for low-rise SMRF buildings.
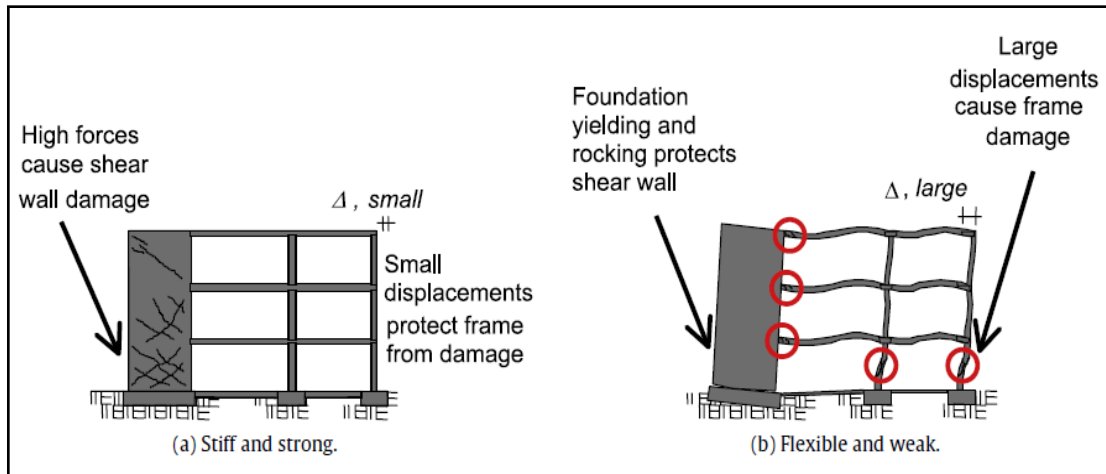
Figure 2-8 Effect of Foundation Flexibility on the Component Response of a Structure, (ATC, 1996)

Figure 2-9 shows that the study concentrated on modelling the nonlinear SSI behaviour using a beam on the nonlinear Winkler foundation (BNWF) method. Once nonlinear SSI is considered, the peak moment and peak shear at the base of the columns are reduced up to 60% and 30%, respectively. The displacement demands are also reduced significantly. Moreover, the study concluded that SSI must be considered critically for heavily loaded footings due to high inertial consequences; Developing a rational basis for seismic design, including SSI effects, is necessary.

(Sáez, Lopez-caballero & Modaressi-farahmand-razavi, 2013) examined the effect of inelastic DSSI on the response of moment-resisting frame structures. They performed a 2D FEM analysis. Two buildings resting on sandy soil in dry and fully saturated conditions were analysed (Figure 2-10). The study concluded that inelastic dynamic soil behaviour effects are more pronounced in the case of fully saturated sands. The effective stresses decrease due to pore water pressure, resulting in large soil deformations. However, the analysis of the results showed that the effect of DSSI on the dry soil case is highly erratic. The importance of considering SSI may vary according to site conditions.
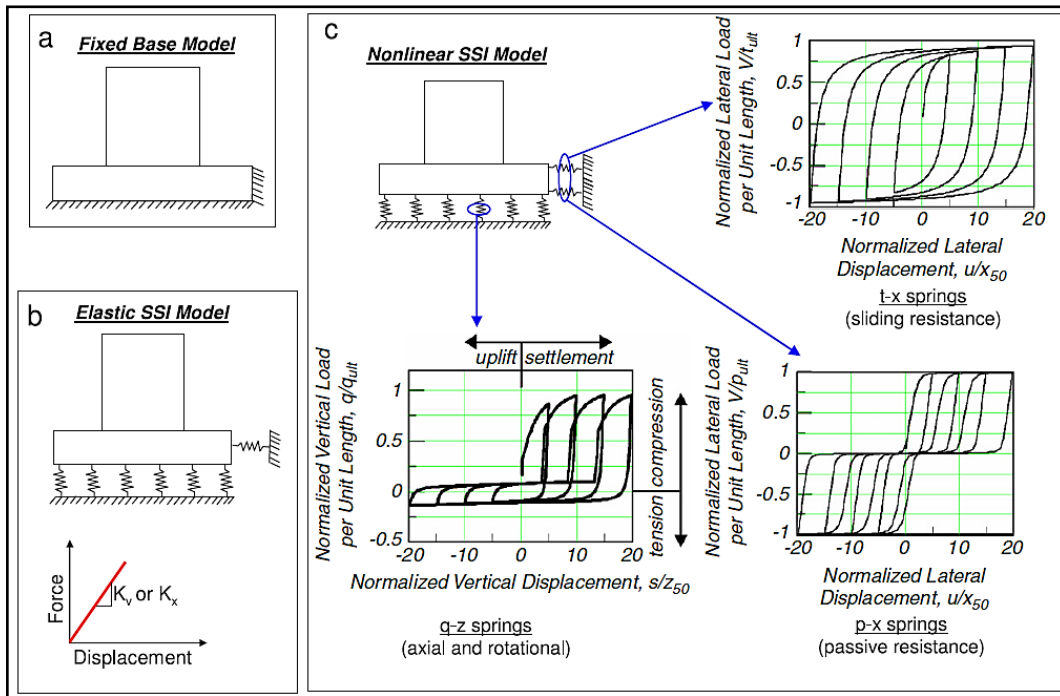
Figure 2-9 Different Base Conditions Considered: (a) Fixed Base, (b) Elastic Winkler-Based SSI Model, (c) Nonlinear Winkler-Based SSI Model, ((Harden & Hutchinson, 2009); (Raychowdhury and Hutchinson 2009))
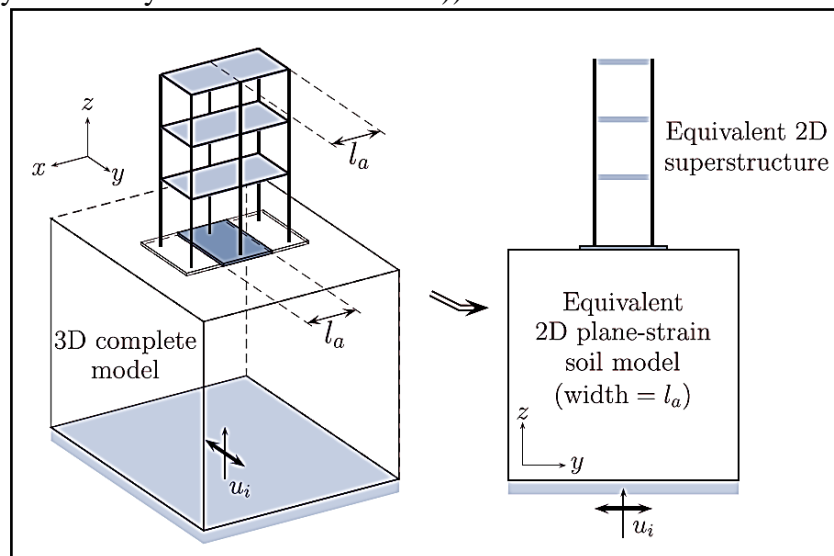
Figure 2-10 Typical Model of Regular Multi-Storey Building, (Sáez, Lopez-caballero & Modaressi-farahmand-razavi, 2013)

(Reza & Fatahi, 2014) developed an SSI model using the direct analysis method with FLAC 2D software to examine the behaviour of soil and structure during seismic loading (Figure 2-11 and Figure 2-12). Three mid-rise moment-resisting building frames comprising 5-, 10- and 15 storey buildings were nominated with three soil categories of shear wave velocities less than 600 m/s, signifying soil classes C, D and E according to Australian specifications. The aforementioned situations were analysed under two

different boundary conditions with and without SSI, namely, incorporating the soil model and not incorporating the soil model, respectively.
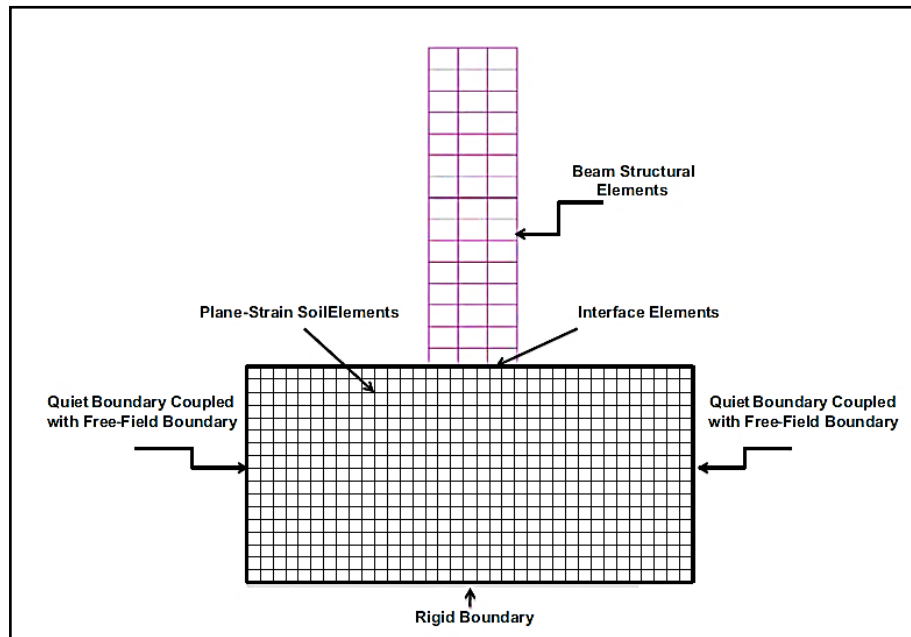
Figure 2-11 Components of the SSI Model, (Reza & Fatahi, 2014)
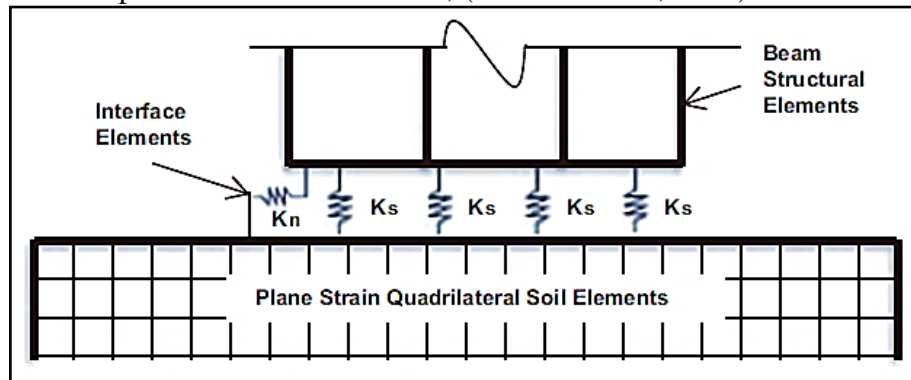
Figure 2-12 Interface Elements Including Normal and Shear Stiffness Springs, (Reza & Fatahi, 2014)

Figure 2-13 shows that considering the effects of SSI in seismic design is essential, especially in the case of structures resting on soft soils. The analyses ignored the effect of pile–foundation interaction and SPSI. Considering a fully nonlinear effect of SSPSI enables the examination of the mechanism of gap-slap concept and other DSSI components, such as kinematic and inertial interactions. The distance to the free field is a significant parameter which is noted in this analysis.
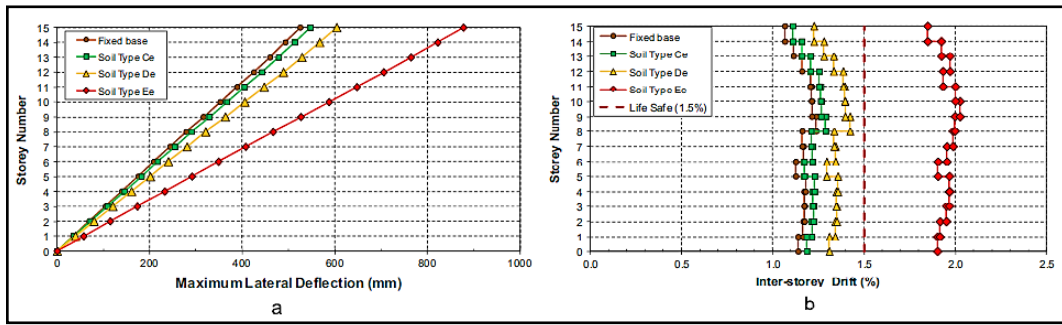
Figure 2-13 Average Results of Inelastic Dynamic Analyses of Model (15 Storey) for Two Cases of Fixed Base and Flexible Base Resting on Three Different Subsoils: (a) Lateral Deflections, (b) Inter-Storey Drifts, (Reza & Fatahi, 2014)

(Aydemir and Ekiz 2013) addressed the behaviour of multi-storey buildings under earthquake excitation considering SSI for the reinforced concrete of 1, 3, 6, 9, 12 and 15 storey buildings, corresponding to the aspect ratios (h/l) of 1/3, 1, 2, 3, 4 and 5, respectively. Figure 2-14 shows the five case studies, the buildings were designed according to the Turkish seismic design code (2007).
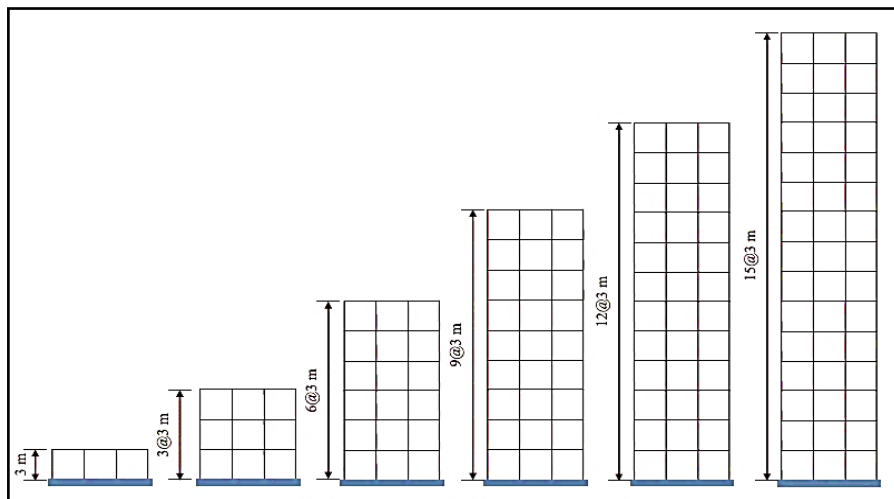
Figure 2-14 Geometry of the RC Frames Cases, (Aydemir and Ekiz 2013)

The analyses were performed in the time domain using incremental dynamic analysis. Figure 2-15 indicate that the strength reduction factors of the structure where the SSSI has been considered are smaller than design strength reduction factors for the same structure which is designed according to the current available seismic design codes. This scenario leads to a hazardous design condition and nonconservative design forces. Moreover, inelastic displacement ratios of fixed base and interacting cases are significantly different.
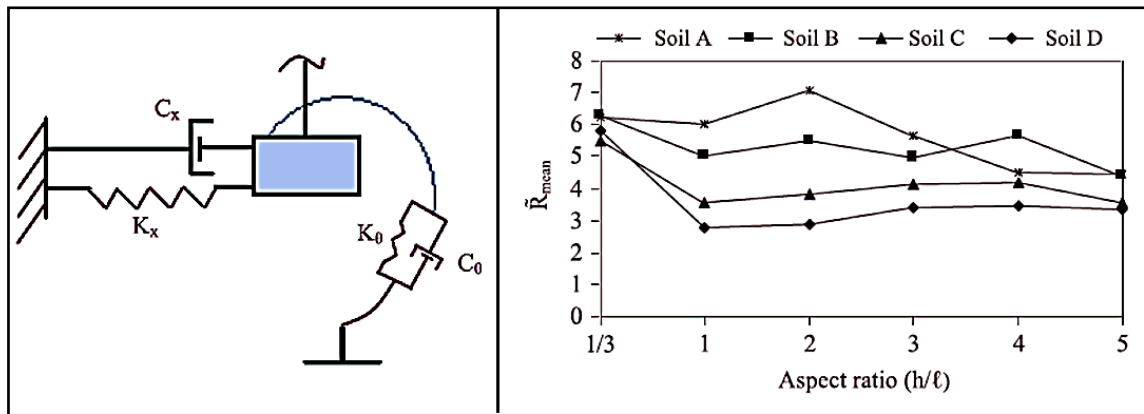
Figure 2-15 (a) Mathematical Model of Supports with SSI, (b) Variation of Mean Strength Reduction Factors of Interacting Case with Aspect Ratio for Different Soil Classes, (Aydemir and Ekiz 2013)

(Zdravković *et al.*, 2019) presented a combined in situ and FE modelling study in order to develop an enhanced design procedure for larger-diameter piles in overconsolidated glacial clays under monotonic lateral loading condition. A series of 3D FE models were performed before the field tests for the medium-scale pile testes using Imperial College Finite Element Program (ICFEP) (Potts & Zdravković, 2001), and employing modified Cam-clay as a constitutive soil model (see Figure 2.16). The target of places highlighting on the consistent interpretation of the soil data determined from the available field and laboratory information was the main aim of the study. Excellent agreement between the physical and numerical behaviour was accomplished for a range of pile-diameter geometries, indicating the precision of the numerical model and the suitability of the calibration process for the constitutive model (e.g., see Figure 2.17). The study revealed that developing advanced numerical modelling can facilitate the development of new soil response curves for utilizing in piles of design models founded in stiff clay and subjected to lateral load.

(Hassani, Bararnia & Ghodrati, 2018) broadened the examination of the range of effects of SSI to incorporate the consequences on the inelastic displacement ratios of structures which experience strength and stiffness degradation. Consequently, the significance of considering SSI in the inelastic design of structures is recognised. A comprehensive range of valid parameters of hysteresis models and SSI systems was studied by (Hassani, Bararnia & Ghodrati, 2018). Four various hysteretic models were designated to signify the response of the force displacement of the superstructure which were bilinear, modified Clough, stiffness degrading and strength-stiffness degrading.
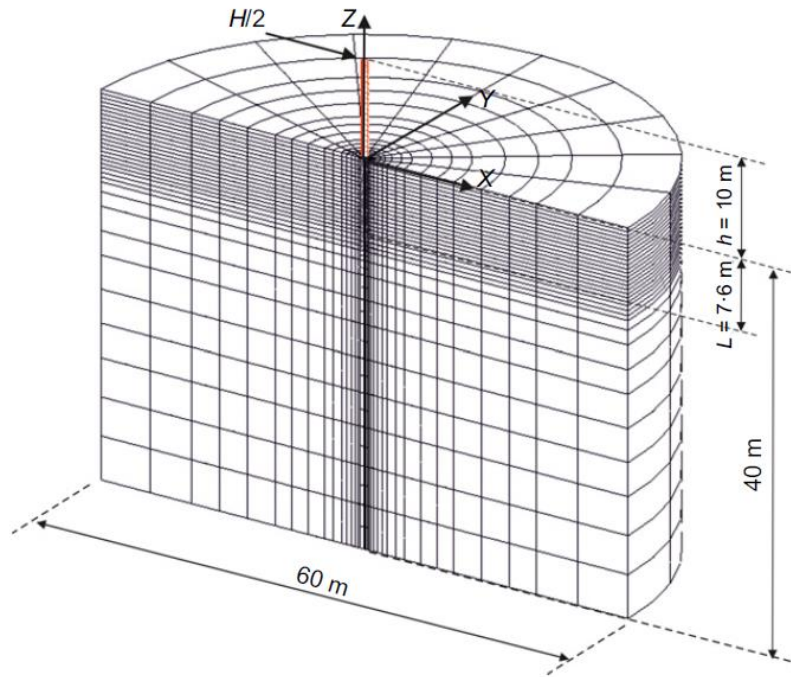
Figure 2-16 Example 3D FE Model , (Zdravković *et al.*, 2019)
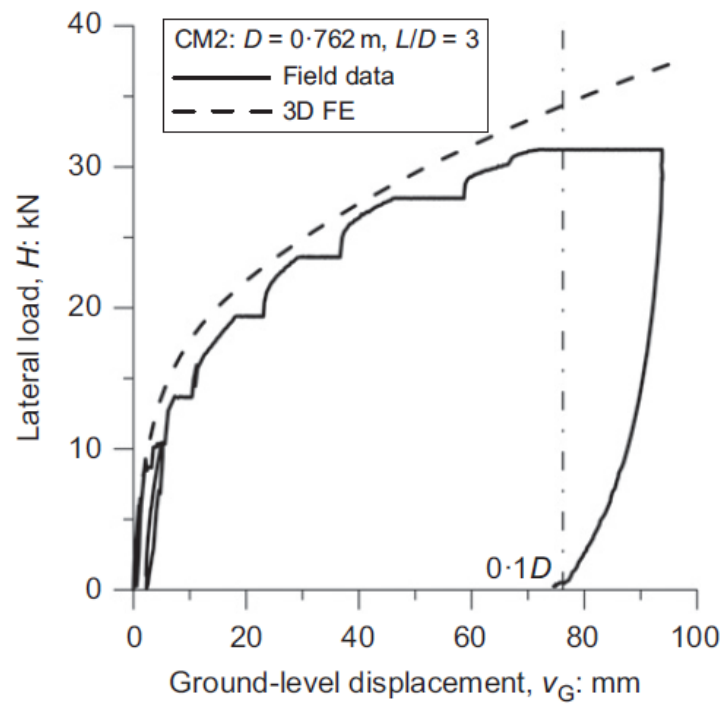
Figure 2-17 Load–Displacement Curve , Measured Vs 3D FE Analysis (Pile with 0.76 m Diam., Embedded Length of 2.3 m, and 10 mm Wall Thick., (Zdravković *et al.*, 2019)

The parametric statistical test was performed to observe the factors which may influence the nonlinear response of structures with a strength-stiffness degrading hysteretic model. The study identified that incorporating SSI resulted in increases in the inelastic displacement ratios, except for the structures with short period. Similarly, the soil–structure systems with stiffness degrading hysteresis model in short period range may experience more significant inelastic displacement in contrast to those in non-degraded soil–structure systems. In particular, the SSI substantially increases the intensity of inelastic displacement ratios of strength-stiffness degrading structures. In consideration of the massive capital required, the significance of accessibility in post-disaster circumstances and the level of hazards involved, incorporating DSSI in the design of bridges, dams, wind turbines and other important structures is essential. Given the inadequate SSI provision included in existing seismic codes, paucity of DSSI in the design of various structures is noted despite the substantial research in the field of DSSI. An accurate and efficient methodology of developing a DSSI model must consider the nonlinearity of soil and substructure appropriate boundary conditions which can simulate the real situation and free field conditions. The significance of choosing and modifying the input motion in such a way that can represent the actual situation in the site should also be taken into account. The development is achievable only with an efficient comprehension of different DSSI solution methods offered in the literature which are reviewed in the next section along with their strengths and weaknesses.

2.4. Approaches to Solving the Problems of Soil–Structure Interaction

Initial attempts to solve SSI problems were focused mainly on finding an analytical solution approach. (Kaynia & Kausel, 1991) presented a general formulation for the dynamic response analysis of piles and pile groups in a layered half-space media based on Green's functions. These functions were computed numerically using the integral transform method, accompanied by analytical solutions for the dynamic piles' response. These analytical derivations and extended formulation to cover the seismic analyses were described. (Gazetas & Stokoe, 1992) proved the reliability of impedance functions employed in (Gazetas, 1992) by performing a set of shaking table tests, in which Gazetas presented a set of algebraic formulas and dimensionless charts for computing the dynamic stiffness (k) and damping coefficients (C) of foundations with oscillation on/in half-space. Most of the possible modes of vibration, a realistic range of Poisson's ratios and a practically adequate range of oscillation frequencies were considered. Rigid bases with

embedded foundation models were adopted in the two studies aimed to advocate the application of the results obtained for the dynamic response of the foundation area. (Durante *et al.*, 2016) experimentally investigated the seismic SSI by performing a physically scaled shaking table model (Figure 2-18). The model consisted of an oscillator tied to a single or a group of piles embedded in two layers of soil deposit. Free and fixed head pile conditions were adopted in addition to different head pile head masses installed at the top of the SDOF model. The model was excited by three different input motions, namely, white noise, sine wave and real earthquake record. The inertial and kinematic bending moments and effects of oscillator mass and pile head conditions on soil–pile response were underlined (Figure 2-19).
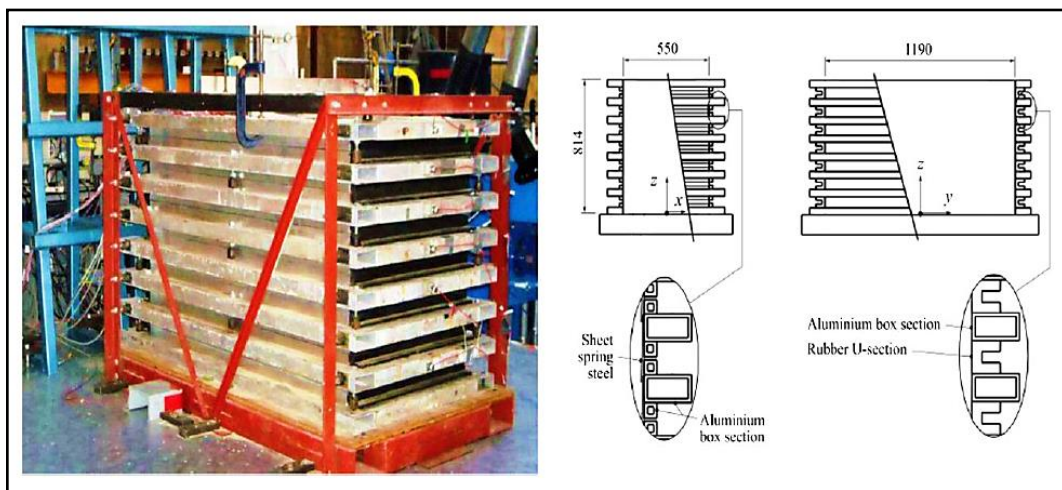
Figure 2-18 Equivalent Shear Beam Container of Bristol Laboratory, (Durante *et al.*, 2016)
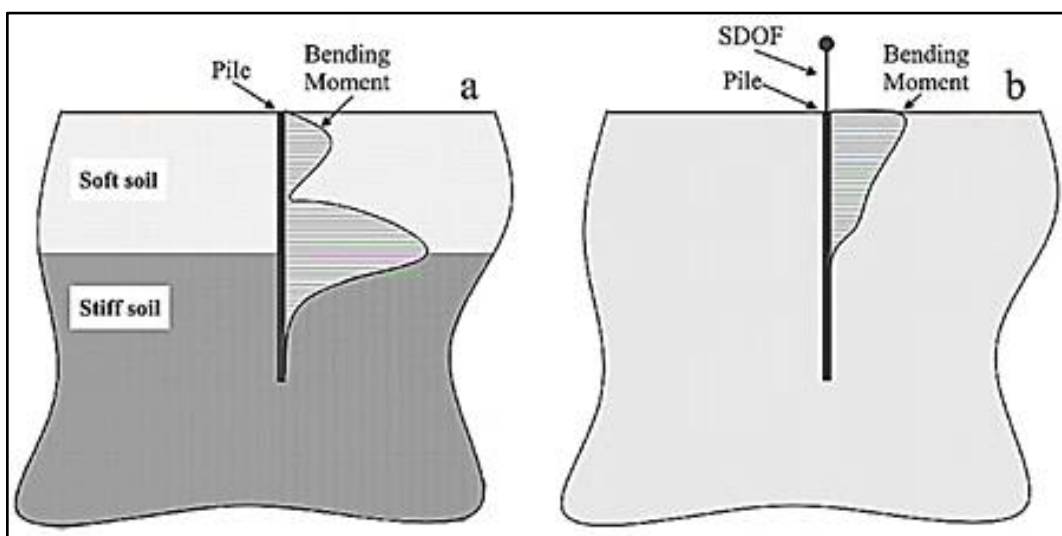
Figure 2-19 (a) Kinematic and (b) Inertial Bending Moments (Qualitative Patterns), (Durante *et al.*, 2016)

The study by (Durante *et al.*, 2016) concluded that the complicated SSPSI phenomenon can be adequately examined by testing models on a shaking table. Doing so offers insights into their behaviour, leading to simple yet reliable suggestions for analysis and design developments.

(Hussien *et al.*, 2016) performed a series of centrifuge tests analysing the dynamic responses of a single pile and pile group embedded in sand and subjected to a set of sinusoidal waves. The study indicated the relationship between the structural response and the frequency content of the input motion and observed both kinematic and inertial components. The distribution of pile bending moments in the pile group was a function of the pile location and the frequency of the excitation. Figure 2-20 shows that the internal piles experience the maximum kinematic bending moments, and the external piles experience inertial bending moments.
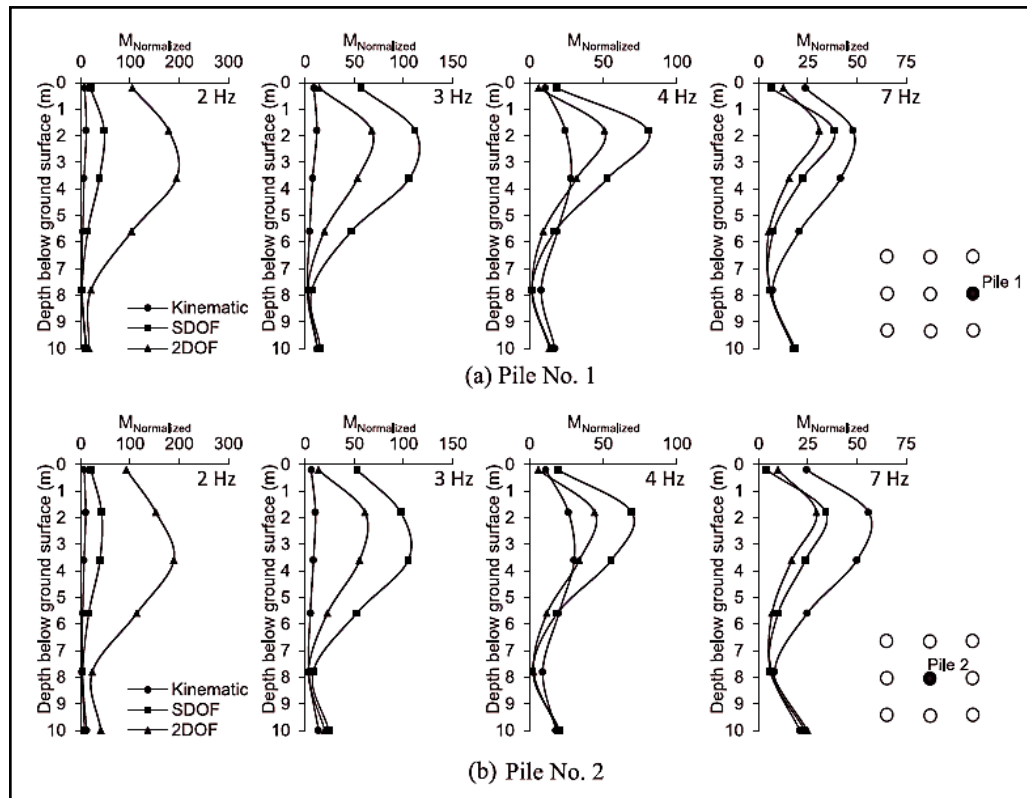
Figure 2-20 Distributions of Normalised Steady-State Bending Moments of Piles in the Group at different Hz: (a) Pile No. 1(external) , (b) Pile No. 2 (internal), (Hussien *et al.*, 2016)

(Martakis *et al.*, 2017) accomplished a series of dynamic centrifuge tests to examine the influences of soil properties and structural parameters on the SSI behaviour and thereby obtained an experimental dataset which might serve as a benchmark for engineering practice. Period lengthening was significantly correlated to the corresponding

superstructure-foundation stiffness (Figure 2-21). The study dealt with the small strain close to the linear range, and the test response indicated development of nonlinearity.

Most of the experimental attempts on SSI are either shaking table or dynamic centrifuge model tests. However, a small number of full-scale dynamic tests have been published. for instance, a portal frame railway bridge by (Zangeneh *et al.*, 2018). While these investigations were generally cumbersome and expensive, researchers were involved in developing practical and economic modelling strategies to analyse SSI effects. Adopting a realistic and accurate modelling method for developing DSSI model of structures resting on soft soil is one of the most challenging issues in the field of seismic design practice. (Far, 2019) comprehensively reviewed available modelling techniques and computation methods for DSSI analysis. The advantages and disadvantages of utilising the methods were compared and listed, with two examples illustrated in Figure 2.22. The review by Far (2019) proposed the most accurate and reliable modelling techniques for the DSSI analysis of structures resting on soft soil.
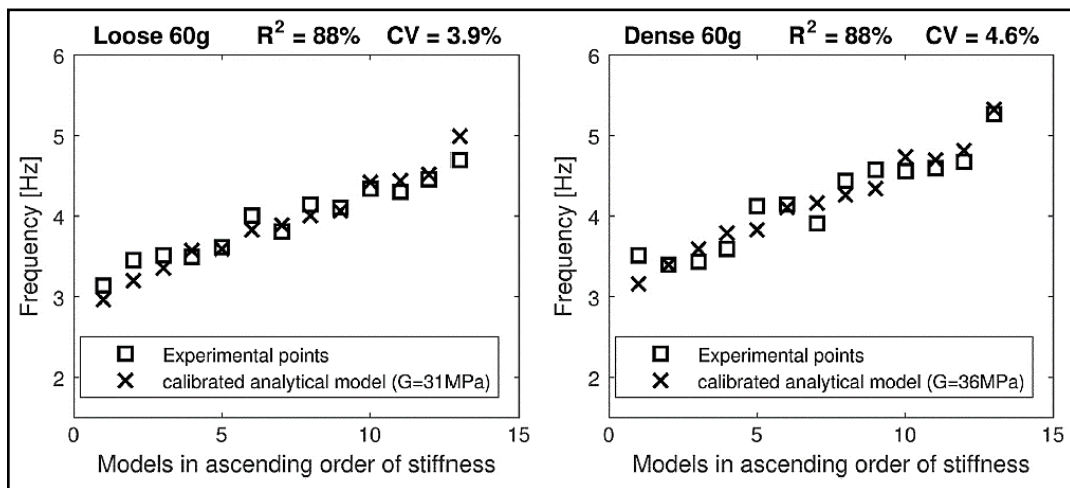
Figure 2-21 Analytical Fit to Experimentally Identified Frequencies, (Martakis *et al.*, 2017)

Employing the direct method of the numerical approach to achieve the aforementioned objective was highly recommended due to its adaptability and ability to deal with complicated geometries and arduous material properties. Nonlinear analyses are achievable in this approach. The review concluded that the fully nonlinear computation method is the most precise and realistic technique for the DSSI analysis of structures founded on soft soils. Figure 2-23 shows that the equivalent linear method is not valid and qualified and cannot sufficiently guarantee the safety and structural integrity of structures resting on soft soil.
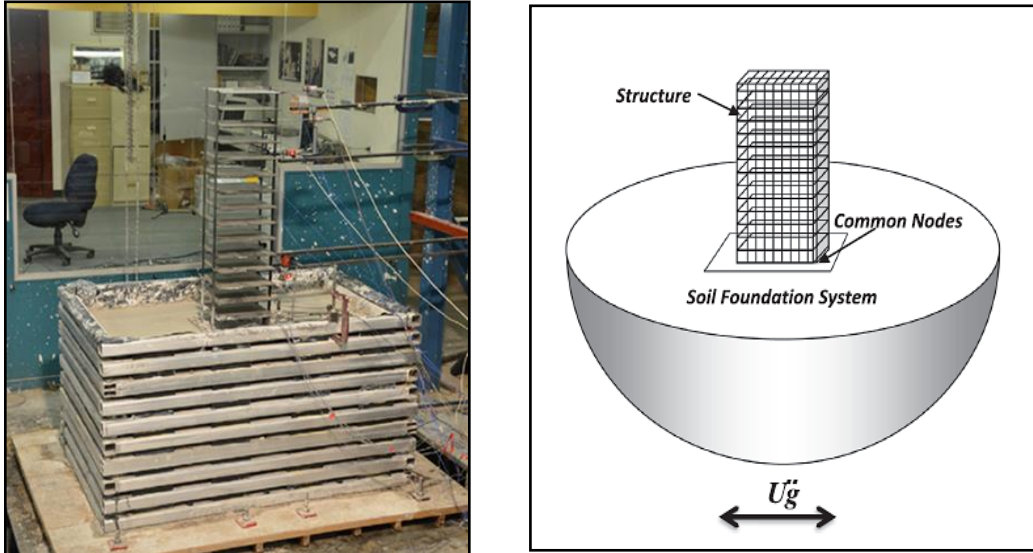
Figure 2-22 (a) Instruments of the Soil–Structure Model, (b) . Soil–Structure System in Direct Method, $\ddot{U}_g$ is the applied seismic load, (Far 2019)
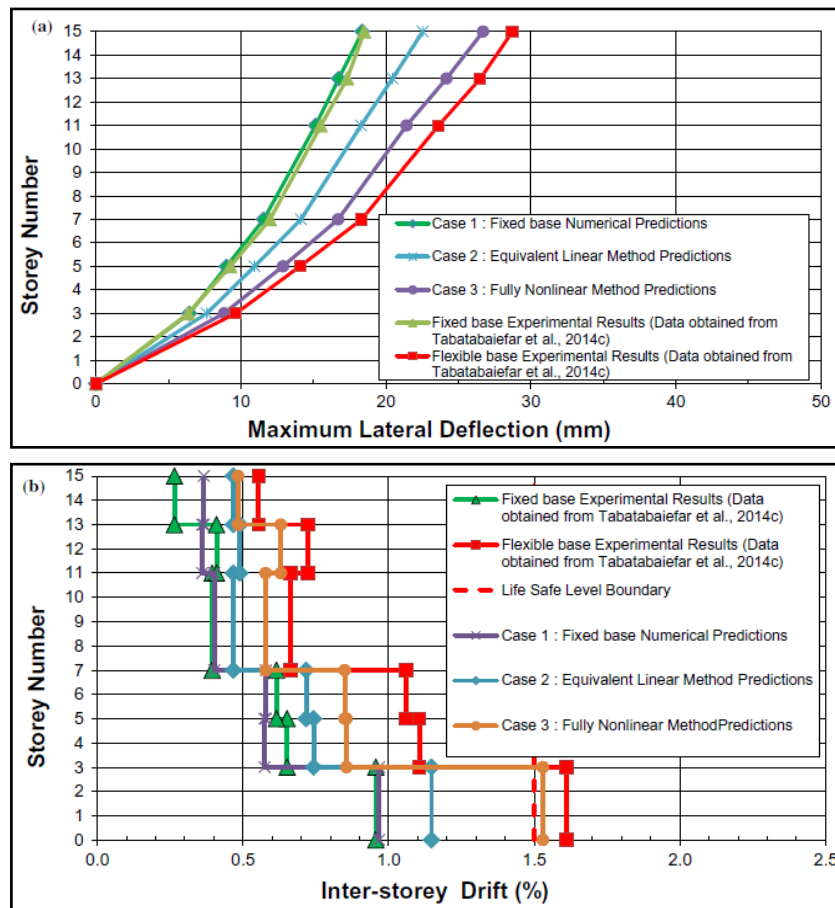
Figure 2-23 (a) Average Values of the Numerical Predictions and Experimental Values of the Maximum Lateral Displacements of Fixed Base and Flexible Base Models, (b) Average Experimental Inter-Storey Drifts of Fixed Base and Flexible Base Models, (Far, 2019)

2.4.1. Discrete and continuum modelling approaches

(Dutta & Roy, 2002) presented a critical review of idealisation and modelling approaches of SSI, which are generally classified as discrete and continuum methods depending on the components and parameters involved in the SSI. Springs and dashpots are typically employed as interface elements in the discrete method. The discrete method comprises a set of approaches: Winkler model, continuous Winkler model, Hetenyi's foundation, Pasternak foundation, Filonenko–Borodich foundation, generalised foundation, beam column analogy model and Kerr foundation. The continuum approach can be accomplished by using either a finite element or boundary element method. Two examples are listed in this section.

(Küçükarslan *et al.*, 2003) developed an inelastic PSSI model using a linear hybrid continuum FEM and boundary element method. This model can include soil material nonlinearity, pile group behaviour, pile settlement and pile–soil slip. The results were validated against static load experiments. The inelastic simulation of soil is demonstrated by introducing a rational approximation to continuum with nonlinear interface springs along with the piles implementing the modified Özdemir's nonlinear model (Özdemir, 1976). The systems of equations were coupled for piles and pile groups at interfacing nodes. Four previous experimental results performed under static loads were utilised to validate the proposed algorithm. (Givens *et al.*, 2012) developed a DSSI model for use in response history analysis which requires a modification of the input motions comparative to those of the free field to successfully incorporate the kinematic interaction effects. The spring and dashpot model that is used to characterise SSI also needs to be represented adequately. The ATC-83 procedure was adopted in the study to model a 13-storey concrete-moment frame building with two levels of basement and a 10-storey concrete shear wall core building without a basement. Figure 2-24 shows the 3D baseline models (MB) that were developed, including SSI components. Figure 2-25 shows that the SSI components comprised horizontal and vertical springs and dashpots that were denoted the horizontal translation and rotational impedance and kinematic ground motion variations. The effects of removing selected components from the models as one part per model was based on several parameters. For instance, inter-storey drifts, shear distributions and accelerations distributions were evaluated to detect suitable models' conditions that can deliver adequate results.
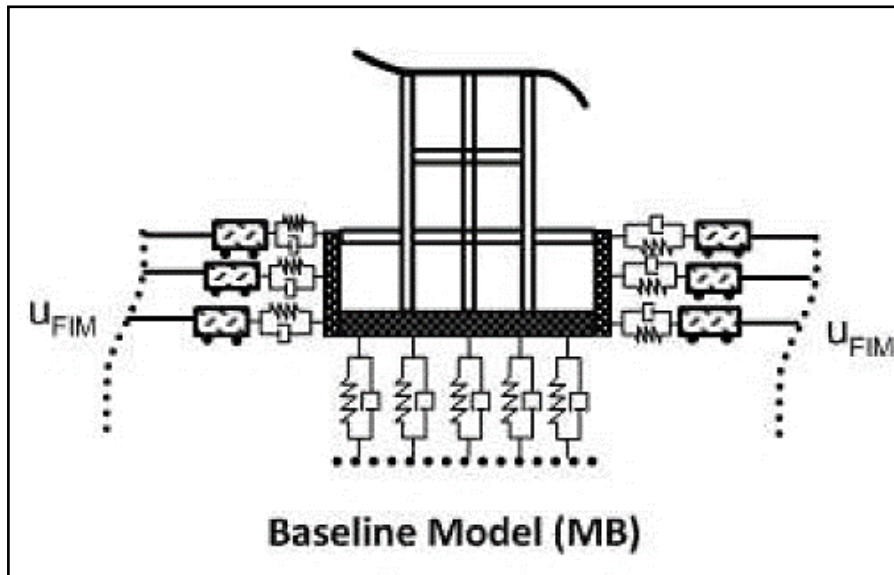
Figure 2-24 Schematic of Baseline Model Considered in Simulations, (Givens *et al.*, 2012)
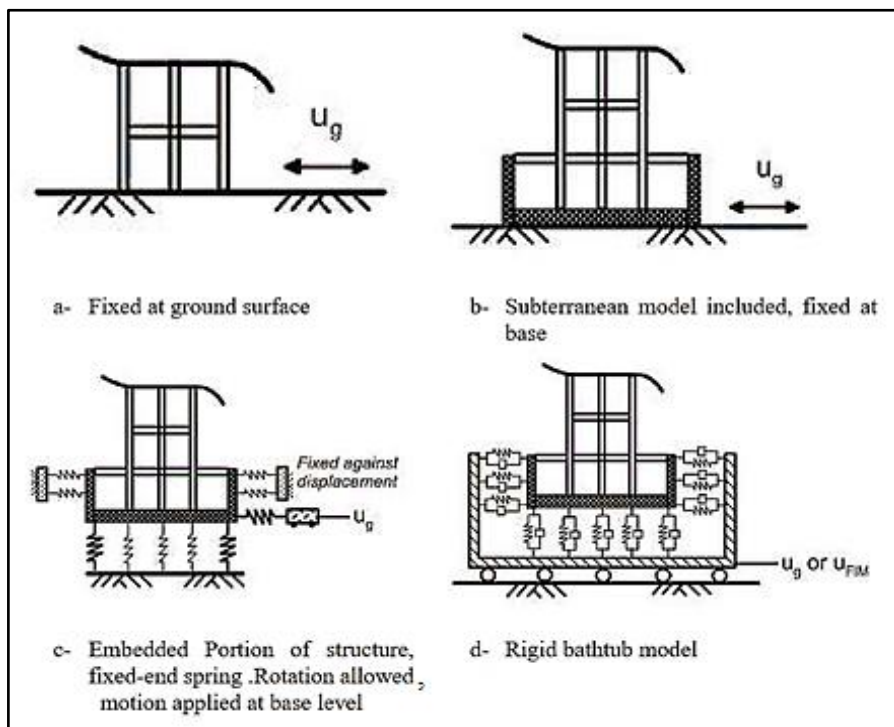
Figure 2-25 Schematic of Simplified Models A to D Considered in Simulations, (Givens *et al.*, 2012)

The bathtub model maintains the crown level of performance, except for the depth-variable motions, generally providing decent above-ground superstructure responses. However, the subterranean demand assessments are biased. Figure 2.26 shows that other conventional methods of applying a fixed-based illustration may produce unsatisfactory results.
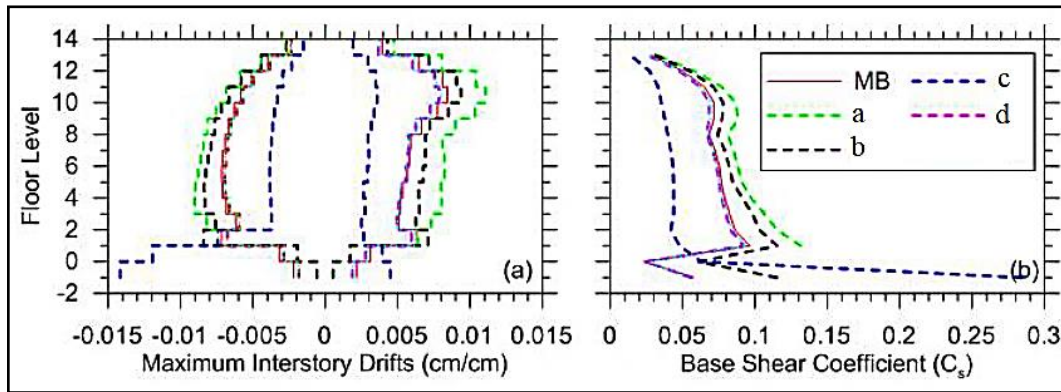
Figure 2-26 Comparison of Peak Drift Ratios and Storey Shears for the Sherman Oaks Building, (Givens *et al.*, 2012)

2.4.2. Linear and nonlinear analysis approaches

A consistent assessment of the seismic response of SSI systems is crucial in the field of earthquake engineering. Given that the seismic structural design has relocated recently to the performance design approach, seismic design problems incorporate the effect of SSI into seismic design, so accounting for the SSI effects becomes essential (Garevski & Ansal, 2010). SSI analysis is a crucial stage in the computation of seismic demands for important structures and is currently achieved using linear approaches in the frequency domain. Such approaches are presumed to predict an accurate response for low intensity shaking. However, their competence for severe shaking, which may cause exceedingly nonlinear soil, structure and foundation response, is ambiguous. Therefore, nonlinear DSSI analysis in the time domain must be employed in such circumstances. Geometric and material nonlinearity in DSSI systems (superstructure, foundation and soil) may arise due to yielding of structural elements, for instance, soil liquefaction state and losing the soil foundation contact. The structural nonlinearity in a structure is described by employing hardening and hysteretic rules. The results are depicted in terms of ductility demands, whereas the nonlinearity in a soil model is accounted for using hardening or softening constitutive models.

In (Ciampolp & Pinto, 1995) and (Mylonakis & Gazetas, 2000a), nonlinearity was only considered in the structure part of the model. The three main methodologies to consider nonlinearity for the foundation system and soil are the continuum model, BNWF model and plasticity-based macroelement (PBM) model. The BNWF model was combined in open system for earthquake engineering simulation (OpenSees) by (Raychowdhury & Hutchinson, 2009b). (Thomas, Gajan & Kutter, 2005) validated several model conditions comprising shear wall strip foundations and rigid structures which were rested on dense

37

sand to the centrifuge model tests. PBM models have been developed relatively recently. (Nova & Montrasio, 1991) initiated the model by employing a single interface element to represent flexibility as well as energy dissipation. Based on the hypotheses of considering both the foundation and the soil as a macro-element for which the loading condition is generalized stress variables and the foundation's displacements and rotations were corresponding to generalized strain variables. The generalised stress-strain in rate relationship is represented according to the constitutive law of the macro-element, which is signified by the rigid-plastic strain-hardening with a non-associated flow rule. The constitutive functions and soil parameters are defined using simple calibration tests. A simplified methodology for loading conditions far from failure conditions is performed. Although the technique is as simple as the elastic approach, it has the benefits of permitting the coupling of displacements and rotations to be forecast accurately.

(Gajan & Kutter, 2009) developed a variant of PBM models, namely, contact interface model (CIM), which is advantageous over BNWF models due to its ability to consider nonlinearity resulting from the gap raised between soil and foundation by incorporating gap geometry. However, a comparison between BNWF and CIM nonlinear DSSI models were presented by (Gajan *et al.*, 2010). They confirmed that the performance of CIM models was exceptional in the circumstances of the coupled moment, shear and axial responses. Moreover, both models turned out to be equivalent. Given the limitation of physical experimental validation, PBM models remained impractical. (Lee, 2018) developed a numerical analysis for a nonlinear DSSI model using poroelastic half-space soil medium. Figure 2-27 shows that the nonlinear soil behaviour is considered using conventional finite elements approach in the near-field zone. The soil far-field zone was introduced using mid-point integrated finite elements and perfectly matched discrete layers (PMDLs) approaches to consider the energy dissipation to infinity. The suggested numerical methodology was validated from a variety of perspectives, and it is applied to nonlinear analysis of the earthquake responses of a structural system on poroelastic soil. The method is demonstrated via the application that the proposed approach can be applied successfully to nonlinear DSSI problems. For realistic simulations of soil model, an advanced plastic model should be used. Two-dimensional problems were considered; however, the behaviours of the 3D dynamic model were different (Raychowdhury, 2011). Therefore, the proposed numerical approach must be extended to 3D analysis. Many researchers have studied the stability of local absorbing boundary conditions.
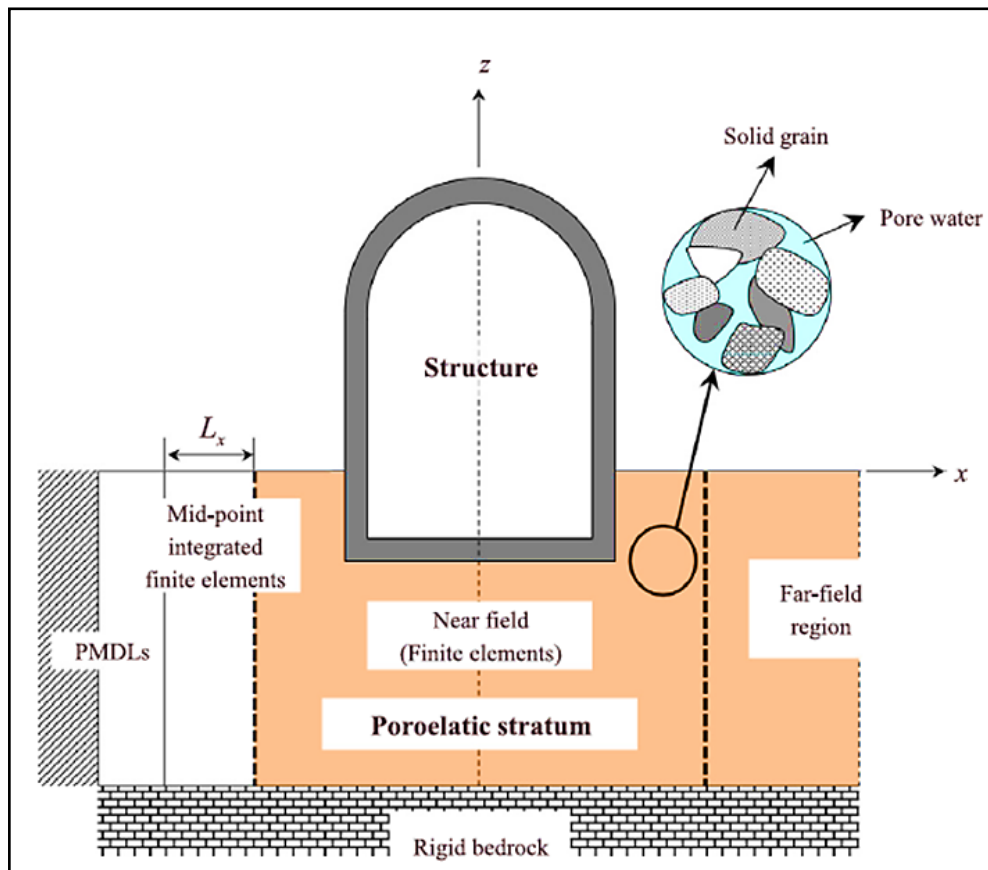
Figure 2-27 Representation of a Homogeneous Poroelastic Stratum with Rigid Bedrock, (Lee, 2018)

The constancy of local absorbing boundary conditions which were studied by a number of researchers was confirmed merely with a small number of numerical models [(Gazetas, 1992), (Boulanger *et al.*, 1999)]. However, the proposed method revealed erratic behaviour, thus requiring further research. The stiffness of soil may experience degradation under cyclic load. Such degradation can be incorporated by reducing the shear modulus for the soil deposit. However, the modulus degradation curves can be obtained according to the methods listed in the literature, for instance, (Kramer, 2014) and (Darendeli, 2001).

2.4.3. Frequency domain and time domain analysis approaches

The nonlinear analysis approaches in the time domain are evidently superior to the corresponding linear approaches in the frequency domain according to purely mathematical modelling point of view. The time domain methods are much less desirable mainly due to their large sensitivity to various numerical modelling aspects involved in the DSSI analysis from the perspective of the practical design. However, practitioners recognised that the results of the nonlinear time-domain analysis are numerically sensitive to the constitutive soil material models type and their parameters in addition to the

modelling circumstance of the soil–foundation interface (Ghiocel, 2012). Additional analysis should be carried out to modify and set the soil–foundation interface parameters and/or soil constitutive model parameters to avoid the implausible DSSI results (Ghiocel, 2012a). In time-domain nonlinear systems analysis which involves incremental step-by-step solutions, numerical errors can occur due to the lack of precise determination of the time at which transition in material properties. As a result, the overshooting and backtracking influences at which modifications in the stiffness happen may induce erroneous noise from high-frequency components. However, the equilibrium corrections are frequently applied once the analysis transfers from linear elastic to plastic. Nonetheless, that the correction is imprecise should be taken into account. No correction from plastic to linear elastic is applied at the reversal stage. These abrupt changes in the material properties generate fictitious noise of the spurious high-frequency components in the system response. Therefore, the researcher proposed to incorporate viscous damping and decrease the time step as much as possible to eliminate this problem. Incorporating viscous damping can enhance the solution and filter the high frequency components, but decreasing the time step increases the effort needed for computational analysis critically. In the time domain, the model is evaluated according to the progression of analysis state with time. In the frequency domain, the model is analysed according to system response to different frequencies.

Adopting frequency domain analysis is one of the safest solutions for simplifying DSSI problems. A fully complicated analysis approach may be developed to directly employ the convolution operator and least squares method. The most critical issues with frequency domain are the required time developing boundary which is related directly to the time domain approach. The filtering requirement must be nonzero in a stated time interval. The attractive factor of adopting the time–domain approach is the ability to use the weighting functions which are appropriate whenever a signal amplitude varies from position to position. However, most time-series analyses in the literature were applied to the limited case of uniform weighting functions, namely, the time series to be 'stationary'. Therefore, their statistical properties do not change with time, which is inconsistent with real-life circumstances. Thus, the time–domain approach can cope with the DSSI analysis with significant complexity and can deliver accurate results with minimum approximations.

(Ülker-Kaustell, Karoumi & Pacoste, 2010) presented a qualitative linear elasticity analysis of the DSSI of a portal frame railway bridge. The effect of SSI on the structural dynamic properties and structure response owing to the high-speed load model (HSLM) of the Eurocode was examined using FEA. The dynamic behaviour of the foundations was presented using dynamic stiffness functions, defining the stiffness and damping of the foundation–soil interface, including solution of equation of motion in frequency domain and employ of (FFT) to find the time domain solution. The frequency dependent functions were used as boundary conditions for the 2D Euler–Bernoulli model. The results of the frequency domain solution have linearity presumed inherently, so it may be inappropriate for inelastic analysis. Moreover, damage and residual strength calculation cannot be achieved in frequency domain. Further attempts were carried out to develop a hybrid approach which has benefits of frequency- and time-domain solutions. The hybrid approached can be categorised as hybrid frequency–time domain (HFTD) and hybrid time–frequency domain (HTFD) methods. (Nimtaj & Bagheripour, 2013) developed a seismic response of a layered soil model using HFTD. In this method, the dynamic equation of motion was written in the frequency domain. The model was subject to pseudo-forces in an iterative analytical technique in the time domain to analyse the nonlinear behaviour of the soil. The simulation was performed using MATLAB algorithm script created by the authors. The accuracy of the proposed method was checked by comparing the results, including the acceleration, displacement and acceleration response spectrum, to the earthquake recorded data and with the results of the equivalent linear and nonlinear approaches given by software SHAKE and DEEPSOIL. The main conclusions of these comparisons were according to the equivalent linear method. The results were overestimated, but the results obtained according to the nonlinear approach were underestimated. Moreover, the proposed approach presents reasonable accuracy due to the acceleration of Fourier amplitude changes in different frequencies. (Bernal & Youssef, 1998) solved equations of motion in the time domain using frequency-independent impedance functions according to HTFD approach. The frequency dependence of these functions is taken into account through pseudo-forces in frequency domain at every iteration. The conclusions of the study are as follows:

- The HTFD method provides a simple alternative for the accurate computing solutions for inelastic DSSI problems.

- The degree of freedom (DOF) at the SSI has restricted the pseudo-forces. Therefore, the convergence of the analysis and the accurate results were limited to the number of DOF at this interface.

- The numerical results achieved for an eight storey shear building indicated that the HTFD method can deliver more significantly efficient results than the alternative HDTD approach when the predicted response is inelastic. Moreover, the former was approximately four to 19 times faster than the latter in the considered simulations.

2.4.4. Direct and substructure analysis approaches

According to the discussion of past studies, the methods for dealing with DSSI problems can be classified as one of the following approaches: discrete versus continuum, linear versus nonlinear and frequency domain versus time domain. These approaches can be further categorised into direct and substructure methods based on several fundamental characteristics (Wolf, 1991). On the one hand, the entire soil-structure system is analysed using free-field motion as an input motion in the direct method. The response of the coupled system is applied in the second stage of the analysis to determine the structural response of the system. On the other hand, in the substructure method, the system is subdivided into several substructures, which are analysed independently. The solutions are represented by superpositioning the individual results of the sub-analysis cases, which will be considered as the final response of the structure. Given that semi-infinite soil media do not need be discrete, the latter is computationally efficient and inexpensive. Subdividing the complicated problem into multiple and straightforward problems offers an option of a practical modelling scenario for each issue, which is also useful in a parametric study.

Unlike the direct method, in the substructure approach the kinematic and inertial components of SSI in the substructure approach are separately considered using transfer and impedance functions, respectively. The substructure approach is typically performed in the frequency domain due to the frequency dependence of both functions (Kutanis & Elmas, 2001). Despite the broad utilisation in analysing DSSI problems, the suitability of the substructure method was recently examined by (Rahmani *et al.*, 2016), who noticed that this method consistently overestimates the design base forces and top displacements, and is therefore relatively simple to capture the major mechanisms involved in SSI. The methods and the corresponding modelling aspects, as used in the new research presented

in this thesis, will be comprehensively described in Chapter 3. The early attempts to evaluate impedance functions were relatively rigorous due to the utilisation of boundary or finite element methods. (Wolf, 1995) developed a physical model to establish the impedance functions of a foundation in a simple and comparatively accurate manner. The analysis can be performed in the time domain. These physical models can be generally characterised as translational and rotational cones with respective lumped-parameter models. Lumped-parameter models designate the foundation in terms of stiffness, damping and mass elements using a particular degree of freedom, whereas cone models characterise load dissipation mechanism using either translational or rotational cones. Most of the lumped-parameter models were developed for ideal circumstances, such as shallow foundation resting on a homogeneous elastic half-space. This gives the cone models an advantage over lumped-parameter ones because the former can deal with foundations and pile embedded in layered soil. (Kaynia & Kausel, 1991) revealed that the non-homogeneity of soil increases the interaction impacts and filters the high frequencies. (NEHRP, 2012) adopted the impedance function based on lumped-parameter models, which have been presented in past studies on shallow (Pals & Kausel, 1988; Gazetas, 1992; Mylonakis, Nikolaou & Gazetas, 2006) and pile foundation types (Mylonakis, 2015). Jaya (2000) used the cone model initiated by Ehlers in 1942 to devise a computational tool called IMFFS (IMpedance Functions of Foundations) which involves four important steps: analytical modelling of the soil–structure system, computing the dynamic stiffness matrix of the free field, assembly of the kinematic constraint matrices and evaluation of the dynamic stiffness matrix of the soil–foundation system. Cone models, which define the foundation as a stack of rigid disks, are also used in DSSI analyses (Khoshnoudian, Ahmadi & Kiani, 2015; Ayough et al., 2017). The thickness of the parts of the soil stuck between two successive disks of the embedded foundations/pile must not exceed $\frac{1}{6}$ or $\frac{1}{10}$ of the smallest wavelength participating in the excitation. The cones arrangements illustrate the mechanism of the load dissipation developing at the surface and the embedded disks. The lateral slopes of the cone are computed using the association between the coefficients of the static stiffness of the disk and cone, which are highly hinged on the properties of the soil deposit. In the stratified approach, cones are substituted with backbone cones with multiple cone frustum. In the analytical modelling for a soil–structure system, the disk subjected to a unit load and the backbone cone is assembled to determine the displacements at all locations on the disk. The dynamic

flexibility matrix of free field can be calculated by repeating such operation for each disk. Unlike the free field, the node displacements located at the foundation element are dependent on each other, which is defined by applying kinematic constraint matrix to remove the dependent degrees of freedom. In the case of long piles, the active pile length is crucial when constructing the matrices, which is 10–20 times the pile diameter and can be computed according to the methods proposed in previous studies (Karatzia & Mylonakis, 2012; Mylonakis, 2015; Gazetas, 1992). When these matrices are established, the matrices of the dynamic stiffness for the independent degrees of freedom, which are the so-called impedance functions, can be computed. However, only impedance functions for a single pile are obtained; the impedance functions for the pile group can be generated by considering the pile–soil–pile interaction amongst the piles.

2.5. Code Standards Soil–structure for SSI

Despite the numerous studies on the solution techniques for DSSI problems, few seismic codes impose standards for containing DSSI because of the dissension among researchers about the influences of SSI on the structural seismic response. However, considering the importance of incorporating SSI in the structural design, coded SSI provision should be involved in the seismic codes. Several SSI standards in some of the existing international seismic codes, such as Eurocode8 and US seismic code, are discussed in this section.

2.5.1. US and European seismic design codes

The Applied Technology Council (ATC) outlined the first generation of SSI guidelines in 1978, which is called ATC 3-06 (ATC, 1978). The guidelines incorporate the effects of the SSI due to lengthening the natural period and increasing the damping induced by the soil structure systems over the fixed-base counterparts of the structure subject to an earthquake. ATC 3-06 also proposed a reduction factor for the design of the base shear. However, this equivalent lateral force was based on the elastic response of the structure. Several studies reported that the influences of the SSI on the structural response declines due to the increase in the inelastic structural behaviour. Consequently, the structures subjected to a particular seismic event and designed according to the above-mentioned standards might not perform adequately. Therefore, a new standard called ASCE 7-10 proposed a 30% maximum limitation of the base shear reduction. (Jarernprasert, Bazan-zurita & Bielak, 2013) stated that the structures designed according to ASCE 7-10 might experience a large ductility demand that can exceed the design target ductility, thereby indicating the necessity of reconsidering these SSI provisions.

NEHRP established the Federal Emergency Management Agency (FEMA) provisions to develop design and analysis practices that can minimise earthquake hazard and structural damage risk. The FEMA provisions signified the limitation of the base shear reduction factor (RF) as a function of the modification factor (FEMA P-1050, 2015). These provisions suggested a low design base shear RF for the systems with substantial response modification factor (i.e. structures with large inelastic deformation capacity) and were incorporated in ASCE 7-16, which validates the linear dynamic analysis as an alternative approach to the equivalent lateral force method. This approach can either incorporate the effects of SSI using the modified general design response spectrum specified by ASCE or modify the site-specific response spectrum, which can be developed by the designer. In the linear dynamic approach, kinematic interaction mode cannot be considered in the DSSI analysis. Therefore, the nonlinear response time history analysis using acceleration time histories, which are scaled to a site-specific response spectrum, is essential once the kinematic interaction is predominant. (Khosravikia et al. 2017) reported the consequences of applying DSSI according to the NEHRP 2015 provisions, which were used to develop the basis of the 2016 version of the ASCE seismic design standard. However, the probability of applying SSI circumstance instead of the fixed-base analysis condition will increase the ductility demand of the structure. They further investigated whether or not the NEHRP standards effectively strengthen the SSI provisions of the existing ASCE seismic design code using 720 structures with various height, structure systems, aspect ratios and embedment ratios founded on different site classes (Figure 2-28). A probabilistic method is used to compensate for the predominant uncertainties in the ground motion and soil structure system properties (Figure 2-29 and Figure 2-30).

In conclusion, NEHRP and the other existing provisions contribute to the hazardous structural designs given the surface foundations founded on relatively soft soil. NEHRP, however, slightly improved the current requirements for squat structures. The provisions offer conservative designs for systems founded on very soft soils, in which that of NEHRP is more restrictive than the other standards. As previously mentioned, adopting a typical code spectrum can lead to a reduction in the spectral acceleration and consequently contribute markedly low rates of superstructure seismic demands. However, fixed-base models can be assumed to be conservative. This concept is not valid for some soil sites condition that n are exposed to specific earthquake motions with particular frequency content properties (Bardakis & Fardis, 2011). Coupled with the inferences mentioned

above, the debatable seismic codes based on design spectrum and the lack of the effects of the SSI provisions should be examined under a loop to set some groundwork for the investigation of this frequently neglected phenomenon.
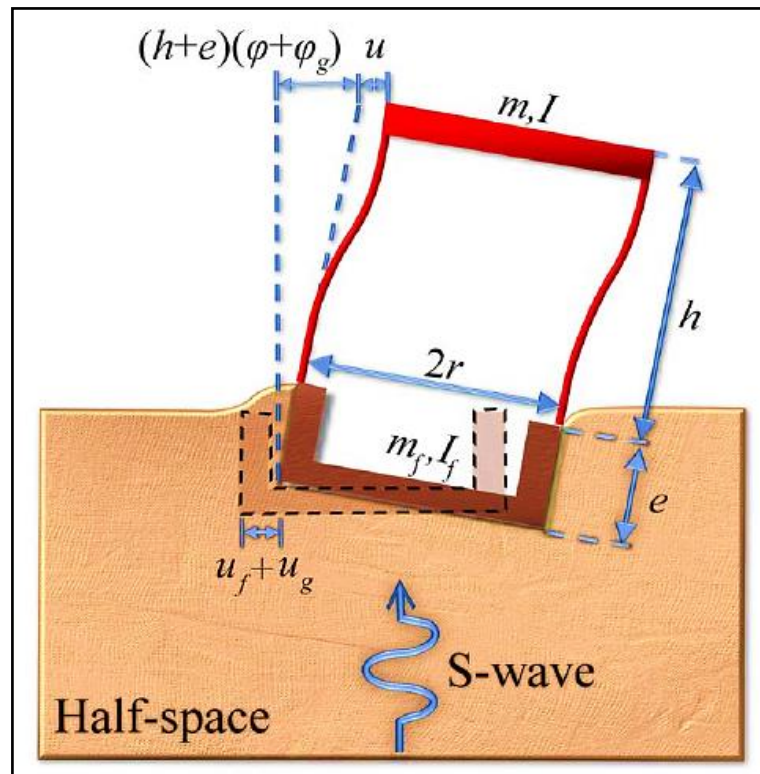
Figure 2-28 Soil–Structure System, (Khosravikia, Mahsuli & Ghannad, 2017)
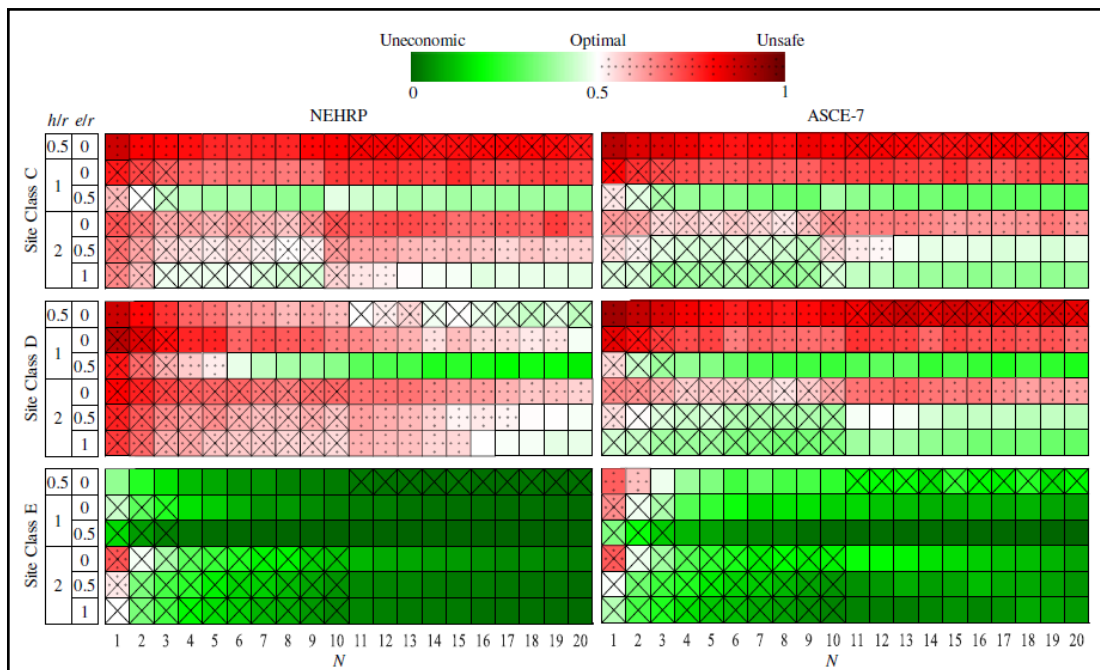
Figure 2-29 Colour-Coded Illustration of $P(\mu_{SSI} > \mu_{fix})$ from NEHRP and ASCE-7 for Stiff Structures, (Khosravikia et al. 2017)
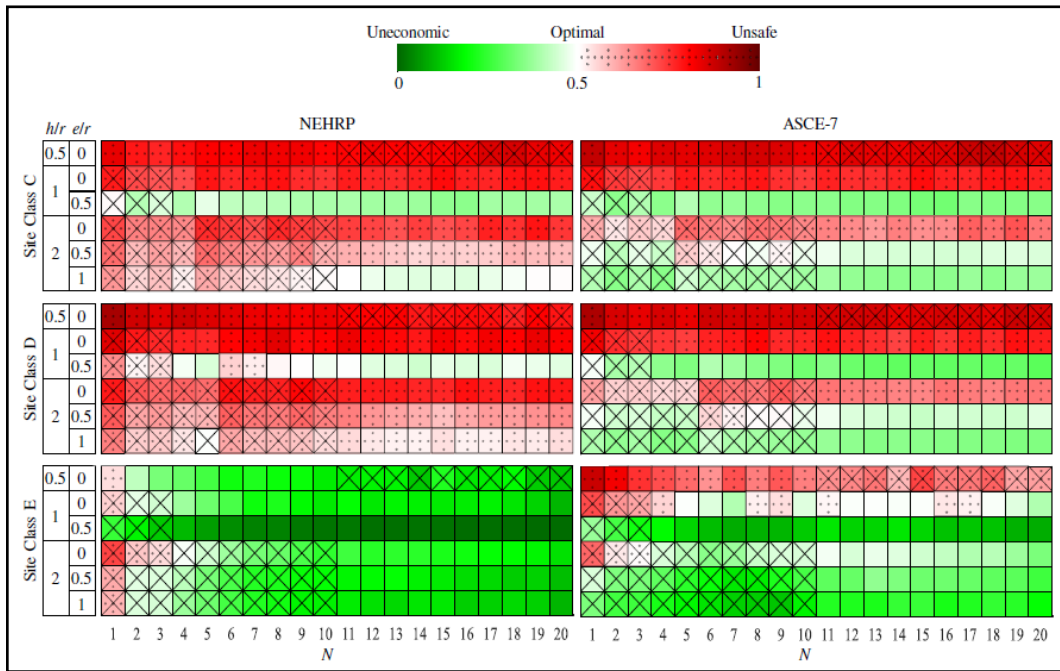
Figure 2-30 . Colour-Coded Illustration of $P(\mu_{SSI} > \mu_{fix})$ from NEHRP and ASCE-7 for Soft Structures, (Khosravikia, Mahsuli & Ghannad, 2017)

A quality estimate of the structure's fundamental period is essential for the performance-based design methodology, which is one of the highly practical methods and has become a modern tool in the field of earthquake engineering (Džakić, Kraus & Morić, 2012). The SSI concept involves various mechanisms (e.g., kinematic and/or inertial components) that induce the linkage of soil and structural displacements. Several basic approaches used to solve SSI problems can be generally categorised as a continuum or discrete, linear or nonlinear, frequency or time domain and direct or substructure approaches (Aydemir & Ekiz, 2013). Given that the experimentation is usually heavy and expensive, researchers have devised economical and explicit modelling strategies to evaluate the impact of SSI. (Far, 2019) conducted a comprehensive critical review on available and well-known modelling techniques and computation methods for DSSI analysis. With the advent of powerful computers and advanced numerical methods, great improvement were observed in the computational aspects. Given that numerical methods have a broader scope of research than analytical methods, adopting numerical approaches, such as FEM and finite difference method, to examining combinations and complex interactive applications has become widespread. Although many researchers developed numerical analysis and solution techniques, few international codes encompass the guidelines for incorporating the effect of SSI due to the lack of consensus amongst the findings regarding the SSI effects on the seismic response of structures. However, considering the significance of

incorporating SSI impact in the structural design, direct and detailed SSI provisions should be included in the seismic codes.

To deliver a distinct vision to the stakeholders of the seismic code committees, a comparison between the provisions in the existing ASCE and EC8 codes and the real impact of the SSI problem in the case of high rise buildings resting on soft clay and exposed to earthquakes is necessary. As previously stated, ATC generated the first serious SSI provisions in 1978 (i.e. ATC 3-06) (ATC, 1996). Considering the unambiguous relationship between the effects of SSI and the lengthening in the natural period and increase in damping (presuming fixed-base counterparts) ATC 3-06 has reported a reduction in the base shear design value. This proposed equivalent force has resulted from the elastic structural response analysis. Conflicting results from subsequent studies showed that inelastic behaviour might dominate. Consequently, inadequate structural performance might be observed during a seismic event. Hence, ASCE 7-10 (ASCE 7-10, 2010) set the limitation for the base shear RF at 30%. (Jarernprasert, Bazan-Zurita & Bielak, 2013) reported that the structures designed according to ASCE 7-10 provisions possess a mean ductility demand that exceeds the design target values. Thus, the SSI regulations should be reviewed. The NEHRP then developed the FEMA provisions (FEMA P-1050, 2015), in which the base shear RF was expressed as a function of the response modification factor. These provisions also recommend low design base shear reduction factor for systems with high inelastic deformation capacity, and was eventually incorporated in ASCE 7-16, (ASCE, 2013). In addition to the equivalent lateral force procedure, ASCE 7-16 specified a linear dynamic analysis method using either the SSI-coded design response spectrum or the SSI-modified site-specific response spectrum, which can be developed by the design engineer. However, the kinematic interaction cannot be considered when using the linear dynamic method. Otherwise, a nonlinear response time history analysis using acceleration time histories scaled to a site-specific response spectrum for predominant kinematic interaction circumstance must be adopted. The kinematic interaction effects are denoted by the response spectral modification factors for the base shear averaging and embedment with no more than 30% reduction factor. (Khosravikia, Mahsuli & Ghannad, 2017) emphasised the importance of practicing ASCE 7-16 in the context of structural design safety and economy, and further reported the scope of enhancements in the latest guidelines. Eurocode8 (EN 1998-5, 2011) recommends considering the effects of DSSI for structures that are slender or have notable second order (P−δ) effects, as well as structures that sit on piles or piers, offshore caissons,

and silos. Amongst these codes, EN 1998-1 (EN 1998-1, 2011) explicitly indicates a typical soil type with deficient shear strength and high plasticity index, whereas EN 1998-5 (EN 1998-5, 2011) prescribes the design consideration for deposits without defining the guideline for the assessment criteria of the SSI effects. With the availability of modern computational platforms, great development has been observed in the field of SSI. Most research can either be exploring the effects of SSI on a specific structure class or investigating the reasons behind these effects on a general structural system. Most studies have investigated the effects of SSI on the seismic vulnerability, seismic fragility, inelastic displacement ratio, strength reduction factor, ductility demand, acceleration demand and modal characteristics (associated frequency and damping) of a general structural system (Bararnia et al., 2018; Mitropoulou et al., 2016; Stefanidou et al., 2017; Karatzetzou & Pitilakis, 2018; Papadopoulos et al., 2017; Cruz & Miranda, 2017).

2.6. Contemporary Dynamic Soil–Structure Interaction Research

Owing to the availability of robust and sophisticated computational analysis platforms, considerable and various developments have taken place in the DSSI field recently. However, most of the research can be categorised under two main themes: research that investigates the influences of DSSI on a particular type of structure; and research that attempts to comprehend the hypothesis behind these consequences, which are usually applied on general structural systems. (Carbonari *et al.*, 2017) examined the consequences of DSSI on bridge piers established on inclined pile group embedded in different soil, using the direct approach and developed a numerical model which is employed in a distinct computer code running in MATLAB (MATLAB, 2020) in the frequency domain. The piles and superstructure are simulated using the beam-column element. The soil is modelled with a visco-elastic medium developed using independent infinite horizontal layers. The consequence of kinematic stress, filtering effect and rotational component of the input motion were investigated. The study falls under the category of understanding of the general concept controlling the dynamic response of the soil–pile–superstructure systems which highlights that current seismic code design approaches do not give reliable predictions of the seismic structural behaviours. (Bigelow *et al.*, 2017) investigated the influence of backfill behind abutments on static and dynamic properties of the composite single-span bridge as a soil–structure system. The main target determines fundamental frequencies and corresponding damping ratios obtained at the different levels. Unlike the previous literature that highlighted that the dynamic performance of structures may hinge

on substantially on the SSI considerations, the results of the present showed that the fundamental frequencies values would experience a negligible influence of the backfill when the first two values would be adopted. Therefore, further research based on a reliable and accurate numerical assumption is essential in examining this problem correctly. (Li *et al.*, 2017) assessed the seismic response of a cable-stayed bridge founded in fault zones considering the effects of DSSI. The likelihood of the position of the bridges crossing fault-rupture zones forward region (FR), middle region (MR) and backward region (BR) relative to the potential position of the fault were examined. The fixed base and SSI numerical model situations were considered using ANSYS software. Four various orientation angles of 0°, 30°, 60° and 90° were related to the fault direction. The dynamic behaviour of the foundation – soil system was represented using systematic lumped-parameter models. The study confirmed the effect of DSSI which elongates the period of the structure due to the stiffness reduction. Moreover, the orientation of the bridge direction compared to fault trace has a considerable effect on the seismic responses of the structure.

A number of researchers covered the DSSI considerations that resulted from other sorts of dynamic loadings, such as wind loading. (Harte, Basu & Nielsen, 2012) performed dynamic analysis of wind turbines considering SSI as soft soil may affect the dynamic response of wind turbines. An MDOF model is developed using a Euler–Lagrangian as a substructure approach. The base shear and bending moment at the base of the tower and in the foundation were computed. No considerable difference between the shear and moment in the foundation and tower base was noticed because the foundation inertia of the modelled foundation was not taken into consideration. The frequency content in the response time history was significantly influenced because of the DSSI effects. (Fitzgerald & Basu, 2016) explored the significance of considering the DSSI in structural control of wind turbines and suggested an active structural control. The study showed that by considering the DSSI, the natural frequencies of the system could be significantly influenced. (Zuo, Bi & Hao, 2018) examined the dynamic responses of a wind turbine exposed to a combination of sea wave and wind loadings numerically using the explicit Abaqus procedure. The effects of SSI are considered. The results reveal that the wind turbine responses in the condition of the operating were much larger than those in the parked situation. Because of the consideration of SSI influences, the vibrations of the tower may be affected significantly, whereas a slight influence on the in-plane vibrations

of the blades is exerted. (Michel, Butenweg & Klinkel, 2018) analysed the dynamics of a realistic pile-grid system of a wind turbine tower incorporating frequency-dependent SSI. Different structures in different soil types have a significant impact on the vibration reaction. Although the amplitude of the vibration is mostly attenuated, certain unfavourable combinations of structure and soil parameters amplify the natural frequencies of the system. This occurrence testifies to the need for overall dynamic analysis in defining dynamic turbine stability and whole frequency setting. (Chatziioannou *et al.*, 2017) highlighted the significance of considering the nonlinearities, which influenced both computing the wave loading and the nonlinear structural analysis. A fully nonlinear 3D model was established to correctly determine an accurate distribution of wave energy in both frequency and direction. The examinations were performed using SAP2000 software, developed with an interface in order to evaluate the forces due to wave loading and employ them on the structural members. The study showed that the consideration of the nonlinearities resulted in substantial changes in both the displacements and stresses of the structure comparing to the conventional design approaches. (Hatzigeorgiou & Beskos, 2010) examined the significance of incorporate DSSI on the inelastic seismic response of tunnels, using the FEA with viscous absorbing boundaries, in the time domain (Figure 2-31). The inelastic behaviour of the materials used by (Hatzigeorgiou & Beskos, 2010) was assumed according to the basis of the continuum damage mechanics theory (Krajcinovic & Lemaitre, 1987). The analyses were performed with and with SSI effects. The results concluded that the effect of SSI for the 3D lined tunnels founded on soft rocks can be disregarded (Figure 2-32).

(Coleman, Bolisetti & Whittaker, 2016) defined a nonlinear SSI method developed for use to nuclear facilities. This approach involves sequential steps to provide realistic results using time-domain numerical analysis (Figure 2-33). The nonlinear soil constitutive model comprising energy dissipation were described in the study, as shown in Figure 2-34. (Farahani *et al.*, 2016) and (Solberg, Hossain & Mseis, 2016) performed two time-domain analyses for the seismic SSI analysis of nuclear structure rest on soil with degraded concrete stiffness condition and nonlinear seismic SSI analysis of embedded structure, respectively. (Bolisetti, Whittaker & Coleman, 2018) described a nonlinear seismic SSI analysis technique of nuclear structures performed in time domain using LS-DYNA and correlated the results alongside the traditional frequency-domain code SASSI, considering their high stiffness and weight. Significant consequences arising

from these reactors' structural failure indicate the need for sufficient SSSI consideration in their structural design. Studying the effect of SSI is no longer limited to seismic response as (Venanzi, Salciarini & Tamagnini, 2014) extended it to wind loading response of high-rise buildings. The study observed that the permanent displacements and rotations accrued at the foundation level can induce substantial permanent displacements at the top level of the structure.
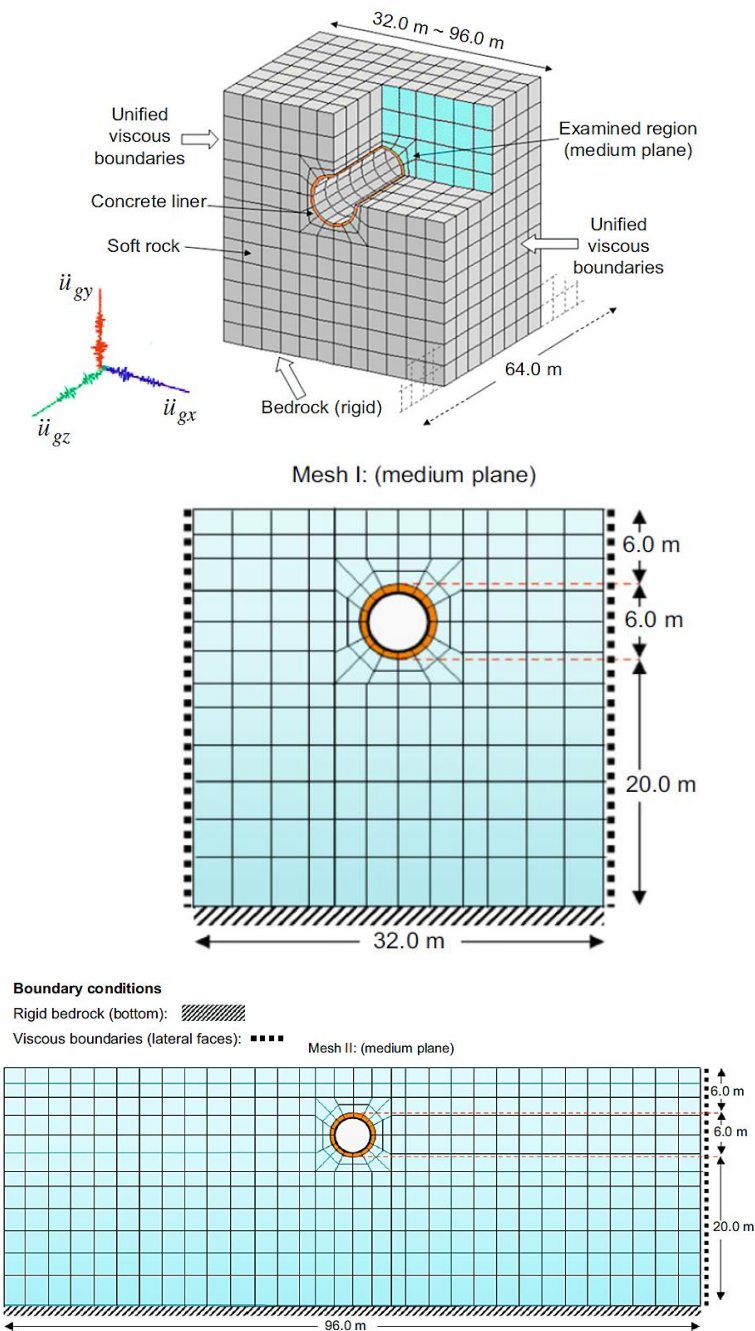
Figure 2-31 Geometry, Discretisation and Boundary Conditions of the 3D Rock–Tunnel System, (Hatzigeorgiou & Beskos, 2010)
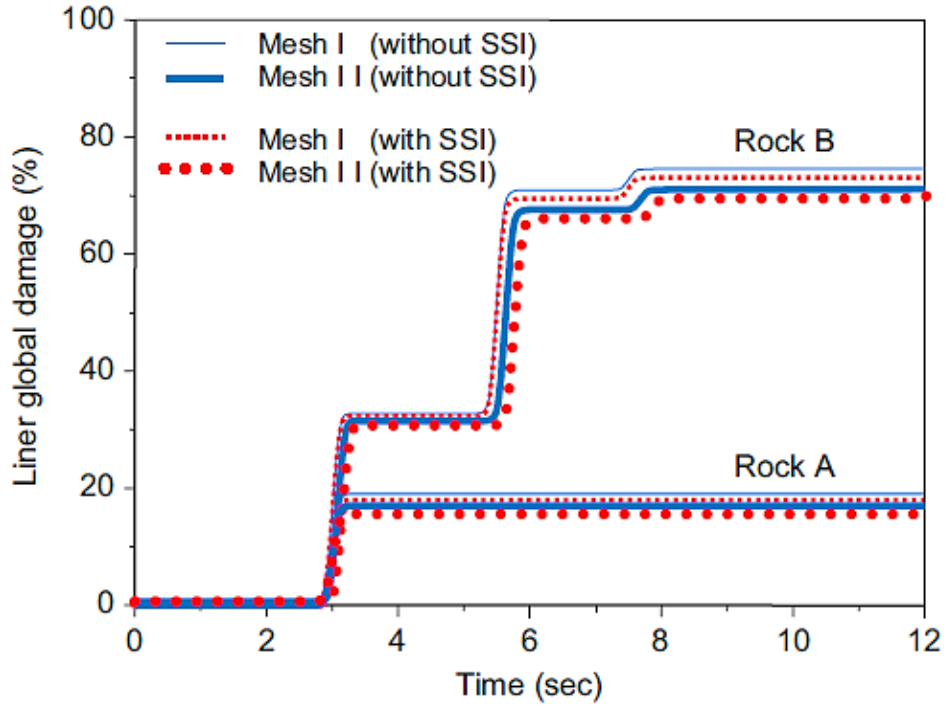
Figure 2-32 Time History of Total Damage in the Liner for Analysis of Various Rock Sand Types, (Hatzigeorgiou & Beskos, 2010)
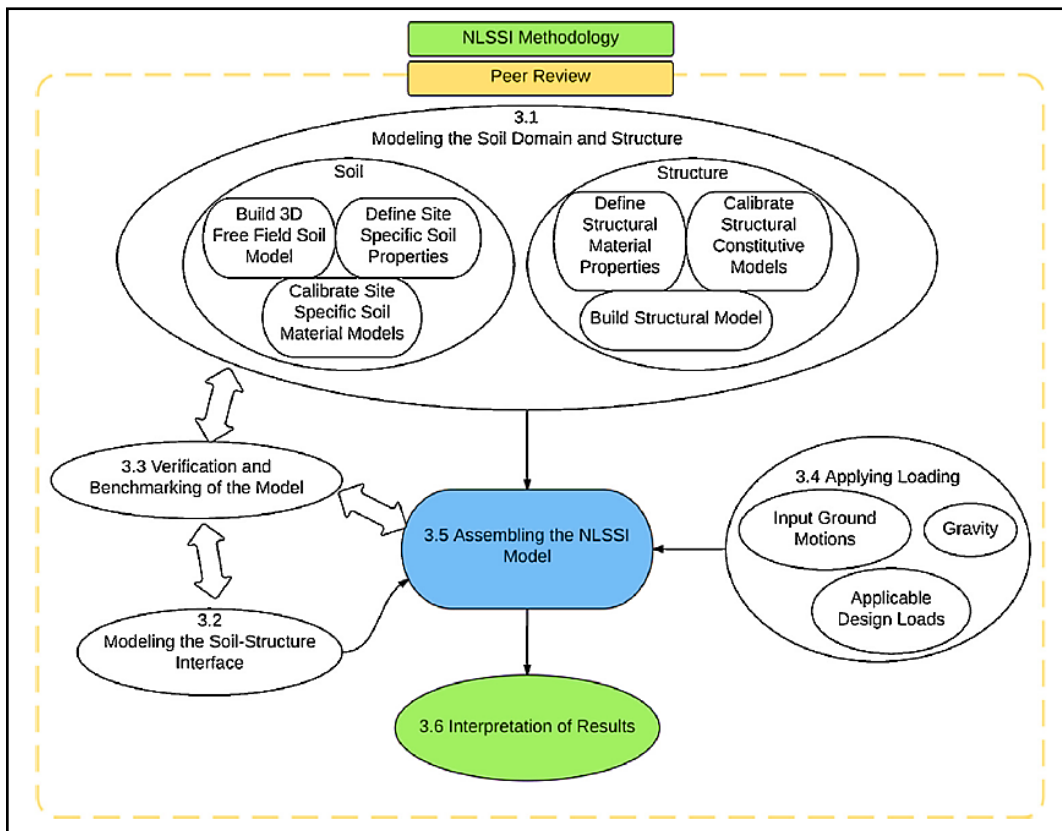
Figure 2-33 INL DSSI Methodology in Time Domain, (Coleman, Bolisetti & Whittaker, 2016)

53
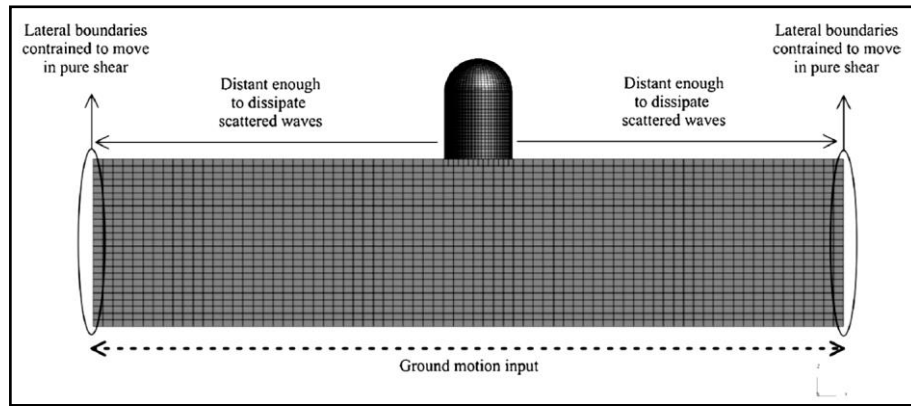
Figure 2-34 FEM for SSI Analysis Using the Direct Method, (Coleman, Bolisetti & Whittaker, 2016)

(Mekki *et al.*, 2016) formulated a procedure for analysing SSI system and evaluated the significance of its effects and the influence parameters of the analysed system involved, such as performance and reduction factors. The nonlinear response of a structure under seismic loading was developed by (Mekki *et al.*, 2016) counting the effects of SSI. Several parameters associated with SSI analysis were examined, such as the significance of soil parameters and foundation/soil stiffness ratio. The study confirmed that structural response not merely hinges on the dynamic characteristics of the structure and the excitation characteristics. However, the external environment nearby the base of the structure will have significant impact on the structure–structure interaction and foundation–soil interaction. (Tomeo *et al.*, 2017) examined the effect of seismic SSI on the performances of 2D RC moment-resisting frame founded on soft clay, which were studied using nonlinear dynamic analyses. The numerical modelling was applied using the OpenSees software. A number of parametric studies were investigated, such as soil properties, modelling method and different seismic design levels (Figure 2-35).
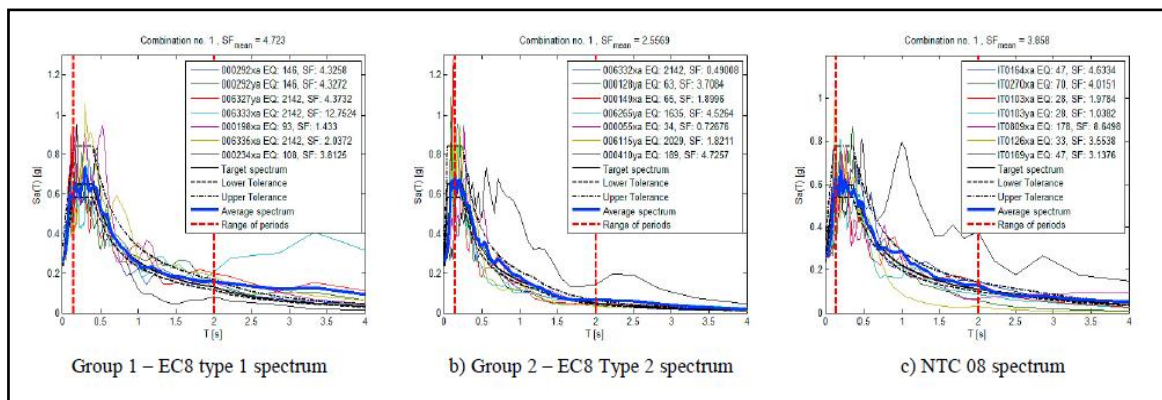
Figure 2-35 Selected Spectrum, (Tomeo *et al.*, 2017)

The soil classes were indicated according to EC8 (Tomeo *et al.*, 2017). The substructure and the direct method were adopted in this study (Figure 2-36). The SSI affects the seismic demand with respect to maximum base shear and inter-storey drift ratio, which depends on the modelling method, with various significances (Figure 2-37). Recently (Bararnia et al., 2018) suggested a simplified definition for inelastic displacement ratios of the soil–structure system with embedded foundations incorporating kinematic and inertial DSSI components. The nonlinear analysis of the soil structure system was modelled by the sub-structure method. The foundation was considered as a rigid cylinder embedded in the soil with different embedment ratios. The study concluded that employing the inelastic displacement ratios for the fixed-base circumstance system resulted in an underestimation peak inelastic demands because of the increase of the foundation embedment.

(Ghandil & Behnamfar, 2017) investigated the nonlinear response of MRF resting on soft soils, considering the SSI effects and using the direct analysis approach. The analysis was performed using OpenSees software. The soil deposit was simulated employing the equivalent linear technique once the shear modulus and damping ratio of soil are substituted with values representative of the nonlinear soil behaviour. A modification of this procedure regarding extensive strains of soil was proposed. However, the results concluded that the storey drift and ductility demand at the lower floors increase by considering the SSI effect, and a checking tool of asses the significance of considering the SSI for nonlinear analysis application signified as ductility demands with SSI to those of fixed-base circumstances. (Karatzetzou & Pitilakis, 2018) proposed a reduction factor to estimate the acceleration demand for SSI systems. This reduction is influenced predominantly by the soil conditions lower than $\frac{1}{\sigma} \geq 0.1$, whereas the impacts of the frequency content of the input motion and foundation-structure slenderness ratio are negligible. (Papadopoulos et al., 2017) computed the modal characteristics of a frame structure with respect to the soil stiffness exposing the key effects of DSSI, using finite element model. The analysis reveals that SSI influences the fundamental period and higher modes of the system because of the rise in modal damping ratios and generation of composite mode shapes as shown in Figure 2-38.

(Cruz & Miranda, 2017) evaluated the modification in damping ratio of structures subjected to seismic excitation because of the effects of SSI. The study reveals that the effects of SSI may increase or decrease the effective modal damping ratio of the

55

fundamental period. A reduction in effective damping in circumstance of slender high-rise structures and an increase for short and medium period structures have been reported. Moreover, SSI effects contribute to an essentially linear trend in efficient modal damping ratios with increasing modal frequency. (Zhang, Wei & Qin, 2017) described the damping characteristic of the soil–structure system using physical shake table tests (Figure 2-39 and Figure 2-40).
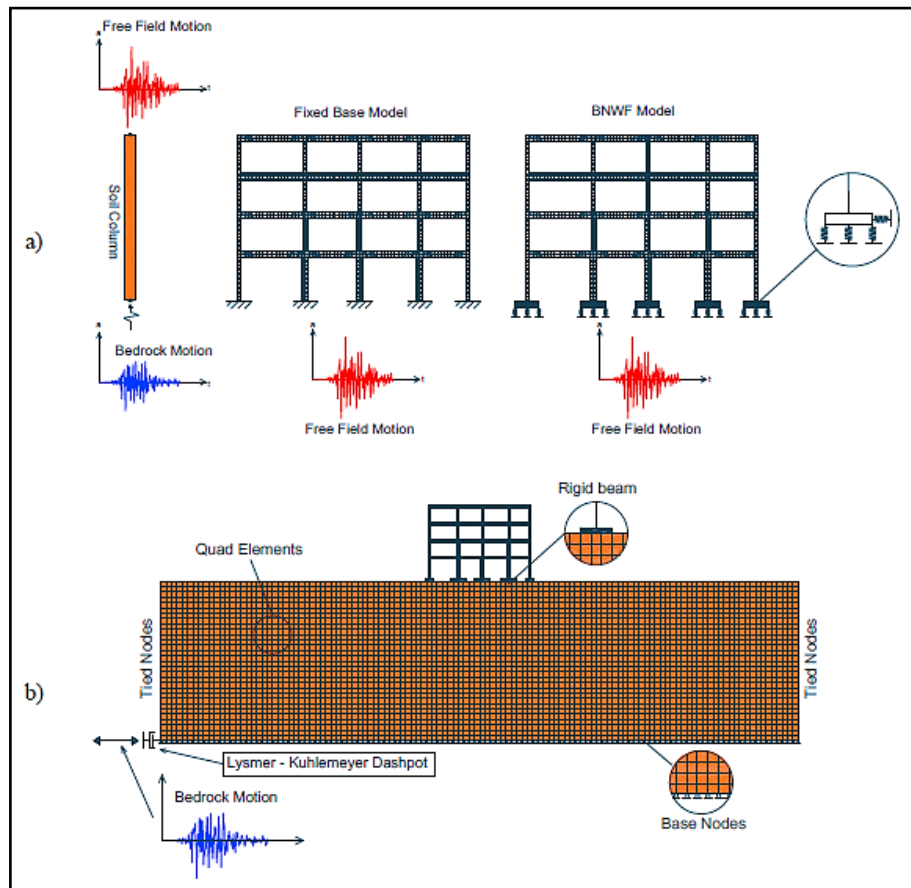
Figure 2-36 Schemes for DSSI Analyses: a) Fixed Base and BNWF Models and b) FEM Model, (Tomeo *et al.*, 2017)
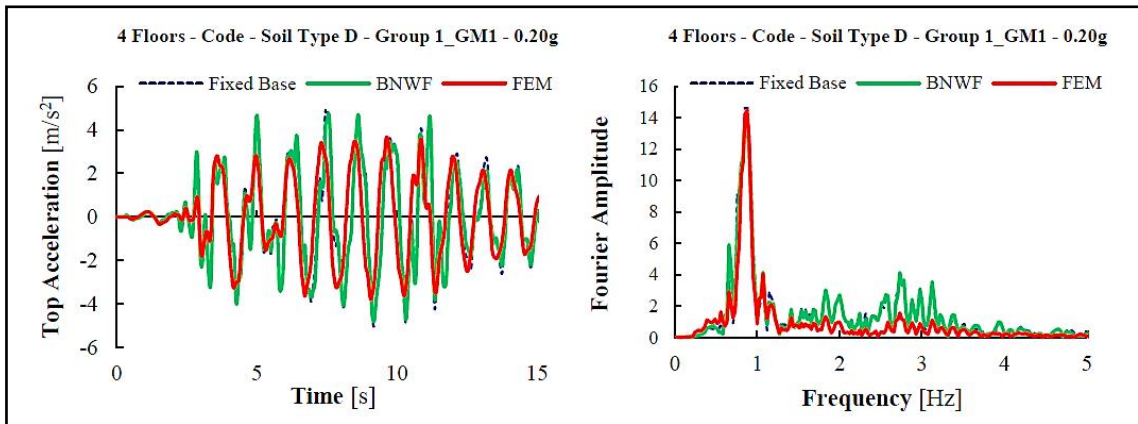
Figure 2-37 Figure 81. Time Acceleration and Corresponding Fourier Spectrum, (Tomeo *et al.*, 2017)
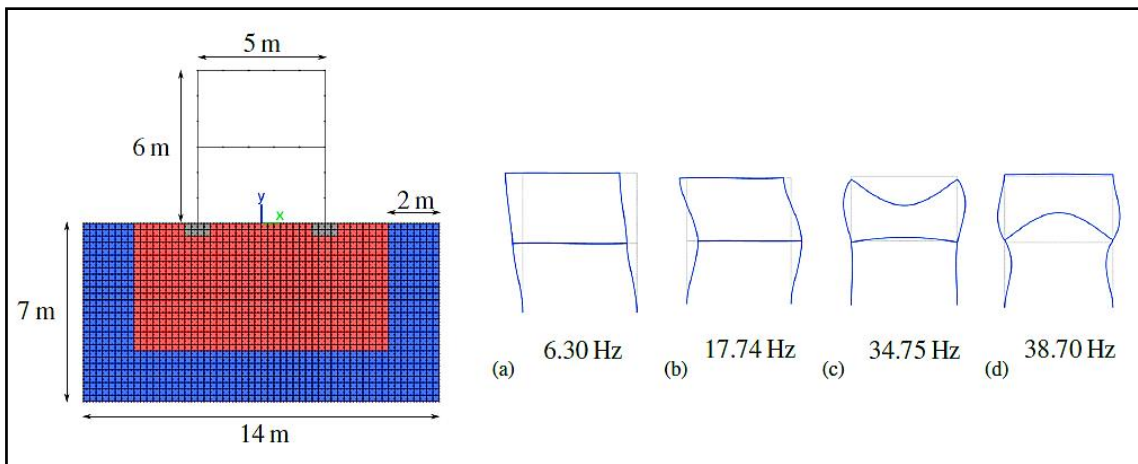
Figure 2-38 First Fixed-Base Modes of the System, (Papadopoulos et al., 2017)

Figure 2-39 Physical Model and Loading System, (Zhang, Wei & Qin, 2017)
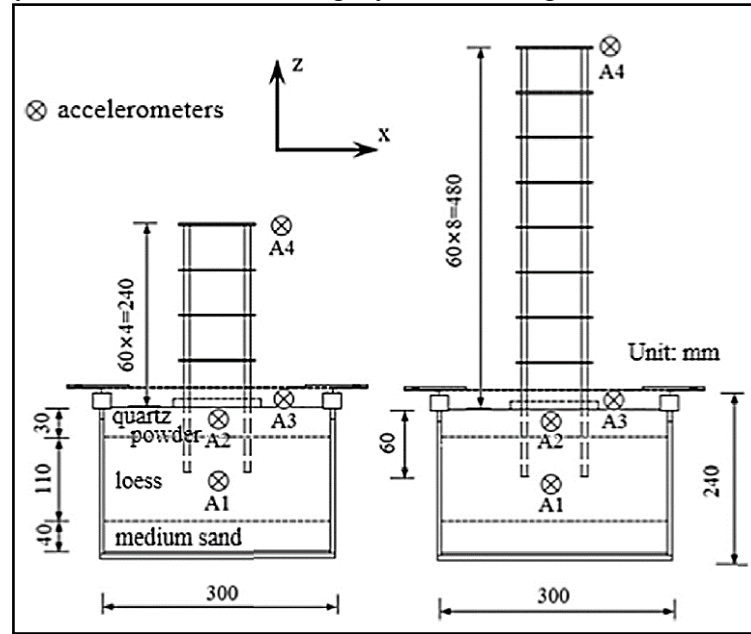
Figure 2-40 Arrangement of Sensors, (Zhang, Wei & Qin, 2017)

The study observed that predominant period and the system mode shape tend to be compatible, the amplitude of transfer function rises, the interface motion state is coordinated, and the modal damping ratios are identical. The SSI system can be considered as the engineered classical damping mechanism by selecting a dynamic analytical approach in practical projects (Figure 2-41).
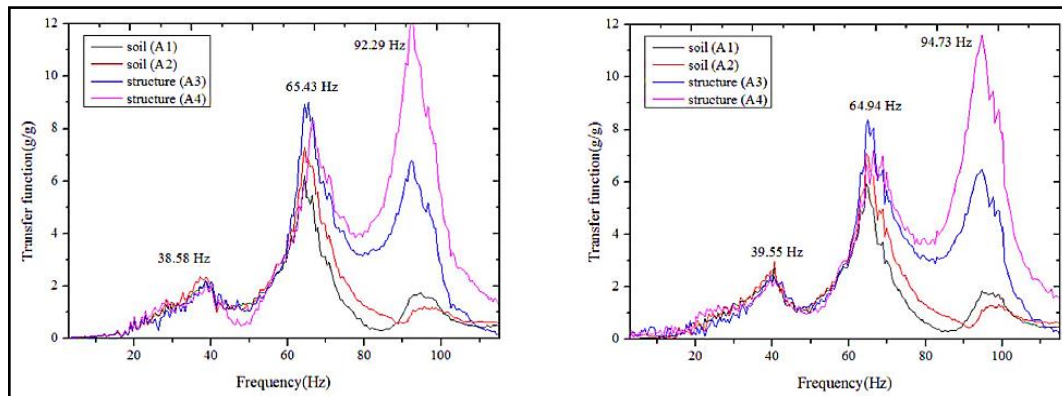
Figure 2-41 Transfer Function of the Four-Storey Model, (b) 1.0 g El Centro Wave (Test E5), (c) 2.0 g El Centro Wave (Test E7), (Zhang, Wei & Qin, 2017)

(Menglin *et al.*, 2011) reviewed the concept, development, research methods and available analysis platforms in the field of DSSI, based on systematic literature reviews and status of DSSI research that considers adjacent structures as a guideline for researchers. The study attempted to review the main and appropriate computer software; the benefits, drawbacks and existing challenges and the future trend in research in the

field. (Yang, Li & Lu, 2019) captured the effect of SSPSI on the dynamic behaviour of structure and soil by employing two groups of large-scale shaking table tests of 12 storey RC frame-founded pile group embedded in soft soil for two different test conditions, i.e. with (PS6) and without (RS6) considering SSI effect (Figure 2-42). The results revealed that SSPSI amplified the storey drift and peak displacements. However, the peak acceleration and base shear force of the structure were reduced (Figure 2-43).
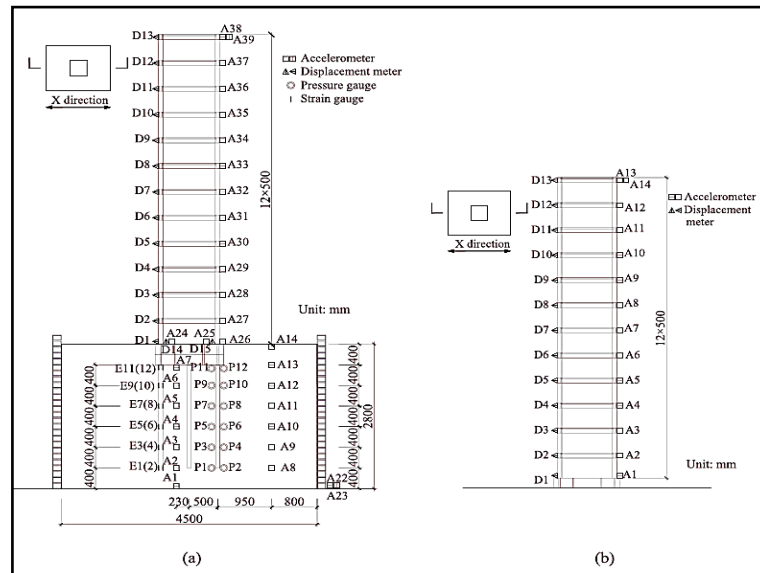
Figure 2-42 Experiment Setups for (a) (PS6) with SSI Effects and (b) (RS6) without SSI Effects, (Yang, Li & Lu, 2019)
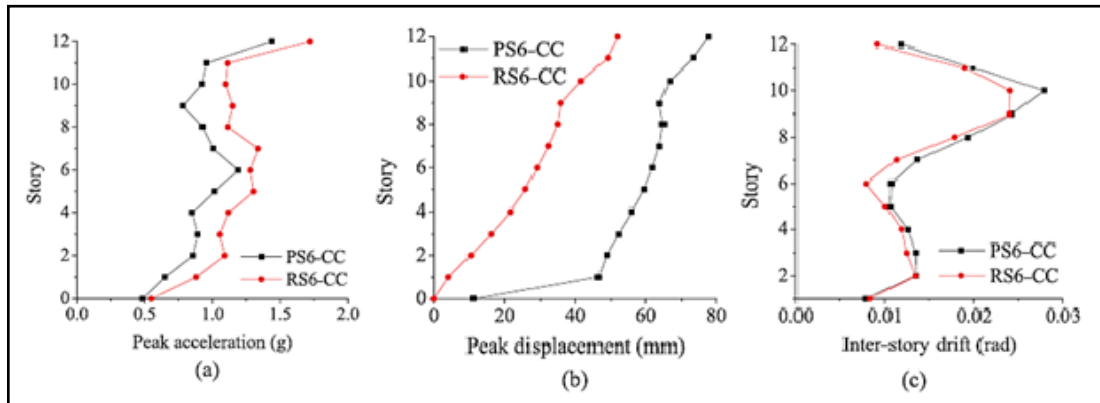
Figure 2-43 (a) Average Peak Acceleration of PS6 and RS6 Tests under the Excitation of Chi-Chi Earthquake, (b) Average Peak Displacement of PS6 and RS6 Tests under the Excitation of Chi-Chi Earthquake, and (c) Average Inter-Storey Drifts of PS6 and RS6 Tests under the Excitation of Chi-Chi Earthquake, (Yang, Li & Lu, 2019)

The study recommended that the DSSI should be considered realistically to offer insight into the realistic seismic design provision of structures founded on soft soils. (Xiong & Mao, 2019) addressed the comparison between dynamic and static pile behaviour because

59

of the high strain pile impact. The static load-settlement curve elevated gradually, and the side resistance along the pile developed prior than pile base resistance. The pile base showed hardening characteristics once the lateral displacement increased. The relative pile displacement is directly proportional to the ultimate frictional resistance. The larger the pile end bearing layer strength, the higher negative reflection of the measured velocity.

The bearing capacity of the high-strain test analysis is generally smaller than that of the static load test. The pile displacement at the top is significantly smaller than the one of static load test related to the ultimate bearing capacity of a single pile. (Yan *et al.*, 2020) investigated the seismic response. The damaged patterns of the tunnel lining with steel reinforced rubber joint passed through normal faulting in the laboratory. The results revealed that the damage of the lining with the joints generally occurred in the fault section because of the readjustment of joints. However, no shear failure was noticed in the test. Nonlinear 3D FEA models with and without joints using concrete damaged plasticity model were performed. The numerical results showed that the relative displacement significantly decreased for the case of without joints, whereas the failure location still at same positions. Good agreement was noted between the physical and numerical test. (Ramadan, Mehanny & Kotb, 2020) investigated the effects of non-synchronised motion on the seismic behaviour of a 430 m-long, nine-span bridge founded on deep pile embedded in three different sand soil ranging from medium to stiff soil, considering the effect of DSSI. The results proved that the wave passage and SSI effects substantially influence the seismic response of the structure and probability of exceeding life-safety limit state (see Figure 2-44). The selection of the input motion to predict the structure behaviour may significantly be affected by the two aforementioned aspects. This activity may lead to an overestimated prediction, particularly for situations of low velocity and with soft soil. (Lin *et al.*, 2020) examined the effect of structures position by studying the performance of bridges crossing fault experienced the surface fault rupture. The study investigated the seismic behaviour of SCCRFB frame supported by CFDST piers. However, for this purpose, a shaking table test with 1:10 scale factor in addition to 3D FEM has been employed. The results indicated that the residual pier displacements are very different. The numerical model can correctly predict the seismic responses and damages of the bridge. The damage mainly depends on rupture-structure relation position. Moreover, the transferred ground motion components resulting from different fault-crossing angles can produce different damages.

a) Apparent velocities (100m/s)

b) Apparent velocities (420m/s)

— ▲ — Soil (1) Flexible Base(βCL=0.1 - βM = 0.1)
— ▲ — Soil (2) Flexible Base(βCL=0.1 - βM = 0.1)
– ▲ – Soil (3) Flexible Base(βCL=0.1 - βM = 0.1)

— ■ — Soil (1) Flexible Base(βCL=0.2 - βM = 0.2)
— ■ — Soil (2) Flexible Base(βCL=0.2 - βM = 0.2)
– ■ – Soil (3) Flexible Base(βCL=0.2 - βM = 0.2)

— ● — Soil (1) Flexible Base(βCL=0.3 - βM = 0.3)
— ● — Soil (2) Flexible Base(βCL=0.3 - βM = 0.3)
– ● – Soil (3) Flexible Base(βCL=0.3 - βM = 0.3)

c) Apparent velocities (1000m/s)

Figure 2-44 Relative Change in Probability of Exceeding Life-Safety Limit State Because of Wave Passage Consequence Related to Uniform Excitation for Different Soil Circumstances. X-axis, (wave passage/uniform motions) -1, (Ramadan, Mehanny & Kotb, 2020)

2.7. Investigated Pile Seismic Performance

2.7.1. Post-earthquake observations

In this section, several case histories are presented to show a representative review of the detected pile damage and/or failure during severe earthquakes. The event details are comprehensive but not all-inclusive because many other cases prevail worldwide. Nevertheless, the enumerated instances contribute a remarkable indication of the dynamic SPSI and pile performance during strong shaking and insight into the system's behaviour and failure mechanism.

2.7.1.1. San Francisco earthquake (18 April 1906)

The 7.9-magnitude San Francisco earthquake caused intense damage at the boundaries of the historic shoreline, which was reclaimed with loosely dumped fill consisting of dune sand, silty sand and rubble (Figure 2-45). Underneath the fill is a soft bay mud, which is underlain by stiff cohesive soil (Seed et al. 1990). The enormous horizontal displacements and rupture length confused geologists (see Figure 2-46 a).
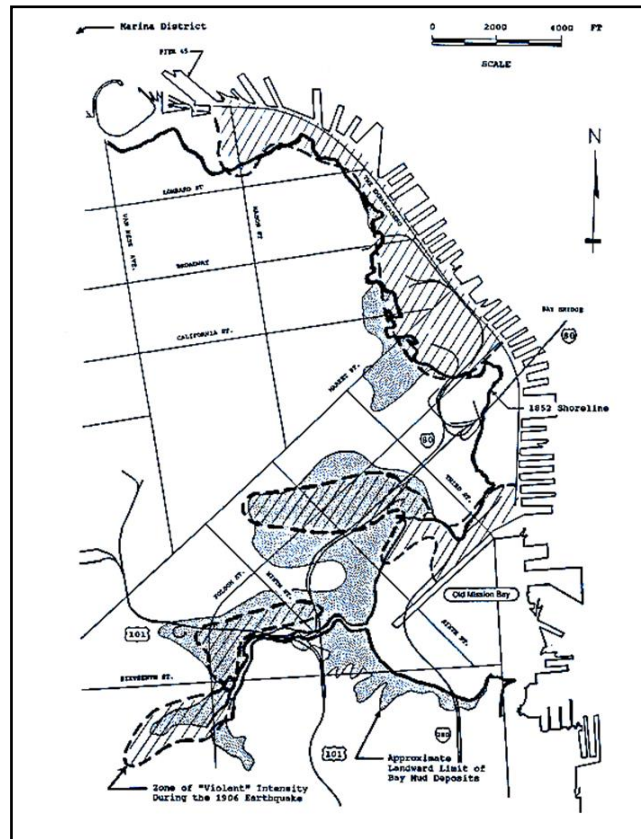
Figure 2-45 Regions Most Intensively Damaged During the 1906 San Francisco Earthquake and the Historic Shoreline, (Seed et al. 1990)

The analysis of the displacements and crust strain induced by the San Francisco earthquake inspired Reid (1910) to formulate the elastic-rebound theory of the earthquake source, which is represented by the current earthquake cycle principal models. A quantitative comparison between the 1906 San Francisco and 1989 Loma Prieta earthquakes was performed by David Wald (Figure 2-46 b). The records were processed using the same seismograph instrument in Gottingen, Germany. The displacement time history of the Loma Prieta earthquake is significantly smaller than that of San Francisco, which released around 16 times of the former's energy. The strong shaking induced the extensive liquefaction of the dune sand and the consequent failure of numerous buildings due to fire (Seed et al., 1990). The San Francisco earthquake was ranked as one of the most severe earthquakes in the world. The rupture was located in the northernmost 477 km San Andreas fault, from the northwest of San Juan Bautista to the triple junction at Cape Mendocino. The earthquake was a predominately right-lateral strike-slip with a peak horizontal displacement of 6.4 m (Wald et al., 2014).
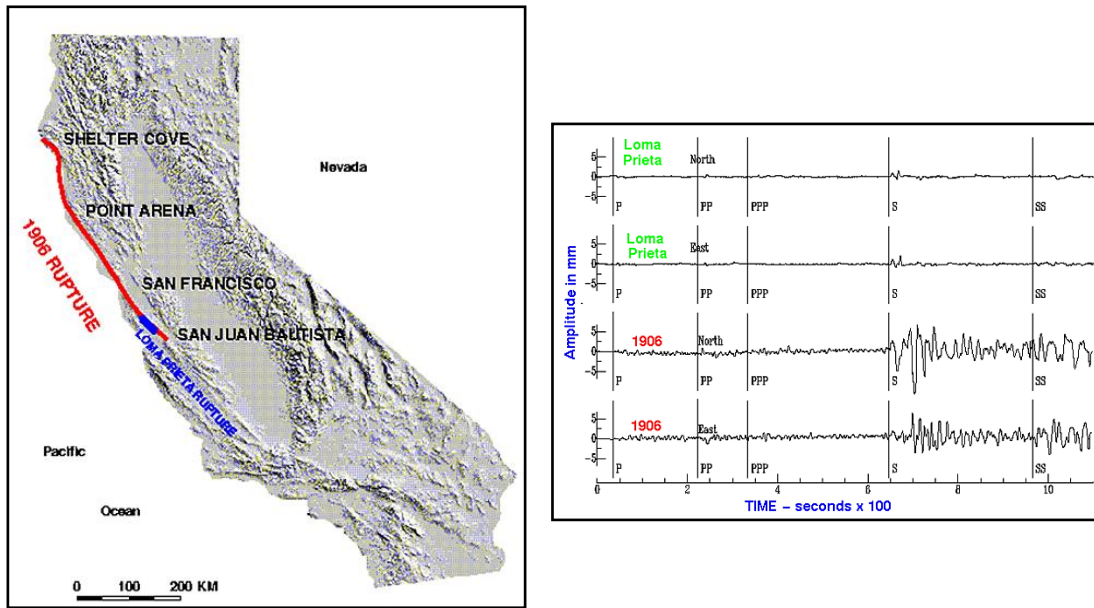
(a)   (b)

Figure 2-46 Comparison Between 1906 San Francisco and Loma Prieta Earthquakes (a) Fault Rupture, (b) Acceleration Time History Record at Gottingen, Germany, (Wald et al., 2014)

Some pile-supported structures suffered from broken concrete pile casings. However, class I structures established on deep pilings, such as the Ferry Building, did not experience severe damage (Lawson *et al.*, 1990). The southwest corner of the US Post Office building was on the edge of the filled marsh and experienced significant differential settlement as the ground deformed into excessive waves with a magnitude of at least 0.915 m, resulting in gaps and a severe compression strip. Differential settlements were also created amongst pile-supported cable car conduits, which settled about 0.61m beneath the tracks. Outside the city, many pile-supported bridges experienced failure. In Mendocino, the bridge across the Big River collapsed due to the pile's shifting, which caused a drop in the span. Wooden piles supporting the Gonzales Bridge with length of 23 m cracked and tilted at the southwest side. The south pier of the two-span Salinas Bridge, which comprised 26 piles, moved between 1.83 and 2.15 m to the south. The piles were unbroken at ground level, but the whole pier was inclined (Wood, 1908). At the Neponset county bridge, the piles bent and shifted more than 3.0 m towards the river. The ground spread laterally at the Moss Landing due to the movement of the railroad bridge piles towards the Salinas River before failing. In the Inverness, the underlying tidal mud has been dragged towards the bank in a ridge and was deformed into two light wooden

piers built on timber piles. Figure 2-47 displays the piles located on the firm ground and the tilted mud.
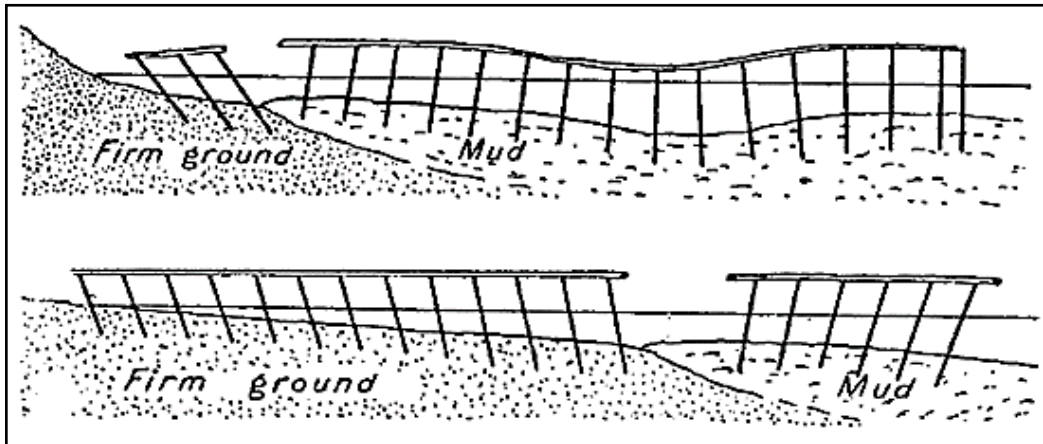
Figure 2-47 Deformation of Pile-Supported Inverness Piers due to Lateral Spreading, (Wood, 1908)

2.7.1.2. Alaska earthquake (27 March 27, 1964)

The 9.2-magnitude 1964 Alaska earthquake caused extensive damage to highway bridges. The earthquake rupture began around 25 km below the soil surface (Figure 2-48), producing an estimated peak ground acceleration PGA of 14–0.18 g (Alaska, 1968). The fault type was a reverse fault induced by a compressional force (Figure 2-49).
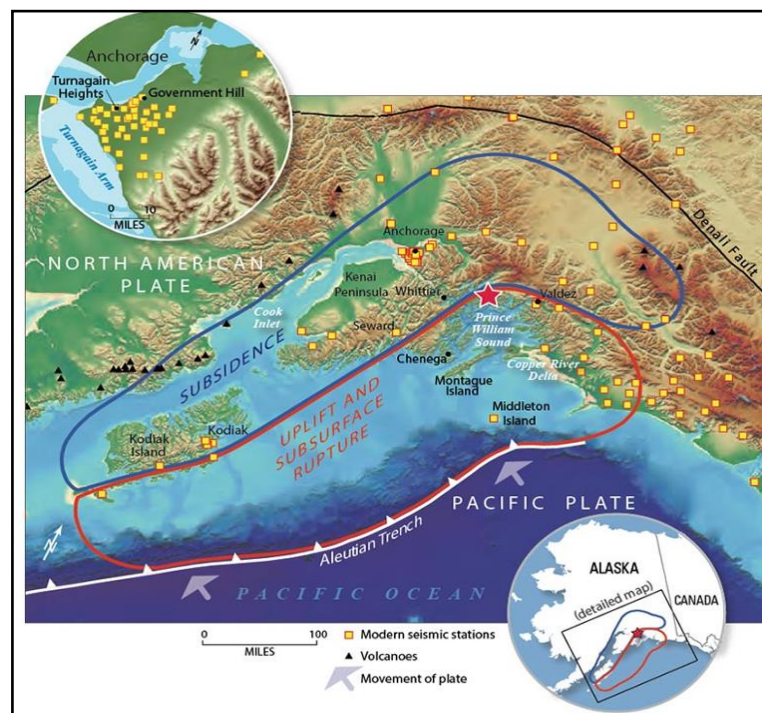
Figure 2-48 Map of Southern Alaska Showing the epicentre of the 1964 Alaska Earthquake, (Alaska, 1968)
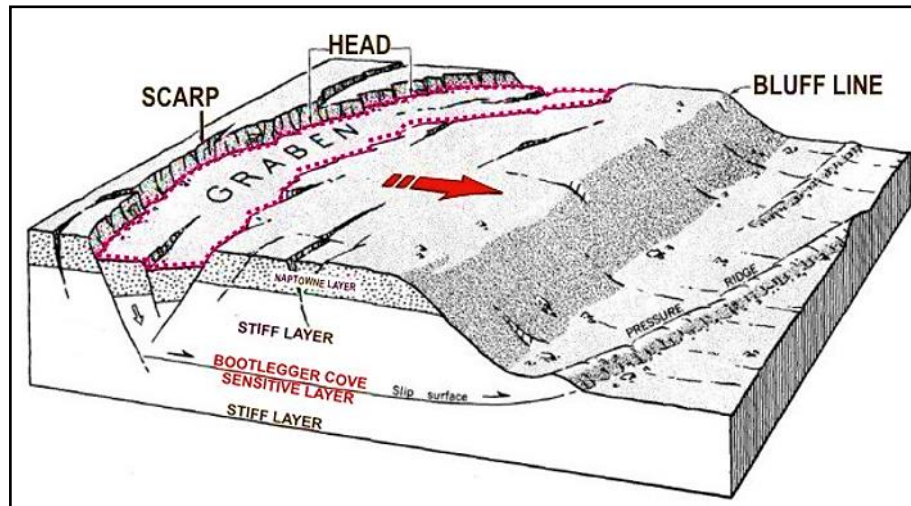
Figure 2-49 Schematic of Fault Movements of the Alaska Earthquake on 27 March 1964, (Pontbriand, 2014)

The intensity of the damage was related to the sensitivity of the soil to liquification rather that the vicinity to the epicentre. (Ross, Seed & Migliacio, 1973) and (Dickenson, Barkau & Wavra, 2002) conducted a comprehensive survey to reveal the pile damage due to the earthquake. Four bridges over the Snow River on the Seward Highway, which were made up of wooden piles founded on fine granular soils, sustained various degrees of damage. The piles of Bridge 603 were driven towards the bedrock and caused minor damage to the bridge. Bridge 604 experienced significant settlement of the abutments. The timber piles of Bridge 604 had been driven 12.0–18.0 m through the inter-bedded fluvial soil with a standard penetration test (SPT) blow count of N = 5 – 10, but the bridge was destroyed due to the driving of the abutments against each other, and the bends of the timber experienced a settlement of 3.0 m (see Figure 2-50). At the time of the earthquake, the foundations for Bridge 605 A were under construction. The soil deposit experienced liquefaction-induced foundation failure in the heavy piers, each of which were supported by 21 steel pipes filled with concrete piles extending 27.5 m deep and has a lateral displacement and inclination of 2.44 m and 15°, respectively (see Figure 2-51). The two Seward Highway bridges over the Resurrection river with similar construction and with similar silty sand gravel soil deposit (N = 30 – 60) exhibited contrasting behaviours. Both bridges suffered lateral displacement in abutments (towards the river) but Bridge 596 experienced a slight clearance between the abutment and the pier. The movement applied substantial lateral loads, resulting in severe damage to the bridge.

Figure 2-50 Snow River Bridge 605 Collapse due to Liquefaction, (Ross, Seed & Migliacio, 1973)
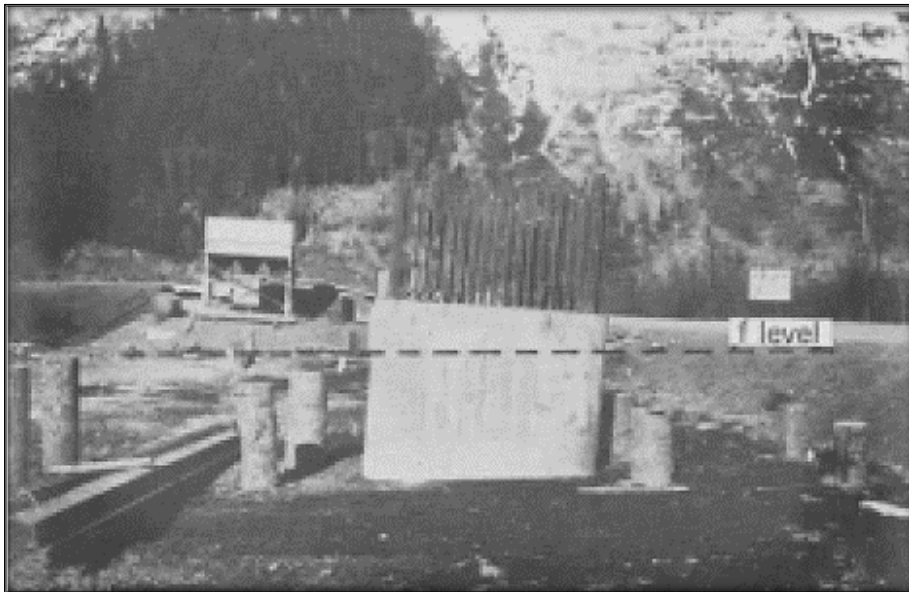
Figure 2-51 Tilt (15°) of the Foundations of the Snow River Bridge 605A due to Liquefaction, (Dickenson, Barkau & Wavra, 2002)

Bridge 598, which was designed with a large separation between the abutments and piers, sustained only moderate damage (Dickenson, Barkau & Wavra, 2002). Many bridges on the Seward Highway in the Turnagain Arm area experienced serious damage and entirely or partially collapsed (see Figure 2-52).

Figure 2-52 Concrete Deck of Bridge 629 that Collapsed due to Penetration by Timber Piles, (Dickenson, Barkau & Wavra, 2002)

The collapsed bridges consisted of concrete superstructures established on timber piles resting on a gravel layer over inter-bedded silty sand and underlain with silt deposit. The SPT blow counts ranged between N = 15 – 30 (closes to the surface) and N = 35 − 85 (at the base of piles). The structure experienced damage including collapsed decks, twisted and shifted timber bents and abutments. In the Copper Highway, 25 bridges extending across the Scott and Sheridan Glaciers' outwash plains suffered severe damages due to soil liquefaction. Some brittle rail piles were sheared near the head (e.g., Figure 2-53).
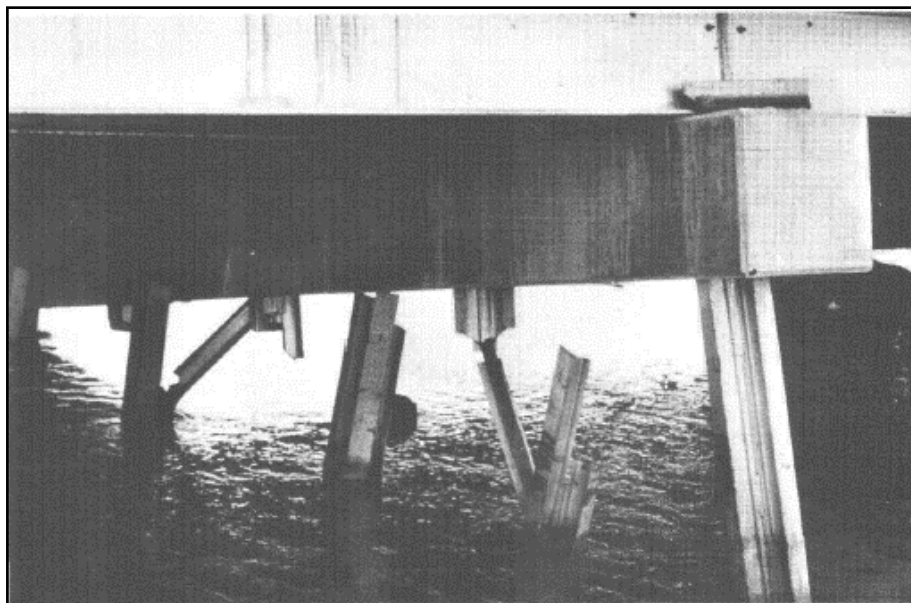
Figure 2-53 Sheared Rail Piles on Scott Glacier Bridge 6, (Kachadoorian, 1968)

In the Scott Glacier region, timber and rail pile bents were assembled on loosely to moderately dense silty sands (SPT N = 10−20) with a percentage of organic components. The soils deposit in the Sheridan Glacier area comprised of loose sand and gravel (SPT N = 5−10) in depths above 6−7.6 m level but were denser (SPT N =15 − 50) at the deeper levels. Moreover, most of the 19 Copper River Delta bridges exhibited moderate to serious deformations, and at least six spans collapsed. Although the information of the soil profile during Ross and Seed's (1973) survey was unknown, considerable evidence of liquefaction in this area was observed. The Million Dollar Bridge collapsed due to the abutment and stream-bed rocking (Figure 2-54).
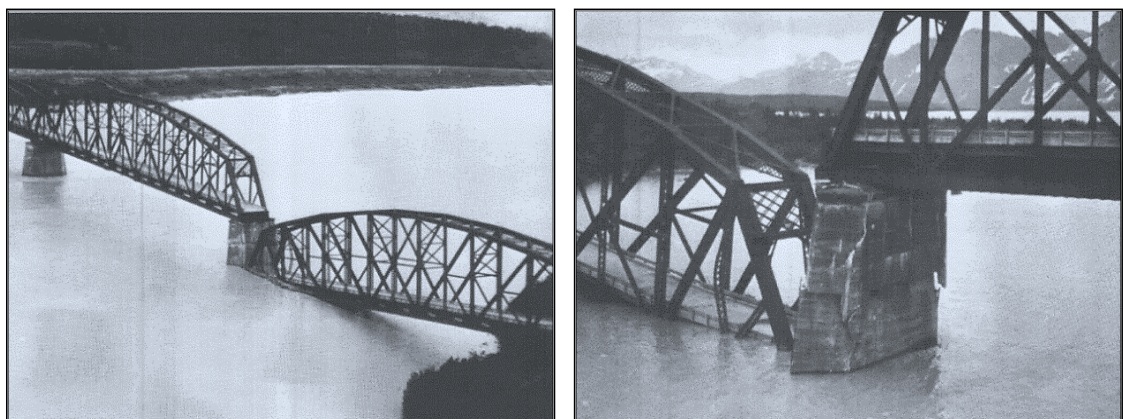
Figure 2-54 Collapse of the Million Dollar Bridge, (Kachadoorian, 1968)

The 1966 US Geological Survey delivered a report including the description of the pile damage, as well as the effect of the pile displacement on the stress condition in Anchorage, which was one or a combination of the following (Waller & Stanley, 1966):

- *At the top of the pile:*
a. A bending moment has been induced at the pile cap due to the rigid connection.
b. Under the rigid connection, the pile has yielded, resulting in an indeterminable residual bending moment.
c. The concrete has cracked due to the induced failure of connection and exhibited slight or no bending moment.

- *At the tip of the pile:*
a. The soil and pile base constraints resulted in a bending moment.
b. Under the above-mentioned constrain and yielded pile condition, a residual bending moment is induced and blew the mud line.
c. The rotation of the pile dismissed the bending moment.

68

- *Along the pile length:*

a. The pile yielded and was deformed, maintaining bending moments in a quantity that depends on the depth.

The resulting dynamic pile loading sequence is various and complicated. On the one hand, piles that experienced substantial stiffness reduction at the end but remained straight were able to maintain loads along the length by exerting a horizontal load to the dock, which was transmitted to the other piles according to the SSI concept. On the other hand, piles that maintained stiffness at one or both ends and experienced deformation along the axis experienced combined loads of axial and bending stress. The bending stress generated in the piles resulted in a reduction in the pile load capacity. This highly robust analysis is a comprehensive investigation of the complicated seismic SPSI system. The inadequate pile response is particularly apparent due to the pile's horizontal load association; the load was transmitted to the structure and to other piles.

2.7.1.3. Niigata earthquake (16 June 1964)

The second major earthquake in 1964 is the Niigata earthquake, which has a magnitude of 7.3 and a reverse dip–slip faulting with predicted PGA of 0.245 g. The epicentre was about 50 km from Niigata City and possessed a deep focal depth of 34 km. The Niigata earthquake produced extensive liquidation and numerous structural failures. (Seed & Idriss, 1967) related the building damage trends and the associated damage intensity to the SPT blow count of soil and the embedment depth of the foundation. (Nakakuki, 1986) recorded many specific cases of pile damage caused by liquefaction at sites where the piles are pushed into loose sand soil with an SPT of $N = 5 - 10$. In Saiseikai Hospital, a 7.2 m-long concrete piles of 0.18 m diameter experienced bearing capacity failure because of the liquefaction, thereby causing the structure to tilt and crack (Figure 2-55).

Piles with similar specification at the Ishizue Primary School also experienced bearing capacity failure, and the differential settlement caused substantial damage to the structure (Figure 2-56). The East Police Station did not experience significant damage, although soil liquefaction occurred. A post-earthquake investigation showed that the concrete piles cracked at the head and formed pile–cap connection positions (Figure 2-57). A direct consequence of the liquefaction of the top loose sand layer was the failure of the Showa River Bridge, in which ten spans with a length of 307 m have collapsed (Figure 2.58 and Figure 2.59). (Yoshida *et al.*, 2007) and (Fukuoka, 1966) investigated the post-earthquake failure and restoration of the damaged piles.
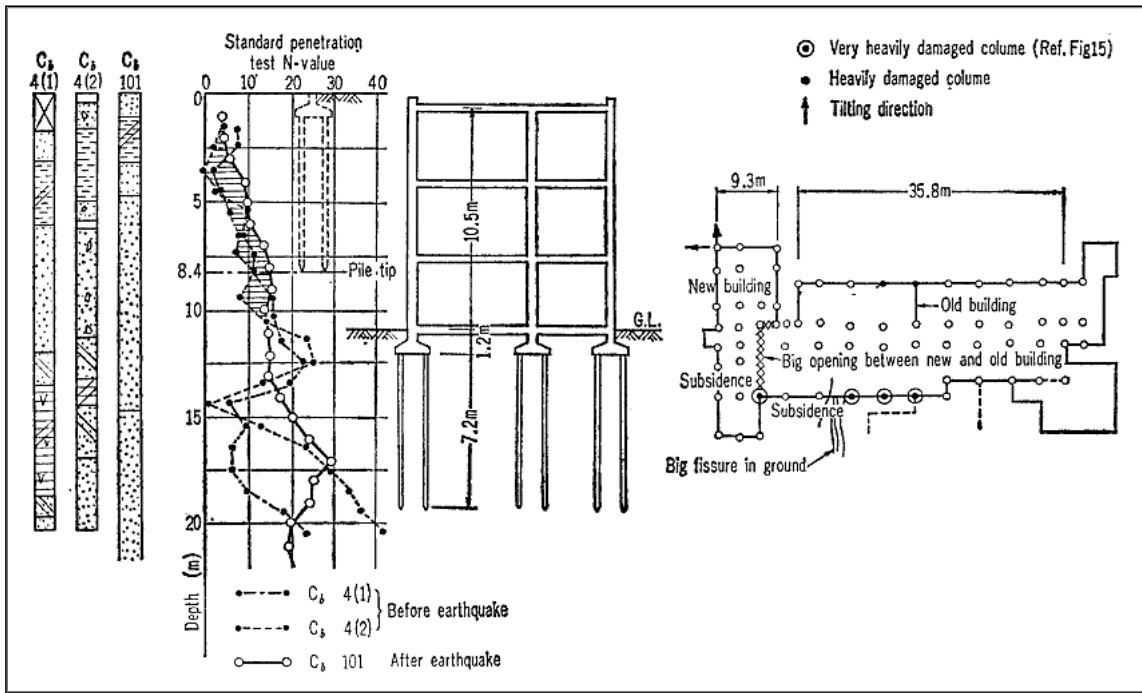
Figure 2-55 Saiseikai Hospital, (Nakakuki, 1986)
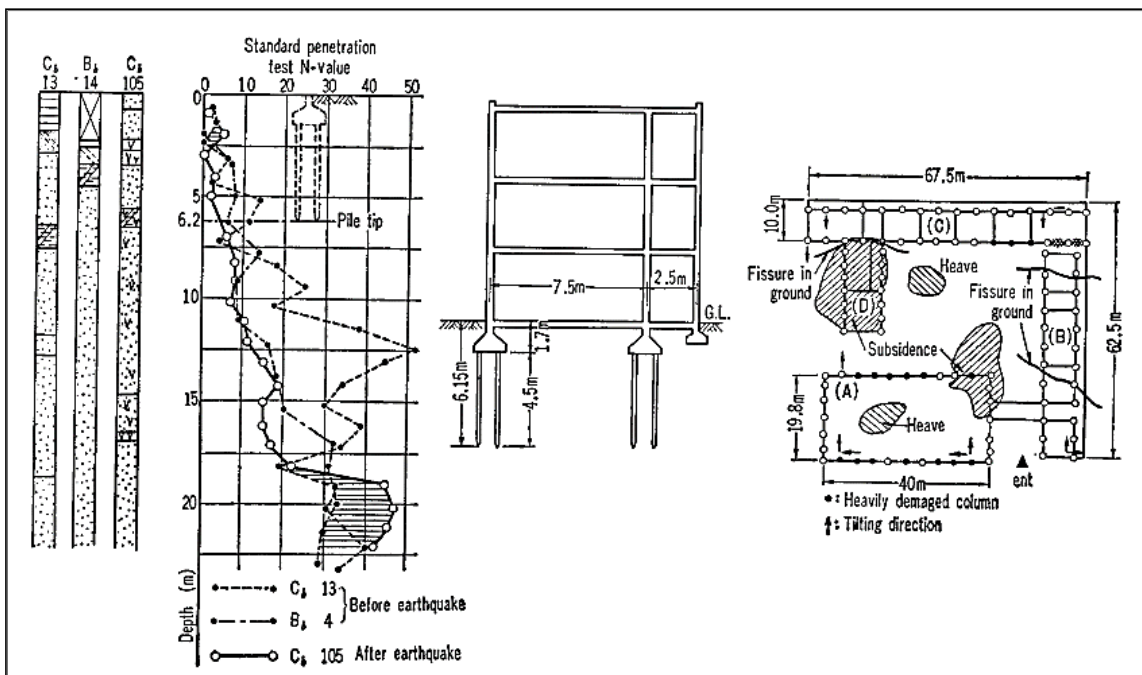
Figure 2-56 Ishizue Primary School, (Nakakuki, 1986)
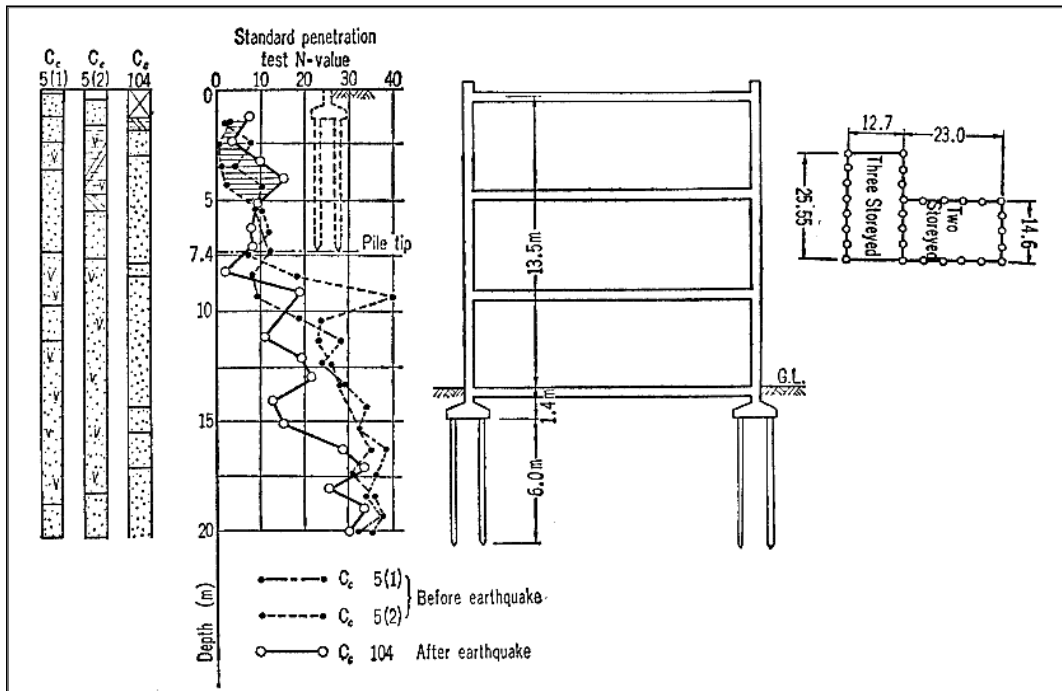
Figure 2-57 East Police Station, (Nakakuki, 1986)
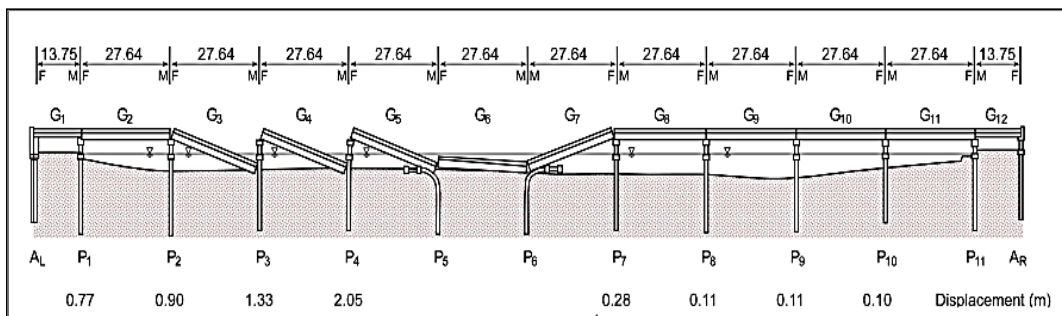
Figure 2-58 Elevation of the Showa Bridge, (Yoshida *et al.*, 2007)

Figure 2-59 Collapse of Showa Bridge due to Liquefaction, (Yoshida *et al.*, 2007)

Figure 2-60 displays the permanent displacement of the pile head, which is approximately 1 m, the transition zone between the loosely and moderately dense sand and the local buckling located at the mid-elevation of the profile depth. A robust structural response has been detected due to resonance consequences, which transmitted significant inertial forces into the piles and produced local buckling.

Another liquefaction consequence describing pile failure mechanism was addressed by (Hamada, 2000) and Hamada (2014), in which the permanent ground displacements during the Niigata earthquake were appraised from aerial photographs and correlated to the damage detected in the piles excavated 20 years after the earthquake. A 12 m-long concrete pile with a diameter of 0.35 m supporting the NHK Building have cracked at two locations (near the pile's top and bottom part) and tilted towards the direction of the permanent ground displacement. During the reconstruction of the Niigata Family Courthouse, similar damages were revealed, including the severe damages near the pile head and at the boundary between the liquefied and non-liquefied soil layers (Figure 2-61 and Figure 2-62). (Yoshida & Hamada, 1990) compared the liquefaction-related damages in the Niigata Family Courthouse and in the NHK building. The soil profile, patterns of pile deflection and patterns of pile crack are illustrated in Figure 2-63. (Nishizawa, Tajiri & Kawamura, 1984) reported that the Daiyon Bank's three storey branch office settled up to 1.3 m and inclined, but sustained only minor structural damages. This building was demolished in 1984, and the severely damaged original precast concrete piles were revealed during the excavation. The piles experienced damaged in two zones: at the maximum bending moment position and near the base where a stiffness contrast in the soil layers raised. The fact that the structures remained in service without any indication of the damaged foundation condition illustrates the complexity of predicting pile performance and/or damage during and after earthquakes.
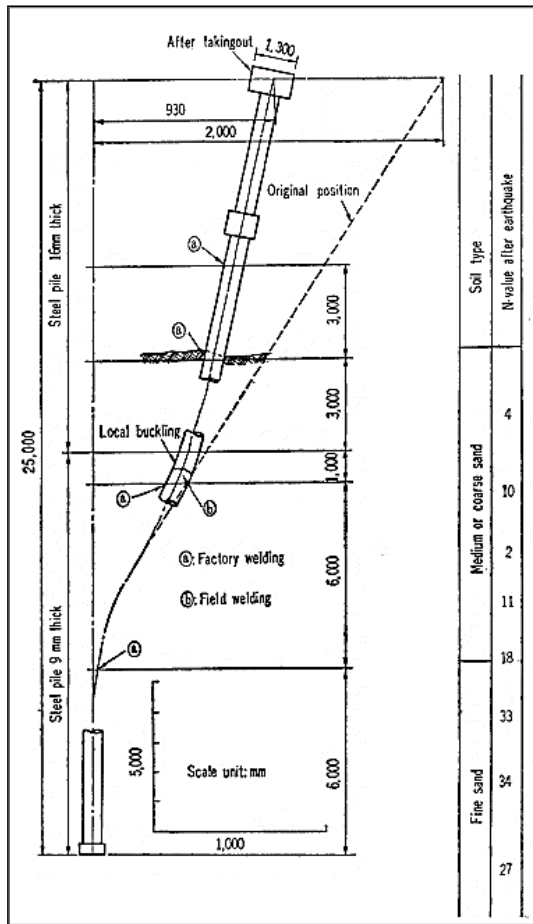
Figure 2-60 Permanent Deformation of Piles Extracted from Showa Bridge, (Fukuoka, 1966)
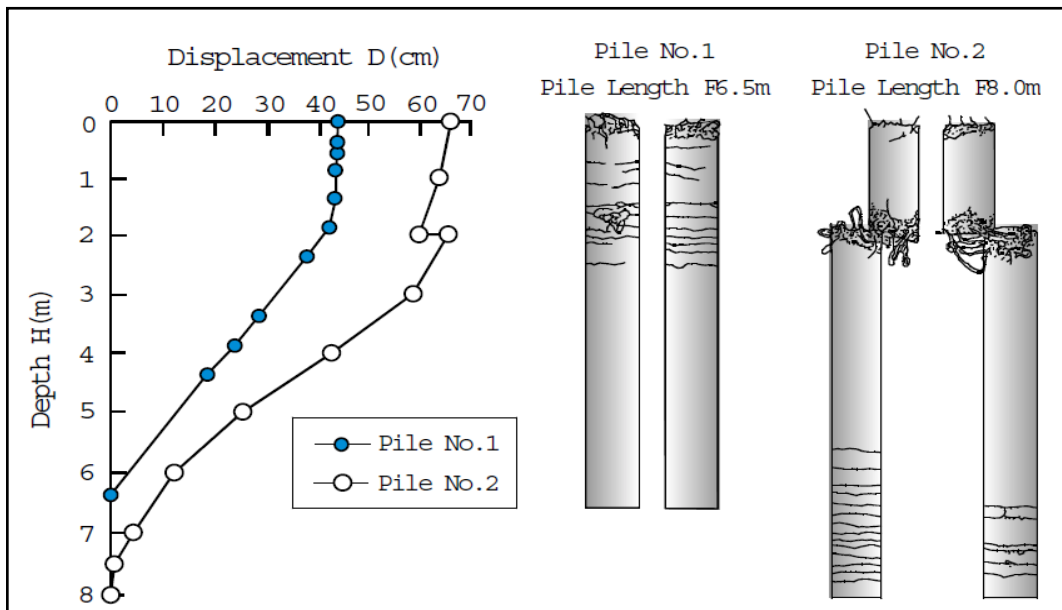
Figure 2-61 Damaged Form of Piles Supporting the Niigata Family Courthouse, (Hamada, 2000)
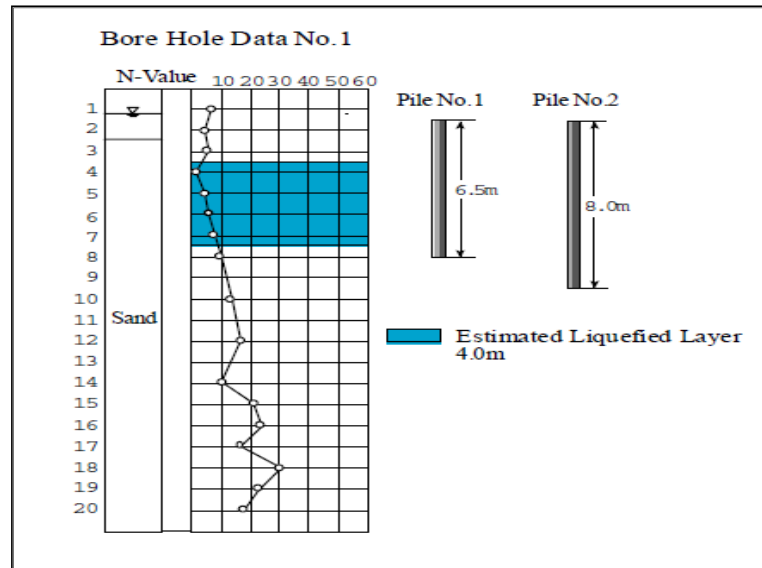
Figure 2-62 Soil Condition and Expected Liquefied Soil, (Hamada, 2000)
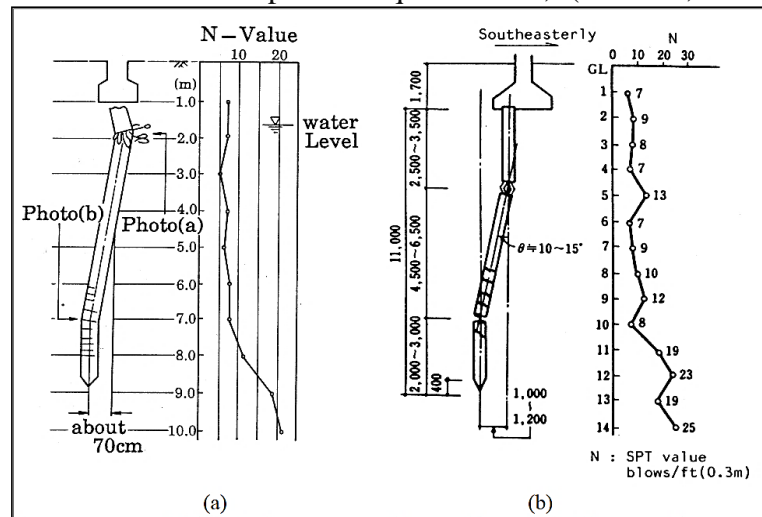
Figure 2-63 Correlation of Pile Damage to Site Conditions at (a) Niigata Family Courthouse and (b) NHK Building, (Dobry, 1995)

2.7.1.4. San Fernando earthquake (9 February 1971)

The San Fernando earthquake was classified as a major earthquake from an engineering perspective. This earthquake has a 6.5 magnitude, 8.5 km depth and oblique thrust fault type and 0.7 g PGA (see Figure 2-64 above). Given the major consequences, Jennings (1971) collected numerous research and reports from a wide variety of resources that describe the engineering features of the earthquake. The Building Science Series published the research results, test methods and performance criteria associated with the engineering aspects of the 1971 San Fernando earthquake (Lew, Leyendecker & Dikkers, 1971). The report provides the documentation of the induced damage to serve as reference for further research.

74
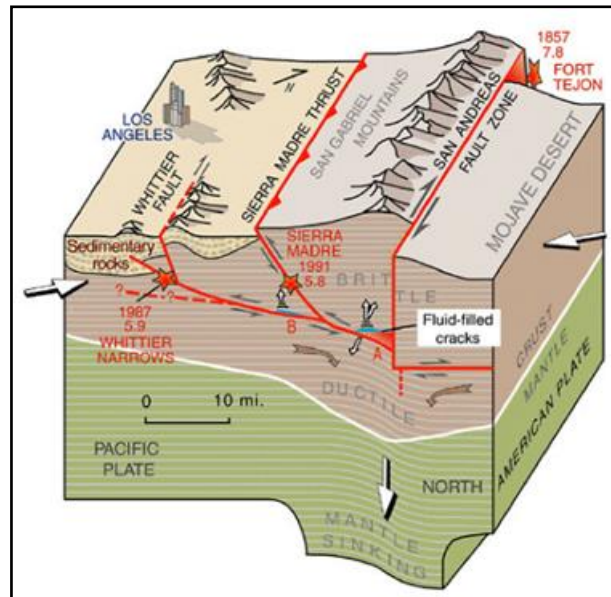
Figure 2-64 . Schematic of Fault Movements of San Fernando Earthquake on 9 February 1971

The epicentre of this earthquake was located less than 16 km from four major freeway bridges. Fifteen bridges experienced substantial damage. The Golden State Freeway/Foothill Freeway Interchange experienced the collapse of seven concrete box girder spans; such spans were supported on single columns, which were lap-spliced into single 1.83 m diameter drilled piers. The soil conditions at this junction consisted of dense silty sand. Failure was intense at the base of the columns, where the bond failed in the main reinforcement bars of the pile. No damage was observed on the deck nor abutments at the Foothill Freeway's Roxford Street Undercrossing, but the piles supporting one abutment were found to be severely damaged in the subsequent excavation to repair a wingwall. This supports the inference about the Niigata earthquake, in which overtly undamaged structures may conceal seismic pile damage.

2.7.1.5. Mexico City earthquake (19 September 1985)

The epicentre of the 8.1-magnitude earthquake was approximately 400 kilometres from Mexico City, but a convergence of the site response factors resulted in the significant damage of the 'Lake Zone' of Mexico City. The 20 km deep normal dip–slip fault type with a PGA of 0.17 g. The seismic waves were productively filtered in long periods because of their movement through the deep soft clay deposits in the Mexico City region. The shaking intensity was considerably amplified to a period of approximately 2 s. This motion of low frequency induced resonance of many structures of intermediate height, causing significant damage and/or failure, especially for those supported by friction piles (Stone & Yokel, 1987). A survey of the types of pile foundations employed in this area

is crucial before defining the damage mechanism of pile-supported structures (Figure 2-65).
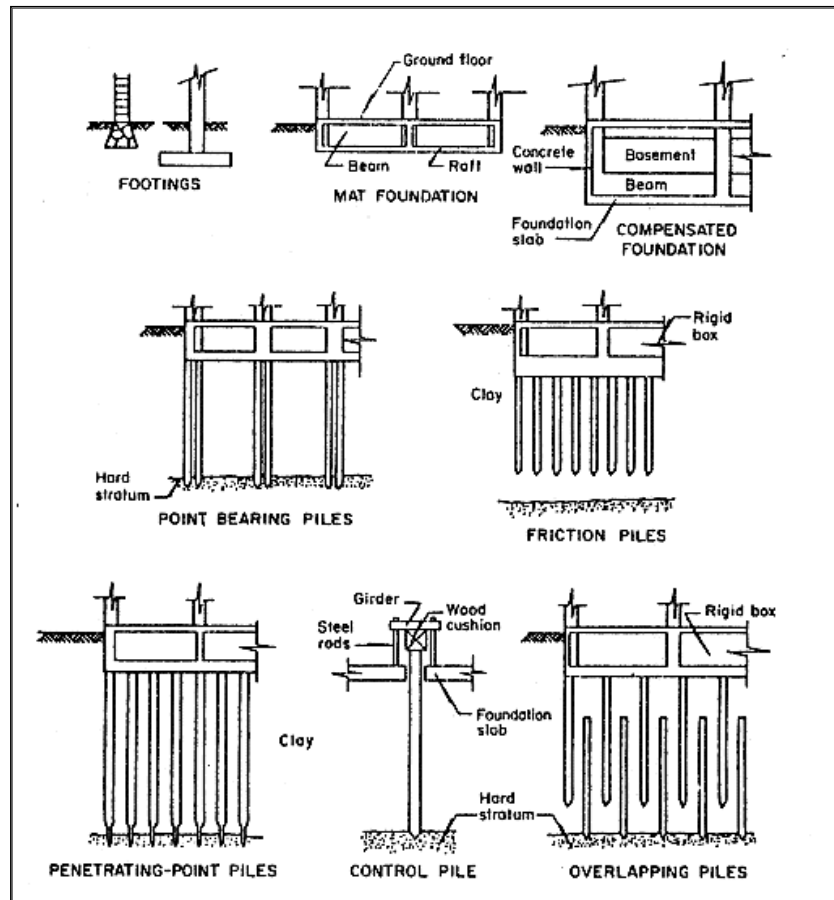
Figure 2-65 Types of Foundations Used in the Soft Soil of Mexico City, (Mendoza & Auvinet, 1988)

The main concerns of the foundation design in Mexico City's highly compressed clay are that they are designed according to settlement limitations and the negative skin friction influences in deep foundations are considered. Friction piles are employed without compensated foundations for light structures and with compensation for medium weight structures. Many structures are placed on end-bearing piles with 'hydraulic-control' devices on their heads to enable the pile to penetrate the foundation slab. The slab is then permitted to settle at the same rate as the surrounding soil. The control systems are usually provided by wooden blocks that compress and hydraulically operated jackets at a predetermined speed rate (Mendoza & Auvinet, 1988). According to (Girault, 1986), 25 buildings founded on raft-friction piles foundation system have tilted after experiencing significant differential settlement (up to 1.30 m). The mechanism of these settlements was due to loosening of the pile-negative skin friction as a result of the reduction in soil shear strength when the sensitive clays were loaded cyclically. (Mendoza & Auvinet, 1988)

76

stated that low safety factors and soil–pile stress condition be close to yielding concerning static loading accelerate foundation failure under seismic loading. Overturning and tilting of the building due to cyclic loading may have been aggravated by P–δ influences associated with inadequacy of plumpness of continually settling structures. For instance, a 10-storey building entirely overturned, as one side dipped roughly 6 m into the soil and the other lifted out 3 m, pulling the piles out. The site profile and damage to this structure are shown in Figure 2.66

(a)

(b)
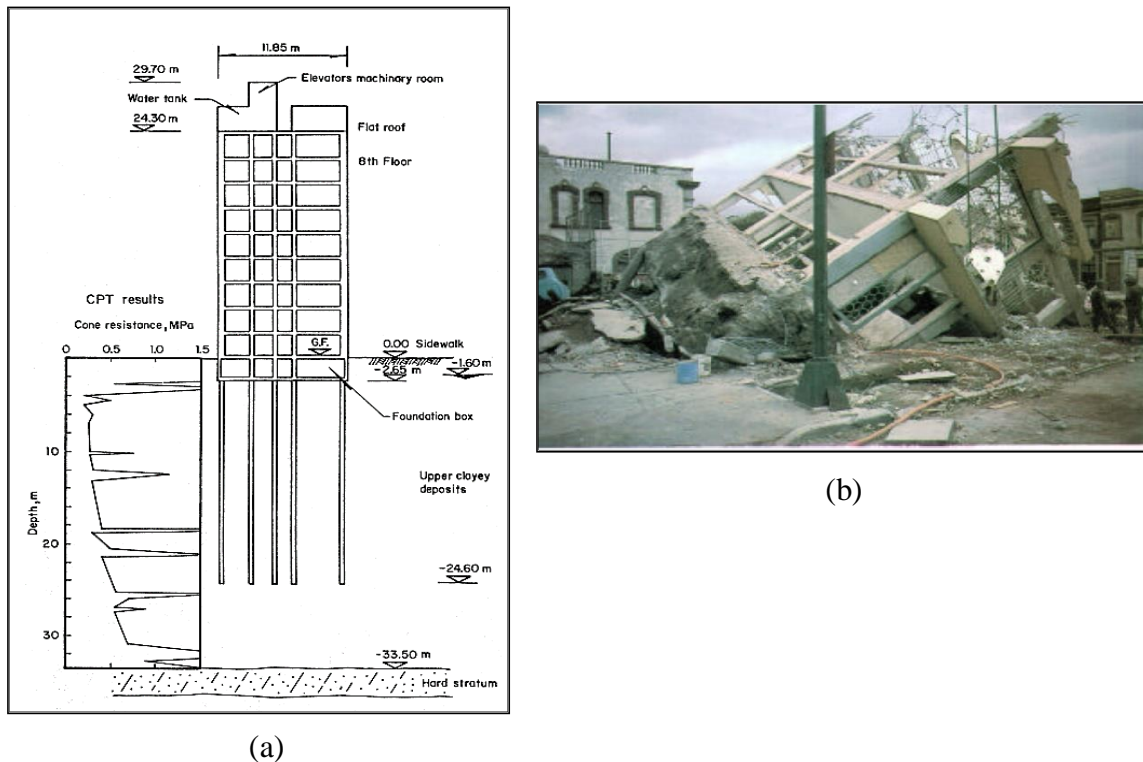
Figure 2-66 Ten Storey Pile-Supported Building Founded on Soft Soils: a) Elevation Including Geotechnical Conditions, b) Overturned Structure, (Mendoza & Auvinet, 1988)

The performance of the structures rested on base-bearing piles were better than those based on friction piles, with smaller settlements and less structural failures. Slender structures with hydraulic-control piles that underwent tilting because of the wooden blocks were damaged, and hydraulic jacks burst. However, the hydraulic-control devices were not designed to maintain seismically inertial loads. In summary, the cyclic strength degradation which contributed to a partial loss of soil–pile friction were the main sources of failure of pile because of the structural resonance overturning moments.

2.7.1.6. Loma Prieta earthquake (17 October 1989)

The 7.0-magnitude Loma Prieta earthquake is an oblique-slip faulting with PGA of 0.07 (g). The epicentre was roughly 14.5 km northeast of Santa Cruz, 96.5 km south-southeast

of San Francisco with a relatively deep focal depth of 18.5 km, as shown in Figure 2-67. Loma Prieta earthquake produced a dramatic failure for many pile-supported structures. The Cypress Freeway supported piles were founded along an alignment which transitioned from stiff to soft soil deposit. However, the site response and the connection of the structure elements were the principal mechanisms of the failure of the structure. The SSPSI contributed a significant component of the structural seismic response of the San Francisco–Oakland Bay Bridge, which experienced a primarily structural failure. In Watsonville, the Highway One Bridge across the Struve Slough which was a pile-supported bridge collapsed. Several piles punched through the slab (see Figure 2-68), (Seed et al., 1990). Soil liquefaction did not contribute to the bridge failure. The upper soil comprised organics soft clays with alluvial sand. The piles showed no signs of settlement. However, gaps of 30–45 cm wide created between the soil and pile circumference, revealed inadequate pile shift strength (Figure 2-69), which indicated excessive lateral pile displacement in addition to flexural and/or shear failures to bent connections (Figure 2-70).

(Yashinsky, 1998) offered a comprehensive overview of road damage in the Loma Prieta earthquake, including many examples of pile-supported bridges founded on soft soil. These included the Southern Freeway Viaduct, the China Basin Viaduct, the Embarcadero Viaduct, and the Terminal Separation Structure, in San Francisco. The Route 92/101 Separation Interchange in San Mateo, the Mococo Overhead in Martinez, the Napa River Bridge in Vallejo, the Richardson Bay Bridge near Marin City, and the San Mateo–Hayward Bridge suffered minor damage. These structures did not exhibit foundation failures, although the performance of the foundation contributed to the structural response and subsequent damage of structures.
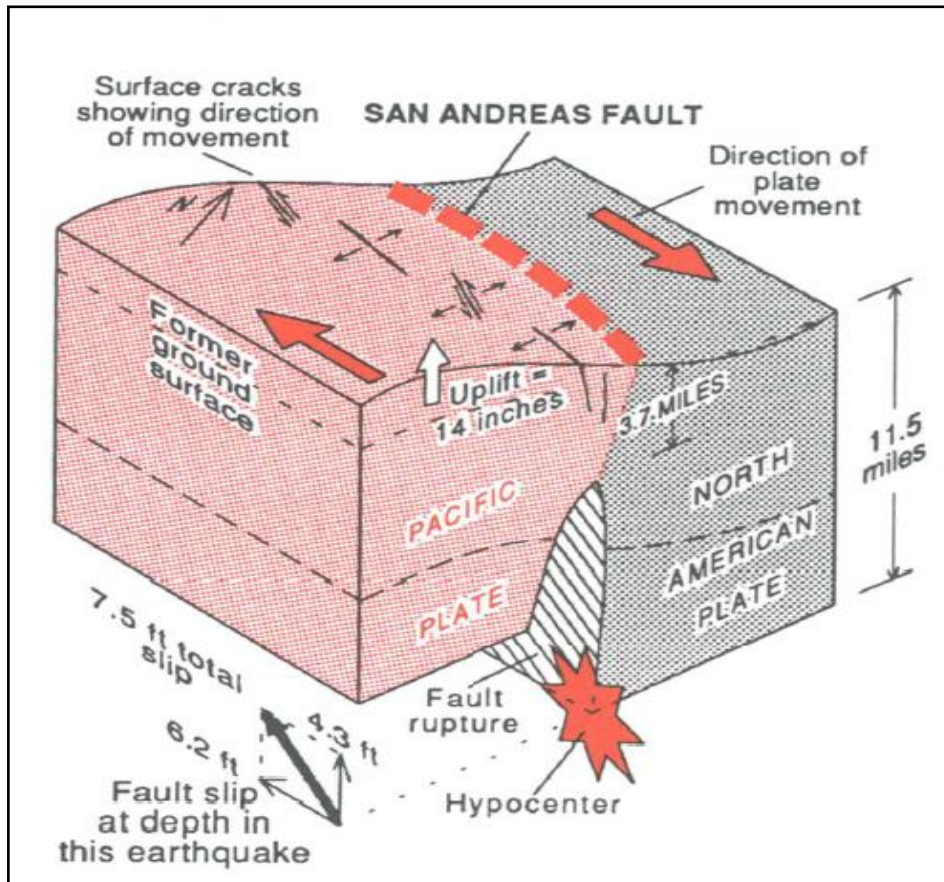
Figure 2-67 Schematic of Fault Movements of Lorna Prieta Earthquake on 17 October 1989, (Seed et al., 1990)

Figure 2-68 Collapse of Highway One Crossing Struve Slough due to Pile Punching Through Deck, (Seed et al., 1990)

Figure 2-69 Creation of Gap Between the Soil and One of the Piles Supporting the Collapsed Struve Slough Crossing, (Seed et al., 1990)

Figure 2-70 Flexural Shear Failure of Pile-Bent Connection of the Struve Slough Crossing, (Seed et al., 1990)

2.7.1.7. Costa Rica earthquake (22 April 1991)

The 7.5-magnitude Costa Rica earthquake caused severe damage over a large area, including liquefaction related collapse of several pile-supported bridges (Carvajal-Soto *et al.*, 2020). The three-span Rio Banano Bridge was located at a river crossing that showed extensive signs of liquefaction. The south abutment rotated approximately 9°, causing movement of the 36 cm square precast concrete piles 66 cm towards the river (Figure 2.71).

The front battered piles suffered flexural and shear damage, but the vertical piles at the rear showed less damage, as shown in Figure 2-72, (Ravazi, Fakher & Mirghaderi, 2007). Two of the three spans on the Rio Viscaya Bridge collapsed because of severe abutment rotation, pile distress and failure of one interior support, also resulting from extensive soil liquefaction (Figure 2-73). The two-span Rio Bananito Bridge suffered collapse of the central pile-supported pier because of liquefaction, and both abutments experienced slumping and rotation towards the river.

Figure 2-71 Rotation of Rio Banano Bridge Pile Cap, due to Liquefaction, (Ravazi, Fakher & Mirghaderi, 2007)

Liquefaction in the river channel caused rotation of 2.1 m-diameter steel caissons supporting the Rio Bananito rail bridge, which tilted the bridge downstream. Steel caissons supporting the Rio Matina rail bridge experienced similar damage. At the Almirante port facility in Panama, concrete pilings supporting a railroad trestle were sheared at the head. Priestly et al. (1991) observed that inadequate pile penetration into stable materials contributed to structural failures. However, this justification made by Priestly disregards the warnings from 1964 which indicated that liquefaction merely in the upper soil layers can also cause structural failure.

Figure 2-72 Differentiation Damage Induced to Front Batter Piles of Rio Banano Bridge, (Ravazi, Fakher & Mirghaderi, 2007)

(a)   (b)

Figure 2-73 Damaged Piles of (a) the Rio Viscaya Bridge and b) Rio Viscaya Bridge due to Liquefaction, (Ravazi, Fakher & Mirghaderi, 2007)

2.7.1.8. Hyogoken-Nanbu (Kobe) earthquake (17 January 1995)

The 7.2-magnitude Kobe earthquake had a strike-slip faulting with PGA of 0.35–0.85 (g), and epicentre of roughly 17.6 km. Figure 2-74 shows that the soil map of Kobe City area (Huzita & Kasama, 1983). When it happened, the Kobe earthquake was the most destructive earthquake to strike Japan in over 60 years. The earthquake was a direct hit on a major metropolitan area, which resulted in the devastation of all modes of infrastructure, and losses exceeding 200 billion dollars (U.C. Berkeley, 1995). Damage to piles due to soil liquefaction was observed in a variety of locations. The number of instances are shown in this section. During the Kobe earthquake, the most dramatic structural failure was for an elevated section of the Hanshin Expressway, a pile-supported structure (Figure 2.75).(Gazetas & Mylonakis, 1998) reported that during the earthquake,

period lengthening owing to foundation flexibility may result to increased structural forces, as shown by the response spectra from near instruments 'Fukai' and 'Takatori' in Figure 2.76. Global settlements of up to 1 m were seismically induced on Rokko. Port Islands and many pile-supported structures stayed at the same constructed elevation, as the surrounding soil deposit settled around them, for instance, the piers supporting an elevated railway on Port Island (Figure 2-77). On Rokko Island, the gaps around a pile supporting a crane rail were indicative of relative pile–soil movement (Figure 2-78), and the piles were stayed safe.
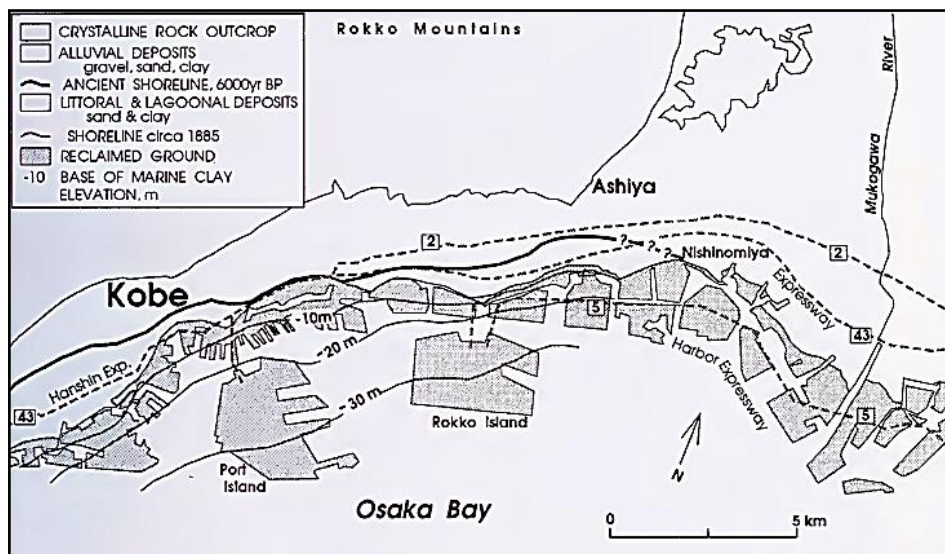
Figure 2-74 Figure 64. Soil Map of Kobe City Area, (Huzita & Kasama, 1983)

Piles supporting bridges, such as at Nishinomiya, experienced dual liquefaction consequences: a decline of lateral resistance and seismic load inflicted by lateral spreading, inducing displacement, shifting and tilting of bridge piers (Figure 2-79). (Fujii *et al.*, 1998) investigated 13 cases of pile damage detected in precast concrete, cast-in-place concrete and steel pipe piles. Damage mechanisms comprised the separation between piles and pile caps, damage close to the pile head and damage at deeper sections of piles. The external sources of the damage were categorised based on the inertial forces from the superstructure and lateral soil flow as a result of soil liquefaction. Near Takatori station (Matsui & Oda, 1996), three precast prestressed pile foundation system supporting 12 storey buildings experienced shear and compressive failure close to the pile head. However, the entire buildings had to be demolished. No empirical evidence of liquefaction was observed, and the damage was assigned to superstructure inertial forces.
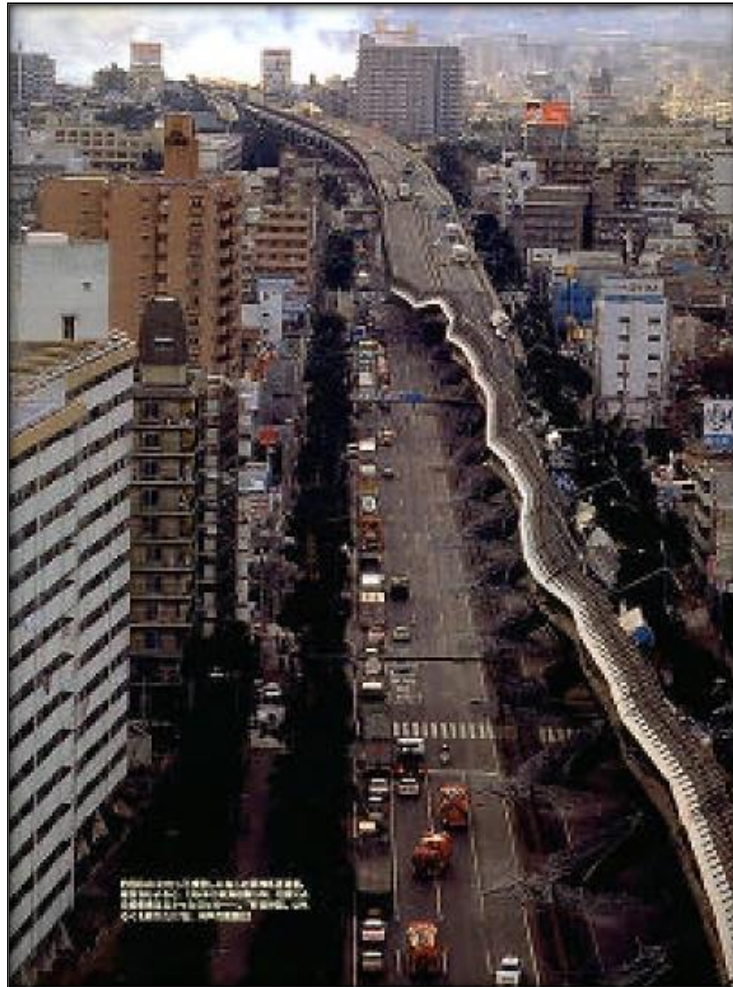
Figure 2-75 Collapsed Section of Hanshin Expressway, (U.C. Berkeley, 1995)
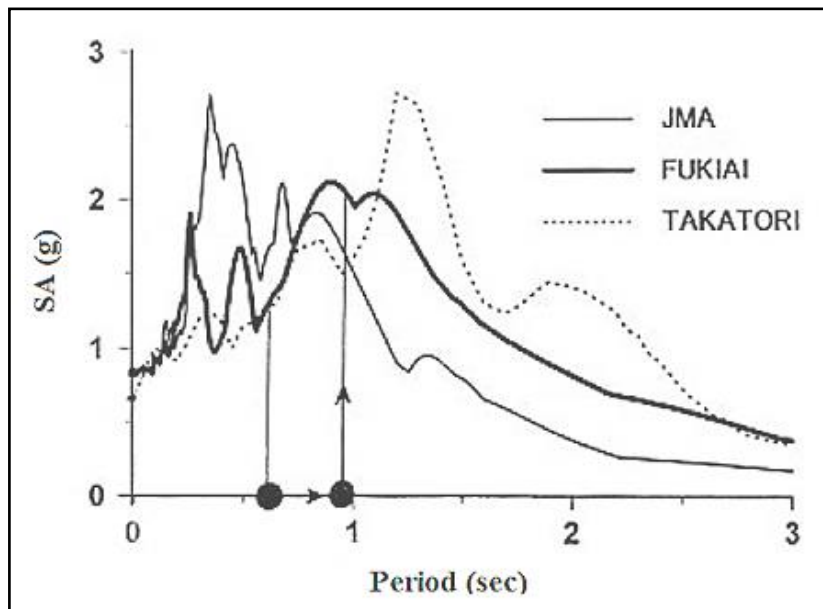
Figure 2-76 Effects of Period Lengthening due to Foundation Flexibility on Structural Forces. Vicinity of Collapsed Hanshin Expressway Response Spectra, S_A is the Acceleration Response Spectrum, (Gazetas & Mylonakis, 1998)

Figure 2-77 Differential Settlement of the Piers Supporting an Elevated Railway on Port Island, (Akia *et al.*, 1995)

Figure 2-78 Pile–Soil Gap of Rokko Island, (Akia *et al.*, 1995)

(Matsui & Oda, 1996) reviewed the damage to piles of the six major elevated highways in Kobe. A borehole TV system was used to directly inspect the condition of the bored piles that support these road structures. On the Hanshin Expressway No. 5 Bay Route, 11% of the investigated piles were categorised as severely damaged, and 37 % with minor damage. On Expressway No. 3, 16% of the examined foundations exhibited minor damage. Other structures experienced less damage. Cracks were detected in the piles close to the pile head (the location of the maximum bending moment), at locations where the steel reinforcement density had altered and at the soft–hard soil layers interface zones. Interestingly, significant superstructure damage was not always directly correlated to

significant sub-structure damage. Thus, structures may appear undamaged after an earthquake because the damaged foundations are disguised. Matsui and Oda (1996) also described case histories of waterfront steel pipe pile-supported structures subject to liquefaction and lateral spreading consequences. In one case, even though the jetty revetment relocated laterally and has damaged, the x-ray of the piles has found these piles were undamaged. In a second case, 0.7 m-diameter steel pipe piles supporting a landing pier were dragged out and detected to be aligned at the same elevation corresponding to a replaced sand layer as shown in Figure 2-80, Figure 2-81, and Figure 2-82.

Figure 2-79 Collapse of the Nishinomiya Bridge Span, (Akia *et al.*, 1995)

(Tokimatsu, Mizuno & Kakurai, 1996) detected different liquefaction influences in Fukaehama. Steel pipe pile-supported structures performed adequately according to the design condition and precast concrete pile suffered a significant settlement and tilted. Pile-supported structures in central Rokko Island showed a same excellent performance which were partially attributed to the building design that can accommodate the higher lateral force on piles in accordance with new seismic codes revised in the 1970s and 1980s (i.e. in response to the earthquake in Off-Miyagi Prefecture).

On the shorelines of Kobe and Port and Rokko Islands, liquefaction, lateral spreading, and ground subsidence destroyed many piles and structures. Inadequately and well-connected precast concrete and steel pipe piles failed either at the connection to the pile cap or into the cap. Borehole television and non-destructive sonic tests discovered damage to concrete piles at different depths. However, Port and Rokko Islands were reclaimed from 1966–1980 and 1971–1985, respectively using Rokko Mountain soils.

Figures 64 and 65 demonstrate the boring logs in Port Island at Sites I and A and in Rokko Island Sites G and B. (Tokimatsu & Asaka, 1998) employed aerial surveys to appraise liquefaction-induced displacements of three 11 storey buildings and excavated six pile caps to identify the degree of the damage to the foundations. Two specific pile damage mechanisms were identified which were observed to be directly associated with the liquefaction-induced displacements of the surrounding soil deposit.

(Tokimatsu *et al.*, 1998) described two buildings of substantial permanent ground displacement in Fukae in the zones that did not experience structural damage and therefore presumed that severe pile damage because of lateral spreading might have arisen. This finding was validated by a slope indicator and a borehole camera examination and has been modelled analytically using a pseudo-static p-y method. The development of SSPSI during liquefaction and the consequences of uniform and non-uniform ground displacements on pile bending moments are shown schematically in Figure 2-83.
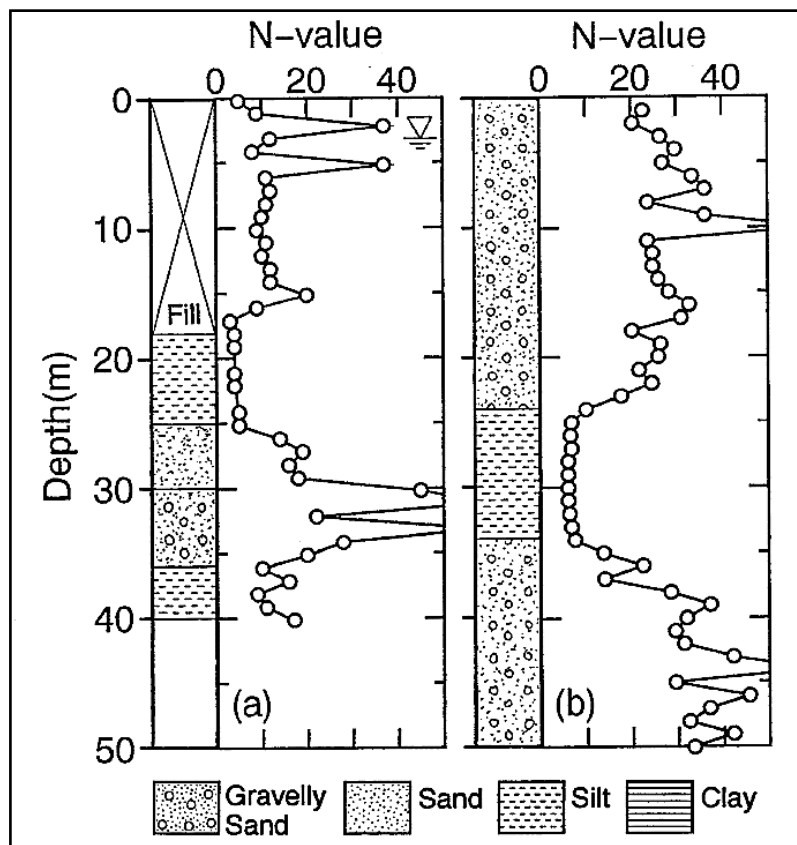
Figure 2-80 Typical Boring Logs on Port Island: (a) Site I, (b) Site A, (Tokimatsu, Mizuno & Kakurai, 1996)
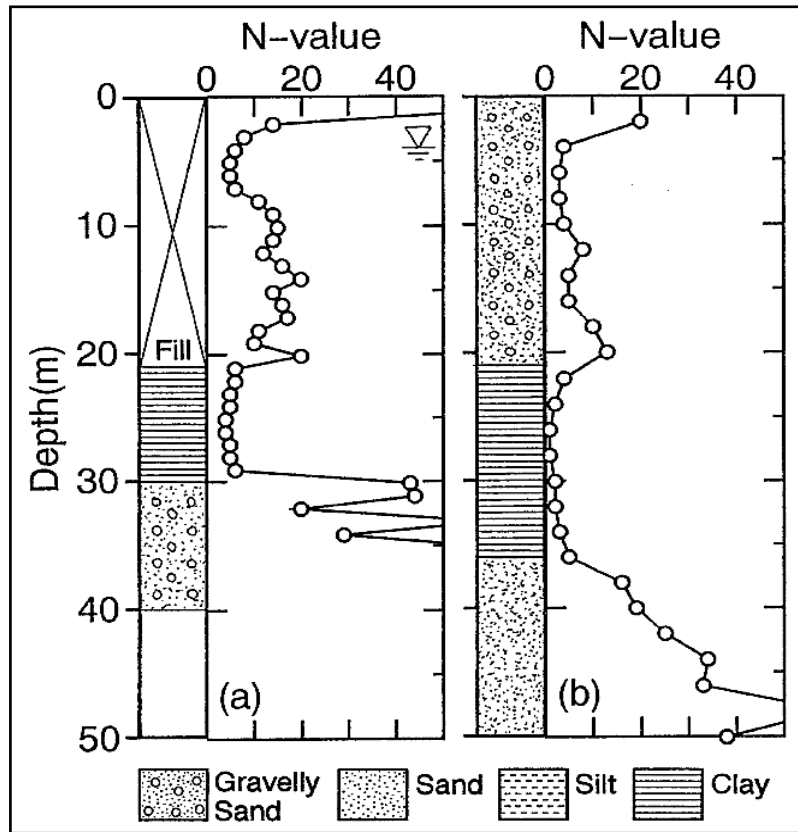
Figure 2-81 Typical Boring Logs on Rokko Island: (a) Site G, (b) Site B, (Tokimatsu, Mizuno & Kakurai, 1996)
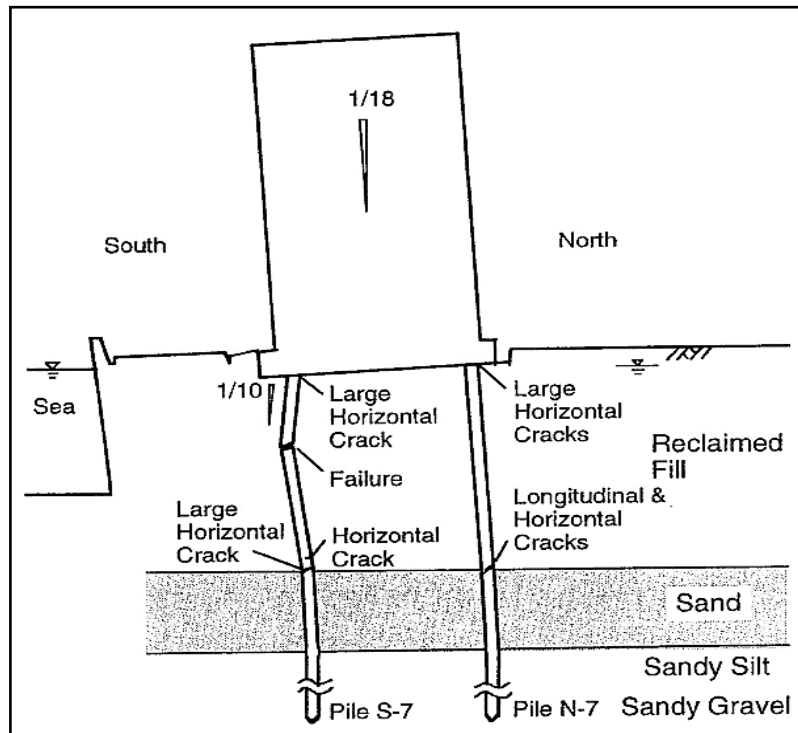
Figure 2-82 Deformation Settlement of Piles Near Waterfront, (Tokimatsu & Asaka, 1998)
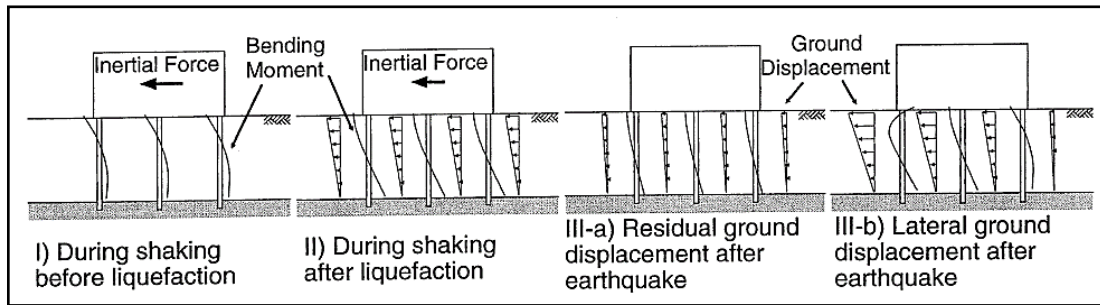
Figure 2-83 Evolution of SSPSI and Bending Moments of the Pile during Liquefaction, (Tokimatsu & Asaka, 1998)

2.8. Multi-Hazard Analysis of Post-earthquake Fire

There has been limited research into multi-hazard extreme events and their effect on building structures compared with single extreme events such as a fire or an earthquake. Nevertheless, as more has become known and understood about single hazard events, researchers have begun to study the more complex case of PEF. Della Corte et al. (2003) investigated the fire resistance rating for unprotected steel frames for the PEF condition, assuming elastic-perfectly plastic steel behaviour. This study considered second-order effects, whereby the lateral displacements caused by the stresses and strains resulting from reduce the structural stability under gravity loads. However, this study did not include stiffness degradation in the analysis.

A comprehensive study which considered the effects of geometry and stiffness degradation in the PEF condition was conducted by Ali et al. (2004), including the development of a 3D numerical model. The behaviour of an unprotected, single-storey, multi-bay steel frame, was analysed after exposure to a seismic load followed by a sizeable uncontrolled fire. The effect of the fire on the behaviour and collapse of laterally deformed frames was assessed. It was shown that the PEF resistance is significantly dependent on both the particular fire scenario as well as the gravity loads. Mousavi et al. (2008) presented a review on the key issues and hazards related to PEF for a building and showed that the principle influential factors are the intensity and duration of the earthquake and fire, the level of protection which is included in the original design and the structural materials used. Zaharia and Pintea (2009) examined two types of steel frame designed for different return periods of ground motion (2475 and 475 years, respectively). The seismic response of the system was evaluated by conducting a nonlinear static analysis, i.e. a pushover analysis. Despite the fact that the weaker structure (after earthquake event) suffered from significant inter-storey drift in the plastic range, the

frame designed for the longer return period continued to respond in the elastic range. A fire analysis was then performed for both frames and the results showed that the fire resistance of the frame with a shorter return period which had experienced greater deformations during the earthquake is lower than for the other frame which did not have any history of deformation before the fire.

Ghoreishi et al. presented a review of the existing experimental and numerical studies on structural systems under fire included a multi hazard analysis of PEF in 2009. This study revealed that traditional design methods based on the concept of fire resistance ratings do not consider many significant typical structural conditions such as size, control conditions and loading. Moreover, fire resistance of a single structural element is different than for the whole structure, due to the influences of continuity, interaction between elements and load and stress redistribution. Memari et al. (2014) presented insight into the consequences of earthquake caused fires on low-, medium- and high-rise steel moment resisting frames, using FE and nonlinear time history analysis. An uncoupled thermal–mechanical analysis was conducted, and a fire was applied at the reduced beam section connections (RBS). The material properties were assumed to be elastic-perfectly plastic in this analysis but it is noteworthy that one-dimensional beam elements were employed to represent the structure components which are incapable of depicting local buckling failure in the members.

Jelinek et al. (2017) presented a PEF examination of a protected MRSF. Two input motion and several fire scenarios were considered. Due to the utilising of 1D beam element and the unreasonable earthquakes motions, the results revealed a minor difference in the obtained fire resistance. Moreover, for the same mentioned above reasons, only global failure could be recognised—the structure designed following the EN1998-1, British Standards (2004) damage limitation, thus the residual deformations caused by earthquakes were relatively small. Jelinek et al. (2017) concluded the effects of PEF are expected to be arisen in case increasing the applied the PGA for the earthquake.

Chicchi and Varma (2018) published a state-of-the-art review for the analysis and design of moment resisting framed structures subjected to PEF, largely focussed on events in the USA. This review included an assessment of the consequences of non-structural damage produced from earthquakes on the subsequent fire resistance. A methodology was suggest for analysing and designing these types of structure to resist a PEF event using incremental dynamic and fire analyses. Zhou et al. (2020) proposed an integrated multi-

hazard analysis framework using FEA and the OpenseeS software. This framework provides a practical solution for measuring the residual fire resistance of a system with cementitious passive fire protection (PFP) subjected to fire following a moderate earthquake. This study analysed individual structural members rather than the complete structure.

In general, the research which has been conducted to date illustrates that the behaviour of a building subjected to a PEF is not significantly affected by the nonlinear geometric effects caused by an earthquake if the initial design of the structure complies with the serviceability limit state. However, there are shortcomings in the assumptions of the available research analysis conditions such as element type, method of analysis and the applied input motion. The nonlinear geometric effects are generally assumed without considering the influence of structural resonance and the frequency effect. Moreover, if an inaccurate design spectrum is determined in accordance with Eurocode 8, the acceleration time history to be applied during the seismic stage of the multi-hazard event would lead to an underestimation of the structural behaviour of the building. Consequently, the applied analysis condition mentioned above cannot be reliable and assertive to be a basis for assessing PEF effects. This is the basis for the current work which provides a novel approach to quantifying the effect of PEF event on structural behaviour using a coupled nonlinear sequential analysis method. The study highlights the unique relationship between the geotechnical and geological properties of applied motion (during earthquake stage) and system behaviour during multi-hazard event. The coupled nonlinear time history analysis is used to identify the residual material properties of the subsequent fire analysis.

Chapter 3: Soil-Structure Interaction Analytical Methods, Theory and Utilised Software

3.1. Analytical Methods

The development of seismic soil-pile-structure interaction SSPSI analytical methods has been driven mainly by the requirements of offshore. In offshore circumstances, lateral loads have been applied to piles under the cyclic wave loading conditions (Abadie, 2015), and limited studies of in-situ and laboratory tests were developed that are empirically based and broadly agreed p-y approach of the static analysis of the laterally loaded pile. This analysis method has been modified with the time by many researchers and extended to cope with the circumstances of cyclic loading and consistently employed to dynamic and seismic loading conditions.

By contrast, dynamic soil–pile analysis methods have been developed for the idealisation of piles embedded in viscoelastic deposits, and these methods have found their way into practice. The dynamic soil–pile analysis methods are more theoretically based than the p-y approach (Gerolymos *et al.*, 2009). The former, simultaneously with the finite element method (FEM), are consequences of the significant effort of studying the problems of SSI for partially embedded nuclear power plants in the 1960s and 1970s. However, such methods typically do not permit the proper characterisation of localised yield at the soil–pile interface and are better suited to relatively low-seismic loading rates. In addition to these analysis groups, defining four levels of progressively 'complete' SSPSI analyses is possible (((USACE), 2007); (Gazetas & Dobry, 1984)):

a) The basic level is a single-pile-kinematic seismic response analysis, which usually involves nonlinear response and is conducted as a pile integrity assessment. A pseudo-static technique of evaluating pile integrity involves two steps. The first is transforming the horizontal soil displacement profile obtained from the analysis of a free-field site response to a curvature profile. The second is comparing peak values with allowable pile curvatures. This approach presumes that piles follow the soil entirely, and no inertial interaction arises. Alternatively, the displacement time history can be applied along the analysed pile (at the nodal points) when dynamic pile integrity analysis is adopted.

b) In the second level of analysis, head stiffness of pile or impedance functions can be simplified from (linear or non-linear analyses) and assembled into the stiffness matrix of

the pile group for employ in global response analysis (see Figure 3-1). Secant stiffness values are usually excluded from nonlinear soil–pile reaction experiments at design level deformations (see Figure 3-2).

c) In the third level of analysis, inertial and kinematic interaction can be measured using sub-structuring analysis, and pile head impedance and input motions can then be defined at foundation level (see Figure 3-3).

d) In the fourth level, a completely coupled seismic soil-pile-structure interaction analysis can be executed to determine the complete response of the system.

$$\begin{bmatrix} K_{11} & 0 & 0 & 0 & 0 & 0 \\ 0 & K_{22} & 0 & 0 & 0 & K_{26} \\ 0 & 0 & K_{33} & 0 & K_{35} & 0 \\ 0 & 0 & 0 & K_{44} & 0 & 0 \\ 0 & 0 & K_{53} & 0 & K_{55} & 0 \\ 0 & K_{62} & 0 & 0 & 0 & K_{66} \end{bmatrix} \begin{Bmatrix} D_1 \\ D_2 \\ D_3 \\ D_4 \\ D_5 \\ D_6 \end{Bmatrix} = \begin{Bmatrix} F_1^1 \\ F_2^2 + F_6^2 \\ F_3^3 + F_5^3 \\ F_4^4 \\ F_5^5 + F_3^5 \\ F_6^6 + F_2^6 \end{Bmatrix} = \begin{Bmatrix} F_1 \\ F_2 \\ F_3 \\ F_4 \\ F_5 \\ F_6 \end{Bmatrix}$$

$\underline{K}$ X $\underline{D}$ $F_{DIR.}$ $F_{COUP.}$ F

STIFFNESS   DISPLACEMENT   DIRECT FORCE   COUPLED FORCE   TOTAL FORCE

Figure 3-1 Single Pile Behaviour and Flexible Pile Stiffness Matrix, ((USACE), 2007)

Figure 3-2 Design Level Displacement –Selection Procedure of Secant Stiffness Value, ((USACE), 2007)

Figure 3-3 Concept of Substructure Method: (a) Definition of Problem, (b) Decomposition into Inertial and Kinematic Interaction Problems, (c) Two-step Analysis of Inertial Interaction, (Gazetas & Dobry, 1984)

Each level of analysis can be employed for various levels of analysis. For instance, beam-on-Winkler-foundation analysis can be performed as a pile integrity assessment or applied to obtain pile head stiffness (Mylonakis et al. 2006). The elastic continuum

analysis may be applied to ascertain pile head impedance or employed in the sub-structuring pattern (Mylonakis and Gazetas 2000). Finite element have been utilised to develop other classes of analysis and execute complete SSPSI analyses (David, Krishnamoorthy & Mohamed Jais, 2015). Static, cyclic, and dynamic loading conditions are considered in the SSPSI problem. FE approach has been employed successfully in the present study. Figure 3-4 demonstrates the idealised soil–pile load-displacement diagrams for all aforementioned loading conditions. Simplified techniques for determining static stiffness of pile head are commonly applied for dynamic response analysis because the static stiffness is approximately equal to dynamic stiffness within the range of seismic frequencies of interest. Lateral and axial stiffness are essential components of impedance functions for pile group because the structural inertial response can induce shaking mode and mobilise axial pile resistance. Pile group effects must be considered in SSPSI analysis, and they are described in detail in Section 1.1. Pile group effects can be applied implicitly in substructure and 'complete' analysis and must be employed separately with interaction factors once pile group impedance matrix is assembled from single pile terms.
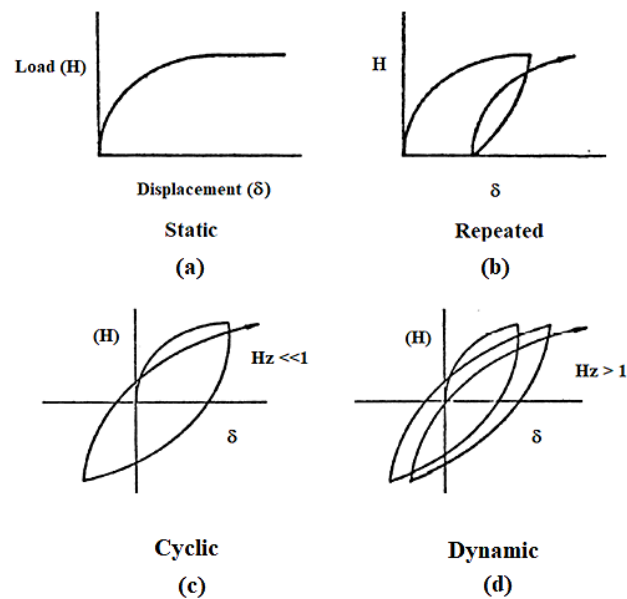
Figure 3-4 Load-Displacement Curve for Different Conditions of Loading , (Meymand 1998)

Differentiations are commonly observed between the type of boundary conditions and material properties of the analysed piles. These distinctions are produced between fixed or free head (pinned connection) piles, and the pile behaviour, whether rigid or flexible, depends on the relative soil–pile stiffness (see Figure 3-5). The flexible behaviour of piles is a fundamental hypothesis of the beam-on-Winkler-foundation method (Kulhawy and

96

Chen, 1995) and is an underlying plane strain hypothesis to elastic continuum approaches. Rigid pile behaviour implies that the cross-coupling stiffness associated with the other modes of pile resistance can be considered in this analysis technique (see Figure 3-6). Many researchers suggested criteria for rigid and flexible behaviour which are listed in Table 3.1.
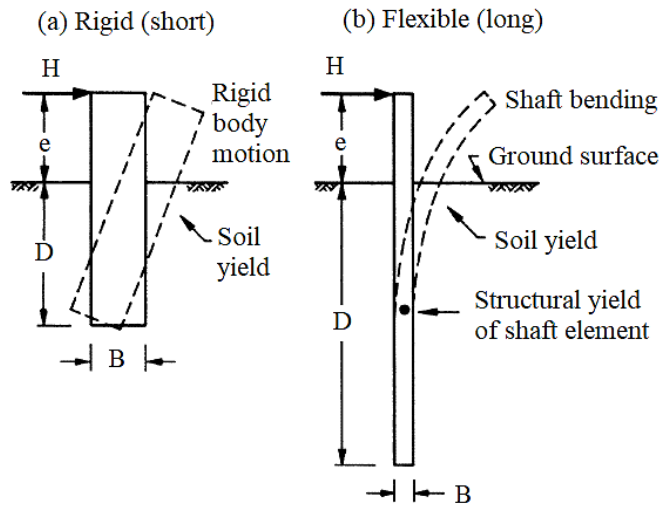
Figure 3-5 Rigid Versus Flexible Pile Behaviour, (Modified from (kulhawy & Chen, 1995))
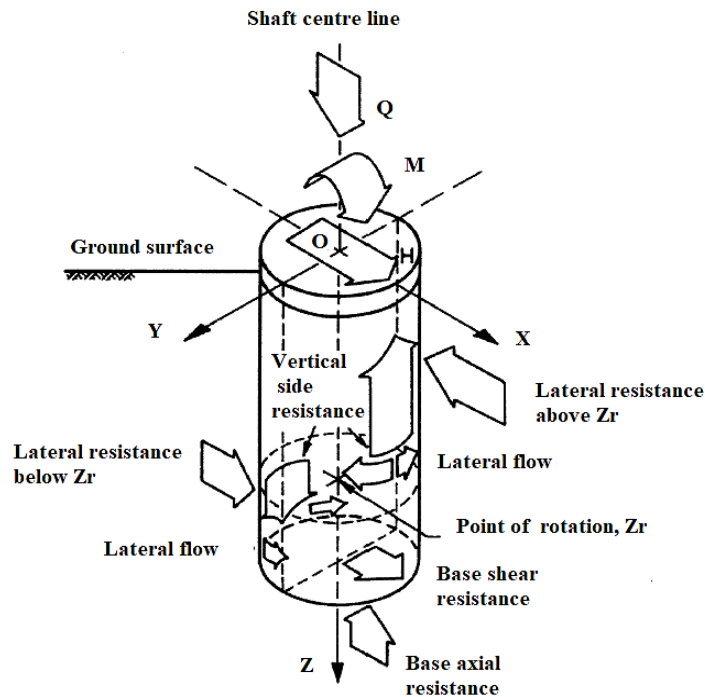
Figure 3-6 Components of Rigid Pile –Lateral Loading conditions (Modified from (kulhawy & Chen, 1995))

Table 3.1 Criteria for Pile Rigidity, (kulhawy & Chen, 1995)

Source	Criterion for Rigid Behaviour	Criterion for Flexible Behaviour	Note
Broms (1964a)	$\beta_r D < 1.5$	$\beta_r D > 1.5$	a
Poulos and Davis (1980)	$K_r > 10^{-2}$	$K_r < 10^{-3}$	b
Bierschwale et al. (1981)	$D/B < 6$	$D/B > 6$	c
Dobry et al. (1982)	$S_H < 5$	$S_H > 5$	d
Davies and Budhu (1986)	$D < 1.5BK^{0.36}$	$D > 1.5BK^{0.36}$	e
Budhu and Davies (1987)	$D < 1.3BK^{0.222}$	$D > 1.3BK^{0.222}$	f
Carter and Kulhawy (1988)	$D/B < 0.05(E_p/G^*)^{0.5}$	$D/B > (E_p/G^*)^{2/7}$	g
Poulos and Hull (1989)	$D < D_P/3$	$D > D_P$	h

Note: B = pile diameter, D = pile depth, Ep = pile elastic modulus, Ip = pile moment of inertia, Es = soil elastic modulus, Vs = soil Poisson's ratio, Gs = soil shear modulus

a - $\beta_r = (K_h B/4E_p I_p)^{0.25}$, K_h = coefficient of subgrade reaction

b - $K_r = (E_p I_p / E_s D^4)$ = flexibility factor

c - may be rigid for D/B < 10 in some cases

d - $S_H = (D/B)/(E_p/E_s)^{0.25}$ = flexibility factor

e - $K = (E_p/E_s)$ = stiffness ration, for constant soil modulus with depth

f- $K = (E_P/mB)$, m is E_s rate of increase, for linear variation of soil modulus with depth

g- $G^* = G_s(1+3V_s/4)$ = modified soil shear modulus

h- $D_p = 4.44(E_p I_P/E_s)^{0.25}$ = critical pile depth

3.1.1. Pile Group Effects

The pile properties identified from the results of single soil–pile interaction analyses are commonly extended to reflect the group configuration piles and employed for full SSPSI analyses. This concept is in contrast with substructure and complete analysis approaches in which the full pile group response is inherently considered. Once the piles are assembled in group with pile-to-pile spacings greater than 6–8 pile diameter, the interaction effects for the pile group are commonly ignored in the static loading condition (see Figure 3-7). This technique may tend to be incorrect when the piles are subjected to dynamic loading condition due to the pile group interaction effects arising from the wave energy exposed between neighbouring piles which (the interaction effect) do not diminish as expeditiously compared with the static loading pile group interaction.

The dynamic response of pile group is a function of load level (Rocscience, 2018), (Rajapakse, 2016) ,and (Bogard & Matlock, 1983). Many researchers addressed small strain elastic response, and few of them considered nonlinear pile group interaction (AASHTO LRFD Bridge Design, 2015). However, evidence suggests that pile group effects decrease with rising soil–pile nonlinearity which prevents wave energy transmission between piles.
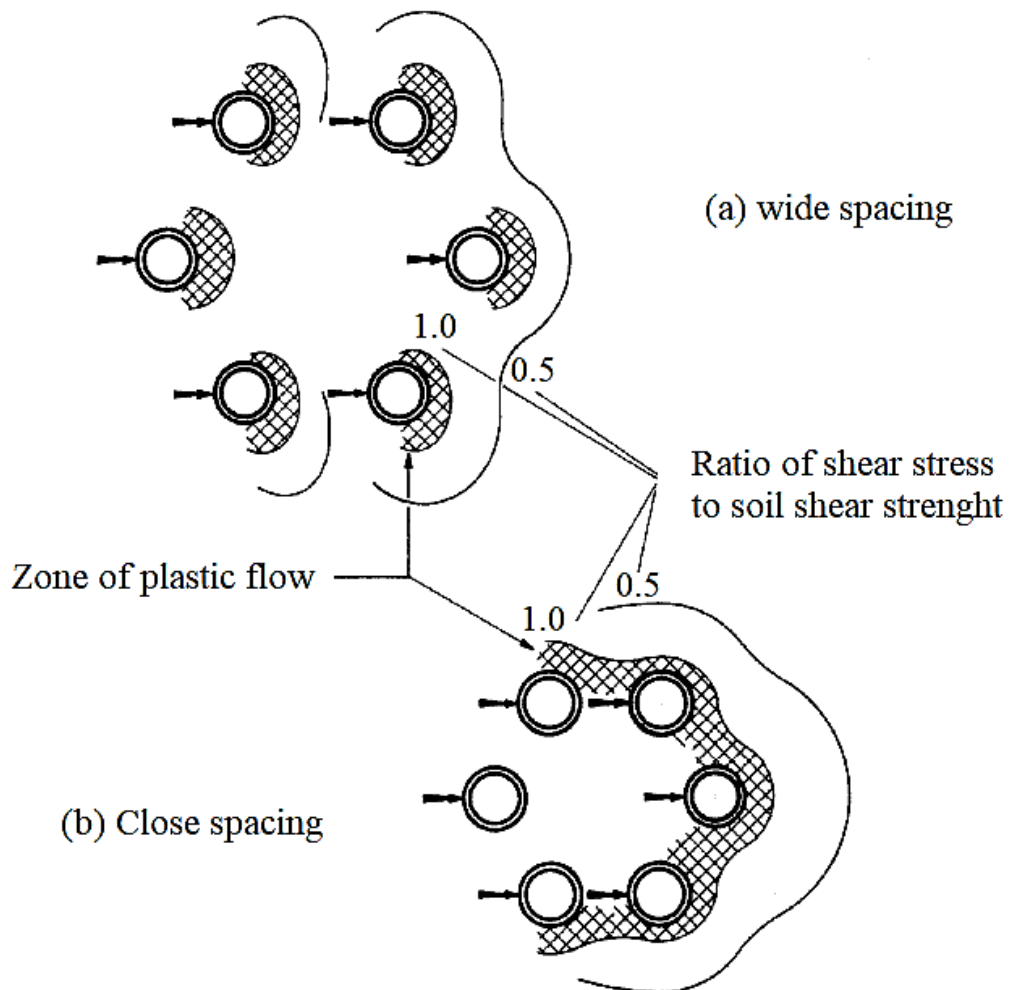
Figure 3-7 Association of Pile Group Interaction with Pile Spacing, (Modified from (Bogard & Matlock, 1983))

Figure 3-8 illustrates the behaviour of a pile group subjected to lateral loading and overturning moment (Dunnavant & O'Neill, 1985). The pile group response components, the aspects that are controlled the pile group response and the objectives of performing a pile group analysis are demonstrated include the following (Meymand 1998):

(1) **the pile group response components**	• pile group rotation that causes axial tensile/compressive forces which are most severe at end piles
	• pile group translation and relative pile translations
	• single pile head rotations located at pile to cap connections
	• single pile deflections and consequent bending moments
(2) **The aspects that control the group response**	• single pile response: small strain elastic or nonlinear behaviour
	• loading condition: static, cyclic, or dynamic loading condition
	• soil properties: particularly as modified by pile group installation
	• relative soil–pile stiffness: more flexible piles undergoing more significant interaction
	• group geometry: including single pile cross-sections and group spacing
	• head fixity: idealised as free or fixed head and an intermediate case
	• pile base condition: either floating or end bearing
	• superstructure mass and flexibility: expose inertial loads to the pile group
	• pile cap embedment depth, stiffness and damping properties
(3) **The objectives of performing a pile group analysis**	• pile group and single pile deflections
	• single pile head shear forces and moment distributions
	• input ground motion modification for superstructure analysis

The method in which these objectives are achieved correlates to the level of single pile analysis. In most practised provisions, the kinematic response analyses of a single pile can be modified to represent approximately the effects of pile group and superstructure (Nikolaou *et al.*, 2001). The impedance functions of a single pile may be mobilised into group impedance functions with group interaction theory. The impedance function of the pile group is then employed in the global structural analysis to deliver the forces and deflections of the pile group. The calculated force and deflection values can be allotted to the individual single piles with group interaction theory, with the checking of that the

single pile head forces must be not to exceed the pile to cap connection capacity. Then, the most critically loaded pile(s) in the group may be evaluated in a single pile integrity analysis mode to ascertain whether pile moment distributions exceed the allowable capacity. The consequences of pile group on the modification of ground motion input to the superstructure must be analysed either with a sub-structure approach or a complete SSPSI analysis.
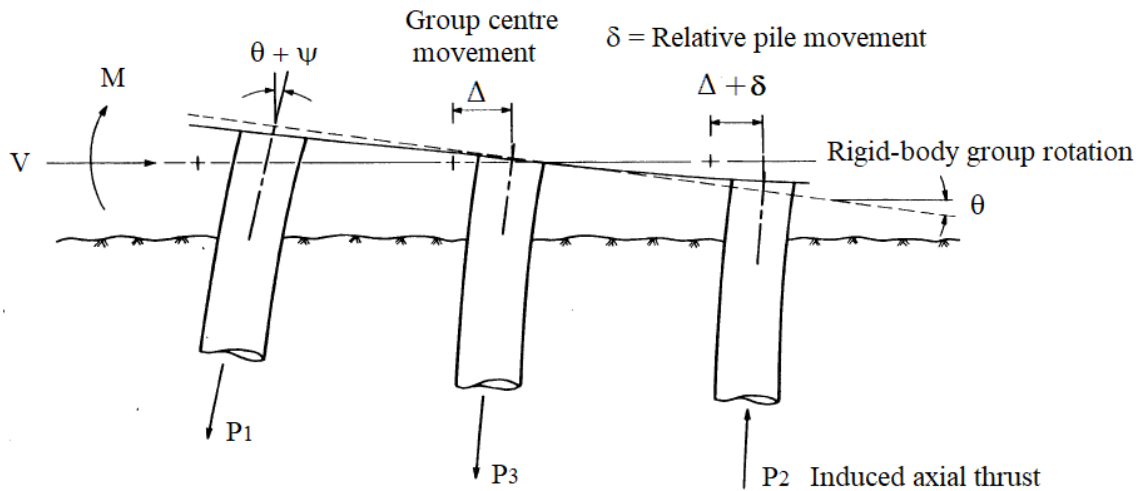
Figure 3-8 Group Response Components Subjected to Lateral Loading, (Modified from (Dunnavant & O'Neill, 1985))

Static and dynamic pile group response theories can be categorised into two groups: (*i*) pile group interaction methods utilised with regard to single pile analysis results to group behaviour and (*ii*) complete dynamic analysis of pile group in which the complete group response is analysed in one phase (Roesset, 1984), and (Novak 1991).

3.1.1.1. Methods of Pile Group Interaction

The concept of pile group interaction factor was first introduced by (Poulos 1971,I) and (Poulos 1971,II) using Mindlin's elasticity equations to compute stress and displacement for two interacting piles subject to horizontal point loads in elastic half-space. The pile group interaction methodology has been widely use since then in SSPSI analysis, (Cairo, Conte & Dente, 2005). Poulos (1971) described the interaction factor in Eq. (3.1). A chart shows the different values of α_p factors for two different pile boundary conditions, fixed and free head piles, subject to lateral and moment loads and as functions of pile flexibility K_r (see Table 3.1), pile spacing S_p , pile diameter D , pile length L and departure angle δ (angle between piles and direction of loading).

$$\alpha_p = \frac{displacement/rotation\ of\ pile\ due\ to\ adjacent}{displacement/rotation\ of\ pile\ due\ to\ its\ own\ loading} \quad (3.1)$$

The pile group was analysed by computing the individual pile's interaction with all other piles that contributed in the group and then using the superposition for the findings. However, the presence of intervening piles was not included in this approach. Meymand (1998) stated that this technique is proven "to underestimate pile group interaction at small pile spacings and overestimate interaction at large spacings, (Poulos, 1980)".

3.1.1.2. Complete Dynamic Analyses of Pile Group

The first pile group complete dynamic response analysis approach was initiated by (Wolf & Von Arx, 1978) when they generalised the solution of (Blaney, Kausel & Roesset, 1978). A horizontal layer, viscous–elastic soil deposit and piles were equal in diameter and length, and either floating or end bearing was considered in any group configuration. An axisymmetric FE model was employed to compute the Green's functions, generating displacements at any point in the earth's mass given a discreetly layered ring load. Green's functions were then utilised to measure the flexibility matrix of the soil at each frequency and assemble the dynamic stiffness matrix of the complete dynamic system. The results revealed a strong dependency on the frequency content, number of piles and spacing between piles, (Roesset & Angelides, 2015).

3.1.2. Finite Element Method

The FEM involve the ability to execute the SSPSI analysis of pile groups with fully-coupled mode without applying independent calculations of site conditions and/or structural response or application of pile group interaction factors and the ability to model any specific soil profile and conduct 3D effects. The author in current study addresses that the challenge of implementing this technique successfully lies in delivering a suitable soil constitutive model that can model small to extremely large strain behaviour, rate dependency and resistance degradation. A particular condition must be employed to consider the effects of pile installation and soil–pile gapping and gap–slap mechanism.

3.1.2.1. Consideration of Finite Element Method

In FEM, a numerical approach that can achieve an approximate solution and its model system is broken down into smaller parts called elements which are interfaced with one another at common points called nodal points. In the FE system, neighbouring elements share the same degree of freedom. The name of the technique is derived from the concept of splitting an infinitely divisible continuum into smaller, simpler finite parts (i.e. FEs).

102

Thus, a set of differential equations which is valid in the mechanics of continuum is transformed to a set of equations compatible to the domain of the continuum problem. Most commercial FEM software packages, such as Abaqus and Ansys, originated from the 1970s and have been widely upgraded and utilised ever since (Fu, 2015). Finite Element analysis (FEA) is composed of the three following stages:

- Pre-processing stage: The FE model is built as elements and nodes. The parts are assembled to gather in a particular shape and property in a process called meshing. However, the geometric domain and properties, element type(s), material properties, element connectivity, physical interaction, constraints and boundary conditions and load conditions must be defined accurately.

- Solution stage: The numerical analysis is performed. The values of the primary field variable(s) are computed. The system vibration modes for the circumstances of the dynamic system specified in this study are considered primary field variables. The values are consequently employed for the computing of additional derived variables (i.e., proportional frequency factors α and β) to run the model(s) for the main target of finding.

- Post-processing stage: The findings are elicited and visualised.

For the performance of FEA for the nonlinear problems, the general/FE package Abaqus is utilised (Smith 2018). Abaqus may find the solution for a nonlinear problem either by iterating through the implicit approach (Abaqus/Standard) or without iterating by explicitly developing the kinematic state from the prior increment with the explicit approach (Abaqus/Explicit). The implicit approach is appropriate for the scope of this study and is therefore employed. A dynamic equilibrium state is determined at the beginning of each time increment and should be small enough for the stability of the solution. However, the FE stages apply analysis technique and steps for individual circumstances according to the objectives, and the purpose of simulations are described in detail in the chapters corresponding to these cases (Chapters 4, 5, 6, 7 and 8).

3.1.2.1.1. Elements

A number of different element types can be employed under the spectrum of the FE modelling approach. These element types are characterised according to their families, such as solid or (continuum), shell, beam, rigid and membrane elements; the number of nodes, such as linear or first-order, quadratic or second-order and cubic or third-order; the degrees of freedom and the formulation and integration scheme, such as full and

reduced. The wide range of element types in the Abaqus library offers flexibility in modelling different geometries and systems. Each element type may be characterised by considering its family, number of nodes, degrees of freedom and formulation and integration. Elements in the same family share many essential features, and variations exist within a family. Nonetheless, this study used the largest category, the family of FEs, to classify the element type as continuum or solid, shell, beam, rigid and membrane elements (see Figure 3-9) , (Hibbitt *et al.*, 2012)

continuum (solid elements)   shell elements   beam elements

rigid elements   membrane elements
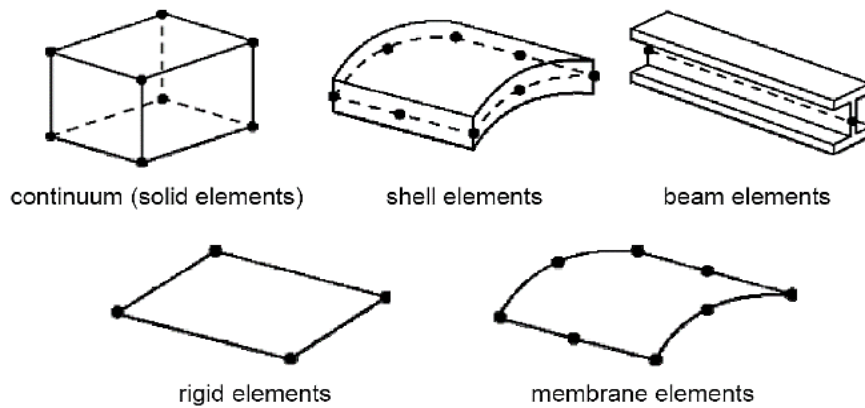
Figure 3-9 Most Utilised Element Types in FEA Approach, (Modified from (Hibbitt *et al.*, 2012))

The number of nodes (interpolation) of each element type defines how the nodal degrees of freedom are introduced over the element domain. Abaqus' library comprises elements with first and second-order interpolation (see Figure 3-10). The elements' degrees of freedom in the FEA represent primary parameters which exist at the nodes of an element.

CPE4 element   CPE8 element
First-order interpolation   Second-order interpolation
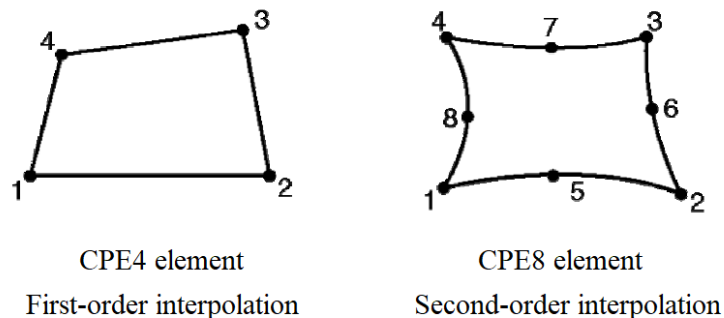
Figure 3-10 First and Second-Order Interpolation, (Modified from (Smith 2018))
The mathematical formulation employed to describe the element behaviour is another wide group that is utilised to categorise the models' elements. Abaqus includes different element formulations, and the compatible model situations are listed as follows:

Plane strain	Plane stress	Hybrid elements	Incompatible-mode elements
⬇	⬇	⬇	⬇
Small strain	Finite strain	Thick shells	Thin shells
Shells	Shells		

The first two types are used in this study.

The stiffness and mass of an element can be computed numerically at sampling points within the 'integration points' of the element. In Abaqus, a numerical algorithm employed to integrate these variables affects and signifies element behaviour. Abaqus is composed of elements with 'full' and 'reduced' integration properties. For the full integration types, a minimum integration order is expected for exact integration of the strain energy for an undistorted element and linear material properties (Kim, 2015). For the reduced integration types, one of the integration rules is one order less than the full integration rule (see Figure 3-11). Elements are named based on the aforementioned principle properties, and Figure 3-12 shows examples.

Choosing an appropriate element type is usually based on the number of parameters. Solid element models may be large and expensive, especially in 3D analysis problems. For economic reasons, the structural elements of shells and/or beams can be used instead, and this change influences the accuracy of the findings. A structural element model typically needs fewer elements than an analogous continuum element model.
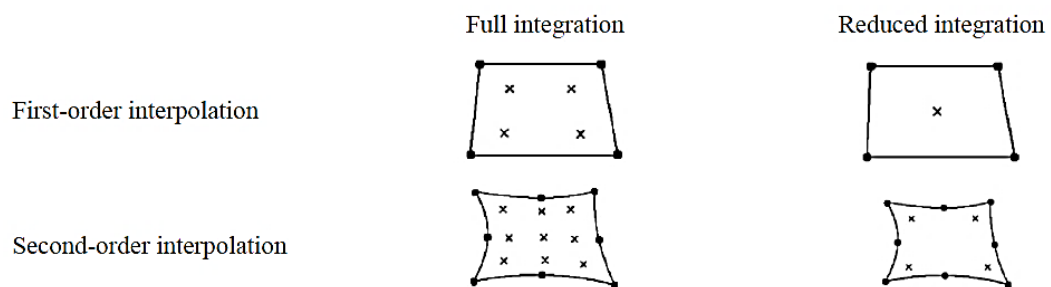
Figure 3-11 First- and Second-Order vs Full and Reduced Integration, Modified from (Smith 2018)

Once structural elements are selected, producing acceptable findings require selected shell thickness and/or beam cross-section dimensions to be less than $1/10$ of a global structural dimension, for instance, the distance between structure supporting location, positions of applied point loads, distance between total alterations in part cross-section

and wavelength of the peak vibration mode. Shell element is an approximate 3D continuum with a surface model (see Figure 3-13). It can model bending and in-plane deformation problems effectively. Once a local detailed analysis is required, a 3D solid model must be incorporated employing multipoint constraints or submodelling technique.

B21:Beam, 2D, First-order interpolation

S8RT: Shell, 8-nodes, Reduced integration, Temperature

CAX8R: Continuum, Axisymmetric, 8-node, Reduced integration

CPE8PH: Continuum, Plane strain, 8-nodes, Pore pressure, Hybird

DC3D4: Diffusion (heat transfer), Continuum, 3D 4-nodes

DC1D2E: Diffusion (heat transfer), Continuum, 1D, 2-nodes
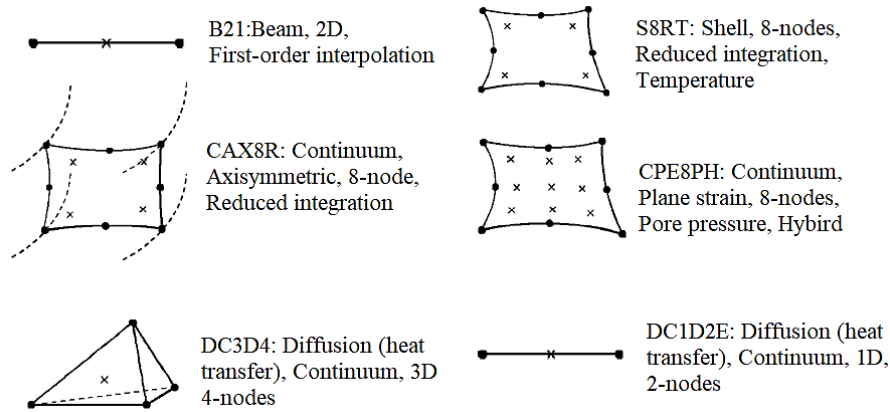
Figure 3-12 Examples of Element Naming Conventions, Modified from (Hibbitt *et al.*, 2012)

(a) 3D continuum (solid) model   (b) Surface model

(c) Shell model of a hemispherical dome subjected to a projectile impact
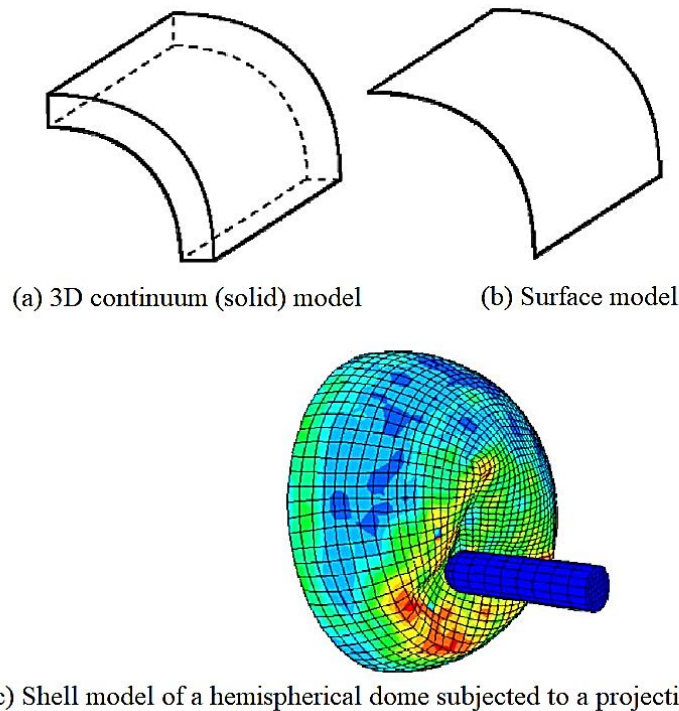
Figure 3-13 Examples of Three Different Element types (Modified from Hibbitt et al., 2012)

The beam element is an approximate 3D continuum using a line model (see Figure 3-14). Bending torsion and axial forces can be modelled effectively by using this type of element. Various cross-section shapes are available in the Abaqus tool, in addition to

cross-section properties which may also be specified by providing an engineering industry library. The modelling of bending employing continuum element process can be understood and controlled by understanding the physical characteristics of pure bending. The behaviour of materials that attempt to be modelled using FEA is assumed to behave according to the following conditions:

- The element plane cross-sections continue plane throughout the deformation.
- The axial strain ε_{xx} changes linearly over the thickness (see Figure 3-15).
- If the value of Poisson's ratio for the modelled material is equal to 0, then the strain in the direction ε_{yy} of the thickness is 0.
- No membrane shear strain in the beam element type indicates that the lines parallel to the beam axis are located on a circular arc.

3D continuum model   Line model
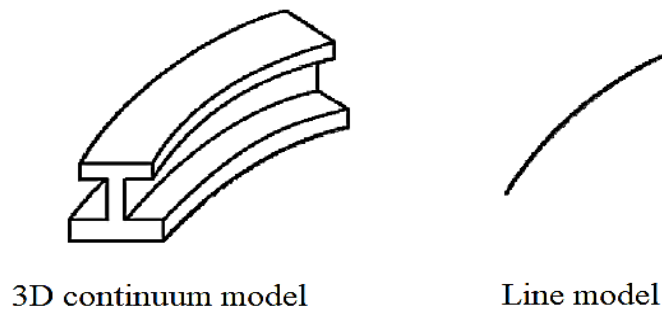
Figure 3-14 Types of Beam Element, (Hibbitt *et al.*, 2012)
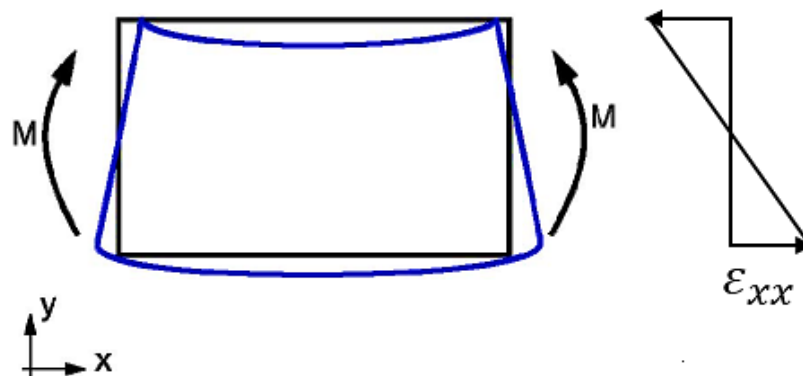
Figure 3-15 Physical Characteristics of Pure Bending, (Modified from (Hibbitt *et al.*, 2012)

Moreover, second-order full or reduced integration solid elements can model the bending accurately. The axial strain equates the difference in the length of the initial horizontal lines. The strain along the thickness direction and shear strain is 0 (see Figure 3-16).

Modelling bending using first-order fully integrated solid elements can detect model shear strains at the integration points. However, excessively stiff behaviour results are due to energy turning into shearing the element rather than bending it which is the so-called 'shear locking' mechanism. Consequently, this type of element is inappropriate for models dominated by bending (see Figure 3-17).
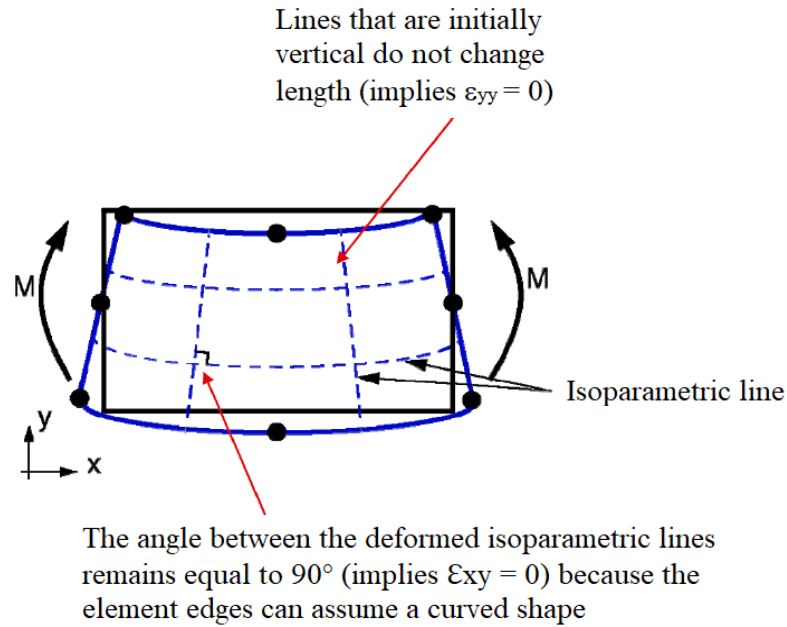
Figure 3-16 Second-Order Elements Under Pure Bending, (Modified from (Hibbitt *et al.*, 2012)
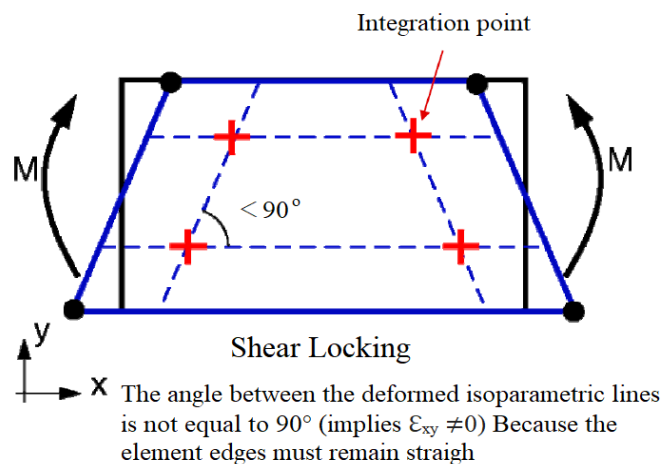
Figure 3-17 First-Order (Shear locking) Elements Under Pure Bending, (Modified from (Hibbitt *et al.*, 2012)

However, bending modelling using first-order reduced integration elements eliminates the shear locking, and hourglassing would be considered. Only one integration point is considered at the element centre, indicating that a single element across the thickness does

not detect strain value during bending response. Consequently, the element deformation is a zero-energy mode and called the hourglassing element due to the presence of deformation without strain (see Figure 3-18). Hourglassing propagates easily through a mesh of first-order reduced integration elements, producing unreliable results. Multiple elements, therefore, at least four along the element thickness are necessary to get rid of this problem. Each single element can capture either one compression or tension axial strain, and they can be evaluated correctly. The thickness and shear strains in this element are 0, and this element can be considered as cheap and effective (see Figure 3-19).
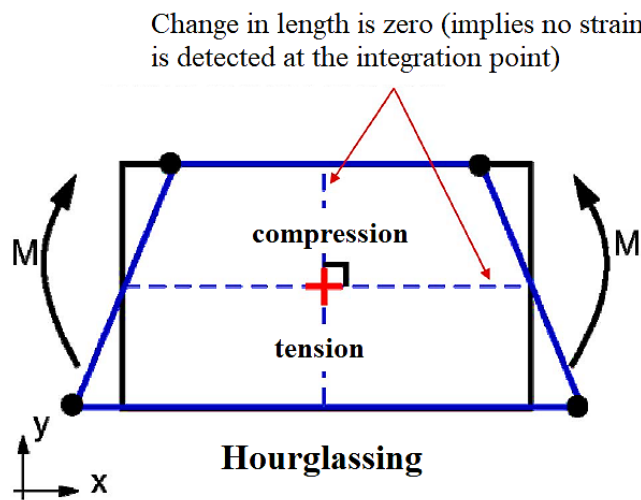
Figure 3-18 Bending behaviour for a single first-order reduced integration (Hourglassing) Elements (Modified from (Hibbitt *et al.*, 2012)
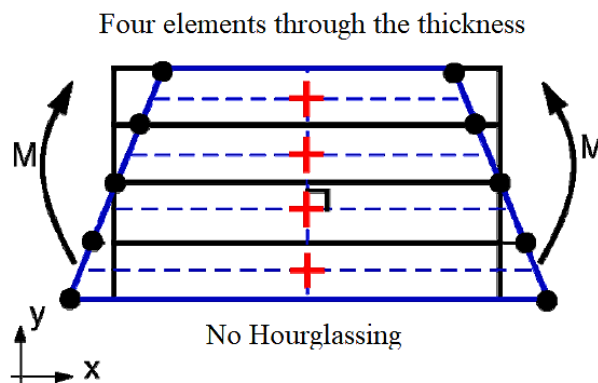
Figure 3-19 First-Order (Non-Hourglassing) Elements Under Pure Bending, (Modified from (Hibbitt *et al.*, 2012)

Stress concentrations in the element model can be determined by using second-order elements which can capture an accurate finding compared with first-order elements, especially for the problems with stress concentrations, and are preferably appropriate for

the analysis of stationary cracks. Although fully integrated and reduced integration elements can capture reliable results, the reduced integration elements tend to be more productive, and the captured results are often better than full integration at a lower computational cost. Most element types are formulated in such a way as to capture appropriate behaviour during contact modelling circumstance. Three element types are considered unless they are exceptions of the rule, due to the following convergence problems:

- second-order quad/hex elements
- 'regular' second-order tri/tet, as opposed to 'modified' tri/tet elements
- 6-node shell and membrane elements

The subsequent direction of the consistent nodal forces is not uniform when classical hard contact is employed due to the pressure. Therefore, the penalty-based contact option must be the alternative. Different contact and interaction conditions have been used in the present study, and all properties and details are described carefully in the corresponding Chapters 4, 5, 6, 7 and 8.

Many nonlinear analysis problems occur once incompressible materials with Poisson's ratio of ($\upsilon = 0.5$), such as some fully saturated clay soil types, are involved in the analysis. Typical FE meshes commonly indicate excessively stiff behaviour due to material volumetric locking, which tends to be more severe when these materials are highly confined (see Figure 3-20).

For an incompressible material, the volume of every integration point remains constant, constraining the kinematic allowable displacement field and producing volumetric locking. For instance, an average of 1 node with 3 degrees of freedom and fixed integration point volume exists in a fine 3D meshing of 8-node hexahedra element. This fully integrated hexahedra element uses 8 integration points; therefore, 8 constraints per element occur for the above example, but only 3 degrees of freedom are presented to manage these constraints.

This observation indicates that volumetric locking is pronounced in fully integrated elements. Reduced integration elements have less volumetric constraints and successfully reduce volumetric locking in many problems, in which incompressible materials are modelled.
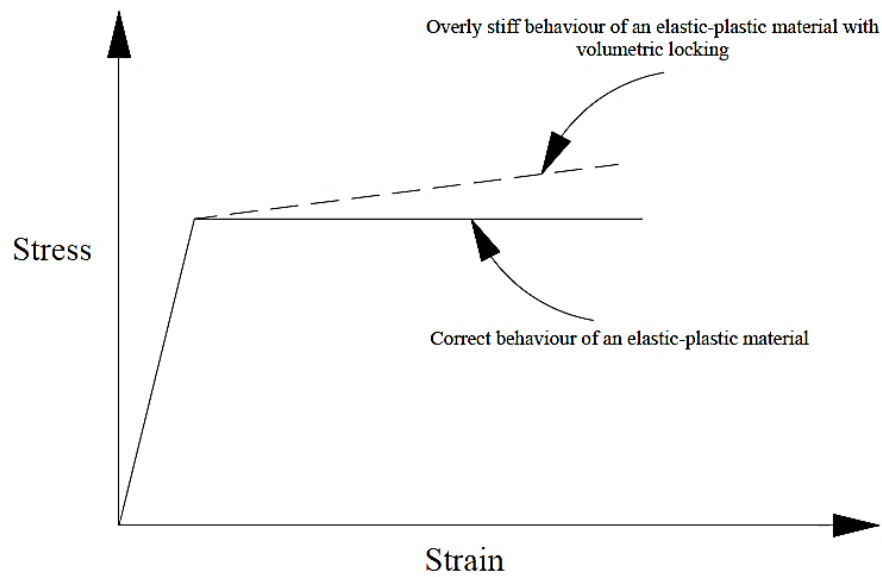
Figure 3-20 Effect of Volumetric Locking

3.1.2.1.2. Mesh Generation

Elements are created in the Mesh module of Abaqus/CAE, and meshes, including the element shapes, are shown Figure 3-21. Most elements in Abaqus are topologically equivalent to these shapes, and each element type is suitable to use for a specific purpose. For instance, CPE4 for stress and DC2D4 for heat transfer are equivalent to a linear quadrilateral type for modelling. Once the mesh of a model has generated the decision, whether to use a particular element type, especially quad/hex and tri/tet elements, represents a particular significance aspect. Quad/hex element must be employed wherever possible due to it producing the best results with minimum cost. In modelling complex geometry systems, using triangular and tetrahedral elements is compulsory.

Sufficiently fine meshes are usually used to certify that the results captured the real behaviour accurately. However, coarse and/or non-uniform meshes tend to yield inaccurate results that complete two of the targeted level of accuracy. The fine meshes are used in high gradient region, whereas the coarse meshes are used in low gradient regions, signifying that the category of gradient regions must be decided before the mesh stage. An appropriately sophisticated mesh that can deliver precise solutions is crucial in FE modelling technique. Coarse meshes may yield ineffective solutions, whereas decreasing the mesh size subsequently produces precise analysis. When more refinement creates only insignificant/negligible differences in the solution accuracy, the mesh is stated to be converged. However, the potential level of refinement is normally restricted by the available computational resources. In such situations, more mesh refinement must

be applied mainly for highly stressed regions, in which a refined mesh is essential to capture severe stress verifications.
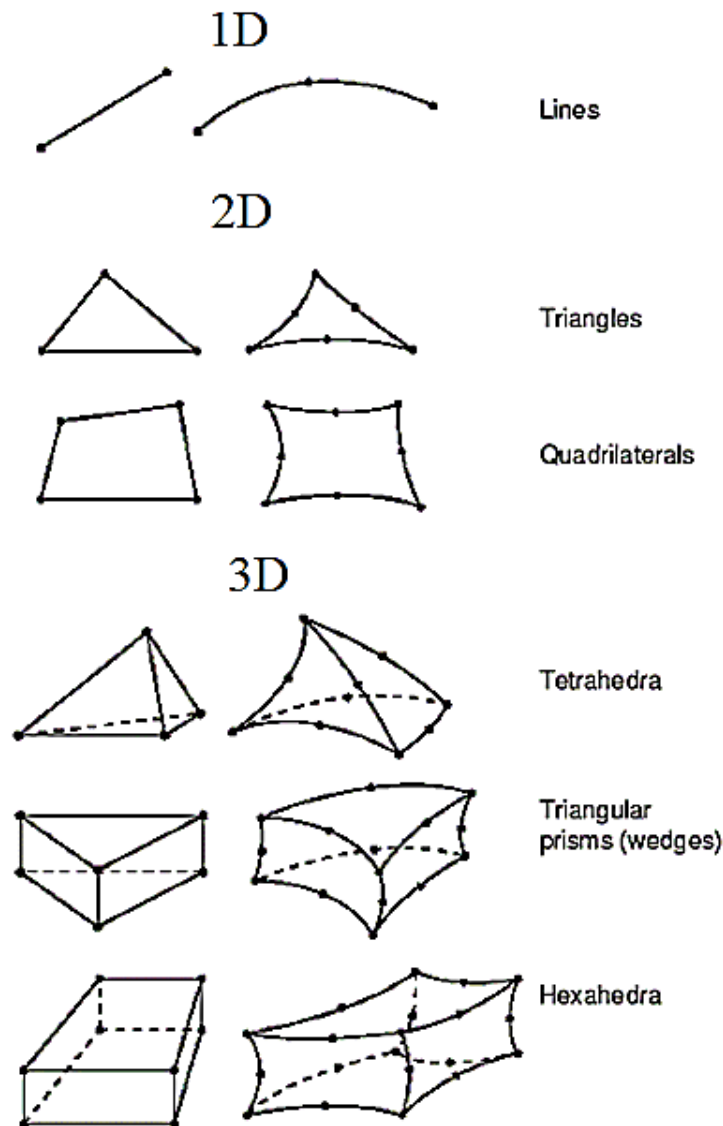
Figure 3-21 Element Shapes, (Smith 2018)

Abaqus offers various techniques for mesh generation, including free, swept and structured meshing. The structured meshing technique is used in this present study. Quadrilateral and hexahedral elements are adopted for the majority of models analysed hereafter. The aspect ratios of the mesh elements are a crucial characteristic towards achieving a successful model by avoiding substantially smaller or larger than particular appropriate values. This phenomenon is examined using mesh controls, and verifications were provided by using Abaqus. Therefore, initial convergence studies are performed employing the mesh size from coarser to finer to achieve the most effective mesh

configuration which can produce the results accurately whilst preserving reasonable computational time from coarser to finer. In each case, once the mesh is required, this technique is used according to the analysis condition. A sensitive analysis of mesh convergence study related to the FE models was developed according to the corresponding analysis circumstance in Chapters 4, 5, 6, 7 and 8.

Detailed descriptions of the models are given in the respective chapters. This section focuses only on the influence of mesh size on system performance and level of accuracy. The precision of the findings is reduced when the size of meshing is increased. This phenomenon is evident for all FEM models produced in the present study. However, sensitivity analysis is performed for every case study to ensure the targeted, appropriate mesh size.

3.1.2.1.3. Constraints and Boundary conditions

The consequence of the system supporting conditions and applied loading patterns on the system behaviour for every test circumstance is described in each modelling chapter through appropriate boundary conditions and constraints. The displacement and rotation, in addition to dynamic conditions of acceleration and angular acceleration degrees of freedom, are appropriately restrained to obtain the exact test conditions, whereas appropriate constraint conditions according to the modelling situation are employed. For instance, the rigid body allows constraining in the region's motion of an assembly to the motion of a reference point, and kinematic coupling offers constraints between the reference node and nodes on a surface (the coupling nodes). Moreover, tie constraint affords a uncomplicated approach to bond surfaces using a master–slave system.

In the case of geometry, boundary conditions, loading and the observed failure mode of the symmetry test configuration, only the structural part is modelled, and appropriate symmetry boundary conditions are applied along the presumed symmetry axis (i.e. X, Y or Z). Boundary conditions and models corresponding to constraints are fully discussed and described in Chapters 4–8, in which the applied boundary conditions and constraints for each model are fully depicted.

3.2. SeismoSignal and SeismoMatch Software

The seismic input for the analyses of nonlinear dynamic of structures is typically described in terms of acceleration time histories which their acceleration response spectra are matched a specific target. The spectral matching in time domain utilised to produce

reasonable design acceleration time histories is generated using SeismoMatch and SeismoSignal software (Al Atik & Abrahamson, 2010). SeismoSignal and SeismoMatch are a set of software that are employed to perform earthquake record operations, such as the managing of strong motion data, deriving elastic and inelastic response and power and Fourier spectra, designing many of the commonly used ground motion parameters, modifying earthquake records to match a definite target response spectrum or generating artificial earthquake accelerograms for the same purpose. SeismoSignal signifies an efficient package for the processing of strong-motion data. It permits the derivation of elastic and constant ductility inelastic response spectra, calculation of Fourier amplitude spectra, filtration of undesirable high and low frequency content and estimation of important strong-motion parameters, such as the Arias Intensity and the significant and operative duration.

SeismoMatch application can adjust earthquake accelerograms to match a definite target response spectrum, employing the wavelet algorithm proposed by (Abrahamson, 1992) and (Hancock *et al.*, 2006). It can also simultaneously match several accelerograms and then achieve a required matched spectrum, in which the maximum misfit considers a predefined tolerance. Therefore, this application can be employed in combination with other record selection tools and appropriateness verification algorithms such as UUSG PEER to describe sufficient sets of records which are essential for nonlinear dynamic structural analysis. For further discussion on the issue of selection, scaling and matching of records, referring to the considerable literature, such as (Bommer & Acevedo, 2004), (Goulet *et al.*, 2008), (Haselton *et al.*, 2009), (Iervolino, Galasso & Cosenza, 2010) and (Jayaram *et al.*, 2011), that focuses on this issue is useful.

The program is efficient in perusing accelerograms saved in different text file formats. This collection of ground motion records may then be modified to match spectral acceleration within a certain tolerance according to predefined response spectrum which can be specified using EC8 or ASCE seismic provisions. SeismoMatch permits the numerical and graphical results to be replicated to any Windows application such as MS Excel in a particular extension due to its full integration with the Windows environment.

Chapter 4: Nonlinear Numerical Simulation of Physical Shaking Table Test

4.1. Introduction

The possibility of structures supported by situated piles on soft soils within earthquake hazard zones stipulates much demand on the piles. Potential resonance consequences amongst soft soil sites, which are classified as prolonged period sites, may amplify ground motions, and high-rise buildings may further aggravate the problem. Potential liquefaction and/or strain softening in soft soils can also dictate extra demands on pile foundation systems. Seismic soil-structure interaction (SSI) analysis is a sophisticated process that simultaneously involves pore water pressure generation, ground and foundation/pile deformation and gap/slap mechanism. In traditional seismic design practice, the effect of the pile on the ground motions applied to the structure is ignored or simplified (Emadi, Shakib & Shadlou, 2014),(Fan *et al.*, 1992) and (Stone & Yokel, 1987).

SSI effects have often been disregarded in the seismic design procedure, to facilitate analyses and avoid intricacies (Ganjavi & Hao, 2013). This practice is generally accepted as a conservative design approach for spectral analysis because a flexible pile foundation lengthens the natural period of the structure and increases damping provided (Fan *et al.*, 1992). Moreover, SSI effects are presumed advantageous during earthquake excitation because they can increase the structural flexibility and natural period of the structure and consequently decrease structural base shear forces (Khalil & Shahrour, 2007). Simplified and non-standardised analyses are widely used to assess pile integrity during seismic loading (Stone & Yokel, 1987). Two of the most relevant discussions currently in SSI research are (i) increasing residual deformations and (ii) decreasing the stiffness of the pile foundation system, which in turn may affect the seismic response and structural displacement (Phanikanth et al. 2013).

The ground motions experienced by a superstructure are influenced by the pile system, and piles may experience extreme damage and/or failure under earthquake loading. In general, there is insufficient information in the public domain regarding seismic soil–pile response cases, and several of the cases that are published only involve piles equipped to record the dynamic response. These cannot provide a reliable basis for calibrating and

validating the analytical techniques which have been developed for seismic soil–pile–superstructure interaction (SSPSI) problems.

In this context, in recent years researchers have been conducting centrifuge and shaking table tests under controlled laboratory conditions. The majority of these tests have investigated seismic responses in cohesionless soils with liquefaction potential (Varghese & Madhavi Latha, 2014). However, many piles are located on soft clays that have the potential for cyclic strength degradation during seismic loading (Stromblad, 2014), and (Meymand, Riemer & Seed, 2000). Therefore, the need for a greater research focus into SSPSI is clear. Laboratory shaking table tests on specimens with a flexible wall offer an opportunity to extend the limited performance data of SSPSI in soft clays, under various controlled test conditions (Tipsunavee & Arangjelovski, 2015). The flexible wall container allows the soil to move horizontally along the depth and therefore this test method can provide a realistic response compared with those using other types of container (Meymand, Riemer & Seed, 2000). Moreover, these experiments can fully represent the coupled behaviour of the soil–pile–superstructure system.

In the past, the majority of numerical soil-pile/foundation models presented in the available literature have employed a Winkler spring model, which uses beam elements to represent the pile, spring elements for the soil along the pile surface that is embedded in the ground, and applied earthquake time history at the bottom of the structure or at the side boundary condition (Durante *et al.*, 2016). The wave propagation and output data are unrealistic however as the soil model is usually restricted to being either linear elastic or viscoelastic, owing to the limitations of finite element analysis (FEA) and computer resources. Moreover, to apply the nonlinear FEA approach in engineering practice, the resulting numerical simulations should be further verified through experiments ((Brown, 2011), (Jahromi, Izzuddin & Zdravkovic, 2009)).

One of the key challenges in modelling geotechnical materials is representing the dynamic response of the soil accurately under various external loading conditions. Soil materials can have a range of diverse and complex properties, including their elasticity, viscosity and plasticity. Nevertheless, reliable constitutive models are capable of simulating the material as a complex, heterogeneous and strongly nonlinear material ((Romo, Mendoza & García, 2000), (Zdravković & Potts, 2020)) for various soil types and conditions, such as cohesive or non-cohesive and saturated or unsaturated soils (Khodair & Abdel-Mohti, 2014).

116

In this context, the current study is focussed on the development of a three-dimensional (3D) finite element (FE) model, including the gap/slap mechanism to simulate a physical shaking table test with a flexible wall barrel, to simulate the dynamic response of a soil structure interaction system founded in a soft clay. The study proceeds with a description of the shaking table tests which are later employed to validate the numerical analysis (Meymand 1998). This is followed by a detailed description of the finite element model, which is developed using the Abaqus software (Smith 2018). The model is then employed to further understand the behaviour.

In accordance with the physical reference case study conditions (Meymand 1998) , the soil material properties were obtained and numerically modelled with three typical soil constitutive criteria, i.e. modified Mohr–Coulomb, Drucker–Prager and Cam–Clay models. The target was achieving and specifying the closest dynamic system behaviour compared with the physical behaviour of shaking table test concerning soil simulation related to seismic excitation.

4.2. Reference case

A series of physical shaking table tests comprising flexible wall barrel containers were conducted by Meymand (1998) at the UC Berkeley PEER Centre Earthquake Simulator Laboratory, and the data from these experiments are employed herein for validation of the numerical modelling. The principal objectives of the physical shaking table tests were to achieve insights into SSPSI behaviour modes and produce a set of performance data, which could then be employed for further analysis. Two specimens from Phase II of this study are selected as reference cases for the current work, namely tests 1.15 and 2.26. Both of these comprised soil which was embedded with a single pile supporting the superstructure. The experimental set-up was able to physically model the entire seismic soil–pile–superstructure interaction (SSPSI). The main aim of the experimental campaign was to provide an insight into specific SSPSI issues, such as the frequency response of the structure, multidirectional excitation, kinematic and inertial responses and pile/cap soil contact.

The individual model piles were tested simultaneously and arranged in the test container in a manner that minimised element interactions (Al-Isawi, Collins & Cashell, 2019). The piles were simulated in one model or each pile was allowed in individual models in accordance with the physical test conditions (Meymand 1998). After a series of trial simulations, the authors of current study found that individual piles models led to more

accurate validation. In terms of instrumentation, there were twenty-three accelerometers arranged in two vertical arrays embedded in the soil deposit, which were attached to the head masses of the piles (i.e. the superstructure) to capture translation and rocking motions. In addition, seven pairs of bending strain gauges were attached to each pile see Figure 4-1 and Table 4.1. Based on the soil strength and shear wave velocity profiles, the soil in the tests was defined as being lightly over-consolidated soft to medium stiff clay. Accordingly, in the numerical model, the positions of the dial gauges were considered when the output data were obtained (see section 4).

Table 4.1 Physical model instrumentation

Test code	Sensors	Test code	Sensors
Test 1.15		Test 2.26	
S_1, S_2, S_3 and S_4	• Seven pairs of bending strain gauges • One pile head accelerometer	$S_1, S_2, S_3,$ and S_4	• Seven pairs of bending strain gauges • One pile head accelerometer
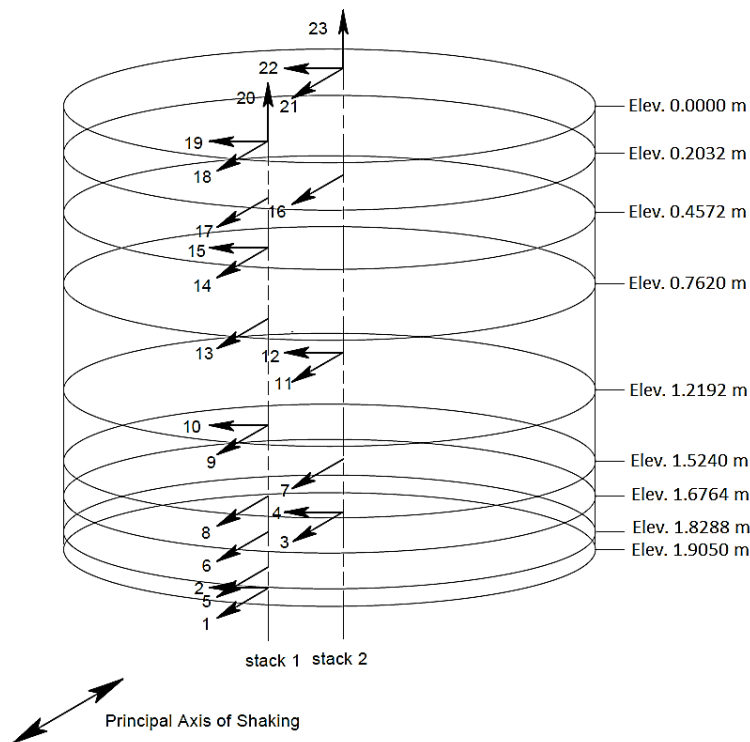
Figure 4-1 Phase II Accelerometer Array, Modified from, (Meymand 1998)

4.2.1. Scale modelling

As with all shaking table tests, the scaling details are very important and the relationship between the scale model and the desired full-scale prototype behaviour requires careful

118

consideration. Kline (Kline, 1986) defined three approaches for enhancing the power and complexity for scale modelling applications: dimensional analysis, similitude theory and governing equations. However, none of these approaches in isolation is capable of representing the true behaviour of this highly nonlinear and complex scenario. Therefore, in the physical experiments (Meymand 1998), a combined scaling method system was developed by identifying and modelling the primary forces and processes in the system whilst suppressing minor effects. Considering the complexity of the SSPSI problem and the significance of the approach for defining the variables and modes of the system, the scaling method was designed to capture the behaviours of the principal interests adequately. The accuracy of this combined scaling method was classified as being either "distorted", "adequate" or "true" depending on the degree of precision required for a particular scenario (Moncarz and Krawinkler 2006), (see Chapter 5 in the current study).

In the current study, this combined method is applied to create a "adequate" model that can represent all primary parameters that are involved in the SSPSI mode in the produced scaled model. All primary parameters of the prototype elements, i.e. the soil and the piles, are demonstrated in dimensional form using an appropriate scaling factor, see Table 4.2.

Table 4.2 Geometric scaling factor λ , (Meymand 1998)

Variable	Factor	Variable	Factor
Mass Density		Force	λ^3
Acceleration	1	EI	λ^5
Strain		Frequency	$\lambda^{-\frac{1}{2}}$
Length		Stiffness	λ^2
Stress	λ	Time	$\lambda^{\frac{1}{2}}$
Modulus		Velocity	

summarises the main model parameters defined in terms of the geometric scaling factor (λ) employed in this study, where *EI* is the product of the Young's modulus (*E*) and the second moment of area for the section (*I*). The geometric scaling factor employed in the reference case had a value equal to 8 (Meymand 1998), and therefore this value is also adopted in the current study.

4.2.2. Details of the physical shaking tests

The shaking table employed in these physical tests was 6.1 m × 6.1 m in plan, and had a load capacity of 580 kN, a frequency range of 0–20 Hz and six controlled degrees of freedom (Meymand, Riemer & Seed, 2000). In geotechnical scaled modelling, a container is typically utilised to confine the soil and to impose boundary conditions that may not occur in the prototype full-scale field scenario. Accordingly, in these tests, a suitable container was designed that could minimise the effect of free boundary conditions on the overall system response and also enable the model to replicate the seismic behaviour at the level ground (i.e. the free field). On this basis, a laterally flexible and radially stiff cylindrical container was selected for the quasi-free field response. This design extends the centrifuge testing laminar box concept to permit multi-directional excitation (Mylonakis, Nikolaou & Gazetas, 1997).

The container constrained a soil column which was 2.3 m in diameter and 2.0 m in height and installed on the surface of the shaking table, as shown in Figure 4-2. The top steel ring was supported by four steel pipe columns connected by heavy-duty universal joints, which allowed the ring full translational freedom but prevented overturning rotations. The flexible wall of the container comprised a neoprene rubber membrane that was 6.4 mm thick, which was suspended from the top ring and fastened at the base. The flexible wall was confined by a set of woven Kevlar straps which were 45 mm in width and arrayed in circumferential bands around the exterior of the membrane and arranged at intervals of 60 mm. The elastic modulus (E) of the combined membrane was designed to be identical to that of the soil to ensure that the free-soil boundary condition was not affected. The combination of the rubber membrane and the set of straps provided lateral flexibility and radial stiffness for the container boundary conditions.

This arrangement provides internal shear strips arrayed vertically around the circumference. In this manner, it can transfer complementary shear stresses developed in the soil and stimulate the soil-free field boundary. A plastic sheet sealed the top of the soil specimen during the period between tests, and water was sprayed on top of the soil to prevent the soil surface from drying out. For each test series, the pile was driven into the soil. After each test, the test arrangement was dismantled by removing the piles and backfilling the holes with soil. However, a new pile was driven into the soil the following day in order to perform the next test. The model was left approximately five days before performing the next test due to the beneficial effects of soil thixotropy.

(a)

(b)
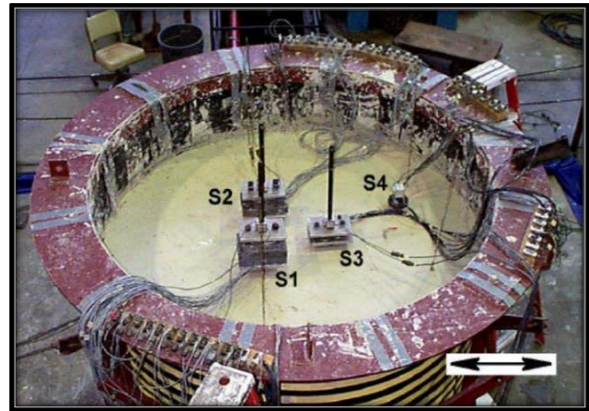
(c)

Figure 4-2 (a) Full Scale Container Mounted on Shaking Table, with Support Struts, and Soil Mixer/Pump in Background, (b) Container on Shaking Table Filled with Model Soil, (c) Layout of the Physical Test (Test 1.15), (Meymand 1998)

4.2.3. Model soil

A soil model with appropriately scaled stiffness and strength properties was developed for the physical shaking test program (Meymand 1998). This model consisted of a weight percentage of 72% kaolinite, 24% bentonite and 10% and 20 % type C fly ash. It has a mass density of 1505.74 kg/m^2, plasticity index of 75, undrained shear strength of 4.8 kPa and shear wave velocity of approximately 32 m/sec. The undrained shear strength with fly ash contents ranging from 20%–60 % is illustrated in Figure 4-3. The figure indicates that the percentage of the fly ash had negligible effect on the shear strength of the model soil. The shear wave velocity was measured at a water content of 130% and cure time of 5 days. A series of unconsolidated-undrained triaxial compression (UUTX) tests on model samples of 20 % fly ash as a percentage of dry weight is presented in Figure 4-4. Undrained shear strength S_u is specimen water content dependence.

A constant rate of strain (5.08e-8 m/sec) consolidation test was executed on a soil model of 20 % class C fly ash at an initial water content of 100 %. The e-log p curve is presented in Figure 4-5, in which the coefficient of consolidation C_v is 2.0458e-10 m^2/sec. This slow rate of consolidation signified relatively stable soil properties during the shaking table testing time. A series of the UUTX tests on model soil specimens was accomplished in the reference case study and was used to identify the numerical properties of soil constitutive models in the current study. The model soil specimens 20 % class C fly ash were prepared at water content 100%. Testing was executed under a confined condition of 1 kilogram per square centimetre and unconfined conditions of normal and fast strain rates of 1905e-6 and 1905e-8 m/sec, respectively, as shown in Figure 4-6. The soil indicated increased peak strengths under fast strain rates loading and decreased sensitivity under confining pressure. However, the failure strains remained rather constant and behaved as a strain-hardening material for both loading rates.

The prototype values implicit in these model properties with a geometric scale factor of 8 are a 25 KN/m^2 static undrained shear strength with 0.75 correction factor of the dynamic strength and a 111 m/sec shear wave velocity. These values are consistent with Dickenson's equation (Al-Isawi, Collins & Cashell, 2019). Accordingly, the model soil constituted an adequate scale model of higher plasticity soft to medium stiff clay, such as San Francisco Bay mud. Table 4.3 represents the material soil properties for the full-scale prototype and the model used in the shaking table tests.
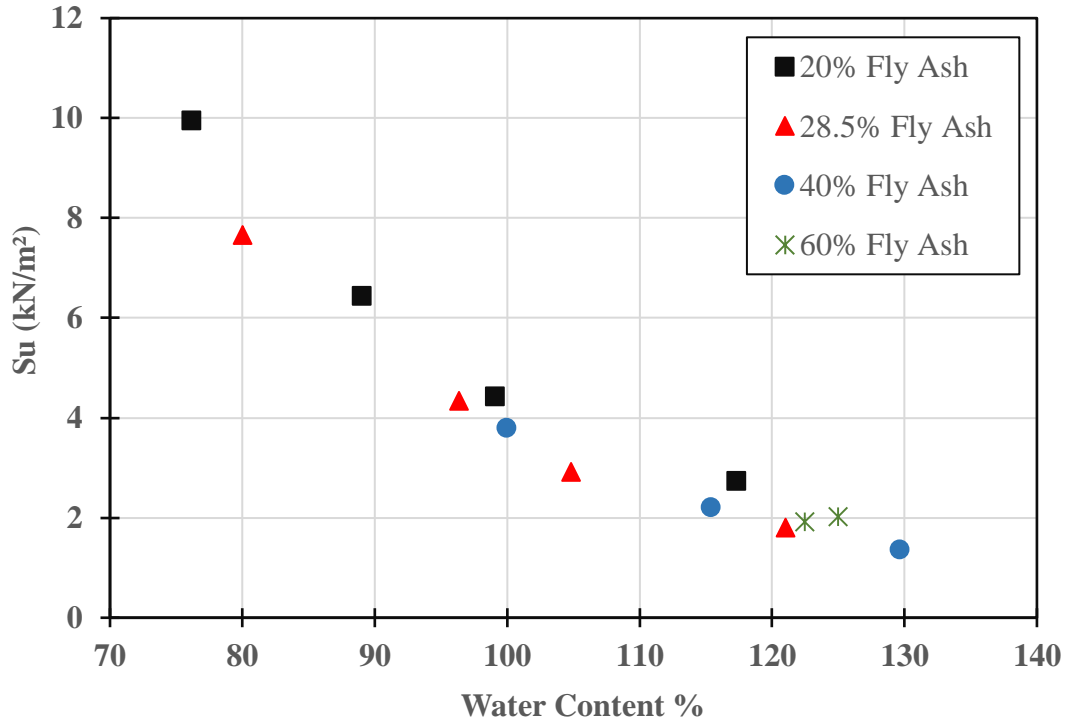
Figure 4-3 Model Soil Undrained Shear Strength versus Water Content of Clay Fraction with different fly ash content
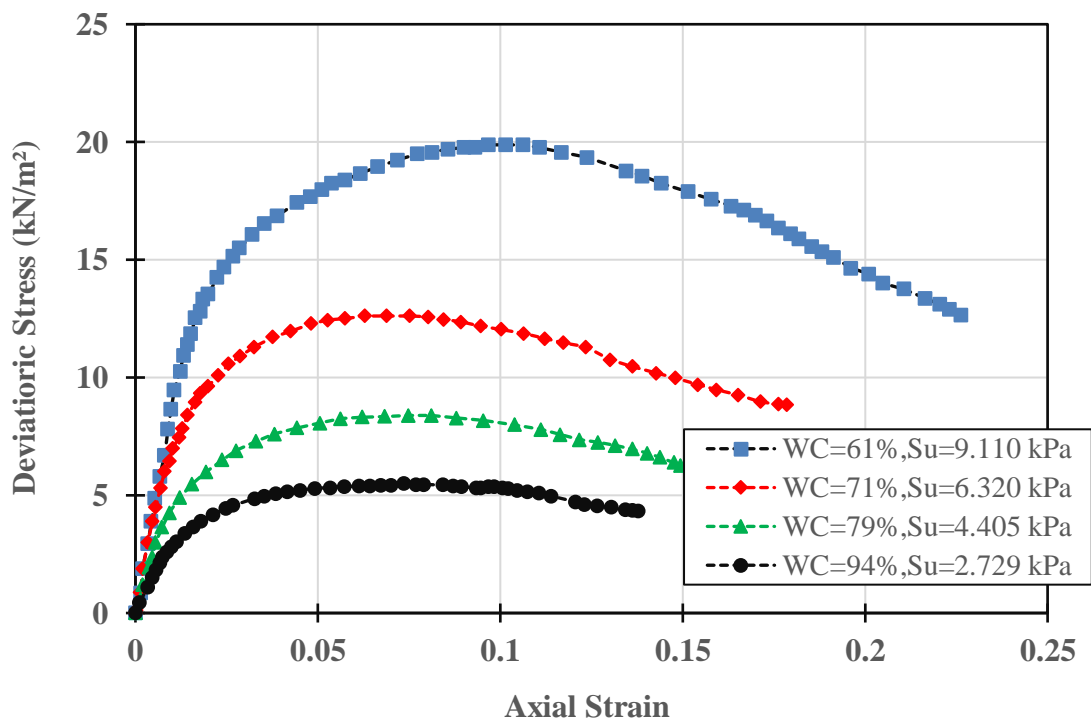
Figure 4-4 Unconsolidated-Undrained Triaxial Compression Test Results for Model Soil Mixture with 20% Fly Ash at 61%,71%,79% and 94% Water Content
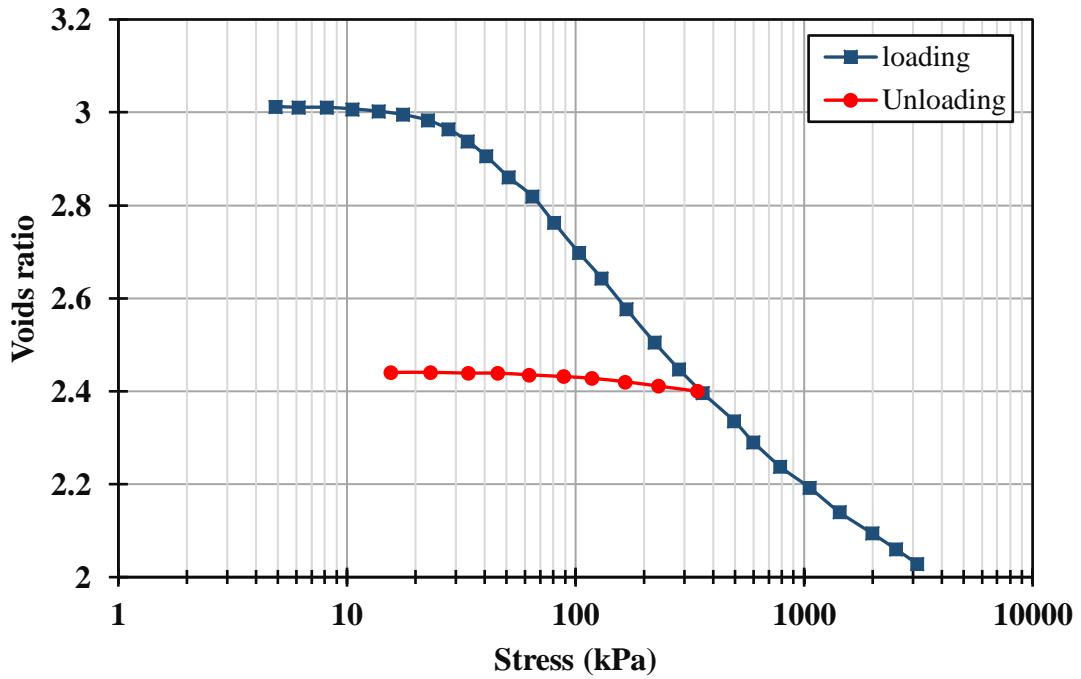
Figure 4-5 Void Ratio versus Log Pressure for Constant Rate of Strain Consolidation Test of Model Soil Specimen (20 % Class C Fly)
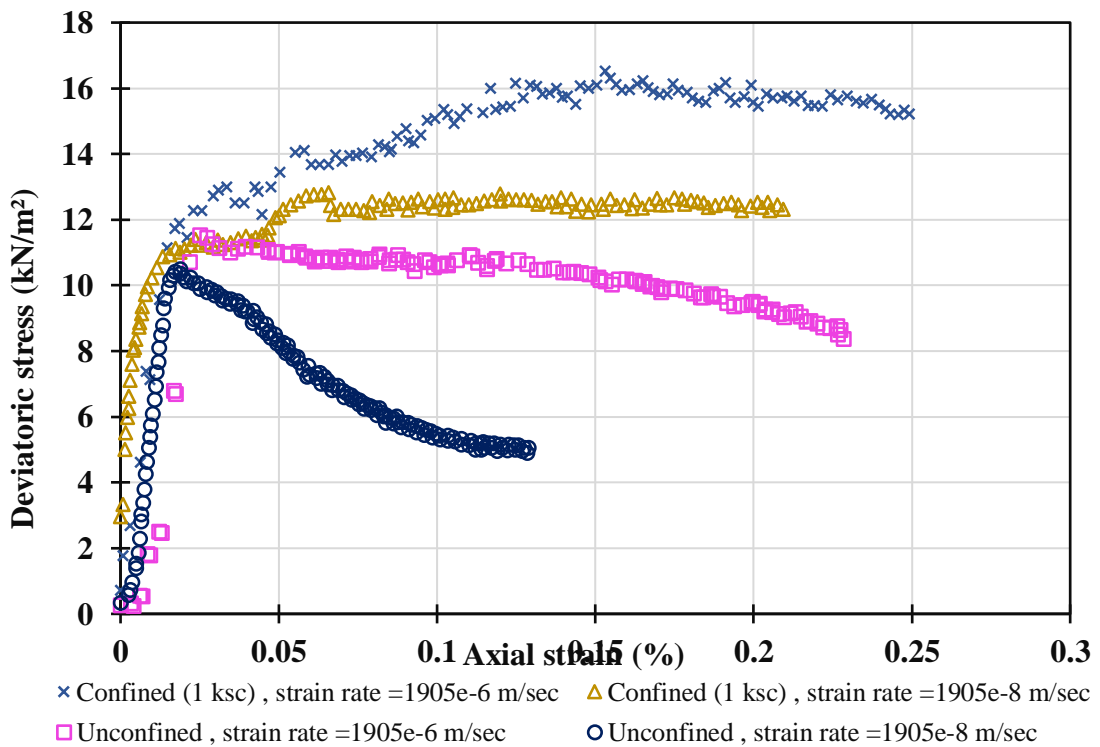
Figure 4-6 Model Soil Unconsolidated-Undrained Triaxial Compression Test Results Showing Effects of Strain Rate and Confining Pressure, (Gruber, 1996)

Table 4.3 Soil Properties for Prototype and Model

Parameters	Prototype	Model
Density [Kg/m^3]	1505.74	1505.74
Undrained shear strength (S_u) KN/m^2	25	4.8
(E) KN/m2	33600	4200
Poisson's ratio	0.5	0.5
Shear wave velocity m/sec	111	39.625
Water content	94%	94%
Liquid limit	115%	115%
Plastic limit	40%	40%
Plasticity index	75%	75%
Rayleigh damping	5%	5%

4.2.4. Pile model

In the full-scale prototype structure that was scaled and replicated in the shaking table tests (Meymand 1998), the pile comprised a steel pipe which was 410 mm in diameter (d) with a wall thickness of 12.7 mm (t_{wall}) and was filled with concrete, in accordance with the California Department of Transportation Highway Design Manual (Tang *et al.*, 2010). The scaling limitations described earlier resulted in a maximum prototype pile length of 12.8 m, thereby giving a pile length to diameter (L/d) ratio of 33, which is acceptable for a slender pile (Durante *et al.*, 2016). The stability conditions of the pile, which are crucial in terms of the lateral response, required that the pile should be fixed against rotation at the top and also relative displacement or translation at the base. The flexural rigidity of the pile was determined as 75.2 kN/m^2. The scaled model pile used in the shaking table tests was designed with due consideration given to the scaling limitations and hence a 6061 T-6 aluminium tube with a diameter (d) of 50.8 mm and wall thickness (t_{wall}) of 0.7 mm was employed. The pile provided an appropriate scaled flexural rigidity (EI) of 2.4 kN/m^2 and a L/d ratio of 36. Table 4.4 lists the properties of the pile for both the prototype and the model, including E_s, E_c and E_{pile} which are the elastic moduli for the steel, concrete and pile model (made from aluminium), respectively, G_{soil} is the shear modulus of the soil and EI_{comp} is the flexural stiffness of the steel and concrete section, (see Chapter 5).

Table 4.4 Pile Properties for Prototype and Model

Parameters		Prototype	Model
Outer Diameter (mm)		406.4	50.8
Wall thickness (mm)		12.7	0.7112
Length (m)		13.4112	2.25
E Steel – Prototype (kN − m^2)	E model (kN − m^2)	1.99948 E+8	6.89480 E+7
E Concrete- Prototype (kN − m^2)		2.75790 E+7	
L/D Ratio		33	36
d/t Ratio		32	71.4
E pile/G soil		1392	3840
Composite Concrete/Steel EI (kN − m^2)		75,179.06	2.42
Rayleigh damping		5%	5%

4.3. Development of the numerical model

The finite element model was developed using the Abaqus software (Smith 2018), implementing the data from Phase II of the shaking table tests previously described (Meymand 1998). Tests 1.15 and 2.26 from that test programme are selected for the validation, and these specimens had a flexible wall barrel container, and adopted a single pile model arrangement. More details on the representation of these tests in the numerical model are presented hereafter.

4.3.1. Input into the numerical model

In Test 1.15, a set of single pile models with head masses of 3.0, 11.40, 45.4 and 72.70 kg were examined whilst Test 2.26 studied free field models; both tests were subjected to unidirectional shaking. Similar to the shaking table tests loading condition, two levels of excitation are applied in the numerical model, namely medium and high excitations of the peak ground acceleration (PGA) corresponding to 0.2 g and 0.69 g, respectively. The input is taken from two different seismic events: (i) the 90 degree component from the Yerba Buena Island record during the Loma Prieta Earthquake (YBI90), and (ii) the Port Island station corresponding to the 79 m record north 00 east component during the Kobe Earthquake (KPI79N00). The YBI90 record had a predominant period of 0.67 sec, a time step of 0.02 sec and a PGA of 0.07 g, which for this physical and numerical testing programme was scaled to 0.2 g to provide the medium level of excitation. The KPI79N00 record had a predominant period of 0.345 sec, a time step of 0.01 sec and a PGA of 0.69 g, which was scaled to 0.7 g for the high level of excitation (U.S. Geological Survey, 2018). In accordance with the scaling relations given in Table 1, the time steps of these two records were divided by $\lambda^{0.5}$ in the both physical and numerical model, resulting in compressed time scales compared with the original records. The acceleration time

histories, and acceleration response spectra for these two records, are shown in Figure 4-7 and Figure 4-8.
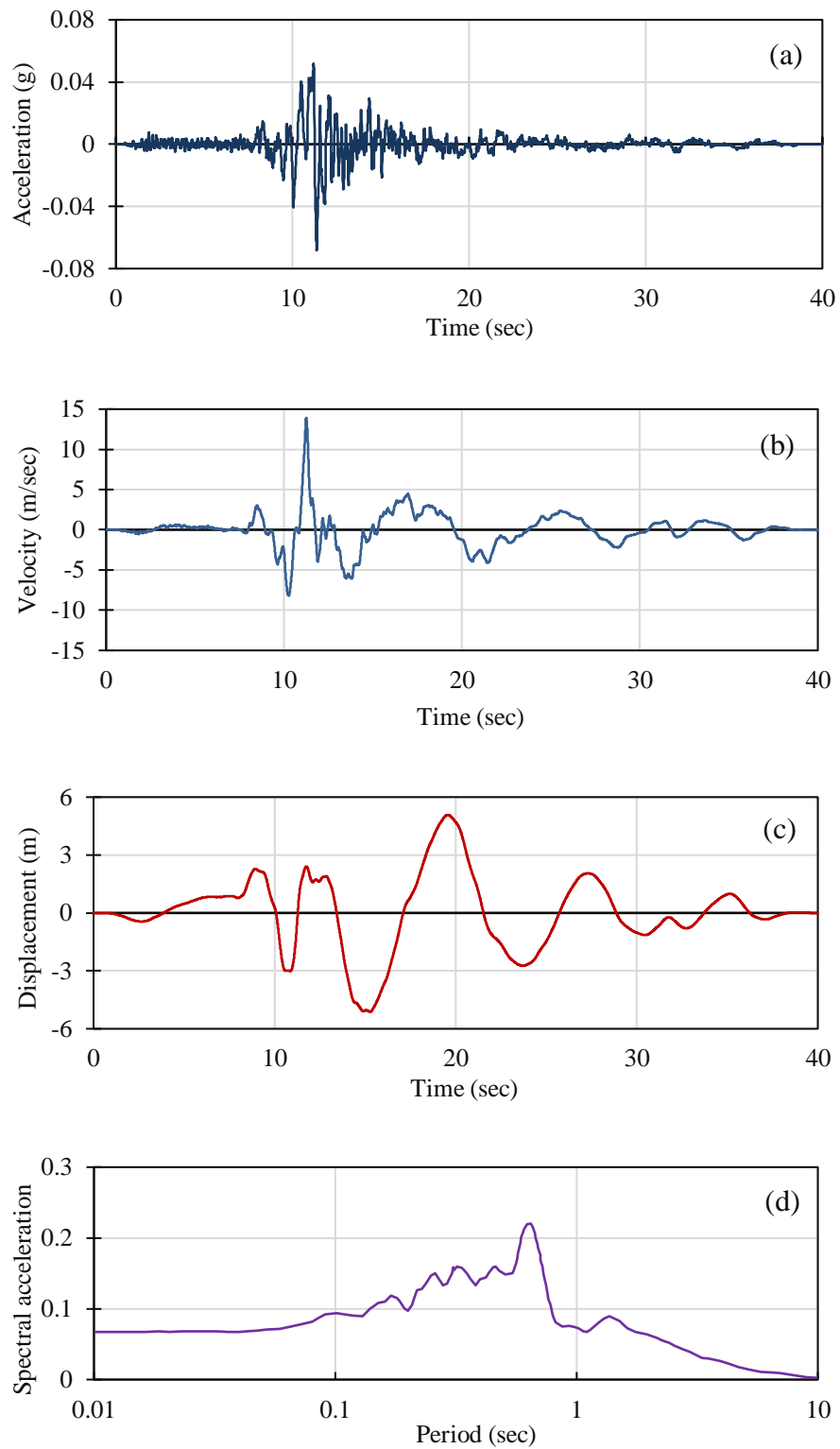
Figure 4-7 Input motions including (a) acceleration, (b) Velocity, (c) Displacement (d) acceleration response spectra for the YBI90, Modified from (U.S. Geological Survey, 2018)
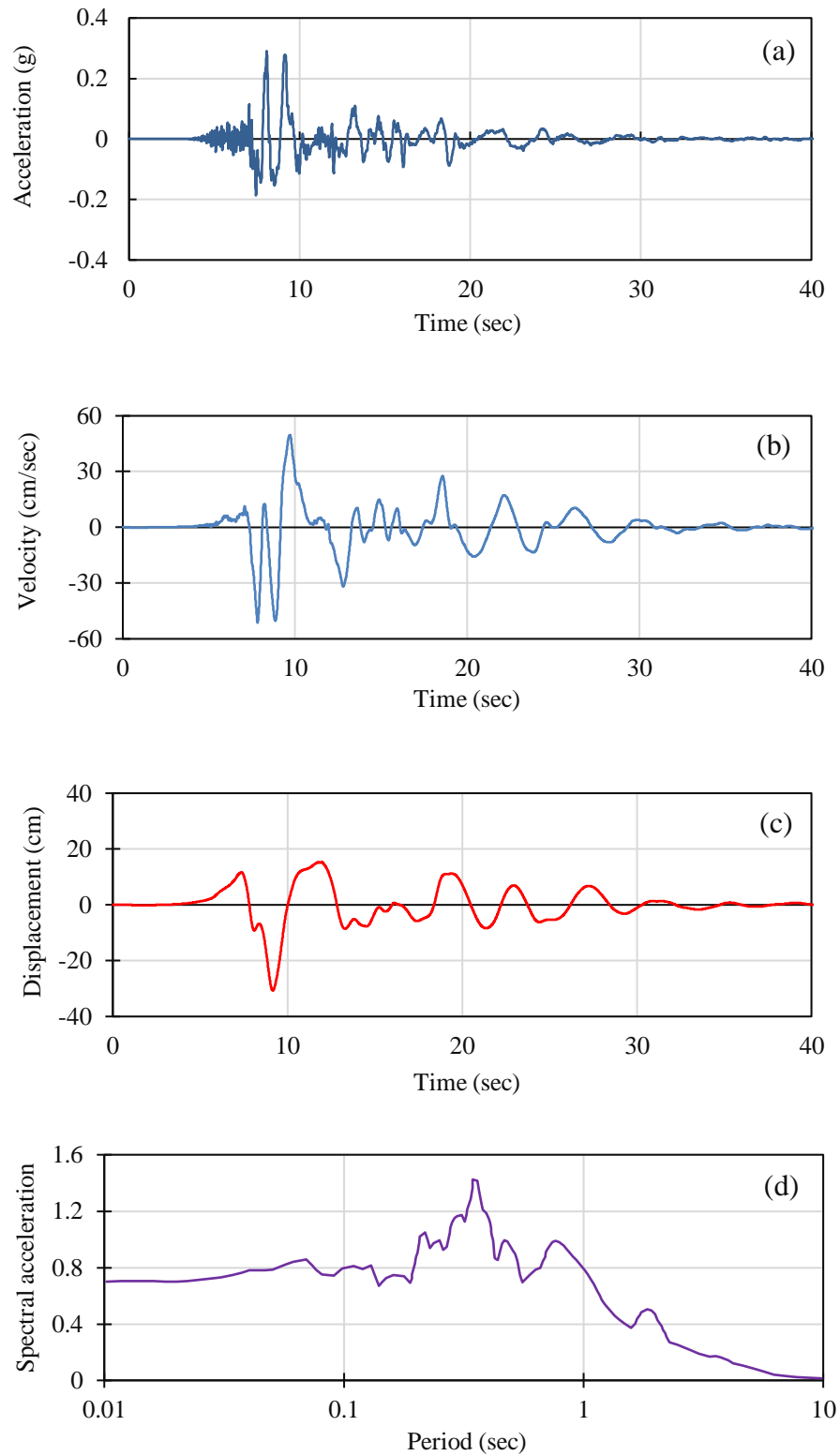
Figure 4-8 Input motions including (a) acceleration, (b) Velocity, (c) Displacement (d) acceleration response spectra for the KPI79N00, Modified from (U.S. Geological Survey, 2018)

128

A 3-dimensional finite element analysis is carried out in Abaqus using the sequential analysis method, which is capable of modelling the SSI under geostatic, static and dynamic loading. The different steps in the analysis are outlined hereafter:

(i) First is the geostatic step, in which only the soil body force is included. Consequently, the forces and initial stresses must be precisely established and equilibrated for minimal soil displacement.

(ii) This is followed by the first loading stage of the analysis, to create stability between the soil and the pile and prevent negative shear stress between them. This represents the piles' installation stage during model construction.

(iii) Then, the static-friction loading step is employed for the application of gravity loads, which are assumed to be static and uniform, in accordance with the loading conditions in the reference case study.

(iv) Next is the dynamic analysis step in which the time history input data are applied to the bottom of the clay soil (at the base of the shaking table). The displacements were restrained in the horizontal direction for the geostatic and static step and changed to the vertical direction allowing in this step, allowing free movement in the horizontal direction. The base of the model is restrained with roller supports in the vertical direction. By contrast, the other two direction boundary conditions, which are perpendicular to shaking direction, are constrained.

Both the soil and the superstructure are modelled using 3D solid elements (C3D8R in the Abaqus library) which are eight-node linear brick elements with reduced integration. For the piles, linear shell elements (S4R) are used, which are a four-node doubly curved shell elements (Smith 2018). As this is a cylindrical application, a radial mesh is the most appropriate meshing type and it is employed in accordance with the approach of other researchers (Pitilakis *et al.*, 2008). As discussed in Chapter 3, a mesh sensitivity study was conducted to achieve accurate and reliable results, resulting in which are 50 mm in each dimension at the boundary of the model and refined to 10 mm near and at the pile. The piles were simulated individually as this was found to give the most accurate results. Given the similarity between the approach of using the combination system of flexible wall material properties, which was chosen in the reference case study, and the alternative method of using the soil sample properties directly, the combination system was not adopted further in the numerical analysis. Alternatively, the soil boundary was

constrained in accordance with the physical test conditions. as shown in Figure 4-9 and Figure 4-10

(a)   (b)
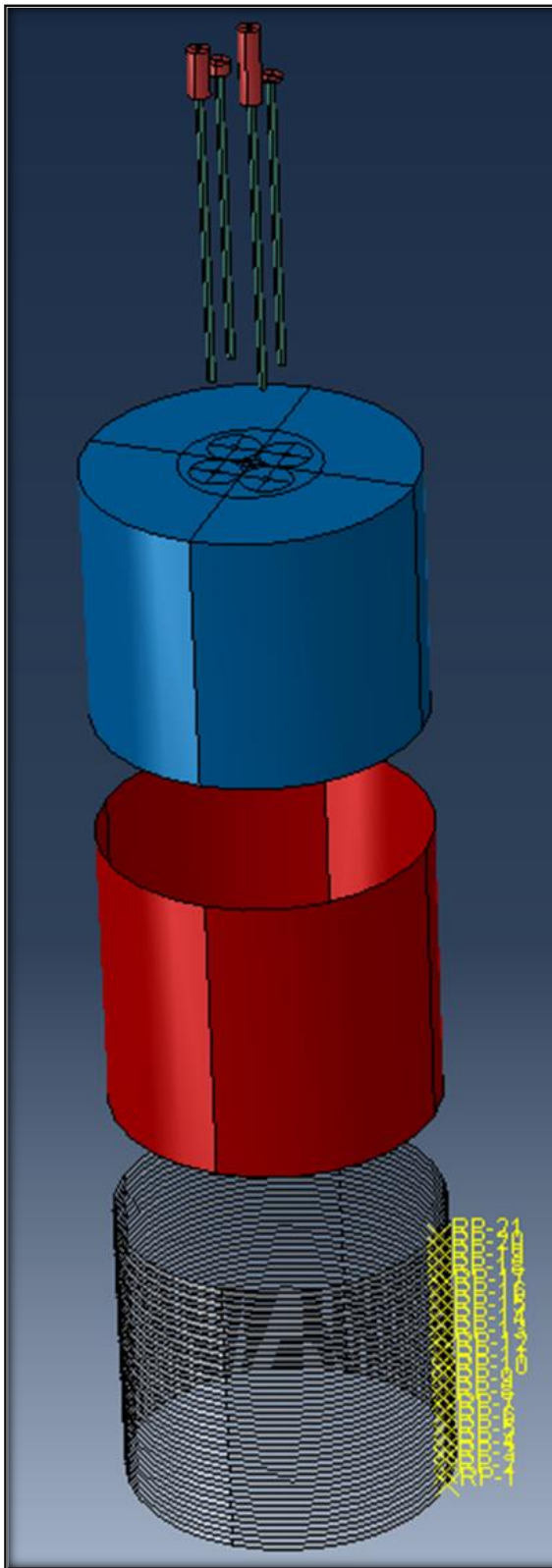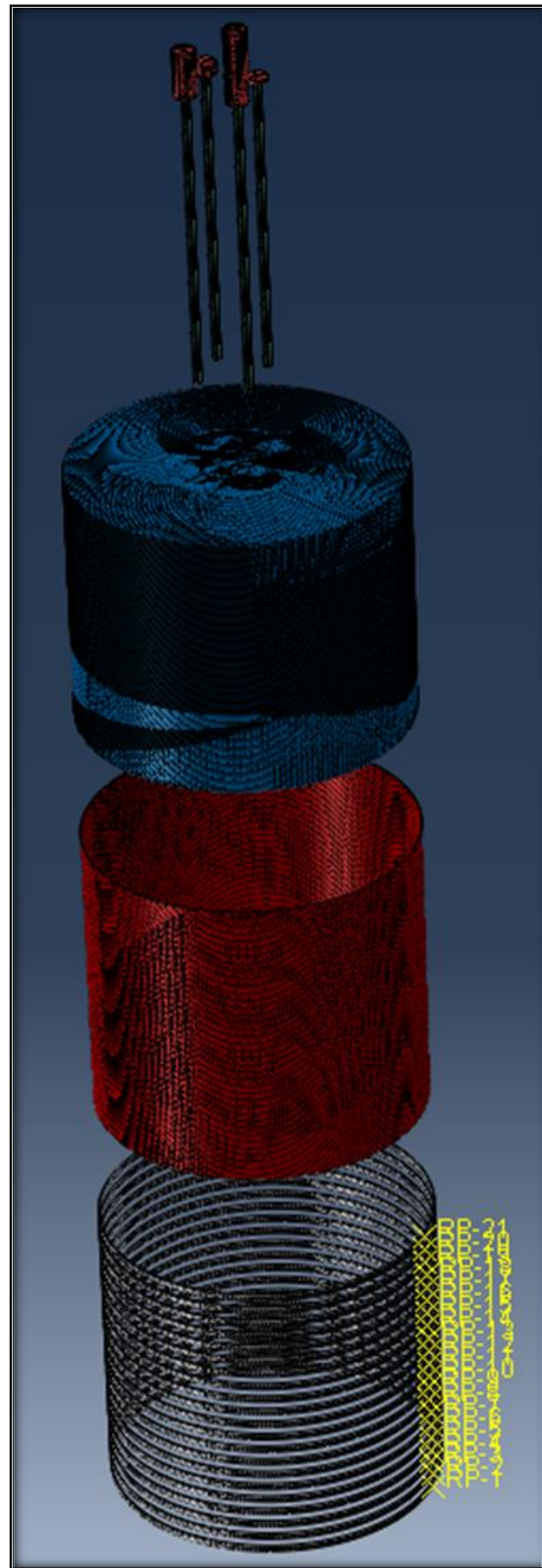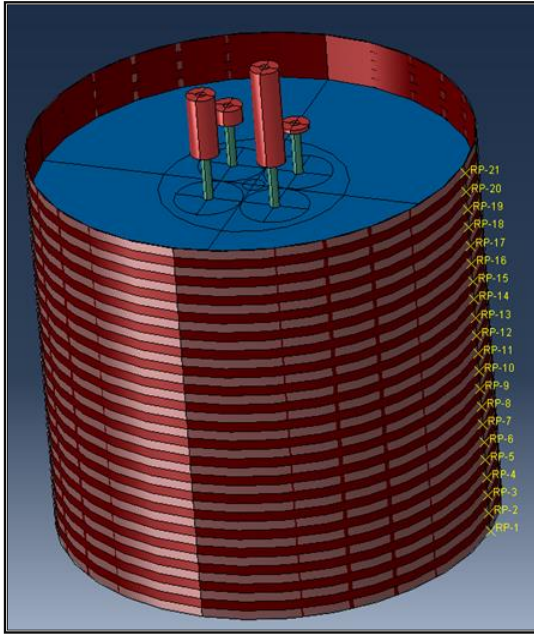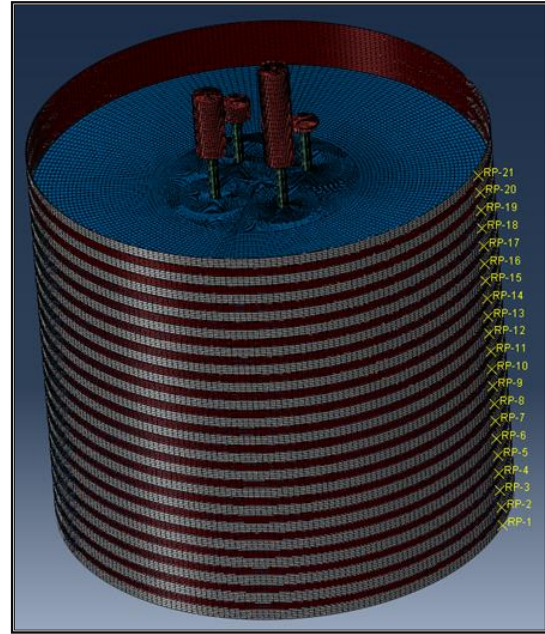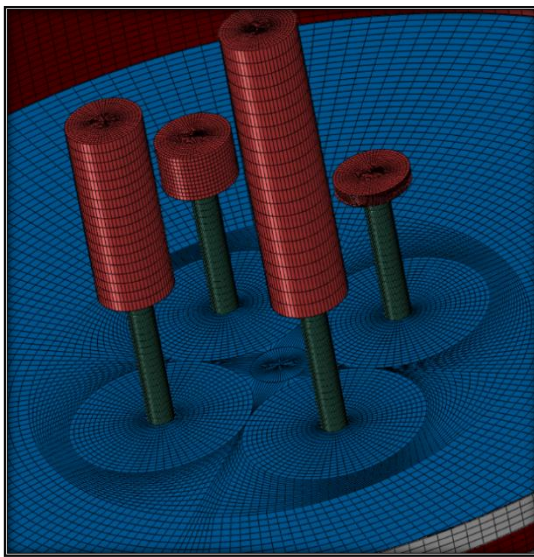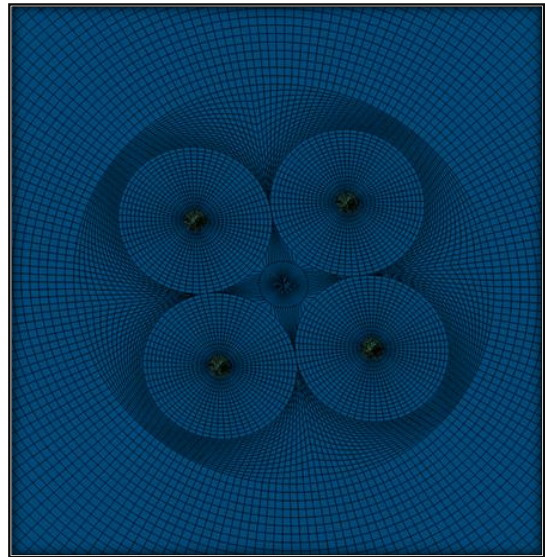
Figure 4-9 Layout of the Numerical Simulation, Geometry and 3D Finite Element model, (a) Model Features Assembly (Model of all Physical Test Parts- Membrane and Straps. (b) 3D Finite Element Meshing for the Case Illustrates in Figure 10-a, (c) Whole Assembly Geometry and 3D Finite Element Model, (d) Whole Assembly 3D Finite Element Meshing, (e) Soil-Pile Contact-Top View, (f) Model Base and Soil-Pile Contact

(a)

(b)

(c)

(d)

133
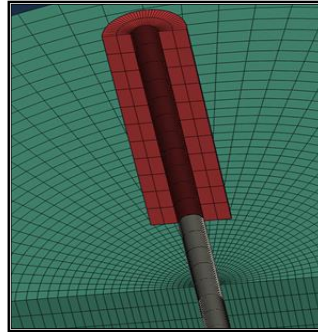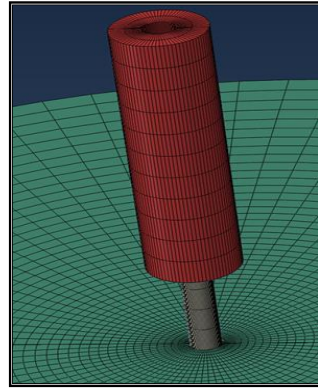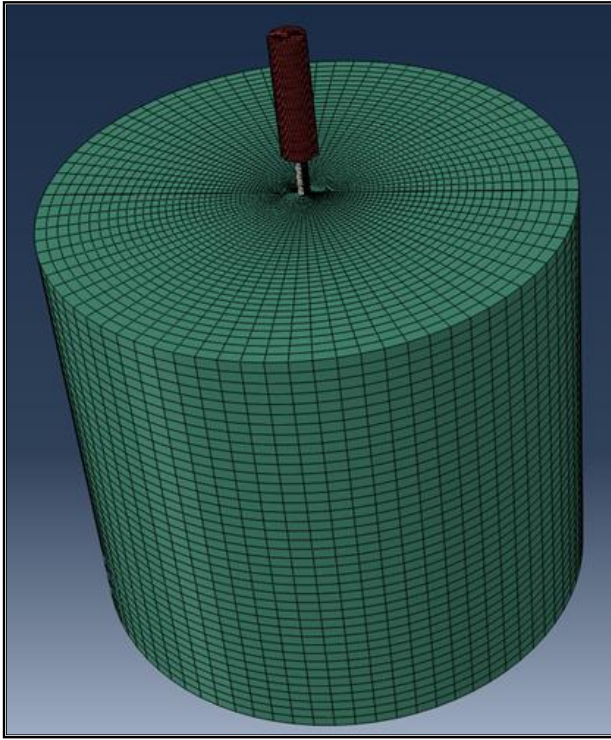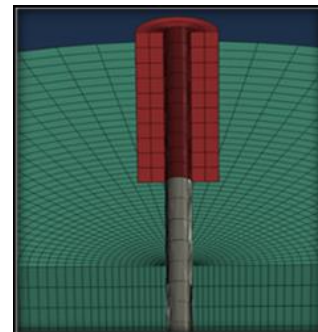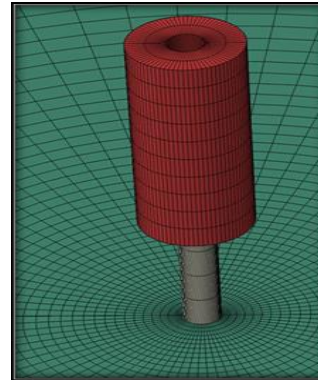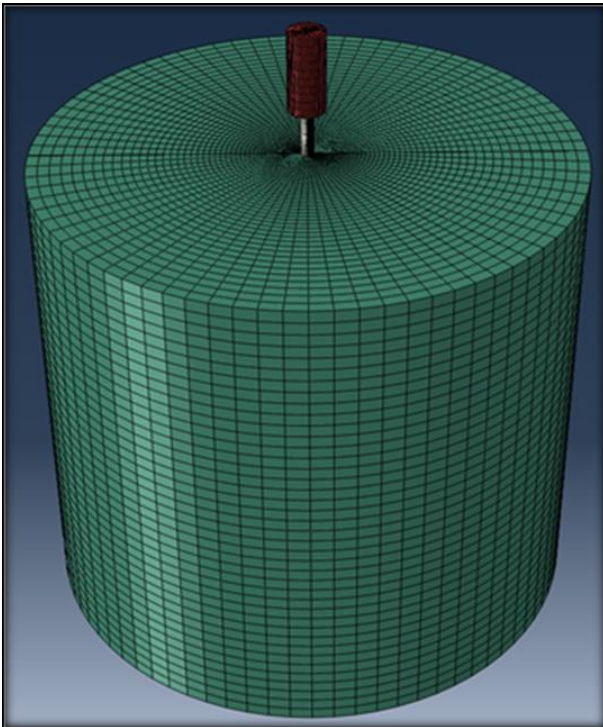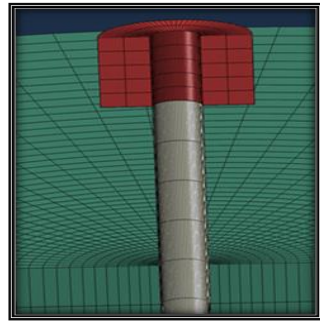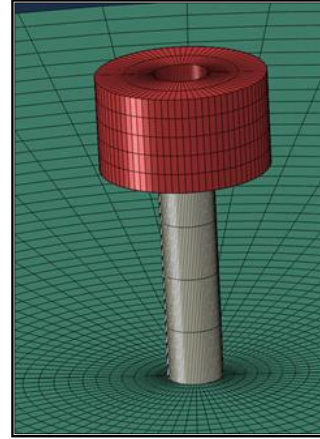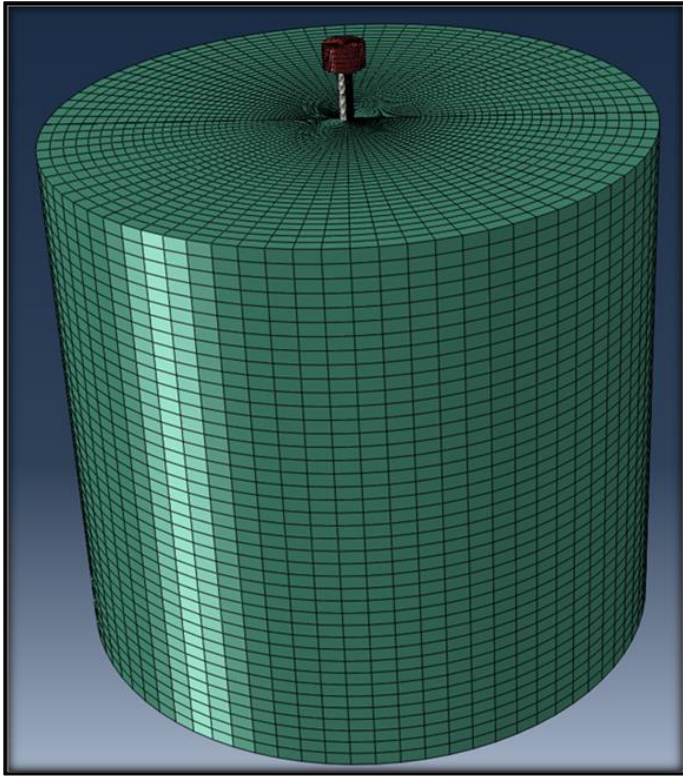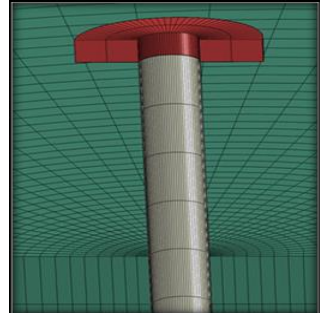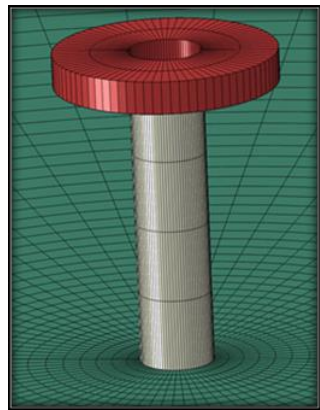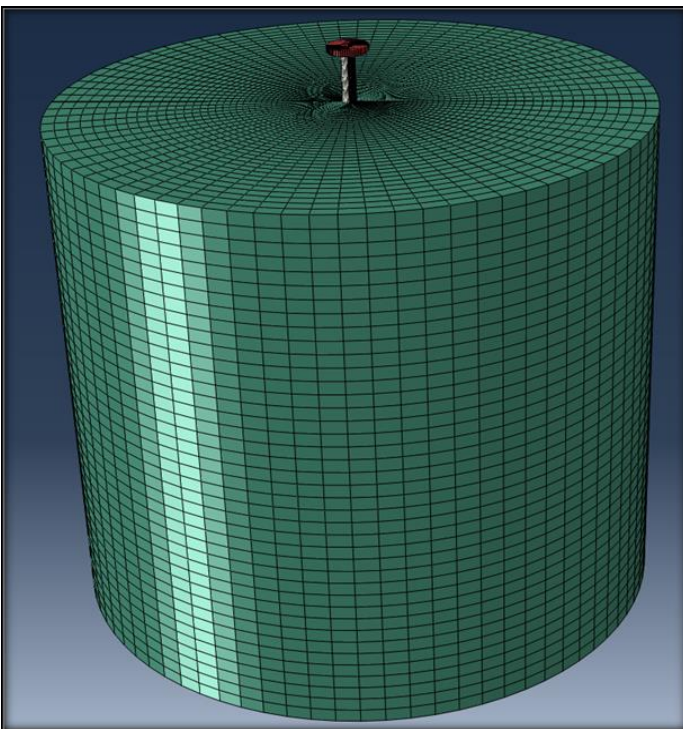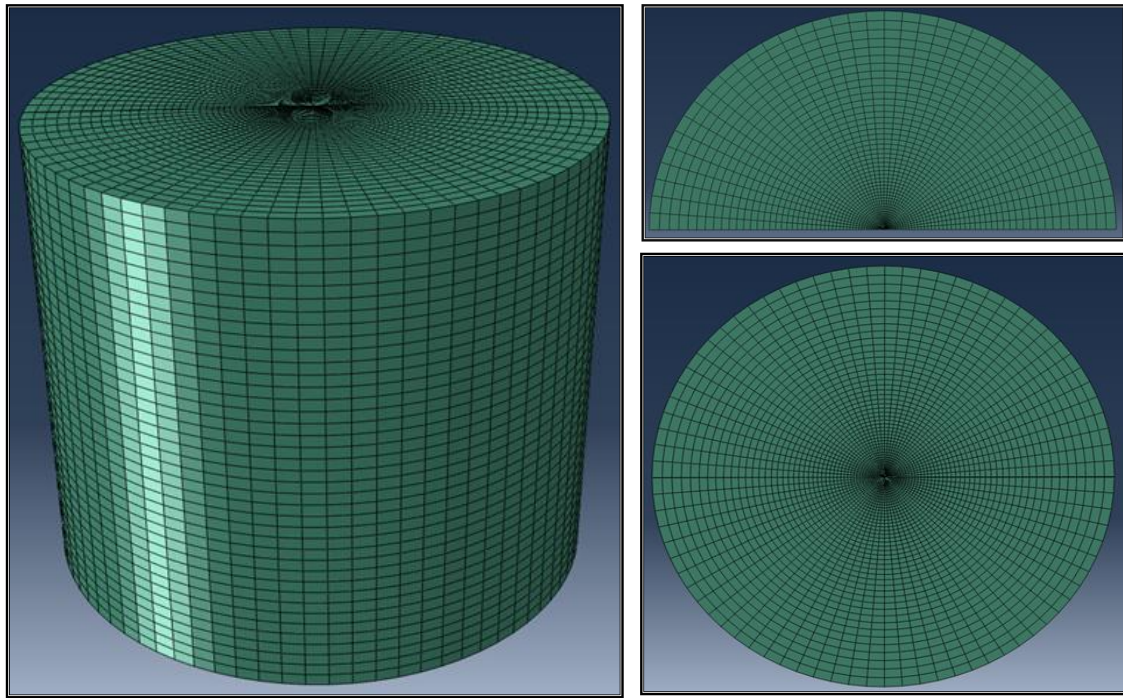
(e)

Figure 4-10 11 Layout of the Numerical Simulation, Geometry and 3D Finite Element Models–(Boundary constrained condition), (a) Pile Head Mass 72.7 kg, (b) Pile Head Mass 45.36 kg, (c) Pile Head Mass 11.40 kg, (d) Pile Head Mass 3.0 k, (e) Free Field

4.3.3. Simulation of the soil–pile–superstructure interaction (SSPSI)

One of the most challenging issues in the numerical modelling of soil-structure interaction, and in particular seismic soil–pile–superstructure interaction (SSPSI), is accurate simulation of the contact between the piles and the surrounding soil. There are a number of different stress components including normal, tangential and relative surface sliding stresses as well as frictional shear stresses. In the numerical model, this contact is considered to be a discontinuous constraint, which can occur when loads transfer between contacting elements under contact conditions. In this case, once the two surfaces detach, the constraint is removed (i.e. the gap condition), and the slap condition takes place during the return of the contact. Abaqus includes two different formulations for modelling this scenario: (i) a small sliding formulation with limited sliding and some arbitrary rotation of the contact surfaces and (ii) a finite sliding formulation with separation and sliding of finite amplitude and some arbitrary rotation of the contact surfaces. In the case of the laterally loaded pile, the relative surface motion is categorised as small sliding. To model the normal behaviour, the 'hard contact' option is selected in the model as a contact property for defining the pressure-clearance relation. Moreover, the model removes the contact constraint when the value of the contact pressure becomes zero or less. Contact

134

surfaces in dynamic circumstances usually transmit normal and shear forces along with their contact interface. The Coulomb friction model, which is included in Abaqus, defines the interaction relation between the constraint surfaces which are in contact. In this study, both the static and kinematic friction coefficients are considered directly and the model identifies the exponential decay relation between the static and kinematic values. Accordingly, both normal and tangential behaviours are considered. Normal behaviour enables the pressure to transmit between the soil and the pile and both surfaces are in contact. This type of behaviour allows the soil to separate when the contact pressure reduces to zero. On the other hand, tangential behaviour enables the shear stress (or shear drag) to transfer between the soil and the pile surface, as shown in Figure 4-11.
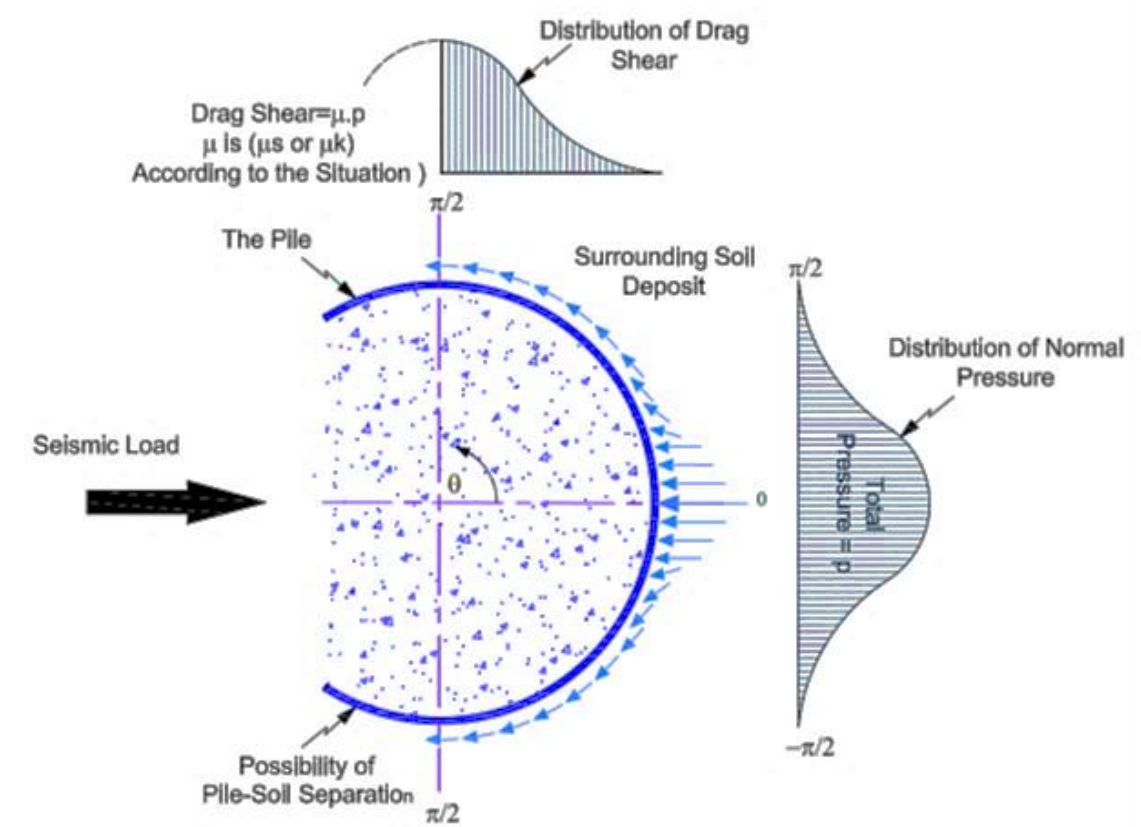
Figure 4-11 Schematic of Normal-Pressure and Drag-Force Distribution (Seismic-Soil-Pile-Structure Interaction with Cap/Slap Mechanism)

4.3.4. Soil constitutive models and parameter

Soil is a heterogeneous material, and its behaviour is substantially affected by a variety of geotechnical and geological parameters, such as particle size and structure, mineralogy, pore water pressure and initial stress state. It is characterised by time-dependent behaviour (i.e. soil creep), and also includes many rheological aspects (Šuklje, 1969).

Over the past five decades, there have been many developments in the modelling of the stress–strain behaviour of soil (Lade, 2005). These models are used to represent the soil behaviour in finite element and/or finite difference approaches of the soil–structure interaction problem under axisymmetric, plane strain and/or general 3D conditions (Helwany, 2007). Simple and advanced models have been developed using the fundamental principles of soil mechanics and their complexity and accuracy can be categorised using experimental evidence or/and theoretical principles. The capabilities and shortcomings of these models can be arduous to determine, and choosing which model is most appropriate for a particular application is challenging. Therefore, the selection of an appropriate soil model relies on many parameters, such as soil type, problem category, solution procedure, complexity, and level of accessibility of the required parameters. For this reason, the current paper includes a detailed analysis of three of the most relevant models, including:

1. The Mohr–Coulomb model, which is commonly used for soil, both for static and monotonic dynamic loading conditions due to its clarity and the case with which the modelling parameters are defined. It is a linear elastic–perfectly plastic model;

2. The Drucker–Prager cap model is also very popular amongst the research community owing to its accurate depiction of the behaviour, and because it simulates a nonlinear elastic–hardening plastic response; and

3. The Cam–Clay approach which is the newest of these three common approaches and also adopts a nonlinear elastic–hardening plastic response.

A fully nonlinear dynamic soil–structure interaction analysis with the application of the gap-slap mechanism is implemented in the current model and the capability of these three constitutive models for modelling the dynamic soil–structure interaction is assessed through comparisons with the physical shaking table experimental results.

4.3.4.1. Mohr–Coulomb model

The Mohr–Coulomb theory was proposed by Charles-Augustin de Coulomb in 1773, in which the soil pressure theory of soil or rock failure is expressed as

$$\tau = c - \sigma \tan \phi \tag{4.1}$$

where σ is the normal stress, τ is the shear strength, c is the soil cohesion and ϕ the angle of internal friction. Christian Otto Mohr developed this to produce a generalised model of shear failure in the 19th century, which is called Mohr–Coulomb yield

criterion (Alex, 2019). In general, in the space of principal stresses, this failure surface F (defined by Eq.(4.2)), is a pyramid with a hexagonal section having the line $\sigma_1 = \sigma_2 = \sigma_3$ as an axis.

$$F(\sigma_{ij}) = (\sigma_1 - \sigma_3) + (\sigma_1 + \sigma_3)\sin\phi - 2c\,\cos\phi \leq 0 \qquad (4.2)$$

However, F can be expressed as a function of stress invariants (Labuz & Zang, 2012):

$$F = \sigma_m \sin\phi + \bar{\sigma}\left(\cos\theta - \frac{1}{\sqrt{3}}\sin\emptyset \sin\theta\right) - c\,\cos\emptyset = 0 \qquad (4.3)$$

where σ_m is the average of the three principal stresses, $\bar{\sigma}$ is equal to the square root of the second deviatoric stress invariant J_2 and θ is the Lode angle, which ranges between $-30°$ and $-30°$.
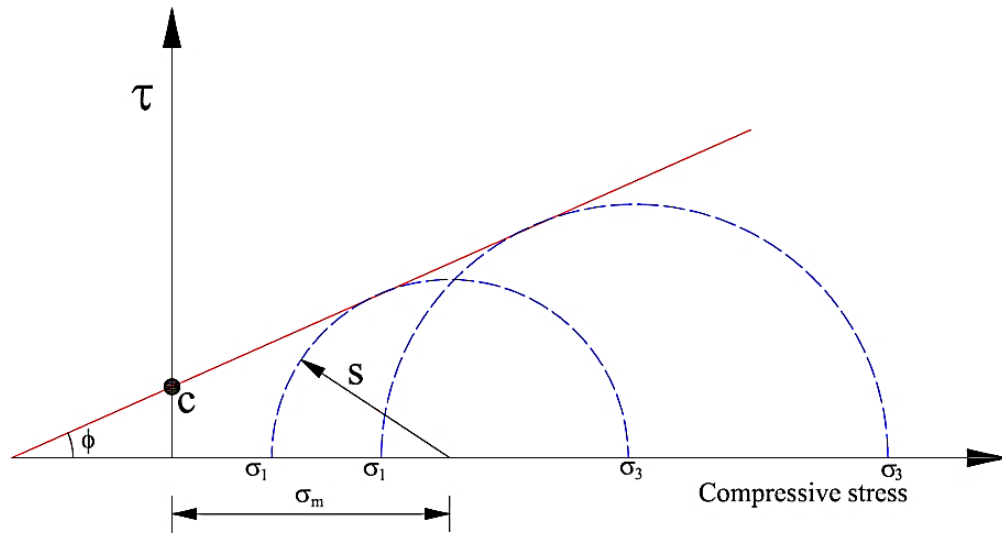
Figure 4-12 Mohr–Coulomb Failure Model, Modified from (Smith 2018)

In Abaqus/standard, the Mohr–Coulomb criterion presumes that soil failure happens once the shear stress approaches a value, which depends linearly on the normal stress in the failure plane (Smith 2018) . This model is based on Mohr's circle of Stress states at failure in the plane of the maximum and minimum principal stresses. The line of the failure is the best straight line that touches these series of circles, as shown in Figure 4-12 above. Once σ is negative (in compression), as shown in Figure 4-12, τ and σ can be expressed as in Eqs. (4.4) and Figure 4-12, respectively.

$$\tau = s\,\cos\emptyset \qquad (4.4)$$

$$\sigma = \sigma_m + s\,\sin\emptyset \qquad (4.5)$$

Thus, the equation of the model can be written as follow:

$$s + \sigma_m \sin\emptyset - c\cos\emptyset = 0 \tag{4.6}$$

where s is the maximum shear stress, where $s = \frac{1}{2}(\sigma_1 - \sigma_1)$ and $\sigma_m = \frac{1}{2}(\sigma_1 + \sigma_1)$.

However, for general stress states, the criterion is conveniently expressed in terms of three invariant stresses, as given in Eq. (4.7):

$$F = R_{mc}q - p\tan\emptyset - c = 0 \tag{4.7}$$

where $R_{mc}(\theta,\emptyset) = \frac{1}{\sqrt{3}\cos\emptyset} \cdot \sin\left(\theta + \frac{\pi}{3}\right) + \frac{1}{3}\cos\left(\theta + \frac{\pi}{3}\right)\tan\emptyset$.

The friction angle of the soil $\emptyset$ denotes the slope of the Mohr–Coulomb yield surface in the $P - R_{mc}q$ stress plane, as shown in Figure 4-13, and it can depend on the following predefined field variables:

θ is the deviatoric polar angle defined as $\cos(3\theta) = \left(\frac{r}{q}\right)^3$

p is the equivalent pressure stress, $p = -\frac{1}{3}\ trace\ (\sigma)$

q is the Mises equivalent stress, $q = \sqrt{\frac{3}{2}(S:S)}$

r is the third invariant of deviatoric stress, $r = \left(\frac{9}{2}S \cdot S:S\right)^{\frac{1}{3}}$

S is the deviatoric stress, $S = \sigma + pI$

The shape of the yield surface in the deviatoric plane is controlled by the friction angle $\emptyset$, which ranges between $0° \leq \emptyset \leq 90°$, as shown in Figure 4-13. For $\emptyset = 0°$, once the Mohr–Coulomb model cuts to a perfectly hexagonal deviatoric section−pressure independent Tresca model (Smith 2018). For $\emptyset = 90°$, it reduces to the tension cut-off Rankine model—a triangular deviatoric section with $R_{mc} = \infty$—which is unsupported in Abaqus as Mohr–Coulomb model (Helwany, 2007). However, Abaqus/Standard sets the output variables as SP1, SP2 and SP3 correlate to the principal stresses σ_1, σ_2 and σ_3, respectively.
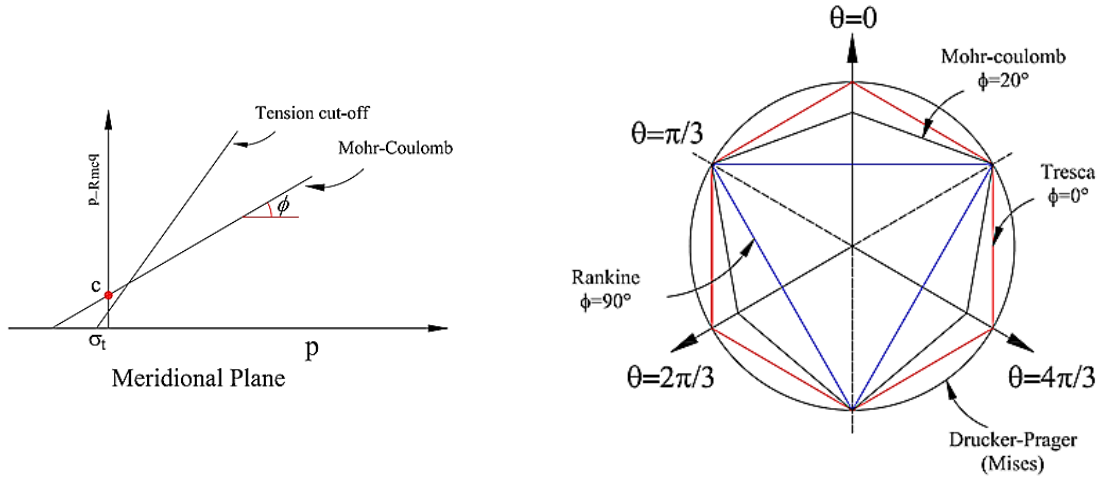
Figure 4-13 Mohr–Coulomb and Tension Cut-off Surfaces in Meridional and Deviatoric Planes, Modified from (Abaqus, 2018)

4.3.4.1.1. Flow potential

Following the proposal of (Menétrey & William, 1995), the hyperbolic function is adopted to represent the flow potential G_f in the meridional stress plane and smooth elliptic function in the deviatoric stress plane:

$$G_f = \sqrt{(\epsilon c_0 \tan \psi)^2 + (R_{mw} q)^2} - p \tan \psi \qquad (4.8)$$

where

$$R_{mw}(\theta, e_{dev.}) = \frac{4(1-e^2)\cos^2\theta + (2e-1)^2}{2(1-e^2)\cos\theta + (2e-1)\sqrt{4(1-e^2)\cos^2\theta + 5e^2 - 4e}} R_{mc}\left(\frac{\pi}{3}, \emptyset\right),$$

$$R_{mc}\left(\frac{\pi}{3}, \emptyset\right) = \frac{3 - \sin\emptyset}{6\cos\emptyset},$$

ψ is the dilation angle measured in the $p - R_{mw} q$ plane at high confining pressure and it can be predefined field variables dependent

c_0 is the initial cohesion yield stress

ϵ is the meridional eccentricity parameter, which defines the rate at which the hyperbolic function reaches the asymptote (the flow potential tends to a straight line in the meridional stress plane whilst the meridional eccentricity turns to zero), $e_{dev.}$ is the deviatoric eccentricity parameter, which defines the 'out-of-roundedness' of the deviatoric section in terms of shear stress along the extension meridian, $\theta = 0$, to shear stress along the compression meridian, $\theta = \frac{\pi}{3}$, ratio. However, a default value of 0.1 is given for the

meridional eccentricity ϵ, and the deviatoric eccentricity $e_{dev.}$ is computed by default as follows:

$$e_{dev.} = \frac{3 - \sin \emptyset}{3 + \sin \emptyset} \qquad (4.9)$$

This procedure corresponds to match the flow potential to the yield surface in both triaxial tension and compression in the deviatoric plane. Alternatively, Abaqus allows this deviatoric eccentricity to be considered as an independent material parameter; by providing its value directly. The convexity and smoothness of the elliptic function need the limitation of $\frac{1}{2} \leq e_{dev.} \leq 1$. When the value of e is not specified, the upper limit ($e = 1$), or the lower limit $e_{dev.} = \frac{1}{2}$, has to be chosen and leading to the Mises circle in the deviatoric plane Eq. (4.10) or the Rankine triangle in the deviatoric plane Eq. (4.11), respectively. However, Abaqus does not support the second limiting case within the Mohr–Coulomb model.

$$R_{mw}(\theta, e_{dev.} = 1) = R_{mc}\left(\frac{\pi}{3}, \emptyset\right) \qquad (4.10)$$

$$R_{mw}\left(\theta, e_{dev.} = \frac{1}{2}\right) = 2 R_{mc}\left(\frac{\pi}{3}, \emptyset\right) \cos \theta \qquad (4.11)$$

The flow potential, which is continuous and smooth, ensures that the flow direction is consistently explicitly defined. Figure 4-14 shown above illustrates a group of hyperbolic potentials in the meridional stress plane.
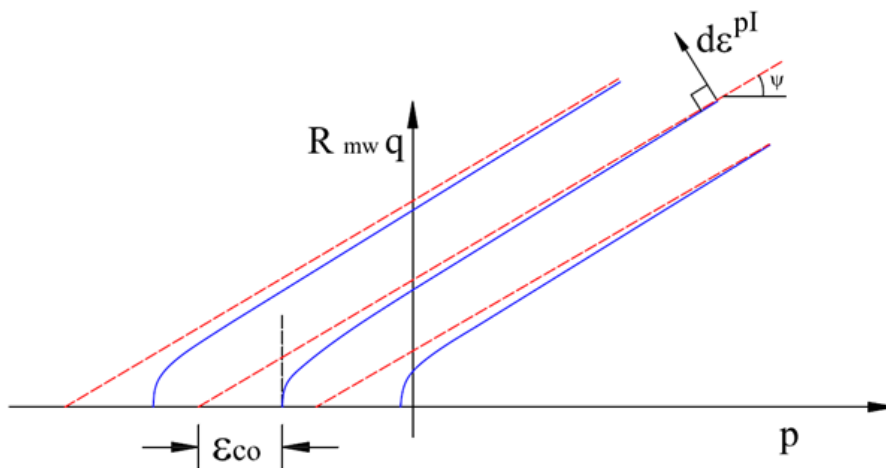
Figure 4-14 Family of Hyperbolic Flow Potentials in the Meridional Stress Plane, Modified from, (Smith 2018)

Figure 4-15 shows the flow potential in the deviatoric stress plane. Flow in the deviatoric stress plane is always non-associated. However, the flow in the meridional stress plane can be close to be associated in the condition that the angle of friction Ø and the angle of dilation ψ are equal and the value of the meridional eccentricity ϵ is small. However, flow in this plane is generally non-associated. The use of the Mohr–Coulomb model involves asymmetric matrix storage and solution scheme in Abaqus/Standard because the plastic flow is usually non-associated.
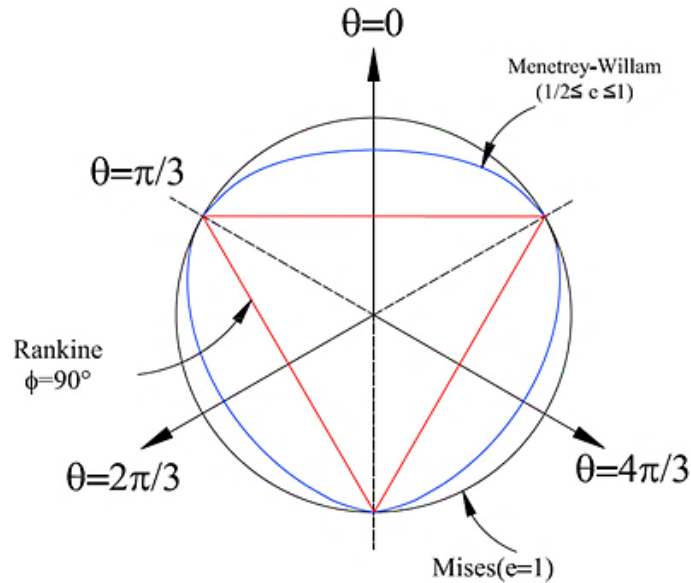
Figure 4-15 Mentrey–Willam Flow Potential in Deviatoric Stress Plane, Modified from, (Menétrey & William, 1995)

4.3.4.1.2. Element type

The Mohr–Coulomb plasticity model can be used with any stress/displacement element in Abaqus/Standard except 1D beam-column element as well as elements for which the stress state is assumed to have plane stress, such as shell and membrane elements.

4.3.4.1.3. Model parameters

The parameters of the Mohr–Coulomb criterion can be determined using a triaxial compression, axial symmetric laboratory test. Figure 4-16 presents the results of such a test and the manner in which the parameters can be determined (ε_1= main specific strain; ε_v= volumetric strain). In case of cohesive soils, a minimum of two laboratory tests are required to be conducted under different consolidation pressures for determining the parameters Ø and c. For each test, the axial stress at failure, σ_1 and the consolidation pressure were plotted in the $((\sigma_1 + \sigma_3)/2, (\sigma_1 - \sigma_3)/2)$ axis system. The obtained points were approximated by a linear regression, as shown in Figure 4-17.
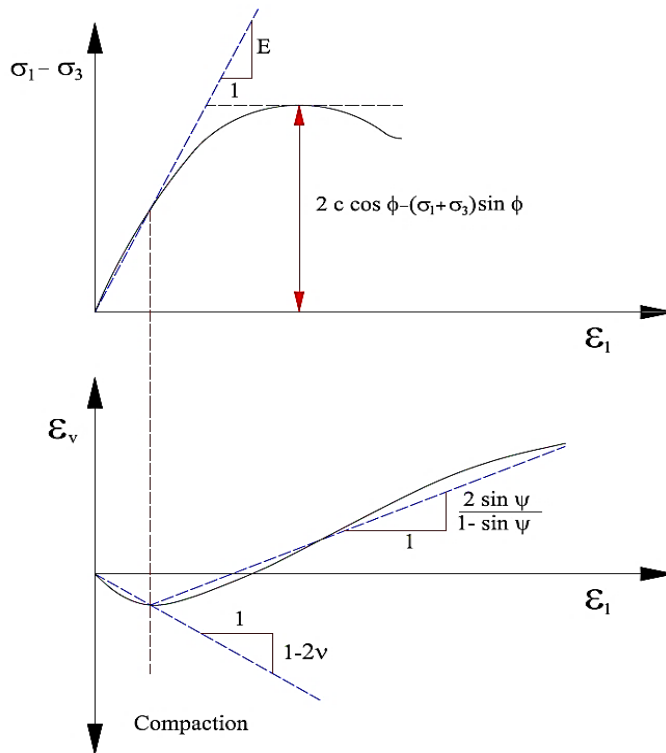
Figure 4-16 Axial Symmetric Triaxial Compression Test Modelled Using Mohr–Coulomb Criterion
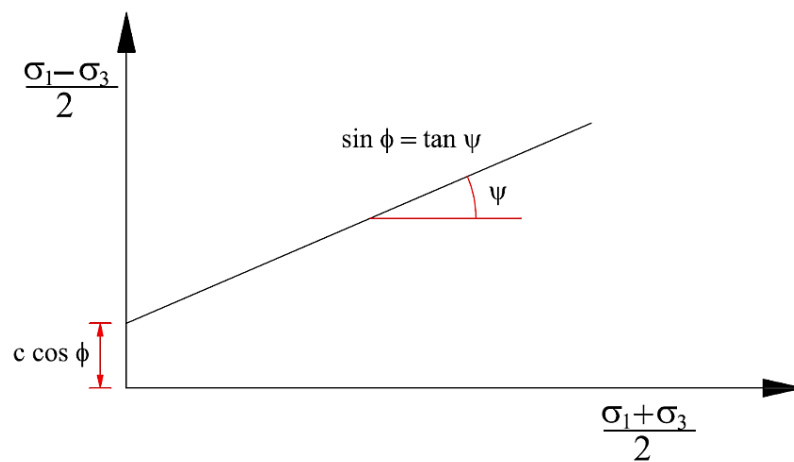
Figure 4-17 Determination of ψ and c

4.3.4.2. Drucker–Prager/cap model

The cap model is suitable to simulate the soil behaviour due to its ability to analyse the influence of stress history, stress path, dilatancy and the effect of the intermediate principal stress. Figure 4-18 illustrates the three main components of the modified Drucker–Prager/cap yield surface plasticity model: model shear failure surface, elliptical cap and smooth transition region. The elliptical cap part converges the mean effective stress axis at a right angle. Elastic behaviour can be modelled as linear elastic using the

142

generalised Hooke's law. Alternatively, an elasticity model in which the bulk elastic stiffness K_b develops as the material experiences compression was used to compute the elastic strains. K is computed as:

$$K_b = \frac{(1 + e_0)\, p\,'}{\kappa}$$

(4.12)

where $p\,'$ is mean effective stress, e_0 is the initial void ratio and κ is the unloading–reloading line slope. These parameters are described in detail in Section 4.4. However, Abaqus either uses direct linear elastic or porous elasticity model involving tensile strength (Helwany, 2007). Plastic behaviour can be modelled by determining the development of the failure surface and the cap yield surface as a function of stress invariants.
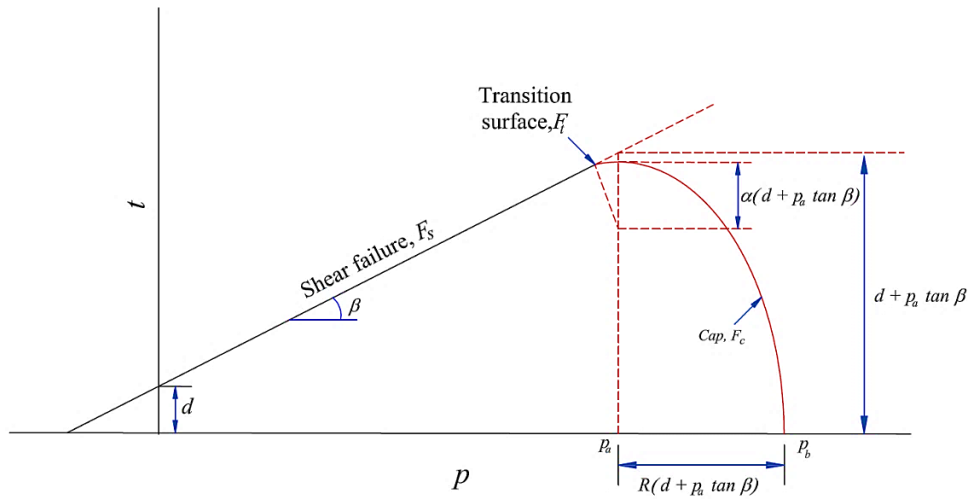
Figure 4-18 Figure 19 Yield Surfaces of the Modified Cap Model in the p–t Plane , Modified from (Abaqus, 2018)

Two invariants were used; equivalent pressure stress p, expressed as Eq. (4.13), and Mises equivalent stress q_{Mises}, expressed as Eq. (4.14):

$$p = -\frac{1}{3}\begin{vmatrix} \sigma_{11} & \tau_{12} & \tau_{13} \\ \tau_{21} & \sigma_{22} & \tau_{23} \\ \tau_{31} & \tau_{32} & \sigma_{33} \end{vmatrix}$$

(4.13)

$$q_{Mises} = \sqrt{3(J_{2D})} = \sqrt{3\left(J_2 - \frac{J_1^2}{6}\right)} =$$

$$\sqrt{\frac{1}{2}[(\sigma_1 - \sigma_2)^2 + (\sigma_2 - \sigma_3)^2 + (\sigma_1 - \sigma_3)^2]} = \sqrt{\frac{3}{2}\,(S{:}S)}$$

(4.14)

where S is the stress deviator defined as $S = \sigma + p\,I$, in which I is the stress invariants. However, the Drucker–Prager failure surface is given as follows:

$$F_s = t - p\,\tan\emptyset - c = 0$$

(4.15)

143

where $\emptyset$ is the slope of the linear yield surface in the p–t stress plane, which is the friction angle of the soil. The t term is defined later in this section. The yield criteria for MDPs are based on the shape of the MDP/cap failure surface in the meridional plane (t–p), which can have a linear, hyperbolic or general exponent form. These surfaces are demonstrated in Figure 4-19.

$$F_s = t - p \tan \emptyset - c = 0$$

$$F_s = \sqrt{(d'|o - p_t|o \tan \beta} - d' = 0$$

$$F_s = a\, q^b - p - p_t = 0$$
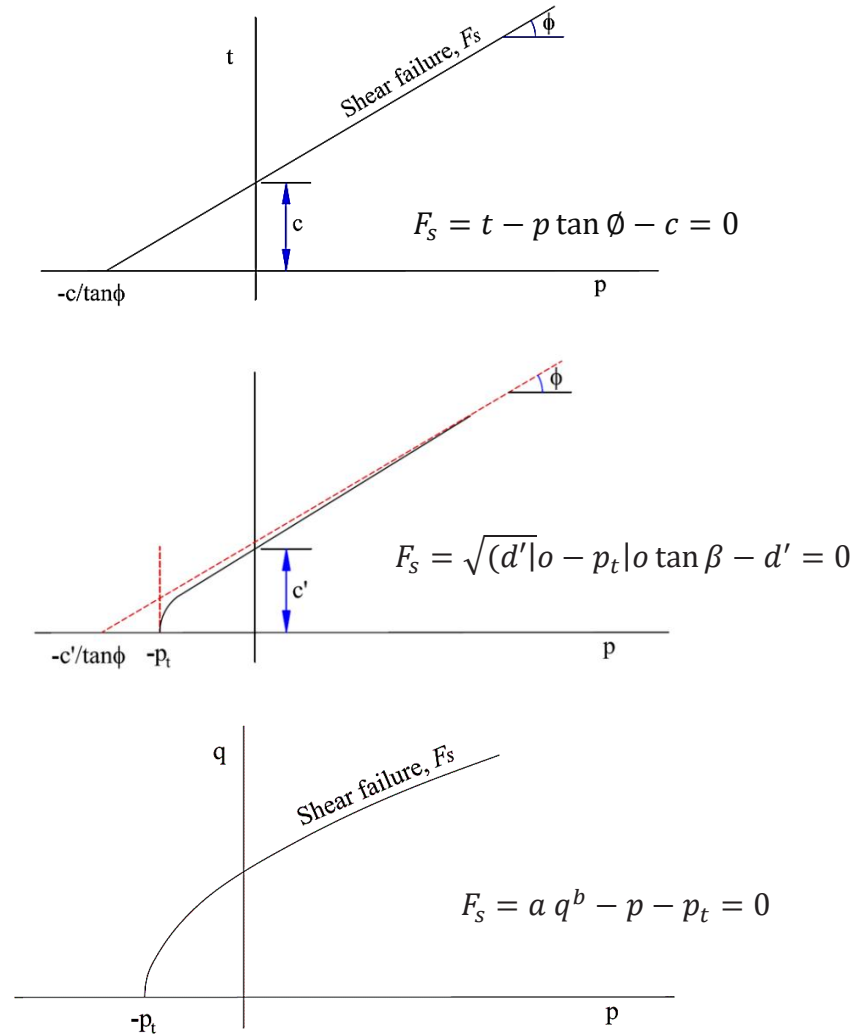
Figure 4-19 Drucker–Prager Yield Criteria Form, (a) Linear Form, (b) Hyperbolic Form, (c) General Exponent Form , Modified from, (Abaqus, 2018)

The cap yield surface is an ellipse with eccentricity R, where its shape may be identified by t, which is expressed in Eq. (4.16). This equation depends on K_r, which is the value of the ratio of the yield stress in triaxial tension to the yield stress in triaxial compression. Thus, this value controls the dependence of the yield surface on the value of the intermediate principal stress, as shown in Figure 4-20, and the third invariant of deviatoric stress r, as expressed in Eq. (4.17).

$$t = \frac{q}{2}\left[1 + \frac{1}{K_r} - \left[1 - \frac{1}{K_r}\right]\left[\frac{r}{q}\right]^3\right] \qquad (4.16)$$

$$r = \left(\frac{27}{2}J_{3D}\right)^{1/3} = \left(\frac{27}{2}J_3 - 9J_1J_2 + J_1^3\right)^{1/3} = \left(\frac{9}{2}\,S.S:S\right)^{1/3} \qquad (4.17)$$
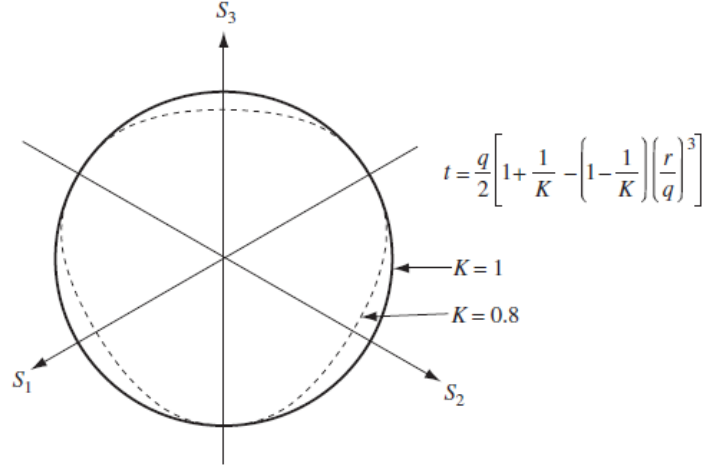
Figure 4-20 Projection of the Modified Cap Yield/Flow Surfaces on the Π Plane, (Smith 2018)

The hardening or softening behaviour of the cap surface F_c is a volumetric plastic strain dependant. In other words, during the stress state, once the yielding occurs on the cap and results in volumetric plastic strain, it leads to cap expansion or hardening. When the yielding arises on the shear failure surface, volumetric plastic dilation develops, inducing the cap softening. The cap yield surface F_c is given as follows:

$$F_c = \sqrt{(p - p_a)^2 + \left(\frac{R_t}{1 + \alpha - (\alpha/\cos\varnothing)}\right)^2} - R(d + p_a\tan\varnothing) = 0 \qquad (4.18)$$

where R is a material parameter that controls cap shape and α is a numeral parameter ranging between 0.01 and 0.05. The numeral parameter is utilised to define the smooth transition surface component F_t as follows:

$$F_t = \sqrt{(p - p_a)^2 + \left[t - \left(1 - \frac{\alpha}{\cos\varnothing}\right)(d + p_a\tan\varnothing)\right]^2} \qquad (4.19)$$
$$- \alpha(d + p_a\tan\varnothing) = 0$$

where p_a, is the evolution parameter which controls the hardening–softening behaviour as a function of the volumetric plastic strain. However, the hardening–softening behaviour is commonly defined by a piecewise linear function, which is associated with

the mean yield effective stress p_b and the volumetric plastic strain (ε_{vol}^{Pl}), as shown in Figure 4-21.
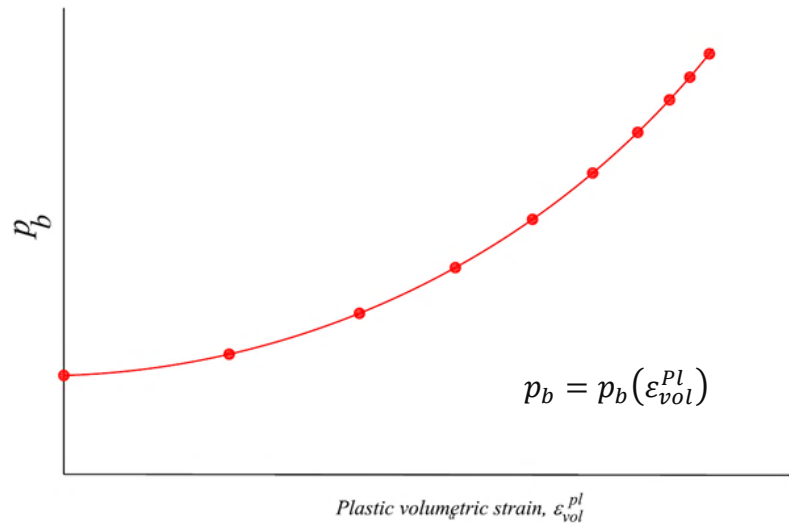
Figure 4-21 Typical Cap Hardening Behaviour, Modified from, (Abaqus, 2018)

This relation can be obtained by the uniaxial isotropic consolidation test with several loading-unloading–reloading cycles. Accordingly, the evolution parameter p_a can be defined as follows:

$$p_a = \frac{p_a - R_d}{1 + R \tan \phi} \tag{4.20}$$

4.3.4.2.1. Flow rule

As shown in Figure 4-22, the potential plastic flow surface in the *p–t* plane contains two segments. The cap region part is defined by a flow potential. Its associated flow yield surface is identical to its elliptical flow potential surface, as specified by Eq. (4.21). For the failure surface and the transition yield surface, the non-associated flow is presumed, and its potential flow surface expressed with Eq. (4.22).

A=(1+α - α sec β)(d + p_a tan β)

B=d + p_a tan β

C=R(d + p_a tan β)
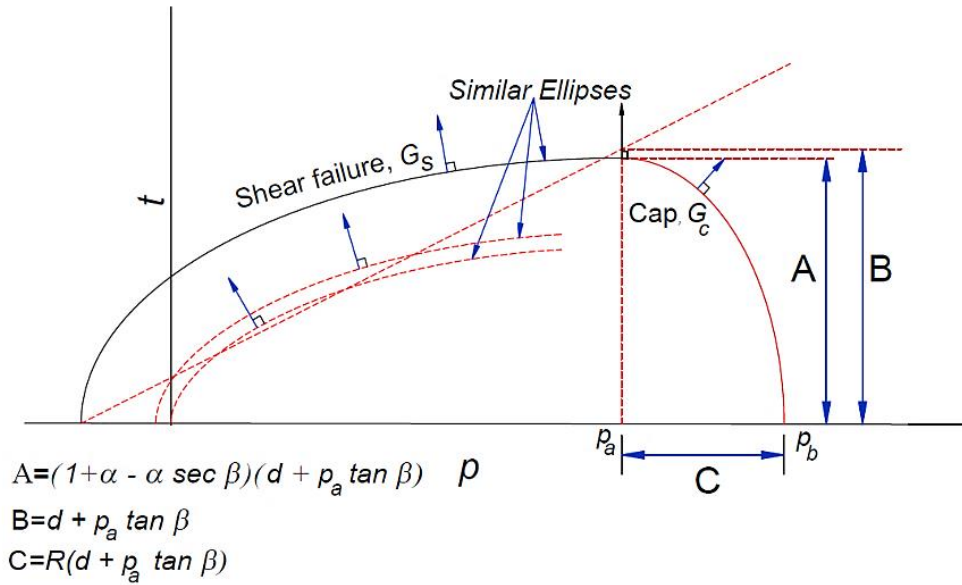
Figure 4-22 Flow Potential of the Modified Cap Model in the p–t Plane, Modified from (Abaqus, 2018)

$$G_c = \sqrt{(p - p_a)^2 + \left(\frac{R_t}{1 + \alpha - \alpha/\cos\beta}\right)^2} \qquad (4.21)$$

$$G_s = \sqrt{[(p_a - p)\tan\beta]^2 \left(\frac{t}{1 + \alpha - \alpha/\cos\beta}\right)^2} \qquad (4.22)$$

The two elliptical parts, G_c and G_s, produce a continued potential surface. The material stiffness matrix is not symmetric due to the availability of non-associated flow. Consequently, an asymmetric solver Abaqus option should be adopted in association with the cap model. For granular materials, the linear model is generally adapted with non-associated flow in the *p–t* plane, presuming that the flow direction and the yield surface are perpendicular in the $\prod$ plane and at the angle of ψ to the $t - axis$ in the *p–t* plane. However, typically $\psi < \beta$, as shown in Figure 4-23. The associated flow may arise due to the setting of $\psi = \beta$. This phenomenon can illustrate the original Drucker–Prager model once set $K_r = 1$. For $\psi = 0$, the inelastic deformation is in incompressible condition. For $\psi \geq 0$, the material dilates. Therefore ψ is usually cited as the dilation angle.
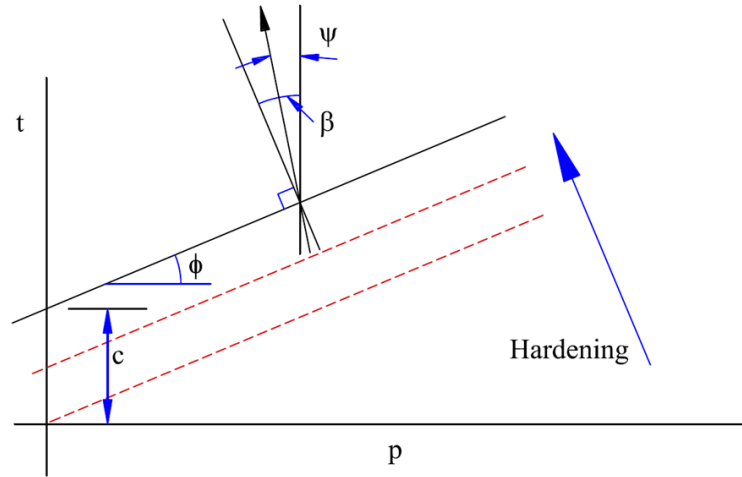
Figure 4-23 Linear Drucker–Prager Model: Yield Surface and Flow Direction in the p–t Plane, Modified from, (Abaqus, 2018)

4.3.4.2.2. Element type

The modified Drucker–Prager/Cap model may be used with plane strain, generalised plane strain, axisymmetric and 3D solid−continuum elements. However, it can never be used with elements in which the stress state is presumed as plane stress, such as shell and membrane elements.

4.3.4.2.3. Model parameters

Three triaxial compression tests are needed as a minimum requirement to compute the c and ϕ parameters. Initially, the at-failure conditions results can be plotted in the *p–t* plane, and then a straight line is best-fitted data points. Consequently, the line intersection with the *t*-axis is *C*, and its slope is ϕ. Secondly, isotropic consolidation test is needed to define the hardening–softening behaviour as a hydrostatic compression yield stress p_b and the corresponding volumetric plastic strain $\left(\varepsilon_{vol}^{Pl}\right)$ function, as shown in Figure 4-21. However, the absolute value of the volumetric inelastic strain can be obtained by subtracting the volumetric elastic strain, which is calculated by means of the unloading–reloading slope values as follows:

$$\varepsilon_v^p = \frac{\lambda - \kappa}{1 + e_0} ln \frac{p'}{p_0'} \qquad (4.23)$$

4.3.4.3. Cam–Clay model

The cam-clay and modified cam-clay (MCC) models were developed in the 1960's by researchers at Cambridge University (Schofield, 1993) to describe the behaviour of soft soils. These models predict the pressure-dependent soil strength, compression and

148

dilatancy caused by shearing, based on the philosophy of the critical state. On this basis, the models can forecast unlimited soil deformations without alterations in stresses or volume at the critical state. The MCC model adopts a fully saturated soil condition, and its formulations are based on plasticity theory. It can define three significant aspects of soil behaviour, i.e. the soil strength, the volume change that occurs due to shearing, and the critical state which represents the location of unlimited distortion without any changes in stress or volume. However, as mentioned previously, in critical state mechanics, the state of a soil sample is characterised by three main parameters, i.e. the effective mean stress (p'), the shear stress q_{shear} and the specific volume V. The effective mean stress and the shear stress can be computed in terms of principle stresses σ_1', σ_2' and σ_3', as expressed in Eqs. (4.24) and (4.25), whereas the specific volume can be defined in terms of void ratio e in Eq. (4.26).

$$p' = \frac{\sigma_1' + \sigma_2' + \sigma_3'}{3} \tag{4.24}$$

$$q_{shear} = \frac{1}{\sqrt{2}} \sqrt{(\sigma_1' + \sigma_2')^2 + (\sigma_2' + \sigma_3')^2 + (\sigma_1' + \sigma_3')^2} \tag{4.25}$$

$$V = 1 + e \tag{4.26}$$

Under the assumption of isotropic stress and perfectly drain condition, i.e. the consolidation stage of a consolidated–drained triaxial compression test, $(\sigma_1' = \sigma_2' = \sigma_3' = p')$, where σ_3' is the confining pressure, and $q = 0$. However, these values have a different relationship during the shearing stage $(\sigma_1' \neq \sigma_2' = \sigma_3')$, thereby resulting in $p' = \frac{\sigma_1' + 2\sigma_3'}{3}$ and $q = \sigma_1' - \sigma_3'$. However, in the triaxial test, the effective stress path (which is a straight line whose slope can be computed according to Eq. (4.27)) describes the condition of the effective stress state in the $p' - q$ plane, and it can be easily calculated following the relationship described above under the condition of constant $\Delta\sigma_3'$.

$$slope = \frac{\Delta q}{\Delta p'} = \frac{\Delta \sigma_1'}{\Delta \sigma_1'/3} = 3 \tag{4.27}$$

The relationship between specific void ratio e and the natural logarithm of the mean effective stress $\ln p'$ consists of a straight virgin consolidation line, whose slope can be calculated using Eq. (4.27), and a set of straight swelling lines, as expressed in Eqs.(4.28) and (4.29), as shown in Figure 4-24. The normal consolidation line (NCL) develops in

the $e - p'$ plane, as displayed in **Error! Reference source not found.**. Its equation in the $p' - q$ plane is $q = 0$.

$$e = e_N - \lambda_{NCL} \ln p' \tag{4.28}$$

$$e = e_C - \kappa \ln p' \tag{4.29}$$
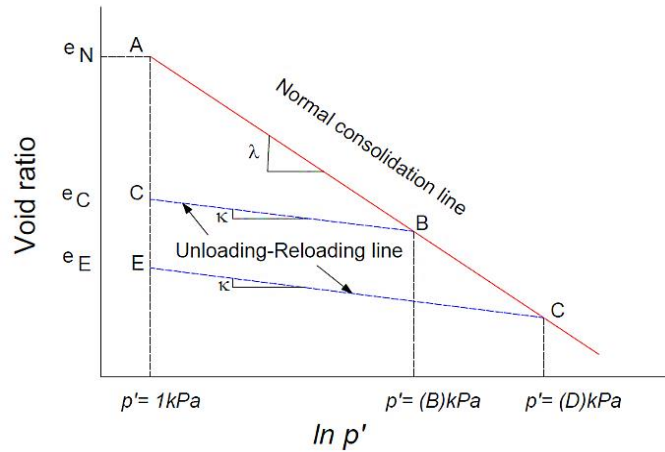
Figure 4-24 Consolidation Curve in the $e - lnp'$ Plane, Modified from (Helwany, 2009)
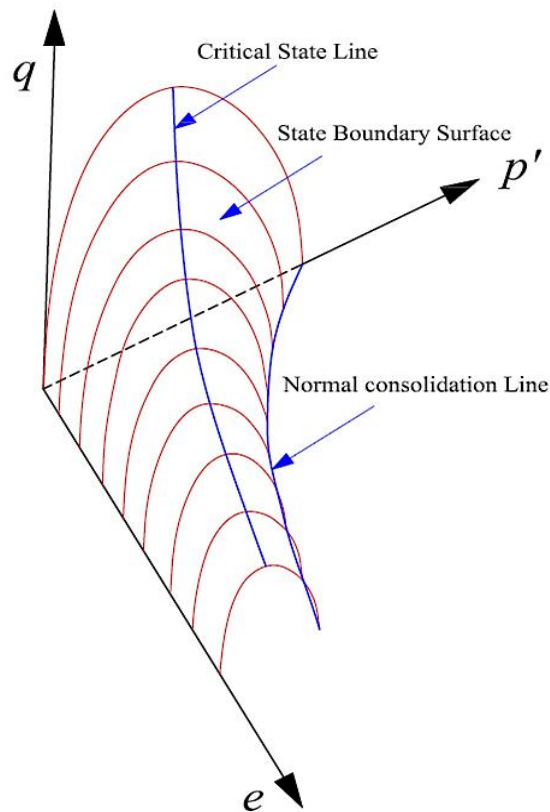
Figure 4-25 State Boundary Surface of the Cam–Clay Model, Modified from (Helwany, 2009)

The values $\lambda_{NCL}, \kappa, e_N \ and \ e_C$ are the characteristic properties of a particular soil. Specifically, λ is the slope of the normal compression line, κ is the slope of the swelling

line, e_N is the void ratio on the NCL at a unit mean effective stress and e_C varies for each swelling line and depends on the loading history of the soil. However, λ and κ can be expressed as a function of soil consolidation parameters, such as compression index C_c and swelling index C_s, where $\lambda_{NCL} = \frac{C_c}{2.3}$ and $\kappa = \frac{C_s}{2.3}$ (Lade, 2005). The application of rising shear stress on soil specimen may lead to a state where further shearing can happen without volumetric change. This phenomenon is known in the MCC model as critical state condition, as illustrated in Figure 4-26, and can be represented by defining the critical-state line (CSL), using triaxial compression tests results under consolidation conditions which can be developed from Mohr's circles. However, CSL is parallel to the NCL in the $e - lnp'$ plane, as shown in Figure 4.27, and its slope in the $p' - q$, M (see Figure 4-28), which is the ratio of the shear stress, can be expressed in terms of internal friction angle $\emptyset'$ as follows:

$$M = \frac{6\sin\emptyset'}{3 - \sin\emptyset'} \qquad (4.30)$$
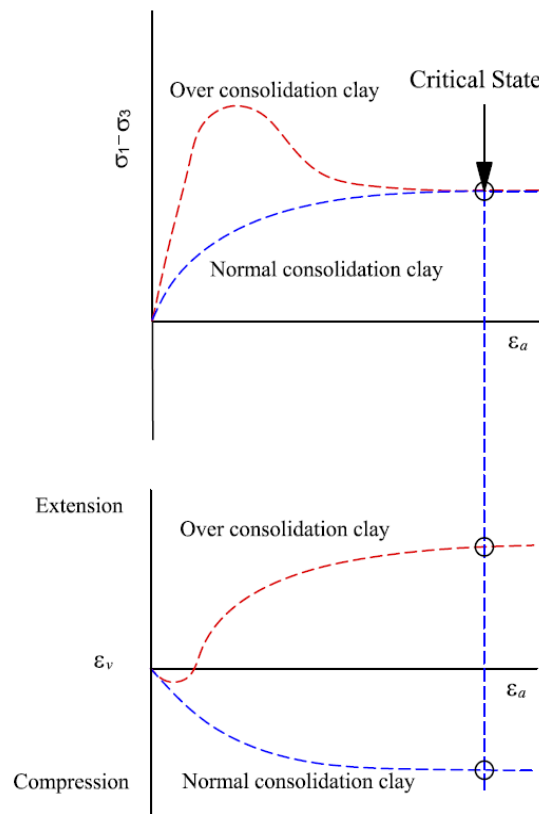
Figure 4-26 Critical-State Definition, Modified from (Helwany, 2009)
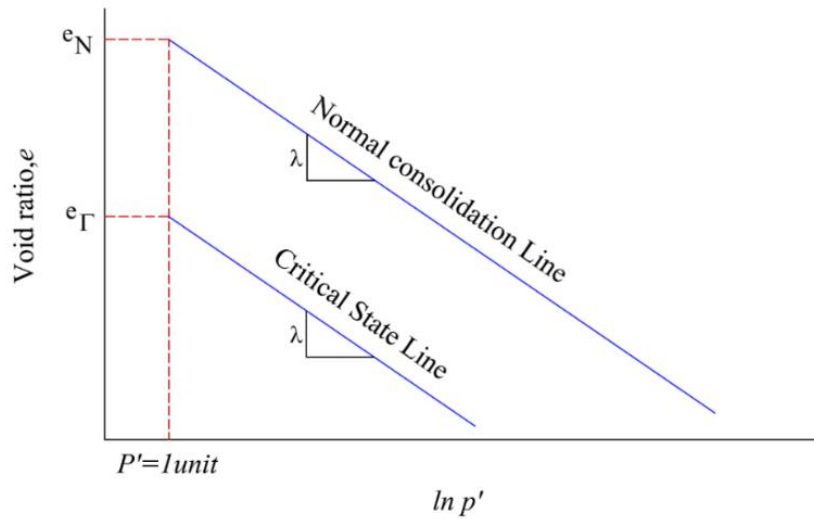
Figure 4-27 Normal Consolidation and CSLs in the e–$\ln p'$ Plane
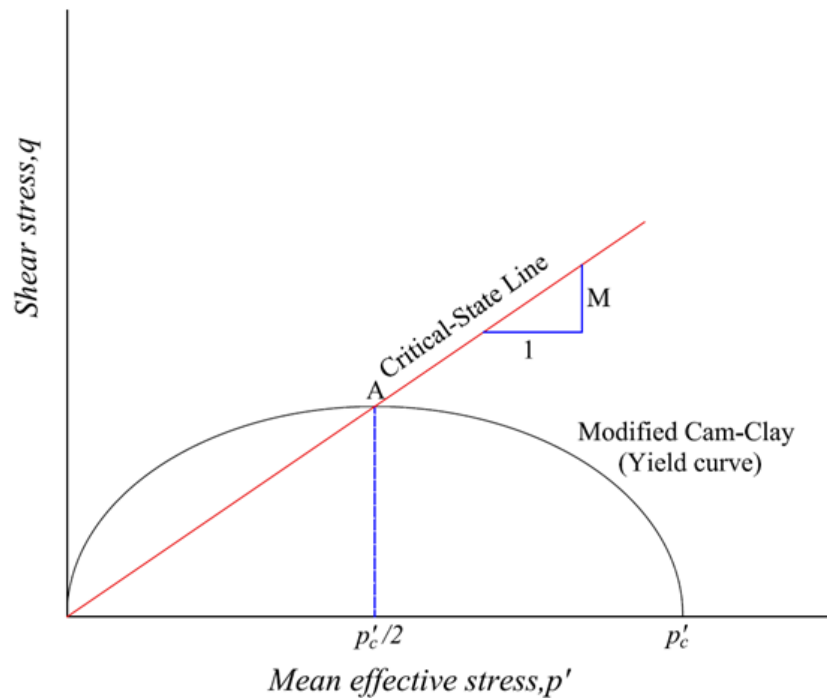
Figure 4-28 Yield Surface of a Cam–Clay Model in the q–p' Plane, Modified from (Abaqus, 2018)

As shown in Figure 29, the shear stress at failure (shear strength) q_f is a function of the mean effective stress at failure p'_f. This relation refers to the slope of the CSL, M dependence, as expressed in Eq. (4.11). It is similar to the Mohr–Coulomb failure criterion, where c' is presumed zero for sands and soft clays. However, this relation also refers to the CSL in the $e - \ln p'$ plane by employing Eq. (4.31).

$$e_f = e_\Gamma - \lambda_{NCL}\, \ln p' \tag{4.31}$$

152

where e_f and e_Γ are the void ratios at failure and of the CSL at $p' = 1 \ unit$, respectively. The initial void ratio (e_N) and the void ratio of the CSL (e_Γ) can be related by Eq. (4.32).

$$e_\Gamma = e_N - (\lambda_{NCL} - \kappa) \ln 2 = e_N - 0.693(\lambda_{NCL} - \kappa) \qquad (4.32)$$

In other respects, the modified Cam–Clay yield surface is demonstrated in $(p' - q)$ plane as an elliptical curve and can be expressed by Eq. (4.33), (see Figure 4-28).

$$\frac{q^2}{p'^2} + M^2 \left(1 - \frac{p'_c}{p'} \right) = 0 \qquad (4.33)$$

where p'_c is the preconsolidation pressure which controls the size of the yield surface and varies in values for each unloading–reloading line. This parameter is utilised to define soil hardening behaviour. The significant parameter q results from the intersection between the CSL and the yield curve at point A, as shown in Figure 4-28.

In geotechnical engineering, the elastic material properties usually used to correlate the stress—strain relationship are Young's modulus E, shear modulus G, Poisson's ratio v and bulk modulus K_b, some of which are expressed in Eqs. (4.34) and (4.35). Several of these parameters must be specified in an analysis.

$$E = 3K_b(1 - 2v) \qquad (4.34)$$

$$G = \frac{3K_b (1 - 2v)}{2(1 + v)} \qquad (4.35)$$

However, in soil modelling, shear modulus G and bulk modulus K parameters are preferred due to the permit of decoupling the influences of volume change and distortion. In MCC models, K_b is not constant, and it is a function of p', e_o and κ, as expressed in Eq.(4.37). Therefore, specifying either $G \ or \ v$ will let the other parameters no longer constant. The following relations define the elastic behaviour of the soil. E and G are not constant, and constant Poisson's ratio is commonly assumed for simplicity.

$$v = \frac{3K_b - 2G}{2G + 6K_b} \qquad (4.36)$$

$$K = \frac{(1 + e_0) \cdot p'}{\kappa} \qquad (4.37)$$

$$E = \frac{3(1 - 2v)(1 + e_o)p'}{\kappa} \qquad (4.38)$$

$$G = \frac{3(1 - 2v)}{2(1 + v)} \cdot K = \frac{3(1 - 2v)(1 + e_o)p'}{2(1 + v)\kappa} \qquad (4.39)$$

4.3.4.3.1. Hardening and softening behaviour

Assuming that a soil specimen has been isotropically consolidated to a mean effective stress p_c' and then unloaded to p_0' Figure 4.29 a, where p_0' is a current pressure, for normally consolidated and lightly overconsolidated soil$-OCR = p_C'/p_0' < 2$, the size of the initial yield surface can be determined in accordance with p_c' value (Smith 2018). Once the specimen shears under drained conditions, the effective stress bath of the consolidated–drained (CD) triaxial test is represented by a straight line having a slope value of 3. However, a compression hardening behaviour is performed once the stress path touches the initial yield surface to the right maximum shear stress (q_f)−the wet side.
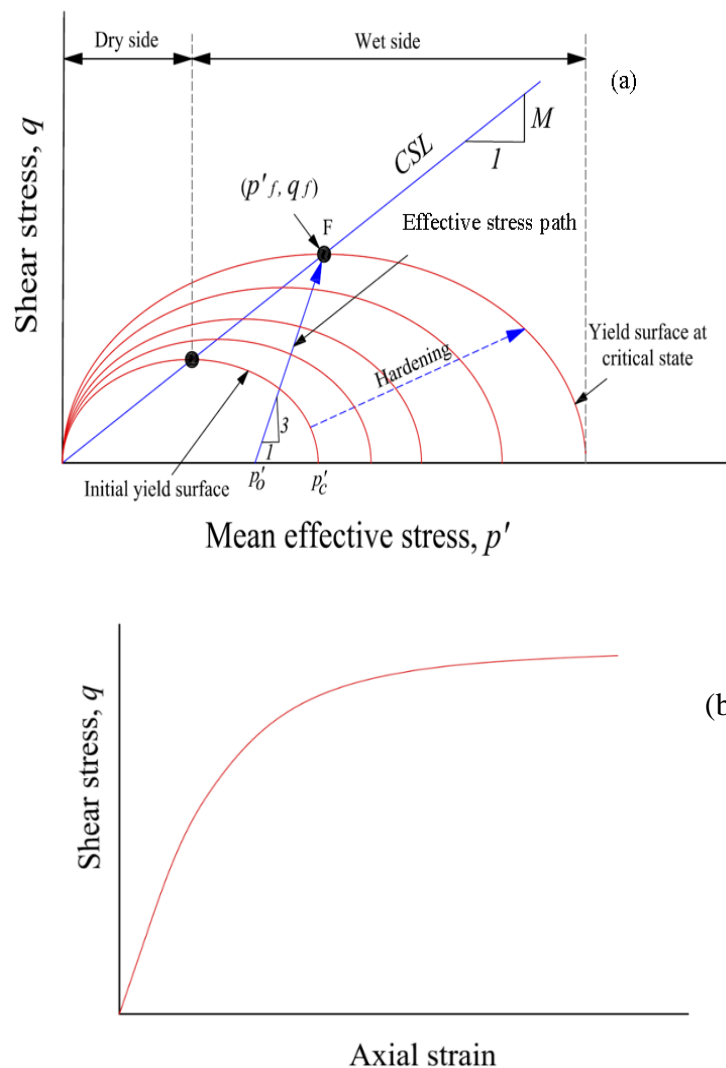
Figure 4-29 Cam–Clay Hardening Behaviour: (a) Evolution of Yield Surface during Hardening, (b) Stress–Strain Curve with Strain Hardening

The specimen experiences only elastic strains within the initial yield surface. Elastic and plastic strains are maintained when the stress state touches the yield surface, thereby promote hardening and further develop plastic strain until the stress state hits the CSL at

point F, as shown in Figure 4.29 a, where the failure happens. However, the distortion of the soil is continuous without changes in shear stress or volume, Figure 4.29 b. Once the specimen is heavily overconsolidated, i.e. $-OCR > 2$, the stress path traverses the initial yield surface to the left of the point F, thereby inducing softening behaviour characterised by dilatancy (expansion) at the dry side, as shown in Figure 4.30 a
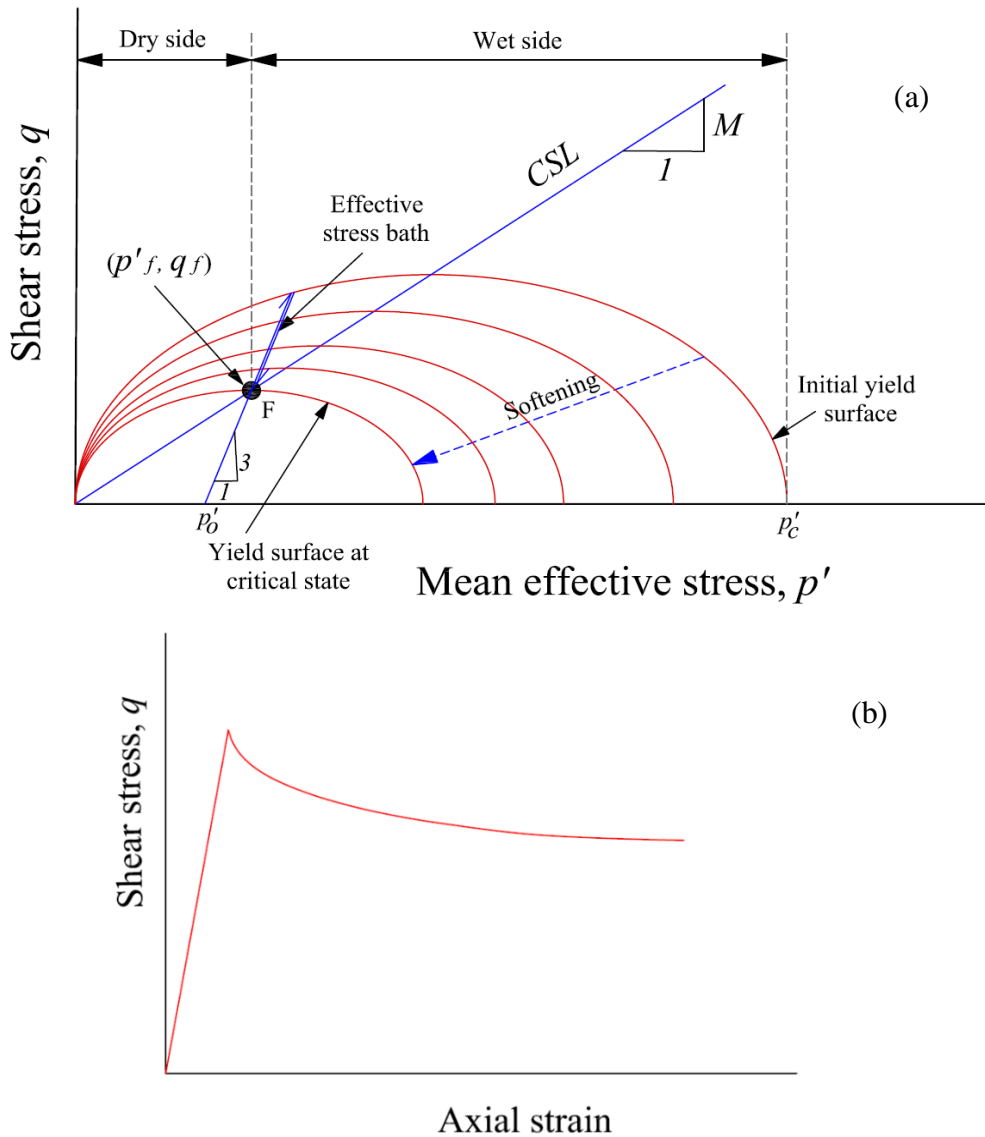
Figure 4-30 Cam–Clay Softening Behaviour: (a) Evolution of Yield Surface during Softening, (b) Stress–Strain Curve with Strain Softening

However, in this case, the specimen experiences only elastic strains within the initial yield surface. Once the effective stress path hints the yield surface, the yield surface experiences softening, thereby further producing plastic strains until the stress state hints the CLS over again at point F and failure arises, as illustrated in Figure 4.30 b The modified Cam–Clay model described earlier is a special case of the extended Cam–Clay model, and the principle concept of the ECC model is illustrated in Figure 4-31. The

elastic model in which the bulk elastic stiffness increases as the material experiences compression is employed to compute the elastic strain. The plastic strain is considered following theory of plasticity, i.e. a yield surface with an associated flow and a hardening rule that allows the yield surface to expand or shrink in the 3D stress space is applied. The critical-state surface is presumed a cone in the space of principal effective stress. Its vertex concurs with the origin−zero effective stress, whereas its axis coincides with the hydrostatic pressure axis− $\sigma_1' = \sigma_2' = \sigma_3'$ (see Figure 4-31).
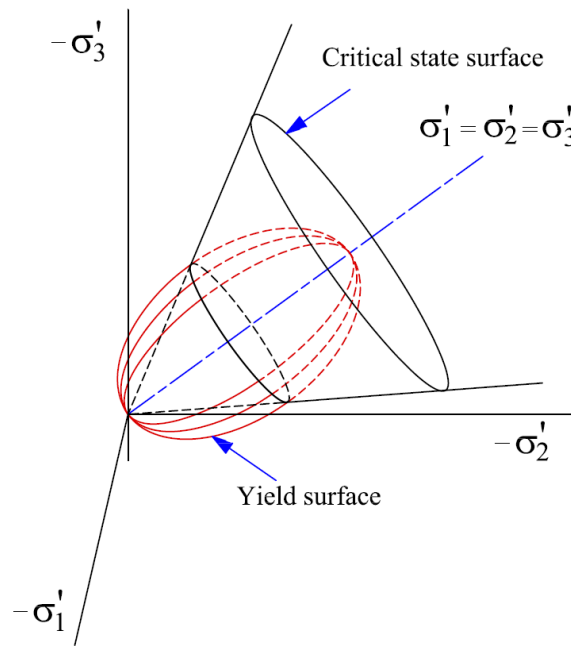
Figure 4-31 Elements of the Extended Cam–Clay Model: Yield and Critical-State Surfaces in the Principal Stress Space

The projection of the yield surface on the Π plane has a general shape, as illustrated in Figure 4-32, where the Π plane is the plane in the principal stress space perpendicular to the hydrostatic pressure axis. The conical critical-state surface projection on the $p - t$ plane is a straight line crossing through the origin with slope M, as shown in Figure 4-33, where t is a shear stress measurement factor as described below. However, the yield surface in the $p - t$ plane comprises two elliptic curves: the first arc passes through the origin and converges on the CSL, where its tangent is parallel to the $p -$ axis, and the second curve intersects this p- axis in right angle, as shown in Figure 4-33. However, the plastic flow is presumed normal to the yield surface (Smith 2018).

156
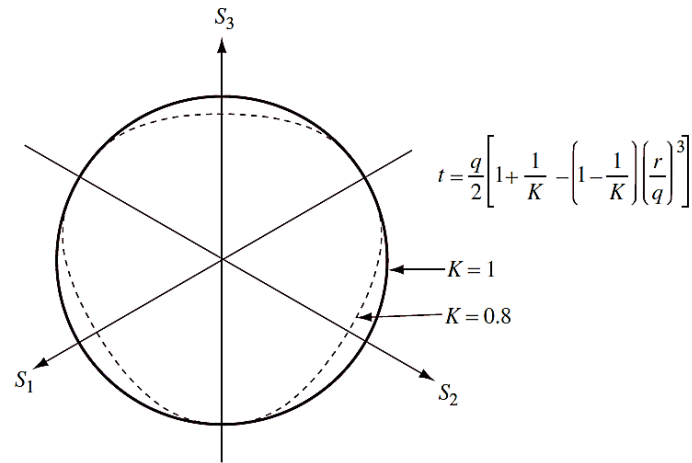
Figure 4-32 Projection of the Extended Cam–Clay Yield Surface on the $\prod$, (Smith 2018)
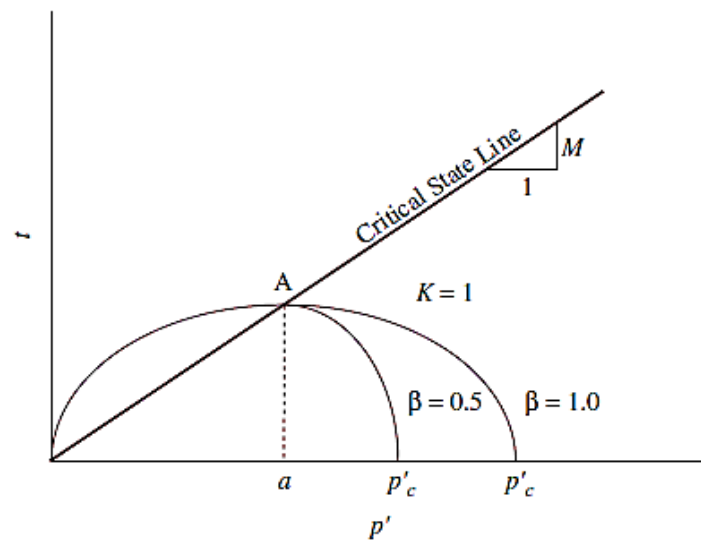
Figure 4-33 Extended Cam–Clay Yield Surface in the p'–t Plane, (Smith 2018)

The hardening rule controls the size of the yield surface, which has volumetric plastic strain dependence. The 3D yield surface is defined as follows:

$$f(p, q, r) = \frac{1}{\beta^2}\left(\frac{p}{a} - 1\right)^2 + \left(\frac{t}{Ma}\right)^2 - 1 = 0 \qquad (4.40)$$

where β is a constant used to modify the shape of the yield surface on the wet side of the critical state. This constant represents the curvature of the cap part of the yield surface. It can be calibrated from a number of triaxial tests at high confining pressures. It ranges between 0 and 1.0 (Bezgin, 2014), but 0.787 was used in this study. α is the hardening parameter characterised as the point on the $p - axis$ at which the developing elliptic curves of the yield surface cross the CSL, as designated in Figure 4-33; (t) is a measure

157

of shear stress, in which $t = \frac{q}{g}$, where g is a function employed to control the shape of the yield surface in the Π plane (the plane in the principal stress space orthogonal to the hydrostatic pressure axis), as defined as follows:

$$g = \frac{2k}{1 + k + (1 - k)\left(\frac{r}{q}\right)^3} \tag{4.41}$$

where k is a constant ranging from $0.778 \leq k \leq 1.0$ to assure convexity of the yield surface. Applying $(k = 1 \rightarrow t = q)$ results in the reduction of the modified Cam–Clay yield surface. The value used in this study was 0.778. The projection of the 3D elliptic yield surface on the Π plane has a typical shape, as presented in Figure 4-32. The factor (t) can be expressed as follows:

$$t = \frac{q}{2}\left[1 + \frac{1}{K} - \left[1 - \frac{1}{K}\right]\left[\frac{r}{q}\right]^3\right] \tag{4.42}$$

Associated flow is utilised in the extended Cam–Clay model. The size of the yield surface is described using the parameter α. Consequently. the progression of this variable identifies the hardening or softening of the clay, as shown in Eq. (4.43).

$$\alpha = \alpha_0 \exp\left[(1 + e_0)\frac{1 - J^{pl}}{\lambda_{NCL} - \kappa J^{pl}}\right] \tag{4.43}$$

where J^{pl} is the plastic volumetric change. The volume change J can be defined as in Eq. (4.44), where J^e is the elastic volumetric change.

$$J = J^e + J^{pl} = \exp(\varepsilon_{vol}) = \frac{(1 + e)}{(1 + e_0)} \tag{4.44}$$

α_0 is a constant that designates α locus at the preconsolidation pressure, which represents the beginning period of the analysis. However, the α_0 can be obtained as follows:

$$\alpha_0 = \frac{1}{2}\exp\left(\frac{e_N - e_0 - \kappa ln p_0}{\lambda_{NCL} - \kappa}\right) \tag{4.45}$$

where p_0 is the initial mean effective stress and e_N is the intercept of the NCL with the void ratio axis in the $e - ln p'$ plane.

4.3.4.3.2. Element type

The Cam–Clay model can be used in Abaqus with plane strain, generalised plane strain, axisymmetric and 3D solid elements. However, this model cannot be used with elements for which the supposed stress state is plane stress, such as shell and membrane elements, (Helwany, 2007) and (Hibbitt *et al.*, 2012).

4.3.4.3.3. Model parameters

At least two laboratory experiments are needed to calibrate MCC model (Smith 2018). An oedometer test in addition to a one or more triaxial compression tests are essential to delivering a precise calibration. The onset of yielding in the odometer test will directly give the initial location of the yield surface α_0. Before the logarithmic bulk modulus, κ and λ are also determined from pressure versus void ratio figure. For a valid model, $\lambda_{NCL} > \kappa$. However, the void ratio e can be computed by Eq. (4.44).

The triaxial compression tests permit the calibration of the yield parameters M and β, where M is the ratio of the shear stress q to the pressure stress p at a critical state, which can be obtained from the stress values when the material has become perfectly plastic, i.e. in a critical state. To calibrate the parameter K, which controls the yield requirement on the third stress invariant, cubical triaxial test results were used. However, these results are generally unavailable. Hence, the value of K is generally between 0.787 and 1.0, (Smith 2018).

Table 4.5 Model parameters for the soil constitutive models

Parameter		Value	
Density, (kg/m^3)		1505.75	
Log Bulk Modulus		0.05	
Poisson's Ratio		0.47	
Tensile Limit (MPa)		0.00	
Log Plasticity Bulk Modulus		0.27	
Stress Ratio		1.26	
Wet Yield Surface Size		1.00	
Flow Stress Ratio		0.78	
Angle of friction (Degrees)		10.00	
Cap Eccentricity		0.90	
Transition surface radius (m)		0.04	
Initial Void Ratio		1.50	
Cyclic loading parameters			
Freq. (Hz)	CSR	ξ_{d1}	ξ_{d2}
0.1	0.6	4.2	75
0.25	0.6	4.2	97
1	0.6	4.1	420
2	0.6	4.1	600
5	0.6	4.2	825
10	0.6	4.2	1065

4.4. Validation of the numerical model

In this section, the finite element model developed in the previous section is employed to simulate the physical shaking table experiments discussed previously, namely tests 1.15

and 2.26 from phase II of the PEER Centre test programme (Meymand 1998), to validate the numerical approach. In the first instance, the three different soil constitutive models are examined, denoted as the MC (Mohr-Coulomb), DP (Drucker-Prager) and CC (Cam–Clay) models, respectively, to determine which is the most appropriate for this type of problem.. The FE simulation consists of four single piles with head masses varying from 4.5 kg to 72.7 kg embedded in 2.0 m of soil deposit. The layout of the physical test and numerical simulation are shown in Figures 4 ,10 and 11. As in the reference case study, the model was subjected to a series of scaled seismic excitation, such as the YBI90, which is the input motion for Test 1.15, and the KPI79N00, which represents the test 2.26 loading. The results are assessed in terms of acceleration time histories, fast Fourier transforms (FFTs) and 5% damped response spectra. In addition, bending moment envelopes were calculated as the absolute peak strain at the nodes located in the same position as the physical model pile strain gauges in the shaking table tests, to enable a comparison of this data.

4.4.1. Simulation of free-field response

In an SSPSI analysis, one of the most critical factors is achieving an accurate depiction of the free-field site response as any error in this calculation can directly propagate into and intensify during the soil–pile analysis (Turner, Brandenberg & Stewart, 2017). However, this component is valid for uncoupled and coupled analyses. Therefore, the effectiveness of the numerical simulation of a flexible barrel shaking table is assessed to select the procedure with the suitable soil constitutive model.

To evaluate the dynamic soil–structure interaction problem correctly, the free-field responses of the numerical simulation of the three soil constitutive models were compared. These responses were represented as the soil accelerations recorded at different levels along the soil column depth, with the physical shaking table response. Finally, the results were validated with those numerically simulated using the ground response analysis software SHAKE91, which is designed to performing an equivalent linear seismic response analyses of a horizontally layered soil (Idriss & Sun, 1993). The model container for the physical and numerical tests in addition to the distribution of soil displacements are shown during strong shaking in Figure 4-34 and Figure 4-35, respectively. An advanced cyclic triaxial testing device was utilised in (Meymand 1998) study to obtain modulus degradation and damping curves for the model soil, as shown in Figure 4.36, with the best estimate curve fit. Comparison modulus degradation and

damping curves recommended by (Sun, Golesorkhi & Seed, 1990) for Young Bay Mud and Vucetic and (Vucetic & Dobry, 1991)for cohesive soils as a function of plasticity index are also shown in the figure.

A test-specific shear wave velocity profile was developed using the methods formerly presented as well as input parameters to simulate the Test 2.26 analyses, which are focused on the Phase II tests in the reference case. Consolidation and triaxial tests that are provided in the reference study were used to produce soil properties, which are essential to use in FEA. As mentioned before in section 2.0, the accelerometer arrays were denser and located away from structures in this test.

Figure 4-34 Model Soil Container in Motion during Strong Shaking, (Meymand 1998)

(a)

(b)

(c)

162
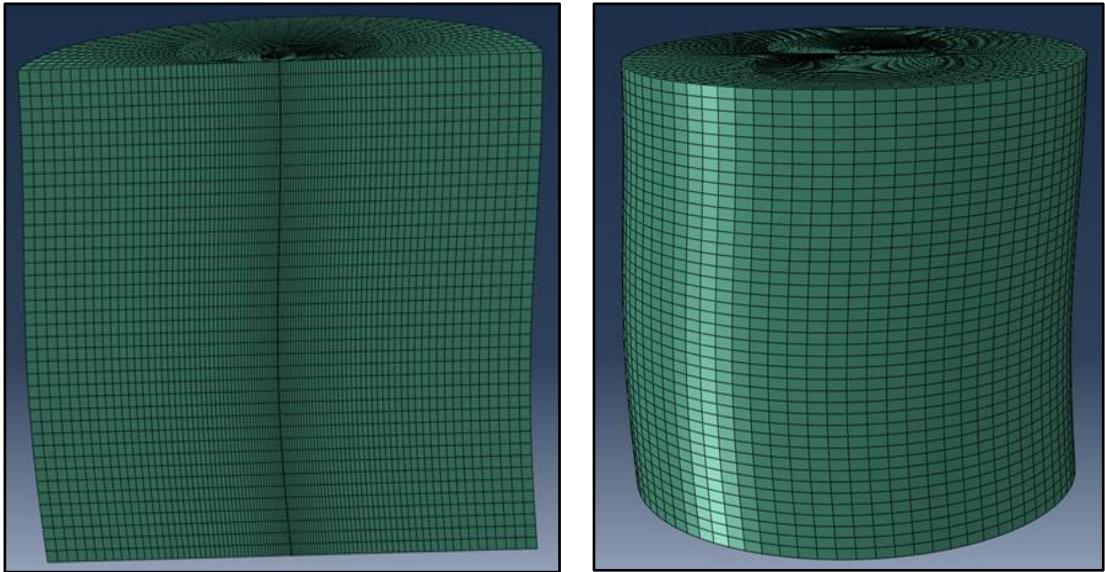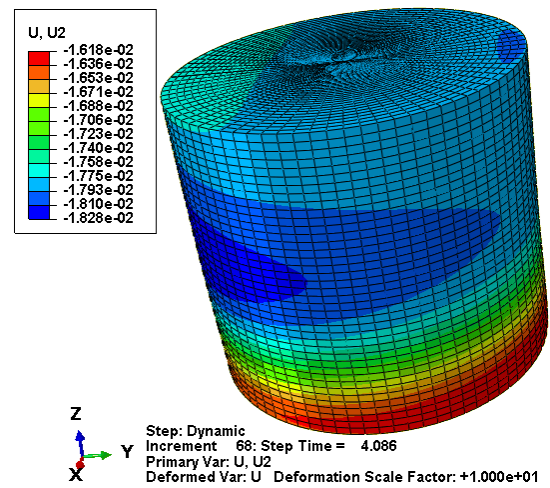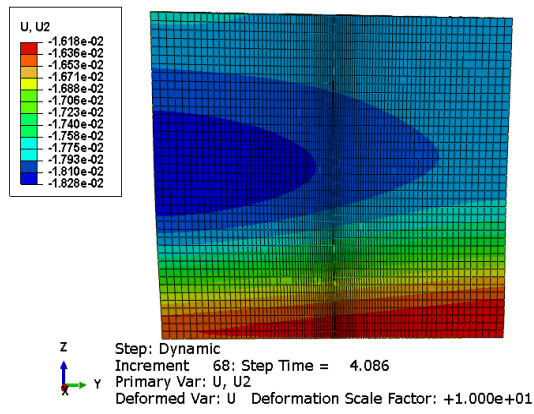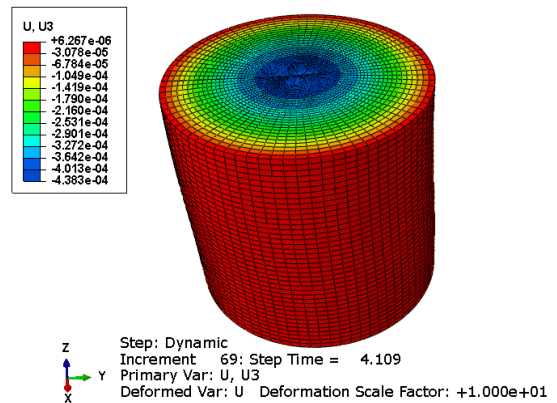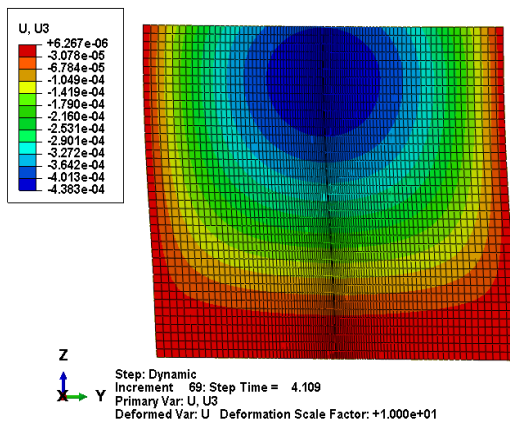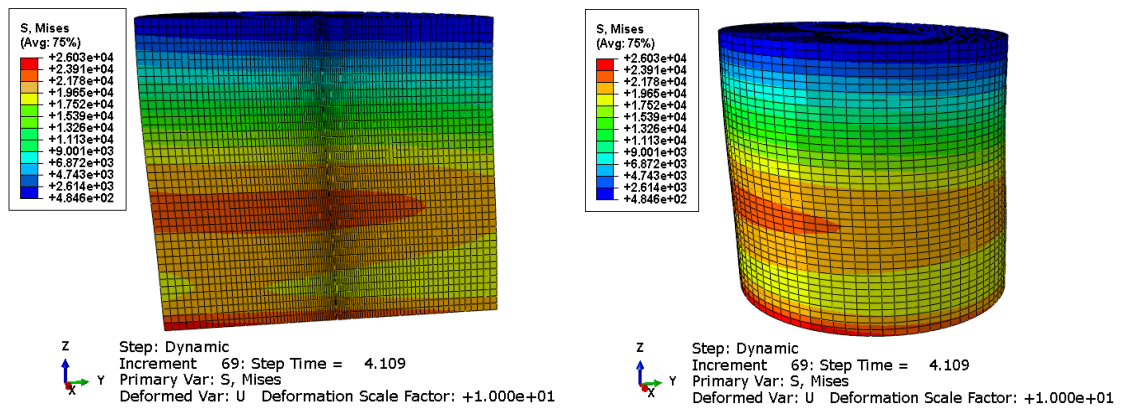
(d)

Figure 4-35 Numerical Model Soil Container in Motion during Strong Shaking, (a) Numerical Model Soil Container in Motion, (b) The Distribution of Soil Displacement (Y-direction) in Motion, and (c) The Distribution of Soil Displacement (Z-direction)in Motion, (d) Distribution of Stress distribution in Motion(Mises)

A series of SHAKE91 trial simulations was performed in the reference case study to examine the model performance following several parametric studies, i.e. the shear wave velocity profile and the modulus degradation and damping curves. Indeed, these tests confirmed the strong sensitivity of the results to variations in the shear wave velocity profile and the modulus degradation and damping curves. Based on the analysis of other researchers [e.g.(Boulanger *et al.*, 1999), and (Novak 1991)] it was found that enlarging the shear wave velocity values by 30% from the test-specific stiffness profiles provided optimal results and therefore this strategy is also adopted in the current work.
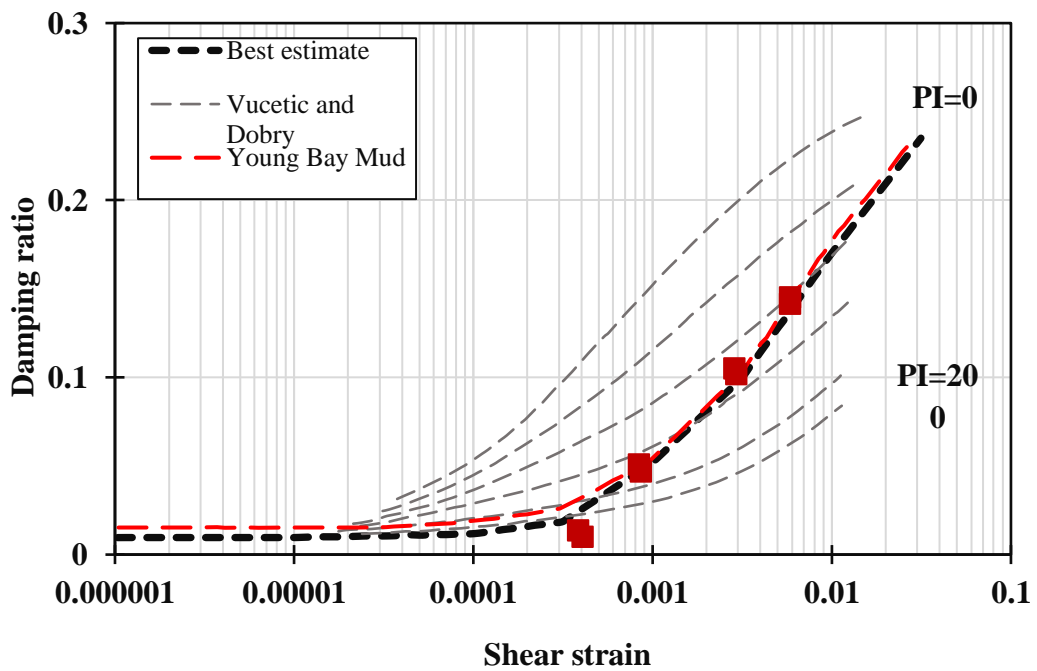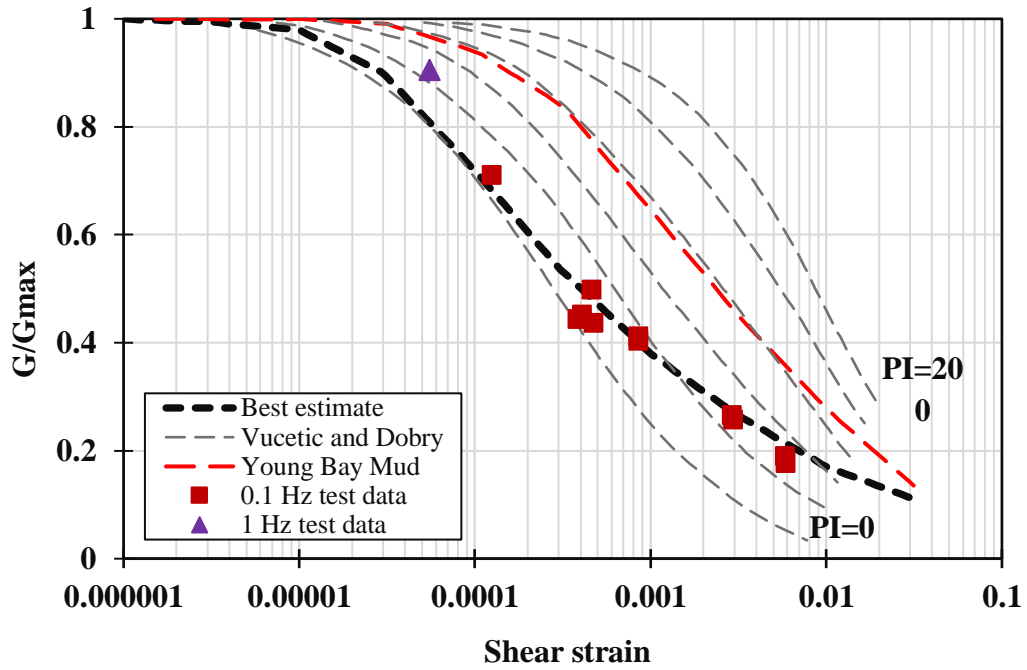
Figure 4-36 Model Soil Modulus Degradation and Damping Curves

Figure 4-37 presents the results of the spectral acceleration response along eight elevations of the soil deposit depth for the free field analysis case for Test 2.26. To ensure that the accelerations in the soil response are accurately predicted, these results have been selected at the model elements in accordance with the accelerometer positions during the physical test. Depending on the applied soil constitutive criteria, four different levels of

accuracy (Accuracy of being close to physical test findings) have been achieved, ranging from the best to worst accuracy for CC, DP, SHAKE91, and MC model, respectively.

Based on the results presented in Figure 4-37, it is concluded that the numerical simulation model is successful in depicting the free field case. The model boundary conditions are sufficiently restrained from simulating the free field conditions in the soil effectively, and therefore this aspect of the numerical modelling is validated. The predicted values of the peak ground acceleration (PGA) obtained by SHAKE91 at the soil surface is slightly lower than that from the physical test. On the other hand, the MC model tends to over-predict the PGA whilst the DP model provides an acceptable PGA predicted value which has a small deviation to physical test value. The CC model produces the most accurate depiction of the true behaviour.

Moreover, the spectral acceleration response accomplished in physical test at the predominant input motion periods of 0.12 sec, is 0.35 (g). The CC model precisely predicts these values, and lesser degrees of accuracy are achieved for the SHAKE91, DP and MC models. In conclusion, both the CC finite element model and the SHAKE91 approach provide an accurate depiction of the physical model soil response in two different scale levels of precision. The numerical model of the soil-container system can replicate the free-field site response accomplished by physical test adequately.

There are some small deviations between the results from the physical test and numerical model but these are considered to be in the acceptable range as there is only one material dependence model (only soil model has been simulated), i.e. kinematic interaction function response. However, the propagation of these errors into the complete soil-pile structure interaction analysis requires careful consideration and the selection of an appropriate soil constitutive model and precise scaling methodology are critical.
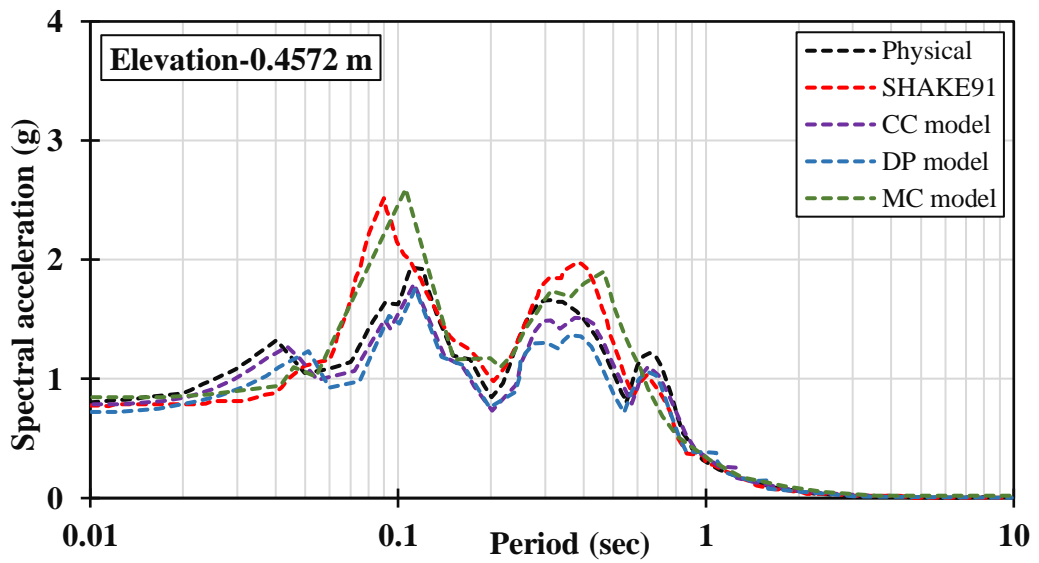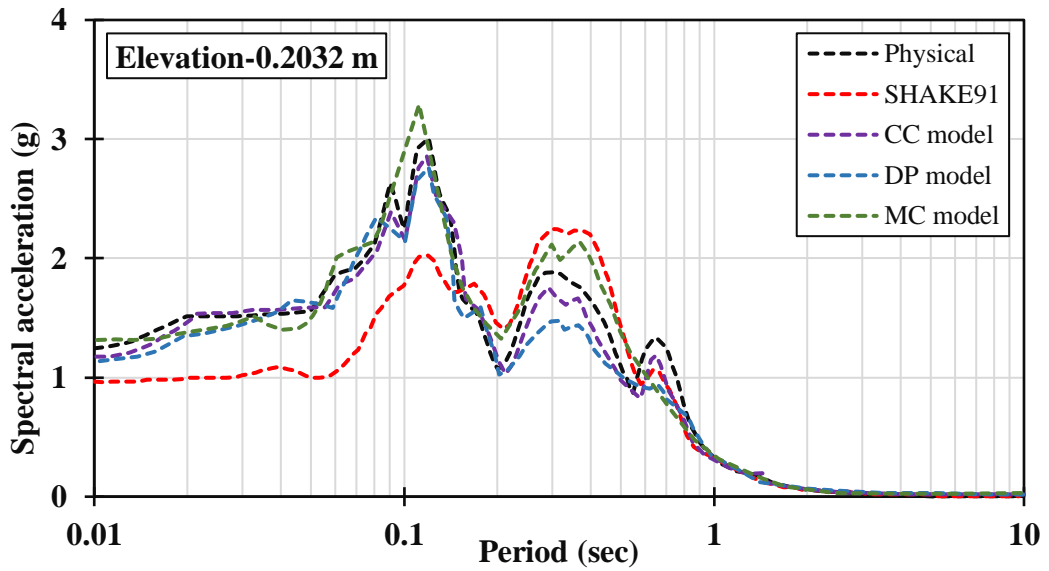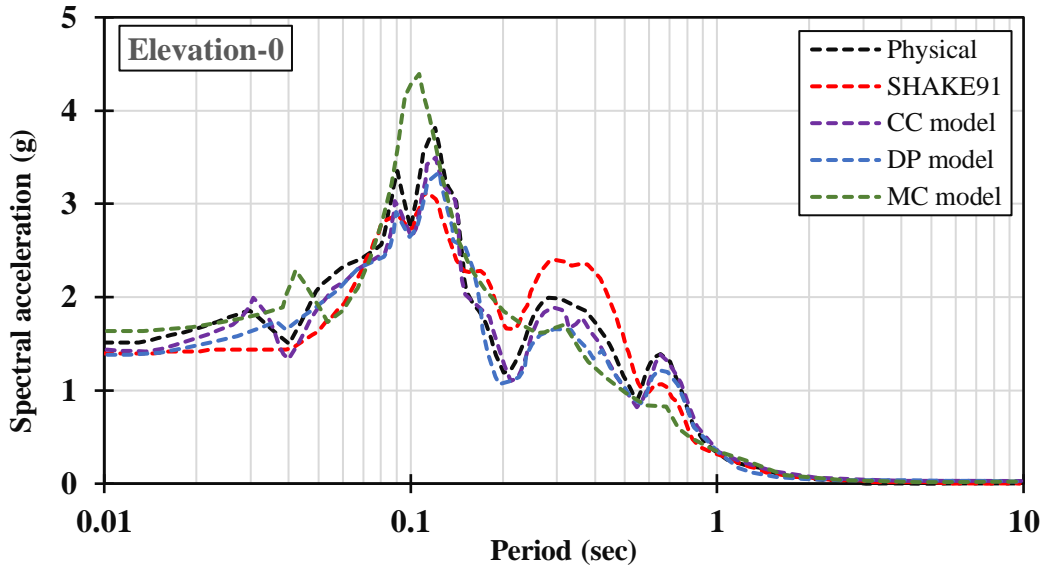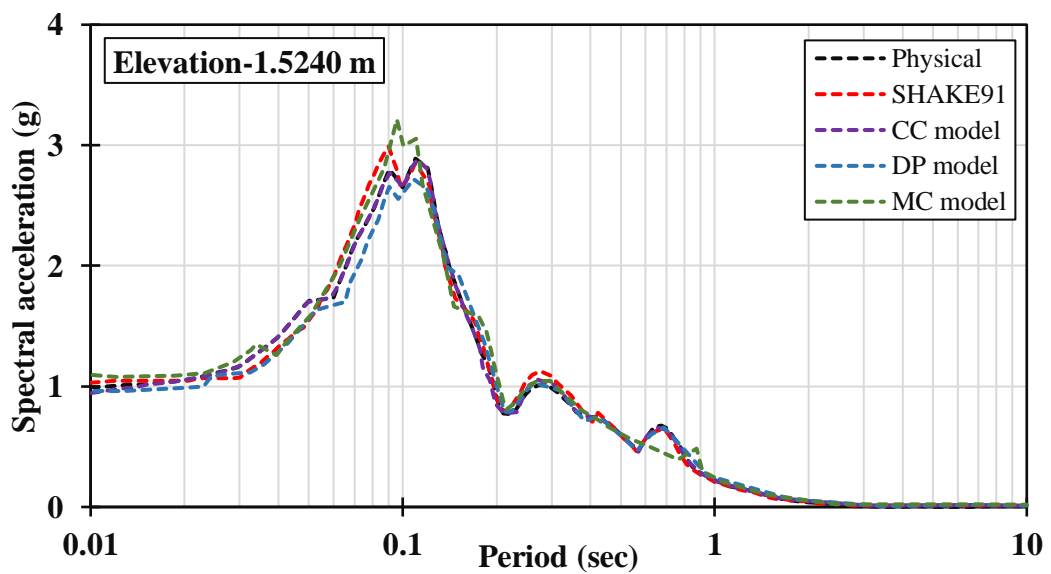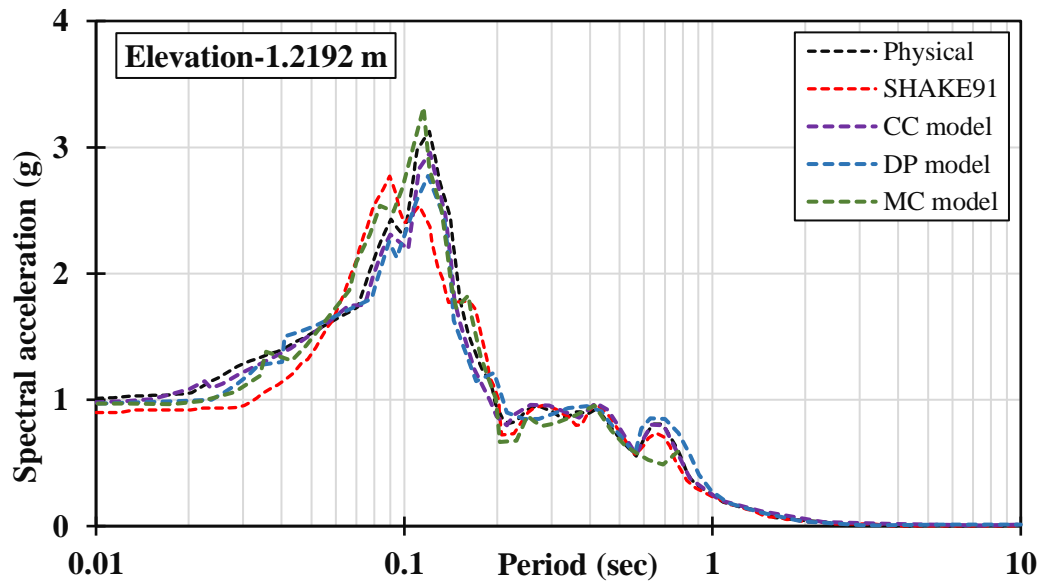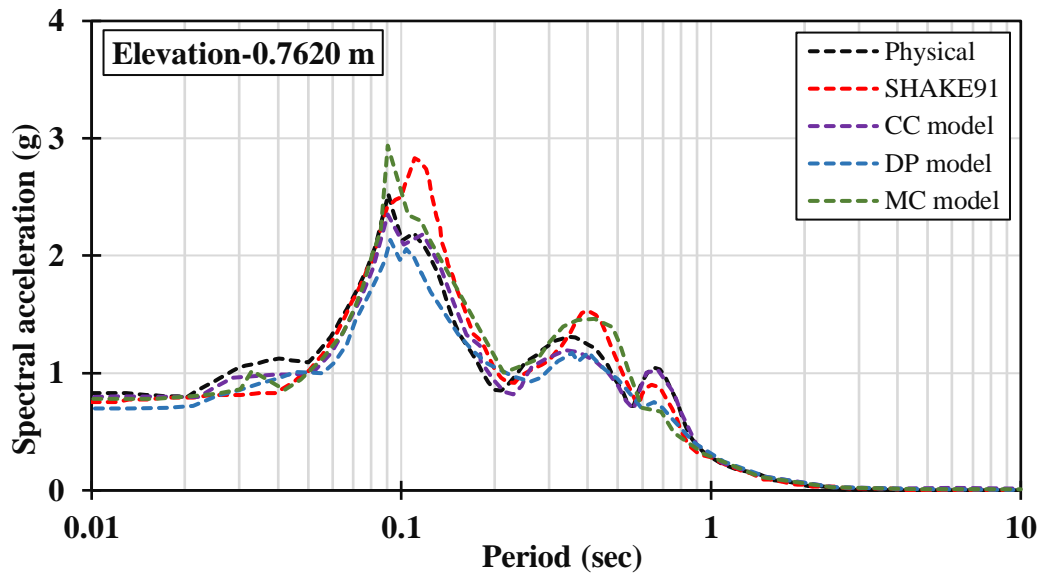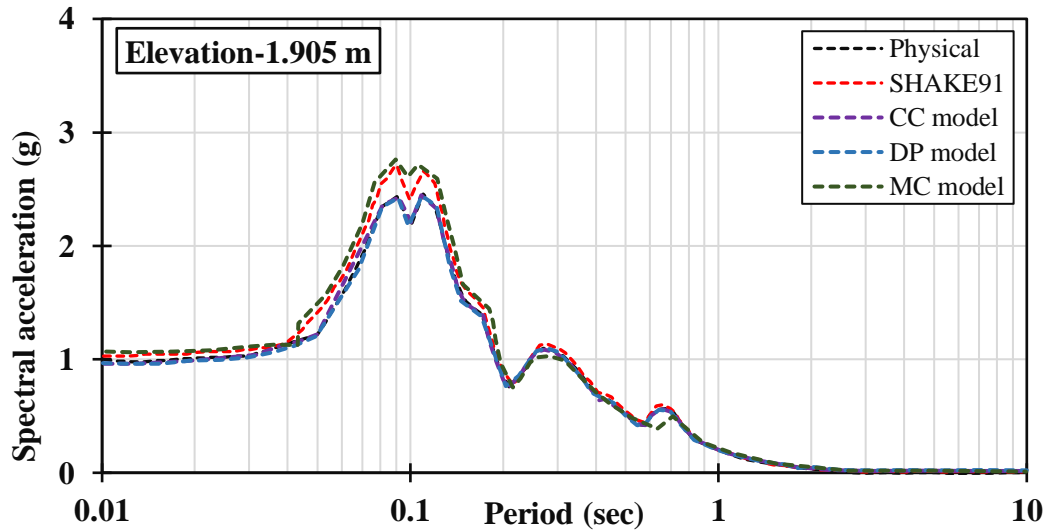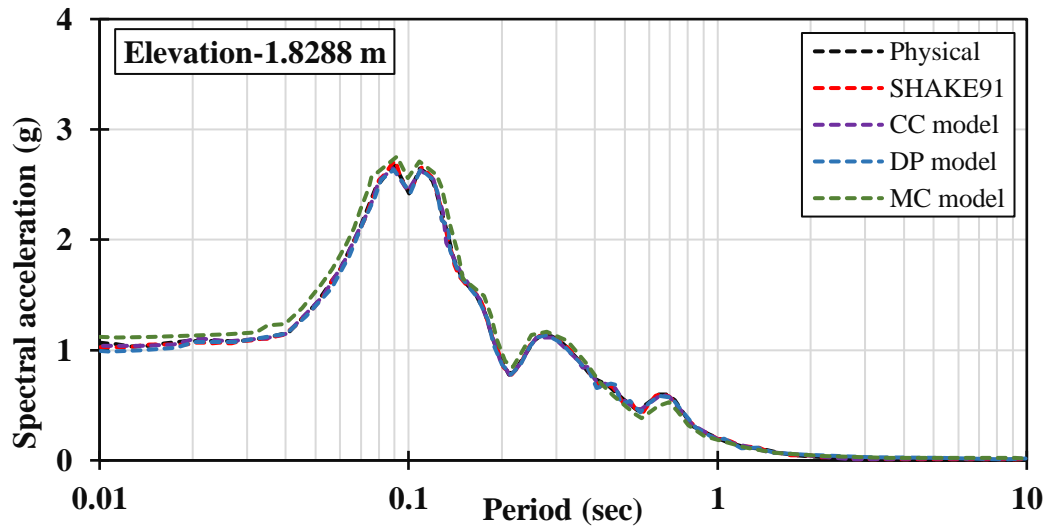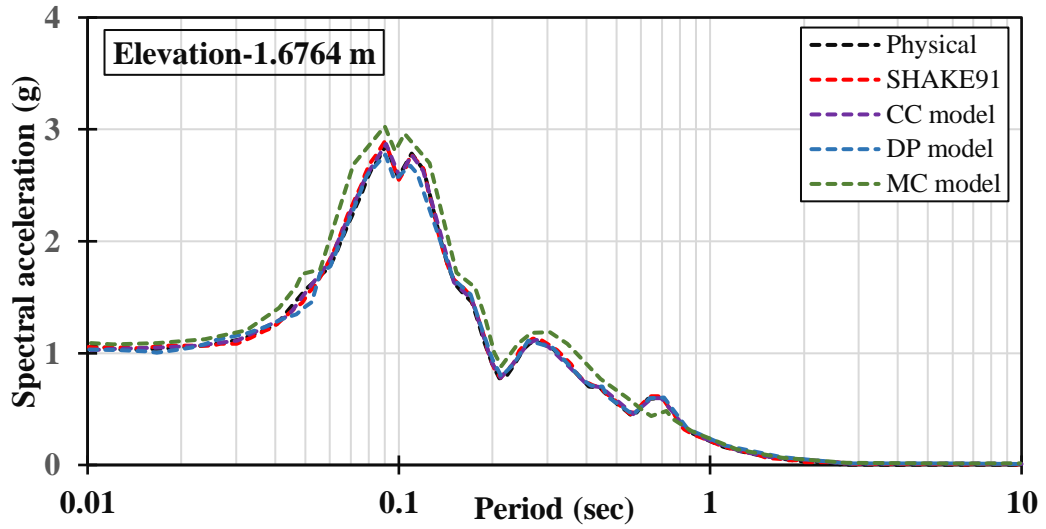
Figure 4-37 Test 2.26 Physical Test Site Response versus Numerical Simulation, Acceleration Response Spectra (Elevations in m, Relative to Top Surface)

4.4.2. Kinematic versus inertial pile response

As previously identified, SSPSI response modes comprise components of the superstructure inertial forces and also the kinematic forces exerted by the soil on the pile. Decoupling these variables and analysing the inertial and kinematic interaction independently for their corresponding contributions to SSPSI is important to understand the individual effects. However, the crucial issue is that the relative proportions of inertial and kinematic interaction are magnitude dependent. Therefore, determining these components from the physical or numerical model and then examining the decoupling assumptions provides an effective approach. However, physical and numerical dynamic simulation for single piles offers the best opportunity for isolating these mechanisms of SSI. A strong relationship between SSPSI and the pile response was reported in the case study (Meymand, 1998a), and this relationship has also been captured in numerical analysis with different degrees of accuracy depending on the type of soil constitutive model. Figure 4-38, Figure 4.39 Figure 4-40 and Figure 4.41 illustrates four examples of the numerical simulation model response for Test 1.15 for the four loading cases.

Figure 4-42 presents the experimental and numerical data of the bending moment envelopes for the four head pile cases. The bending moment response along the pile for each loading cases are shown by Figure 4-43. The comparison of the two set of results reveals that the interaction mode of the inertial forces which develop due to the effects of the superstructure (pile head masses) dominate the heavily loaded pile response. This inertial interaction induces a significant bending moment at the vicinity of the pile heads. The interaction of kinematic forces significantly influences the lightly loaded piles and induces maximum bending moments at a depth of 0.762 and 0.762 m, respectively. The differences between the physical test results and the numerical simulation are relatively small indicating the following:

(i)   the FE simulation of the physical shaking table test is performed successfully,

(ii)   (ii) both inertial and kinematic interaction of the SSPSI system can be captured accurately, and

(iii)   (iii) using an effective soil constitutive model and appropriate numerical modelling aspects (constraint, contact, loading and boundary conditions) are the key of achieving accurate results.

(a)

(b)

(c)
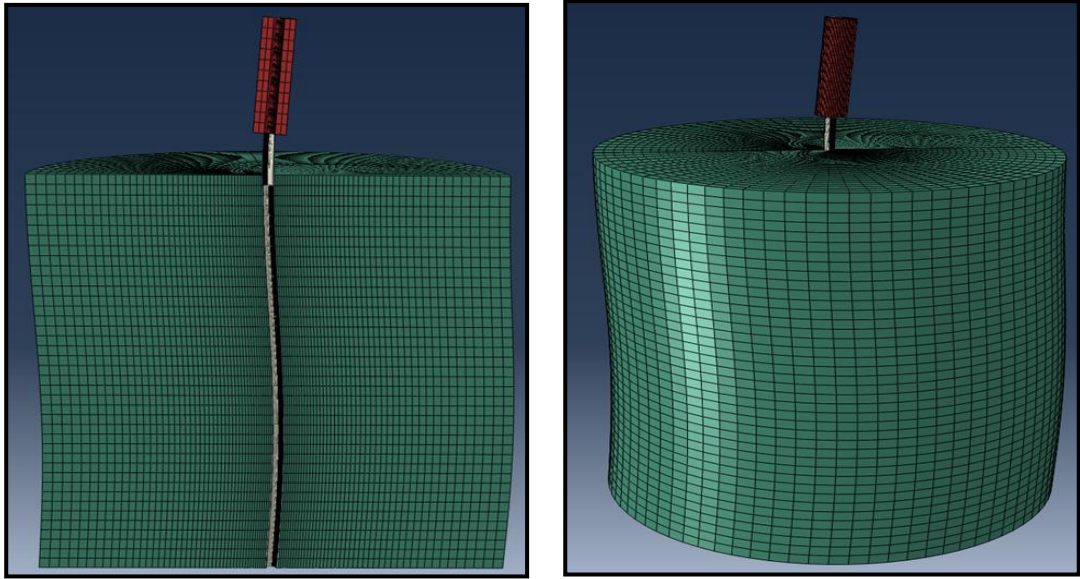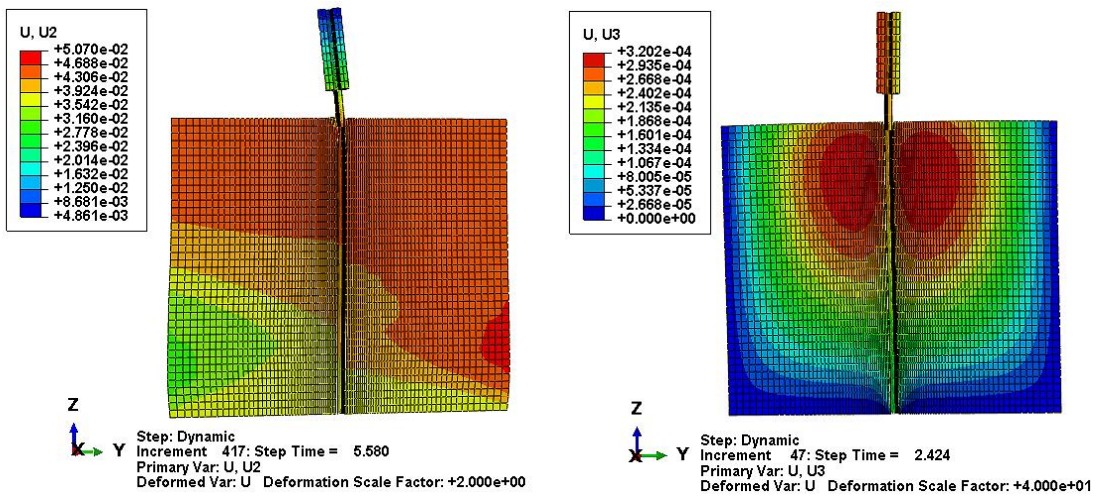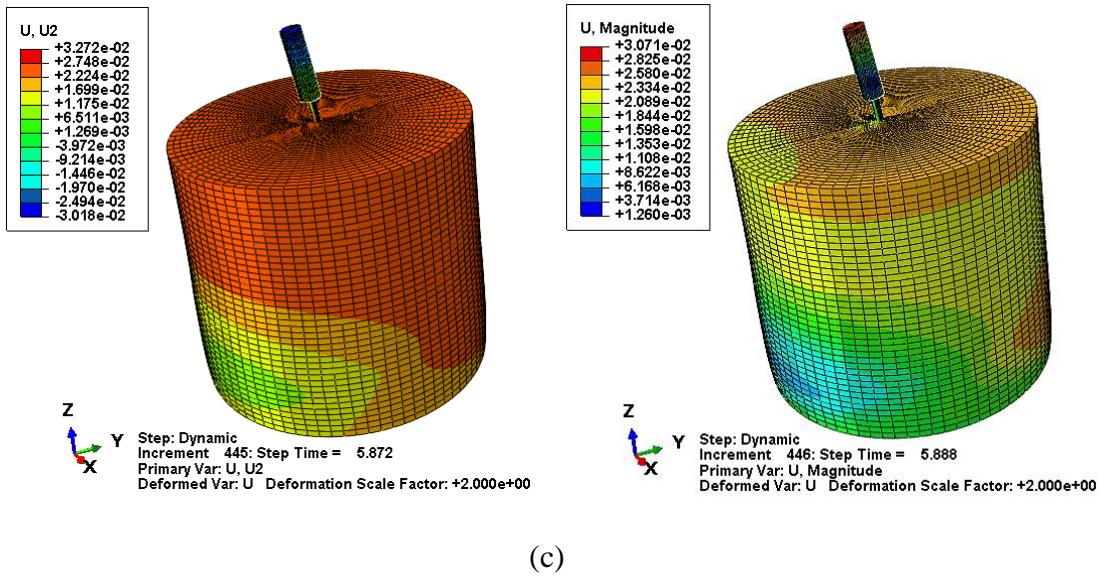
Figure 4-38 Pile Mass Head 72.7 kg (a) Numerical Model deformation in Motion, (b) Distribution of Soil Displacement (Y-Direction, Z-direction and Total Magnitude) at Different Time Period in Motion

(a)
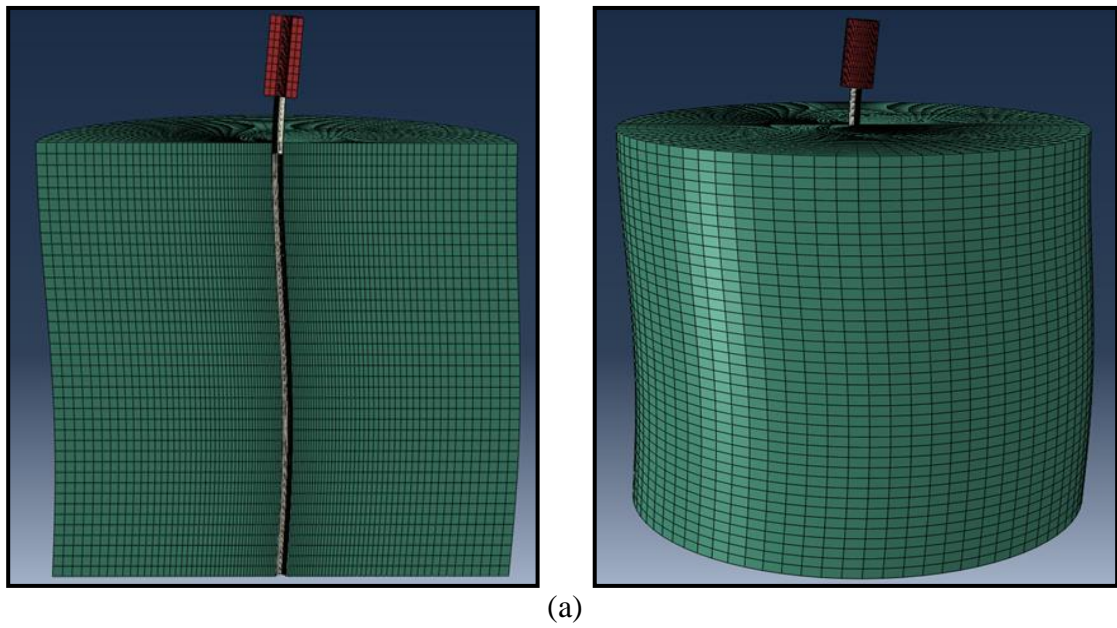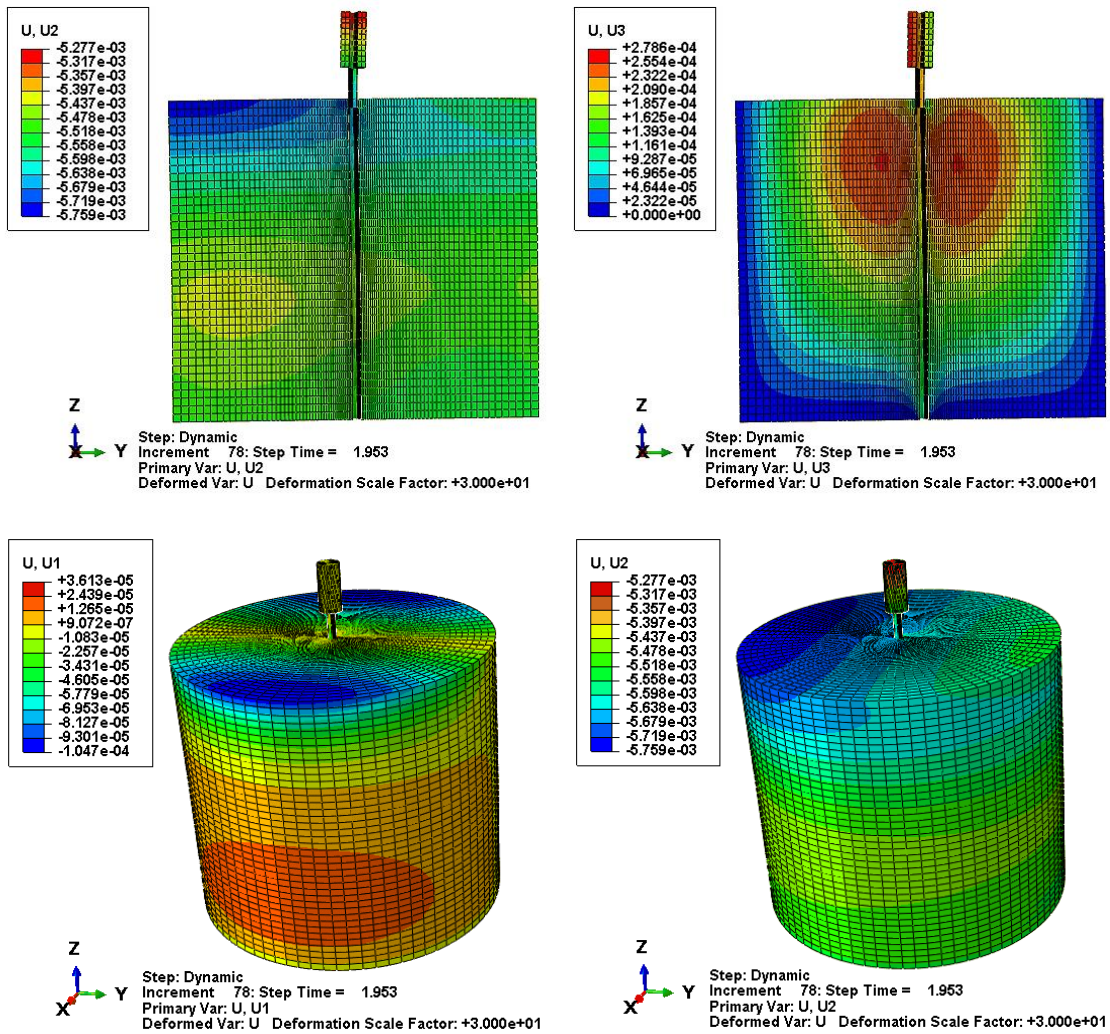
(b)

Figure 4-39 Pile Mass Head 45.36 kg (a) Numerical Model deformation in Motion, (b) Distribution of Soil Displacement (Y-Direction, Z-direction and Total Magnitude) at Different Time Period in Motion

(a)

(b)

173
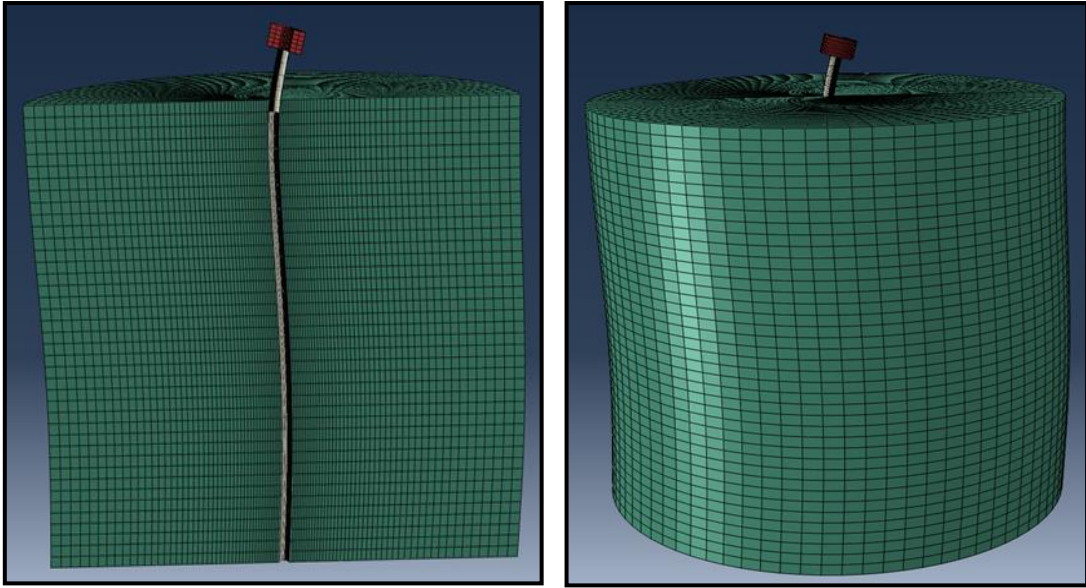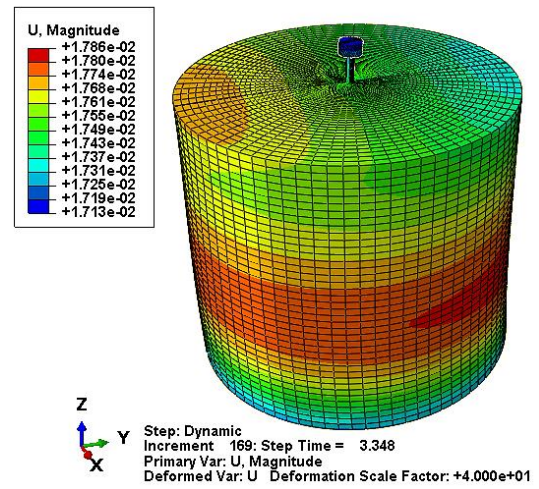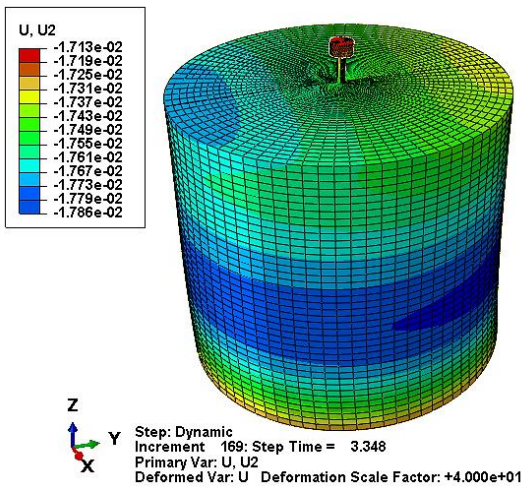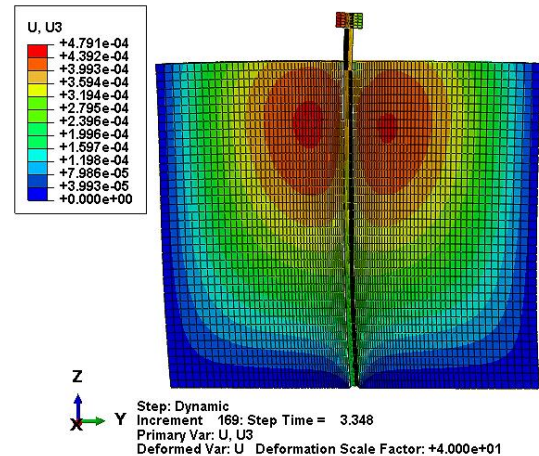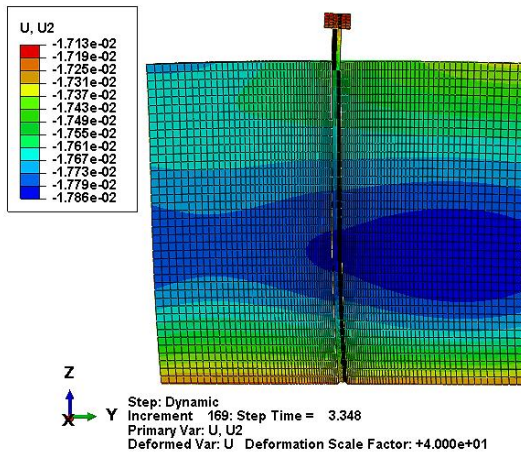
Figure 4-40 Pile Mass Head 11.40 kg (a) Numerical Model deformation in Motion, (b) Distribution of Soil Displacement (Y-Direction, Z-direction and Total Magnitude) at Different Time Period in Motion

(a)

174

(b)
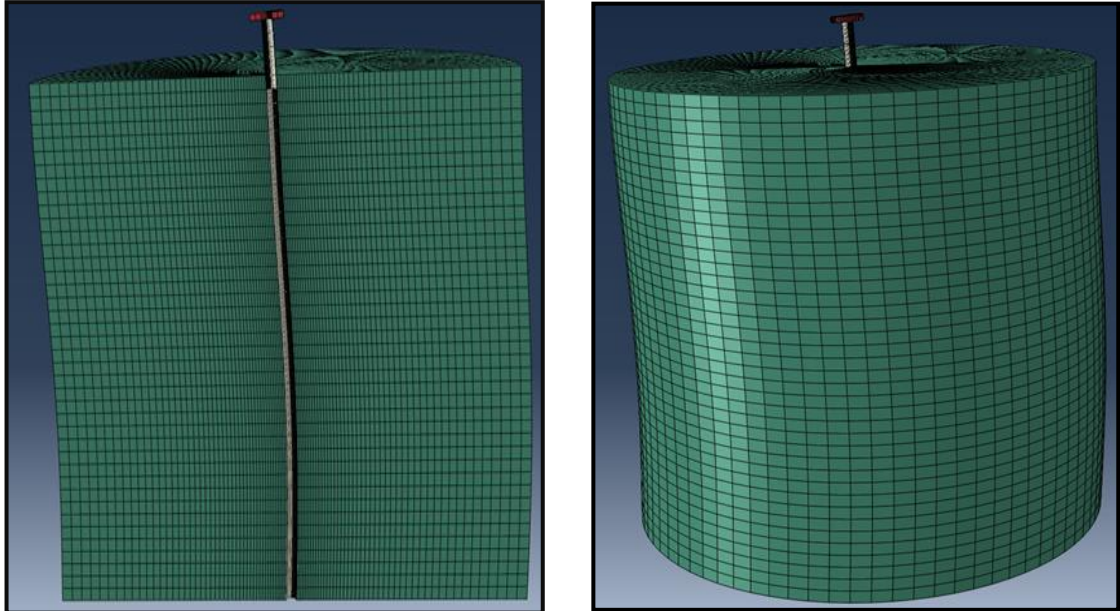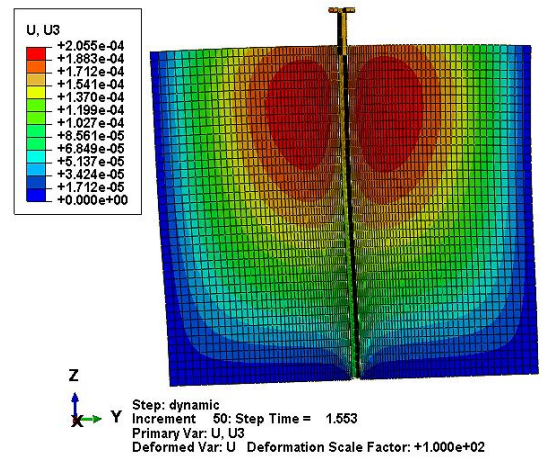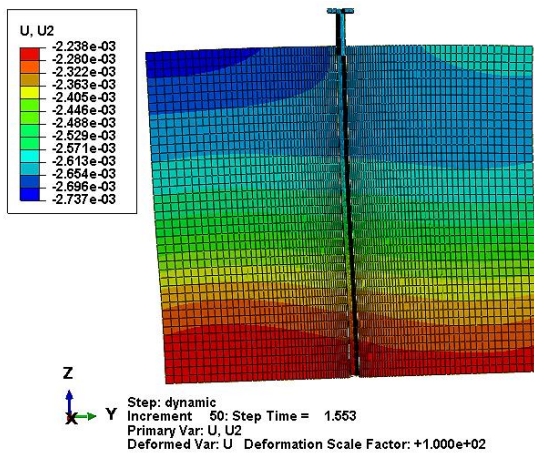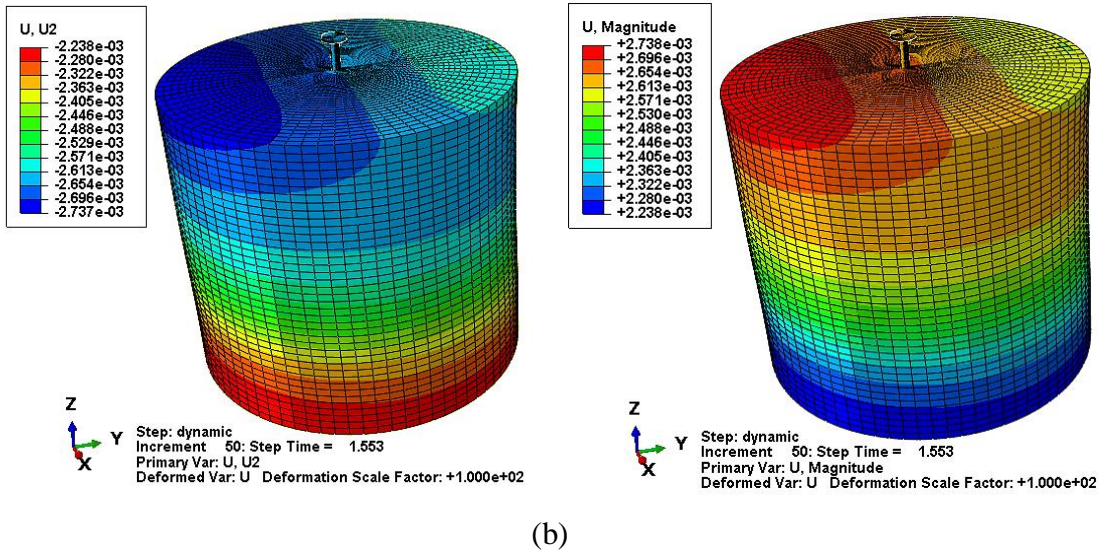
Figure 4-41 Pile Mass Head 3.0 kg, (a) Numerical Model deformation in Motion, (b) Distribution of Soil Displacement (Y-Direction, Z-direction and Total Magnitude) at Different Time Period in Motion
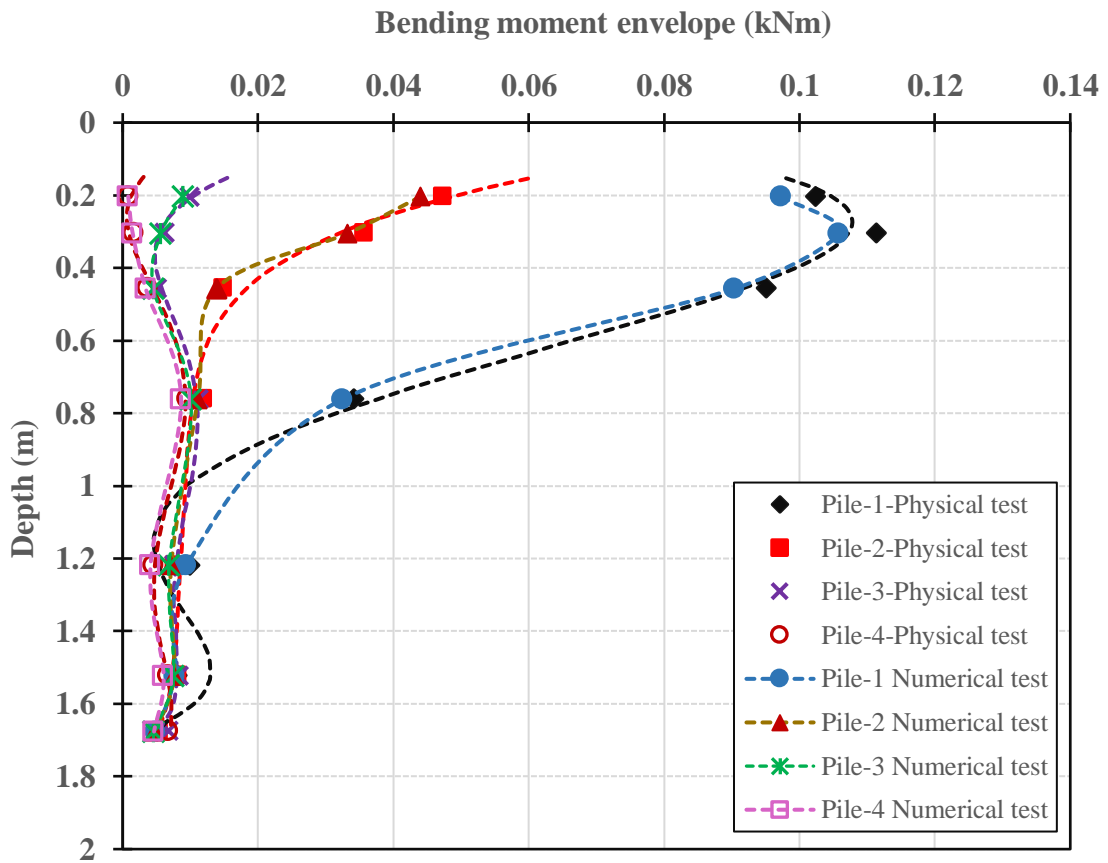
Figure 4-42 Test 1.15 Pile Bending Moment Envelopes
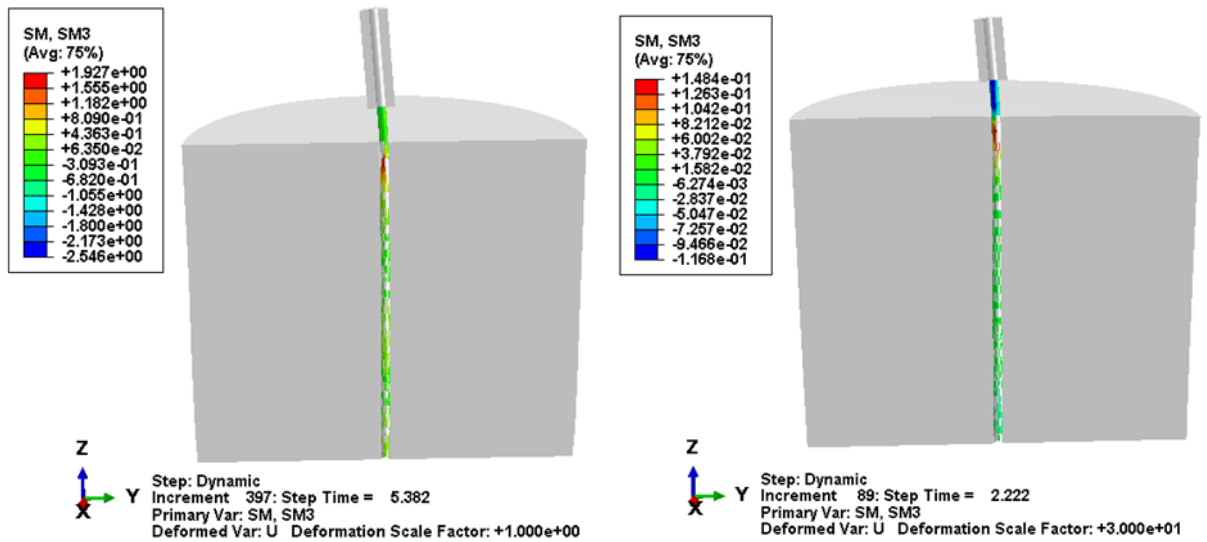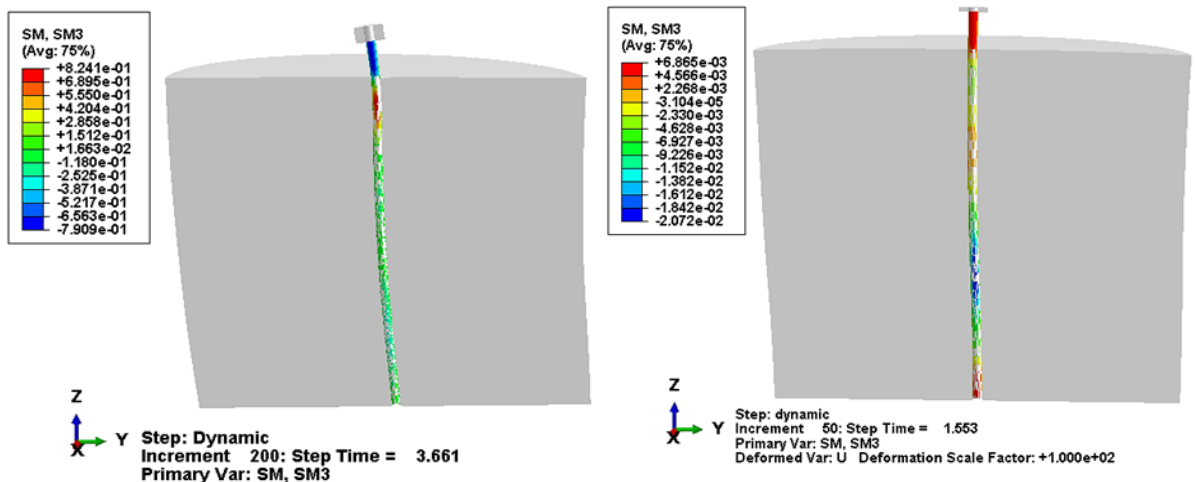
Figure 4-43 Test 1.15 Pile Bending Moment along Z-axis during shaking, (a) Pile with Mass head 72.7 kg, (b) Pile with Mass head 45.36 kg, (c) Pile with Mass head 11.4 kg, (d) Pile with Mass head 3.0 kg

Figure 4-44 to Figure 4-55, present the pile head accelerations, the FFTs and the acceleration response spectra for a single pile model with a head weight equal to 72.7, 45.4, 11.4 and 3.0 kg, respectively for Test 1.15 (Meymand 1998). Three different soil constitutive models are included in the images, as well as the physical test data. Although the structure and soil deposit interact with the foundation system and may behave in the

plastic range under specific earthquakes, most studies focus on the elastic response system to simplify the problem, especially for soil material.

The results when the MC model is employed, as shown in Figure 4-44 to Figure 4-55, indicate that significant errors in the SSPSI system behaviour develop during seismic loading. There are a number of explanations for these errors, which are outlined as:

1. The MC soil constitutive model is most appropriate for monotonic loading conditions, rather than during seismic events,

2. The MC model is more appropriate for simulating less soft clays subjected to monotonic loading. Therefore, when the soil is shearing beyond the elastic limit (into the plastic range), the model tends to overestimate the effective stress values. This is indicated clearly in Figure 4-44 to Figure 4-55, through the significant jump in Fourier amplitude values in the values obtained using the MC model.

3. The stress and stress-path dependency of the soil stiffness are not incorporated in the MC model, and the model does not include the strength reduction component, which is essential for simulating cyclic behaviour (Mylonakis and Gazetas 2000).

A number of previous studies have revealed that using the MC model provides reasonable results, but the analyses were performed within the small-strain range and monotonic loading conditions and therefore do not capture the issues with seismic conditions (Phanikanth et al. 2013). The results presented in Figure 4-44 to Figure 4-55 also indicate that although these errors exist to some extent when the Drucker–Prager model is used, the errors are smaller than for the MC soil model. In accordance with the reference case study, the piles with larger head masses experience more significant bending moments at the pile head, leading to high plastic strains in this region. Consequently, damping increases dramatically, contributing to a significant reduction in the acceleration amplitude of the pile head. This phenomenon may justify the greater divergence between the simulation results and those from the physical test simulated using MC and DP models, as the inertial force increases significantly due to seismic excitation effect.

The gap-slap mechanism is employed in this simulation. The gap evolution develops in the unconfined space along the pile length. Consequently, the pile has a large space to move horizontally, and then free vibration can occur. Permanent gap deformity is monitored after the shaking phase with the values matching those that occurred the reference physical case study. However, the comparison of the size of the generated soil-

pile gap values with those from the reference case study depends largely on the type of the modelling criteria and the best results were provided by the CC model, followed by the DP model and then the MC simulation. Similar to the physical shaking table results, the piles with relatively higher mass heads develop greater gap-slap mechanisms. By contrast, the influence of the soil kinematic force dominates the piles with relatively lower head mass. Once the gap between the soil and pile develops, the friction resistance of the pile skin reduces as does the pile capacity, and more space develops between the two components allowing for pile free vibration. This is mainly relevant for pile systems with high head masses. From the results presented in this paper, it is observed that nonlinear numerical analyses are a practical and useful way of simulating the SSPSI problem, although the accuracy is very dependent on the selection of a suitable soil constitutive model. For a dynamic soil-structure interaction analysis, as presented herein, the Cam-Clay (CC) model is considered to give the best results. Furthermore, the small deviation between the physical and numerical results when the CC model is employed may reflect the conditions of constructing the physical shaking structure, which include a close proximity between the accelerometer array to the adjacent part of the shaking table and other model structures, which in turn added to the feedback energy that arises from those members and being recorded by the accelerometers. This phenomenon has been observed in several field case studies presented in the literature (Ashory, 1999). Moreover, the strong twist motions provided by the shaking table, which cannot be isolated from the test data and are difficult to consider in the numerical analyses, may represent another possible justification for the under-prediction of behaviour from the CC model.
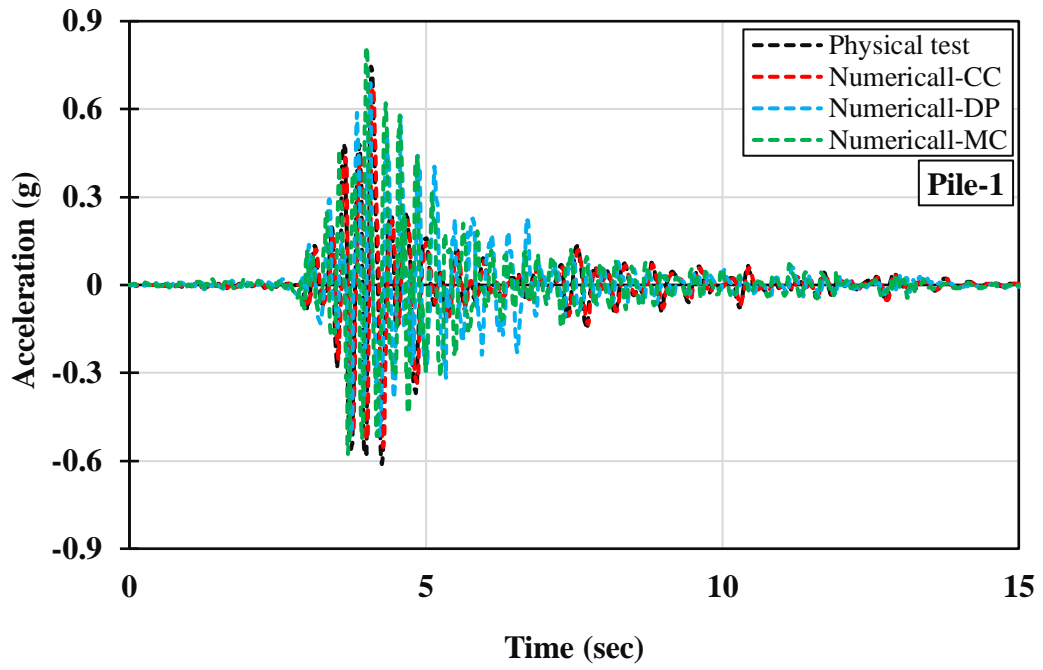
Figure 4-44 Physical Test versus Numerical Simulation: Pile Head Acceleration Time History (Pile-1)
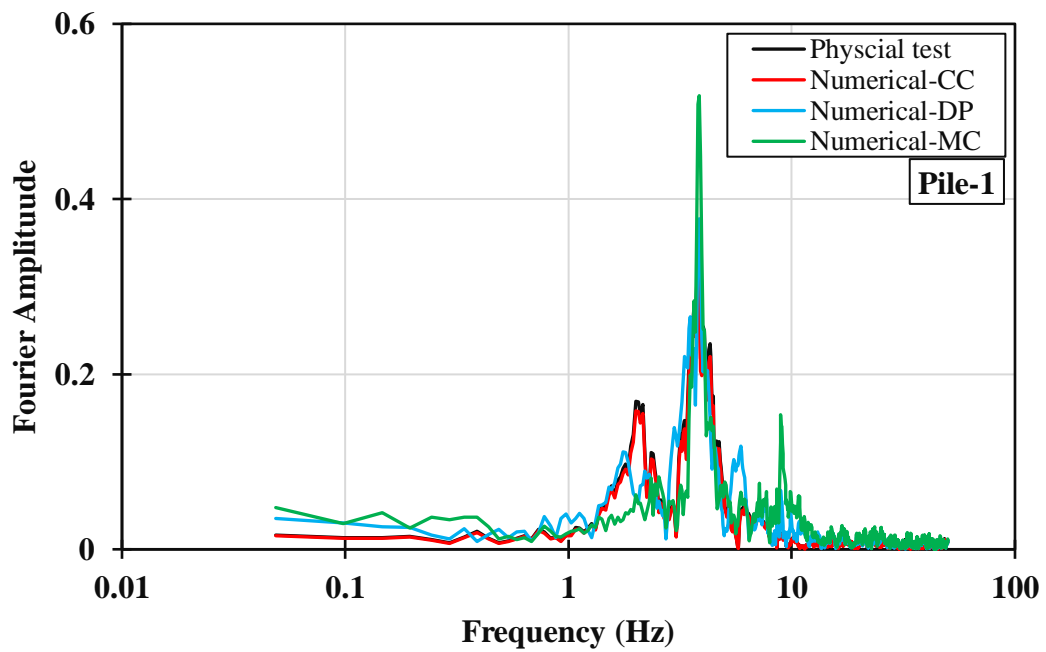
Figure 4-45 Physical Test versus Numerical Simulation: FFT (Pile-1)
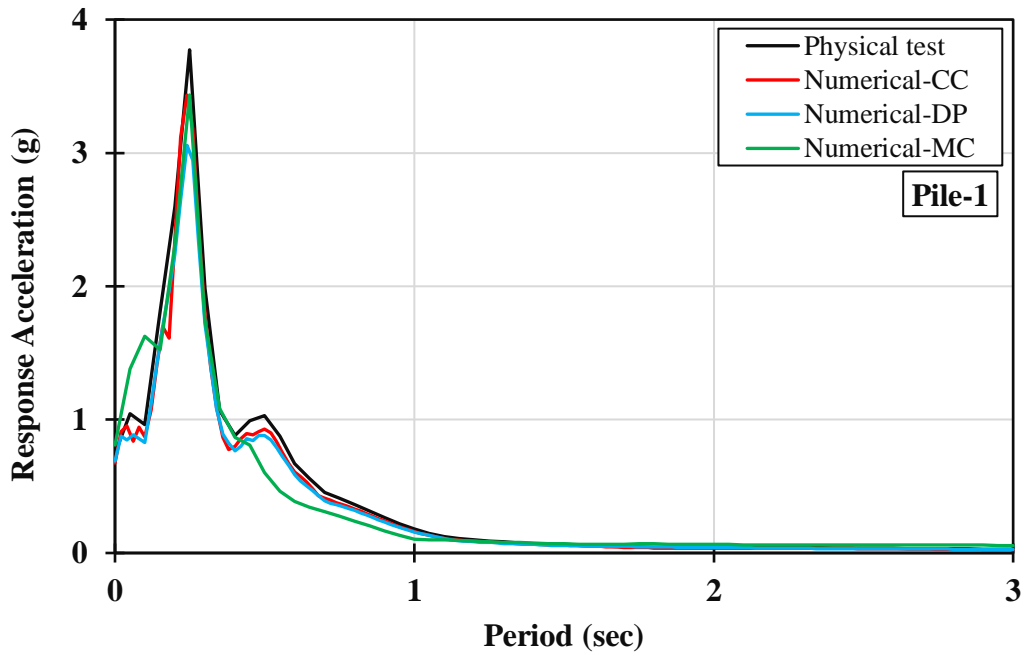
Figure 4-46 Test 1.15 Physical Test versus Numerical Simulation: Acceleration Response Spectra at Top Surface (Pile-1)
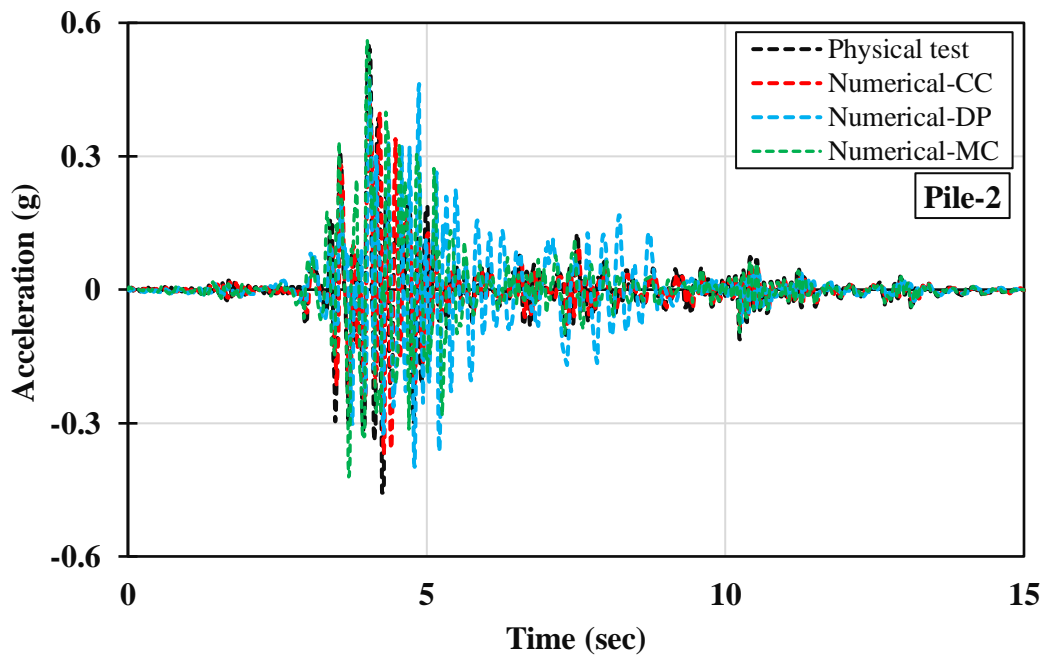
Figure 4-47 Physical Test versus Numerical Simulation: Pile Head Acceleration Time History (Pile-2)
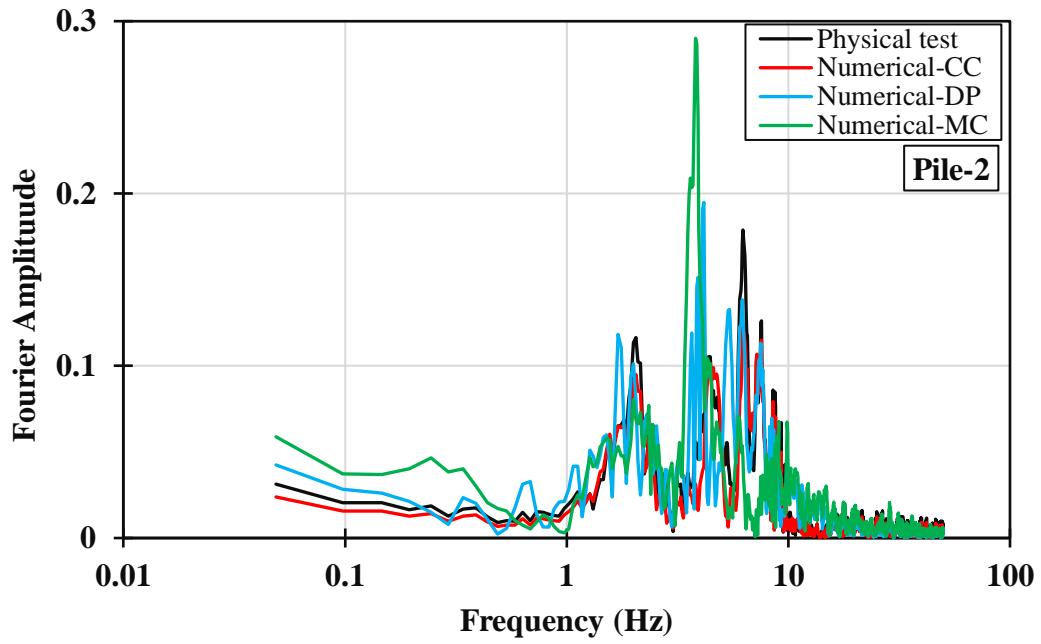
Figure 4-48 Physical Test versus Numerical Simulation: FFT (Pile-2)
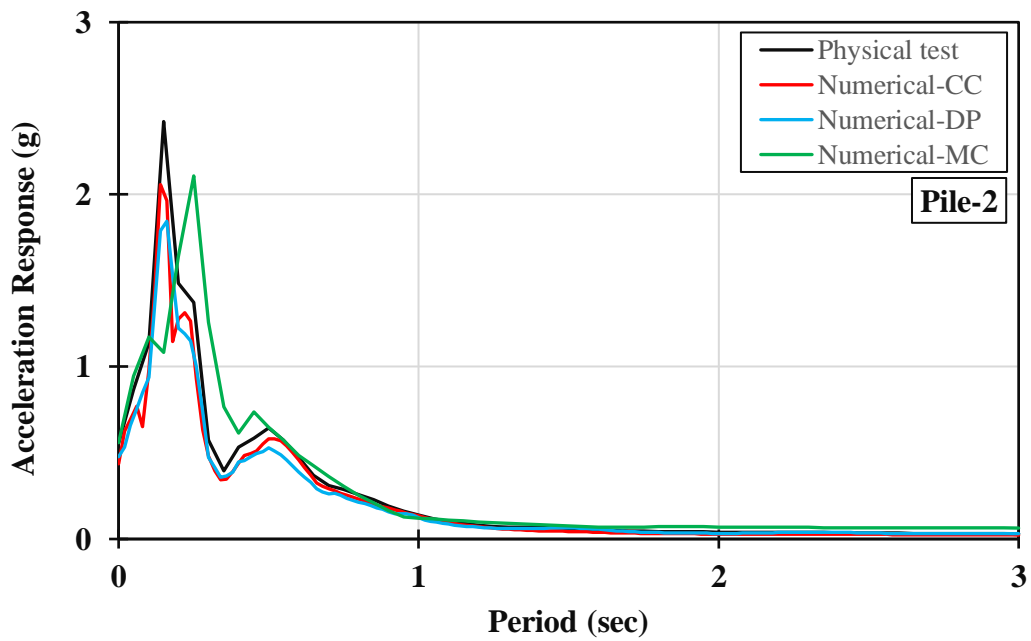
Figure 4-49 Test 1.15 Physical Test versus Numerical Simulation: Acceleration Response Spectra at Top Surface (Pile-2)
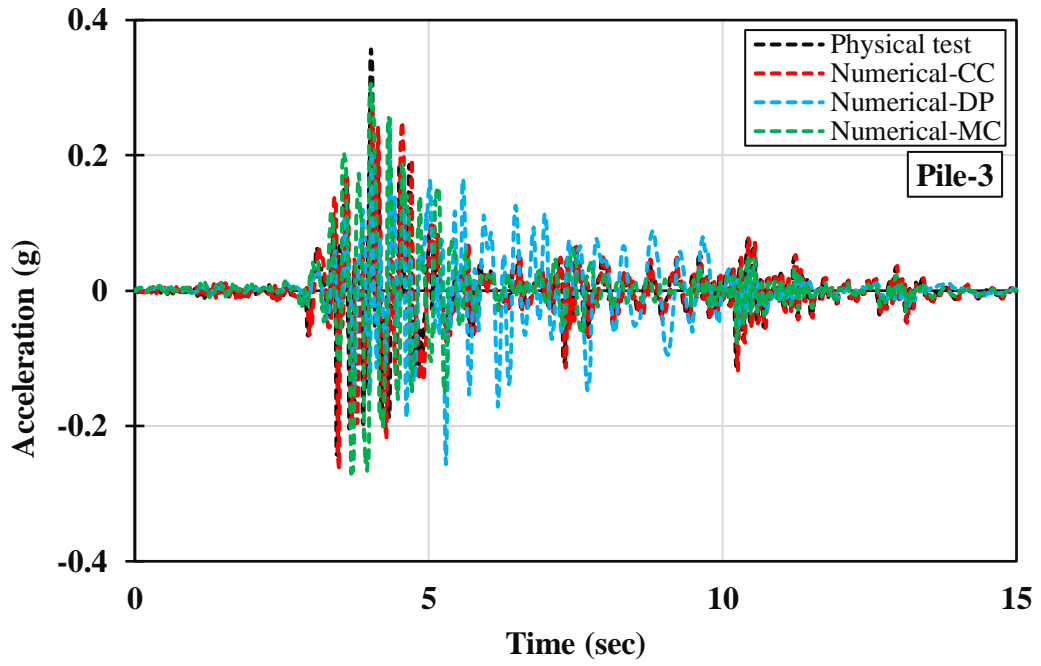
Figure 4-50 Physical Test versus Numerical Simulation: Pile Head Acceleration Time History (Pile-3)
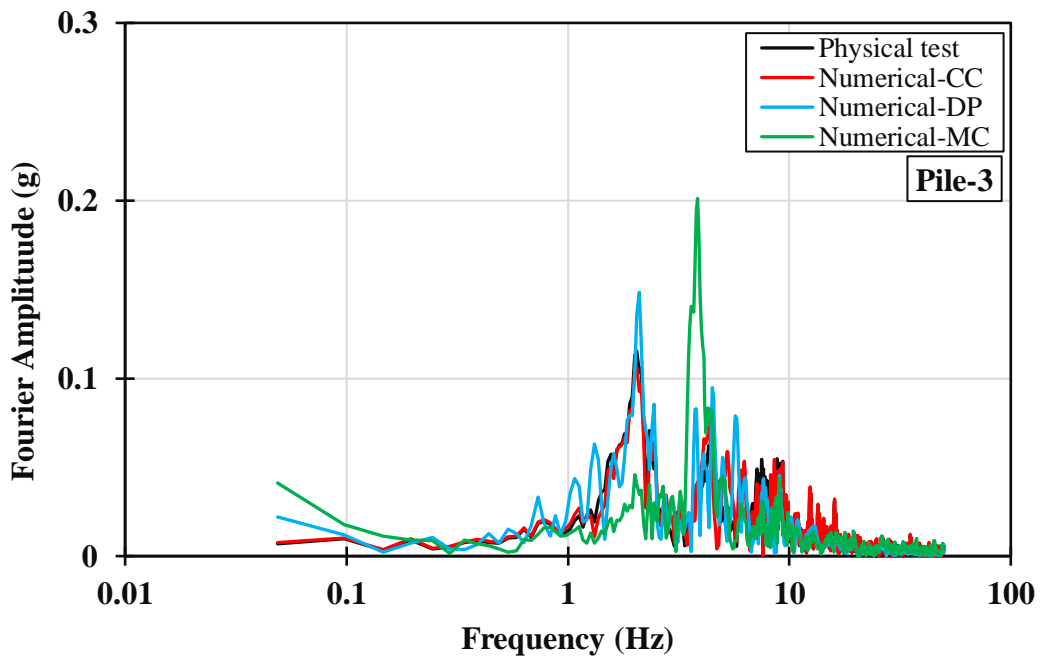
Figure 4-51 Physical Test versus Numerical Simulation: FFT (Pile-3)
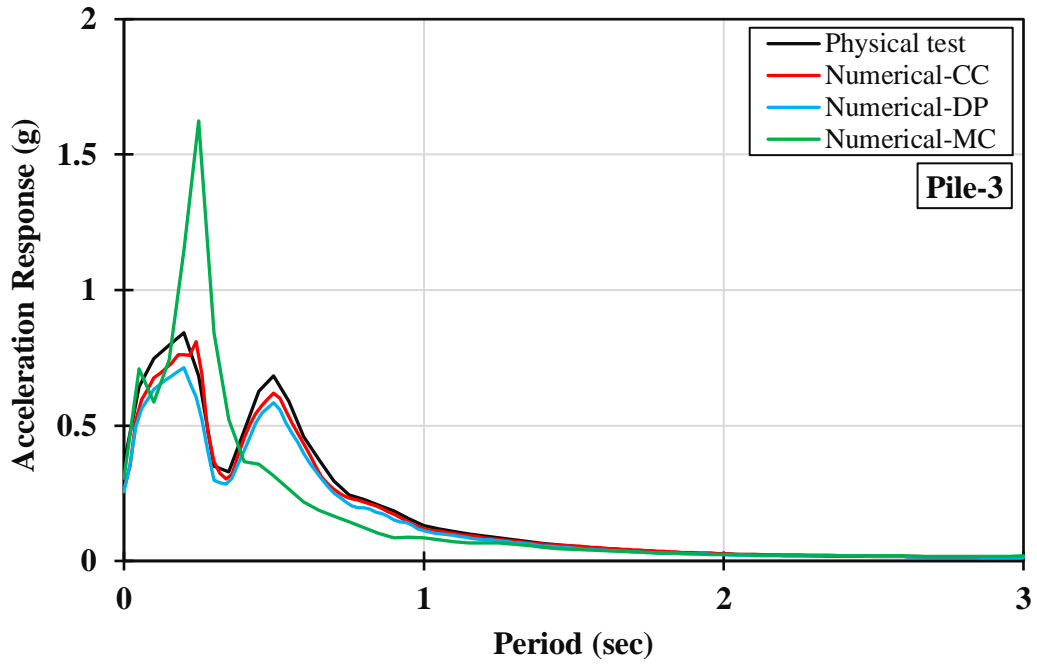
Figure 4-52 Test 1.15 Physical Test versus Numerical Simulation: Acceleration Response Spectra at Top Surface (Pile-3)
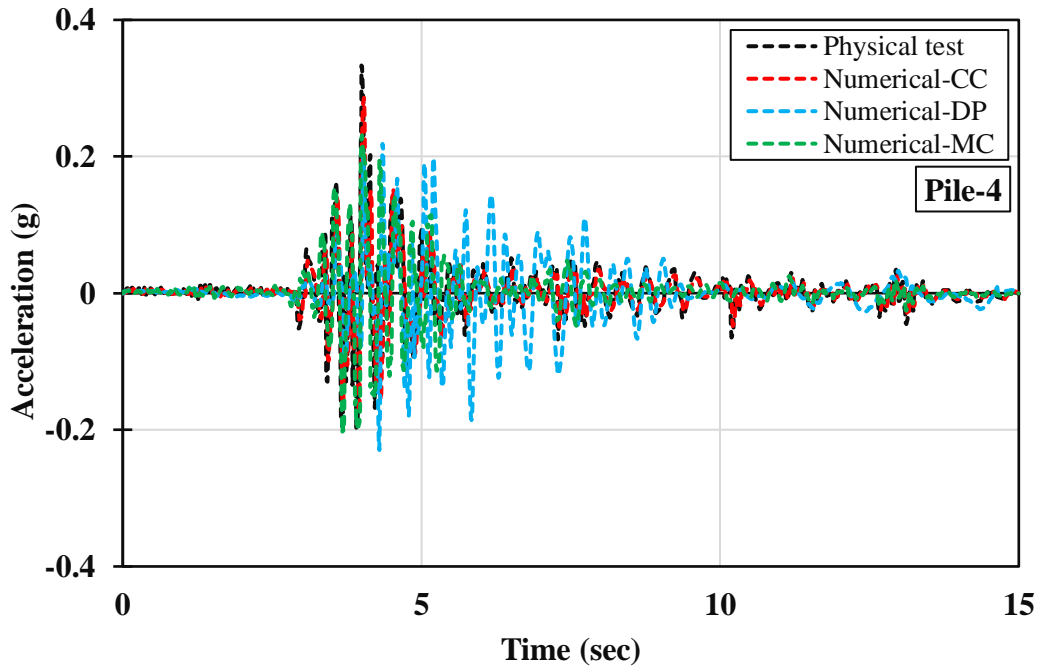
Figure 4-53 Physical Test versus Numerical Simulation: Pile Head Acceleration Time History (Pile-4)
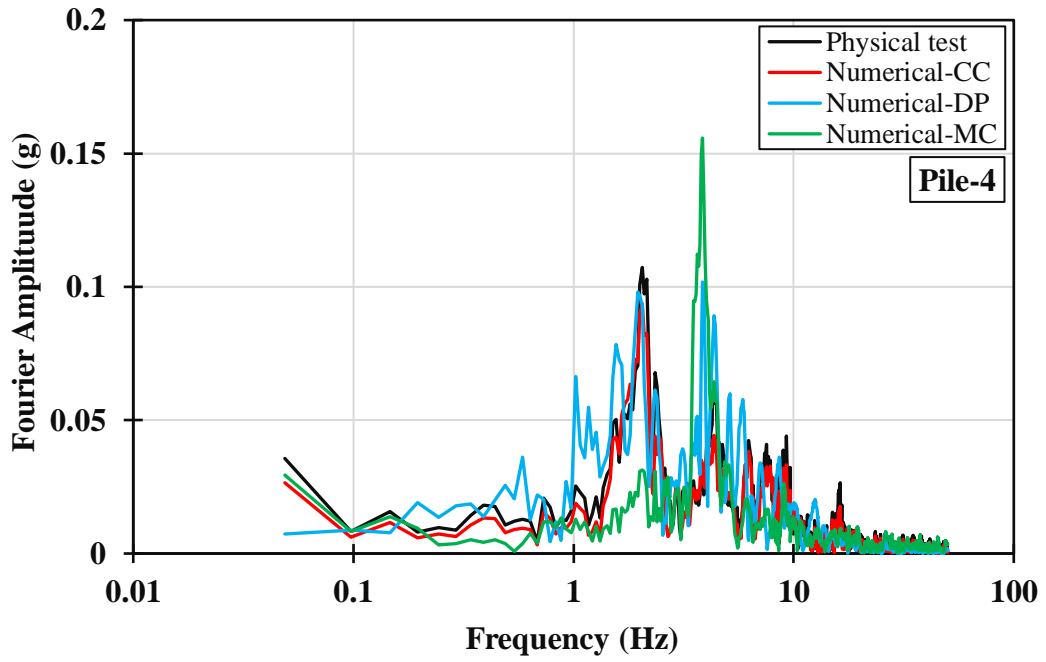
Figure 4-54 Physical Test versus Numerical Simulation: FFT (Pile-4)
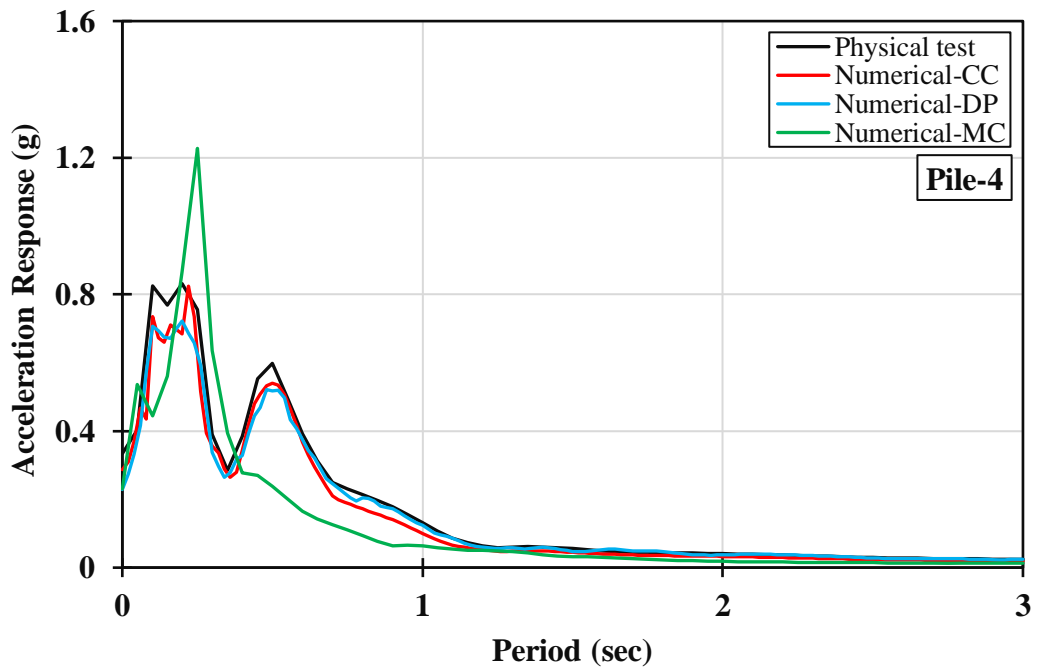
Figure 4-55 Test 1.15 Physical Test versus Numerical Simulation: Acceleration Response Spectra at Top Surface (Pile-4)

A qualitative comparison between the resultant motion properties for both the physical and numerical tests are given in Table 5, which represent the values of the motion parameters such as maximum acceleration (g), time of maximum acceleration (sec), predominant period (sec), number of effective cycles, sustained maximum acceleration (g) and effective design acceleration (g). Vibration period is an essential factor in base-shear design methodology, and is a critical parameter in defining the design response spectrum and consequently controlling the value of the base shear force. It is observed in Table 5 that the predominant periods and number of effective cycles from the numerical analysis for all four pile head masses is quite similar to the equivalent values from the physical test when the cam-clay soil constitutive model is used.

Table 4.6 The resultant motion properties for both physical and numerical tests

Parameters	Pile-1				Pile-2				Pile-3				Pile-4			
	Test	Numerical simulation			Test	Numerical simulation			Test	Numerical simulation			Test	Numerical simulation		
		CC	DP	MC		CC	DP	MC		CC	DP	MC		CC	DP	MC
Max. Acc. (g)	0.745	0.74	0.689	0.812	0.534	0.438	0.477	0.560	0.356	0.305	0.256	0.307	0.333	0.287	0.230	0.231
Time of Max. Acc. (sec)	4.09	4.1	4.06	4.03	4.03	4.03	4.04	4.0	4.02	4.03	5.29	4.07	4.0	4.03	4.29	4.05
Predominant Period (sec)	0.24	0.24	0.25	0.27	0.15	0.14	0.16	0.26	0.23	0.24	0.2	0.26	0.22	0.22	0.2	0.26
No. of Effective Cycles	1.359	1.359	2.690	1.727	2.030	2.137	3.730	2.106	1.978	1.776	4.214	3.126	1.461	1.417	4.006	2.410
Sustained Max. Acc. (g)	0.370	0.365	0.576	0.578	0.304	0.256	0.363	0.407	0.198	0.236	0.206	0.258	0.141	0.154	0.202	0.196
Effective Design Acc. (g)	0.767	0.707	0.636	0.845	0.558	0.532	0.482	0.572	0.358	0.335	0.254	0.378	0.336	0.286	0.231	0.268

4.5. Concluding remarks

This chapter has described the development of a numerical model which can accurately depict seismic soil–pile–superstructure interaction (SSPSI) problems. This is a very challenging problem, but essential in order to develop a greater understanding of this behaviour for real structures. The novelty of this work is in the development of a fully coupled nonlinear seismic soil-structure interaction numerical model for a scaled shaking table test. This includes both material and geometric nonlinearities for both the soil and pile behaviour, and three elastoplastic soil constitutive models were analysed.

The research presented herein has largely focused on the influence of the soil constitutive model, and three different models have been examined. The dimensional analysis procedure to determine appropriate scaling criteria to develop a scaled soil and pile-supported structure in the model, is described. A unique methodology is outlined which allows multi-directional simple shear deformations, minimises boundary effects and replicates the free-field site response. The output data from the model is validated using available physical test data and it is shown that the model provides an accurate representation of the test behaviour.

The finite element analysis software Abaqus is employed to develop a 3D numerical model to replicate a physical shaking table test. Three different soil constitutive models are examined including the Mohr–Coulomb model, the Drucker–Prager cap model and the Cam–Clay approach. It is shown that using an appropriate soil constitutive model is key to providing an accurate representation of the physical test. The dynamic pile response is also studied, and a fully-coupled analysis procedure is developed which can accurately represent the dynamic response of complex soil–pile–superstructure systems.

The majority of soil–structure interaction effects such as the gap-slap mechanism, the consequences of the soil-pile kinematic force, and the superstructure inertial force, are clearly shown and depicted in the model. The consequences of SSPSI illustrates that the gap-slap mechanism amplifies the pile head acceleration, lengthens the period of the superstructure and activates the pile free vibration, thereby leading to a reduction in stiffness of the pile. Therefore, ignoring the gap-slap mechanism due to simplification of numerical analysis results in misleading stiffness and strength capacity of the analysed piles. It is important that this is included in the numerical model. Although there are some small differences between the numerical results and those from the physical tests, these are within an acceptable range and the physical shaking table test is successfully simulated using FEA, particularly when the Cam-Clay soil model is employed. The Mohr–Coulomb and Drucker–Prager cap models provide a less accurate representation of the considered problem and are generally shown to be unsuitable for non-monotonic loading conditions.

Chapter 5: Scaling and Validation Methodology

5.1. Introduction

In geotechnical engineering, the use of scale models enables the controlled modelling of complicated systems and offers the opportunity to understand the fundamental mechanisms involved in operating these systems. In certain situations, such as a static lateral pile loading test, the scale modelling test can be an effective alternative to the corresponding full-scale one. In investigations of dynamic soil–pile interaction, the scale modelling test allows the simulation of cases which can never be accomplished in a full scale prototype, (Heib *et al.*, 2014).

The scale modelling approach can be employed when performing parametric studies to augment case histories and/or prototype investigations for the areas where existing investigations provide sparse data. In addition to qualitative analysis, the results of scale modelling tests are frequently applied as calibration benchmarks for analytical approaches and/or quantitative forecasts of the prototype response. To successfully achieve this, a set of scaling relationships which can describe the examined model and accurately predict the behaviour(s) of the prototype must be developed.

In this chapter, the theories of scale modelling approach are described, and the development of scale modelling criteria for shaking table test is explored. The adoption of scaling criteria and design of the soil and pile models utilised in the programme are explained. The sub-scale models are examined to predict the behaviour of involved prototype materials using sophisticated scaling approach (see Section 3). The results are then validated through a series of experimental tests. With the association between the scaled experimental test and full-scale numerical analysis for the prototype system as basis, this study attempts to develop a practical technique to scale and validate the dynamic soil–structure problem. The physical shaking table test following the selected reference case study (Meymand, 1998) is adopted, the full description of which is in Chapter 4. For the numerical modelling of this methodology, the analysis aspects used in Chapter 4 are adopted in this simulation for full-scale modelling.

5.2. Scale Model Similitude Theories

The relation between a scale model and analogous prototype behaviour can be characterised using the theory of 'scale model similitude'. (Kline, 1986) described three

approaches of increasing intricacy and the power of developing complex scale models. These theories are 'dimensional analysis theory', 'similitude theory', and 'the method of governing equations'. Dimensional analysis theory (Jonsson, 2014) is based on the principle of dimensional homogeneity. This theory involves converting a dimensionally homogeneous equation stating a physical association between quantities and defining the physical circumstance to the corresponding equation involving dimensionless products of powers of the physical quantities. Dimensional analysis theory can be employed particularly to comprehend the problem–solution form without the application of scale modelling. Similitude theory is a category of engineering science involved with setting up the necessary and appropriate conditions of correlation between phenomena. This theory can accurately predict the behaviour of a prototype by using scaling laws applied to the experimental results of a scale model related to the prototype through similarity conditions, as schematically illustrated in Figure 5-1 (Szücs, 1980, Simitses, 1992, Murugan, V. & P. R., 2013).
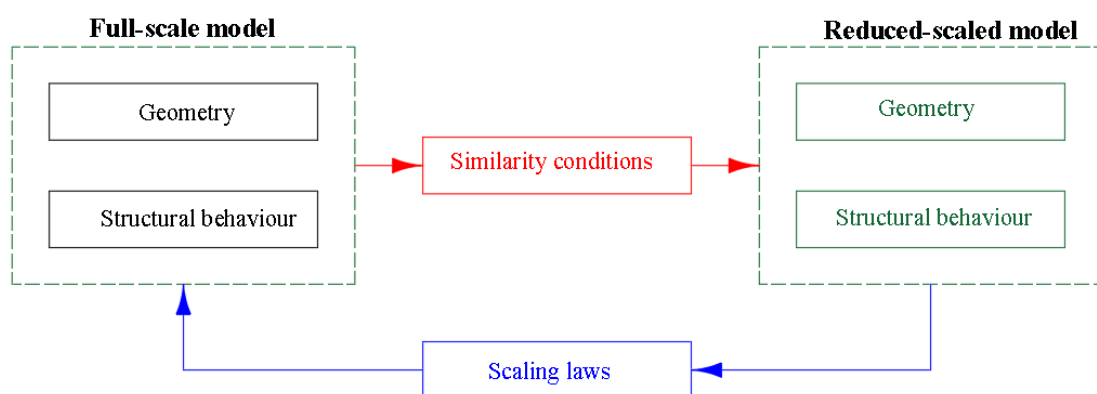
Figure 5-1 Flow Chart of Forecast of the Structural Behaviour of Full-Scale Prototype Using Physical Test of a Scale Model

Similitude theory identifies the forces functioning in a system and employs dimensional analysis to form and associate the dimensionless terms for the scale model and full-scale prototype (Coutinho, Baptista & Dias Rodrigues, 2016). The scaling relationships between model and prototype are also known as prediction equations. The method of governing equations includes changing the differential equation characterizing the process to a nondimensional one and developing similarity of the model to prototype variables, which must also be concluded for the initial and boundary conditions of the system. In addition, similarity variables should be established for the initial and boundary conditions which are operating the system.

Scale models of dynamic loading and SSI conditions can be described as those involving geometric, kinematic and dynamic similarities to the prototype (Langhaar, 1980). Geometric similarity describes a situation wherein model and prototype have analogous physical dimensions. Kinematic similarity refers to a phenomenon in which model and prototype have analogous particles at similar points and times. Dynamic similarity defines a circumstance in which analogous parts of the model and prototype undergo homologous forces. Scale models may fulfil the criteria of similarity to the prototype in different degrees of accuracy. The systematic literature uses the nomenclature of 'distorted', 'adequate', or 'true' to describe the degree of accuracy with regard to meeting the requirements of similitude (Moncarz and Krawinkler 2006). A 'distorted' model is a scale model in which the prediction equation is distorted due to significant deviation of similitude requirements. Compensating distortions are introduced to preserve the prediction equation in other dimensionless products. A scale model is 'adequate' when the primary features of the phenomenon are correctly scaled with minor deviation consequences and the equation of prediction is not considerably influenced. A 'true' model refers to a scale model that fulfils all similitude requirements.

Dimensional analysis essentially intends to reduce the parameters of a model to the fundamental 'measures of nature', i.e. *mass, length and time*, while developing a scale factor for all three quantities. For instance, modulus of elasticity is a stress indicator with units of force/area and corresponding dimensions of $M\,L^{-1}T^{-2}$ which represent the mass, length and time dimensions. Therefore, the scale factors for mass μ, length λ , and time τ can be combined to develop a scaling relation of $\mu\,\lambda^{-1}\tau^{-2}$ which correlates model–prototype stress response. As strain is a dimensionless parameter, the scaling relation between model and prototype strains can be considered as $1::1$ according to the same line of interpretation. The densities of the materials of model and prototype are ordinarily applied as a basis for defining the relationship between scale factors μ and λ . Once $\rho_{model}/\rho_{prototype} = 1$, m refer to model quantities, and p refer to the prototype quantities. μ , λ and τ can be expressed as Eqs. (5.1), (5.2) and (5.3).

$$\frac{L_m}{L_p} = \lambda \tag{5.1}$$

$$\frac{M_m}{M_p} = \mu \tag{5.2}$$

$$\frac{T_m}{T_p} = \tau \tag{5.3}$$

Then,

$$\frac{\rho_{model}}{\rho_{prototype}} = 1 = \frac{M_m}{M_p} \cdot \frac{V_p}{V_m}.$$

Once $\frac{M_m}{M_p}$ is μ and $\frac{V_p}{V_m} = \frac{1}{\lambda^3}$, μ can be computed as equal to λ^3.

The scale factor τ of the time quantity can be computed using the equation of the inertial force ratio, expressed as Eqs. (5.4) to (5.7).

$$\left(\frac{M_m A_m}{M_p A_p}\right) = \left(\frac{\gamma_m}{\gamma_p}\right) \cdot \lambda^3 \cdot \left(\frac{A_m}{A_p}\right) \tag{5.4}$$

with the weight ratio

$$\left(\frac{\gamma_m}{\gamma_p}\right) \cdot \lambda^3 \tag{5.5}$$

The model accelerations must be equal to the prototype accelerations. Thus,

$$\left(\frac{A_m}{A_p}\right) = 1 = \frac{\left(\frac{L_m}{T_m^2}\right)}{\left(\frac{L_p}{T_p^2}\right)} = \frac{L_m}{L_p} \cdot \frac{T_p^2}{T_m^2} = \lambda \cdot \left(\frac{T_p}{T_m}\right)^2 \tag{5.6}$$

in which

$$1 = \lambda \cdot \left(\frac{T_p}{T_m}\right)^2, \lambda = \left(\frac{T_m}{T_p}\right)^2 \tag{5.7}$$

where $\tau = \frac{T_m}{T_p}$. τ can then be computed as equal to $\lambda^{\frac{1}{2}}$.

By determining the mass μ, length λ and time τ scaling factors in terms of λ, a set of dimensionally correct scaling relationships can be developed for all variables desired to be studied. In the methodology adopted by (Clough & Pirtz, 1956) and (Clough & Seed, 1963), scale models are used to examine the earthquake resistance of rock-filled dams and sloping core dams, respectively. A drawback of this approach is that each variable is handled independently, disregarding its system function. A sophisticated methodology of dimensional analysis involves the Buckingham pi theorem approach of scale model. With this theorem, '*any dimensionally homogeneous equation involving certain physical quantities can be reduced to an equivalent equation involving a complete set of*

dimensionless products' (Candeias, 2012). Consequently, the solution for a studied physical quantity of interest $(X_1, X_2, \ldots, X_n)$ can be expressed as Eq. (5.8):

$$F(X_1, X_2, \ldots, X_n) = 0 \qquad (5.8)$$

and stated in the form of π such as in Eq. (5.9):

$$G(\pi_1, \pi_2, \ldots, \pi_m) = 0 \qquad (5.9)$$

π(s) are independent dimensionless products of the physical quantities, $X_1, X_2, \ldots, X_n$. (m) is the number of dimensionless products, and (n) is the number of physical variables. The relation between these two terms can be expressed as Eq. (5.10):

$$m = n - \text{the number of involved fundamental measures} \qquad (5.10)$$

The definitions of individual π terms are developed by categorizing the physical variables into dimensionless ones. All these variables must be included, and the term m must be independent. Theoretically, for a given scale modelling issue, there is no unique set of π, but the variables should be correctly identified and the π terms should be formed appropriately. The scaling relationships may then be determined by equating the model $\pi_{i,m}$ and corresponding prototype $\pi_{i,p}$. As previously mentioned, the theory of the similitude attempts to define the problem realistically by developing forms of the π terms basing on the dominant forces in the system (Moncarz & Krawinkler, 2006a). The stress components of time history $\sigma_{ij}(r, t)$ for a scale model are determined by considering the formation of π terms resultant from an imposed acceleration time history $a(t)$. Two requirements are necessary to meet (true) scale modelling criteria, which are the aforementioned Froude and Cauchy conditions. The indicated stress is a function of a number of variables involved in the system (see Eq. (5.11)). Subsequently, the π terms can be developed as in Eq. (5.12).

$$\sigma = F(r, t, \rho, E, a, g, l, \sigma_o, r_o) \qquad (5.11)$$

$$\frac{\sigma}{E} = \left(\frac{r}{l}, \frac{t}{l}, \sqrt{\frac{E}{\rho}}, \frac{a}{g}, \frac{gl\rho}{E}, \frac{\sigma_o}{E}, \frac{r_o}{l} \right) \qquad (5.12)$$

Variables $r, t, \rho, E, a, g, l, \sigma_o$ and r_o represent the factors of position, time, material density, modulus of elasticity, acceleration, gravitational acceleration, length, initial stress and initial position vector, respectively. In $one - g$ scale modelling, the dimensionless product a/g and Froude's number v^2/lg must be equal to unity, which means that the model–prototype ratio of a specific stiffness (E/ρ) is equivalent to the geometric scaling

factor λ. This is referred to as the Cauchy condition and may be expressed in terms of shear wave velocity as in Eq. (5.13).

$$\left(\frac{(V_S)_m}{(V_S)_p}\right) = \sqrt{\lambda} \qquad (5.13)$$

Moncarz and Krawinkler (2006) also revealed that in a dynamic model system, the Cauchy condition is an essential requirement for synchronous replication of restoring, inertial and gravitational forces. However, the challenge in designing a (true) scale model is in selecting the materials of the model that satisfy the Cauchy condition with a combination of small modulus and large mass density. Alternatively, Moncarz and Krawinkler (2006) put forward two alternatives to perform scale modelling tests, that is, simulating artificial mass and ignoring gravity effects.

5.2.1. Scale Model Similitude Applied to Soil Mechanics

The scale modelling of geotechnical problems was first systematically described by (Rocha, 1958), who differentiated between total stress and effective stress circumstances and developed independent similarity relationships for each situation. For scale modelling to be employed in various sorts of stress system present in a one-g scale model, Rocha (1958) presumed a linear stress–strain relation between the model and prototype. Accordingly, the soil constitutive model can be scaled. This hypothesis is shown in Figure 5-2, where α represent the stress scaling factor; β, the strain scaling factor. The scaling of strain conflicts with the concept of the dimensional analysis method. However, the restriction of derivations within elastic deformations is justified by the analysis becoming insurmountably complicated once the nonlinear response is considered.

(Roscoe, 1968) examined the complexity of replicating the constitutive behaviour of prototype in scale models for soils whose response is hinging on confining pressure loading condition, i.e. soil self-weight. The assumptions of (Rocha, 1953) have been extended and recast in the critical state of soil mechanics. That is, the strain behaviours of the scaled and prototype elements of a soil will be identical only if these elements are exposed to two geometrically comparable stress paths when their initial states in $e - \ln\sigma'$ relation are equidistant from the critical state line. This hypothesis is illustrated in Figure 5-3, and validated by limited physical tests. Roscoe also asserted that a centrifuge programme is an applicable approach to such a method.
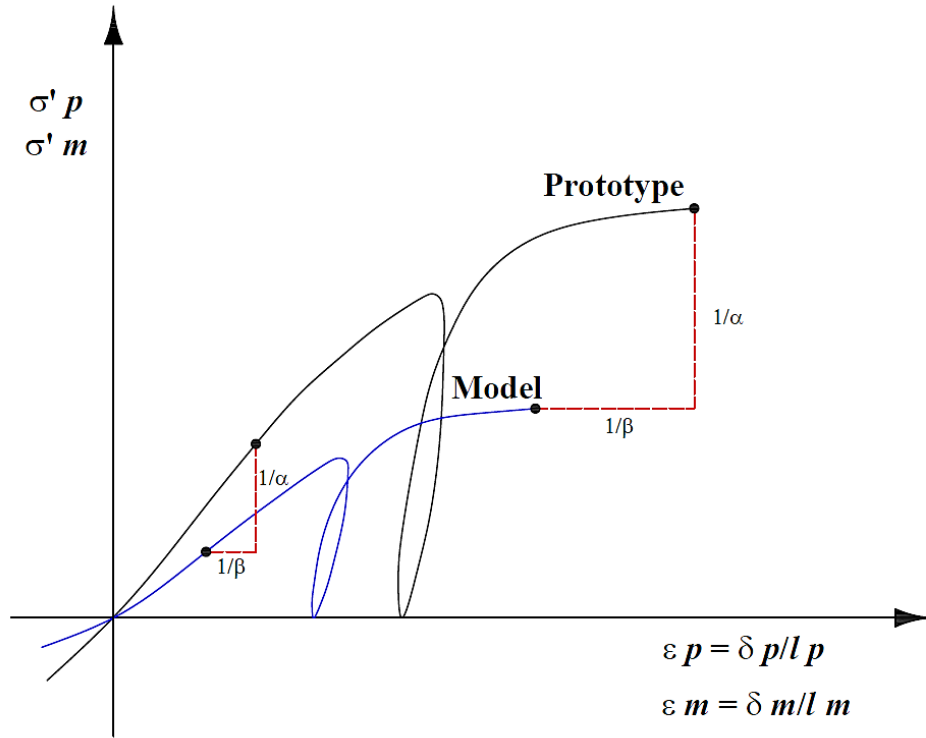
Figure 5-2 Constitutive Behaviour of Scale Model Defined by Stress and Strain Scaling Factors, modified from (Rocha, 1958)

The 'Buckingham pi theorem' is employed to solve the scale modelling problem of the dynamic interaction of a pile founded in clay soil (Kana, Boyce & Blaney, 1986). They then developed a nondimensional equation to define this theory by choosing D, EI and M to be reference parameters (see Eq. (5.14) and Figure 5.4).

$$\frac{x}{D} = f\left(\frac{y}{D}, \frac{M_c}{DM}, \frac{J_c}{D^3 M}, \frac{M}{\rho D^2}, \frac{EI}{E_r D^4}, \frac{EI}{E_l D^4}, \frac{FD^2}{EI}, \frac{M_p D^4 \omega^2}{EI}, \omega T_O, \frac{\omega^2 D}{g}\right) \quad (5.14)$$

where x is the pile lateral displacement, y is the y-coordinate of maximum lateral deflection, D is the pile diameter, M_c is the pile cap mass, M_p is the pile mass per unit length, J_c is the moment of inertia of the pile cap, ρ is soil mass density, E is Young's modulus of the pile, I is moment of inertia of pile section, E_r is soil storage modulus, E_l is soil loss modulus, F is the applied lateral load, ω is frequency of vibration, T_o is the linear frequency sweep period, and g is the acceleration of gravity which indicates the necessity for significant gravity in the last term.
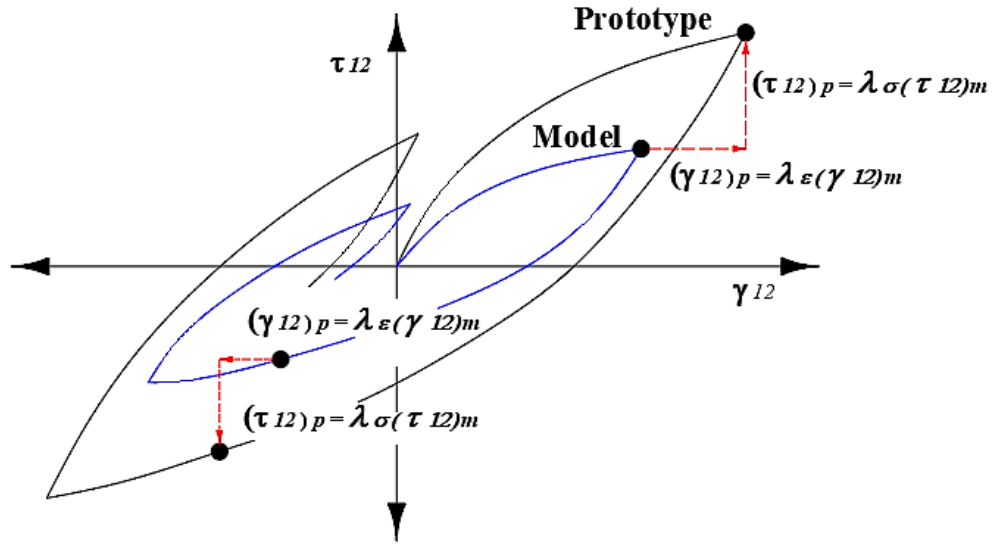
Figure 5-3 Critical State of Soil with Geometrically Similar Stress Paths for Prototype and Model, modified from (Roscoe, 1968)

(Kana, Boyce & Blaney, 1986) concluded that the gravity effects for the lateral pile response for overconsolidated clay were negligible, so the experiments were performed within this scaling system and under one–g environment. The results showed that the gravity effects for the particular test conditions are imperceptible. The frequency response is predominantly dependent on the material properties of the soil and pile tested. (Gohl, 1991) also employed dimensional analysis to develop the following functional relation for scale model similarity which is used in shaking table tests to evaluate the effect of soil–pile interaction for several intensities of shaking (see Eq. (5.15)).

$$\frac{y}{b} = K\left(\frac{l}{u_o}, \frac{\rho_p}{\rho_s}, \frac{EI}{G_s u_o^4}, \frac{\omega^2 u_o}{g}, \frac{m_o}{\rho_s u_o^3}\right) \tag{5.15}$$

where y is the lateral displacement of the pile, b is the pile diameter, l is the pile length, u_o is the input motion amplitude (applied at the base of the model), ρ_p is the pile density, ρ_s is the soil density, EI is the flexural rigidity of the pile, G_s is the shear stiffness of the soil which depends on depth and strain, ω is the natural frequency of input motion, g is the acceleration of gravity, and m_o is the superstructure mass. Gohl (1991) revealed that fulfilling the second and third scaling laws simultaneously is challenging. The former involves the same model and prototype material densities, and the latter obtains the ratio of the prototype to model pile flexural rigidity which equals λ^5. Imperfect model similitude is only accepted by considering the tests as prototype cases, against which

194

analytical simulations can be validated. He also indicated that the test results can be represented in terms of dimensionless variables to permit contrast with the results from the full-scale test.

(Iai, 1989) developed a scale model for shaking table test to simulate a constitutive behaviour for saturated soils by considering a tangent modulus method and basing on the results published by Rocha (see Figure 5-4). A set of scaling relationships for a soil–structure–fluid interaction system subjected to dynamic loading condition is derived, and the scaled dynamic problem is defined in terms of geometric, density and strain scaling factors. The methodology proscribes the geometric (λ) and density (λ_ρ) scaling factors, and the strain scaling factor (λ_ε) is then derived using shear wave velocity tests for the prototype and model of the soil (see Eq. (5.16)).

$$\lambda_\varepsilon = \frac{\lambda}{\left(\dfrac{(V_S)_p}{(V_S)_m}\right)^2} \tag{5.16}$$
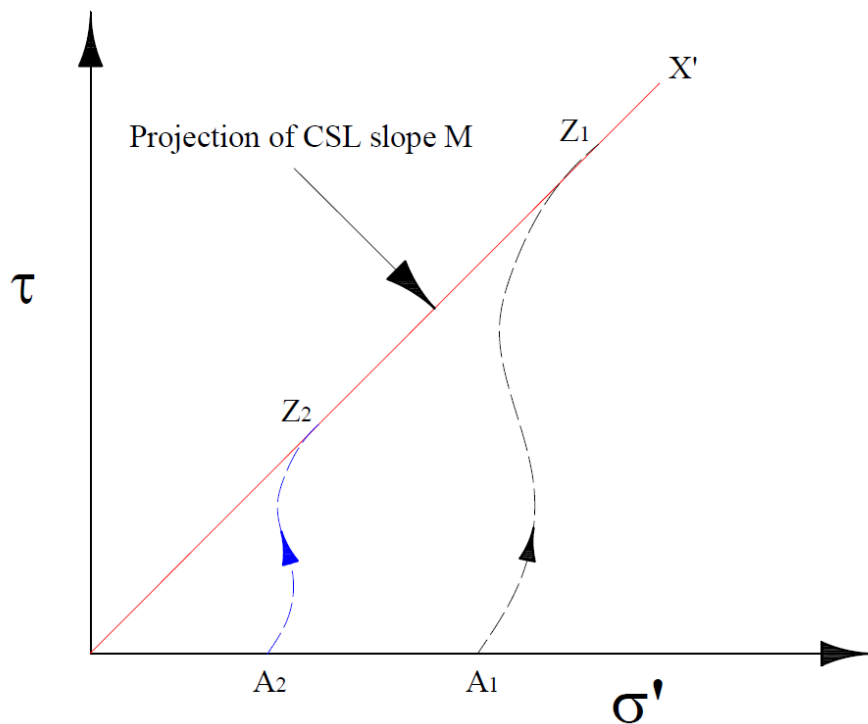
Figure 5-4 Formulation of Tangent Modulus of the Constitutive Behaviour of Scaled Soil, modified from (Iai, 1989)

The non-intuitive consequence in this approach is that quantities for a particular model with the same dimensions may have different scaling factors, such as length and

deflection. Nevertheless, the validation of this technique is supported by laboratory tests. According to Iai (1989) statements, this approach is only applicable for low strain circumstances once the soil particles do not lose contact but contribute application to liquefaction issue involving medium to dense sand soil deposits.

(Scott, 1989) employed the method of governing equations to dynamic equilibrium for developing scaling factor relationships for the soil model to apply centrifuge testing. This derivation was refined and postulated by (Gibson, 1997) to be employed for a granular saturated soil subject to centrifuge modelling programme or one–g environment. The expression for the developed relationships is expressed as Eq. (5.17):

$$\left(1 - \frac{x^*}{\sigma^*} \cdot \frac{x^*}{t^{*2}} \cdot \rho^*\right) \rho_m \left[\frac{\partial^2 u_{im}}{\partial t_m^2} + \frac{\partial u_{jm}}{\partial t_m} \cdot \frac{\partial}{\partial x_{jm}}\left(\frac{\partial u_{im}}{\partial t_m}\right)\right] = \left(1 - \frac{x^*}{\sigma^*} \cdot X^*\right) X_{im} \quad (5.17)$$

where x is the model length, σ is the stress, t is the time, r is the mass density, X is the body force and (*) quantities denote the prototype to model ratio. Gibson (1997) also identified the dynamic behaviour of the scaling soil constitutive problem for one-g testing and proposed modification to the material properties of the model for that purpose. Consequently, under one–g stress conditions, the model demonstrates strain behaviour comparable to that of the prototype. The method proposed by Gibson applies a steady-state line which is presented in Figure 5-5. This method is different from Rocha's and Iai's which are both adopted to modify the soil constitutive relationship rather than the soil material properties.

Gibson (1997) also observed that the scale factors of the dynamic and diffusion time which are associated to pore pressure response and potential liquefaction are incompatible for one–g testing conditions unless finer grain soil and more viscous pore liquid can be used.

This section highlights an important fact that must be clarified regarding the studies of geotechnical researchers. They have included the crucial feature of constitutive similarity to the set of scale modelling demands for the problems of soil response. A system with its full range of nonlinear behaviour must be considered because simplifying a model to a discrete elastic parameter system is inadequate. Constitutive similarity is discussed with regard to the designs of the soil and pile models in Sections 4 and 5, respectively.
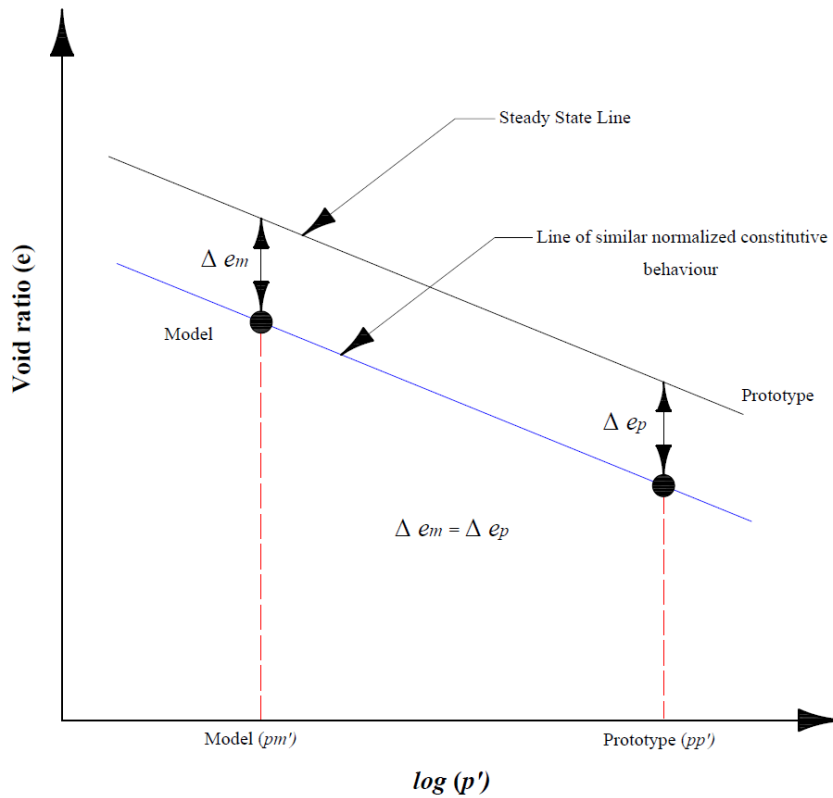
Figure 5-5 Definition of Model Soil Properties Based on Steady-State Line, modified from (Gibson, 1997)

5.2.2. Implied Prototype Scaling Methodology

The interdependent processes of an SSPSI problem and its components constitute an imperative segment of the scale modelling approach in which the variables involved in the process and the modes of the system are defined. The design of the scale model programme must be developed to enable the system to capture the behaviour(s) of principal interest adequately. No governing equation can be devised to describe a full-scale SSPSI system. No similitude theory or dimensional analysis can also be directly utilised to achieve 'true' model similarity of this complicated system.

Consequently, a viable modelling methodology involves pinpointing and modelling the primary forces and processes within the system successfully while suppressing the secondary effects. In doing so, an 'adequate' model can be yielded. This scale modelling design technique is performed as an iterative process (see

Figure 5-6). In this scale modelling approach, the essential modes of the system response are initially identified, and the prototype value is defined for the variables that contribute to these modes. The scaling relationships are derived and employed to determine the parameters of the scale model for the variables of interest. Scale model components are

197

then produced and examined to corroborate their concrete behaviour. Subsequently, scaling relationships are applied to ascertain whether the determined model behaviour indicates a reasonable prototype response.

This technique of implied prototypes offers an appropriate modelling approach for the wide range of potential soil, pile, and superstructure conditions of the prototype. Caution must be taken when interpreting the scale model test results in terms of the prototype. The most precise use of numerical analysis employed to the modelling process is analysing the scale model rather than predicting the behaviour of the implied prototype. The approach used to determine the precision of the scale modelling technique is known as 'modelling of models' [e.g. (Meymand 1998), and (Schellart & Strak, 2016). In this technique, individual and independent tests of the same prototype are executed at various scaling factors, and the modelling technique can be considered sound if the findings consistently meet similarity requirements. Many factors must be identified throughout the entire development of scale modelling process, and these factors may influence the accuracy level of the scale model. (Harris & Sabnis, 1999) addressed these factors by discussing the 'accuracy and reliability of structural models' in detail. In the scale model design phase, the similitude and size consequences may influence the produced model; thus, the careful development of the scale modelling process used for this programme is described above. In the material fabrication phase, imperfections or overstrength may change the performance of the scale model during the test. Therefore, corroboration testing and in-situ testing for the model components must be performed to validate the actual material properties. In the construction phase, the procedures for installation and application of boundary conditions may yield different stress conditions between the model and prototype. Consequently, the laboratory model should minimise the influence of boundary conditions and installation procedure. In the reference case study (Meymand, 1998), the design of the flexible container attempted to mitigate the effect of boundary conditions, and the model pile installation technique was designed to emulate that of the prototype. Another source of inconsistency between model and prototype is the loading phase in this test program. Nevertheless, the minor deviation between the command signal and actual input are acceptable once the actual input signal is identified and recorded. Instrumentation defects and reading errors may arise while arranging the sensors, sensing and/or recording data. Uncertainty evolving from the analysis of the output data is

primarily due to human error. Application of model test data to prototype also must use scale model similitude.
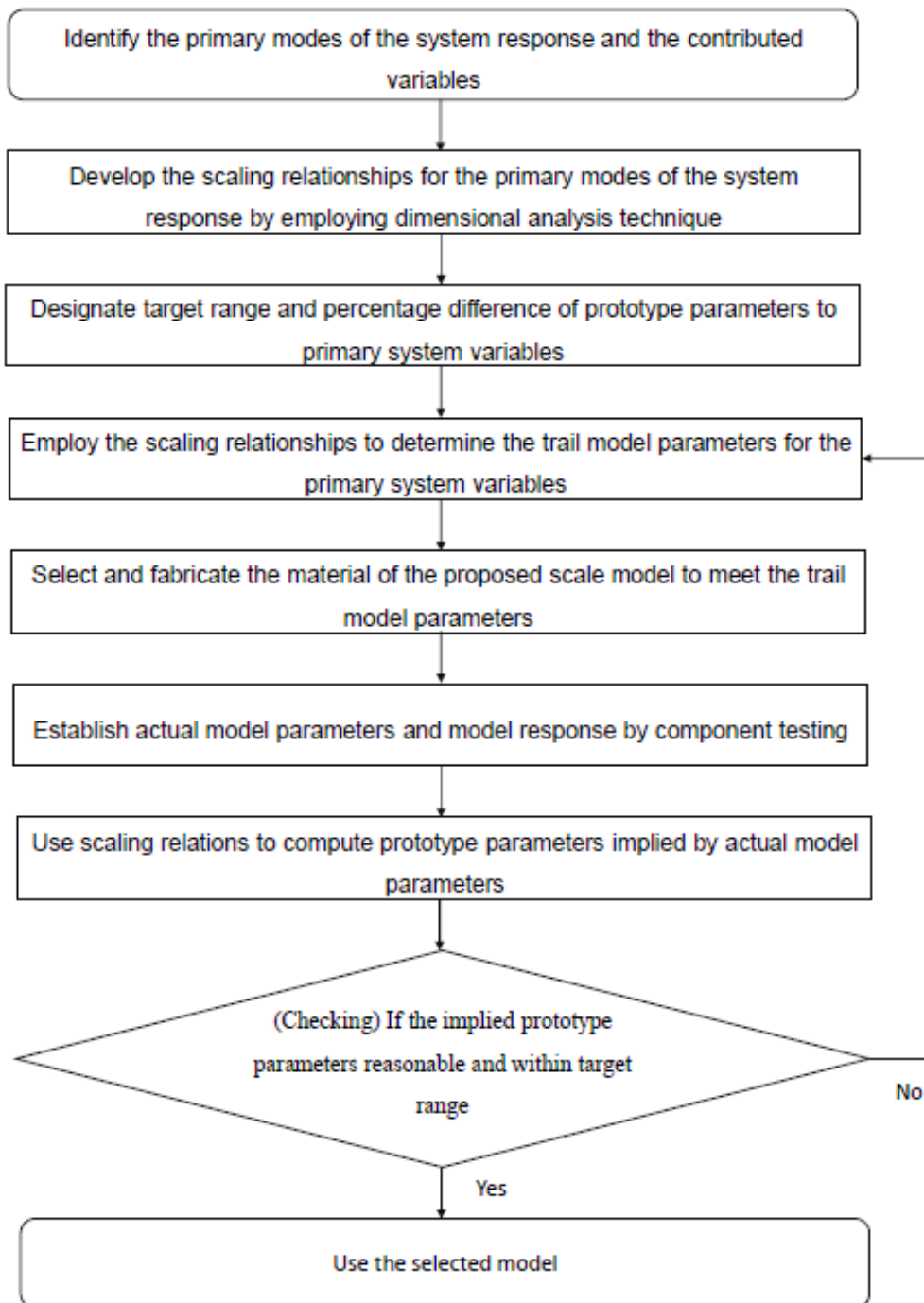
Figure 5-6 Flowchart of Implied Prototype Scaling Methodology

As previously mentioned, the appropriate application of scale models is to achieve insight into prototype behaviour not to develop accurate prototype performance. The sources of errors occurring from instrumentation compromise the inherent accuracy of sensor and sensor arrangement. High efficiency of the instrumentation is necessary to diminish this

error. In the reference case study, the IC sensor accelerometers were rated with a flat response ranging between 0 and over 300 Hz which was beyond the frequency range of interest. The maximum nonlinearity was less than 0.2%, and the accelerometers were positioned in soil deposit using manual surveying methods. If they were not wholly orthogonal to the shaking axis, then they might cause a noticeable reduction in output signal. Moreover, individual accelerometer arrays could have undergone small permanent movements during testing. Even a $10°$ off-axis shift would cause a reduction in the output signal of <1.5%. According to the test environment, the installed strain gauge was with a transverse sensitivity of 1.2±0.2%. Inaccurate gauge mounting or driving the piles in a not perfectly perpendicular line to the axis of shaking may result in negligible signal distortions. The wire potentiometers were rated with linearity within 0.1%.

5.3. Scale Modelling Factors for SSI Problem

In Figure 1-3 of Chapter 1, the significantly related interaction modes of a seismic soil–pile–structure interaction system response can be identified as the free-field soil site response mode, soil–pile lateral kinematic interaction mode, soil–pile lateral inertial interaction mode, soil–pile axial response mode, and pile and pile cap radiation damping mode. Table 5.1 catalogues the variables connected with each interaction mode. The purpose of the scale modelling technique for such a test is to accomplish what has been formerly characterised as dynamic similarity once the scale model and prototype experience analogous forces. Dimensional analysis is the basis for scale model similarity in this program. Three main test circumstances create many of the scaling parameters. Firstly, the examination should be performed in a one–g environment which characterises equal accelerations of the model and prototype. Secondly, model soil and prototype soil must be of similar density. This condition fixes another component of the scaling relations. Thirdly, the test medium must predominantly comprise saturated clay whose undrained stress–strain response confines pressure dependence and, thus, simplifies the constitutive scaling requirements.

Table 5.1 Identification of SSPSI Primary System Modes and Associated Variables

No.	SSPSI Interaction Mode	Variables
I.	Free-field Site Response	$[V_s(Z), \rho(Z),$ modulus of degradation and damping $(Z)]_{soil}$
II.	Soil–Pile Lateral Kinematic Interaction	I, $[EI, \text{length, diameter, fixity}]_{pile},$ $[(\text{stress–strain behaviour}), S_u(Z)]_{soil}$

III.	Soil–Pile Lateral Inertial Interaction	II, $(M, K)_{superstructure}$
IV.	Soil–Pile Axial Response	I, $[E, \text{length, diameter}]_{pile}$, [(stress–strain behaviour), $S_u(Z)]_{soil}$, $(M, K)_{superstructure}$
V.	Radiation Damping	I, (length, diameter, $M, E)_{pile}$

By defining the scaling conditions for the density and acceleration, the mass, length and time scaling factors can all be signified in terms of the geometric scaling factor λ. A correct set of dimensionally accurate scaling relationships (ratio of prototype: model) for studied variables can be derived. The scaling relationships for all the potential variables contributing to the primary modes of system response are obtained according to the technique above and are listed in Table 5.2. Geometric scaling factor λ that equals to 8 is selected as a benchmark for the dimensional scaling procedure (Iai, 1989). A comprehensive set of scaling relationships for a soil-structure interaction system subjected to dynamic loading condition is derived. The scaled dynamic problem is entirely defined in terms of geometric scaling factor λ. The corresponding scaling relationships for the variables which contribute to the primary system response modes are density, acceleration, length, force, shear wave velocity, stress stiffness, time, strain, modulus, frequency and flexural rigidity. Accordingly, with the scaling factor of the shear wave velocity equals to $\lambda^{\frac{1}{2}}$, the scale model meets the Cauchy condition. The calculated Iai's strain scaling factor equals to 1. Consequently, Iai's set of scaling relationships is in absolute agreement with the values developed for the circumstance in the current study. Table 5.2 is created on the basis of this circumstance.

Table 5.2 Scaling Relationships for Primary System Variables Expressed in Terms of Geometric Scaling Factor λ

Variable	symbol	Factor
Mass density of saturated soil and structure	ρ	
Acceleration of soil and or structure	$acce.$	
Strain of soil and structure	ε	
Strain of the soil due to creep, temperature, etc.	ε_o	
Porosity of soil	n	1
Inclination of the beam	θ_{inc}	
Density of pore water and/or external water	ρ_f	
Inclination angle	θ_{inc}	
Hydraulic gradient of external water	i	
Length	l	λ

Total stress of soil and structure	σ	
Effective stress of soil	σ'	
Tangent modulus of soil	D_T	
Bulk modulus of the solid grains of soil	K_s	
Pressure of pore water and/or external water	P	
Displacement of soil and/or structure	U	
Bulk modulus of pore water and/or external water	K_f	
Young's modulus of the soil and structure	E	
Shear modulus of the soil and structure	G	
Displacement of the soil and/or the structure	U	
Pressure of pore water and/or external water	P	
Average displacement of pore water relative to the soil skeleton	W	
Static soil shear strength	$S_{u_{static}}$	
Dynamic soil shear strength	$S_{u_{dynamic}}$	$\lambda/0.75$
Time	T_t	
Permeability of soil	k	
Velocity of soil and/or structure	V	$\lambda^{\frac{1}{2}}$
Rate of pore water flow	W_f	
Shear wave velocity	V_s	
Stiffness	k	
Mass per unit length	ρ_b	λ^2
Shear force	S_{shear}	λ^3
Axial force	F_A	
Force	F	
Mass	μ	
Longitudinal rigidity	EA	
Bending moment	M	λ^4
Flexural rigidity	EI	λ^5
Frequency	ω	$\lambda^{-\frac{1}{2}}$

The implementation of the scaling relationships and creation of the components of the model soil, pile, and superstructure system are addressed in the subsequent sections. Before doing so, the following problem conditions which may propagate into the process of scale modelling must be understood. They must be considered in the design of the model components and/or testing procedures.

- Initial condition refers to the initial stress states of interacting elements of soil and pile.

- Boundary conditions include the model boundary conditions, interface conditions between soil and pile and soil and pile cap, pile and superstructure connection conditions and the connection condition among the superstructure components
- Constitutive behaviour is the soil scale modelling criterion.
- Ductility must be considered for pile and superstructure.
- Material damping relates to soil, pile, cap, and superstructure.
- Strain rate effects pertain to soil and pile, and superstructure.
- Long term effects include consolidation or creep for the soil.
- Group effects reflect the configuration of piles in groups.

5.4. Design of Soil Model

The properties of the soil model should be reflected in the primary modes of the problem behaviour and based mainly on the type of the analysed problem. The primary modes should be first identified and then subdivided into their general categories of system behaviour to pinpoint the system parameters which are characterised as soil properties. The dimensional scaling factor is then selected for each parameter according to Table 5.2. These steps are key towards achieving a 'true' scale model. Following the reference case study, the five primary modes of SSPSI illustrated in Table 5.1 can be subdivided into two general categories of free-field response and soil–pile interaction. Free-field site response is defined as a function of the small strain of soil material properties, whereas soil–pile interaction is a function of the large strain of soil material properties. The parameters which define these soil properties are shear wave velocity, soil density, modulus degradation and damping, stress–strain behaviour and undrained shear strength. These parameters are independent and nonlinear and can be described as a function of the loading rate, number of cycles and strain reversals. Therefore, the technique of implied prototypes is appropriate to model the complex modelling issue in the current study.

5.4.1. Soil Modelling Criteria

As the density of the soil model is considered equal to the density of the prototype soil according to the analysis conditions given earlier, one scaling condition is revealed. Several parameters, such as nonlinear stress–strain and modulus degradation and damping curves, are not explicitly modelled from a prototype case. Instead, the technique of implied prototypes is employed to determine whether the properties of the scale model for these parameters are reasonable. The undrained shear strength and shear module or shear wave velocity are the key parameters of the scale soil modelling. If the elastic

response is desired for the free-field soil and the soil–pile system, then the soil shear modulus should be modelled appropriately. The undrained shear strength should be modelled appropriately when the inelastic response of the soil–pile system is desired. If the full nonlinear response of the dynamic system is desired, then both criteria should be considered simultaneously as in the current study. These parameters have distinct scaling factors according to the scaling results of the derivative in Table 5.2. The static and dynamic soil behaviours are affected greatly by the plasticity index (*PI*), which is an additional soil modelling parameter that is not reflected in Table 5.1. Therefore, the use of soil model with an analogous *PI* to the prototype is essential. As *PI* is a dimensionless parameter, the 1:1 scale model to prototype can be employed.

5.4.2. Prototype Soil Parameters

The current study follows (Meymand, 1998) and uses shaking table test for validation and application. All material properties and modelling specifications are in accordance with those in the reference case study. The full description of the soil material properties is in Chapter 4. The target prototype soil designated for the current study is the soil adopted in the reference case study which is San Francisco Bay mud, a marine clay with index properties varying in values. This soil is suitable to the implied prototype technique. This soil is also a well-characterised soil according to (Bonaparte & Mitchell, 1979), who performed experiments on bay mud samples from Hamilton Air Force Base in Novato, California. Their results are shown in Table 5.3, which correspondingly reflects the prototype parameters adopted for the current study.

Table 5.3 Selected Properties of San Francisco Bay Mud, (Meymand 1998)

Property	Symbol	Unit	Value
Saturated Unit Weight	ρ	kg/m^3	1 505.74
Natural Water Content	w_c	%	90
Liquid Limit	LL	%	88
Plastic Limit	PL	%	48
Plasticity Index	PI	%	40
Undrained Strength Ratio	S_u/p'	Ratio	0.32
Coefficient of Consolidation	C_v	$m^2/year$	$0.743 - 0.930$

(Dickenson, 1994) investigated the seismic response of bay mud during the 1989 Loma Prieta earthquake and developed an empirical relation expressing the undrained shear strength of the soil as a function of soil shear wave velocity (see Eq. (5.18)). This

relationship is illustrated in Figure 5-7 and is employed to determine the targeted shear wave velocities for the prototype soil.
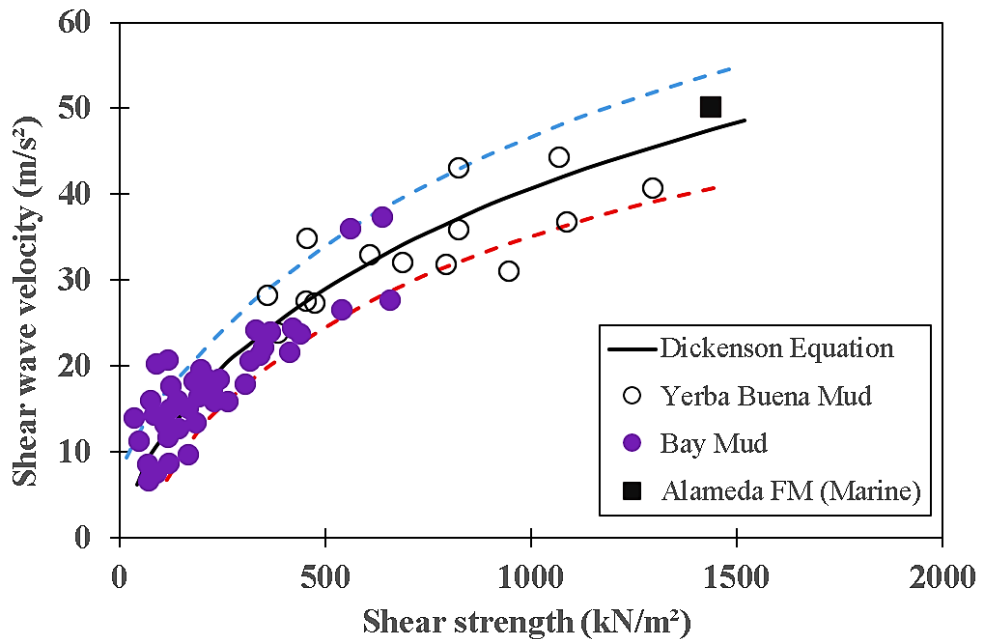
Figure 5-7 Shear Wave Velocity vs. (Static) Undrained Shear Strength of Cohesive Soils, (Dickenson, 1994)

Appropriate shear wave velocities value between 114.3 m/sec and 160 m/sec are computed for the prototype soil's undrained shear strengths values between 28.73 kN/m^2 and 57.46 kN/m^2.

$$V_s = 18 \, (S_u)^{0.475} \tag{5.18}$$

V_s denotes the shear wave velocity in feet per second, and S_u denotes undrained shear strength in pounds per square foot. The conversion to any system of desired units can be done for the resultant value. All soil prototypes, model properties and model soil design characteristics are detailed in Chapter 4.

5.5. Design of Pile Model

The pile model is subjected to different scale modelling criteria. A successful pile model design is achieved by addressing the primary governing factors of pile response, and the same procedure for soil model must be applied. The primary modes should be first identified and then subdivided into their general categories of system behaviour to pinpoint the system parameters which are characterised as soil properties. The dimensional scaling factor is then selected for each parameter according to Table 5.2. In the case of SSPSI of the reference case study, the four principal modes of pile response

according to Table 5.1 are soil–pile lateral kinematic interaction, soil–pile lateral inertial interaction, soil–pile axial response and pile radiation damping.

5.5.1. Pile Modelling Criteria

Several pile properties contribute to the principal pile response modes, such as the slenderness ratio L/d, where L and d are the pile length and diameter, respectively; flexural rigidity EI, where E and I are the pile modulus of elasticity and moment of inertia, respectively; yield behaviour; ductility; moment–curvature relationship, buckling properties P_{cr}; d/t; pile natural frequency and relative ground/pile rigidity. According to the scaling methodology described in Section 5.3, geometric similarity relationship must be applied as a strict modelling constraint. Complete pile slenderness and relative contact surface area are thus preserved in the model properties, ensuring that the pile group's relative spacing and consequent group interaction are replicated into the scale model. The pile moment–curvature relationship is designated as a principal modelling criterion because it comprises the two significant parameters—flexural rigidity and yield behaviour—which enables describing the fully nonlinear response of pile under lateral loading conditions. In this respect, appropriate 'state-of-the-art of the seismic design of pile foundations should be considered. The prevalent scenario is to generally design piles to respond in their elastic range without yielding, concentrating on the ductile behaviour in the columns of the superstructure, (Raoul *et al.*, 2012). The philosophy is that damage to the aerial parts of the structures is easier to detect and repair than damage to subsurface parts. With this approach, the working range of lateral dynamic response of the pile can be correctly modelled by scaling the flexural rigidity EI of the pile and certifying that the yield point is equal to or greater than that of the prototype yield point. By appropriately scaling the resistance properties of the soil, soil–pile kinematic and inertial interaction can be correctly replicated in the model. The nonlinear cyclic response of the pile is therefore captured by the soil behaviour. The soil–pile interaction of the axial response for the end-bearing piles is mainly a function of soil properties in the bearing layers. The soil–pile interface of the friction/cohesion along the pile shaft and the elastic deformation of the pile represent a secondary factor for the axial response of the end-bearing pile, mainly in the circumstance of soft soil deposit. Although the axial loading is dynamic in nature, the pile static axial capacity is a key factor as it defines the inertial load carries by the pile. Pile radiation damping have two behaviour components: (i) the inherent dynamic characteristics of the pile, which is the ability of the pile to generate energy to be radiated

into the surrounding soil, and (ii) this energy propagated away from the pile hinges on the relative soil–pile stiffness. By consistently scaling the soil and pile elastic properties, the relative soil–pile stiffness parameter is automatically scaled from the prototype to the model. However, the inherent pile dynamic characteristics represent a complicated modelling criterion to achieve. The natural frequency ω of an end-bearing pile can be optimised using the equation describing the natural frequency of a cantilever rod as a function of the rod's mass m (see Eq. (5.19)) (Clough and Penzien, 1996).

$$\omega = 3.516 \sqrt{\frac{EI}{mL^4}} \tag{5.19}$$

With pile geometry and EI scaled as discussed above, the scaling factor of the mass per unit length of the model pile is λ^2 (refer to Table 5.2). This scaling criterion should be subjected to an examination to assess that the condition of application can cover the conventional materials and other modelling constraints which are essential to produce a correct scale model. Recognising that radiation damping is most pronounced at lower levels of shaking, it can have a diminishing influence on the intense shaking levels once applied in this test program. Furthermore, the pile is only a component of the soil–pile-superstructure system, and slightly altering the vibration characteristics of the other elements of the system is not expected to affect the vibration characteristics of the entire system significantly.

5.5.2. Prototype Pile Parameters

According to the Highway Design Manual (Caltrans standard,2010), a 410 mm diameter $\times$ 12.7 mm wall dimension steel pipe filled with concrete is designated as a target prototype pile. Scaling restrictions impose a maximum prototype pile length of 12.8 m with a ratio of L/d of 33, which is acceptable for a slender pile, where L and D is the pile length and diameter, respectively. The stability conditions of the pile, perceived to be crucial in lateral response conditions, are as follows. The pile must be set up as fixed against the rotation displacement at the top and fixed against the relative displacement at the base. The flexural rigidity EI of a composite steel filled with concrete pile is nonlinear due to concrete cracking. Therefore, the concrete contribution to the composite EI is reduced by 50% to yield a composite EI of 8710376.7 $kN - m^2$. The first mode period of vibration of a cantilever rod with the prototype pile properties is 0.74 s. The flexural rigidity of the pile is 75.179 $kN - m^2$.

5.5.3. Model Pile Development

An iterative process must be employed to accomplish the primary pile design criteria of flexural rigidity EI and natural period using an appropriate laboratory test and numerical model for validation. According to the reference case study pile boundary condition, an equivalent cantilever rod can be used to identify the targeted principal pile parameters. A geometric scaling factor of 8 is used to develop the scaling requirements for the soil and pile models. In accordance with the target model EI and scaled pile outer diameter, the moment of inertia can be computed according to two pile cases of type conditions (solid and thin wall tube), and then the corresponding lower and upper bound elastic modulus can be determined, respectively. The pile density can be computed at these two bounding values which impart the scaled modes of vibration. The computed density values may range within two different values for solid and thin wall sections, and such materials with these values may be impractical. Thus, this condition must be modified as described previously in Section 5.3.1. In addition, material type must be investigated to determine appropriateness as a model pile material. In the reference case study, for the target EI equals to 2.30 $kN - m^2$ and pile outer diameter fixed at $50.8 \, x \, 10^{-3} \, m$, the lower and upper bound elastic moduli corresponding to solid and thin wall tubes cases are 6894.76 and 68947.6 MPa, respectively. The corresponding pile material density at these lower and upper bound elastic moduli is computed and ranges between 295.30 kg/m^2 and 573.4 kg/m^2 for the solid and thin wall sections, respectively. After material investigations, aluminium 6061 T-6 alloy (see Table 5.4) is the only nominee within an acceptable range of modulus, and the pile is designed as a thin wall section to satisfy the EI criterion. Accordingly, the scale model pile is fabricated according to the scaling limitation employing 6061 T-6 aluminium tube which provides an appropriate scaled flexural rigidity EI of and L/d ratio of 36. A pile wall thickness of $0.67 \, x10^{-3} \, m$ was computed in the reference case, indicating that the scale model pile has appropriate flexural rigidity. The thickness of $0.711 \, x10^{-3} \, m$ is selected according to the commercial availability of aluminium tube cross-section. This pile dimension produces an EI equal to 2.42034 $kN - m^2$ with 5% deviation from the EI target value. Although thin wall tube may experience a possible local buckling mechanism which is not evident in the solid cross section prototype, it was selected in the reference case as this geometry is proven advantageous for external attachment of foil strain gauges and internal routing of the lead wires of the gauges. To make the final decision concerning the selection of the pile cross-

section and material, other pile performance aspects must be examined with respect to axial performance, pile driving stresses static loads and dynamic stresses. In the reference case, the aluminium tube buckling load P_{cr} was satisfied within the allowable range. The theoretical moment–curvature ratio of the trial pile model must be compared to that of the prototype to ensure the elastic response of the selected tube.

The moment–curvature relationship defines the nonlinear response of the pile model to applied loading and is comparable to a soil stress–strain curve. The lower and upper bound prototype circumstances are determined by employing yield stresses in the steel pipe pile of 345 MPa and 483 MPa, respectively, with 0% and 100% concrete EI contributions which signifying intact and fully cracked concrete sections.

Table 5.4 Mechanical Properties of Nominated Model Pile Materials, (Meymand, 1998)

Material	Elastic Modulus (MPa)	Yield stress (MPa)
Steel	200000	415.0
Copper	118000	206.0
Aluminium 6061 T-6	68950	276
Nylon	2895.0	117.0
PVC	2895.0	100.0
Polyamide	2827.0	83.0
Polyacetal	2827.0	69.0-97.0
Acrylic	2689.0-3310.0	83.0 -117.0
Polycarbonate	2068.0-2413.0	93.0
ABS	1724.0	28.0-97.0
Polypropylene	1172.0-1724.0	48.2629
PVDF	2158.0	67.0
Ryton	1103.0	20.0
CPE	1034.0	41.0
Vinyl ester resin fiberglass	965.0	107.0
Epoxy fiberglass	931.0	69.0
High density polyethylene	414.0-1241.0	48.0
Teflon TFE 58	400.0	14.0 -35.0
Teflon FEP	345.0	18.0 -21.0
Polybutylene	241.0	29.0

Low density polyethylene	97.0 -262.0	16.0

These lower and upper bound moment–curvature relationships demonstrated at a prototype scale are defined according to the pile analysis code COM624P (Wang & Reese, 1993). The results are calibrated against a four-point loading test finding performed by Caltrans on $0.61\ m$ concrete-filled steel pipe pile (Brittsan, 1995). The moment–curvature relationship of the pile model can be identified using several modern approaches, and SE:MC is one of the computer programs offering this sort of analysis. SE:MC is a powerful tool for structural design and research where moment–curvature analysis is needed and based on strain compatibility technique. A numerical FEA approach offers an advanced method of validation, which is applied in the current study using Abaqus software to simulate the four-point loading test. Following the time for performing the reference case study, the method of (Langhaar, 1951) is adopted to determine the moment–curvature relationship of the pile in which the equation defining the bending of a ductile beam of circular cross-section is expressed as in Eq. (5.20).

$$M = 2\ r^3 \int_0^1 \beta\ \sigma\ \xi\ d\xi \qquad\qquad (5.20)$$

Where r is the radius, β represent the width of the cross-section at the ordinate divided by r, ξ represent the ordinate from the neutral axis divided by r, and σ represent the stress at the ordinate of the cross-section. The elastic-perfectly plastic stress–strain relationship is presumed by using this derivation. The moment–curvature relationship for the trial aluminium model is superimposed in Figure 5-8 at prototype scale and can be observed to exceed the yield behaviour in the target prototype range. As previously explained, this is an acceptable result as the pile is expected to respond in the elastic spectrum. An 'optimal' model pile material that accurately incorporate the scaled moment–curvature relationship is developed to have a wall thickness of $5.08\ x\ 10^3\ m$, an elastic module of $20685\ MPa$, and a yield stress of $13.8\ MPa$. To capture an ideal model behaviour, such a material must be manufactured due to its unavailability in the market. A four-point loading test was executed physically in the reference case study (see Figure 5-9) and this was replicated numerically in the current study using Abaqus FEA model and COM624P program with a $1.8288\ m$ long and $50.8\ x\ 10^{-3}\ m$ diameter section aluminium tube with a wall thickness of $711 x 10^{-6}\ m$ to corroborate the model pile moment–curvature relationship. The supported beam condition is subjected to equal loads applied at two

points. Foil strain gauges positioned on the tube's compression and tension sides were read at each increment of loading, and moment and curvature were determined from the strain data. This aspect was considered when the results were red in the numerical models. Figure 5-10 shows the experimental moment–curvature relationship for the scale model pile, superimposed on the numerical FEA and theoretical curves, both at model scale. The agreement in the elastic response range is superb, and the test pile fails with a buckling mechanism very close to the FEA and theoretical yield point. The failure load is 725 N which imposes a 386 N − m bending moment. These tests reveal that the aluminium tube is an appropriate model pile for the testing programme of the scale model.

Chapter 4 describes the development of the shaking table test programme for SSPSI analysis with the identified scale model similitude relationships and developed soil and pile models. Table 5.5 lists the input parameters of the prototype pile and soil.

Table 5.6 provides the computed properties and targeted values of the prototype pile and soil. Table 5.7 presents the soil and pile models' input parameters, computed properties and the percentage of result deviation from target values.
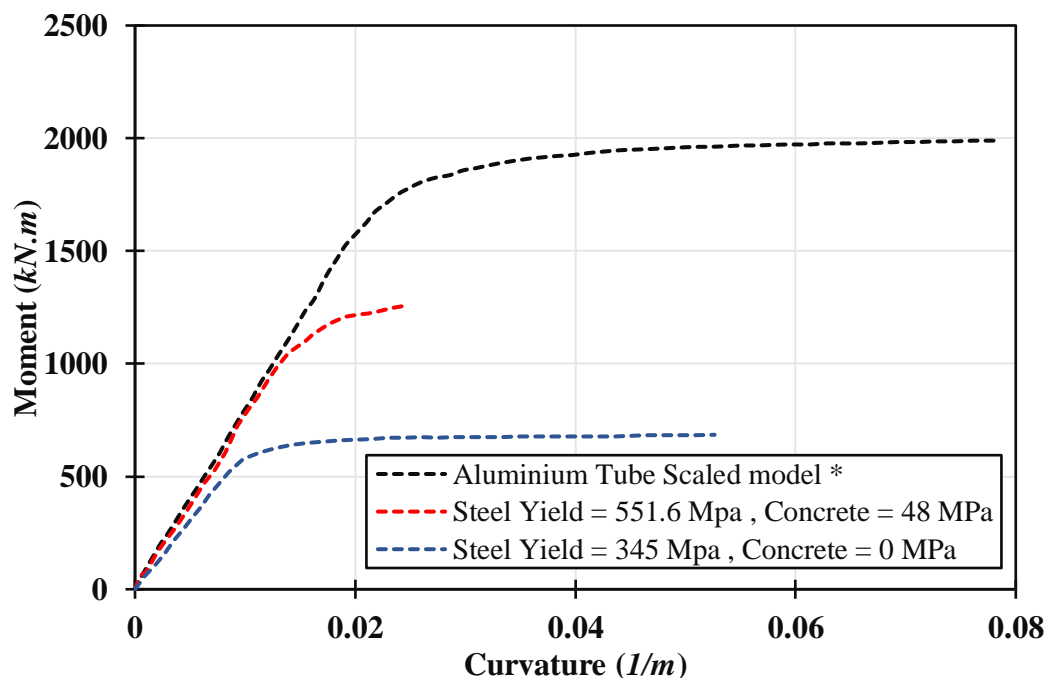
Figure 5-8 Theoretical Lower and Upper Bound Moment–Curvature Relationships for Prototype Pile as Determined by COM624P, (* Aluminium Tube Dimensions, (0.0508 (m) dia. x 0.00071 (m) wall thick.), (Meymand, 1998)

211
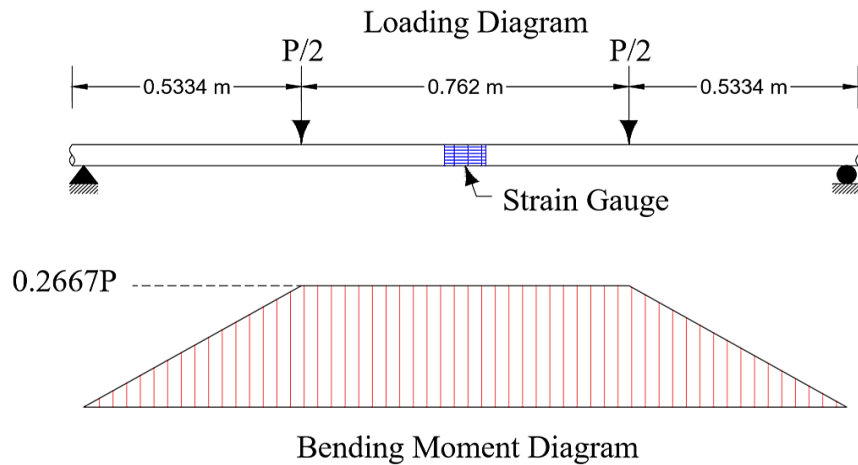
Figure 5-9 Four-Point Loading Test of Model Pile and Bending Moment Diagram, (Meymand, 1998)
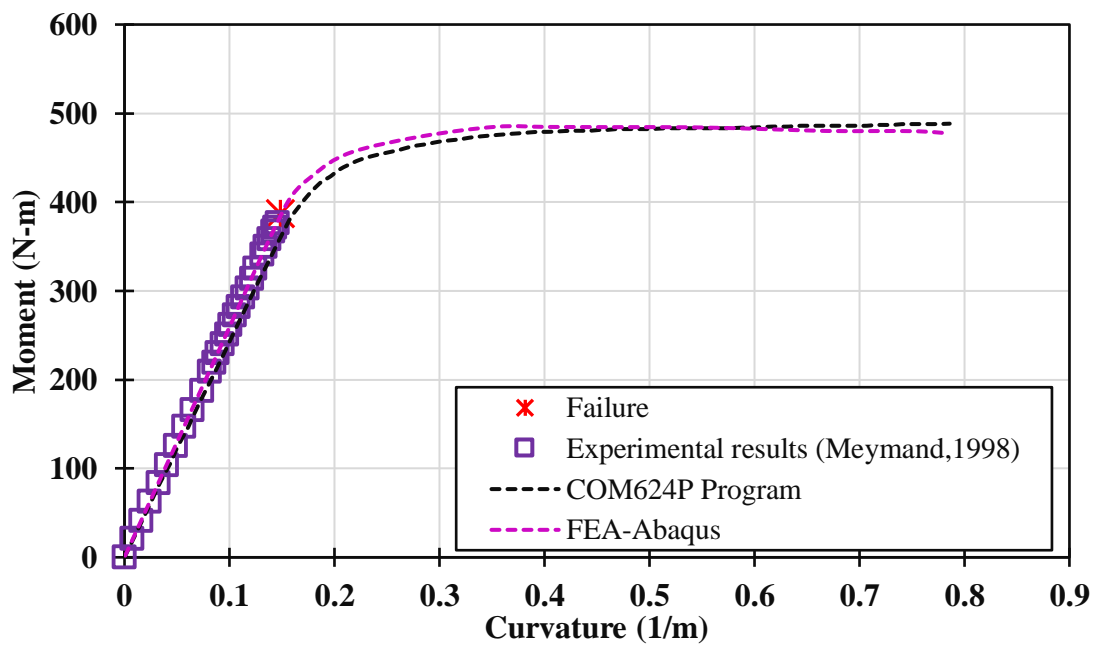
Figure 5-10 Theoretical and Experimental Moment–Curvature Relationships for Dimensions of Aluminium Tube Model Pile (0.0508 (m) dia. x 0.00071 (m) wall thick.)

Table 5.5 Input Parameters of Prototype Pile and Soil

Prototype Input Parameters	Symbol	Value	units
Pile outer diameter	OD	0.4064	m
Pile wall thickness	$t_{wall.p}$	12.7×10^{-3}	m
Pile length	L	13.4112	m
Pile density	ρ	7700	kg/m^2
Soil shear strength	S_u	25.0	kN/m^2

Shear wave velocity	V_s	111.25	m/sec	
Steel Young's modulus	E_{steel}	200	GPa	
Concrete Young's modulus	$E_{concrete}$	28	GPa	
Soil Young's modulus	E_{soil}	28.728	MPa	
Soil shear modulus	G_s	163.8	MPa	
Percentage of concrete EI contribution	EI	50	%	

Table 5.6 Computed Properties of Prototype Pile and Soil

Model Input Parameters				
Pile outer diameter	OD_m	$50.8 \, x10^{-3}$	m	Target
Pile wall thickness	$t_{wall.p}$	$15.875 \, x \, 10^{-4}$	m	Target
Pile length	L	1.6764	m	Target
Pile L/D Ratio	L/D	33	-	Target
Pile d/t Ratio	d/t	32	-	Target
E_{pile}/G_{soil}	k	1392		Target
$EI_{pile}/E_{soil} \, . D^4$	k_r	96		Target
Soil shear strength	S_u	4.167	kN/m^2	Target
Area of steel:	A_{steel}	0.01571	m^2	Scale
Steel moment of inertia	I_{steel}	$304.7 \, x \, 10^{-6}$	m^4	Scale
Steel flexural rigidity EI	EI_{steel}	60915.6	$kN - m^2$	Scale
Area concrete	$A_{concrete}$	0.114	m^2	Scale
Concrete flexural rigidity EI	$EI_{concrete}$	14263.4	$kN - m^2$	Scale
Composite concrete/steel flexural rigidity	$EI_{composit}$	75179	$kN - m^2$	Scale
Composite concrete/steel flexural rigidity	$EI_{composit}$	2.294	$kN - m^2$	Target
Total Mass/m length	Ratio	397.24	kg/m	Target
Prototype first mode period	T	0.7386	sec	Target

Table 5.7 Soil and Pile Models' Input Parameters, Computed Properties and Percentage of Result Deviation from Target Values

Model Parameters	Symbol	Value	units	% difference
Pile outer diameter	OD_m	$50.8 \, x10^{-3}$	m	Scaled

Pile wall thickness	$t_{wall.m}$	711×10^{-6}	m	76
Pile length	L	1.8288	m	Scaled
Pile Young's modulus	E_{pile}	68.95	GPa	Scaled
Pile density	$\rho_{pile.m}$	2700	kg/m^3	Scaled
Soil shear strength (with 0.75 dynamic correction)	S_u	4.07	kN/m^2	2.4
Shear wave velocity	V_s	40.0	m/sec	Scaled
Pile cross sectional area	$A_{pile.model}$	0.115×10^{-5}	m^2	Scaled
Pile mass/m length	Ratio	0.07173	kg/m	Scaled
Pile moment of inertia	$I_{pile.model}$	$3.5105\ e-8$	m^4	Scaled
Pile flexural rigidity	$EI_{pile.model}$	2.420	$kN-m$	5.0
Pile L/D ratio	L/D_{model}	36.0	Dimensionless	8.7
Pile d/t ratio	d/t_{model}	71.4	Dimensionless	76
E_{pile}/G_{soil}	k_{model}	3840	Dimensionless	93
$EI_{pile}/E_{soil}.D^4$	$k_{r.model}$	101	Dimensionless	5.0

The difference values are computed according to the following equation:

$$\% \ difference = 100\% \ \frac{|A-B|}{\frac{(A+B)}{2}} \qquad (5.21)$$

5.6. Methodology of Validation

In the conditions of dynamic loading, full-scale physical tests are complicated and maybe even impossible in some circumstances, such as seismic loading, where no fixed reference point is available to be taken as a benchmark. All the loading areas in an environment are moving during a seismic event. Therefore, most investigations performed after earthquake events are generally intended to analyse the consequences of the earthquake rather than the behaviour of the system or system component during seismic loading, (see chapter 2). Performing an accurate large-scale laboratory test is also complicated and costly and may be impossible depending on the desired degree of complexity and accuracy. All these reasons present researchers with difficulties on how to validate their studies in the seismic area. Resorting to a scaled testing technique, using shaking table or centrifuge tests in the one–g environment is a viable, and often the only, option . Calibration of results remains a serious problem though. As part of this research, it was necessary to develop an accurate, practical and scientific calibration method for

establishing the relationship between full-scale numerical analysis and scaled laboratory tests in the one–g environment. This linkage is applied to one of the two tests to calibrate and validate the other.

This sophisticated and novel validation approach is schematically shown in Figure 5-11. The concept of this approach is based on performing two parallel analyses, i.e. the scaled physical model and full-scale numerical model.
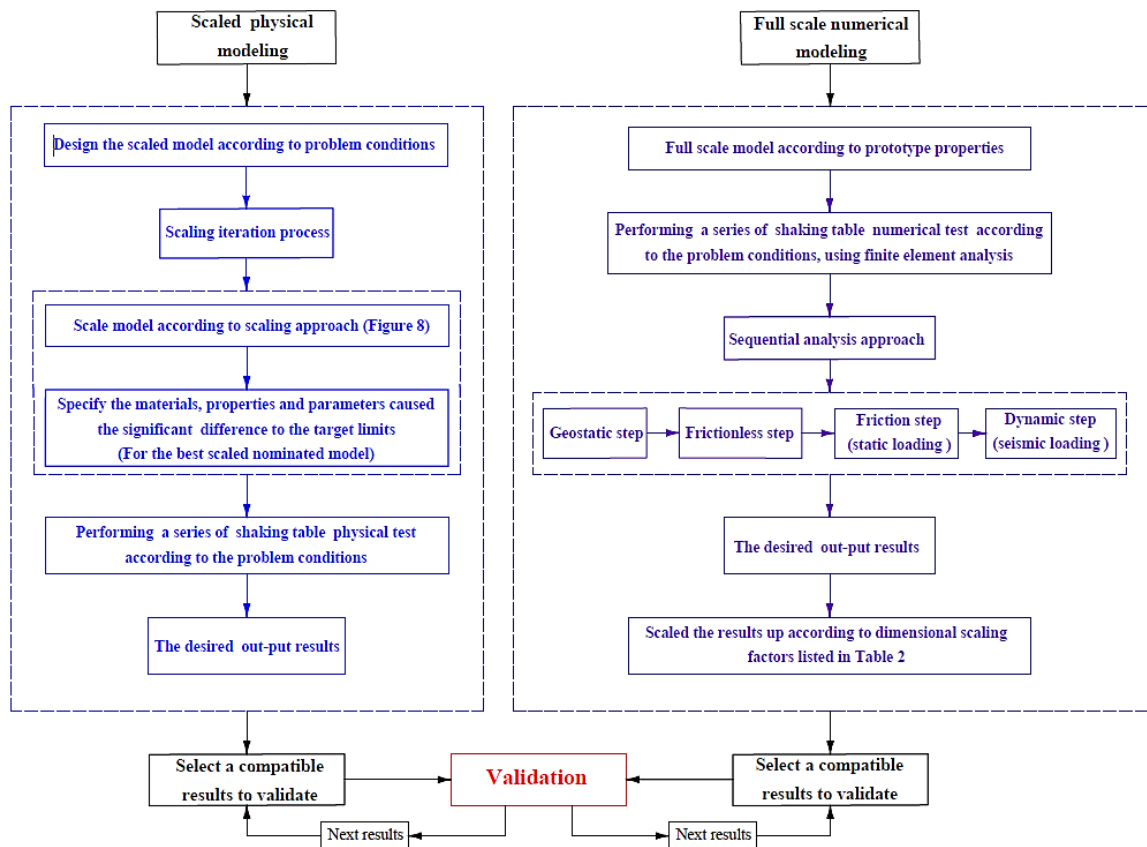
Figure 5-11 Flowchart Describing the Validation Methodology

The first step in this process is to scale the prototype parameter down using the scaling procedure in Section 3. Prior to achieving the scale model, the physical test should be performed according to the problem condition. The shaking table test conducted by (Meymand, 1998) and its results are adopted in the current study as the simulated laboratory test output. After identifying the problem characteristics of the full-scale problem as a prototype which corresponds to the scale model, the full-scale numerical models using FEA approach should be developed in an analysis condition which is comparable to that of the physical test. The reference case study (Meymand, 1998) is adopted (see Chapter 4 for details). Once the full-scale numerical simulation is completed, the desired results of that analysis can be scaled according to corresponding parameter scaling factors listed in Table 5.2. This step is necessary to identify all parameters

involved in the final validation step. Finally, the reference physical shaking table experiment results should be validated against the results captured from the earlier stage of this procedure. A 3D FEA test is carried out using the sequential analysis method for considering the effects of SSI during static and dynamic loading conditions. The sequential analysis method is the most appropriate approach for considering the consequences of the geostatic, static and seismic loads of seismic SSI analysis.

5.6.1. Numerical modelling characteristics

As it has explained in chapter 4, three main steps have been used i.e. geostatic, static and dynamic step. The geostatic step is used as the first step in which , only the soil body force is employed. Consequently, the considerable force and the initial stresses should be precisely equilibrated and established for minimal soil displacement.

Abaqus/Standard offers two methods for developing the initial equilibrium. The first procedure is appropriate to these issues in which the initial stress state is identified approximately. The second improved method is applicable in circumstances wherein the initial stresses are unidentified but only for a limited number of elements and materials. In this respect, the second procedure is followed in this study, in which the pore water pressures vary linearly with depth, and the initial effective stresses are appropriately stated according to the total stresses.

The second step (static step) comprises two sub steps of analysis. Firstly, to create the stability between the two interaction parts, namely, the soil and pile, and prevent negative shear stress between them, the static-frictionless step must be employed. This step represents the piles' installation stage during model construction. Secondly, the static-friction loading step must be applied, which comprise the application of gravity loads, which are assumed static and uniform, and uniformly dead load and live load according to the loading condition of the reference case study. Four pile head masses as a superstructure is used in the current study (see Chapter 4). The third step is the dynamic analysis step. The time history input data from the Loma Prieta earthquake, as mentioned and described in Chapter 4, are applied to the bottom of the clay soil (at the base of the shaking table). All numerical modelling consideration and conditions are the same as those used in Chapter 4.

5.7. Validation of Scaling Methodology

For the piles designed to resist a lateral load, the ultimate and serviceability design limit states must be considered including the potential load-displacement behaviour of a single pile. This adopted potential behaviour of the single pile results are typically based on some theoretical or/and semi-empirical methods available in the foundation's standard and literature. Ignoring or simplifying the 3D aspect of the lateral soil reaction and the variety of primary parameters governing the pile–soil interaction leads to less effective prediction of pile capacity according to the aforementioned approach.

As it mentioned earlier in this chapter that, Full-scale tests can be considered as reasonable alternatives that lead to a realistic evaluation of small pile head deflections, but the expensiveness and difficulties of implementation limit the practical value of these tests. Developing a scale model that represents the primary parameter of the prototype full-scale mode is valuable for the prediction and validation of such a complex system. A number of problems in soil mechanics and structural analysis, primarily in SSI area, can be studied using this validation approach. This method is a mix of two research areas, i.e. geotechnical and structural areas, and is connected between the physical and numerical modelling programmes. A physical shaking table test as a reference case study in addition to 3D nonlinear FEA is used for this purpose. The first set of analyses examine the accuracy of employing the scaling method.

The full-scale 3D numerical model is used to validate the inertial and kinematic behaviours of the scaled physical shaking table test. The bending moment envelope, acceleration time history, acceleration Fourier amplitude and acceleration response spectrum for the model are presented in Figure 5-12 to **Error! Reference source not found.**. The results for these parameters are compared with the corresponding parameters conducted by the scaled physical shaking table test of the reference case study. To do so, these parameters (full-scale numerical results) are scaled according to their corresponding scale factor using Table 5.2 in Section 3.

The bending moment parameter values of the full-scale numerical model are scaled down using the scaling factor equal to λ^4 . Based on the procedure of validation described in Section 6, the resultant bending moment envelope behaviour of the scaled numerical model are compared to those concluded in the reference case study. Figure 5-25 represents this validation. A similar process is done to the output acceleration time histories of the full-scale numerical model. As the test is performed in a one–g

environment, the scaling factor corresponds to the acceleration parameter is considered as 1. According to Table 5.2, the time parameter must be divided by the factor of $\lambda^{\frac{1}{2}}$. To create the other two parameters related to acceleration time history behaviour, namely, acceleration Fourier amplitude and acceleration response spectrum of the four cases of loading, the acceleration time histories data are treated with SeismoSignal software. Figure 5-25 to Figure 5-37 illustrate these comparisons for the four instances of pile head.

Pile behaviour under dynamic loading is substantially affected by the properties of the soil and pile, where pile properties represent pile material and shape properties. The nonlinear pile material modelling must be adopted to identify the pile lateral load capacity, associated bending moment, pile deflection and pile material failure onset. The variation in the bending stiffness (EI) of a laterally loaded pile is evidently a function of the bending moment distribution along the pile length and is represented as the moment–curvature relationship. As concluded in Table 5.7 and 5.8, the targeted EI of the model ($2.94\ kN - m$) experiences an increase of 5.0% than the value of the computed scale model $2.42\ kN - m$).

This deviation is reflected on the bending moment envelope values of the numerical simulation, where the bending moment envelopes have amounts lesser than those of the physical model. Owing to the small difference in flexural rigidity values of the physical and numerical models, slight deviations of bending moment envelopes corresponding to these models are noted in Figure 5.28, indicating that the current scaling and validation method can successfully examine and validate the inertial behaviour of the SSSI system when the primary parameters of the system are identified and scaled correctly.

The pile flexural stiffnesses along the deflected pile vary with the level of loading, pile material, moment–curvature relationship and soil reaction that influences the pile deflection pattern. Therefore, consistency among the primary dominated parameters of the distributions of pile deflection, bending moment, bending stiffness and soil reaction must be maintained along with the pile. Nevertheless, the scale model which is developed to predict the SSPSI response can represent all these primary parameters correctly. It permits the evaluation of the soil–pile modulus based on the properties of the soil and pile, which include pile flexural stiffnesses. The assessed model will thus be influenced by the accuracy of bending stiffness of model-to-prototype similarity and the selected pile cross-section type and dimension. The proposed scaling and validation technique

suggests reducing the model flexural stiffness to simulate the correct prototype flexural stiffness. Considering a rational reduction factor is a crucial aspect that requires further research to provide reasonable guidelines.

In this scaling and validation technique, the static and /or dynamic pile response including pile-head loads and deflection, maximum moment is considered on the basis of a constant bending stiffness (EI) along the pile length. Many studies reveal that the bending moment along the pile length does not significantly depend on the characteristics of the structure e.g. (Reese & Wang, 1994). Therefore, a small deviation between numerical modelling according to prototype properties and scaled physical test can be justified due to the 5% difference in EI values. Moreover, the pile/soil compressibility ratio K can be expressed as follows:

$$K = \frac{E_P}{E_s} \qquad (5.22)$$

the lateral pile/soil stiffness ration K_r is given as:

$$K_r = \frac{E_p \, I_p}{E_s \, D^4} \qquad (5.23)$$

and, K_r can be written as a function of K as in the following equation:

$$K_r = \frac{I_p}{D^4} \, K \qquad (5.24)$$

According to geotechnical codes, such as AASHTO and Eurocode 7, the pile design phenomena hinge mostly on ultimate limit states and serviceability limit states in which the load-deflection behaviour of the pile under lateral loads should be considered correctly. Pile slenderness ratio and pile–soil stiffness ratio are crucial factors controlling the dynamic response of the pile–soil system. Realistic scaling and analysis of such an interaction should consider the nonlinear response of the system and the homogeneity of soil properties.

In pile design practice, L/D ratio represents the effect of embedded length of the pile on pile stiffness associated with pile and soil (Byrne *et al.*, 2019). Increasing L/D ratio results in an accumulative decline in the relative pile–soil stiffness K_r (Poulos & Davis, 1980). These consequences are significantly influenced by pile head conditions. The value of degradation factor indicates less reduction in soil–pile interactive performance for high values of L/D . Low degradation factors induce a remarkable decline in the axial capacity

of the pile owing to less degradation factor values. For comparable dynamic loading properties and pile geometry parameters, the literature reports that the degradation of the free headed pile is less compared to that of the fixed headed pile. The L/D ratio limitation must be identified carefully before starting the scaling process. Accurate L/D ratio must be determined to produce a correct scale model-to-prototype system behaviour associated with this significant scaling parameter.

The minimum wall thickness of the pile based on the D/t ratio is one of the principal parameters that must be considered to produce a scale model. According to (Bala, 2007), the D/t ratio along the pile length must be small enough to avert local buckling at stresses up to the yield strength of the pile material. Loading circumstances occur during the installation, so loading periods of the service life of piling must be considered and standard limitation should be applied as a minimum requirement. The minimum pile wall thickness should not be less than the value in Eq. (5.25).

$$t = 6.35 + \frac{D}{100} \qquad (5.25)$$

where t and D are the wall thickness and diameter of pile in mm, respectively. This condition does not exist in the targeted and scale model properties. The minimum t required is $6.8\ mm$, and the actual values of t are 1.5875 and 0.711 mm for the target and scale model, respectively. Depending on soil type class, pile buckling failure associated with the D/t ratio are documented in standard provisions (Randolph et al., 2005), where D/t ratios range between 15 and 45 (Jardine, 2009). In the current study, the difference between the values of target and scale model is large, with a reduction of 76%. D/t limitation must be considered. The similarity between scale model to prototype for D/t ratio must be identified according to appropriate standard provision, for instance, Section 3.2 in (Bala, 2007).
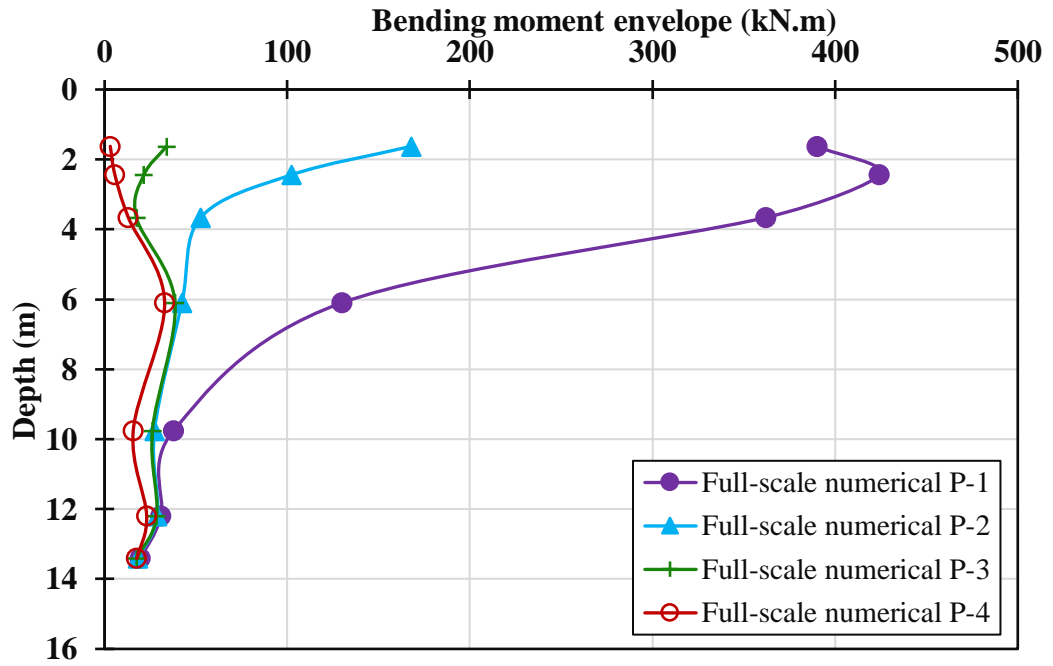
Figure 5-12 Pile Bending Moment Envelopes (Pile-1–Pile-4, see chapter 4): Full-Scale Numerical Model
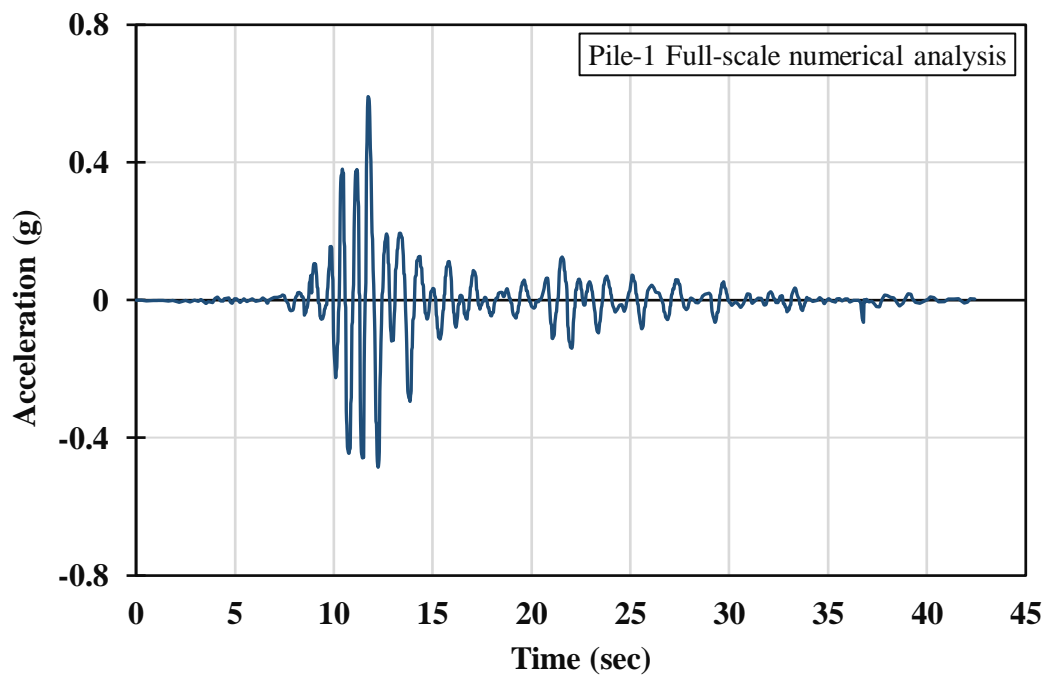
Figure 5-13 Pile Head Acceleration Time History (Pile-1): Full-Scale Numerical Model
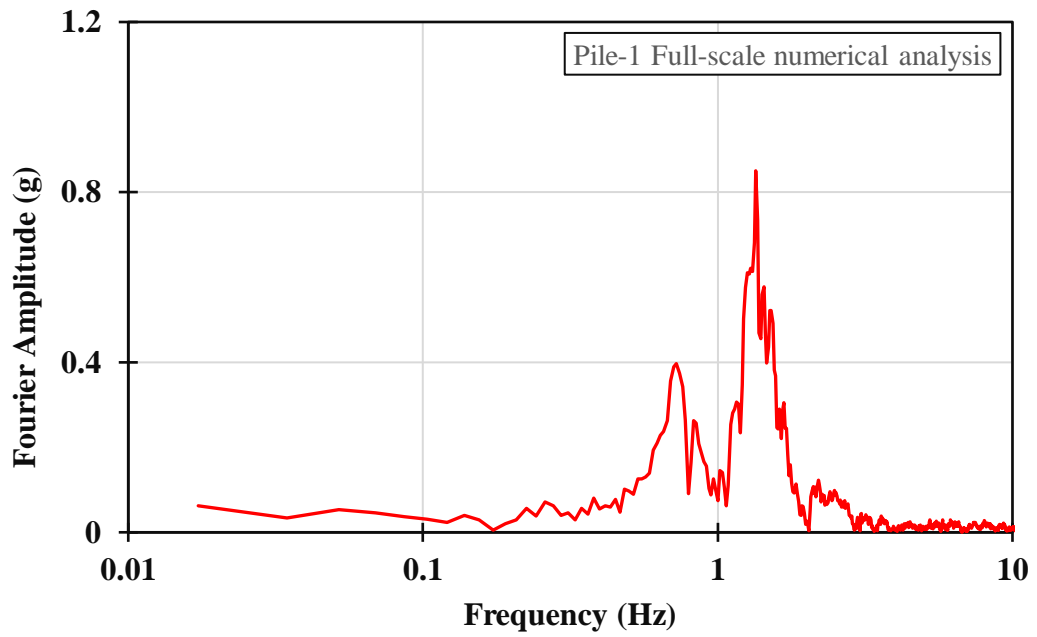
Figure 5-14 Fourier Amplitude vs. Frequency (FFT) (Pile-1): Full-Scale Numerical Model
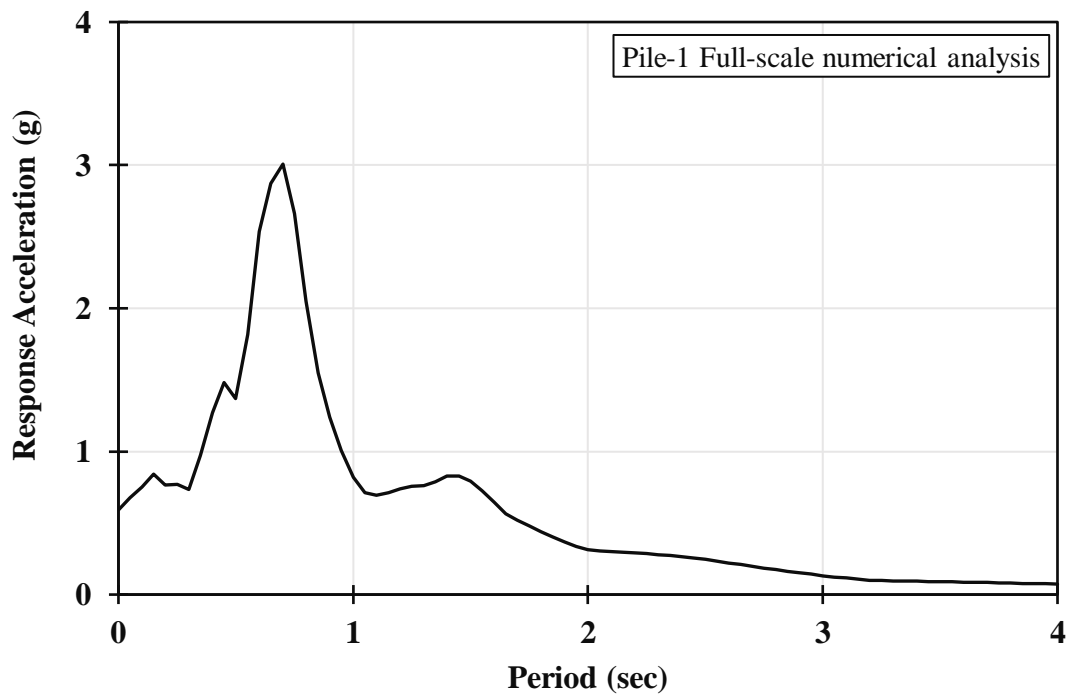
Figure 5-15 Acceleration Response Spectrum (Pile-1): Full-Scale Numerical Mode
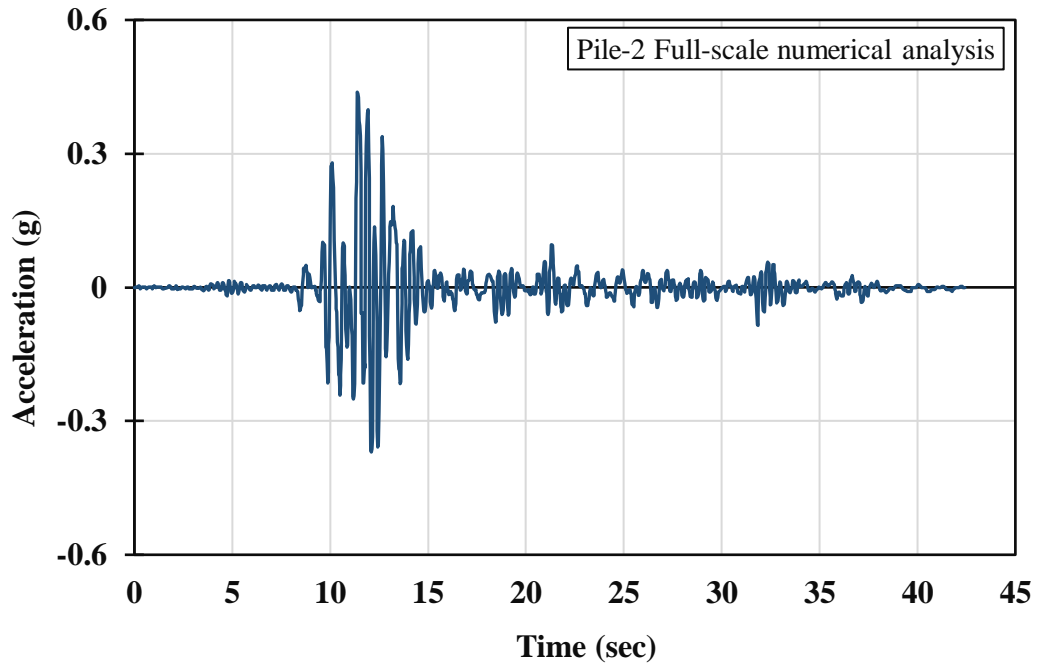
Figure 5-16 Pile Head Acceleration Time History (Pile-2): Full-Scale Numerical Model
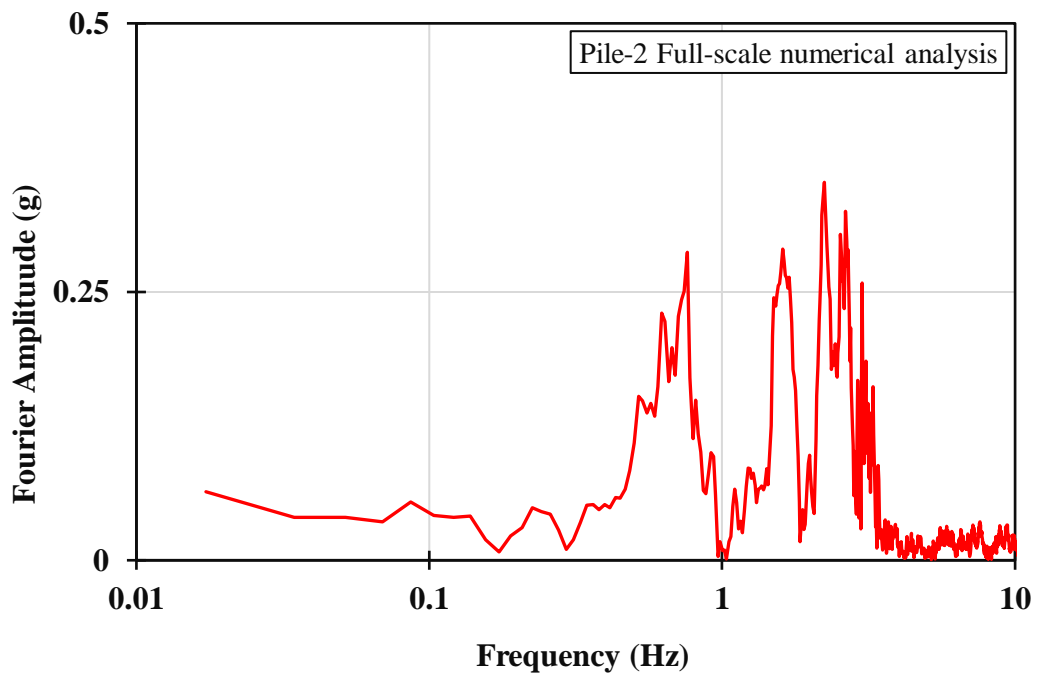
Figure 5-17 Fourier Amplitude vs. Frequency (FFT) (Pile-2): Full-Scale Numerical Model

223
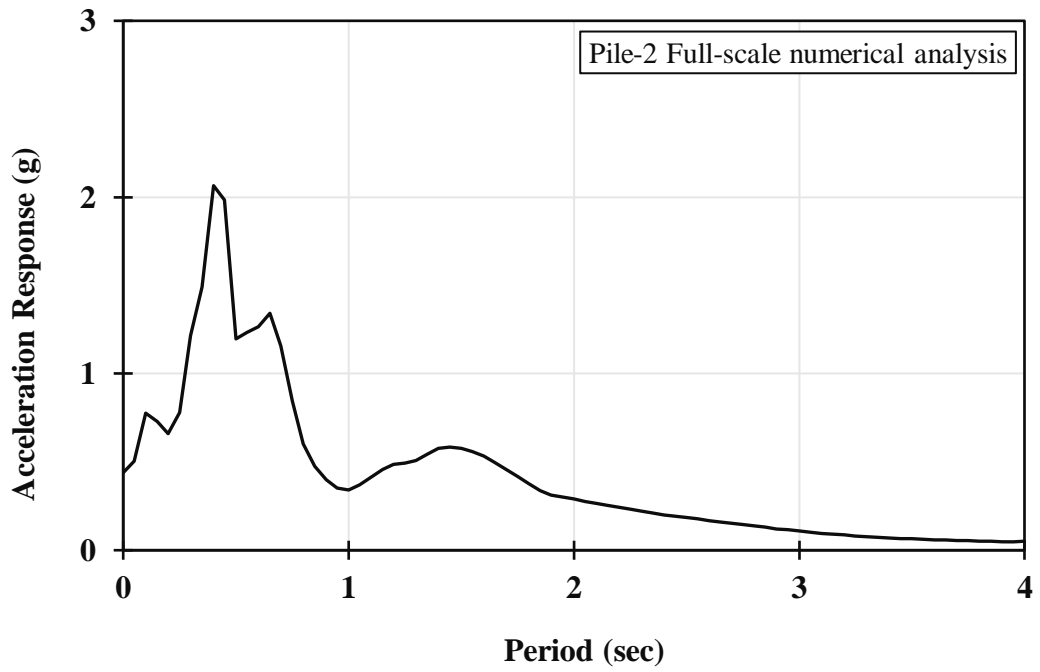
Figure 5-18 Acceleration Response Spectrum (Pile-2): Full-Scale Numerical Model
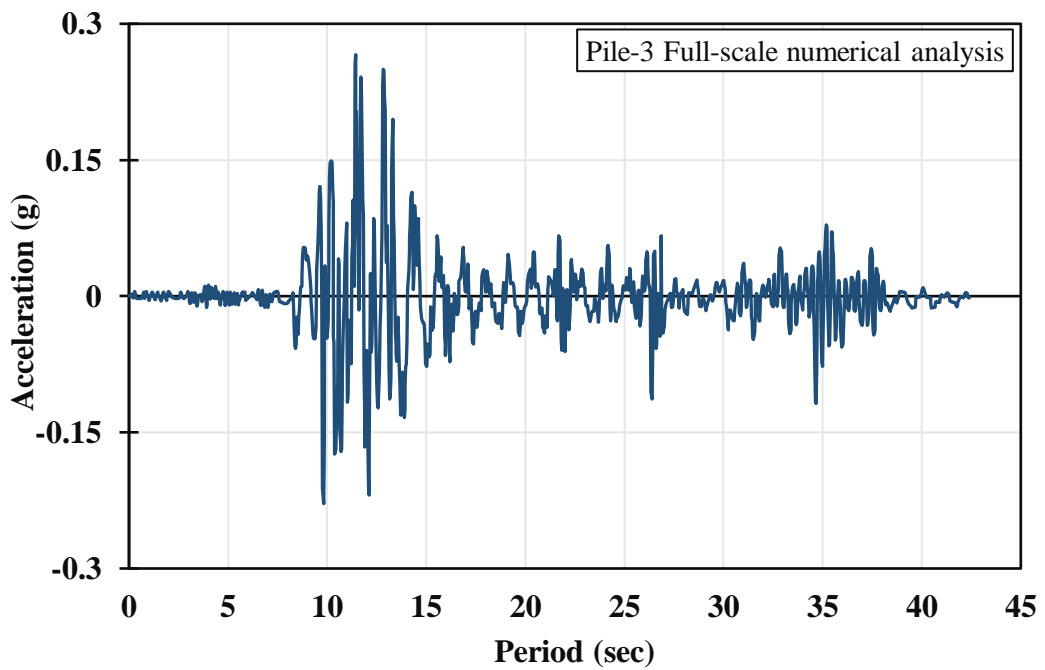
Figure 5-19 Pile Head Acceleration Time History (Pile-3): Full-Scale Numerical Model
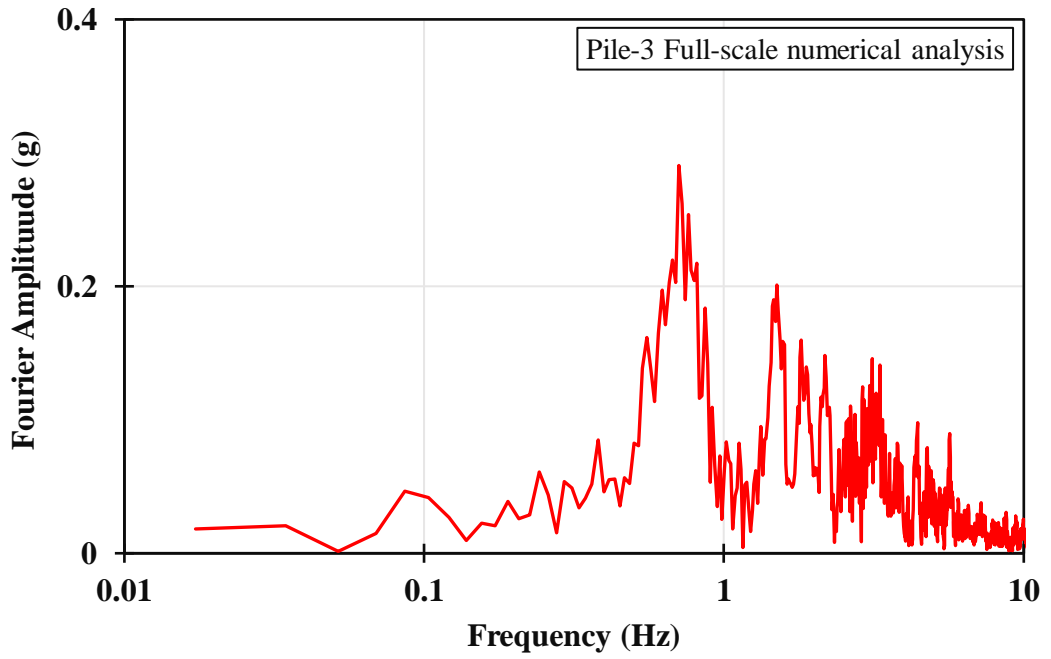
Figure 5-20 Fourier Amplitude vs. Frequency (FFT) (Pile-3): Full-Scale Numerical
Model
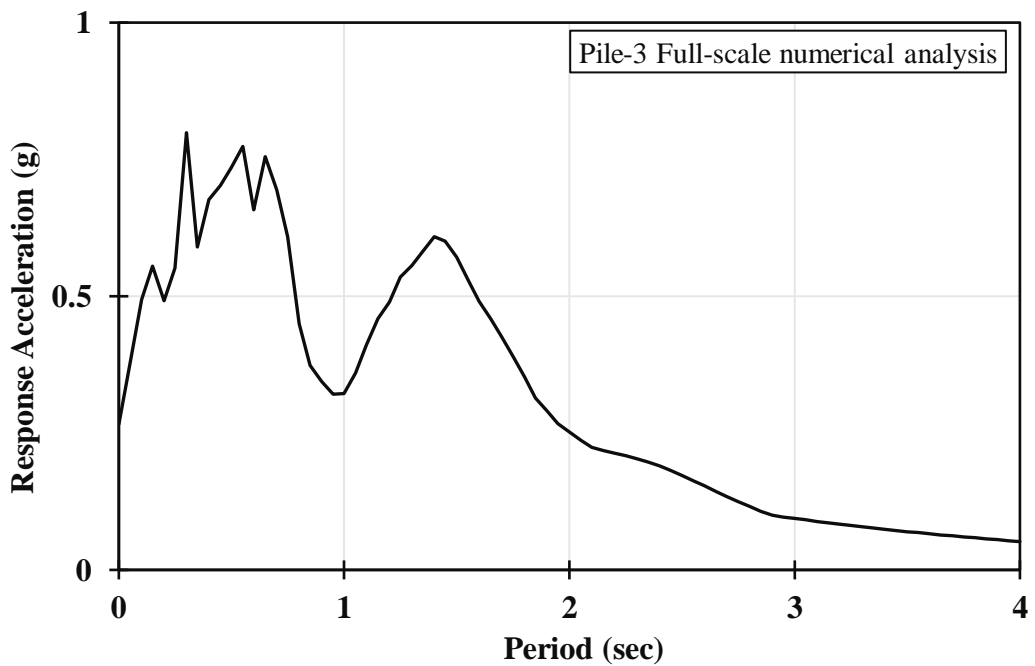
Figure 5-21 Acceleration Response Spectrum (Pile-3): Full-Scale Numerical Model
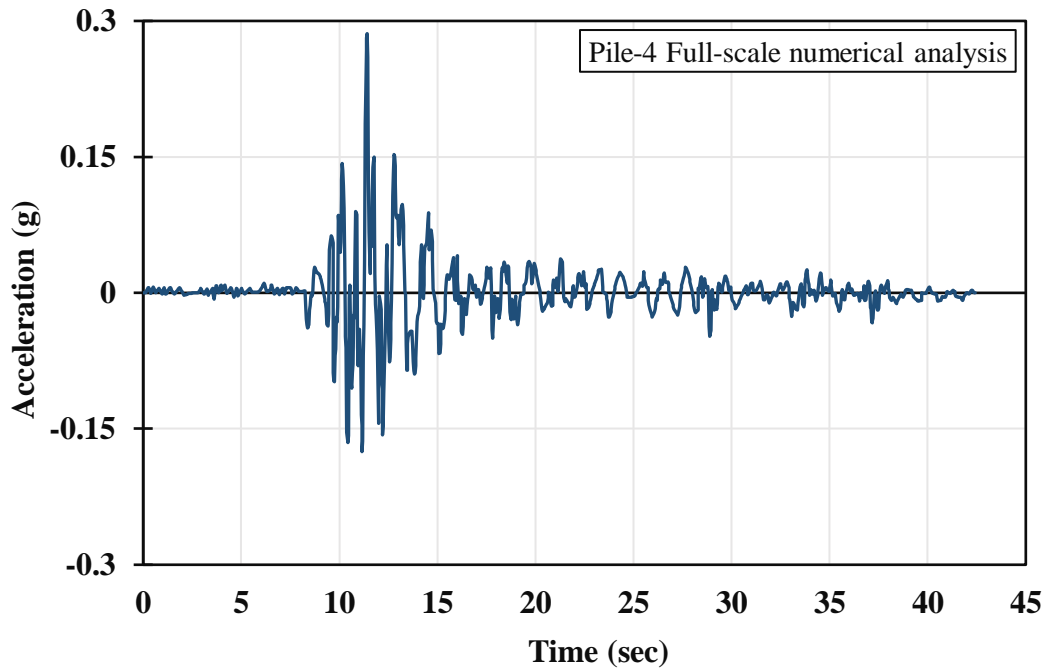
Figure 5-22 Pile Head Acceleration Time History (Pile-4): Full-Scale Numerical Model
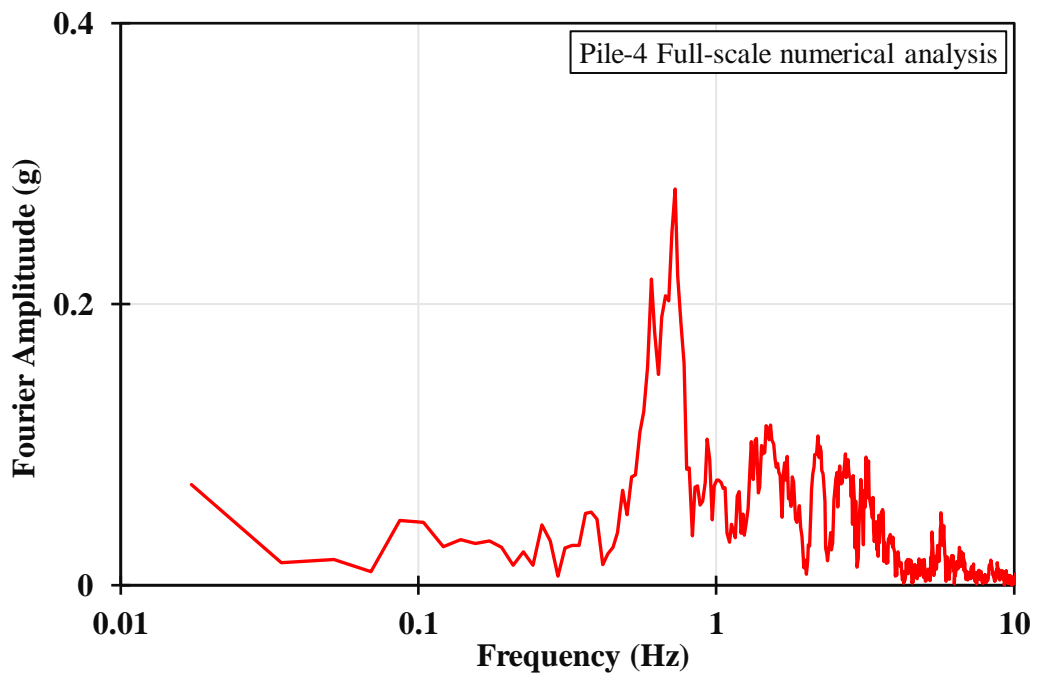
Figure 5-23 Fourier Amplitude vs. Frequency (FFT) (Pile-4): Full-Scale Numerical Model

226
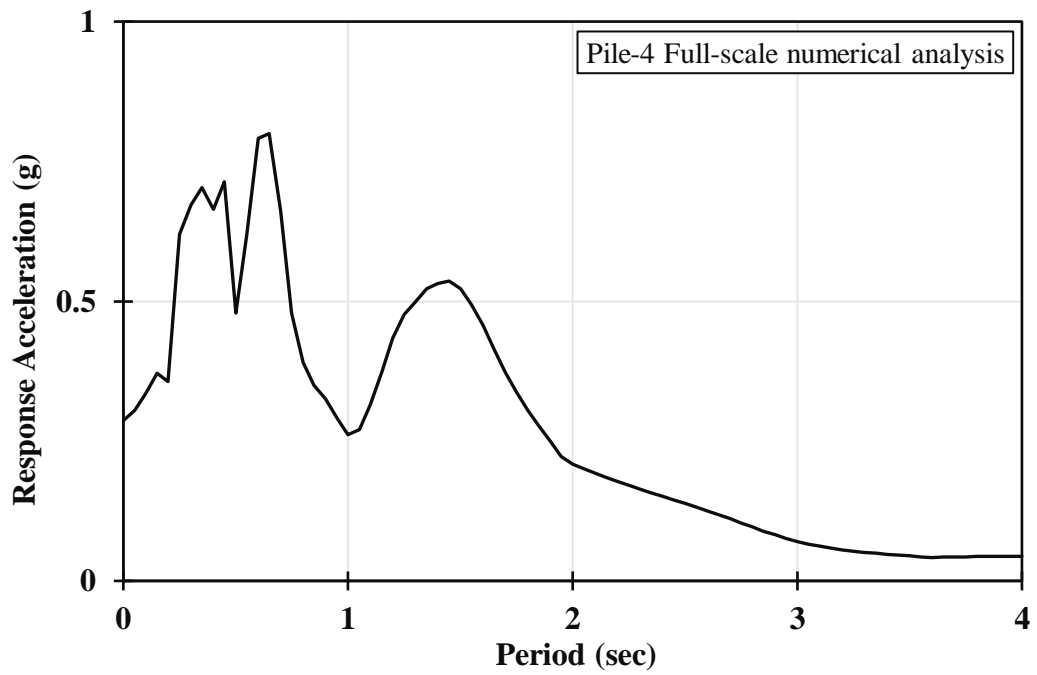
Figure 5-24 Acceleration Response Spectrum (Pile-4): Full-Scale Numerical Model
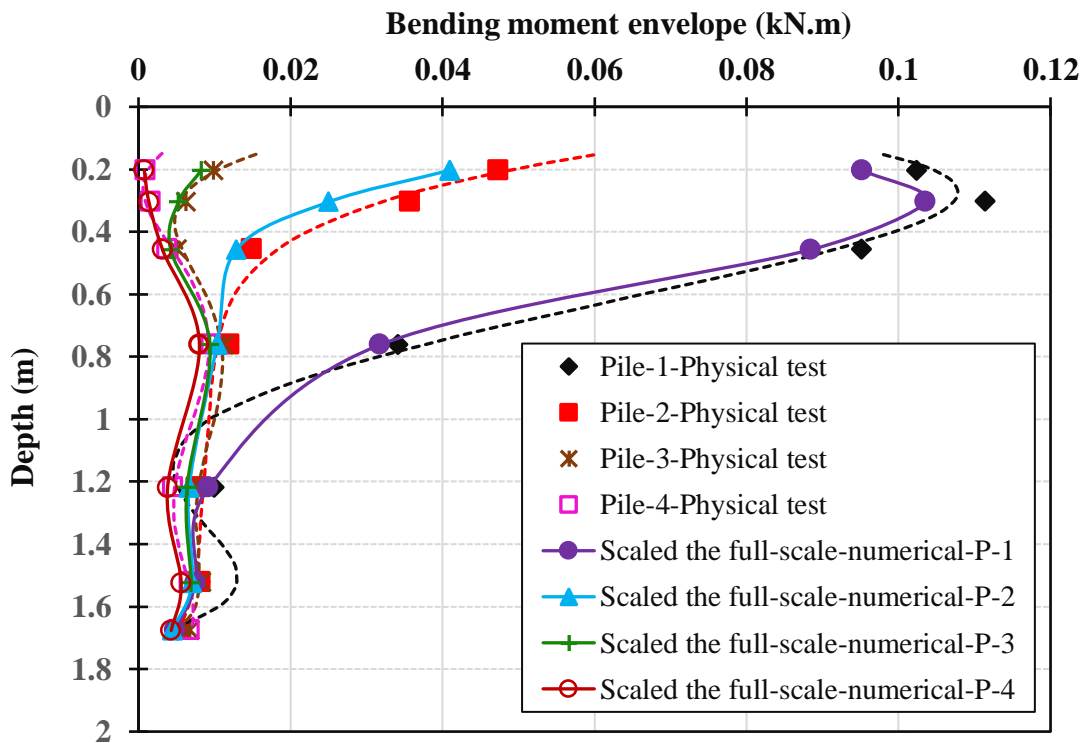
Figure 5-25 Pile Bending Moment Envelopes (Pile-1–Pile-4 see chapter 4): Scaled Full-Scale Numerical Model vs. Scaled Physical Test

227
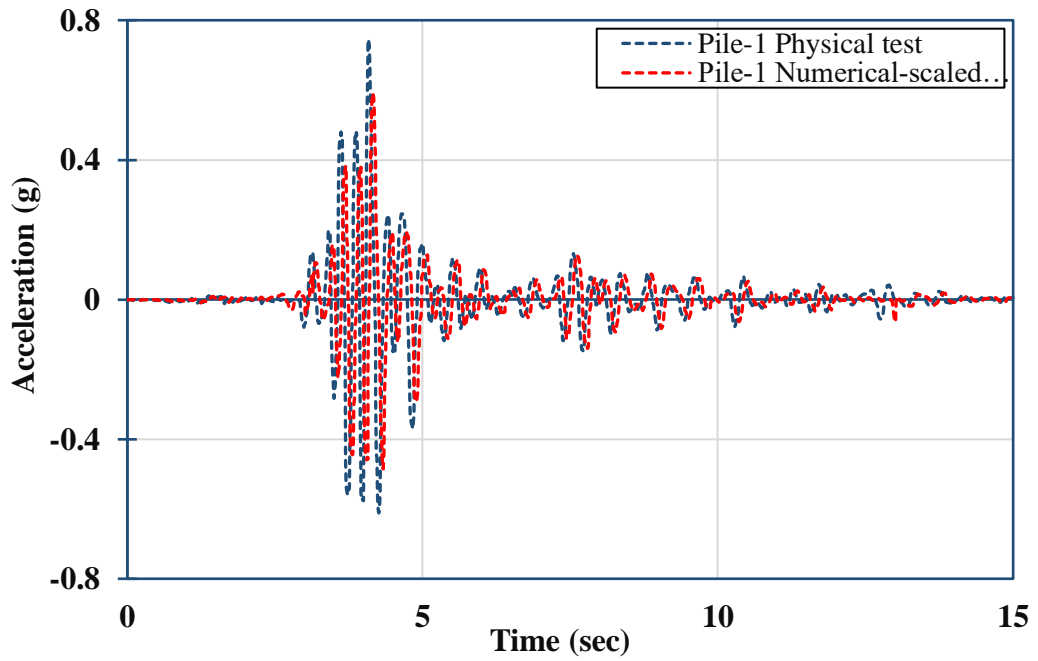
Figure 5-26 Pile Head Acceleration Time History (Pile-1): Scaled Full-Scale
Numerical Model vs. Scaled Physical Test
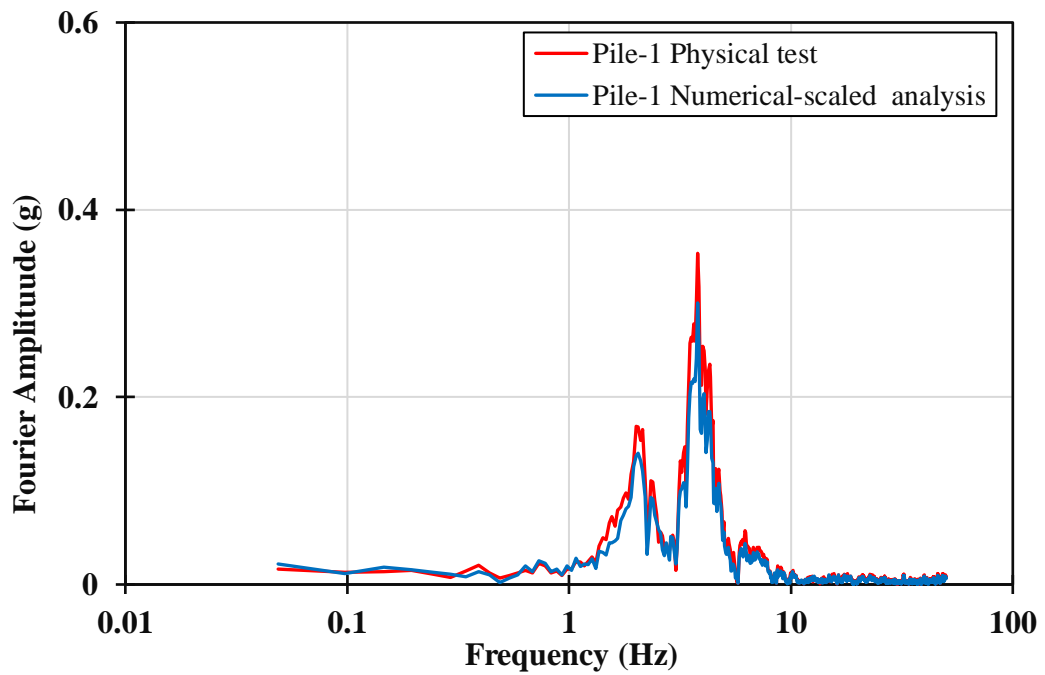
Figure 5-27 Fourier Amplitude vs. Frequency (FFT) (Pile-1): Scaled Full-Scale
Numerical Model vs. Scaled Physical Test
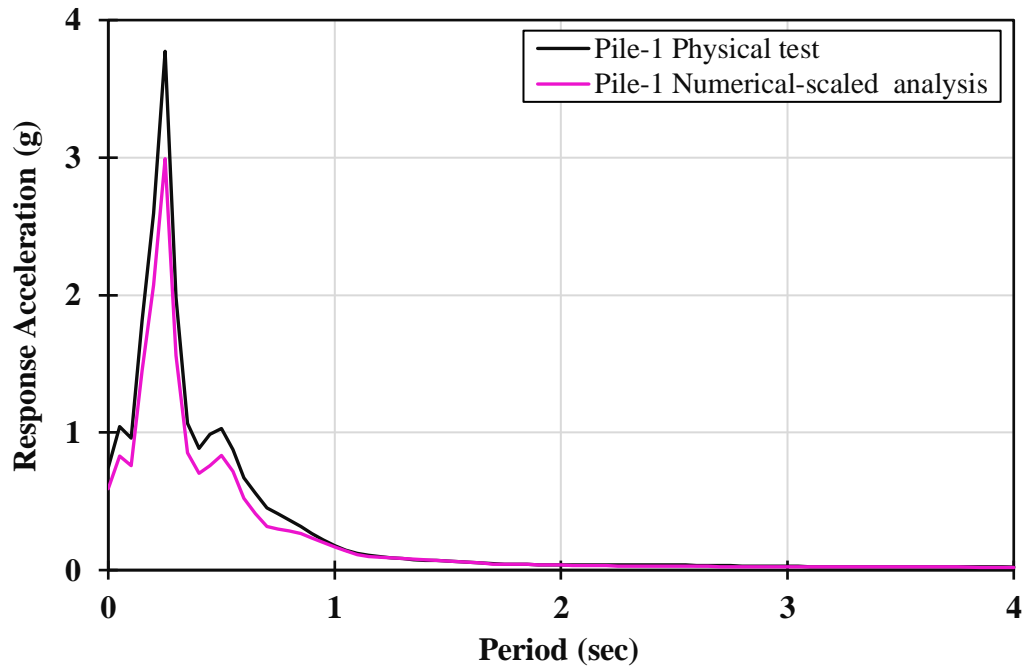
Figure 5-28 Acceleration Response Spectrum (Pile-1): Scaled Full-Scale Numerical Model vs. Scaled Physical Test
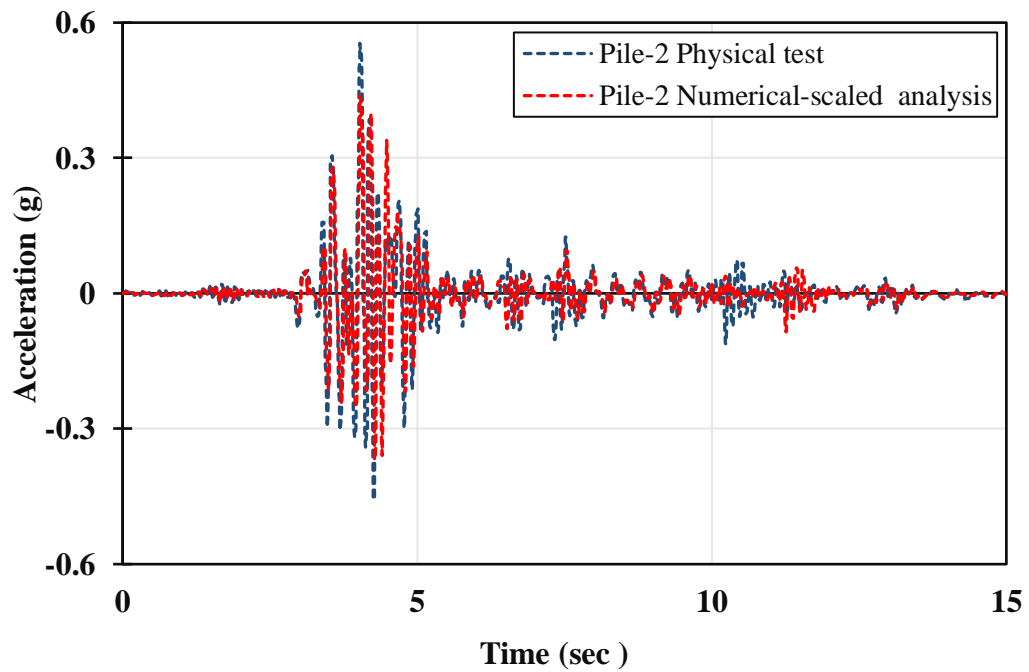
Figure 5-29 Pile Head Acceleration Time History (Pile-2): Scaled Full-Scale Numerical Model vs. Scaled Physical Test
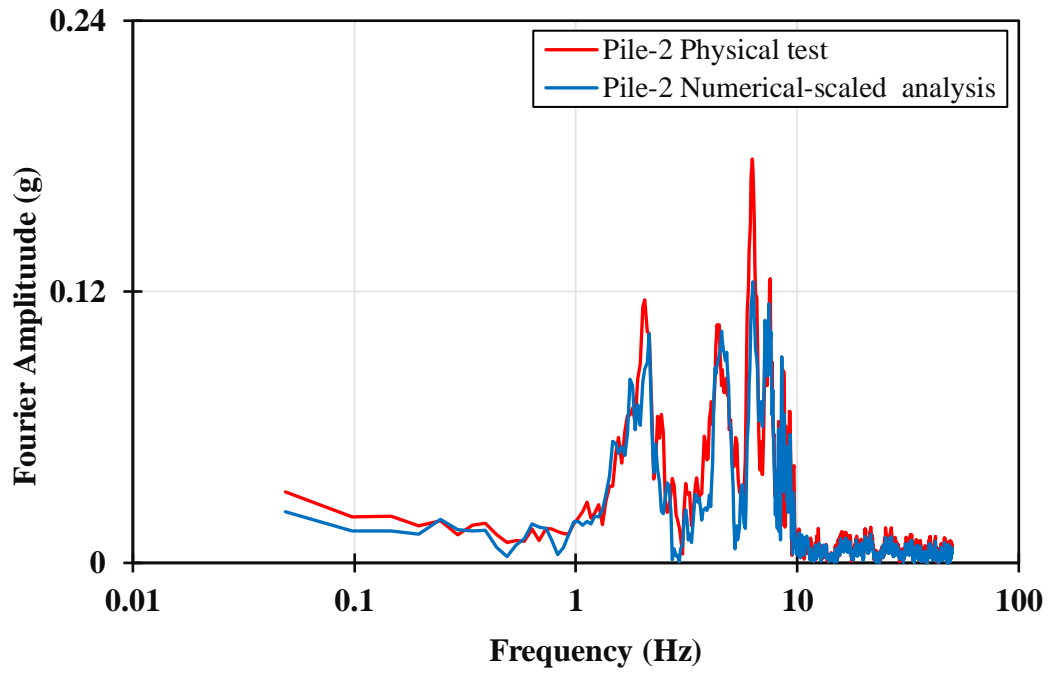
Figure 5-30 Fourier Amplitude vs. Frequency (FFT) (Pile-2): Scaled Full-Scale Numerical Model vs. Scaled Physical Test
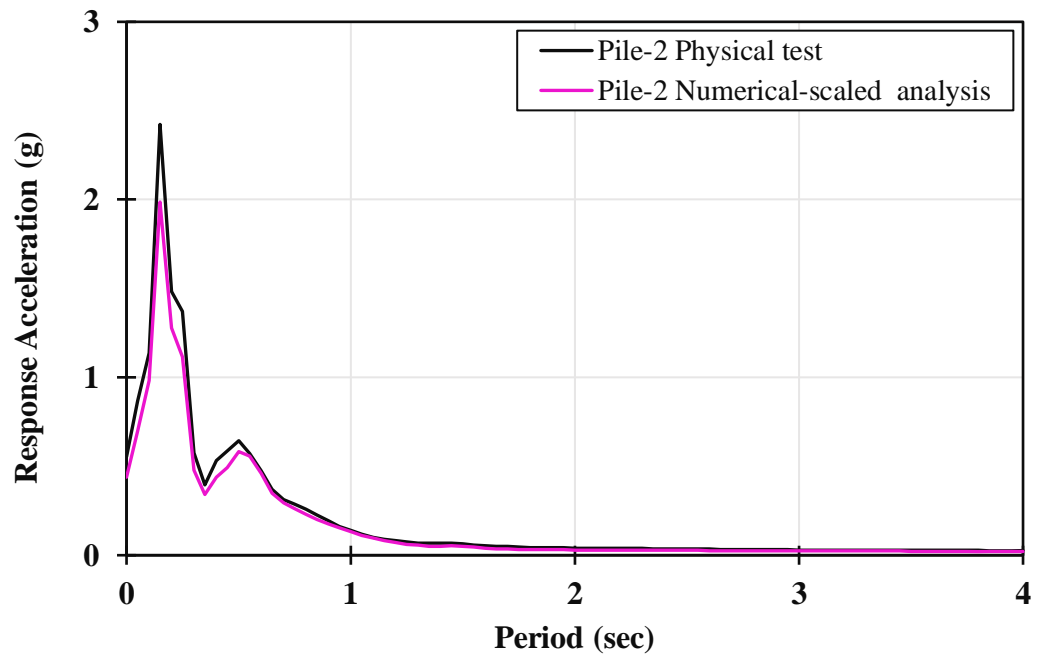
Figure 5-31 Acceleration Response Spectrum (Pile-2): Scaled Full-Scale Numerical Model vs. Scaled Physical Test
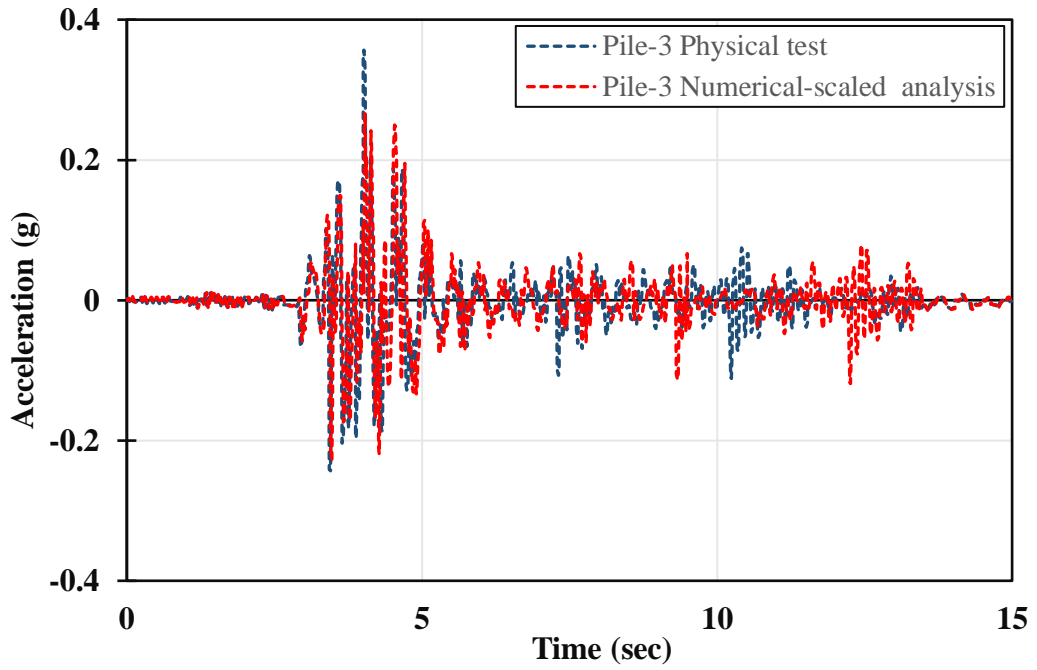
Figure 5-32 Pile Head Acceleration Time History (Pile-3): Scaled Full-Scale Numerical Model vs. Scaled Physical Test
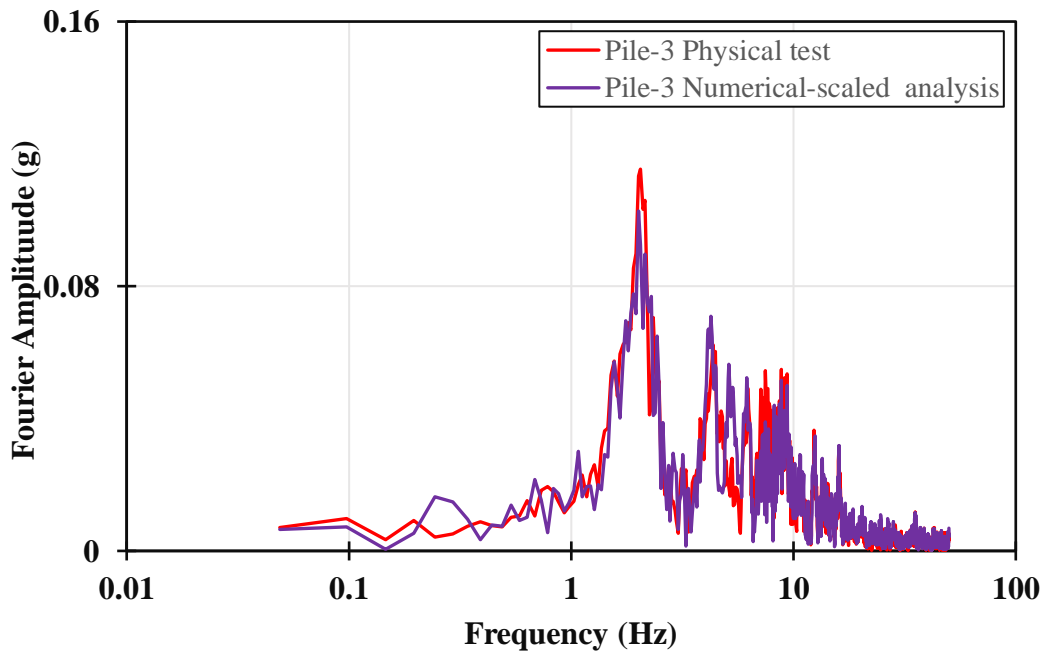
Figure 5-33 Fourier Amplitude vs. Frequency (FFT) (Pile-3): Scaled Full-Scale Numerical Model vs. Scaled Physical Test

231
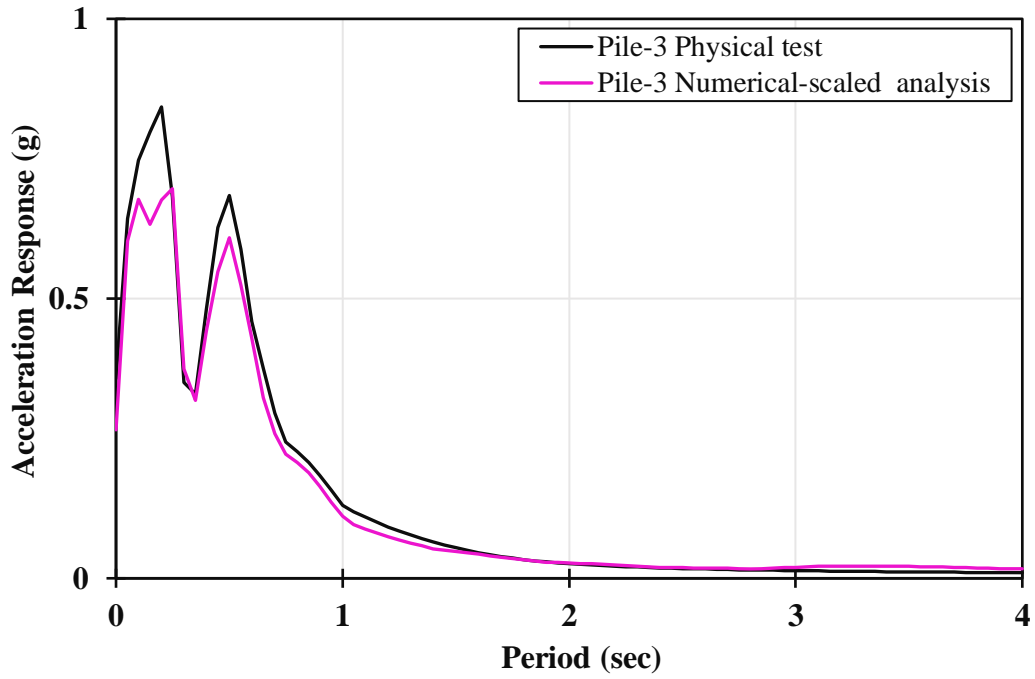
Figure 5-34 Acceleration Response Spectrum (Pile-3): Scaled Full-Scale Numerical Model vs. Scaled Physical Test
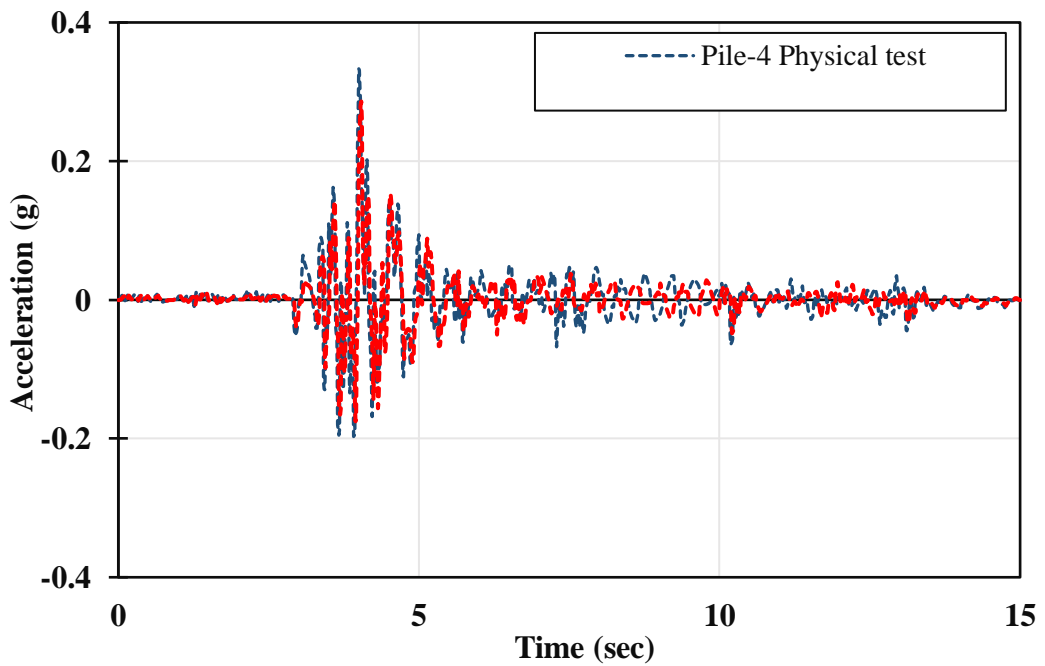
Figure 5-35 Pile Head Acceleration Time History (Pile-4): Scaled Full-Scale Numerical Model vs. Scaled Physical Test
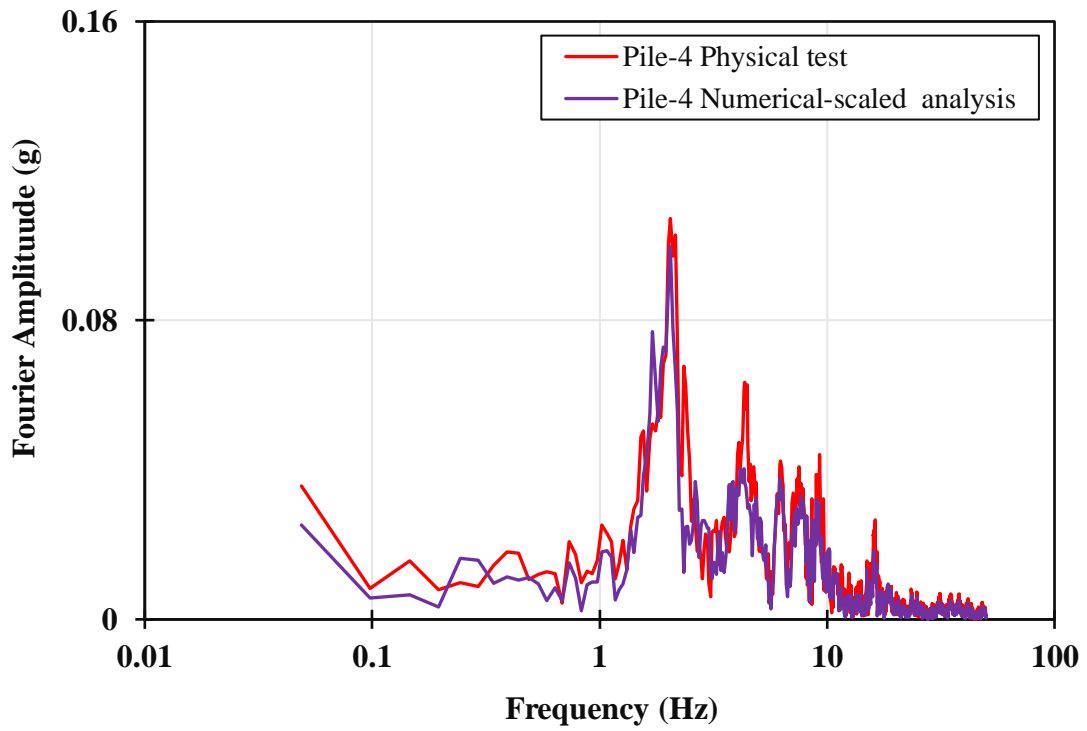
Figure 5-36 Fourier Amplitude vs. Frequency (FFT) (Pile-4): Scaled Full-Scale Numerical Model vs. Scaled Physical Test
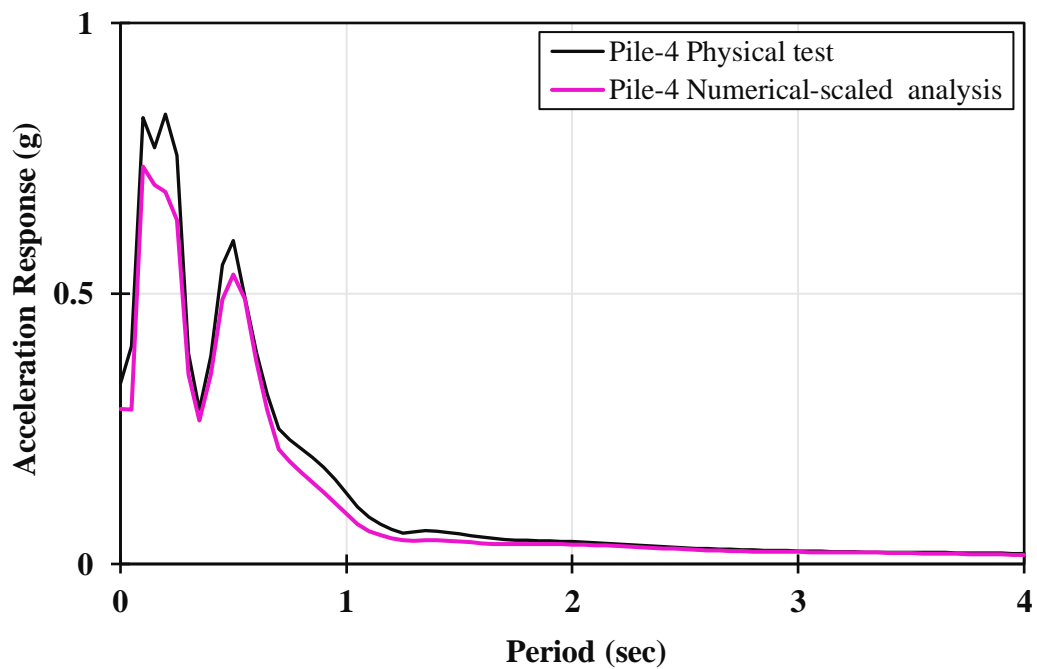
Figure 5-37 Acceleration Response Spectrum (Pile-4): Scaled Full-Scale Numerical Model vs. Scaled Physical Test

5.8. Concluding Remarks

- In this chapter, a sophisticated approach of scaling and validating full-scale seismic soil structure interaction problem is proposed using the association between numerical and physical tests.

- On the basis of an extensive laboratory test which has been previously done by many researchers, a dimensional scaling factor $\lambda = 8$ is adopted in the current study.

- An entire approach is built as a step-by-step procedure. The proposed methodology considers the scaling concept of implied prototypes and 'modelling of models' technique which can ensure a satisfactory level of model accuracy.

- Advanced 3D finite element modelling using Abaqus software is also developed. The characteristics, properties and results of the physical shaking table test presented by Meymand (1998) are adopted as a refence case study.

- The results indicate a good correlation with small deviation between the scaled numerical and physical test when the scaling and validation method is employed.

- The level of accuracy primarily depends on the level of scaling precision, selection of appropriate material that can represent the properties of the prototype materials correctly and the percentage difference for the primary parameter of the system.

- To stimulate the correct prototype flexural stiffness, the proposed scaling and validation technique indicates that the model flexural stiffness must be reduced by a reasonable reduction factor.

- Consideration of a rational reduction factor is critical step that warrants further research to provide reasonable guidelines. According to the scaling law, the preparation of clay specimen model is successfully defined for the physical and numerical tests. Therefore, this method of modelling can be adapted to other scale modelling circumstances that require realistic soil behaviour and validates the results using existing validation methods.

- Most SSPSI modes such as the gap-slap mechanism, the inertial forces of the superstructure and the kinematic soil–pile force can be modelled correctly.

Chapter 6: Comparison of ASCE and Eurocode 8 Seismic Codes

6.1. Introduction

The soil–structure interaction (SSI) of high-rise buildings is most affected by the essential characteristics of seismic soil–pile–superstructure interactions (SSPSI), including nonlinearity, resistance degradation, frequency dependence, dynamic load distribution and pile group effects. The seismic soil–structure interaction (SSSI) analysis procedure addressed in Eurocode 8 (EC8) and ASCE also shows four factors significantly influencing the mode interaction: period lengthening, equivalent damping ratio, base-shear reduction factor and inertial and kinematic mode interaction. However, seismic codes do not specify all these essential factors. Reviewing and upgrading the seismic codes for nonlinear seismic soil–structure analysis of high-rise buildings are crucial to practically account for the seismic SSI effect.

The effects of soil–pile–structure interaction on the applied excitations and behaviour of structures is universally disregarded or simplified in seismic design practice (Durante *et al.*, 2015). These conditions are included in codes as a conservative premise for spectral analysis methodology. The flexibility of the embedded piles leads to lengthening of ground motion period and increase in damping. Consequently, the structural forces are reduced compared with a fixed base case, namely, the base-shear force of the structure is reduced. This design assumption is commonly accepted as a conservative spectral analysis approach. However, in extreme circumstances such as the 1985 Mexico City earthquake, period lengthening may result in increased spectral time history values corresponding to the design spectral time history specified in seismic code provisions (see Figure 1.2 of Chapter 1).

Figure 6-1 demonstrates the acceleration response spectra of the horizontal components of the earthquake of 6.5 magnitude recorded during 30 October 2016, the Amatrice Earthquake in Italy (AMT station) (Iervolino, Giorgio & Cito, 2019). The figure also shows that the design response spectrum suggested by EC8 does not cope the recorded earthquake spectrum for both directions in two different risk scales.
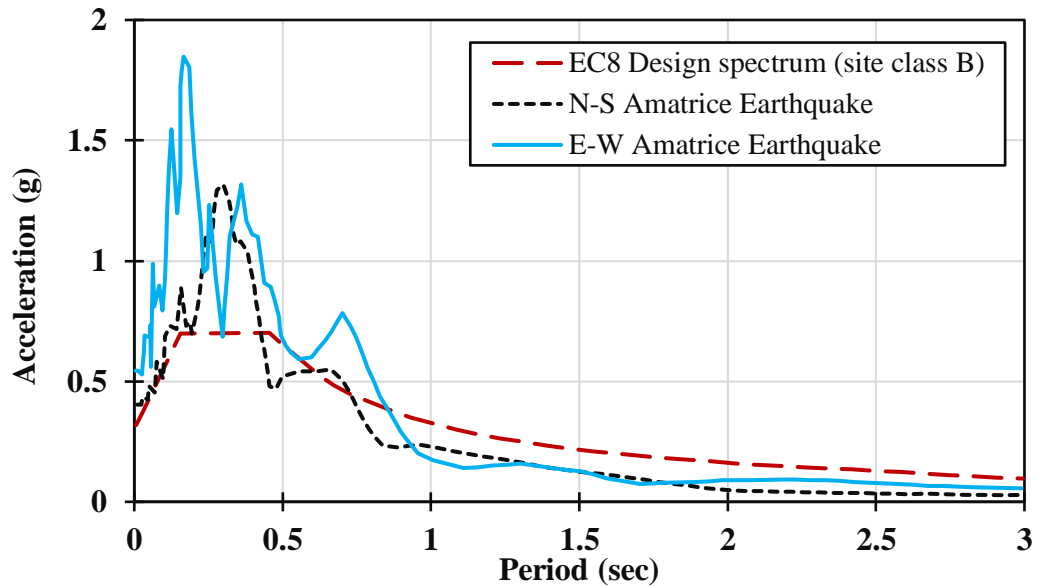
Figure 6-1 East–West (E-W) and North–South (N-S) Response Spectra Recorded at Amatrice (AMT Station) During the 30 October 2016 Earthquake and Design Response Spectrum According to EC8 (Site Class B)

The provisions in EC8 do not sufficiently address the coupled nonlinear dynamic response of pile groups and superstructure. Instead, approximate approaches for extending static and single pile analyses to this complex problem are used, and they disregard essential characteristics of SSPSI, including nonlinearity, resistance degradation, frequency dependence, dynamic load distribution and group effects. During an earthquake, pile performance, behaviour and integrity can be evaluated by simplified and non-coding analytical methods. The stiffness of the pile foundation system can be decreased by including the effects of SSI which is also accountable for increased permanent deformations. Consequently, the displacement and seismic response of a whole structure can be impacted. Two main aspects related to pile performance must be considered during an earthquake. (i) Ground motions experienced by the superstructure are impacted by the pile foundations. (ii) Extreme damage and even failure can occur in the piles due to seismic loading.

Incorporating the effects of SSI in determining the design for earthquake forces can decrease the value of the base shear and consequently the lateral forces and overturning moments. However, lateral displacements may be decreased due to the vibration of the structure. Codes give the maximum allowable base-shear reduction factor which is a function of the flexible base period and damping factors. In circumstances where the pile system majorly contributes to lateral stiffness (i.e. in soft soils), the single pile stiffness parameters determined by field tests or numerical analysis result in unsafe and insufficient

values [(Basack & Nimbalkar, 2017), (Stacul, Squeglia & Morelli, 2017)]. The provisions recommend computing these stiffness factors to calculate the stiffness of the pile group, without reduction factors. Moreover, the procedure should be based on the strain levels expected in the soil response to reduce the effect of nonlinearity limitations (EC8 and ASCE). The SSI of high-rise buildings has the most significant influence, including the development of high vibration modes incorporating inertial and kinematic interaction and the effects of using linear and nonlinear springs to model the soil and foundation system in linear and nonlinear SSI time history analysis. High-rise buildings may be subjected to resonance as a result of SSI during earthquake effects [(Mylonakis & Gazetas, 2000c); (Guin & Banerjee, 2002); (May & Malhotra, 2010); (Phanikanth, Choudhury & Reddy, 2013b)].

In this chapter, the effects of SSI on design and analysis procedures, as well as the provisions for pile performance analysis of high-rise building resting on soft clay soil subject to seismic load, are examined with respect to EC8 and ASCE. Although both codes include simplified approaches to SSI analysis, they recommend specific dynamic analysis for structures resting on soft soils subject to intense levels of shaking. A series of 2D models of a high-rise steel building resting on soft clay soil subject to the input data of two different real filtered matched earthquakes has been developed for many parametric studies using Abaqus software. The results are compared with seismic code limitation.

6.2. Seismic hazards

Seismic hazard analysis is the application of the attenuation relationships to predict ground motions for a particular site. The two basic types of seismic hazard analysis are deterministic seismic hazard analysis (DSHA) and probabilistic seismic hazard analysis (PSHA). As the 'original' method, DSHA represents a single scenario and is intended to be conservative. However, this method has two notable problems. (i) It does not deal explicitly with uncertainty, and (ii) it only deals with the possibility of an earthquake, not the likelihood. PSHA was developed in the 1970s to account for most of the uncertainties involved in a seismic hazard. This method acknowledges the uncertainty of relevant aspects to the problem such as location, magnitude, intensity and timing. Considering the volume and complexity of the information needed to understand and cover this subject, it is excluded in this study. The discussion here focuses on which of the input data to select to deliver an accurate analysis for ASCE and EC8. Earthquake codes are regularly

revised and updated according to the enhancement in the characterization of ground motions, soils and structures. These revisions have been made more frequently in recent years. Studies have attempted to compare the accelerograms—recorded response spectrum and design response spectrum—derived from EC8 and ASCE. For example, the period range corresponding to the pulse periods of the 1999 Düzce earthquake is around 0.5–1.5 sec, which exceeds the design response spectrum value given by codes (Akkar & Gülkan, 2002) and Pantosti *et al.* (2008) (see Figure 6-2).
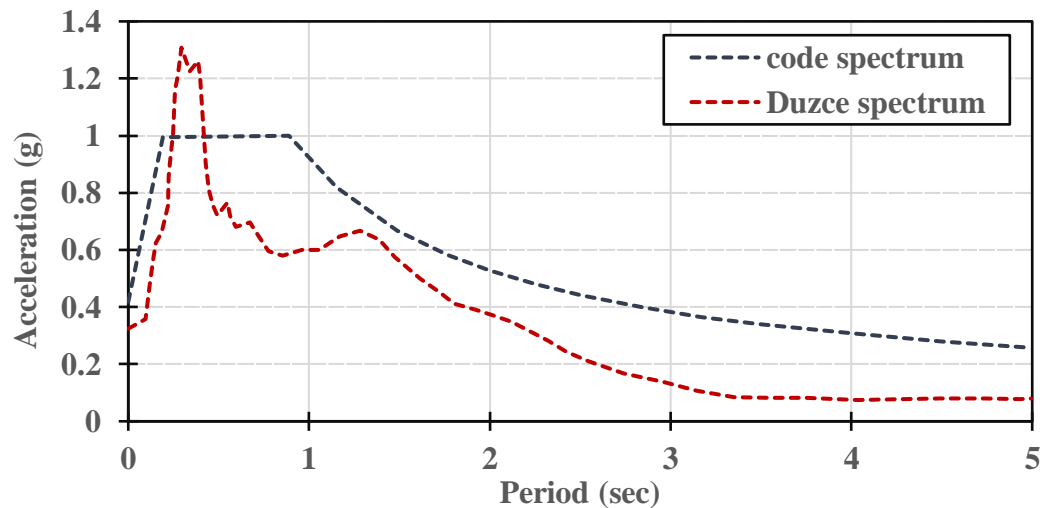
Figure 6-2 5% Damped Linear Response Spectrum of Code and Düzce Earthquake

Faccioli, Paolucci and Pessina (2002) also carried out other comparisons, and they correlated the simulated displacement spectrum results with the EC8 design displacement spectrum results for the Bolu Viaduct earthquake. (Akkar & Gülkan, 2002) concluded that the peak acceleration for much near-source records was not as high as predicted and tended to become saturated for increasing magnitudes. The peak velocities and corresponding storey drift consequences were significant, as confirmed by structural damage. Seismic hazard is expressed in EC8 by a single parameter a_{gR}. This parameter represents the reference peak ground acceleration (PGA) at the rock surface for a specific mean return period. The recommended period is 475 years, corresponding to 10% probability of exceedance in 50 years for noncollapse performance level, (Douglas & Gkimprixis, 2017), (Solomos, Pinto & Dimova, 2008).

The design ground acceleration is equal to a_{gR} multiplied by the importance factor γ_I. Considering the effects of frequency content, which is described by a code response spectrum, and the amplitude of the ground motion on the structural response, a single parameter is insufficient to outline the seismic hazard. According to EC8, the provision

frequency content of any potential earthquake affects two characteristics, namely, the ground conditions and magnitude of the earthquake. However, different standards have been established for defining the return periods. Non-collapse criteria have been recommended in EC8 for considering a return period of 475 years, and the design ground accelerations vary between 0.025 g and 0.32 g. ASCE proposes a recurrence period of 2475 years that corresponds to a probability of 2% of the seismic hazard exceeding 50 years. The design ground accelerations vary between 0.024 g and 0.80 g.

6.2.1. Site class definition

Earthquake codes generally classify the site conditions into different categories called ground type, soil profile type, site class or subsoil class. 'Site class' is used in ASCE, whereas 'ground type' is used in EC8. In this study, 'site class' is selected to represent code site condition. ASCE and EC8 seismic codes categorise the soil site class into six types (A–F) and seven types (A–E, S_1 and S_2), respectively, depending on the average shear wave velocity, standard penetration test blow count ($\overline{N}$) and undrained shear strength value $\overline{S}_u$ of the topmost soil layer. Some of those soil types need a specific requirement to be characterised under their appropriate site classes such as class F in ASCE and S_2 in EC8. Therefore, in addition to the parameters mentioned above, several other factors must be identified, i.e. the thickness of the soil layer (H), plasticity index (PI), and moisture content (w). In this respect, both codes recommend that site class F in ASCE and S_2 in EC8, which represent the deposit of liquefaction soils and/or of sensitive clays require site response analysis in accordance with Section 21.1 and Section 20.3.1 of ASCE and EC8, respectively. Basing on empirical studies, Borcherdt (1994) recommended the average shear wave velocity for the top 30 m of soil that is referred to V_S^{30} as a means to classify the soil class. This recommendation is adopted in ASCE and EC8 site classification. Code design spectrum is a function of site class provided for circumstances wherein the 30 m of soil laid immediately directly underneath the site dominates the frequency content of the design motions (Sabetta & Bommer, 2002). In multi-layered sites, the averaging of these parameters for the first 30 m should be computed as a classification criterion.

6.2.2. Acceleration response spectra

In all current seismic codes, earthquake actions are illustrated in the fashion of a spectrum of absolute acceleration. A typical shape of horizontal elastic design spectrum for ASCE and EC8 can be drawn as in Figure 6-3.
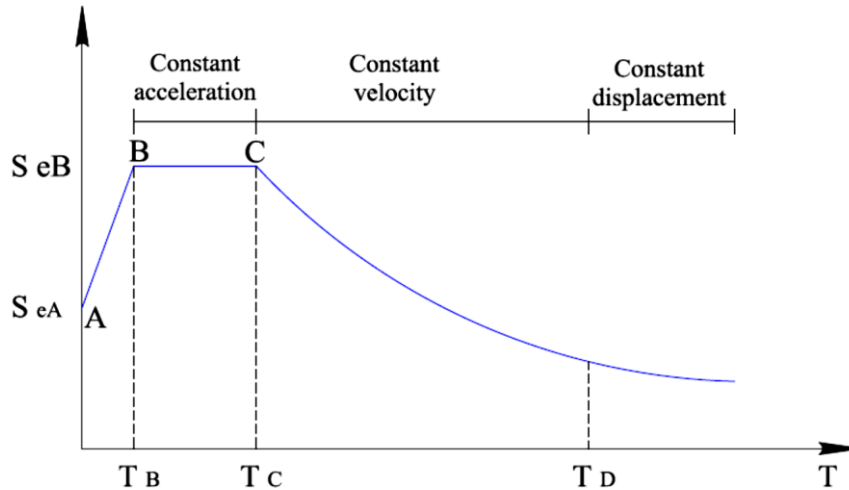
Figure 6-3 Typical Shape of Elastic Design Spectra

In this figure, T signifies periods of the structure, S_{eA} and S_{eB} denote the elastic design spectra corresponding to points A and B on the acceleration response spectrum axis, T_B and T_C are the lower and the upper bands of the period of the constant spectral acceleration part and T_D is the period value that specifies the start of the constant displacement response range of the spectrum. The window of $T_C - T_D$ period is the constant velocity part. EC8 recommends two types of design response spectra (Types 1 and 2) without considering the deep geological characteristics of the site. However, EC8 states that "If the earthquakes that contribute most to the seismic hazard defined for the site for the purpose of probabilistic hazard assessment have a surface-wave magnitude, Ms, not greater than 5.5, it is recommended that the Type 1 spectrum is adopted". Otherwise, the Type 2 response spectrum is used. Many crucial differences are noted between the definitions in EC8 and ASCE. For the response spectrum characteristics T_B, T_C and T_D in EC8 and ASCE, the values of characteristics ordinates of site class $A - D$, S_1 and S_2 in EC8 are in tabular form according to the earthquake type (1 or 2) [EN 1998- 1/Table 3.2], whereas ASCE supplies a set of equations which rely on the mapped acceleration parameters S_S and S_1 (see Table 6.1). In Table 6.2, the soil factor S defined in EC8 is controlled by site class and η (the damping correction factor). In ASCE, this factor depends on site class conditions in addition to the zonation factors S_{MS} and S_{M1}. EC8 defines the parameters β and q as the lower bound factor for the horizontal design spectrum and the behaviour factor, respectively. The recommended value for β is 0.2, although different countries may use diverse values as per their National Annex. Major contrasts are also noted between the seismic design provisions of ASCE and EC8. ASCE does not apply seismic zone phenomena to produce the design

240

earthquake ground motion or establish additional design requirements and structural limitations. Alternately, ASCE uses seismic design category as the mechanism for demanding design restrictions, detailing requirements and setting structural limitations. The seismic design category assigned to a building is essential due to its impacts on the permissible analysis procedures, the applicability of structural redundancy, the method of lateral load distribution, the limitations on structural systems, the applicability of load combinations and the requirements for ductile detailing.

The design ground motion parameters S_{Ds} and S_{D1} are used rather than seismic zone factors which are the ordinate values that equal to 5% damped design spectral response accelerations at short periods and one-second period, respectively. S_{Ds} is the leading factor in computing the design upper-bound base-shear value, i.e. the plateau-top branch of the design spectrum. S_{D1} characterises the descending component or the period-dependent part of the design spectrum. These two parameters are evaluated from the mapped spectral response accelerations prepared for a distinct zone condition. In general, their values are equal to two-thirds of S_{Ms} and S_{M1} which represent the soil modified spectral response accelerations at the short period and one-second period, respectively. The values of S_{Ms} and S_{M1}, are computed by multiplying the mapped spectral acceleration parameters S_s and S_1 by the acceleration-related soil factor F_a and the velocity related soil factor F_a, respectively. F_a is defined over the low period range (T = 0.1–0.5 sec), whereas F_v is defined over a mid-period range (T = 0.4–2 sec). These two site parameters are developed using observational and analysis-based approaches (Dobry *et al.*, 2000). Generally, an important concept relating to the design of response spectrum as an earthquake design requirement is converting the computed elastic response spectrum to inelastic design response spectrum by multiplying by the behaviour factor in EC8 (q) and basing on the experience in practice and observational approaches. The engineer's recommendation 2⁄3 factor in ASCE (for economic reasons) led this standard to allow for a reduction factor of 2/3. EC8 prescribes different behaviour factors. The maximum allowable behaviour factor takes into account the type of structural system, regularity in elevation and prevailing failure mode in the systems containing walls.

Table 6.1 Period Boundaries of Elastic and Inelastic Response Spectra Defined in ASCE and EC8

Code	T_B	T_C	T_D	T_L
ASCE	Controlled by site class and earthquake zone. In addition, for seismic zone 4 it also depends on the near source factors.	Defined depending on ground types and earthquake zone	Section 11.4.5 — Design Response Spectrum figures	$T_L = T_D$ Section 11.4.5 — Design Response Spectrum figures
	$T_B = 0.2\frac{S_{D1}}{S_{DS}}$	$T_C = \frac{S_{D1}}{S_{DS}}$		
Eurocode8	For Type-1 the values of TB corresponding to A, B, C, D and E ground types can be taken 0.15, 0.15, 0.20, 0.20 and 0.15, respectively.	For Type-1 The values of TC corresponding to A, B, C, D and E ground types can be taken 0.4, 0.5, 0.6, 0.8 and 0.5, respectively.	It is equal to 2 for Type-1	4 sec
	For Type-2 the values of TB correspond-ding to A, B, C, D and E ground types can be taken 0.05, 0.05, 0.10, 0.10 and 0.05, respectively.	For Type-2 The values of TC corresponding to A, B, C, D and E ground types can be taken 0.25, 0.25, 0.25, 0.3 and 0.25, respectively.	It is equal to 1.2 for Type-2	4 sec

Table 6.2 Elastic and Inelastic Design Response Spectra (S_e and S_e) According to ASCE and EC8

Code	$0 \leq T \leq T_B$	$T_B \leq T \leq T_C$	$T_C \leq T \leq T_D$	$T_D \leq T \leq T_L$
ASCE Elastic	$S_e = S_{MS}\{0.4 + 0.6\frac{T}{T_B}\}$	$S_e = S_{MS}$	$S_e = \frac{S_{M1}}{T}$	$S_e = \frac{S_{M1}\,T_L}{T^2}$
ASCE Inelastic	$S_d = \frac{2}{3}\,S_{eA}$	$S_d = \frac{2}{3}\,S_{MS}$	$S_d = \frac{2}{3}\cdot\frac{S_{M1}}{T}$	$S_d = \frac{2}{3}\cdot\frac{S_{M1}\,T_L}{T^2}$
EC8 Elastic	$S_e = a_g \cdot S\left[1 + \frac{T}{T_B}\cdot(\eta\cdot2.5-1)\right]$	$S_e = a_g \cdot S \cdot \eta \cdot 2.5$	$S_e = a_g \cdot S \cdot \eta \cdot 2.5\,\frac{T_C}{T}$	$S_e = a_g \cdot S \cdot \eta \cdot 2.5\,\frac{T_C\,T_D}{T^2}$
EC8 Inelastic	$S_d = a_g \cdot S\left[\frac{2}{3} + \frac{T}{T_B}\cdot\left(\frac{2.5}{q}-\frac{2}{3}\right)\right]$	$S_d = a_g \cdot S \cdot \frac{2.5}{q}$	$\begin{cases} S_d = a_g \cdot S \cdot \frac{2.5}{q}\cdot\left[\frac{T_C}{T}\right] \\ \geq \beta \cdot a_g \end{cases}$	$\begin{cases} S_d = a_g \cdot S \cdot \frac{2.5}{q}\cdot\left[\frac{T_C\,T_D}{T^2}\right] \\ \geq \beta \cdot a_g \end{cases}$

6.2.2.1. Code design spectrum

Many seismological and geological parameters influence the shape of the design response spectrum. To better understand these parameters, a number of studies have classified and discussed the shape of the design response spectrum in terms of earthquake magnitude, source-to-site distance, site classification and fault type effects. Damping ratio and fundamental period are other parameters affecting the response spectrum. Ground motion is generally represented in the form of acceleration, velocity or displacement response spectrum.

Many empirical studies have confirmed that ground motion at a particular position is correspondingly affected by the depth of the geological sediments which is also known as 'deep geology' below the surface soil layer (Sokolov & Wenzel, 2014) and (van Lanen & Mooney, 2007). To achieve a correct design response spectrum which can predict real earthquake impacts, these geological aspects must be considered when developing the design response spectrum. The relevance of geological data, such as source-to-site distance, is not mentioned or even recommended as such data is defined per country or region. This parameter seriously influences the peak acceleration and frequency content of a strong ground motion. The properties of ground motions are inherently different for diverse source-to-site distance ranges. Hence, code definition of the design response spectrum based on the surface-wave magnitude is rather rough and imprecise. The elastic response spectrum produced by EC8 is a scaled spectrum and is developed as a function of the design ground acceleration (a_g) for a ground of site class A. The enlargement of the ground motion amplitudes for X times is considered indirectly. In addition to this increase in the earthquake magnitude, the motion frequency content changes. Therefore, in severe earthquakes, much energy and then long period ordinates are generated. An empirical equation is provided in EC8 to compute reference PGA a_{gR}, with reference to source-to-site distance, the magnitude of the earthquake as a direct parameter and deep geology as an embedded parameter (see Eq. (6.1)).

$$log\ a_g = -1.48 + 0.27\ .M - 0.29 \log R \qquad (6.1)$$

Where M is the magnitude of the desired earthquake, and R is the epicentre distance. This expression is valid for 4 < M < 7.3 and 3 km < R < 200 km perimeter condition. Accordingly, the EC8 hands the authority of specifying seismic zonation over to the National Jurisdiction. National site conditions are defined for several zones according to

National Annex, and the common classification in those slandered is the soil investigations made particularly for every site location. The seismic amplification in more or less stiff soil layers affects the characterization of the configuration of response spectrum. That is, soft soil deposits lead to high amplification and, consequently, large soil class coefficients. However, all seismic standards are specified as an autonomous class for liquefiable soils. According to EC8, only one parameter controls the local seismicity, i.e. 'zero period acceleration', representing the reference PGA value a_g at bedrock. In ASCE provisions and through relevant detailed zonation maps, three essential parameters define local seismicity, i.e. ground accelerations (S_e) for the short, one-second and T_L spectral periods.

The EC8 spectral amplitude is scaled with respect to site class (S), the vibration period of a linear single-degree-of-freedom of the structure (T), importance factor (γ_I) and damping correction factor(η). The behaviour factor (q) replaces the importance factor (γ_I). The lower bound factor for the horizontal design spectrum ($\beta_{l.b}$) is added to the aforementioned parameters to develop the inelastic response spectrum (see Figure 6-1 and Figure 6-2). Seismic ground response characteristics are generally defined as a function of 'site effects' that is necessarily reflected in seismic code provisions. The appropriate elastic response spectrum definition according to soil categories and seismic intensity is the uncomplicated method to take site impacts into account for engineering projects and micro-zonation studies. Current seismic codes (i.e. ASCE and EC8) basically authorise the important aspect of site effects and attempt to incorporate their influence either through a constant amplification factor that entirely relies on soil class or other factors such as earthquake intensity and near-field conditions. Although site classification has different approaches, the basic idea of the mean value of shear wave velocity of the first 30 meters is considered a sound parameter for site classification over the last few decades. The estimation of V_{s30} is based entirely on a simplified hypothesis. Thus, it may prompt erroneous results, specifically in deep foundation soil systems or sudden stiffness variation between the soil layer at 30 m and the bedrock layer [(Pitilakis, Gazepis & Anastasiadis, 2004), (Doğangü & Livaoğlu, 2006), (Yue & Wang, 2009), (Bulajic, Manic & Ladjinovic, 2012), (Milev, 2016), and (Anand & Satish Kumar, 2018)]. Several studies on different sites, where the dynamic soil profile along the site surface to the bedrock is adequately known, have reported that the linear approach which assesses the amplification functions may be given sufficient consideration for many types of soils in

case of low- to medium-intensity earthquakes, i.e. <0.2 g. However, this approach completely ignores the soil nonlinearity, which may become critical in circumstances of strong motions and depends on soil type, stiffness, and depth. From this perspective, current seismic design codes (EC8 and ASCE) ignore the influence of geological depth and account for merely the average value of the shear wave velocity over the 30 m (V_{s30}) of a site profile as the primary parameter for site classification.

6.2.2.2. Displacement response spectra

As mentioned in Chapters 2 and 3, Gűlkan and Sözen (1974) developed the substructure method that allows the use of an elastic displacement spectrum for earthquake design. Employing the displacement capacity of an inelastic system—base shear—as seismic design remains forced though. Despite the shortcomings of this procedure, it has been most widely used in seismic codes until recently. However, the recognition of the insufficient correlation between transient inertial forces that induced earthquake shaking and structural failure has driven the development of displacement-based approaches. The first practical methodology to compute the design elastic displacement spectrum S_{De} is converting the code absolute acceleration elastic design spectrum S_e through the pseudo-spectral relationship (see Eq. (6.2)) (Bommer *et al.*, 2001).

$$S_{De}(T) = \frac{S_e(T)}{\omega^2} \tag{6.2}$$

According to the current seismic codes, this transformation does not produce reliable displacement ordinates at extended periods relevant to the displacement-based design ((Bommer & Elnashai, 1999), (Faccioli, Paolucci & Rey, 2004)). It can be applied only for periods that do not exceed 4 sec.

6.2.3. Classification of structures in different importance levels

EC8 and ASCE note that classifying the structures according to importance levels is essential. This classification implies a reliability differentiation according to the estimated risk and consequences of failure. However, the reliability differentiation is directly defined by multiplying importance factor (γ_I) to compute seismic forces. Four importance class values are assigned in EC8 (0.8–1.4). Five risk categories are identified in ASCE/SEI 7/16, with the corresponding importance factor (γ_I) varying between 1 and 1.5. In most seismic excitation problems, the structures do not behave in a purely elastic way. Structures are presumed to behave nonlinearly, develop considerable deformations and dissipate a substantial amount of energy. Thus, they should be designed in such a way

that ensures the essential capacity of energy dissipation and degree of ductility. The transformation of the elastic response spectrum may be considered to design response spectrum, in which the required ductility is implied. On account of these reasons, the reduction factors are defined in the current seismic codes as a function of structural systems and materials. The reduction factor (RF) in ASCE and in EC8 are expressed as a function of the ductility degree, that is, instant medium and high ductility according to EC8 and ordinary, intermediate and appropriate detailing needs according to ASCE. The numerical value of these coefficients is commonly established empirically according to past practice and expert engineering judgment.

6.3. Soil–structure interaction analysis

To meticulously examine the SSI problem in seismic analysis, the dynamic properties of structure, foundation and soil must be understood. The dynamic properties of a structure can be defined through the fundamentals of structural dynamics and soil dynamics properties. Soil dynamic properties highly depends on wave propagation through the soil medium. Therefore, the comprehension of the concept of wave propagation through the soil medium is crucial to understand ground motion modifications due to soil characteristics. Moreover, the understanding of the vibration characteristics of the soil deposit during wave propagation is crucial to the examination of soil resistance using multi-step methods. The concepts mentioned above are essential to clearly define the mechanism of SSI through the two main contributions that occur in earthquake excitation.

6.3.1. Description of the case study

As shown in Figure 6-4 (a, b and c), the main frame of a residential high-rise steel frame building already studied in literature (Fu, 2010) is used as the case study for this exploratory research. The structure replicates 20 storeys with 7.5 m grid dimensions. The total height of the aerial part of the building is 60 m, and the height of each floor is 3 m. The size of the structure plan is 23 m × 23 m. The cross bracings along the middle span of the structure are provided to contribute the maximum lateral stability. However, a British circular hollow section CHCF (273 × 12.5) is used for such a purpose. As a 2D study, the concrete slab is not simulated; instead, the transformation of loads to the beams are taken into account. Table 6.3 lists the necessary information of all the sections mentioned above in addition to the section details of the piles. The structure is designed according to the full structural framing of typical high-rise buildings in the current construction industry with full composite action of gravity and live, dead and seismic load

according to EN 1998-1. In particular, the design PGA is 0.32 g, the damping ratio (Rayleigh damping) of the structure is presumed equivalent to 5%, the design dead load Q_d is $3.5\ kN/m^2$, and the design live load Q_K is $2.5\ kN/m^2$. Pile–raft foundation includes those supporting the superstructure, in which bored pile is used, with a diameter D of 800 mm and a length of 36 m. The dimension of the raft foundation is 28.6 m × 28.6 m, and its thickness is 1.5 m. The supporting layer is assumed as the bedrock layer. The piles for the proposed structure are required to support the characteristics of the permanent vertical load of $G_k = 38824\ kN$ and the characteristics of the variable vertical load of $Q_k = 25806\ kN$. These piles are designed according to EC8 provisions. The design procedure is based on the available information of soil properties.

Table 6.3 Structural Details of the Case Study

Category	Location	Serial size	Depth	Width	Web	Flange	Root radius	Dep. btw. fillets	Mass
Symbols			D	B	t	T	r	d	M
Units			mm	mm	mm	mm	mm	mm	kg/m
Columns	G–6th	[UC 356 × 406 × 634]	474.6	424.0	47.6	77.0	20.0	280.6	933.9
	7th –13th	[UC 356 × 406 × 467]	436.6	412.2	35.8	58.0	20.0	280.6	467.0
	14th–19th	[UC 356 × 406 × 287]	393.6	399.0	22.6	36.5	20.0	280.6	287.1
Beams	All beams	[UB 533 × 210 × 29]	533.1	209.3	10.1	15.6	12.7	476.5	92.10
Category			Outside diameter			Wall thickness			
Symbols			R			w			
Units			mm			mm			
Bracings	Bracings	[CHS 273 × 121.5]	273.0			12.5			80.30
Piles	All Piles	Welded Pipe	800.0			22.0			422.1
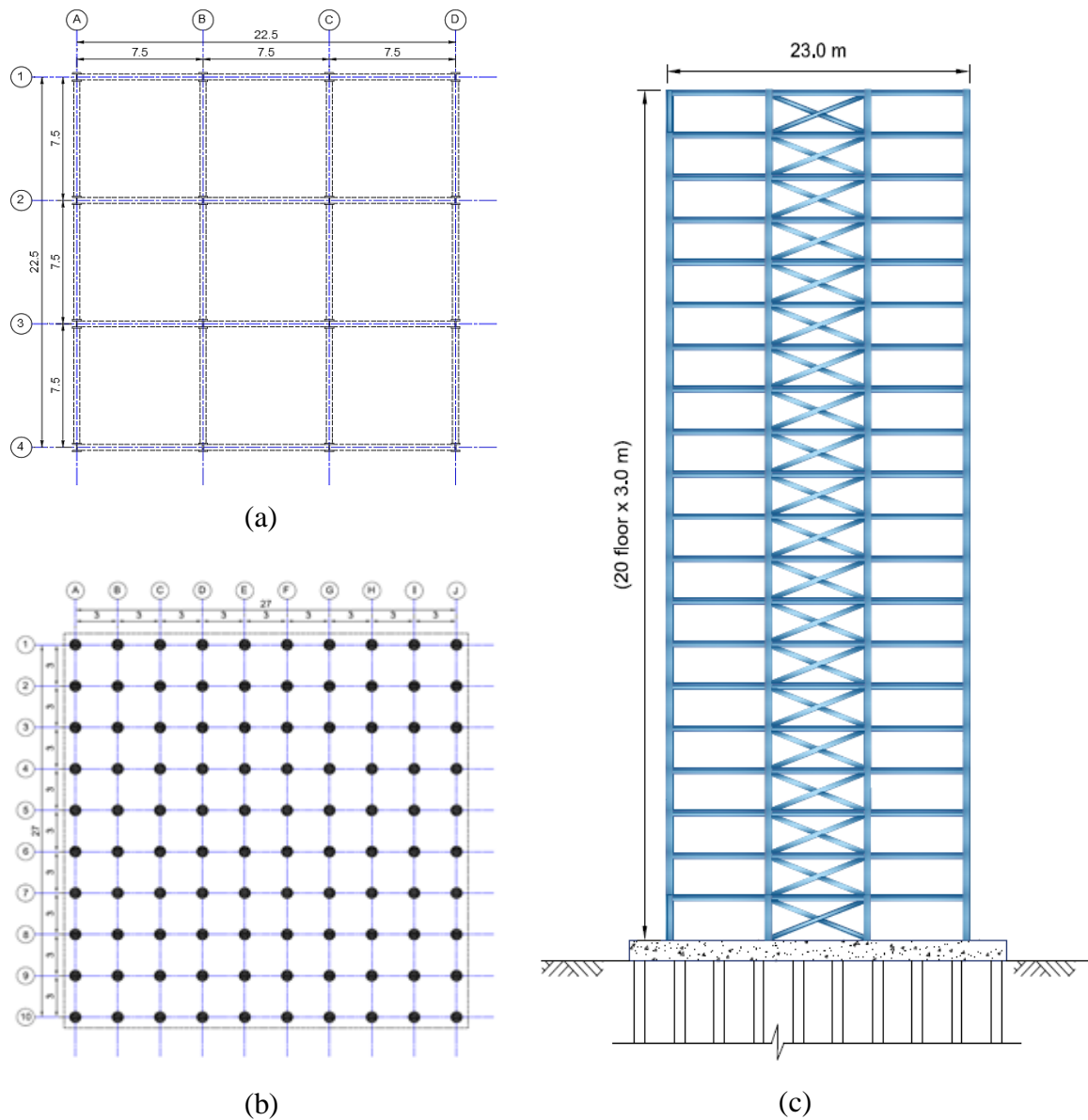
Figure 6-4 Layout of Case Study: (a) Layout of Beams and Columns, (b) Layout of Piles, (c) Main Frame of the Case Study

6.3.2. Methodology

Choosing an appropriate methodology is one of the most challenging and critical decisions in this study. Identifying a proper and capable technique of employing data collection to meet the objectives is crucial in this kind of study. Answering all aspects of the research question is difficult when only a single methodology, i.e. qualitative or quantitative, is adopted. To highlight the vague provisions that concern dynamic SSI in clay soil aspects and manipulate the study environment, longitudinal and cross-sectional approaches are adopted. The author perceives the sequential analysis method appropriate for considering the consequences of the geostatic, static and seismic loads in the case of

249

SSI analysis. Two circumstances are simulated, (*i*) the model with the consideration of the SSI and (*ii*) the situation of only the superstructure exposed to static and dynamic excitation. Several characteristics are measured, i.e. natural vibration characteristics, horizontal absolute acceleration response, storey drift response, for both circumstances by employing ASCE and EC8 design response spectrum standards as input motions. The results of these two different provisions are then compared. According to the basic definition of the cross-sectional study approach, the two standards can be compared at a single point of condition (design response spectrum) concerning the structural behaviour of the two different systems and according to the results of the aforementioned characteristics. Consequently, the longitudinal approach enables the detection of the effect of the developments or changes in input data. In particular, the time history input data result in different fashions for varying wave velocity values owing to the diverse in-situ geological properties of the same earthquake event. The longitudinal approach extends the boundary of explorer beyond a single target situation of standard application by establishing sequences of event case. The simulations in this research are divided into two phases according to analysis type (see Figure 6-5). Phase I represents the frequency analysis for computing the structural modes of the systems. The Rayleigh damping factor is calculated, by which viscous damping is considered in the phase II analysis. Phase II is illustrated by developing three main analysis steps, i.e. geostatic, static and dynamic steps. The geostatic step is generally used as the first step. In such geotechnical analysis problems, only the soil body force is employed. The considerable force and the initial stresses should precisely equilibrate and establish minimal soil displacement. Abaqus/Standard approach for developing the initial equilibrium is employed in which the initial stresses are unidentified but only for a number of elements and materials. The pore water pressures vary linearly with depth. The initial effective stresses are appropriately stated according to the total stresses. The first loading stage is the static step. The application of gravity loads, which are assumed to be static and uniform in additional to uniformly dead load and live load according to the EC8 combination set. The third step, which is the second loading step, is the dynamic analysis step. The time history input data are for two earthquakes events (1989 Loma Prieta and Cape Mendocino earthquakes), and they are modified according to the design response spectra of ASCE and EC8. The input data are applied at the bottom of the clay soil (at the bedrock) in the case of SSI analysis. The modified input motions are applied at the base of superstructure in the case of without SSI analysis. The input modified motion that resulted from using

the SeismoSignal and SeismoMatch software depends on shear wave velocity. Different acceleration time histories are resulted from the same design response spectrum according to the shear wave velocity value of the original motion seeds which are used to create the matched time histories. Thus, the shear wave velocity parameter is taken into account by applying those different time histories to examine the effect of geological properties. Analytical analyses are developed to validate the results of both geostatic and static steps. In many studies on pile–soil–structure interaction, the fundamental period and damping ratio of structures may be lengthened when SSI effects are considered. Therefore, the base shear force and storey drift response of the structure can be reduced according to the response spectra recommended by ASCE and EC8.
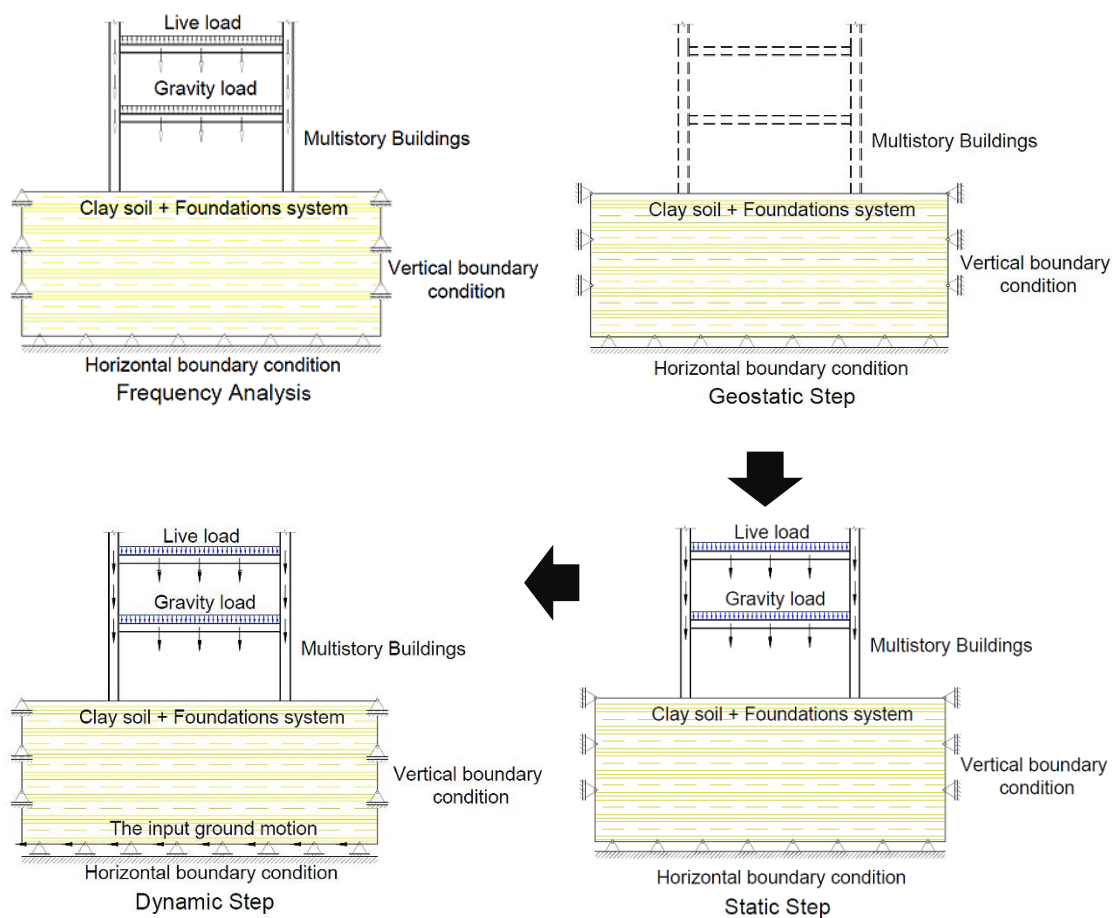
Figure 6-5 Schematic Demonstrating all Stages of Nonlinear Elastoplastic Analysis Simulations

In other studies, SSI effects are satisfied in the code specifications only when the structural response is dominated by the first mode (natural frequency of the system according to the code provisions). However, considerable distinctions can be observed when the impact of higher modes is accounted for. The structural response may increase

251

in some storeys; consequently, the code provisions regarding SSI do not provide safety approach consistently. Several questions remain unanswered at present concerning the pile–soil–structure interaction problem on account of its complexity. Although the structure and soil may operate in plastic range during strong motions, most of the SSI studies have anticipated the elastic systems. Moreover, a number of studies have involved elastoplastic behaviour, utilizing either Mohr–Coulomb model or Drucker–Prager criterion to simulate the soil constitutive relationship which are appropriate for the monotonic loading simulation. Consequently, substantial flaws may be developed in case of dynamic loading like seismic excitation.

6.3.2.1. Numerical model

When the SSI system is a half-infinite space, the finite element analysis method becomes a critical approach for such a finite region analysis. To simulate the horizontal infinity of the system, the continuity of the soil must be cut off at a certain position. The free edges should be replaced by an artificial boundary condition despite the availability of many typical kinds of artificial boundaries, such as cut-off boundary, viscous boundary, penetrating boundary and boundary element. Most of them are only suitable for frequency domain analysis. To deliver a reliable solution for the nonlinear analysis problems in the case of time domain analysis, an outstanding approach is generating the soil boundary of the principal region as far as possible.

One problem emerges here which is the effects of the free boundary. To eliminate this impact, (Zhang, 2006) proposed extending the horizontal direction of the soil to around five times the length of the principal region. From this perspective, free boundary conditions are adopted in the SSI model. Accordingly, the geostatic and static steps uses a free boundary in the vertical direction and constrained boundary in the horizontal direction. This arrangement is in reverse for the frequency and dynamic steps. The boundary conditions for the base of the model, which is the base of clay soil presumed as the surface of the bedrock, are managed as follows: (i) symmetry/anti-symmetry/encastre for the linear perturbation-frequency step, (ii) fixed in horizontal and vertical directions for geostatic and static steps and (iii) displacement and acceleration/angular acceleration boundaries for seismic analysis step. Fixed mechanical displacement in the vertical direction and free mechanical displacement in the excitation in the X-direction represents the first boundary in this case (U1).
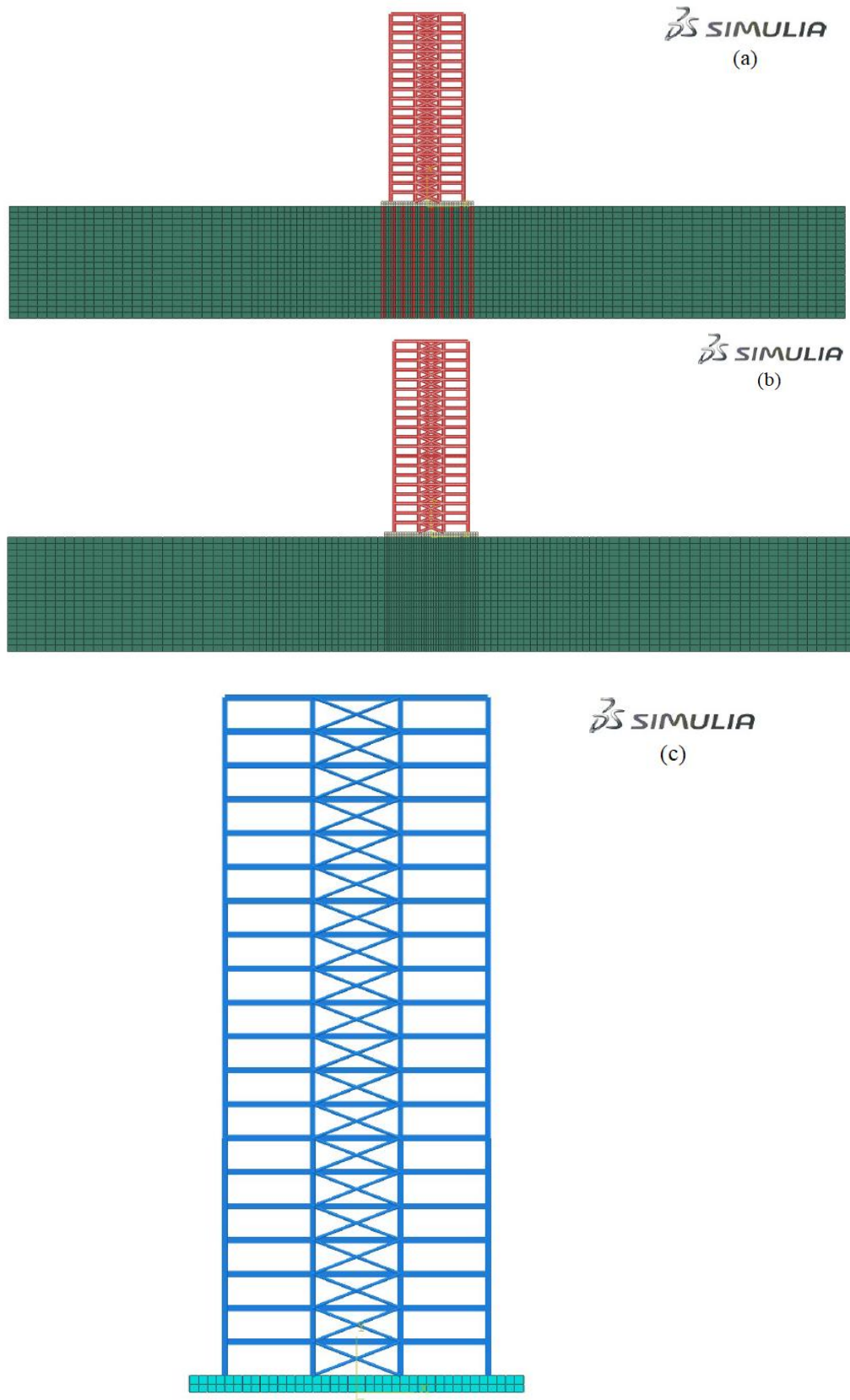
Figure 6-6 Numerical Model; (a) With SSI and Piles, (b) With SSI and WithoutPiles, (c) Without SSI

The moving boundary is illustrated by applying the acceleration/angular acceleration in the direction of excitation. Standard 2D beam–column, stress and linear element types

with reduced integration are used to simulate the piles and superstructure. Standard, linear and shell element types with reduced integration are employed to simulate the soil. The pile–soil interaction is simulated as 'embedded', and beam–column and superstructure–foundation connections are simulated using 'Tie' command. Mesh sensitivity is used to optimise a reliable mesh size (see Figure 6-6).

6.3.2.1.1. Methodology of developing seismic input data

For a reliable comparison between the two standards, a particular location and two specific earthquake events are carefully chosen. As previously mentioned, the second step in this simulation is the nonlinear implicit dynamic analysis wherein acceleration time histories are applied to the base of the structure which represents the earthquake event. The main objective of this study is to achieve a reliable comparison between ASCE and EC8 seismic code provisions that is accomplished only by applying an appropriate input motion. To generate a correct SSI analysis target, an accurate and sophisticated methodology of choosing, modifying and matching the input motion data should be followed. This methodology consists of the following three steps:

- developing the design target spectrum according to ASCE and EC8 provisions,
- selecting the seed motions according to the earthquake database [peer website]
- matching the selected seed motions by following the matching procedure according to the design target spectrum using SeismoSignal and SeismoMatch software, then choosing the best-matched input data

To investigate the structural response for the input earthquake data developed and matched according to aforementioned steps, two real earthquake events are chosen, i.e. 1989 Loma Prieta and 1992 Cape Mendocino earthquakes. The first two time histories to be applied at the base of the superstructure are developed considering that the clay layer filters the wave. Another set of earthquakes are applied at the base of the SSI system, i.e. bedrock. In this case, the modification is applied according to bedrock type and geotechnical and geological site properties. Figure 6-7 and Figure 6-8 show the earthquake properties for the two aforementioned selected motions. Previous studies have been unable to consider the effect of geological aspects based on site soil properties and site class classification in choosing and matching time histories.
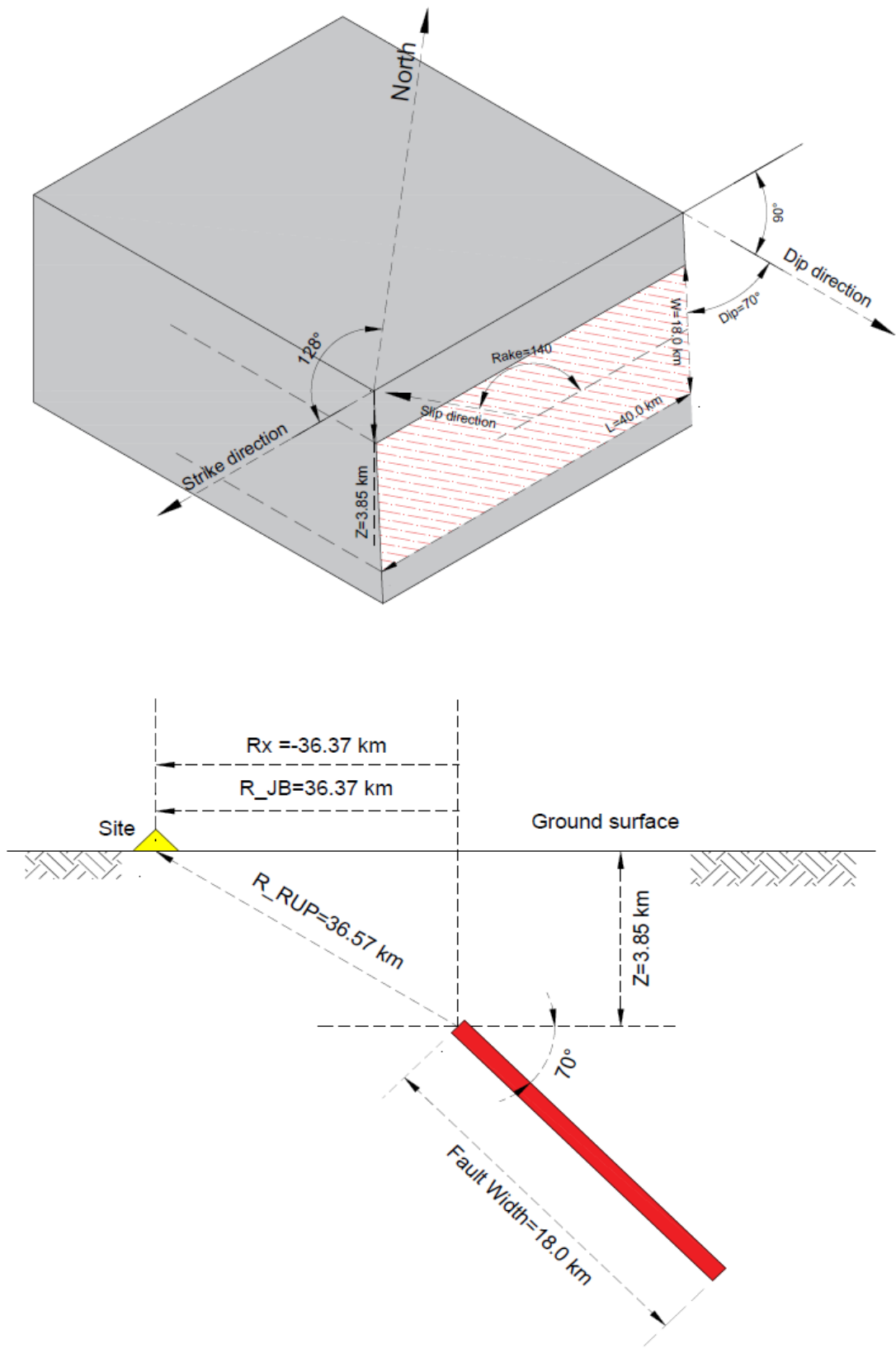
Figure 6-7 Loma Earthquake, Normal Oblique Faulting, Footing Wall Site
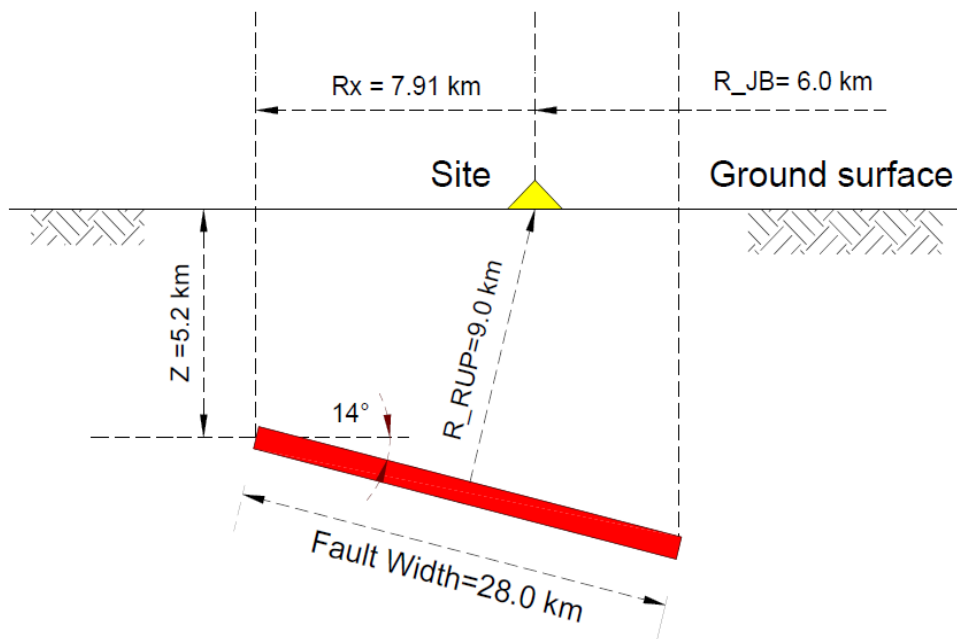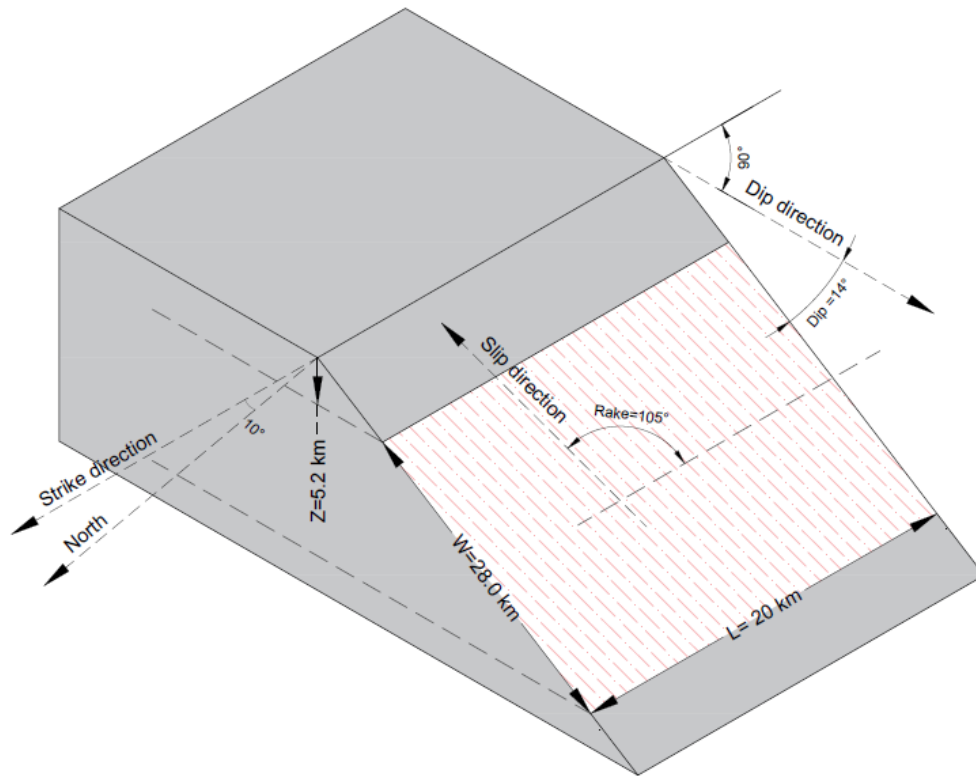
Figure 6-8 Cape Mendocino Earthquake, Normal Oblique Faulting, Hanging Wall Site

When the details regarding site soil properties are insufficient, the main concern is achieving a close matching between design and code response spectra without considering most of the geological and geotechnical aspects.–The author believes that ignoring some of these effects may bring about misleading results. To assign the ground motion records from the available database, several important characteristics must be

identified accurately. The principal characteristics of a reliable ground motion seeds are listed below.

- $R_{\_JB}$ is the closest distance to surface projection of coseismic rupture (km). See Figure 6-7 and Figure 6-8 for illustration.

- $R_{\_Rup}$ is the closest distance to coseismic rupture (km).

- V_{s30} is the average shear wave velocity (m/s) over a subsurface depth of $30\ m$.

- $D_{5-95\ (sec)}$ is the event duration factor.

- Fault type depends on the site region of the fracture [site specification]. In general, according to specialised seismologist, two main fault categories are put forward in literature, and each category has subcategories (see Section 4.2 of Chapter 3). Dip slip fault has normal and reverse faults, and strike-slip fault has left lateral, right lateral and oblique faults.

- Initial scale factor (minimum, maximum) is a perilous and complicated factor due to insufficient identification and unwritten law provision concerning the selection of its minimum and maximum boundary. However, a practical initial scale factor window can be adopted from the recommendation of expert engineers as $\left(\frac{1}{n}, n\right)$ once the value of n can be started correctly from 2.

- Period window is often between $0.2T_N\ and\ 1.5\ T_N$). Researchers have attempted to develop a smooth response spectrum fall within the specified tolerance of the target spectrum. However, cultivating a perfect tolerance over the entire target spectrum is impossible. Therefore, much of the provisions focus on identifying and evaluating the period range of interest.

Eight time histories are matched from the US databases according to EC8 and ASCE provisions. Figure 6-9 to Figure 6-16 illustrate the design and matched response spectra as well as the acceleration time histories for all the input data. All time histories are processed to match the design response spectrum for a time period between 1 and 4 sec. The corresponding effect frequency window depends on the corresponding code design spectrum. Accelerograms are scaled to the design PGA. To examine the site effect for the same earthquake event, three different wave velocities are chosen for each code, i.e. $388.33\ m/sec, 517.06\ m/sec\ and\ 729.65\ m/sec$ for 1989 Loma Prieta earthquake and $378.95\ m/sec, 525.26\ m/sec, 566.26\ m/sec$ for 1992 Cape Mendocino earthquake. Table 6.4 lists the characteristics of the chosen earthquakes.
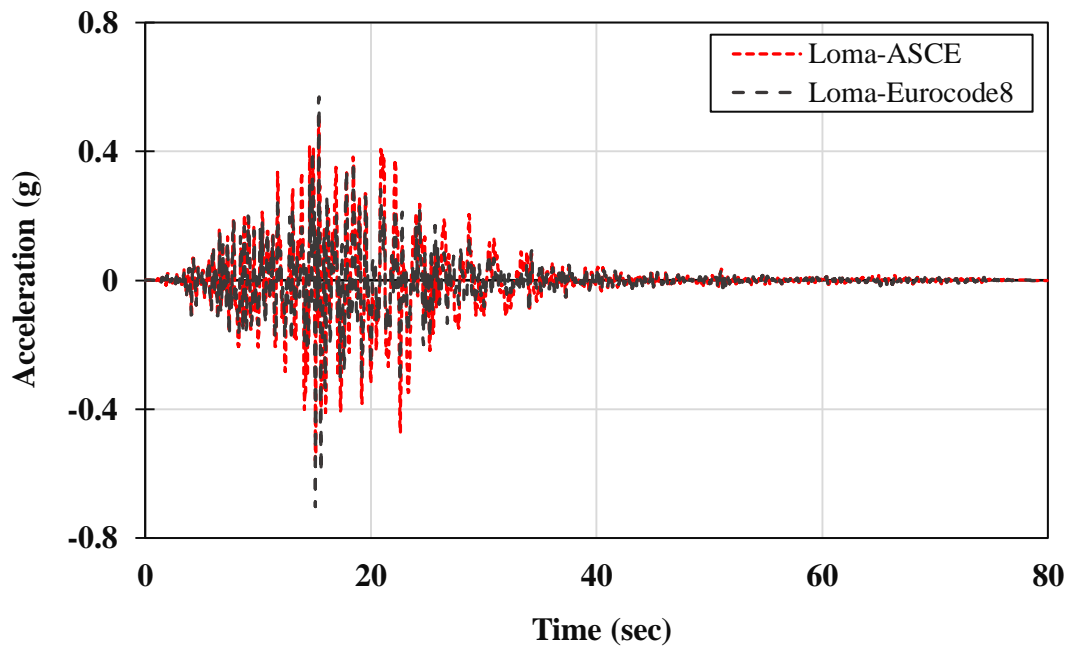
Figure 6-9 1989 Loma Prieta (Modified) Time Histories
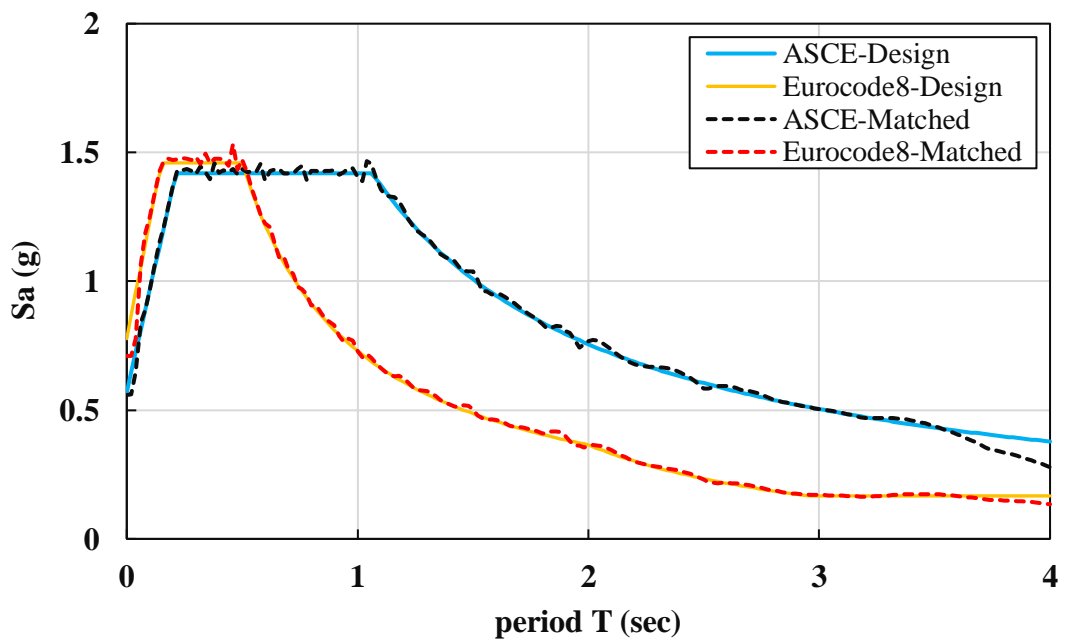
Figure 6-10 1989 Loma Prieta ASCE And EC8 Response Spectra
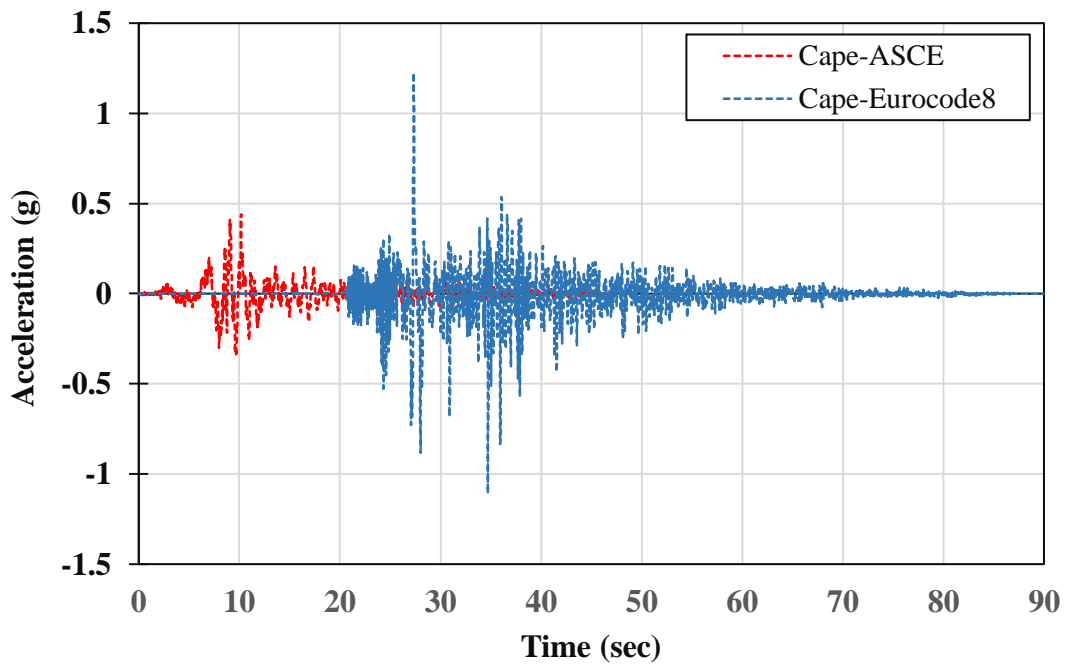
Figure 6-11 1992 Cape Mendocino (Modified) Time Histories
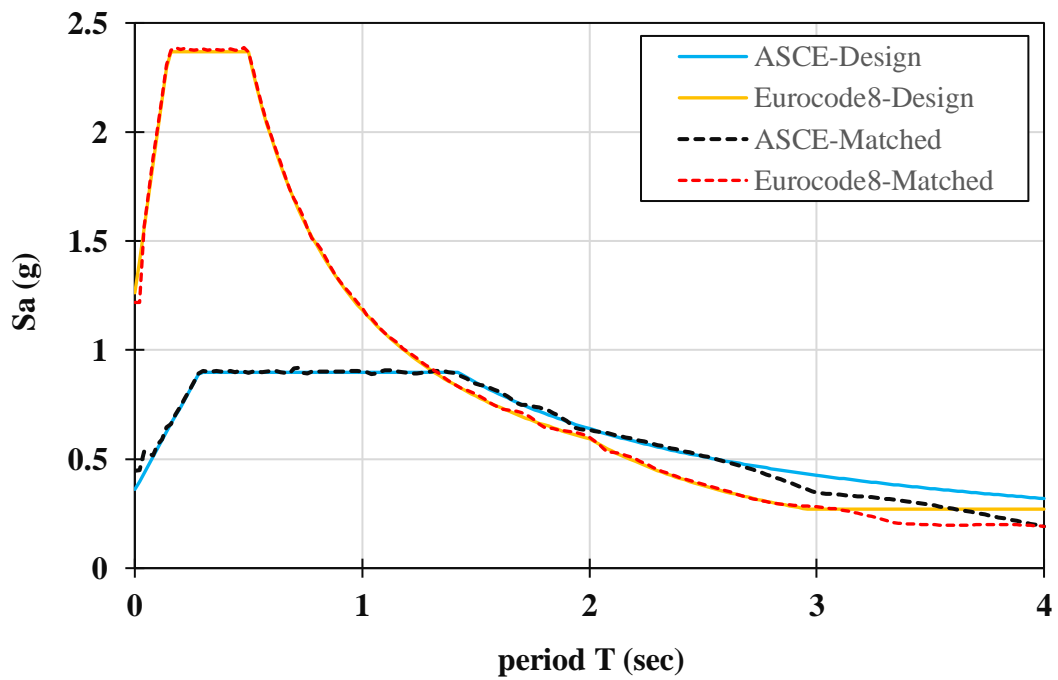
Figure 6-12 1992 Cape Mendocino ASCE And EC8 Response Spectra
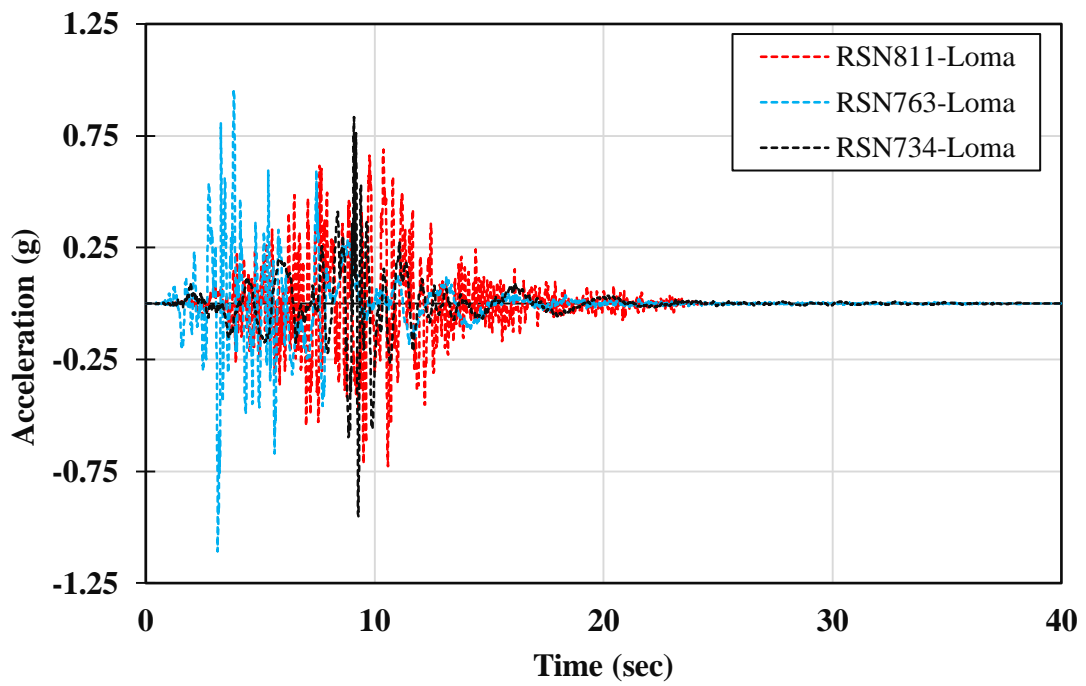
Figure 6-13 1989 Loma Prieta (Modified) Time Histories
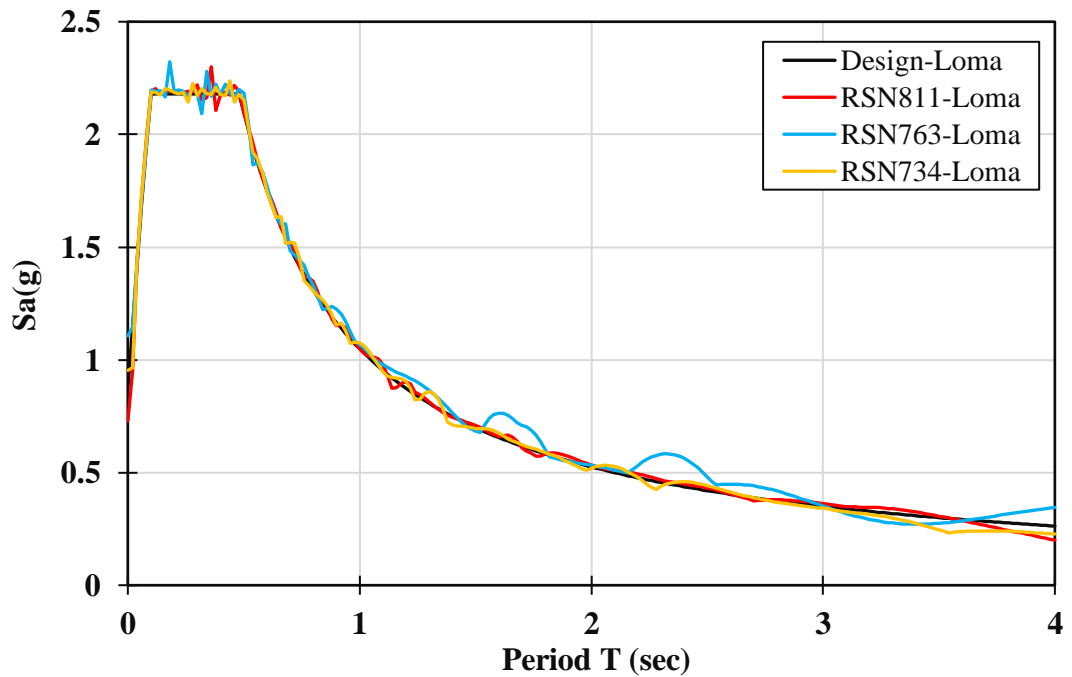
Figure 6-14 1989 Loma Prieta Design and Modified Response Spectra
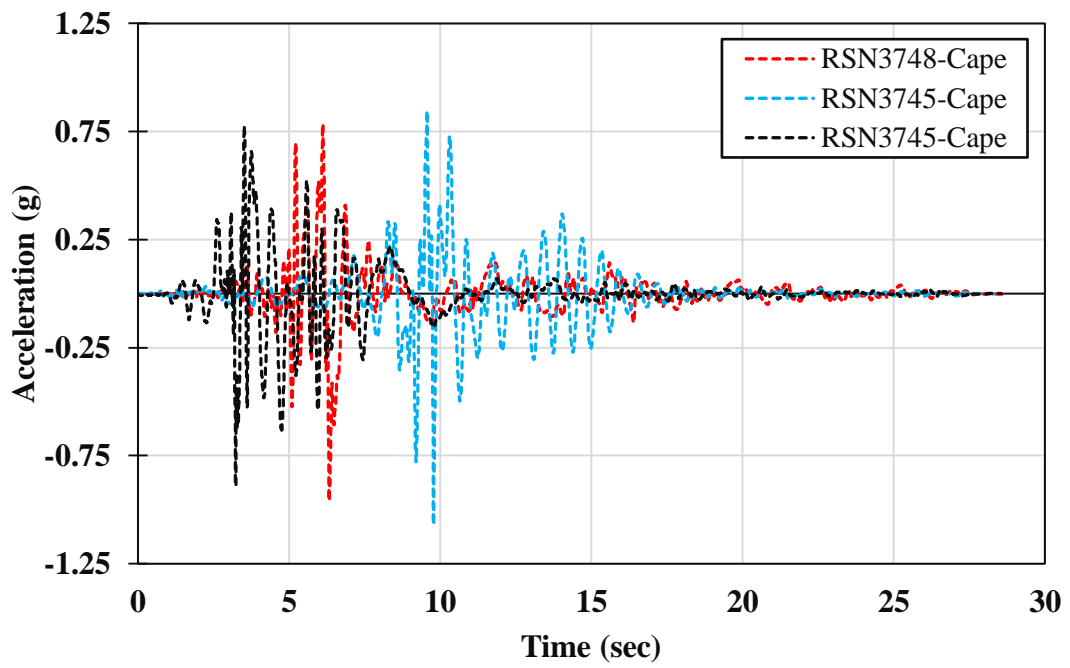
Figure 6-15 1992 Cape Mendocino (Modified) Time Histories
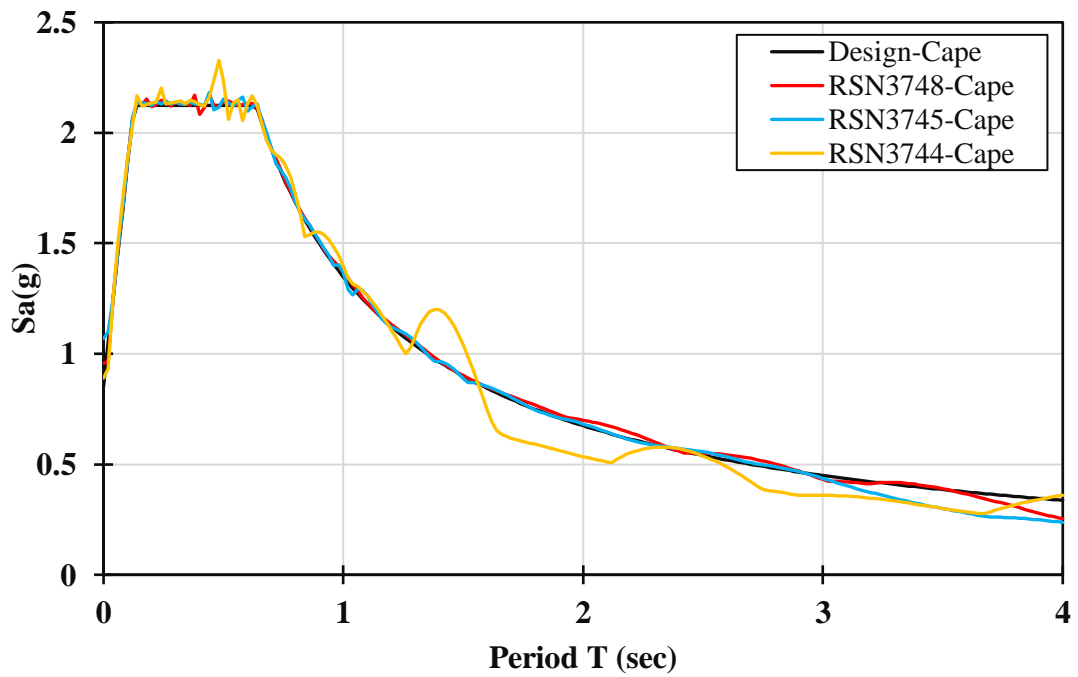
Figure 6-16 1992 Cape Mendocino Design and Modified Response Spectra

261

Table 6.4 Characteristics of Loma Prieta and Cape Mendocino Earthquakes

Characteristic	Units	Loma Prieta	Cape Mendocino
Strike angle	(degree)	128	350
Dip angle	(degree)	70	14
Rake angle	(degree)	140	105
Depth to top of fault rupture model	(km)	3.85	5.2
Fault rupture length (L)	(km)	40	20
Fault rupture width (W)	(km)	18	28
Fault rupture area	(km^2)	719.8	559.7
$V_S 30$	(m/s)	659.81	567.78
Fault type	$-$	*Normal/Oblique*	*Normal/Oblique*
Magnitude (Mw)	(M_W)	6.93	7.01
R_JB	(km)	36.37	11.44
R_ Rup	(km)	36.57	8.85
Damping ratio	$-$	5%	5%
Site condition	$-$	*Footing wall*	*Hanging wall*
R_X	(km)	-36.37	7.91
PGA	(m/sec^2)	0.028404 g	0.73876 g
Epicentre distance (R)	(km)	41.33	9.35
Hypocentre latitude	$(degree)$	37.0407	40.327
Hypocentre longitude	$(degree)$	-121.8829	-124.233
Hypocentre depth	(km)	17.48	9.5

6.3.2.1.2. Soil model

The engineering field chosen for this study lies in San Francisco Bay. The target prototype soil is San Francisco Bay mud, a marine clay whose index properties have ranges of values (Meymand, 1998a), and (Geotechnical Report, 2005). It is also a well-characterised soil that is the subject of a study whose findings are shown in Table 6.5. The table reflects the prototype parameters adopted for this research. The principal parameters of soil layers are also listed in Table 6.5, in which the shear velocity of strongly rock is greater than 300 m/s. As such, it can be considered as bedrock according to ASCE and EC8 codes. In the model, only clay soil over a strong rock layer is simulated. The total depth of the soil model is 36 m, and seismic acceleration is applied at the bottom of bedrock layer. The soil is simulated by solid elements with a length of 1 m in the principal region and by refined elements near to the pile region. The element length is

increased gradually far from the principal region, and the maximum length is 4 m. The critical state model for describing the behaviour of soft clay used in this study is Cam–Clay (CC). All aspects of the modified CC (MCC) are described in detail in Section 4.3 of Chapter 4. The characteristic properties of a model soil λ, κ, e_N and e_C are computed according to the prototype soil properties described in Chapter 4. However, the soil characteristics λ and κ are expressed as a function of soil consolidation parameters, compression index C_c and swelling index C_s; $\lambda = \frac{C_c}{2.3}$ and $\kappa = \frac{C_s}{2.3}$. The critical state line, which is parallel to the normal consolidation line in the $e - lnp'$ plane and is illustrated by the straight line starting from the origin with the slope equal to M, is computed in terms of internal friction angle $\emptyset'$, which is obtained from triaxial test results at failure (see Eq. (6.3)).

$$M = \frac{6 \sin \emptyset'}{3 - \sin \emptyset'} \tag{6.3}$$

The initial void ratio (e_N) is computed according to Figure 6-17. The β term which is a constant used to modify the shape of the yield surface on the 'wet' side of the critical state is given a value of 0.787 in this study. All soil properties used in this study are listed in Table 6.5.

Table 6.5 Prototype Soil Properties, (Geotechnical Report, 2005)

Property	Value
Saturated unit weight (kN/m^3)	14.77
Unit weight (kg/m^3)	1505.75
Natural water content (%)	90
Liquid limit (%)	88
Plastic limit (%)	48
Plasticity index (%)	40
Undrained strength (kN/m^2)	43
Coefficient of consolidation C_v (m^2/sec)	0.01–0.12
Wave velocity (m/sec)	160
Shear modulus G (kN/m^2)	28261.42
Young's modulus E (kN/m^2)	82000
Initial void ratio	1.496
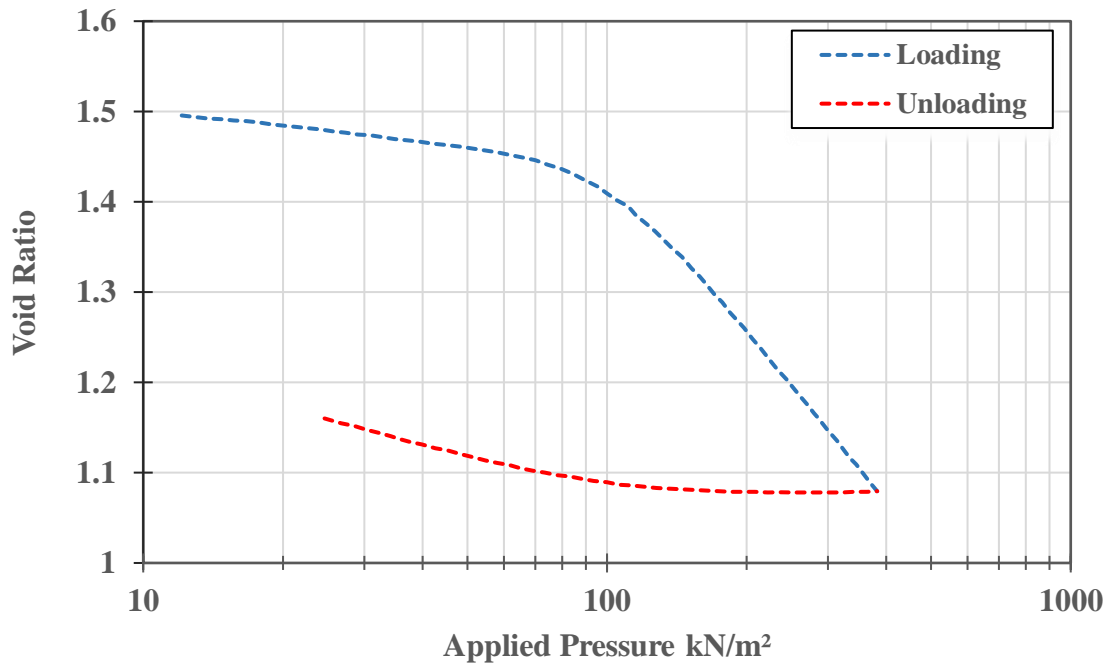
Figure 6-17 Void Ratio Versus Log Pressure for Constant Rate of Strain Consolidation, (Geotechnical Report, 2005)

6.4. Natural vibration characteristics

Vibration period is an essential factor in base-shear design methodology, and it is a critical parameter in defining the design response spectrum and consequently controlling the value of the base shear force. The methods permitted by EC8 and ASCE seismic design codes for designers to estimate vibration period must be reviewed for use in dynamic analysis. Based on this review, a comparison is carried out between the values in the two codes and other numerical model analysis which are considered the effects of SSI and pile group. An accurate assessment of the codes' formula is outlined. For the MCC constitutive model, hysteretic damping and viscous damping are included in the soil model. Hysteretic damping is involved in the restoring force, whereas viscous damping is considered by Rayleigh damping (proportional damping), as expressed in Eq. (6.4).

$$[C] = \alpha_M [M] + \beta_K [K] \tag{6.4}$$

Where α_M and β_K are mass and stiffness proportional damping coefficients, respectively. The damping ratio for different natural frequencies can be computed with Eq. (6.5).

$$\xi_i = \frac{1}{2} \left[\frac{\alpha_c}{\omega_i} + \beta_c \omega_i \right] \tag{6.5}$$

264

According to the orthogonality between system mode and damping matrix and the assumption of 5% damping for the system modes, the corresponding coefficients of Rayleigh damping are calculated by Eqs. (6.6) and (6.7).

$$\alpha_M = \frac{2\omega_i\omega_j}{\omega_j^2 - \omega_i^2}\left(\xi_i\omega_j - \xi_j\omega_i\right) \qquad (6.6)$$

$$\beta_K = \frac{2\left(\xi_j\omega_j - \xi_i\omega_i\right)}{\omega_j^2 - \omega_i^2} \qquad (6.7)$$

Where ω_i and ω_j are any two system modes' frequencies, and ξ_i and ξ_j are damping ratio at ω_i and ω_j, respectively. Codes provide empirical formulas to estimate the fundamental vibration period T of the structure. According to ASCE, the empirical formula is

$$T = C_t \cdot H^{0.75} \qquad (6.8)$$

where H is the overall aerial height of the building, and C_t is a numerical coefficient related to the lateral force-resisting system which is equal to 0.073 for this case study. EC8 recommends using the Rayleigh method which is the expression based on methods of structural dynamics to compute the time period value (see Eq. (6.9)).

$$T = 2\pi\sqrt{\frac{\sum_{i=1}^{n}(m_i \cdot S_i^2)}{\sum_{i=1}^{n}(f_i \cdot S_i)}} \qquad (6.9)$$

Where m_i are storey masses, f_i are horizontal forces, and S_i are displacements of masses caused by horizontal forces. The first six natural vibration periods, damping coefficients and the codes' natural vibration period of all three models are listed in Table 6.6.

The estimated period is very far from the result of the model without SSI. Given the assumption of a rigid base and disregard of the soil effects, the finite element model cannot estimate the natural periods. SAP200, in which the effect of soil is embedded and can be simulated by springs, is more practical than other software. Nevertheless, the data in Figure 6-18 indicate that the first natural period of the model without piles is close to the estimated values, but the natural period substantially decreases when the field effect is considered. The mode values of the model with SSI and piles seem realistic due to their gradual decrease. Many modes are attributed to the response of the SSI model. Figure 6-19 to Figure 6-21 show the first six modes for all studied circumstances.

Table 6.6 First Six Natural Vibration Periods and Factors of Rayleigh Damping

| Model | Natural vibration period (s) | | | | | | | | Damping coefficients | |
| | Models | | | | | | Codes | | | |
	1	2	3	4	5	6	EC8	ASCE	α_m	β_k
SSI-Piles	0.7957	0.7127	0.6655	0.5292	0.4978	0.4160			0.0684	0.03626
without piles	1.1215	0.5762	0.5206	0.4398	0.3122	0.2795	1.3251	1.5737	0.05613	0.04294
Without SSI	0.0778	0.0266	0.0145	0.0098	0.0083	0.0075			1.0820	0.00123
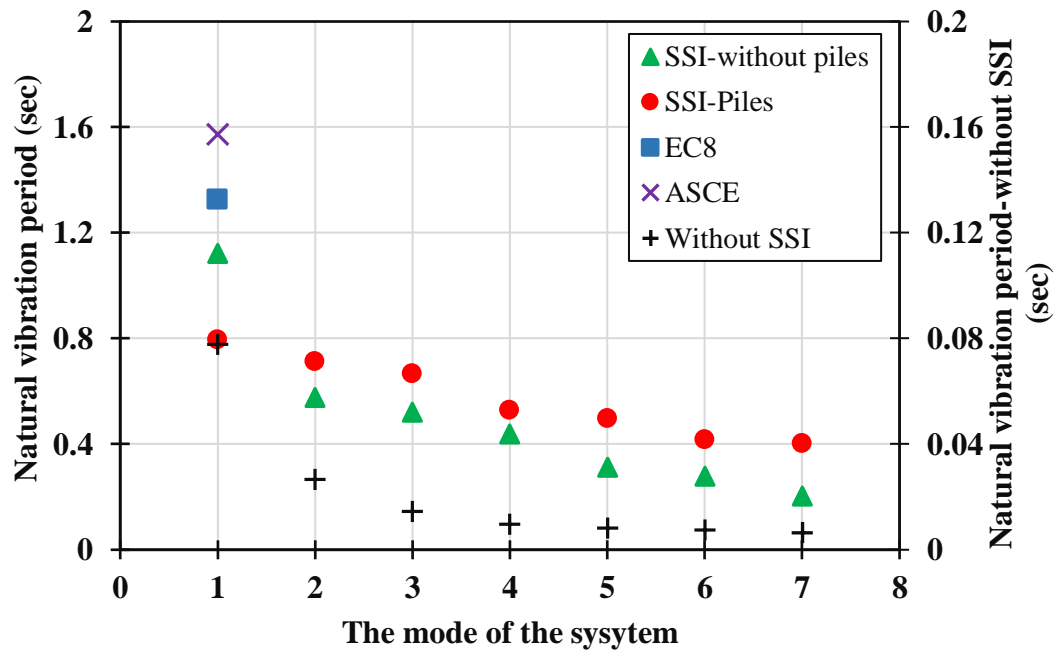
Figure 6-18 First Seven Modes of all Models' Circumstances

Y
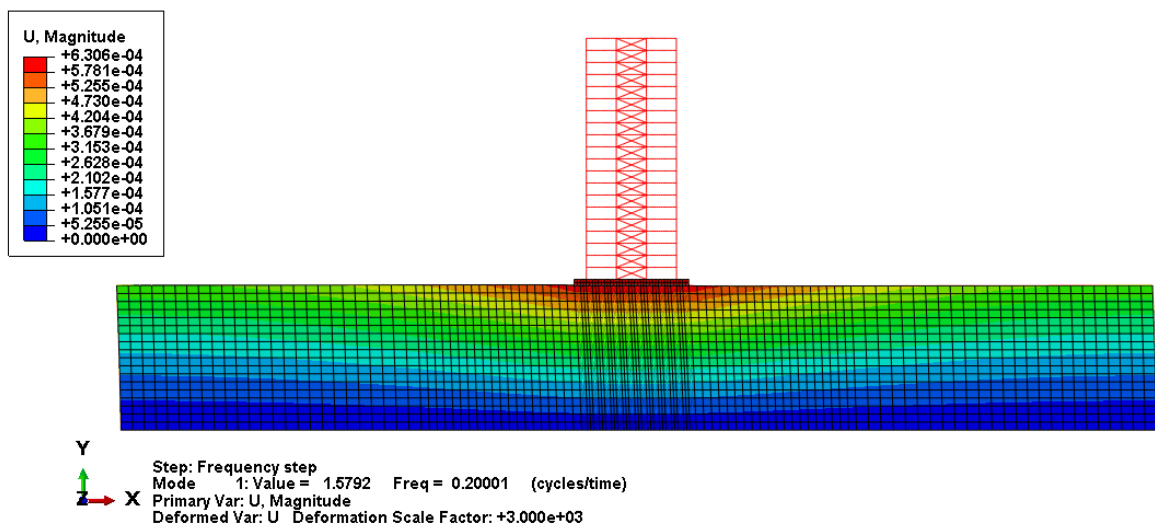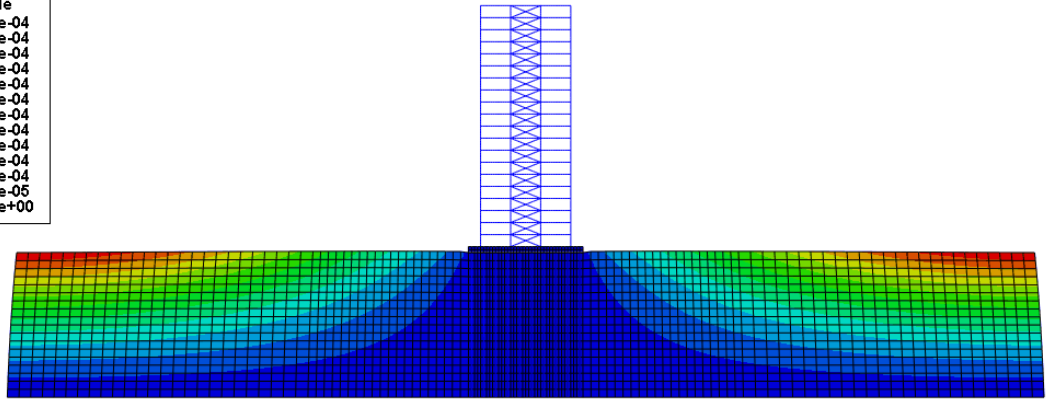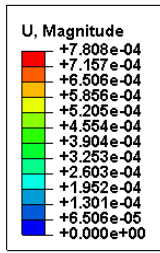
Step: Frequency step
Mode   2: Value = 1.9684   Freq = 0.22329   (cycles/time)
Primary Var: U, Magnitude
Deformed Var: U   Deformation Scale Factor: +3.000e+03

Y
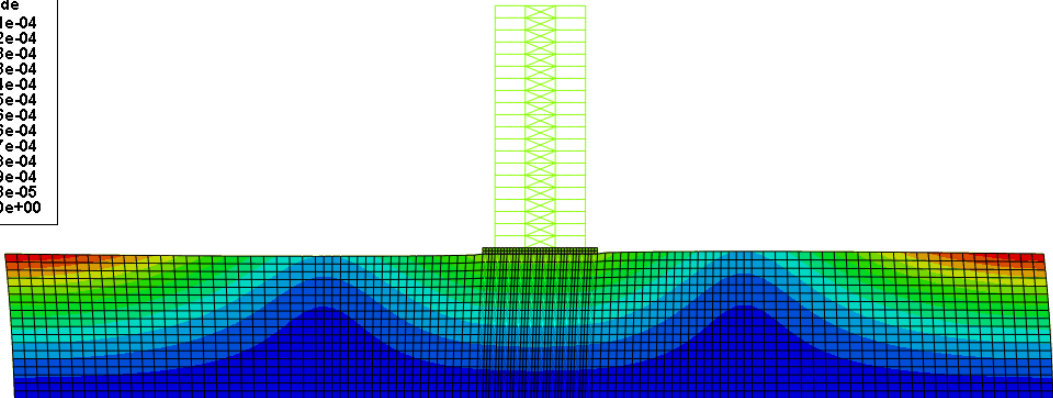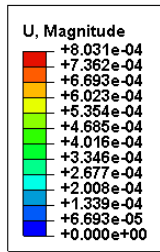
Step: Frequency step
Mode   3: Value = 2.2576   Freq = 0.23914   (cycles/time)
Primary Var: U, Magnitude
Deformed Var: U   Deformation Scale Factor: +3.000e+03

Y
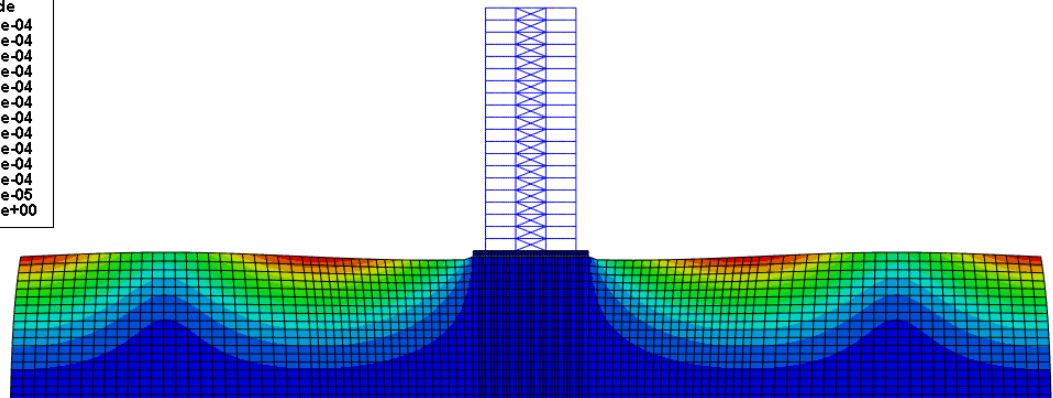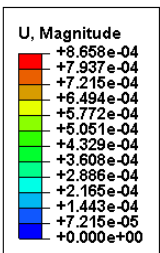
Step: Frequency step
Mode   4: Value = 3.5701   Freq = 0.30072   (cycles/time)
Primary Var: U, Magnitude
Deformed Var: U   Deformation Scale Factor: +3.000e+03

267
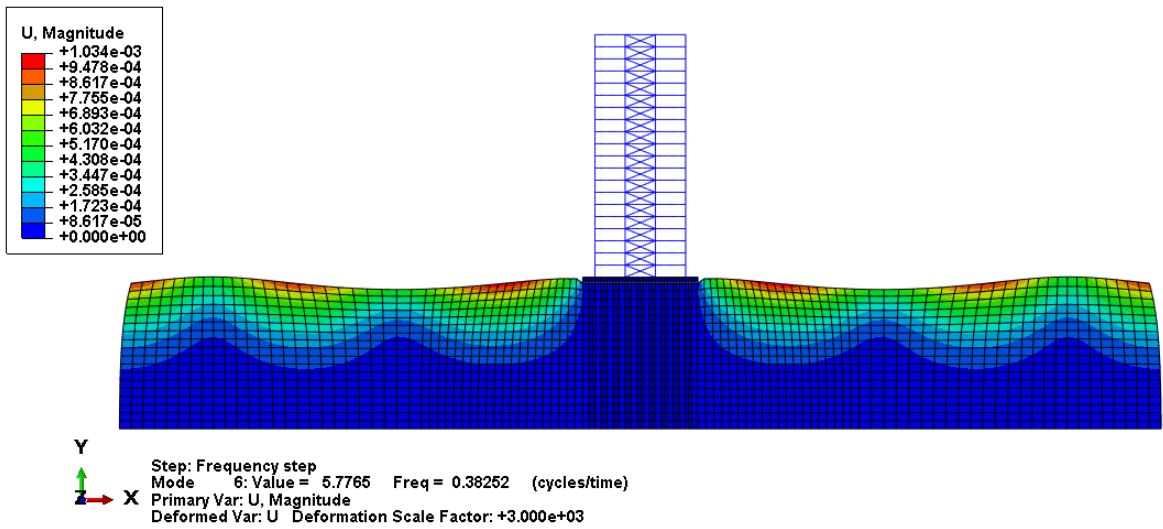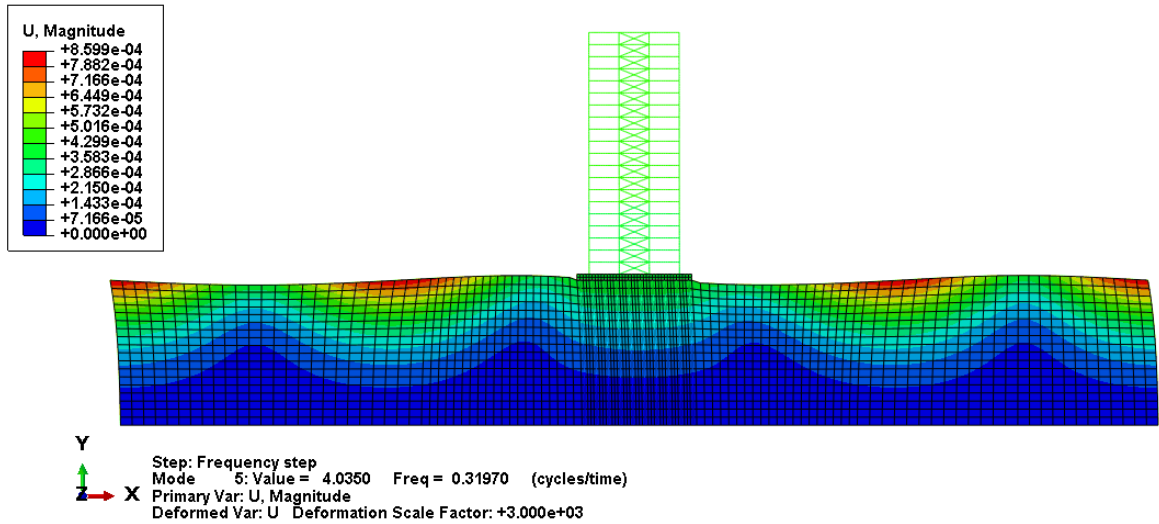
Figure 6-19 First Six Modes of the Model with SSI and Piles

Y
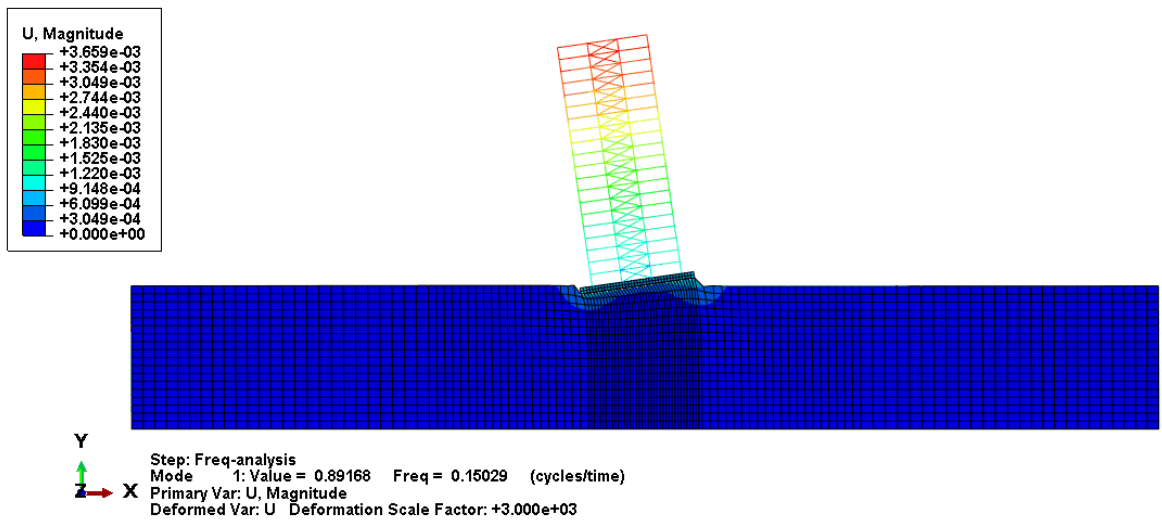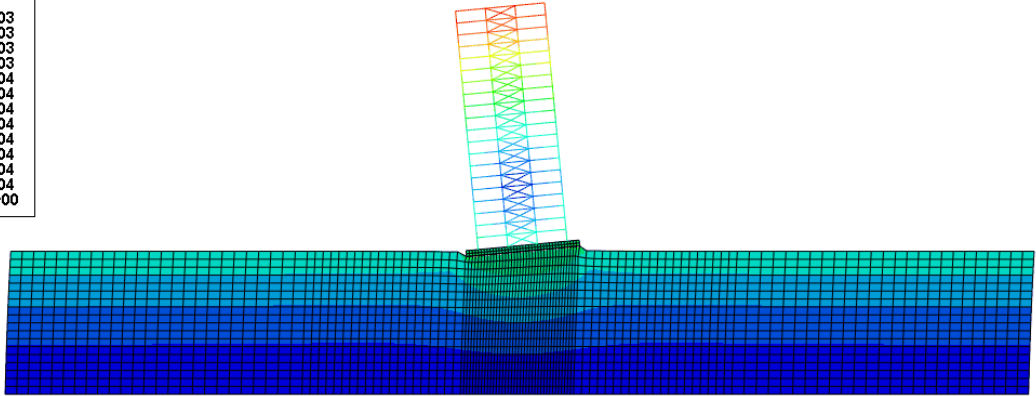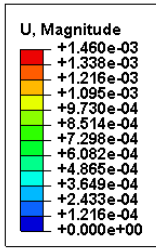
Step: Freq-analysis
Mode   2: Value =   1.7353   Freq = 0.20966   (cycles/time)
Primary Var: U, Magnitude
Deformed Var: U   Deformation Scale Factor: +3.000e+03

Y
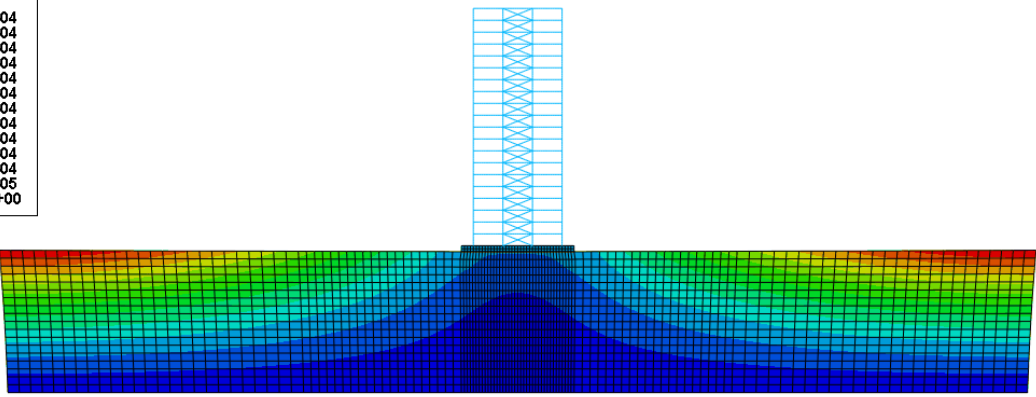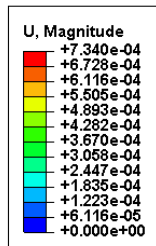
Step: Freq-analysis
Mode   3: Value =   1.9199   Freq = 0.22053   (cycles/time)
Primary Var: U, Magnitude
Deformed Var: U   Deformation Scale Factor: +3.000e+03

Y
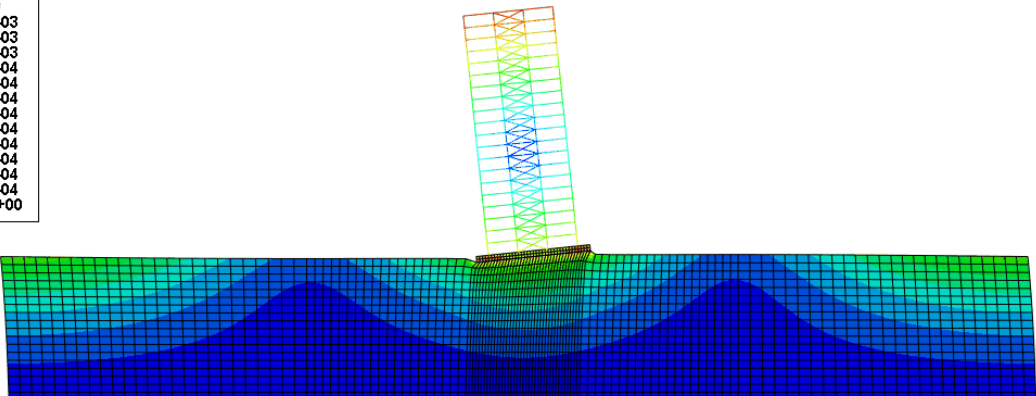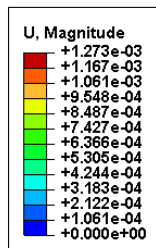
Step: Freq-analysis
Mode   4: Value =   2.2739   Freq = 0.24000   (cycles/time)
Primary Var: U, Magnitude
Deformed Var: U   Deformation Scale Factor: +3.000e+03

269
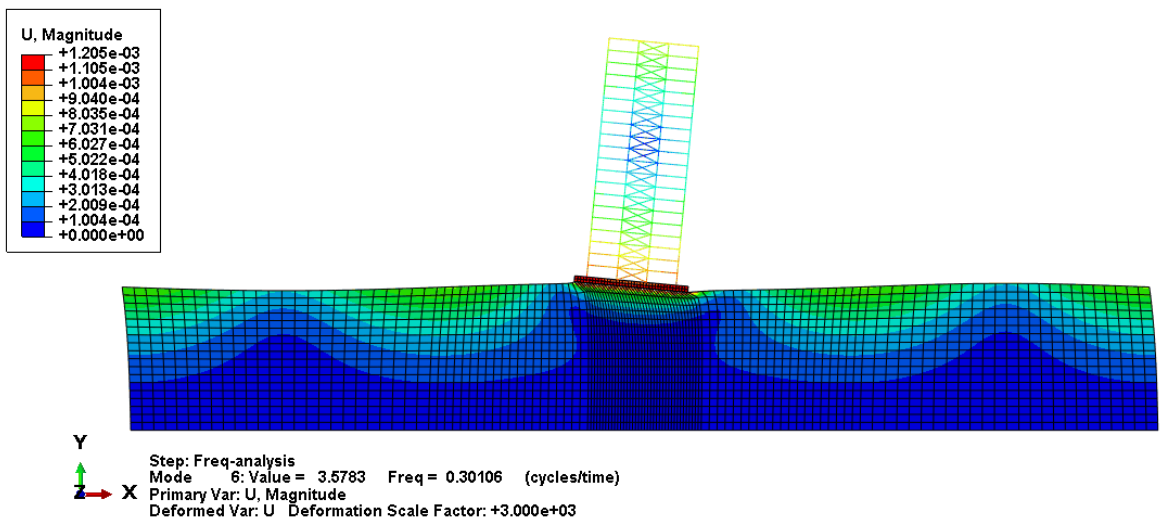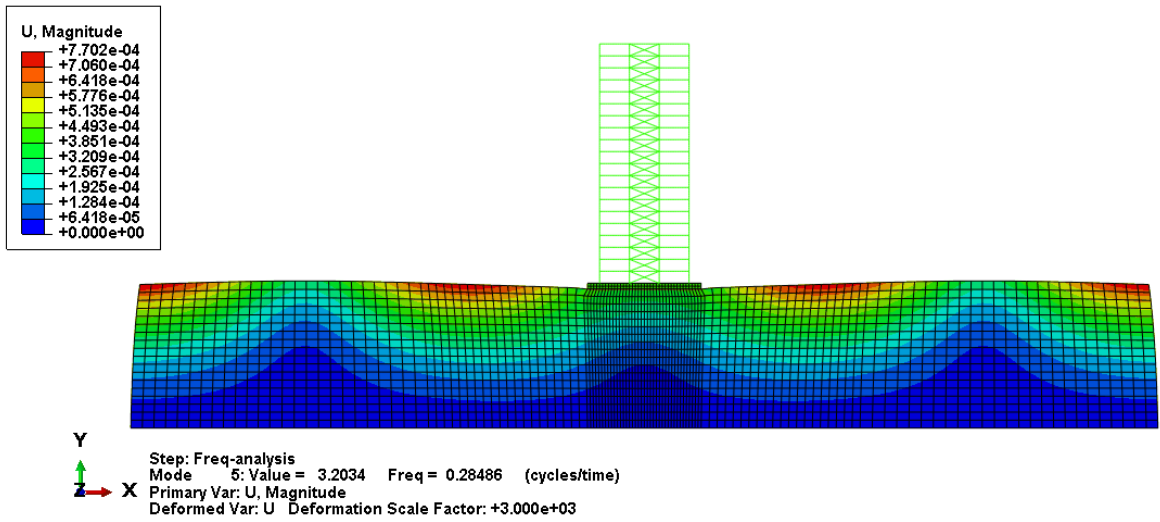
Figure 6-20 First Six Modes of the SSI Model without Piles
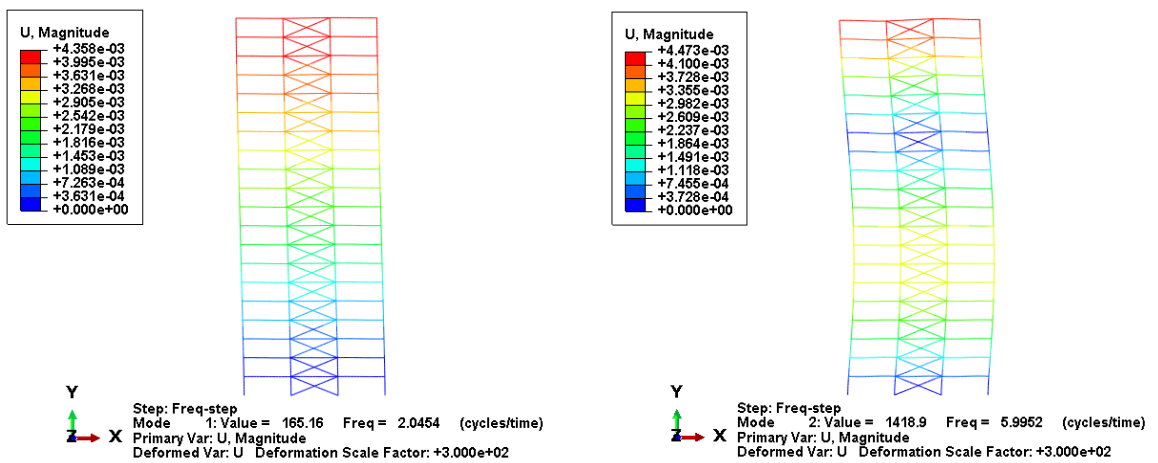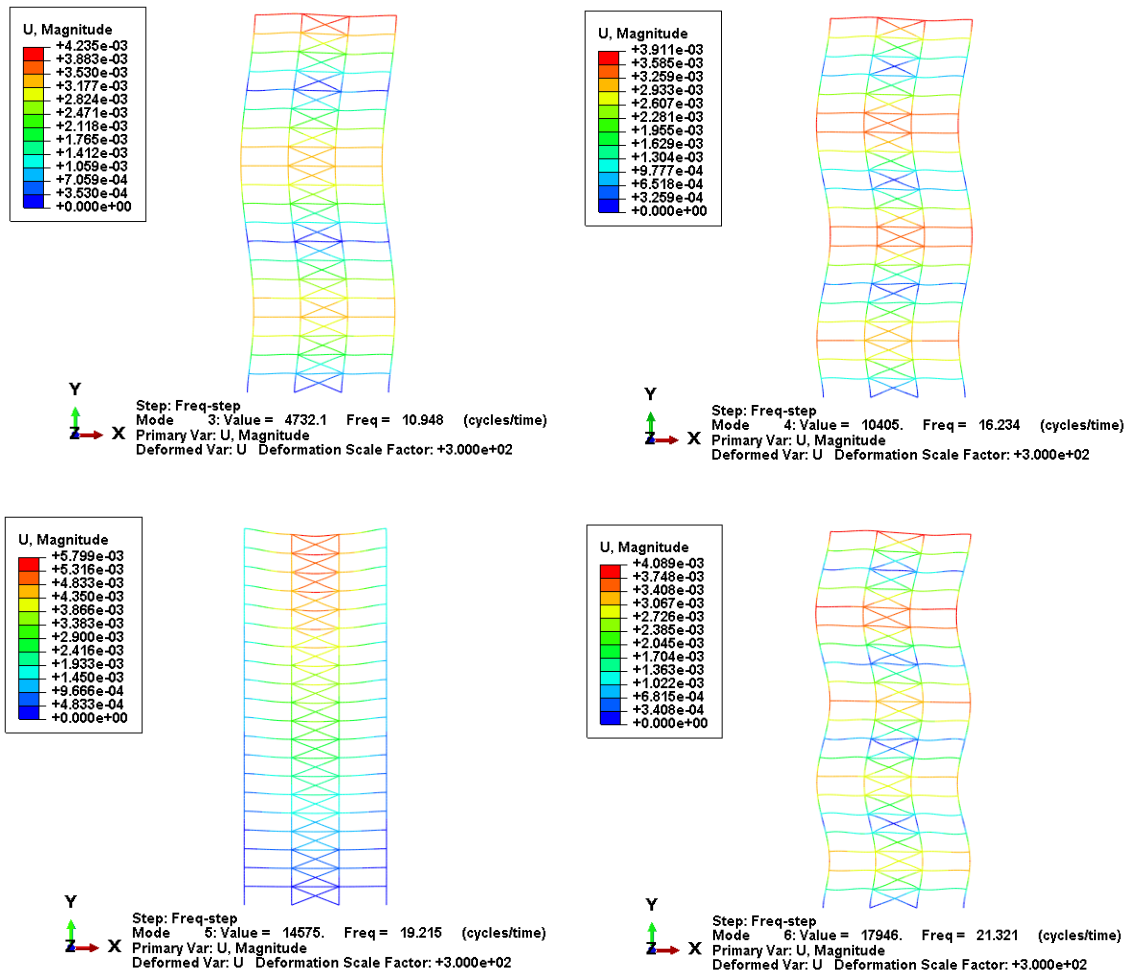
Figure 6-21 First Six Modes of the Model without SSI

6.5. The examination of Soil–structure interaction effects

In this study, the effects of SSI on design and analysis procedures and the provisions for pile performance analysis of high-rise building resting on clay soil subject to a seismic load are examined with regard to EC8 and ASCE standards. Although both codes include simplified approaches to SSI analysis, they recommend that specific dynamic analysis for structures resting on soft soils subject to intense levels of shaking is essential. A set of 2D models of a high-rise steel building resting on soft clay and subject to the two aforementioned seismic excitations are developed using Abaqus software. The set of models include:

i. a model of SSI system with pile–foundation system.
ii. a model of SSI system without piles. These models are subjected to two sets of modified and matched input motions. The data are modified according to the

271

design response spectra of the Loma Prieta and Cape Mendocino earthquake conditions as previously detailed.

iii. Two groups of seismic ASCE and EC8 models are subjected to modified sets of Loma Prieta and Cape Mendocino earthquakes. Figure 6-22 to Figure 6-25 illustrate selective simulation examples.

Absolute acceleration, relative storey drift, moments at beam ends and five absolute peak stress responses along the height of the structure are computed to examine the SSI effects. The results are calibrated with the codes' models.
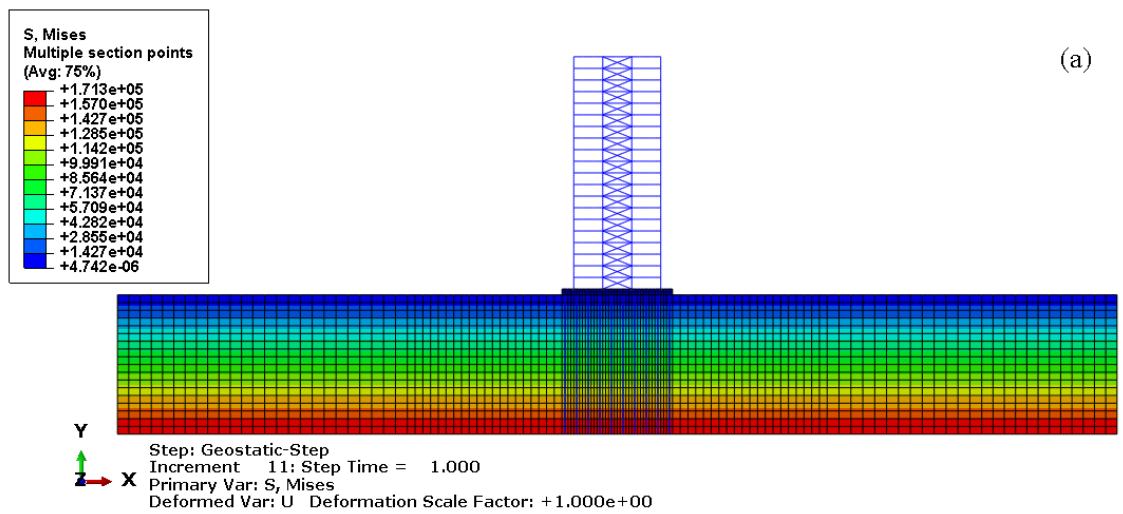
(a)
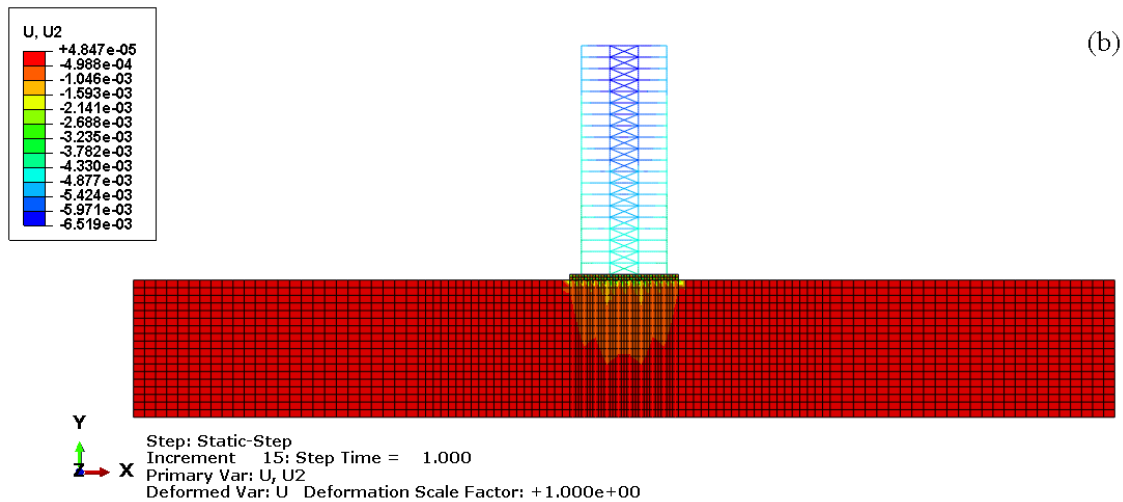
(b)
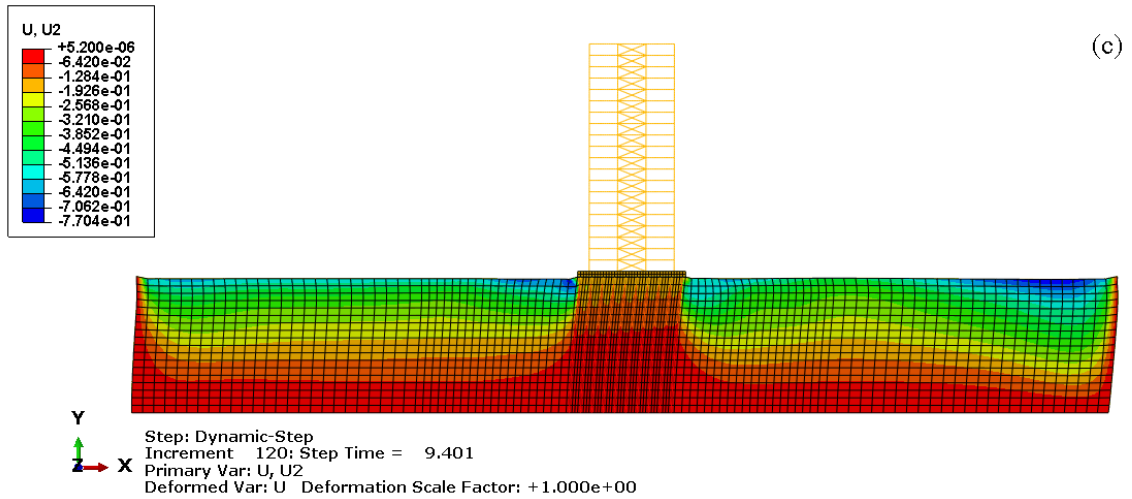
Figure 6-22 Three Steps for the Case of SSI Model with Piles (RSN3744): (a) Geostatic Step, (b) Static Step, (c) Dynamic Step
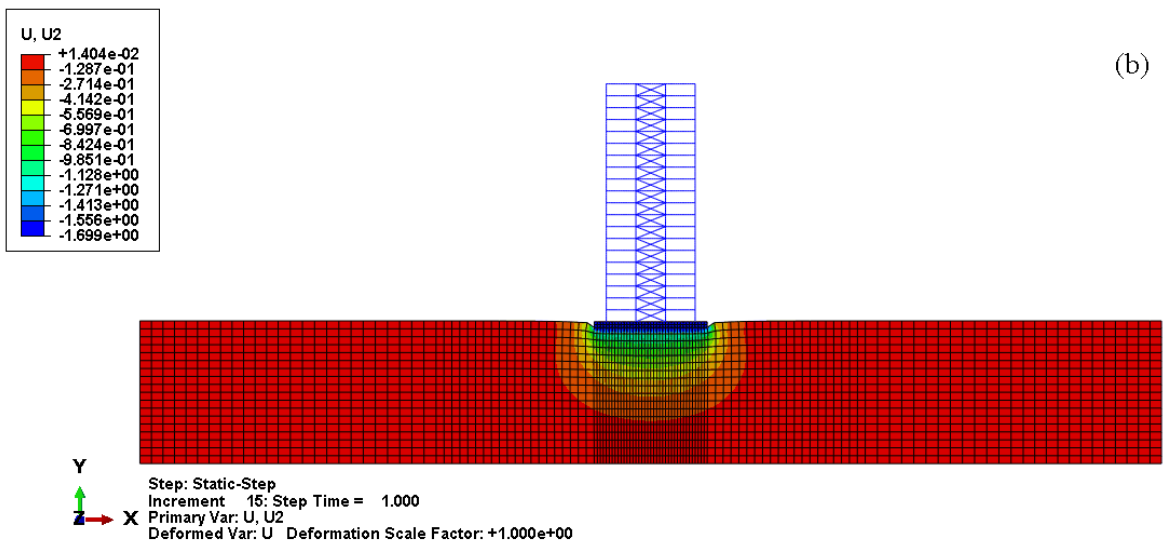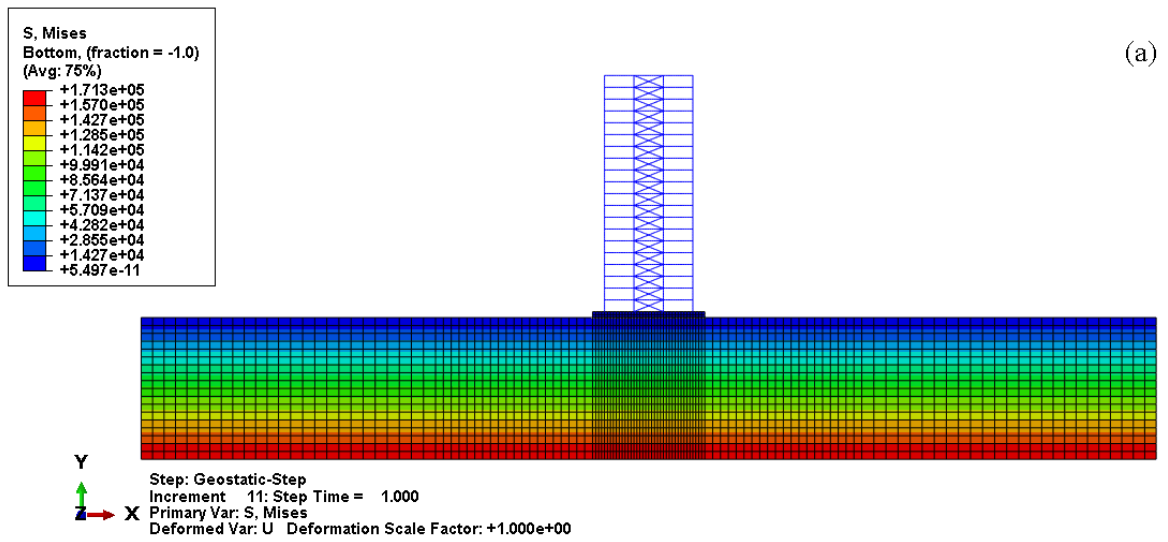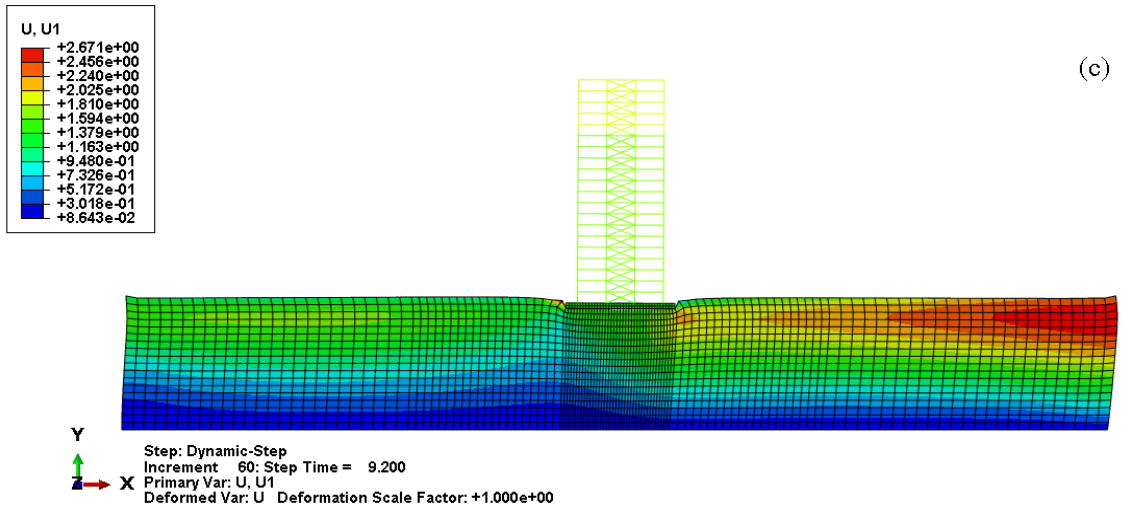
Figure 6-23 Three Steps for the Case of Model without Pile (RSN3744): (a) Geostatic Step, (b) Static Step, (c) Dynamic Step
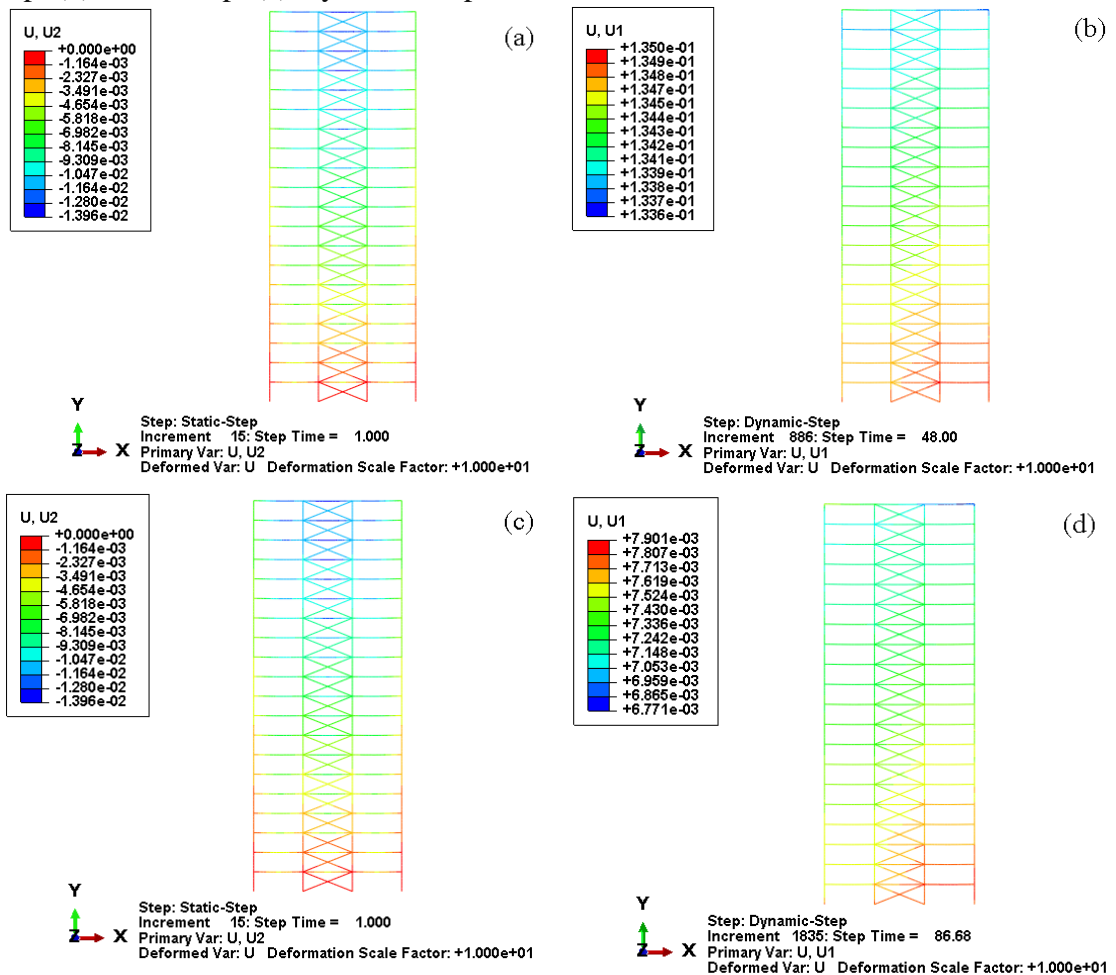
Figure 6-24 Two Steps for Cape Mendocino ASCE and EC8: (a) Cape Mendocino ASCE - Static Step, (b) Cape Mendocino ASCE - Dynamic Step, (c) Cape Mendocin EC8 - Static Step, (d) Cape Mendocino EC8 - Dynamic Step
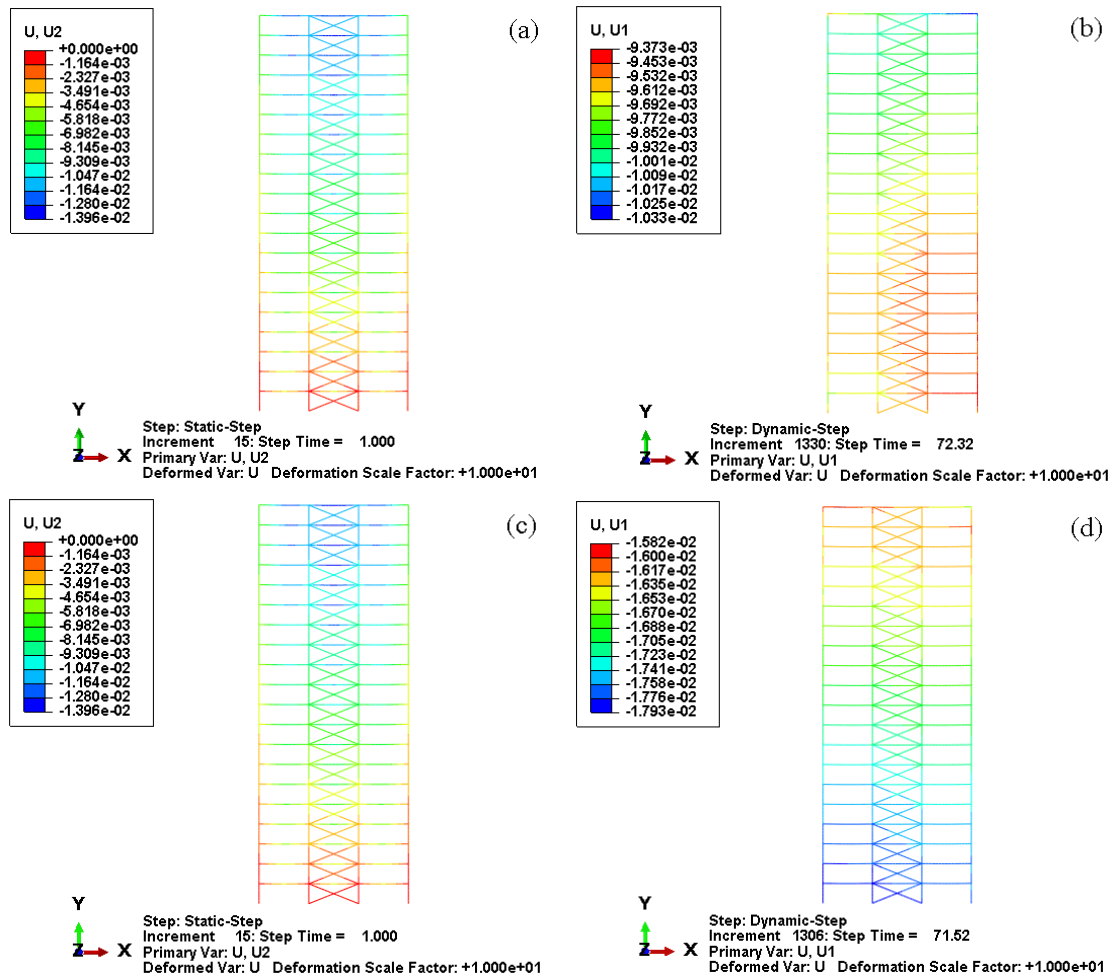
Figure 6-25 Two Steps for Loma Prieta ASCE and EC8 Case: (a) Loma Prieta ASCE - Static Step, (b) Loma Prieta ASCE - Dynamic Step, (c) Loma Prieta EC8 - Static Step, (d) Loma Prieta EC8 - Dynamic Step

6.5.1. Horizontal absolute acceleration response

The purpose of examining three different input data for each real earthquake event is to distinguish between the possibilities of peculiar behaviour according to the input data that have distinct properties reflecting site conditions, fault type and geological properties. The first set of analyses examines the influence of including SSI and piles on structural behaviour by calculating the horizontal peak absolute acceleration response (HPAAR) at each floor. The comparison of the distribution of the horizontal peak absolute acceleration along the building height is illustrated in **Error! Reference source not found.** to Figure 6-30. For the two input earthquake events, the structural response varies according to the earthquake properties of the applied motion, and the values of the peak acceleration variation along the superstructure do not coincide with each other. Firstly, the distributions of the horizontal absolute acceleration response (HAAR) for the case of model incorporating the SSI and pile effects are discussed. Different motion properties

275

are noted, and they are classified according to the shear wave velocity value into three motions and named according to their RSN of the original modified motion, i.e. Cape-RSN 3744, Cape-RSN 3745 and Cape-RSN 3748.

Although the three input motions are matched with the design response spectrum, the three circumstances have different behaviours, as indicated in **Error! Reference source not found.**. However, the value of acceleration for Cape-RSN 3744 decreases gradually in the lower five storeys and increases over the remaining levels. The acceleration reaches its minimum value at the fifth floor and its maximum at the top of the structure. For Cape-RSN 3745, the HPAAR increases gradually from the ground floor level, which represents the position of the minimum value. The maximum value is located at the highest floor. The HPAAR for the Cape-RSN 3748 case increases approximately linearly along the height of the structure. The three input motions tend to have dissimilarity in behaviour for all three input data recorded for the Loma Prieta earthquake (see Figure 6-27). Considerable dissimilarity is noted in the minimum and maximum boundaries of the acceleration values. For Loma-RSN 811, a slight decrease can be seen between the ground and sixth floors and then a sharp increase between the seventh and twentieth floors. For Loma-RSN 763, relatively fixed values remain up to the fifth floor, and then the HPAAR starts to increase dramatically for the rest of the floors. The HPAAR values for Loma-RSN 734 increase almost linearly along the height of the structure. Table 6.7 shows the maximum and minimum HPAAR values in coordination with motion type and shear velocity value.
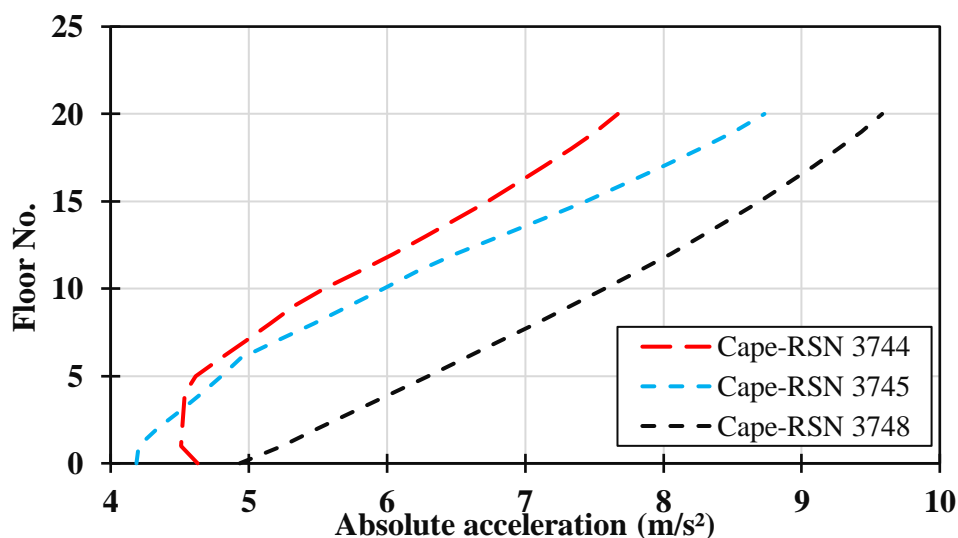
Figure 6-26 HPAAR of Cape Mendocino Model with SSI and Piles
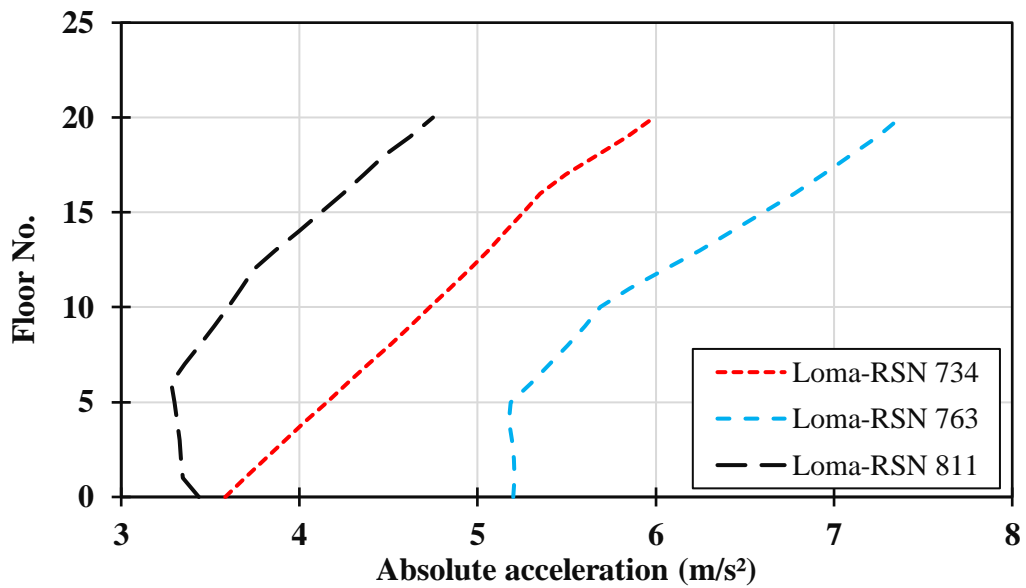
Figure 6-27 HPAAR of Loma Prieta Model with SSI and Piles

Figure 6-28 to Figure 6-30 illustrate the cases in which the SSI effect is considered but piles are not incorporated in the analysis. In Figure 6-28 Cape-RSN 3745 and Cape-RSN 3748 have nearly similar behaviour along the building height's HAAR maximum values with the locus at the top of the structure. The minimum HPAAR values of the two cases slightly differ with the locus at ground floor. One of the most crucial differences between the two cases and Cape-RSN 3744 lies in the maximum values of HPAAR with the locus at the top of the structure. Cape-RSN 3744 has an HPAAR value equal to or greater than double of the values of the other cases. The HPAAR values of Cape-RSN 3745 and Cape-RSN 3748 experience a steady decrease up to the first eight to ninth floors, then the values shot up for the rest of the levels. The HPAAR values in the superstructure for the two data are not always amplified as the values at the top of the building are smaller than the values at the base. The minimum HAAR value is at the 20th level. The behaviour of Cape-RSN 3744 varies from those of others considerably. Its highest value is positioned at the top of the structure, whereas the locus of the lowest value is at the fifth floor.

Table 6.7 Maximum and Minimum HPAAR Values for Cape Mendocino and Loma Prieta Models with SSI and Piles

Records	Minimum HPAAR	Location	Maximum HPAAR	Location	Wave velocity
	m/s²		m/s²		m/s

Cape-RSN 3744	4.510	1	7.670	20	566.26
Cape-RSN 3745	4.186	0	8.731	20	525.26
Cape-RSN 3748	4.934	0	9.583	20	378.95
Loma-RSN 763	5.176	4	7.374	20	729.65
Loma-RSN 734	3.584	0	5.990	20	517.06
Loma-RSN 811	3.281	6	4.750	20	388.33
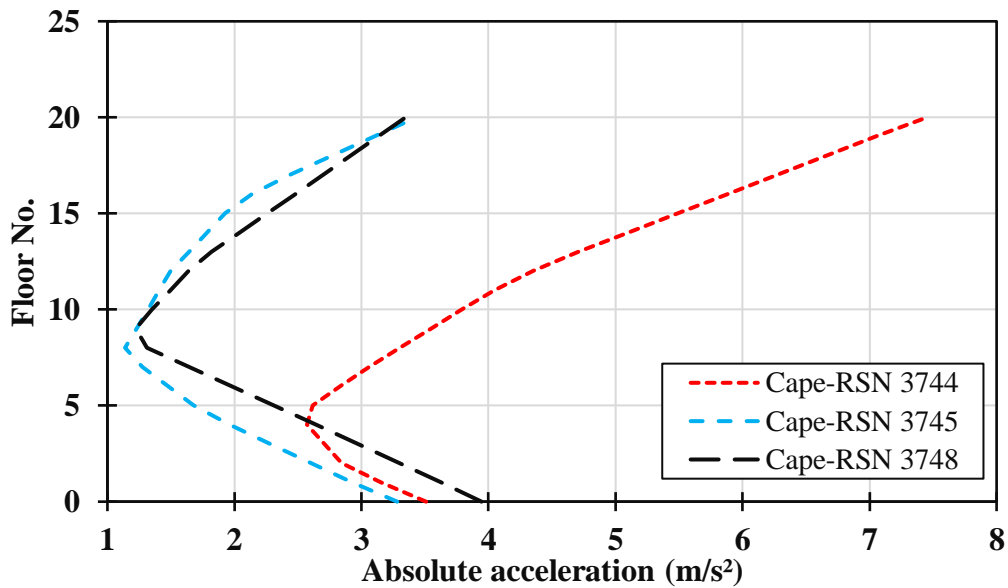
Figure 6-28 HPAAR of the Cape Mendocino SSI Model without Piles

Figure 6.29 compares the Loma Prieta earthquake data for three different cases (RSN 734, 736 and 811). The values of the absolute acceleration for all three records decrease up to the fifth floor for Loma-RSN 734 and Loma-RSN 763 and over the first nine floors for Loma-RSN 811. After these levels, the values rapidly increase over the top 11th and 15th floors. The minimum HPAAR values which are located at the base of the superstructure are slightly diverse for each particular record, whereas the maximum HPAAR values tend to be distinct for each particular record (see Table 6.8).
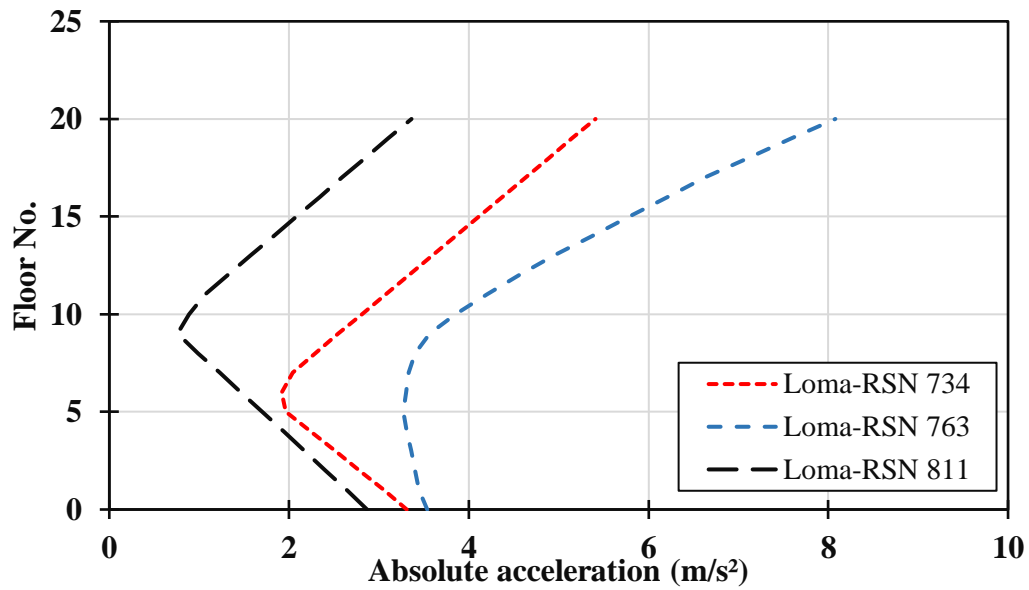
Figure 6-29 HPAAR of the Loma Prieta SSI Model without Piles

To examine the structural dynamic response for the structure designed according to ASCE and EC8 code provisions, the modified seismic loads are applied at the base of the superstructure after involving all aspects listed in the standards of ASCE and EC8. The resulting earthquakes are filtered, and having a new property depends on the clay layer properties that it passes through. The filtration is included by applying the provision of the ASCE and EC8 codes separately. Figure 6-30 reveals similar behaviour in the case of Loma Prieta applying ASCE and EC8 codes. This similarity includes the minimum and maximum HPAAR values for both cases. Both code provisions reflect similar structural dynamic responses, leading to this similarity. The application of Cape Mendocino records concerning these two codes develop very contrasting consequences for the values and behaviour of the HPAAR. Cape-ASCE goes up and down smoothly over the height of the structure, whereas Cape-EC8 fluctuates wildly along the height, as indicated by two peak readings of 38.5 m/s² at the first floor and 43.2 m/s² at the top of the structure.

279

Table 6.8 HPAAR Values Aligned with Motion Type and Shear Velocity Value

Records	Minimum HPAAR m/s²	Location	Maximum HPAAR m/s²	Location	Wave velocity m/s
Cape-RSN 3744	2.571	2	7.453	20	566.26
Cape-RSN 3745	1.140	8	3.432	20	525.26
Cape-RSN 3748	1.224	9	3.946	0	378.95
Loma-RSN 763	3.272	5	8.079	20	729.65
Loma-RSN 734	1.920	6	5.410	20	517.06
Loma-RSN 811	0.760	9	3.363	20	388.33
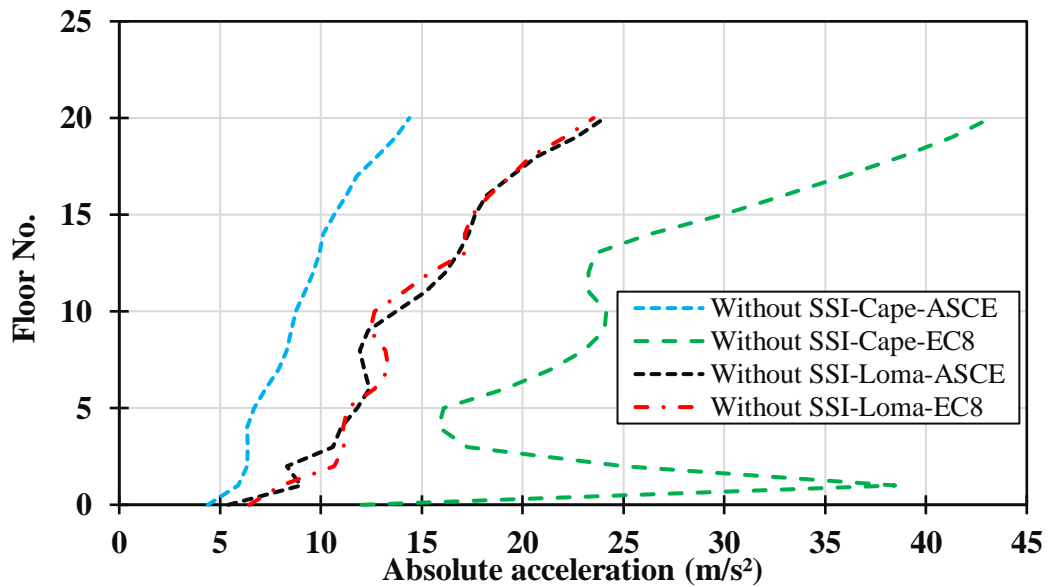
Figure 6-30 HPAAR of Cape Mendocino and Loma Prieta SSI models without piles

Table 6.9 HPAAR Values Aligned with Motion Type and Their Location

Records	Min. HPAAR m/s²	Location	Max. HPAAR m/s²	Location
Cape-ASCE	4.394	0	14.388	20
Cape-EC8	12.020	0	43.213	20
Loma-ASCE	5.409	9	24.067	20
Loma-EC8	3.272	5	8.079	20

In contrast with the Cape-EC8 record, that of Cape-ASCE shows a steady rise in the HPAAR values along the height of the structure. Table 6.9 presents the maximum and

minimum HPAAR values with the corresponding locations. From the results of the SSI time history analysis, the acceleration response in the upper floors is not always amplified and is sometimes equal or less than its value at the ground surface. Variations of acceleration along the structural height of both SSI models are unlike to that of models without SSI. The trend shows a decrease in the first floors (fifth to ninth) and increase in the remaining floors. By contrast, the results of the code provision investigation analysis reveal that the value is amplified and fluctuates along the height of the superstructure, addressing the minimum and maximum values at the base and top of the superstructure, respectively. These results are in line with the assumption that ignoring the SSI effect is a conservative approach. A critical question emerges here: is examining only the behaviour of a structure against the acceleration response enough? This study shows that it is not by supporting the importance of examining other aspects.

6.5.2. Storey drift response

The essential issues of structures subject to an earthquake are stability and not undertaking stress problems. In general, a structure under earthquake action must fulfil two criteria: stability and strength. In case of a multi-storey building, the stability check is outlined by the evaluation of the storey drift d_s criterion which is a dimensionless parameter given by Eq. (6.10).

$$d_s = \frac{U_{up} - U_{down}}{H_s} \qquad (6.10)$$

Where U_{up} is the horizontal displacement at the top of the storey, U_{down} is the horizontal displacement at the bottom of the storey, and H_s is the height of the storey. The distributions of peak storey drift (PSD) over the height of the structure are presented in Figure 6-31 to Figure 6-34. Figure 6-31 and Figure 6-32 show that the PSD variation of the superstructure for the cases of Cape Mendocino and Loma Prieta earthquakes for both code provisions (i.e. Cape-ASCE, Cap-EC8, Loma-ASCE, and Loma-EC8) coincide with each other. They are fluctuating around the y-axis, restricting the maximum and minimum PSD values (see Table 6.10).

Table 6.10 PSD values aligned with motion type and their location

Records	Min. (PSD)	Location	Max. (PSD)	Location	Wave velocity m/s
Cape-RSN 3744	1.16E-04	20	6.780E-04	1	566.26
Cape-RSN 3745	4.20E-05	19	1.920E-04	2	525.26
Cape-RSN 3748	5.233E-05	19	2.043E-04	20	378.95
Loma-RSN 763	3.333E-06	1	1.833E-04	20	729.65
Loma-RSN 734	6.733E-05	14	2.227E-04	1	517.06
Loma-RSN 811	8.123E-06	14	1.298E-04	20	388.33

Throughout the results shown in Figure 6-31 to Figure 6-34, all PSD values of SSI models with piles are at the right of the code standard values with different scales. The maximum storey drift values and structural behaviour of RSN 3745 and RSN 3748 cases are the same, and they hit the maximum at the 20th level. The behaviour, shape and maximum value of RSN 3744 different from those of the two aforementioned cases. In RSN 3744, the maximum value is reached at the 1st floor and the minimum value at the 20th floor. Figure 6-32 shows that the PSD value of the three modified Loma Prieta earthquakes (i.e. Loma-RSN 734, Loma-RSN 763 and Loma-RSN 811) are scattered along the area of the diagram, recording the minimum and maximum values at the 1st and 20th floors, respectively. The last part of the three studied circumstances developed in this study is the situation considering the SSI system without incorporating piles in the analysis for Cape Mendocino and Loma Prieta earthquakes (see Figure 6-33 and Figure 6-34) . The values of PSD for these three cases along the height of the structure is very minimal when comparing the results of both codes. Apart from the two positions, the PSD values experience a sudden change at the third and fifth levels during the structural response of Cape-RSN 3745. Loma-RSN 734 stands on the right-hand side of the code curves with a dramatic fluctuation between 17th and 20th levels. Considering the effect of field nonlinearity, piles and SSI, PSD continually increases in contrast with that of code provision models. Unlike the acceleration response, distributions of PSD along the height of the structure are located in front and back positions and record large values. The interaction of pile–soil structure has an evident peak- enlargement influence (see Table 6.11and   Table 6.12) for maximum and minimum values and their location). On the whole, the aforementioned results indicate that the PSD values do not consistently peak at the top level of the structure.
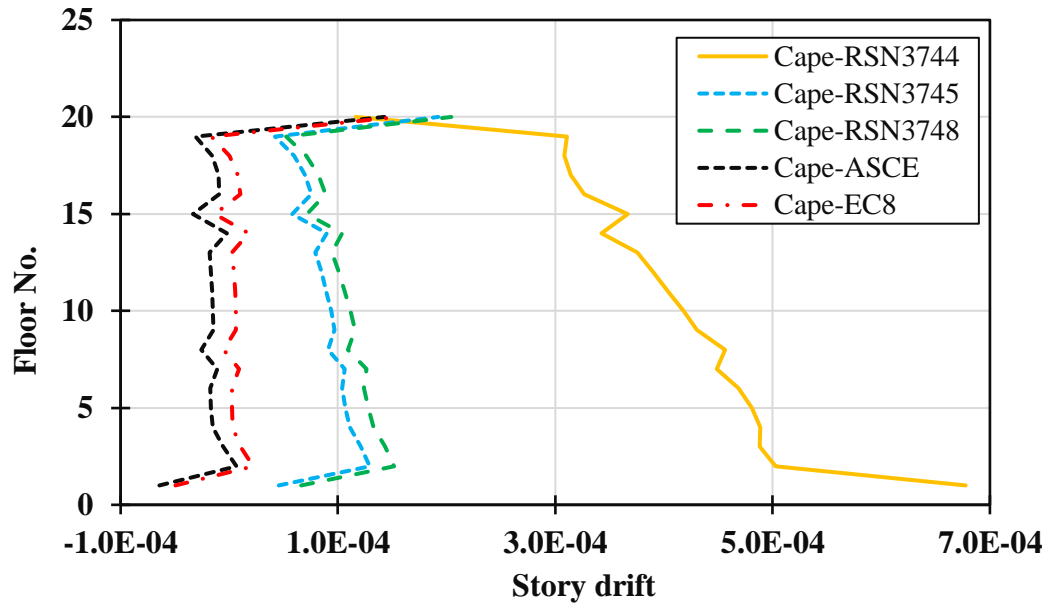
Figure 6-31 PSD of Cape Mendocino Models with SSI and Piles and Code Provision Models
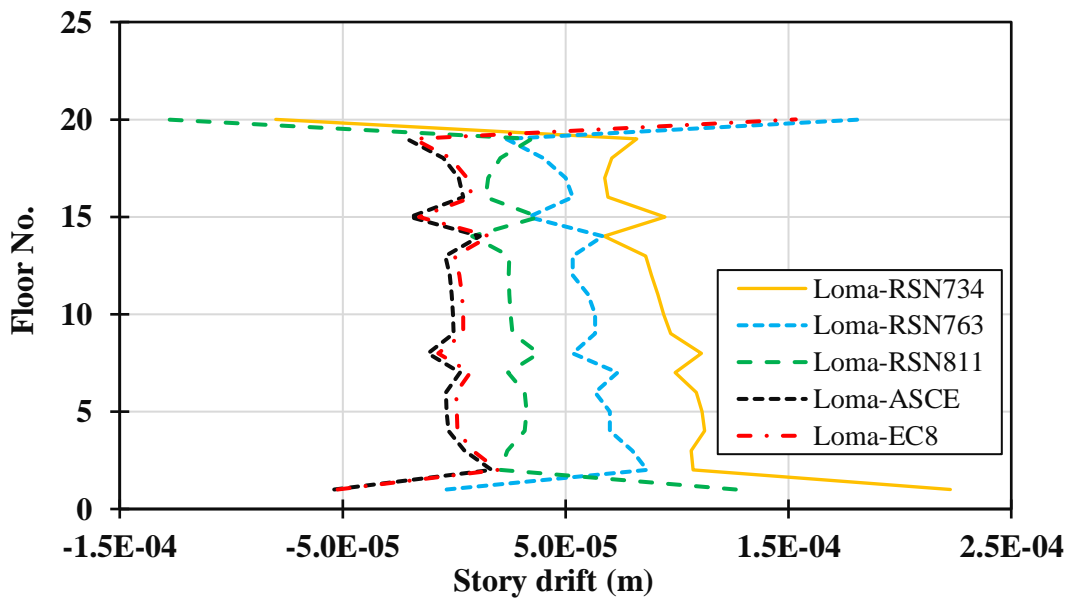
Figure 6-32 PSD of Loma Prieta Models with SSI and Piles and Code Provision Models

Table 6.11 PSD values aligned with motion type and their location

Records	Min. (PSD)	Location	Max. (PSD)	Location
Cape-ASCE	2.333E-06	14	1.427E-04	20
Cape-EC8	2.127E-07	18	1.546E-04	20
Loma-ASCE	3.00E-07	9	1.509E-04	20
Loma-EC8	4.333E-07	13	1.533E-04	20
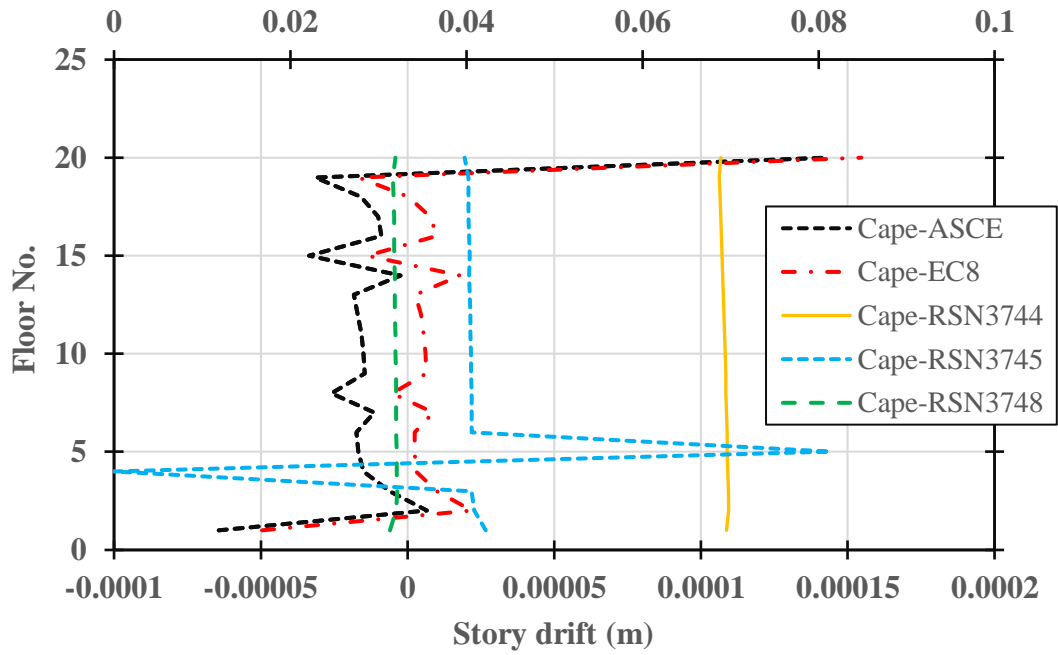
Figure 6-33 PSD of Cape Mendocino SSI Models without Piles and Code Provision Models
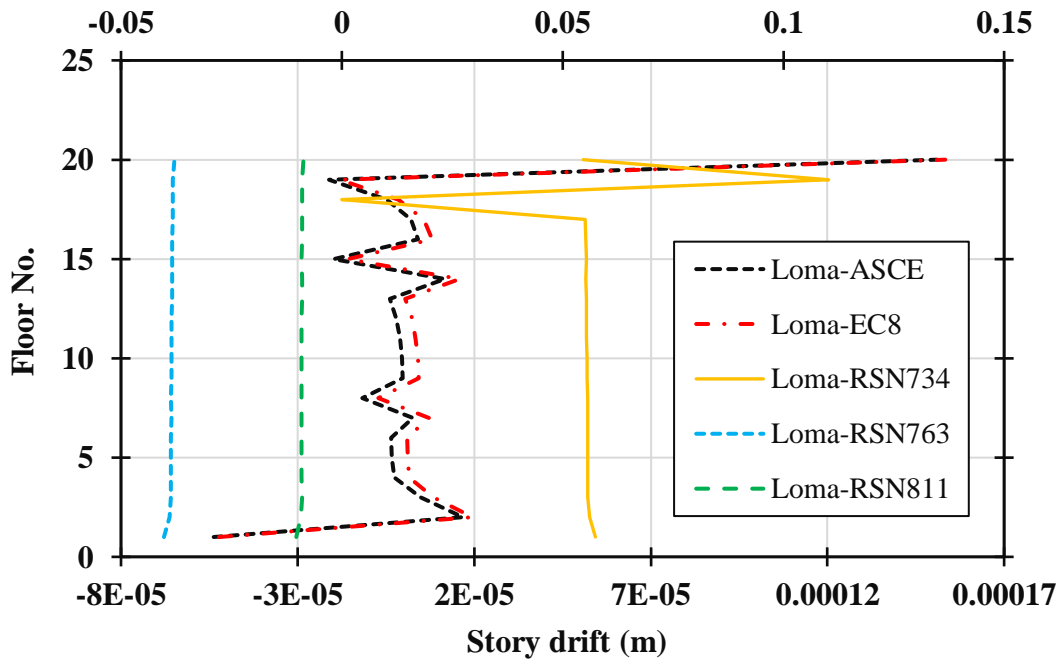
Figure 6-34 PSD of Loma Prieta SSI Models without Piles and Code Provision Models

Table 6.12 PSD values aligned with motion type and their location

Records	Min. (PSD)	Location	Max. (PSD)	Location	Wave velocity m/s
Cape-RSN 3744	68.733E-03	19	69.798E-03	2	566.26
Cape-RSN 3745	0	4	81.320E-03	20	525.26
Cape-RSN 3748	31.336E-03	1	32.164E-03	3	378.95
Loma-RSN 763	37.893E-03	20	40.274E-03	1	729.65
Loma-RSN 734	0	18	110.257E-03	19	517.06
Loma-RSN 811	8.676E-03	20	10.303E-03	1	388.33

6.5.3. Absolute peak stress response

The nonlinearities in a structure's members can be geometric and material nonlinearity describing the consequences of high order strains. Both aspects become increasingly important in the circumstances when the structure experiences high deformations such as when subject to severe seismic excitations. The maximum allowable ductility of structural elements may reduce significantly and critically influence the structural behaviour during earthquakes. To illustrate the distribution of the stress along the height of the structure and make the comparison possible between the chosen cases studies, the stresses at each level are computed for particular consistent points.

Figure 6-35 and Figure 6-36 compare five values in terms of the peak stress (PS) distribution along the height of the structure for the two loading conditions mentioned above. Figure 6-35 illustrates the distribution of PS along the height of the structure for the five cases of analysis, i.e. ASCE and EC8 code provision models without SSI compared with three loading circumstances for the case of Cape Mendocino earthquake which involves the effects of SSI and piles (RSN 3744, RSN 3745 and RSN 3748). Figure 6-36 compares the same aspects for the three loading circumstances for the case of Loma Prieta earthquake which involves the effects of SSI and piles (RSN 734, RSN 763 and RSN 811). All five cases in each loading circumstance have similar behaviour but different maximum and minimum PS values. Figure 6-35 shows that Cape-RSN 3745 and Cape-RSN 3748 are covered completely by code provisions, but the Cape-RSN 3744 is out of the provision spectrum. Figure 6-36 shows that Loma-RSN 763 is covered by both codes' standard limitation requirement for the entire height of the structure.

Only the first lower eight levels, i.e. between ground and eighth levels are out of the standard limitations. The stress values along the height of the structure are amplified for

Cape-RSN 3745 and Cape-RSN 3748 up to the 19th level then decline for the 20th level. The record of Cape-RSN 3744 fluctuates vertically up to the 13th level then decreases for the remaining levels. The minimum and maximum PS values exceed all the other values for all code provision models for Cape Mendocino and Loma Prieta earthquakes.
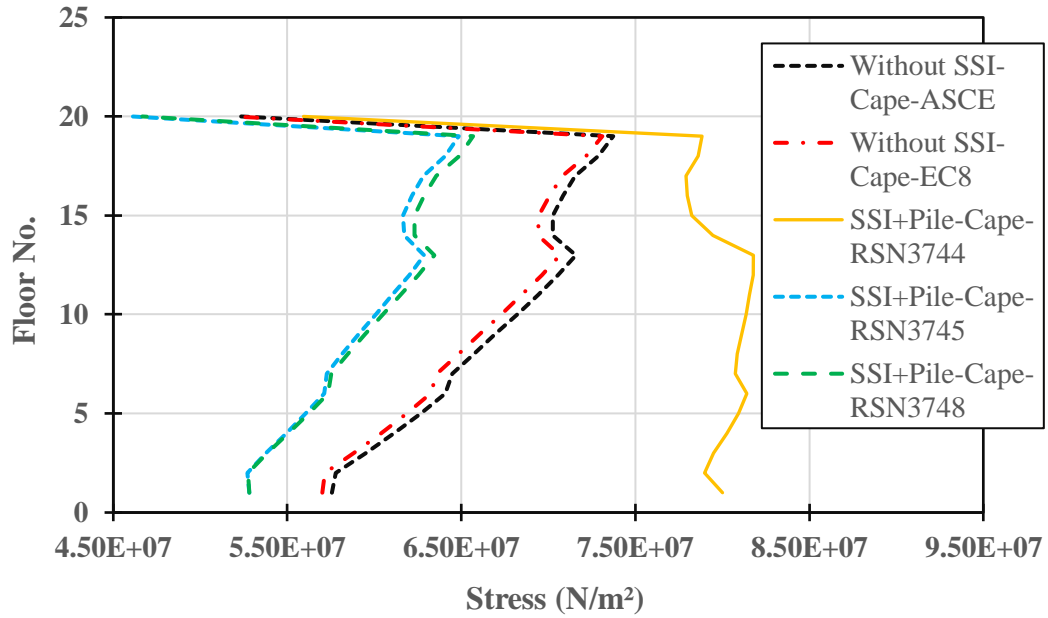
Figure 6-35 PS of Cape Mendocino models with SSI and piles and code provision models
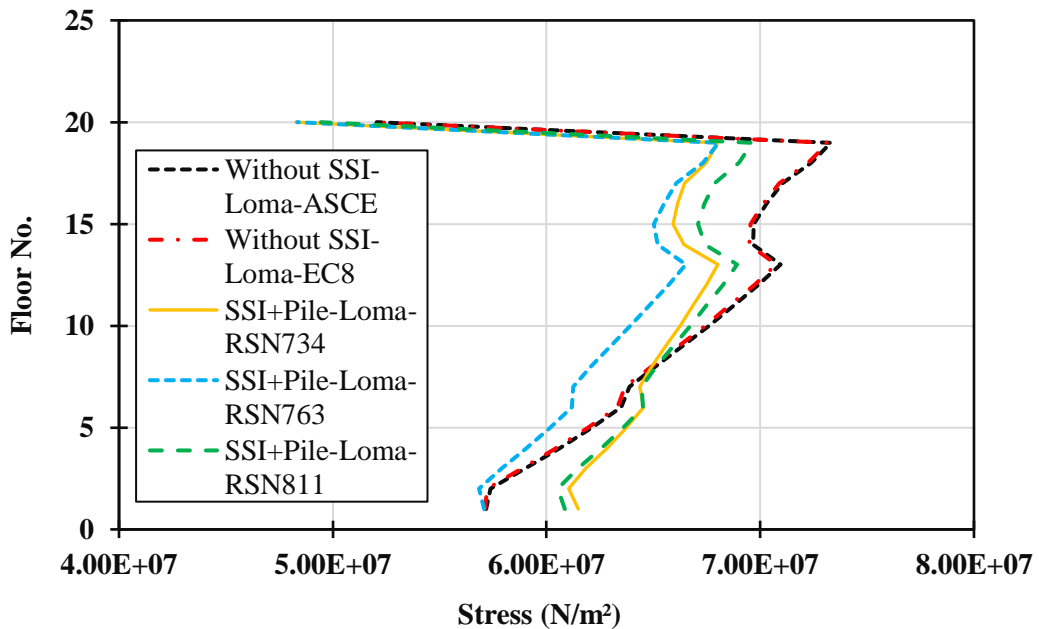
Figure 6-36 PSD of Loma Prieta Models with SSI and Piles and Code Provision Models

Table 6.13 and Table 6.14 show the maximum and minimum PS values along the structure levels and corresponding locations. Figure 6-37 and Figure 6-38 illustrate the

situation when the effect of the piles is removed, and all the records except part of Cape-RSN 3744 exceed the code limitations. Table 6.15 list the maximum and minimum PS values along the height of the structure aligned with the corresponding locations.

Table 6.13 PS values aligned with motion type and their location

| Records | Min. (PS) | Location | Max. (PS) | Location | Wave velocity |
	N/m²		N/m²		m/s
Cape-RSN 3744	5.59E+07	20	8.18E+07	13	566.26
Cape-RSN 3745	4.61E+07	20	6.49E+07	19	525.26
Cape-RSN 3748	4.67E+07	20	6.57E+07	19	378.95
Loma-RSN 763	4.83E+07	20	6.80E+07	19	729.65
Loma-RSN 734	4.83E+07	20	6.80E+07	19	517.06
Loma-RSN 811	4.94E+07	20	6.96E+07	19	388.33

Table 6.14 PS values aligned with motion type and their location

| Records | Min. (PS) | Location | Max. (PS) | Location |
	N/m²		N/m²	
Cape-ASCE	5.23E+07	20	7.37E+07	19
Cape-EC8	5.19E+07	20	7.31E+07	19
Loma-ASCE	5.21E+07	20	7.33E+07	19
Loma-EC8	5.20E+07	20	7.32E+07	19
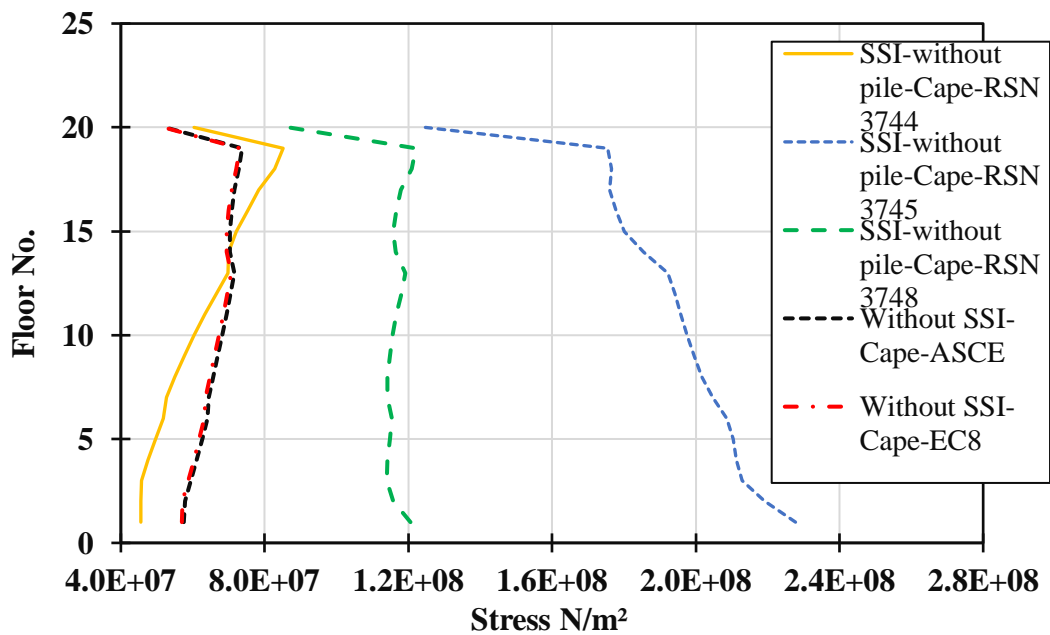
Figure 6-37 PSD of Cape Mendocino SSI Models without Piles and Code Provision Models
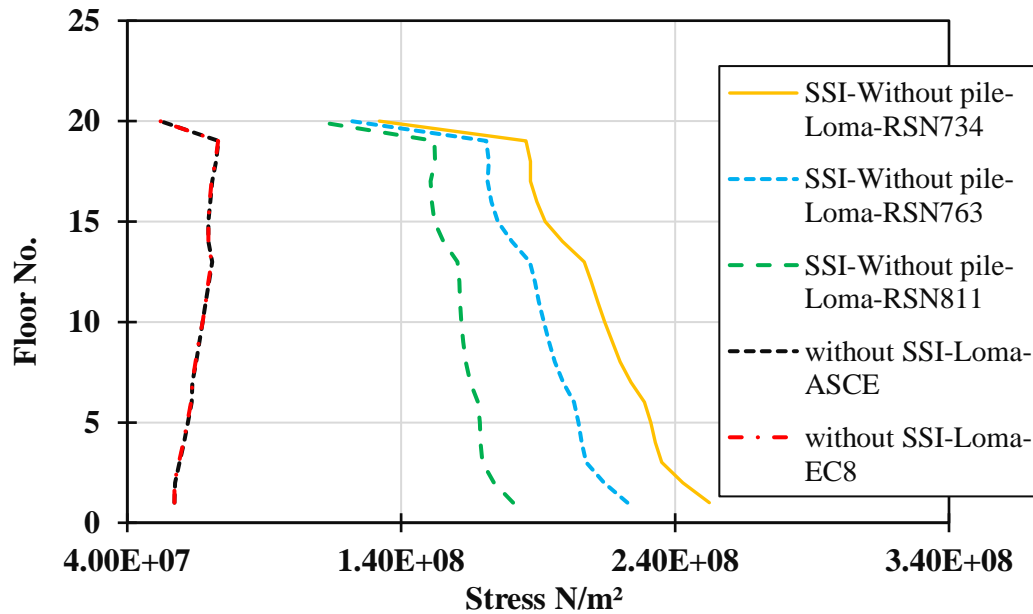
Figure 6-38 PSD of Loma-SSI-without Pile, and Code Provision Models

Table 6.15 PS values aligned with motion type and their location

Records	Min. (PS) N/m²	Location	Max. (PS) N/m²	Location	Wave velocity m/s
Cape-RSN 3744	4.56E+07	1 and 2	8.52E+07	19	566.26
Cape-RSN 3745	1.25E+08	20	2.28E+08	1	525.26
Cape-RSN 3748	8.67E+07	20	1.22E+08	19	378.95
Loma-RSN 763	1.22E+08	20	2.23E+08	1	729.65
Loma-RSN 734	1.32E+08	20	2.53E+08	1	517.06
Loma-RSN 811	1.08E+08	20	1.81E+08	1	388.33

6.6. Results discussion

The philosophy of SSI provisions for clay soil in ASCE and EC8 is to compensate the SSI effect with an extended period and a large damping ratio equivalent for fixed-base model. The designers are thus permitted to curtail the design base-shear force in the equivalent lateral force method. However, this concept is valid only for linear SSI analysis as detecting nonlinear SSI effects accurately is impossible. As mentioned in the literature review, SSI may result in high structural responses that may negatively influence the performance of the structures and then develop a seismic risk. A hypothesis regarding a

purely advantageous consequence of SSI on nonlinear systems, which is the theory of the seismic design codes, needs revisiting. Ideal codes (ASCE and EC8) incorporate the effect of SSI on nonlinear systems by proposing a base-shear reduction factor as a function of the forecasted level of nonlinearity. However, a strong relationship between nonlinearity and base-shear reduction factor has been reported in ASCE, so low contractions of design base-shear force for systems with large nonlinearity are recommended. With respect to the combined methodology, this study assesses the influences of considering the effect of dynamic SSI parameters, method of application and selection of the input motion on relevant ASCE and EC8 seismic provisions. The case study is devised to determine and compare the importance of incorporating these parameters in the context of application the SSI to come up with a reliable and accurate model. The selection, modification and application of the input motions, as well the effect of considering the geological and geotechnical site characteristics on the input motion properties, are examined. For the same earthquake resource, many input motions which match the design response spectrum can be produced. The most critical issue is that the computed input data have different acceleration time histories. Consequently, this difference may influence the structural response due to the discrepancy in the properties of the seed motion collected from the database to modify and produce the input motions required for analysis. According to these data, the author can infer that ignoring the geotechnical and geological properties of an earthquake may lead to contradictory output. This consequence may be explained by the fact that considering these properties leads to reliable input data that represent the desired site properties accurately.

In general, soft clay has a fundamental period that varies between 1.5 and 2.0 sec, so it contributes to expanding the shaking practically 2.0 to 6.0 times that of the bedrock effect. Moreover, the coincidence between the natural period of the soil and the structure may amplify the structural acceleration which is one of the design considerations. In accordance with the present results, previous studies have demonstrated that the effects of SSI induce a linear increase in effective modal damping ratios and a decrease in the natural modal period. For the model that incorporate the pile effects, the percentage of increase in period ranges between 23% and 45%. This value tends to be less for the model without pile by around 7% –19%. The effect of piles lead to an increase in the first time period and a decrease in other periods with a percentage ranging between 20% and 50%. This observation supports the hypothesis that many modes may attribute to the response

of the SSI model. Connections between structural response and the number of modes are likely to exist and thus should be included in the analysis. The results fairly explain why the assumption of ASCE and EC8 of basing analysis on the fundamental period, which is computed by the code equations, may be illogical and inadequate. Further quantitative research should be undertaken to establish a clear procedure for determining the minimum number of structural modes which should be incorporated in analysis. The most prominent finding is that the absolute acceleration values are not proper indicators even if the code provisions cover all seismic design requirements. This study raises the possibility that assessment based only on the acceleration response is insufficient even if the value meets the design requirements. Moreover, both seismic codes propose a method to calculate the storey drift of the system according to the modified storey shear force. The allowable PSD according to ASCE, due to the designed lateral force, depends on the site importance, which is (III) in this study, and it is required to not exceed $(0.015 - 0.045) h$, where h is the storey height. EC8 sets this value to 0.01. Both code provision models and SSI models with piles meet the requirements. However, removing the effect of piles from the analysis leads to results out of the code limitations. To investigate the system behaviour during the application of different motions and not failure analysis, the structure is designed to be strong enough to bear the seismic load. Consequently, the storey drift values are not that important compared with the code limitation and code model response. Hence, that time history analysis results in high structural displacement and then high storey drift response is hypothesised. In contrast with the code standards, there is no evidence to support the view that applying the code limitation can detect safety provisions in case of ignoring the SSI effects and computing the pile and pile group effects. A strong relationship between the nonlinearity of the system and system mode has been reported in the literature [e.g. (Siller, 2004)]. Geometric and material nonlinearities construe consequences of structural behaviour under high-order strains. The aims of this study are to detect the nonlinear behaviour of soil, piles and structure under different seismic load types, evaluate the effects of SSI and PSSI and then assess the ASCE and EC8 seismic provisions in terms of the aforementioned factors. Contrary to expectations, this study does not find a significant relationship between the increase of acceleration response, which is a significant factor in seismic design code load, and the amplitude structural stress. Despite covering the code models and requirements, the stress values exceed the limitations in several circumstances. These valuable results coincide

290

with the recommendation of both codes to further investigate the issues in the analysis of soft soil and/or high-rise building and include the effect of SSI.

6.7. Conclusion remarks

This study is designed to determine the effects of incorporating SSI on the seismic response of a structure and compare the findings with EC8 and ASCE seismic provisions.

The following conclusions can be drawn from this study:

- Seismic design standards according to ASCE and EC8 seismic codes are assumed safe for the high-rise frame structures by considering SSI. However, the findings clearly indicate that the structural response may exceed the limitations, making the provisions potentially unsafe.
- The relevance of the connection between the selecting and matching of input data and the geological and geotechnical site properties is supported by the findings.
- This study raises important questions about the nature and reliability of the base-shear reduction factor recommended in both codes. A smaller reduction factor should be used as the effects of larger field nonlinearity, i.e. geometrical and material nonlinearity, increases the ductility demand of the system.
- The effects of SSI on different members in diverse' positions are dissimilar, so different reduction factors must be considered in member seismic design.
- The SSI problem is complicated. Evidence from this study suggests that further investigation is needed to determine a rational reduction factor.
- Pure reduction according to the reduction factor of the current seismic codes may be unsafe.
- The number of modes is associated with the response of the SSI model. Given this connection, the SSI effects should be involved in the analysis. In this respect, the results explain to an extent why the assumption of ASCE and EC8 to base analysis on the fundamental period, which is computed by the code equations, may be illogical and inadequate. Further quantitative research should be undertaken to establish a clear procedure for determining the minimum number of structural modes which should be incorporated in the analysis.
- These findings have important implications for the understanding of pile and pile group effects.

Chapter 7: Definition of Soil Class F

7.1. Introduction

Seismic design code provisions reveal that, regardless of the quality of seismic provision for the design and construction of structures, structures do not pose the same seismic risk (i.e. not all structures are at the same risk of seismic damage). Two main factors may influence the level of that seismic risk. The first is the ground motion intensity and other earthquake properties (see Chapter 6 Section 3.2.1.1). The second is the level of importance of the structure. Seismic design codes use the concept of seismic design category (SDC) to classify structures according to the seismic risk that they can pose (Georgescu *et al.*, 2018). As mentioned in Chapter 6, six seismic design categories range from A to F, corresponding to the minimal and highest posed seismic risk. As the potential seismic risk of a structure as characterised by the SDC rises, the seismic design provisions need progressively further arduous seismic design as a means to guarantee that the designed structure can withstand an appropriate level of risk (FEMA P-749, 2010). In other words, as a SDC for a structure increases, the strength, detailing requirement and the cost of supplying the appropriate seismic resistance rise. The potential seismic risk related to the type of structure in different seismic design categories and the main protective scales needed for structures in each category are listed in Section 20.3.1 in ASCE and Section 1.2.3 in EC8 (EC8-Part-1, The European Union, 2011; ASCE 7-16, 2017). Accordingly, structures are assigned to a SDC depending on the seriousness of ground motion and other earthquake properties in addition to the nature of the occupancy and function of the structure. The critically important structures located within a few kilometres of major active faults capable of producing a Modified Mercalli Intensity Scale (MMI) of IX or more intense shaking can be classified under class *F* of SDC (SEI/ASCE 7-02, 2013). The nature of a structure's function employed in deciding SDC is classified into four categories of occupancy. The most critical category is IV category, in which the representative structures are essential to post-earthquake response such as hospitals, police stations, fire stations, emergency communications centres or housings with substantially large quantities of perilous materials. The acceptable risk for this category, however, must be very low. Structures under this category should be able to withstand structural collapse because if not, the structures can be damaged seriously, impairing post-earthquake response and recovery efforts and releasing hazardous materials.

Site soil condition is another key factor in deciding the SDC of a structure. Hard, competent rock materials effectively transmit motion with short-period (high-frequency) energy content but manage to lessen and filter the motion out with long-period (low-frequency) energy content. Deep soft soil deposits transmit short-period (high-frequency) motion less efficiently but manage to amplify the long-period (low-frequency) energy content (SEI/ASCE 7-02, 2013). Once type and depth of the different deposits at a site are identified, site response analysis can be performed successfully. The consequences of the type and depth of a deposit may be presumed approximately for most cases when the soil type and properties are available. Seismic design codes recommend seismic provisions to apply the theory of site class in classifying normal soil conditions into comprehensive classes to which typical ground motion reduction or amplification consequences are designated. Site class is defined based on the average properties of the top 30 m layer(s) of the soil deposit, and ASCE and EC8 list six site classes ranging from A to F and A to S1 and S2, respectively (ASCE 7-16, 2017; EC8-Part-1, The European Union, 2011). Geotechnical seismic design properties of these soils can be characterised by employing a set of parameters, including soil classifications as type of soil, number of blows (N) needed for the standard penetration test, shear wave velocity (vs) and undrained shear strength of the soil S_u as calculated using standard laboratory test techniques. However, one of the hazardous seismic code recommendations is that any site is allowed to be classified as site class D unless there is justification to consider that it will be more appropriately categorised as site class E or F.

Traditionally, the previous seismic codes other than 1997 UBC consider that the soil type affects the force level for mid-rise and high-rise buildings, and thus typically does not influence the seismic design force for low-rise buildings. In the current seismic design codes, however, the site classes influence the seismic design force level for all three types of structures directly. In zones of low or moderate seismic activity, a variation in site class may adjust the SDC, leading to differences in design and detailing characteristics. Considerable changes in seismic design force and detailing requirements contingent upon the site class are associated with detected earthquake damage. Typically, structures founded on soft or loose soil experience substantially more damage than similar structures set on hard soil or rock deposits.

7.2. Basis for site classification and problem statements

The basis for site classifications is supplied in Recommended Provisions for Seismic Regulations (NEHRP) for New Buildings and Other Structures (FEMA450) commentary for

ASCE and EC8. The commentary illustrates how soil deposits amplify the level of ground motion comparative to the level of motion at bedrock. The magnitude of ground-motion amplification hinges on characteristics of the wave propagation of the soil deposit which can be determined by measuring shear wave velocity. Soft soils with lower shear wave velocities commonly generate more substantial amplification than stiff soils with higher shear wave velocities. In all seismic design codes, site classes are characterised in terms of shear wave velocity. Although the site class category is described a single type of soil or rock, most sites comprise multiple layers of different types of soil and rock. As previously mentioned, in categorising a site class, all soil and rock layers within the top 30 m of the site profile must be considered. Sites consisting primarily of very dense glacial tills, sand, gravel and very shallow rock deposits are frequently classified as site class C. Once shallow foundations are approved for a structure, site classes C and D are typically applicable, with site class D being more prevalent. In the case when deep foundation is needed, site class E is usually considered appropriate. However, some sites with comparatively shallow deep foundations (foundation depth ≤ 10 m) are classified as site class D. Once a site contains soils which are vulnerable to collapse during an earthquake such as liquefiable soils, quicksand and highly sensitive clay and collapsible weakly cemented soils, site class F is applicable.

Site class F, however, requires a specific site response analysis to evaluate the ground-motion amplification of the corresponding site deposit. For a default site class , ASCE 7-02 and ASCE 7-05 state: 'When the soil properties are not known in sufficient details to determine the site class, site class D shall be used unless the authority having jurisdiction or geotechnical data determines site class E or F soils are present at the site' (SEI/ASCE 7-02, 2013; SEI/ASCE 7-05, 2013). A complicated issue is that most seismic engineers attempt to avoid classifying a soil class as class F, which does not fit an appropriate box of classification according to ASCE Table 20.3.1 and thus requires a specific site response analysis according to Section 21.1. ASCE Table 20.3.1 specifies that a site classification for site class F must be treated according to Section 20.3.1. Where any of four specified conditions (see Section 3) is satisfied, the site shall be classified as site class F and a site response analysis in accordance with Section 21.1 must be performed. Two out of the four conditions are significantly vague in their description and risky to be left to human decision (taken by individual engineers). Firstly, the circumstances of soil are vulnerable to potential failure or collapse under seismic loading, such as liquefiable soils, quicksand and highly sensitive clays and collapsible weakly cemented soils. The definition is hazardous

294

because codes never specify how much the layer thickness of soil constitutes site class F. This situation has always been tricky, and every consultant has their own interpretation of how much should be the soil layer thickness which can filter the wave passing through and changes the soil profile behaviour be considered as site class F.

ASCE states an exception. For structures having a fundamental period of vibration equal or less than 0.5 sec (natural period $\leq 0.5\ sec$), site response analysis is not required to determine spectral accelerations for liquefiable soils. Rather, site class is permitted to be determined in accordance with Section 20.3 and the corresponding values of $F_a\ and\ F_v$ determined from Tables 11.4.1 and 11.4.2. The consideration of site class F goes away, and site response analysis is unnecessary. Secondly, very thick soft/medium stiff clays [H >120 ft. (37 m)] with $S_u < 1000$ psf (50 kPa) exist (ASCE 7-16, 2017). This situation is also tricky due to the circumstances of cutting off the continuity of the thick clay soil, which satisfies the code condition to be considered as site class F, by a thin land of sand. Consequently, the thick layer of soft/medium stiff clays (H $\geq$37 m) is divided into two layers and no longer satisfies the code condition. Thus, specifying the minimum thickness of sand layer which can divide the thick soft soil layer into two parts is essential to define site class correctly and successfully. To minimise the hazardous consequences of making the wrong decisions and accomplish a clear vision and a reliable solution for researchers, designers, analysers and people who are not experts in the geotechnical area, these problems should be coded. The following two critical issues are addressed in the current study:

(i) The minimum thickness of sensitive clay to be considered to meet code condition for soil class F

(ii) The minimum thickness of sand layer that cuts off the continuity of soft clay layer (which meets code condition) to be no longer classified as F

7.3. Effect of soil class according to EC8 and ASCE

Specifying a site class for a certain circumstance of site condition depends completely on several geotechnical soil deposit properties, such as shear wave velocity $\bar{V}_s$ (for upper 30 m), averaged SPT resistance or blow counts $(\bar{N}\ or\ \bar{N}_{cb})$ and undrained shear strength $\bar{S}_u$ for fine-grained the soil. As mentioned before, these site classes vary from A for hard rock soil type to F for highly sensitive or soft clay soils which require site response analysis following Section 21.1 in ASCE or Section 1.2.3 in EC8. Site class F is considered for soft/sensitive soil deposits that can robustly amplify long-period ground motions. Seismic design codes define the most significant soil characteristics and

conditions to categorise site class F. Section 20.3.1 of ASCE or Section 1.2.3 of EC8 specify four conditions. One of them needs to be satisfied to categorise site class of soil as class F.

1. Soil vulnerable to potential failure or collapse under seismic loadings, such as liquefiable soils, quicksand, *highly sensitive clays* and collapsible weakly cemented soils
2. Peats and/or highly organic clays $[H > 10\ ft.(3m)]$ of peats and/or highly organic clays, where H is the thickness of the soil layer
3. Very high plasticity clay $[H > 25\ ft.(7.6\ m)\ with\ PI > 75]$, where PI is the soil plasticity index
4. Very thick soft/medium stiff clays $[H > 120\ ft.(37\ m)]$ with $\bar{S}_u < 1000\ psf\ (50\ kPa)$

By exploring the above four points, the definitions of the first and fourth conditions are vague, and their characteristics are ambiguous. The vague definitions lead to personal interpretations that may create substantial mistakes. Therefore, the present study attempts to specify characteristics of clay soil concerning these two parts and code these characteristics effectively. Consequently, the soil class decision will be based on the coded specification rather than on the opinion of engineers.

7.3.1. Minimum thickness of sensitive clay to meet code condition of class F

Codes specify that soils vulnerable to potential failure under seismic loadings, such as highly sensitive clays fall under site class F (Section 20.3.1, ASCE). Seismic code provisions never specify what thickness of soil layer is needed to be effective and classified as a site class F, so this description tends to be a hazardous definition. These tricky circumstances drive every consultant to apply his/her interpretation of how much is the effective soil layer thickness that can filter the motion effectively before site class F needs to be considered.

The current study intends to answer circumstance (i) adequately. No clear and specific answer for this particular circumstance is found in the seismic standards or the literature on seismic design area. Codes mention the type of soil that falls on the site class F without indicating any thickness limitations, leading to much confusion. To specify the minimum thickness of sensitive clay that is going to filter the passing ground motions and then meet class F code condition, six FE models are developed. Each of them comprises two thick

layers of sand soil (20 m), each with a tiny layer of sensitive clay with thickness starting from 0.25 m to 1.25 m, with 0.25 increases by model. The effective thickness of the sensitive layer is identified after performing a set of analyses and comparing the findings.

7.3.2. Minimum effective thickness of cut-off sand layer

One of the criteria in Section 20.3.1 of ASCE to consider soil class as F is soft, medium or stiff clay soil with a thick layer of 37 m and undrained shear strength of S_u<50 kPa. However, due to soil profile arrangement conditions, a meagre layer of sand soil divides the thick layer ($H \geq 37\ m$) of clay into two layers, inducing a new intricate circumstance that no longer satisfies the seismic code condition of site class F. This relatively tiny layer of sand may cut off the continuity of the clay layer that is supposed to be meeting the seismic code condition of requiring site response analysis following Section 21.1 (ASCE 7-16, 2017). A significantly debated question emerges here: whether the accumulative thickness of clay layers but not the individual layer meets the seismic code condition for soil class F. Moreover, how much is the minimum effective thickness of sand layer that interrupts the profile of clay soil and changes the code classification condition?

This hazardous circumstance is examined carefully in the present study with the objective of defining the minimum effective thickness of sand layer that may cut off the continuity of soft clay layer to be no longer categorised as class F according to Section 20.3.1 of ASCE. This study aims to specify the effective minimum thickness of sand layer that can divide the thick soft soil layer into two parts or the accumulative thickness of the soft clay layer that must be considered to successfully define the condition for this site class.

7.4. Methodology

Choosing a successful methodology that can identify the effects of two different soil classes and the efficient technique of employing clay and sand material properties to meet the targeted objectives is a critical decision in the current study. To highlight the vague provisions that affect the classification of a soil class as F, according to two hazardous seismic design code provisions, the sequential analysis method appropriate for considering the consequences of the geostatic, static and seismic loads in the case of SSI analysis approaches is adopted. Two circumstances described in Sections 7.3.1 and 7.3.2 are performed: (*i*) minimum thickness of sensitive clay to meet code condition for soil class F and (*ii*) minimum effective thickness of sand layer for continuity of sensitive clay layer. The characteristics of motion resulted at the surface of soil layer(s) are evaluated and compared for both circumstances. According to the basic definition of site class F,

two sets of analysis are developed, each set illustrating one of the two cases mentioned above. Whether to consider or not the influence of sensitive soil on system behaviour and the ability of sand layer from cutting off the continuity of thick soft soil are compared for different sensitive soil and (slicer) sand layers' thickness and analysis conditions for both studied circumstances.

Five different soil thicknesses of sensitive clay of (0.25, 0.5, 0.75, 1.0 and 1.25) m are used for circumstance (i) and seven various sand thicknesses of (0.25, 0.5, 0.75, 1.0. 1.25, 2.0 and 4.0) m are employed for circumstance (ii). The resultant acceleration time history at the base and top surfaces of soil system model for circumstance (i) are compared for all five cases (models). The resulting acceleration time history of three different elevations at the base of the soft clay (base of the model), point (C); the top surface of soft clay, point (B) and top surface of sand (cut-off) soil, point (A) for circumstance (*i*) are compared for all five cases (models) (see Figure 7-1). The time history input data modified in Chapter 6, i.e. RSN3744–1992 Cape Mendocino, is used as earthquake loading applied at the base of simulated model(s), (see Chapter 6 Section 3.2.1.1). The simulations in the current research are divided into two phases according to analysis type. Phase I represents the frequency analysis to compute the model modes of the systems. The Rayleigh damping factor is calculated, by which viscous damping is considered in the phase II analysis. Phase II is performed by developing three analysis steps, namely, geostatic, static and dynamic steps for both circumstances mentioned above.

(a)

(b)
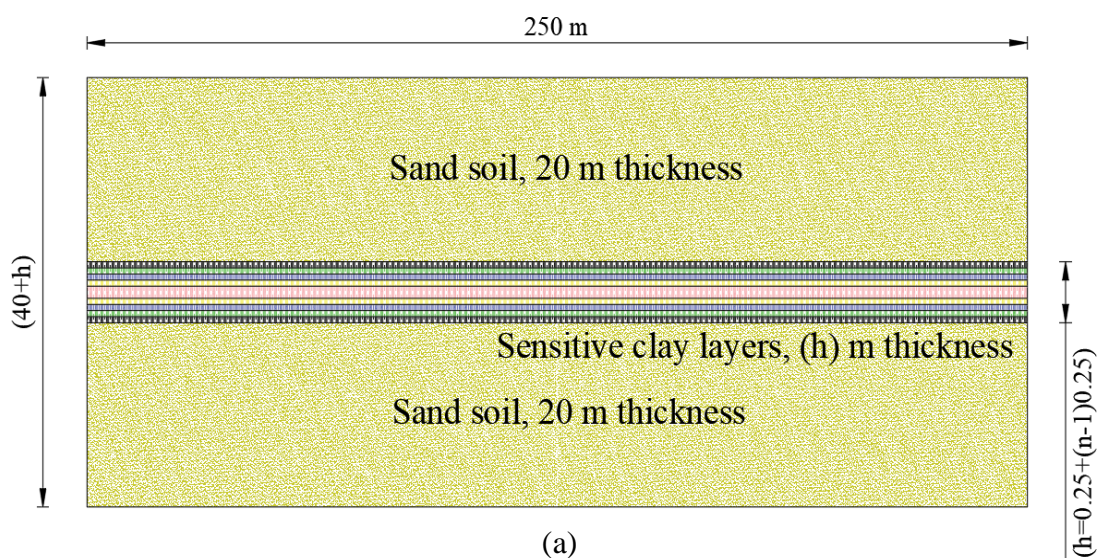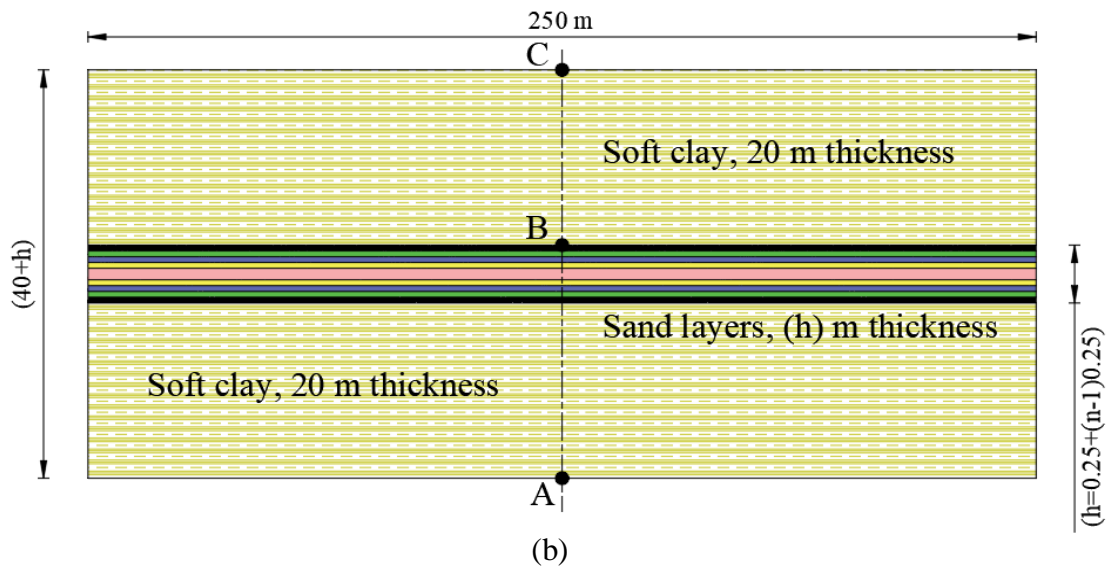
Figure 7-1 Schematic Demonstrating (a) Circumstance (i), h is the Thickness of the Sensitive Cay and n is the Case Number .(b) Circumstance (ii), h is the Thickness of Sand Soil and n is the Case Number.

The geostatic step is generally used as the first step in most geotechnical analysis problems. The nonlinear effects of large deformation and displacement is considered in this step as well as the other two steps (static and dynamic steps). Automatic incrementation with the limitation of maximum displacement change of 0.1 is adopted. Direct method as an equation solver using asymmetric matrix storage and 'full newton' as solution technique is used in the geostatic step.   The second step applied in the analysis is the static step. Damping factor is specified as 0.0002 for the stabilization of unstable problems employing adaptive stabilization with maximum ratio of stabilization to strain energy of 0.05. Automatic incrementation type is applied. Direct method as an equation solver using asymmetric matrix storage and full newton as solution technique is employed. Abaqus presumes that external parameters, such as loads and boundary conditions, are either constant–step function or vary linearly ramped over a step. However, the appropriate option must be selected depending on the analysis procedure. Ramp linearly over static step option is thus used in the current study. The third step is dynamic implicit step, in which automatic incrementation type is applied with default maximum increment size. An asymmetric matrix storage and full newton as solution technique is employed. Ramp linearly over dynamic step option, default time integrator parameter and initial acceleration calculation at the beginning of dynamic step are used in this analysis step (dynamic step). The time history input data Are applied at the bottom of the clay/sand soil (which is presumed to represent the bedrock site class, see Chapter

6) for the dynamic step. The output time history data are treated with SeismoSignal software to compute the motion properties of the resultant time history and then compare the findings according to the objectives of the study.

7.4.1. Soil model properties

Two engineering fields are chosen for this study: the first field lies in San Francisco Bay, where the target prototype soil is fully described in Chapter 6 and represents the soft soil condition in this chapter. The second engineering field is marine clays in Canada investigated by (Nader, 2014), which is used as a sensitive soil model in this study. This type of clay is the result of three main types of sedimentation processes which are water laid tills, lacustrine tills and mudflows. Water laid till is a stratified variety of till deposited in water that usually overlies hard till. These types of clays are generally called Leda clays in Ontario and Champlain Sea clays in Quebec (Nader, 2014). In general, soil sensitivity can be defined as the ratio of the initial undrained shear strength to the remoulded undrained shear strength. In the Con penetration test (CPT), however, the tip resistance and excess pore water pressure can be considered as functions of the undrained shear strength. The sleeve friction can be considered as a function of the remoulded shear strength. Accordingly, the two following relationships can be employed to predict soil sensitivity (Schmertman, 1978), (see Eqs.(7.1) and (7.2) .

$$S_t = \frac{N_s}{R_f} \qquad (7.1)$$

$$R_f = \frac{f_s}{q_t} \qquad (7.2)$$

Where S_t is soil sensitivity, N_s is test constant, R_f is friction ratio and f_s sleeve friction. As the sleeve friction value f_s can be considered equal to the remoulded shear strength, soil sensitivity can be predicted by applying the S_u and the sleeve friction values obtained from CPT following Eq. (7.3), (Bosch & Sotelo, 2015).

$$S_t = \frac{S_u}{f_s} \qquad (7.3)$$

According to the Canadian Engineering Foundation Manual (2006), where the reference study (Nader, 2014) is based, soil sensitivity can be considered high once its value ranges between 4 and 8. Owing to the soft consistency and sensitivity behaviour of these soils, dealing with their geotechnical properties in practice is severely challenging. They may transform from solid-state to liquid consistency only by disturbance, making them

vulnerable to landslides and/or foundation failure. Site 2 has been selected from a larger study that used 15 sites from the Canadian capital region, and a depth of 5m is used as the taken soil properties. These 15 sites were formerly investigated for geotechnical design purposes, where in-situ investigations and laboratory tests were executed (Nader, 2014). The in-situ investigations involved cone and standard penetration tests, split spoon and undisturbed sampling and field vane and monitoring well testing. Laboratory tests involved those on consolidation, grain size distribution, specific gravity, plasticity, moisture content and unit weight. Figure 7-2 illustrates the variation of the soil sensitivity with the depth for Site 2. The soil with high sensitivity of 9.0 at 5 m depth is chosen as a soil model to be employed in the current study, and all other required properties are taken at the same level. Void ratio values at different depths were computed in the reference case study (Nader, 2014) using one-dimensional consolidation test following the ASTM D 2435 standard. The void ratio values of Site 2 range between 1.0 and 2.80 for different soil depths. The void ratio value at 5 m depth is selected as soil model property that equals to 2.0 (see Figure 7-3).

The unit weight was concluded in the reference study in the laboratory (see Figure 7-4). These unit weight values range between 15.3 and 21.0 kN/m^3 and change with depth. Soil unit weight value at 5 m depth of 18.0 kN/m^3 is adopted in the present study. The specific gravity was estimated in the reference study following ASTM D854 (see Figure 7-5). The specific gravity values range between 2.70 and 2.785 in general for Site 2, and the value at 5 m depth is adopted. In the reference study (Nader, 2014), the Atterberg limits were concluded in the laboratory in accordance with ASTM D4318 (see Figure 7-6), and the value at 5 m depth was selected. The OCRs of the sensitive marine clays in Site 2 are demonstrated in Figure 7-7.

The OCR values range between 2.936 and 7.0, the OCR at 5 m depth (4.0) is implemented. The undrained shear strength values obtained in the reference study (Nader, 2014) are presented in Figure 7-8 along with the shear strength values estimated from the SPT test. However, Figure 7-8 indicates that the undrained shear strength values coming from the CPT test at 5 m depth is 6.30 kPa. The compression index values of the marine clays of the studied site (Site 2) are displayed in Figure 7-9. They are computed by running the oedometer tests. No clear relationship with site depth can be seen, and the Cc values range between 0.4 and 2.11. The Cc value for the depth of 5m is 1.037. Figure 7-10 illustrates the variation of the coefficient of consolidation with pressure, and Figure

7-11 demonstrates the variation of the coefficient of consolidation with pressure from oedometer tests for Site 2 at 5 m depth. All soil properties used in this study are listed in Table 7.1.
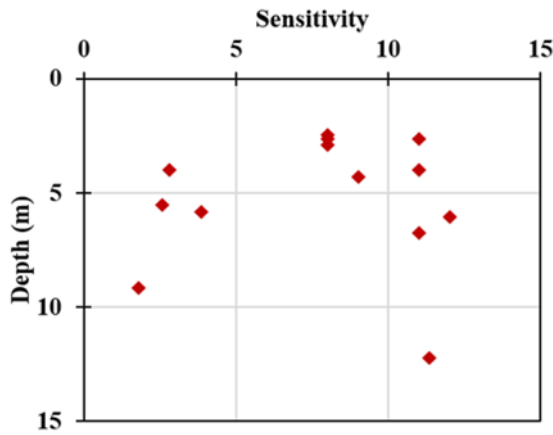
Figure 7-2 Sensitivity with Depth
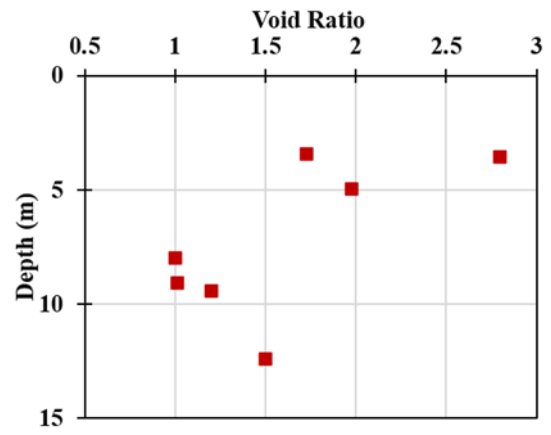
Figure 7-3 Void Ratio with Depth
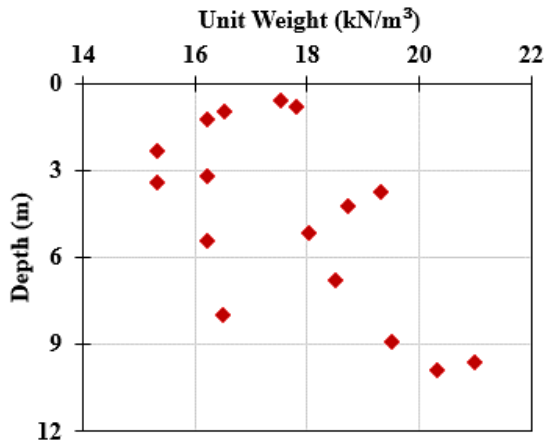
Figure 7-4 Unit Weight with Depth
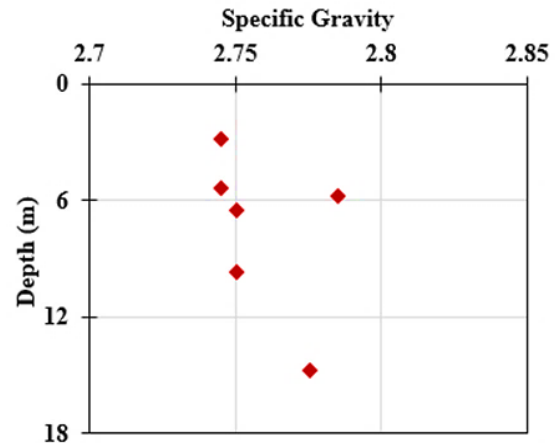
Figure 7-5 Specific Gravity with Depth
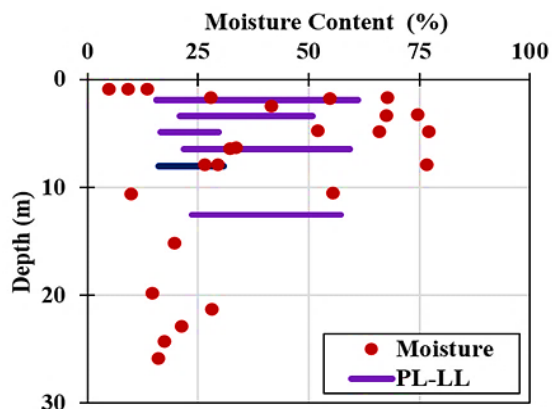
Figure 7-6 Atterberg Limits with Depth
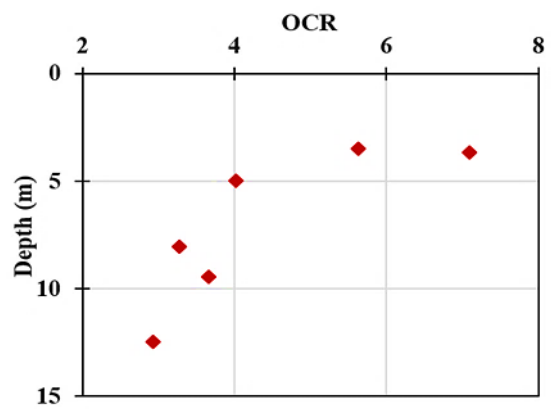
Figure 7-7 OCR with Depth
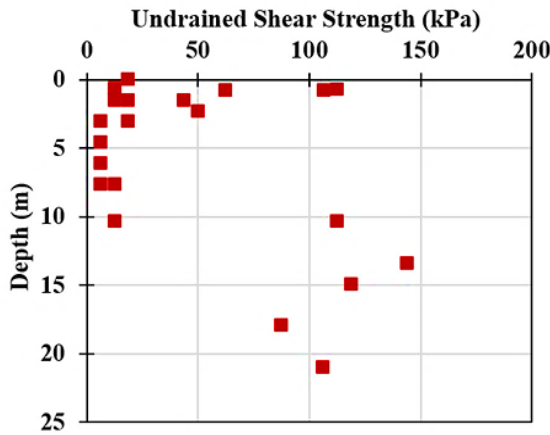
Figure 7-8 Undrained Shear Strength
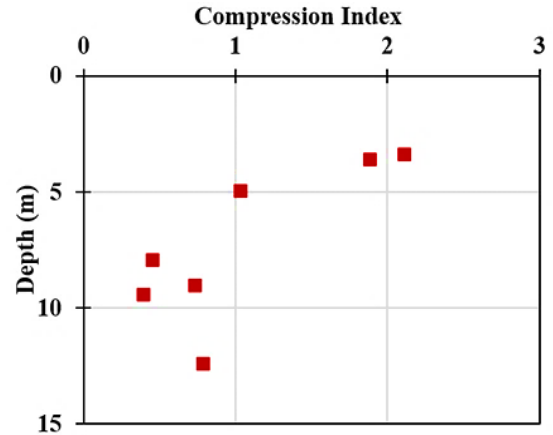
Figure 7-9 Compression Index with Depth
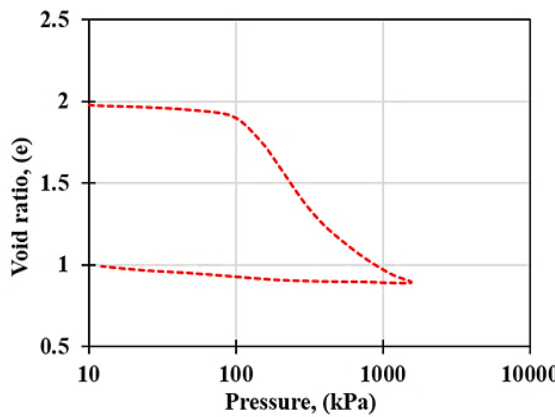
Figure 7-10 Consolidation Curve with Pressure
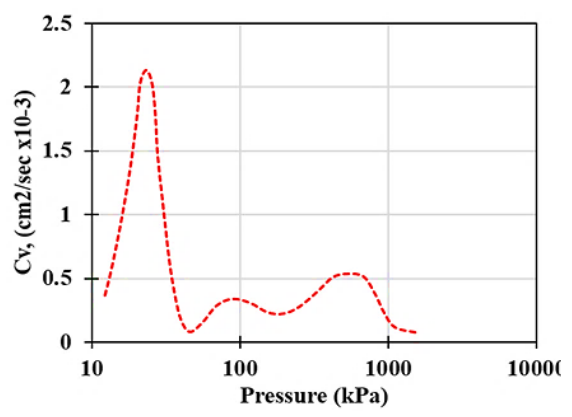
Figure 7-11 Coefficient of Consolidation with Pressure

Table 7.1 Soil Properties for the Sensitive Clay Soil Model

Parameters	Values
Density [Kg/m^3]	1652
Undrained shear strength (S_u) KN/m^2	6.275
Poisson's ratio	0.45
Shear wave velocity m/sec	111
Sensitivity	8-12
Void ratio	1.976
Specific gravity	2.745
OCR	4.0
Compression Index	1.0
Water content	53%
Liquid limit	30%
Plastic limit	17%
Plasticity index	13.5%
Rayleigh damping	5%

303

7.4.2. Numerical model

In simulating a half-infinite space system, FEA is a crucial method for such a finite region. The continuity of the soil at both sides of model must be cut off at a specific location to model the system's horizontal infinity. The two sides' free edge, however, are replaced by an artificial boundary condition by generating the soil boundary of the principal region as far as possible (Yue & Wang, 2009). Sensitive analysis is made to select the suitable model dimension and finer element size that can produce the most successful results. The effective model dimensions are $((40+h) \times 250$ m) for both cases, where h is the variable thickness of sensitive clay soil for circumstance (*i*) and the cut-off sand for circumstance (*ii*) (see Figure 7-1 (a) and (b), respectively). From this perspective, free boundary conditions are adopted in the present study. Free boundaries in the vertical direction and constrained boundary in the horizontal direction are used for geostatic and static steps. This arrangement is in reverse for the frequency and dynamic steps. The boundary conditions for the base of the model, which is presumed as the surface of the bedrock, are managed as follows:

(i)   Symmetry/anti-symmetry/encastre for the linear perturbation-frequency step
(ii)   Fixed in horizontal and vertical directions for geostatic and static steps
(iii)   Displacement and acceleration/angular acceleration boundaries for seismic analysis step

Fixed mechanical displacement in the vertical direction and free mechanical displacement in the excitation in the x-direction represent the first boundary in this case (U1). The moving boundary is illustrated by applying the acceleration/angular acceleration in the direction of excitation. Standard, linear and plain strain shell element types with reduced integration are employed to simulate the soil. The enhanced option is used for hourglass control purpose. The element size for the horizontal direction starts from 4 m at the model far edge and is refined once closer to the model centre to be 1 m. However, this size is stuck at 1 m along the vertical direction. Mesh sensitivity analysis is performed to optimise the selected reliable mesh size.

The geostatic stress field is prescribed for clay and sand soil in both simulated circumstances. According to model condition, the stress in the vertical direction (y-direction in current models) is presumed to vary piecewise linearly with the vertical coordinate. The corresponding soil lateral coefficient (for sand and clay) is applied in predefined field option. Initial void ratio of sand and soft clay materials are applied in

304

initial step (predefined field) as uniformly distribution defined. Cam–Clay soil model is applied to simulate the soil constitutive behaviour for soft clay soil, whereas Drucker–Prager model is employed to simulate the soil constitutive behaviour of sand soil. These two soil constitutive models are described in detail in Chapter 4 (see Sections 4.3.2 and 4.3.3). The material properties corresponding to clay and sand materials applied for the present FEA are shown in Table 7.2.

Table 7.2 Material Properties for Sand Sensitive Clay and Soft Clay

Parameter	Sand	Sensitive Clay	Soft Clay
Density kg/m3	1923	1652	1505.75
Log Bulk Modulus	-	0.03	0.047
Poisson's Ratio	0.3	0.47	0.45
Tensile Limit	-	0	0
Log Plasticity Bulk Modulus	-	1.0325	0.27
Stress Ratio	-	1.467	1.258
Wet Yield Surface Size	-	1	1
Flow Stress Ratio	1	0.778	0.778
Young's Modulus	182000000	-	-
Material Cohesion	0.0001	-	-
Angle of friction	44.56	-	-
Cap Eccentricity	0.2	-	-
Initial Yield surface	0	-	-
Transition surface radius	0.1	-	-
Initial Void Ratio	1.5	1.976	1.496

7.5. Results

7.5.1. Frequency analysis

To understand the effect of soil class and soil profile arrangement on resonance structures during earthquakes, the frequency analysis for the model system is performed according to analysis conditions. However, the resonance of a system is the tendency of a system to oscillate with higher amplitude at some frequencies than at others. In other words, it is the frequency at which the maximum amplitude oscillation occurs, and this state differs depending on system/structure conditions. All types of structures and ground have a specific natural period or resonant frequency. Hard bedrock has higher frequencies than softer soil deposits. Once the period of ground motion matches the natural resonance of a structure, the structure will undergo the most considerable possible oscillations and experience enormous damage (Taranath, 2016). Small buildings of one or two storeys resonate naturally at much less than one-second periods. A one-second period will affect buildings of about ten storeys. For example, a 30-storey building resonates at a period of 3.0 sec, and a 50-storey building at a period of 5.0 sec. As mentioned earlier in (Chapter 1and Chapter 2), during the 1985 Mexico City earthquake, the ground beneath the city

resonated with a 0.5 Hz for over 60 sec. Consequently, the medium-high buildings with the same resonant frequency (natural period) experienced the most damage, whereas short (old, weak stone buildings) and high-rise buildings were relatively undamaged. Such evidence supports the concept that seismic engineers describe as resonance disaster, wherein the destruction of a structure is due to seismic vibrations at a natural period of the system.

The prolonged input energy results in higher system vibration that becomes stronger until exceeding the structural load limit. However, the key concept is that small structures founded on hard rock and large structures founded on soft deposit may experience more damage than small structures sitting on soft deposit and large structures on hard rock as a consequence of natural period matching. Resonance is a crucial factor that contributes to earthquake damage, and it has the most significant influence on achieving effective seismic structural design. Defining the correct resonant frequency (natural period) of the deposit underneath a structural site and modifying the seismic structural design according to obtained natural period can change the function and eliminate the resonance hazard.

The vibration period for both case studies are obtained from frequency analysis models. For the soil constitutive model, hysteretic damping and viscous damping are included in the soil model. Hysteretic damping is involved in the restoring force, whereas viscous damping is considered by Rayleigh damping (see Chapter6 Section 4). According to the orthogonality between system mode and damping matrix and the assumption of 5% damping for the system modes, the corresponding coefficients of Rayleigh damping are calculated by Eqs. 6.6 and 6.7 (Chapter 6). The first 10 natural vibration periods and damping coefficients of all five/seven models for circumstances *i* and *ii* are listed in Table 7.3 and Table 7.4 and illustrated in Figure 7-12 and Figure 7-13. Table 7.3 and Figure 7-12 demonstrate that the estimated first mode periods for circumstance (*i*) are lengthened by 10.1%, 20%, 29% and 37% when the thickness of the sensitive soil layer is extended by 0.25 m. The periods are lengthened as the layer thickness increases from 0.25 m to 1.25 m. This significant increase in mode periods indicates a preliminary effect of minimum sensitive soil layer thickness on system behaviour which is obtained and approved in Section 5.2. According to the findings in Table 7.4 and Figure 7-13 for circumstance (*ii*), the decrease differences between case 1 and case 7 for the first mode values are very small, and these differences range between 0.32% and 0.48%. As the thickness increases to 1.25 m, this percentage tends to range between 0.7% and 1.28%

for the last two cases (case 6 and case 7), when the clay layer expanded to 2 m and 4 m, respectively. Figure 7-13 evinces that the system behaves in a different way and the percentage of difference for the second modes is deamplified more clearly. The estimated second mode periods are decreased by 1.6%, 3.3%, 4.6%, and 5.7% when the thickness of the sand soil layer is expanded by 0.25 m for case 1 to 5 and 8.5% and 13%, when the sand layer is extended to 2 m and 4 m for cases 6 and 7, respectively.

Table 7.3 First 10 Natural Vibration Periods and Factors of Rayleigh Damping for Circumstance (i)

Model	Natural vibration period (s)										Damping coefficients	
	Models											
	1	2	3	4	5	6	7	8	9	10	α_m	β_k
Case1	0.964	0.817	0.605	0.488	0.472	0.468	0.467	0.445	0.442	0.416	0.353	0.007
Case2	1.061	0.875	0.629	0.504	0.483	0.483	0.479	0.460	0.451	0.429	0.324	0.008
Case3	1.154	0.926	0.649	0.518	0.497	0.495	0.491	0.473	0.457	0.441	0.302	0.008
Case4	1.240	0.970	0.665	0.531	0.510	0.506	0.502	0.485	0.463	0.452	0.284	0.009
Case5	1.321	1.008	0.678	0.544	0.523	0.518	0.514	0.497	0.468	0.462	0.270	0.009

Table 7.4 First 10 Natural Vibration Periods and Factors of Rayleigh Damping for Circumstance (ii)

Model	Natural vibration period (s)										Damping coefficients	
	Models											
	1	2	3	4	5	6	7	8	9	10	α_m	β_k
Case1	5.042	4.617	3.895	3.340	2.960	2.686	2.478	2.311	2.250	2.241	0.074	0.034
Case2	5.045	4.543	3.794	3.278	2.932	2.678	2.477	2.312	2.220	2.209	0.076	0.033
Case3	5.026	4.466	3.719	3.240	2.918	2.674	2.476	2.311	2.226	2.192	0.077	0.032
Case4	5.022	4.406	3.665	3.217	2.911	2.673	2.476	2.311	2.234	2.180	0.078	0.032
Case5	5.018	4.353	3.624	3.200	2.906	2.672	2.476	2.311	2.243	2.171	0.079	0.032
Case6	5.006	4.225	3.545	3.172	2.898	2.670	2.477	2.311	2.268	2.170	0.081	0.031
Case7	4.977	4.015	3.455	3.145	2.892	2.670	2.477	2.332	2.309	2.166	0.084	0.030

The compared periods decrease by 13% as the sand layer thickness increases from 0.25 m to 4m. The 13% reduction in values suggests a preliminary sign of the minimal consequence of cut-off on system behaviour which is obtained and approved in Section 5.2.3 in the current study. Figure 7-14 to Figure 7-18 show the first six modes for all five cases of circumstance (i). Figure 7-19 to Figure 7.25.
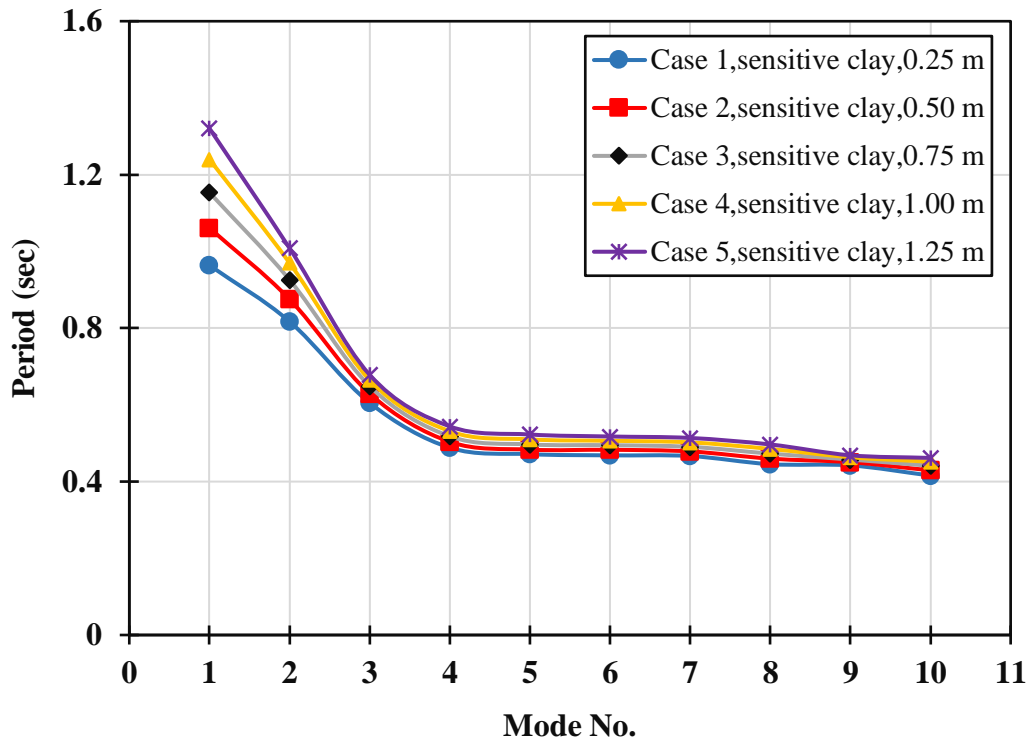
Figure 7-12 First 10 Natural Vibration Periods of the System for Circumstance (i)
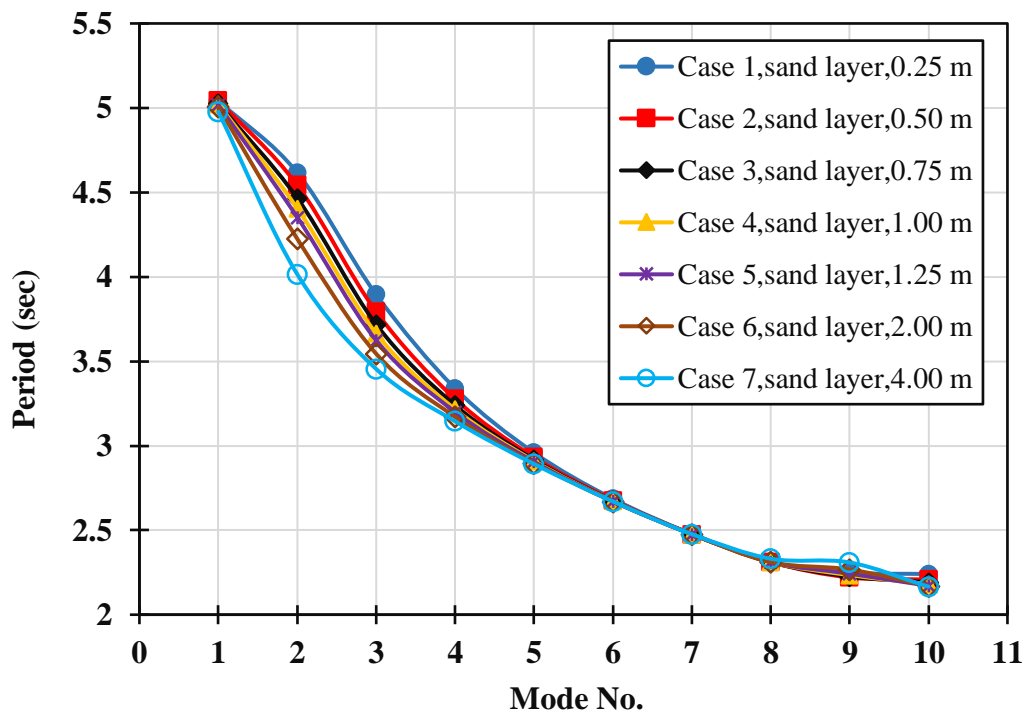
Figure 7-13 First 10 Natural Vibration Periods of the System for Circumstance (ii)
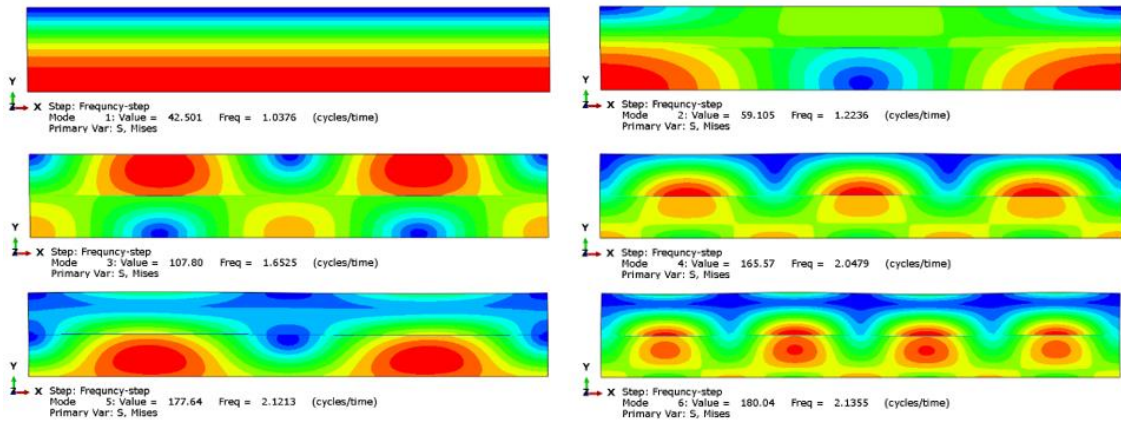
Figure 7-14 First six modes of the system for circumstance (i), Case 1
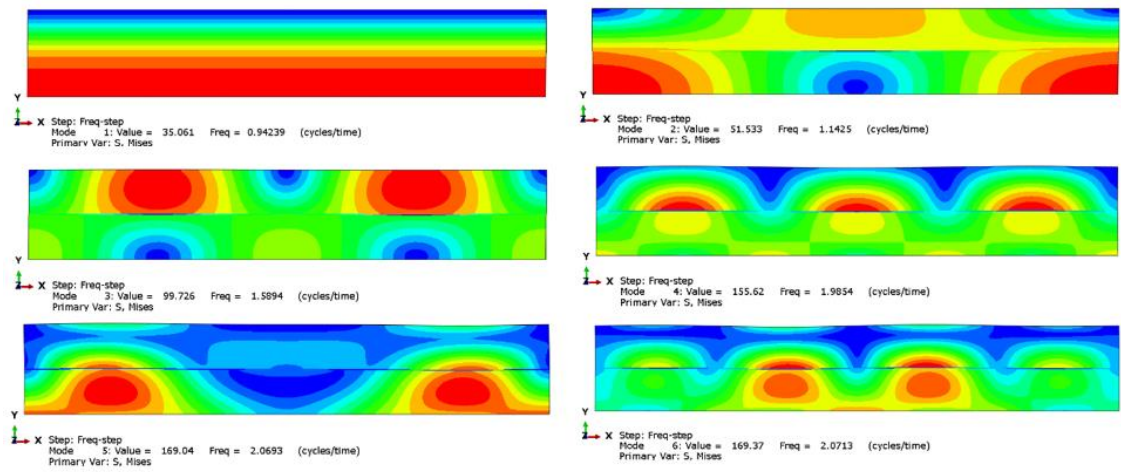
Figure 7-15 First six modes of the system for circumstance (i), Case 2
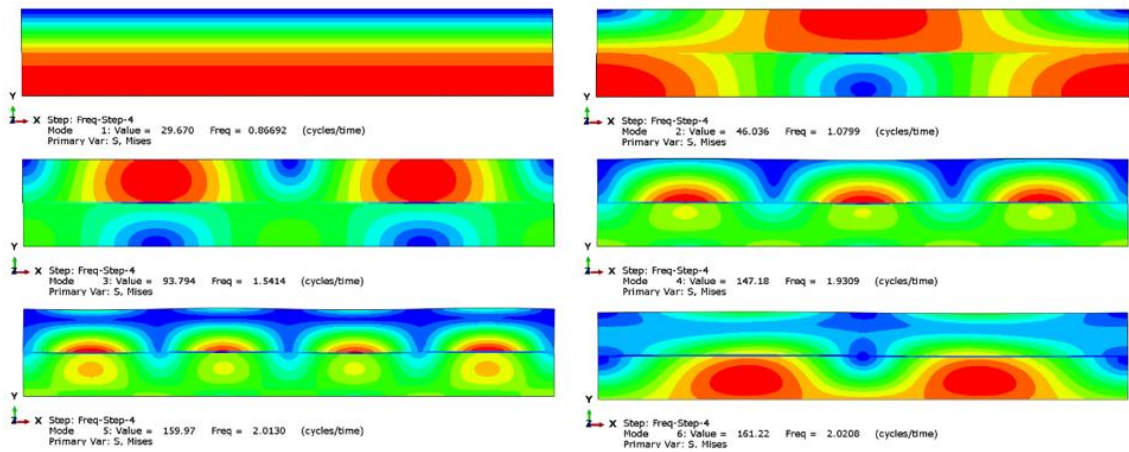
Figure 7-16 First six modes of the system for circumstance (i), Case 3
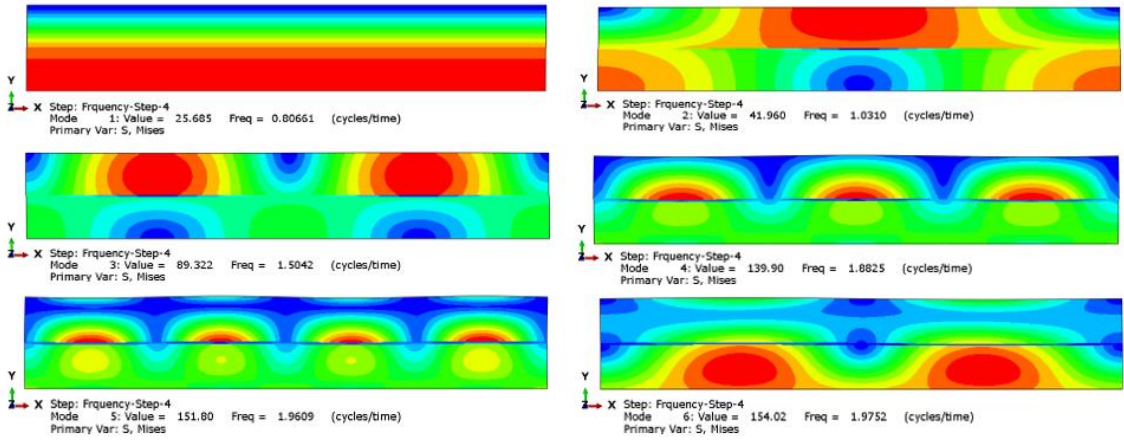
Figure 7-17 First Six Modes of the System for Circumstance (i), Case 4
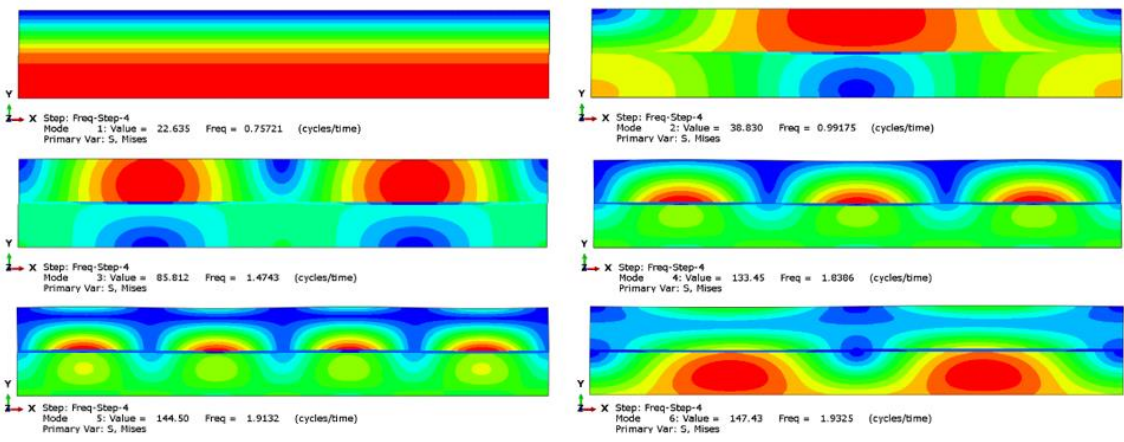
Figure 7-18 First Six Modes of the System for Circumstance (i), Case 5
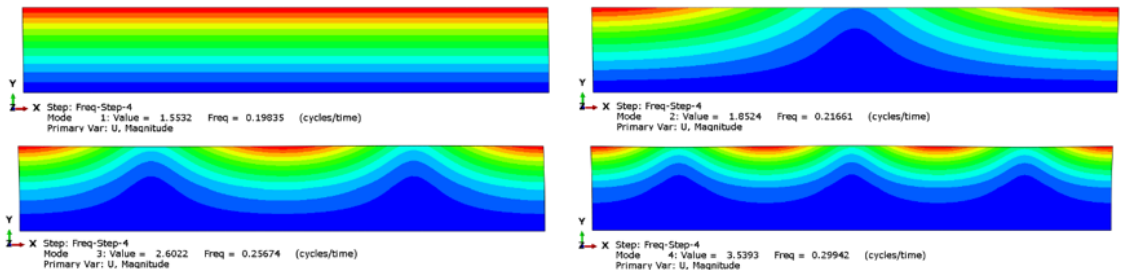
Figure 7-19 First Four Modes of the System for Circumstance (ii), Case 1
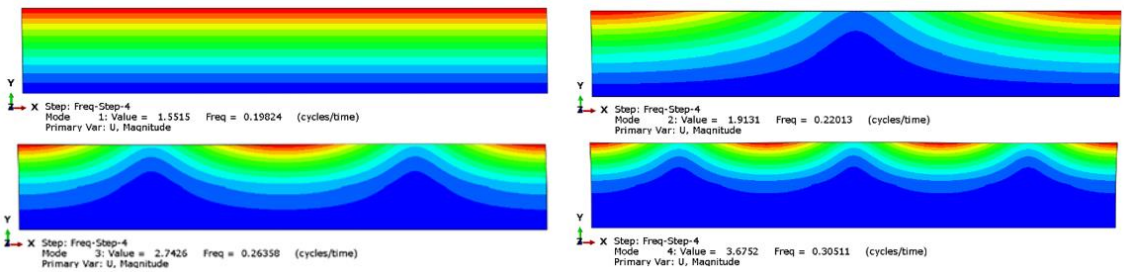
Figure 7-20 First Four Modes of the System for Circumstance (ii), Case 2

310
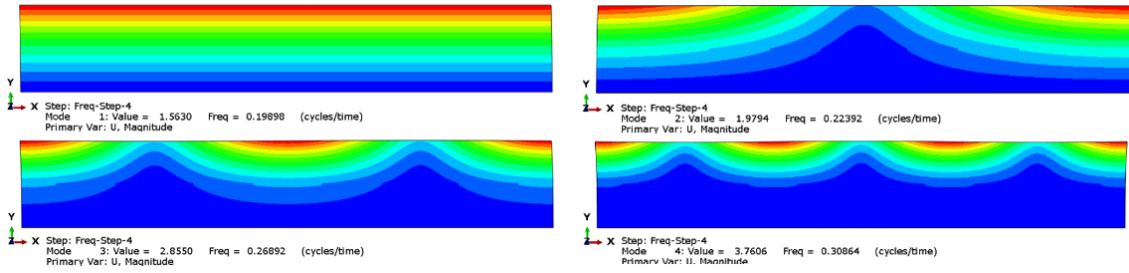
Figure 7-21 First Four Modes of the System for Circumstance (ii), Case 3
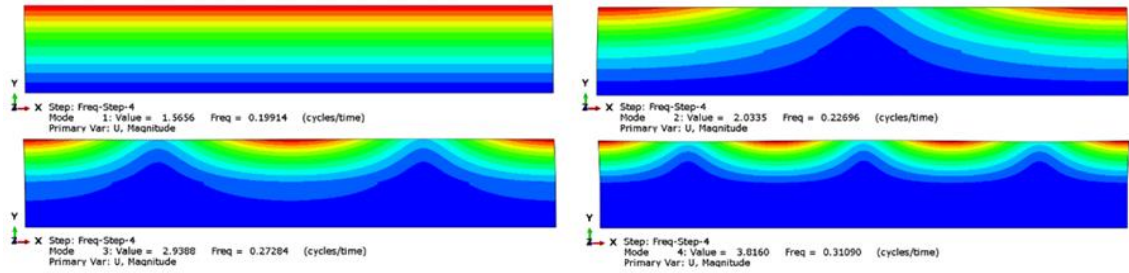
Figure 7-22 First Four Modes of the System for Circumstance (ii), Case 4
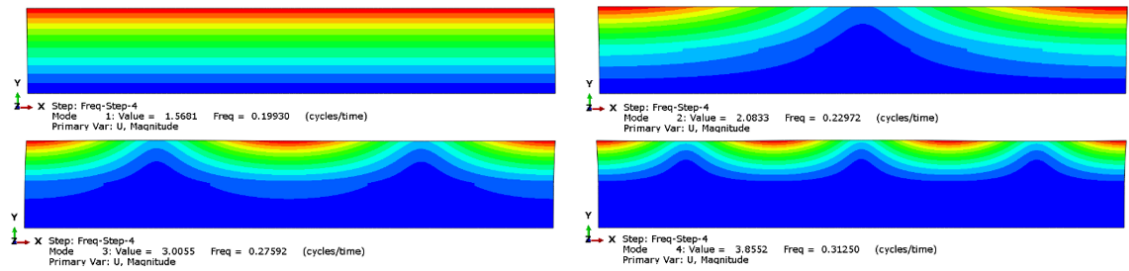
Figure 7-23 First Four Modes of the System for Circumstance (ii), Case 5
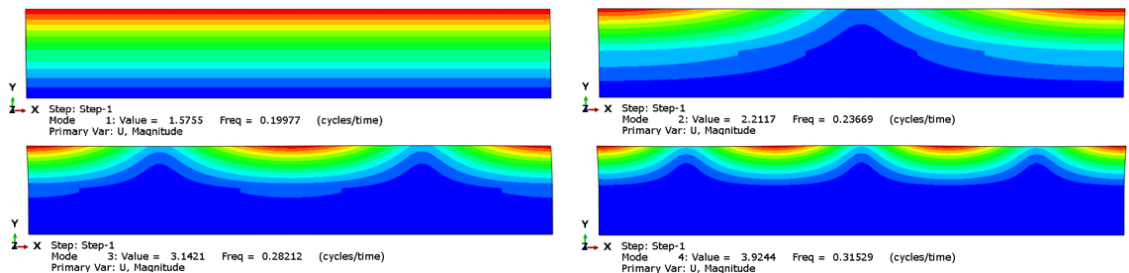
Figure 7-24 First Four Modes of the System for Circumstance (ii), Case 6
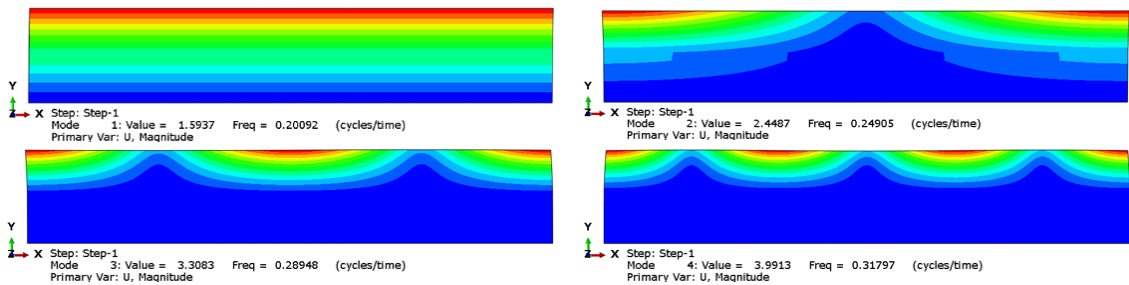
Figure 7-25 First Four Modes of the System For Circumstance (ii), Case 7

7.5.2. Numerical analysis results

7.5.2.1. Ground motion parameter

Peak ground acceleration (PGA) is the most commonly used measure of ground motion amplitude, and it is equal to the absolute maximum value obtained from accelerogram. Estimating PGA accurately is the most crucial for any seismic design process using PGA–MMI relationship (Trifunac & Brady, 1976). PGA data and the frequencies content of an earthquake are the key factors needed to identify the level of structural damage. For instance, high amplitude may not cause significant damage to a structure if earthquake frequency content does not match the natural frequencies of the structure. Peak ground velocity (PGV) is also used to characterise ground motion, and it is useful for describing the motion for intermediate frequencies as velocity is less sensitive to higher frequencies. For some circumstances, PGV may provide clearer indication of structural damage, and PGV–MMI relationship is also employed, (Trifunac & Brady, 1976). The absolute values of maximum accelerations sustained for three or five cycles in acceleration time history are commonly characterised as sustained maximum acceleration. The effective acceleration that induces a structural damage is defined as effective design acceleration. The effective design acceleration depends on several parameters, such as size of loaded area, weight, damping and stiffness properties of structure in addition to its location with respect to epicentre. (Kennedy (1980) proposed effective design acceleration to be equal to 25% higher than three-cycle PGA recorded after filtration. Benjamin (1988) proposed to consider effective design acceleration value that equal to PGA after filtering out all accelerations above 8–9 Hz. The frequency content of an earthquake time history is commonly characterised using Fourier Spectra, power spectra and response spectra. Fourier Spectra is a periodic function that can be written as

$$x(t) = C_0 + \sum_{n=1}^{\infty} C_n \sin(\omega_n t + \emptyset_n) \tag{7.4}$$

where C_n and $\emptyset_n$ are the nth harmonic amplitude and phase angle in the Fourier series, respectively. The Fourier amplitude spectrum is a plot of C_n versus ω_n, whereas the Fourier phase spectrum is a plot of $\emptyset_n$ versus ω_n. The Fourier amplitude spectrum indicates how the motion amplitudes vary with frequencies and signifies the frequencies content of a motion. Two frequencies point the range of frequencies for the largest Fourier acceleration amplitude which are corner frequency f_c and cut-off frequency f_{max}. f_c is a critical parameter, and it represents the inversely proportional of the cube root of seismic

moment. Consequently, it reveals that large earthquakes generate greater low-frequency motions. The most widely used in seismic design engineering area is the response spectrum, which is the relationship of the maximum acceleration response amplitude versus time period of a system to a specific component of ground motion. Response spectrum is used to provide the most descriptive representation of the influence of a given earthquake on a structure or dynamic system. The peak response of a structure to an earthquake can be evaluated, and their natural frequency can be concluded using the response spectrum curve. The vibration period corresponds to the maximum value of the Fourier amplitude spectrum, and this parameter characterises the predominant period (frequency content) of the motion. However, the predominant period for two different motions with different frequency contents can be the same. Therefore, this parameter has to be combined with others to identify the motion properties successfully.

7.5.2.2. Sensitive clay

The purpose of examining six different case studies is to identify the minimum thickness of sensitive clay which causes the system to behave as site class *F* according to ASCE seismic code provisions. The soil then requires a site response analysis in accordance with Section 21.1 in ASCE code/ Section 1.2.3 in EC8. Changes in the seismic parameters of the motion resultant at the topsoil surface for these circumstances are compared using key valid motion parameters from SeismoSignal software, and they are listed in Table 7.5.

Table 7.5 Resultant Time History Properties of Circumstance (i), h in Metre

Parameter	Case1, H=0.25 m	Case2 H=0. 50 m	Case3 H=0.75 m	Case4 H=1.0 m	Case5 H=1.2 m
Max. Acceleration (g)	0.6634	0.6352	0.6	0.587	0.564
Time of Max. Acceleration (sec)	6.37	6.410	8.85	8.86	9.8
Max. Velocity (cm/sec)	172.6	194.3	201.75	198.04	184.92
Time of Max. Velocity (sec)	6.3	8.67	8.72	8.75	8.77
Max. Displacement (cm)	132.3	106.9	117.2	106.53	100.26
Time of Max. Displacement (sec)	31	10.23	10.31	10.38	31
Sustained Maximum Acceleration (g)	0.616	0.574	0.576	0.563	0.55
Effective Design Acceleration (g)	0.663	0.634	0.6	0.586	0.565

Predominant Period (sec)	0.9	1.32	1.34	1.36	1.36

Table 7.5 and Figure 7.31 clearly show that the maximum acceleration of all six cases are close to one other and decrease within a percentage ranging between 2.1% and 4.25% when the sensitive clay layer is expanded by 0.25 m along the six cases. However, amplified or deamplified ground motion accelerations are not always indicative of the right influences of the applied motion. Considering them as a key parameter to assess the system behaviour based only on time history motion properties is not wise (see chapter 6, Section 6.5.1). Despite this fact, the effective design acceleration decreases by 4.4%, 5.36%, 2.5% and 3.6% from 0.663 (g) to 0.634 (g), 0.6 (g), 0.586 (g) and 0.565 (g), where the sensitive clay soil layer thickness is expanded to 0.5 m, 0.75 m, 1.0 m and 1.25 m for cases 1 to 5. The accelerated deamplification does not provide a correct indication to adequately consider the soil Class *F* as a soil profile. The sustained maximum acceleration values present the same decreasing trend. Figure 7-32 shows the significant difference between the acceleration time histories induced due to increasing the sensitive clay layer from 0.25 m to 1.25 m for case 1 and case 5, respectively.

In spite of the aforementioned aspect of considering the effects of the acceleration time history, velocity and displacement time histories curves (see Figure 7-33 and Figure 7-35) may give a better indication to describe the changes in system behaviour according to case study conditions. Shear wave velocity is a function of undrained shear strength of the soil (see Chapter 4 Section 3.2) and the significant relationship between velocity and the displacement. The velocity and displacement time histories are analysed to identify this study object. As shown in Table 7.5, the maximum velocity is increased by 13% between case 1 and case 2 from 172.6 cm/sec to 194.3 cm/sec, when the soil thickness of the sensitive clay is expanded to 0.5 m. These percentage increases fluctuate up for case 3 and case 4 and down for case 5 by 14.3%, 11% and 1%, respectively. The changes in the maximum displacement values are reduced by 20%, 11.4%, 20% and 24% for case 2, case 3, case 4 and case 5, respectively. These results indicate that expanding the layer sensitive clay by 0.5 m demands the system to behave differently, and the identification of the key parameter, which is the predominant period of the motion, becomes essential to signify the targeted minimum thickness. Figure 7-34 indicates the considerable variation between the velocity time histories induced by increasing the sensitive clay layer from 0.25 m to 1.25 m for case 1 and case 5, respectively.

Figure 7-38 and Table 7.5 demonstrate that the wave period of the case 1 motion lengthens substantially induced fundamental changes in the seismic properties of the resultant motion during the next four cases. The predominant period of the case 2 motion is lengthened by 55%, from 0.85 sec to 1.32 sec. The predominant period value for case 3 is lengthened by 58% to the value of 1.34 sec, and the increasing percentage for case 4 and case 5 are increased by 60%. As mentioned above, the frequency content of the ground motion plays the main role in identifying the structural damage of a structure that experienced an earthquake. From this perspective, the minimum thickness of sensitive clay layer that make the system behave under soil class *F* condition starts from 0.5 m. Figure 7-36 and Figure 7-37 reveals the substantial lengthening in the predominant period of the system caused by expanding the sensitive clay layer from 0.25 m to 1.25 m for case 1 and case 5, respectively. Figure 7.26 shows the results of the three analysed steps, i.e. geostatic, static and dynamic steps for case 1, and Figure 7.27 to Figure 7.30 show the results of the dynamic steps for the other four cases in circumstance (i)
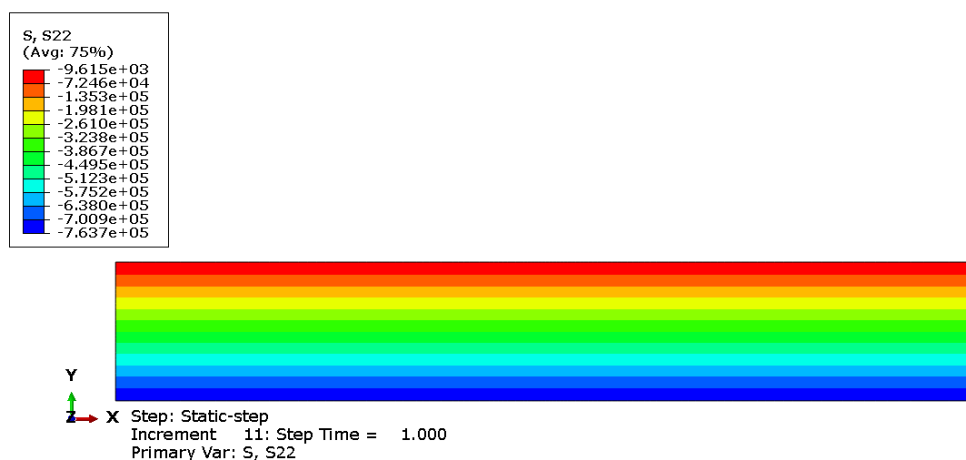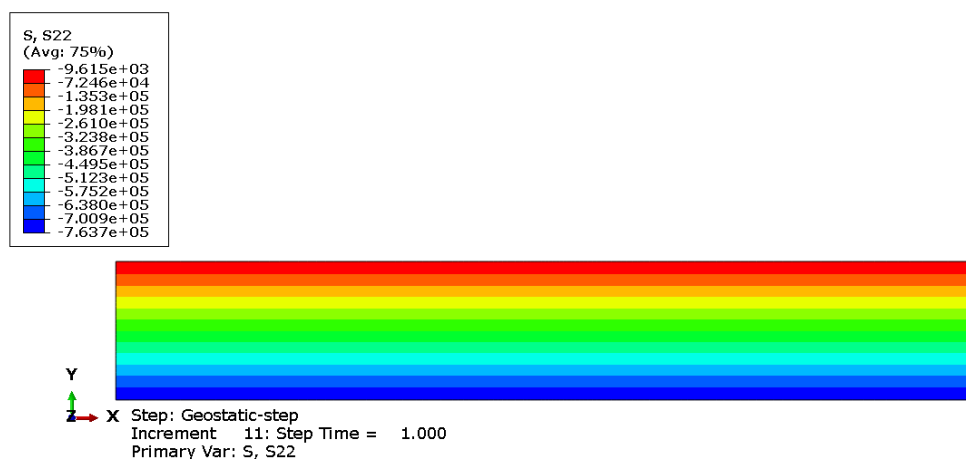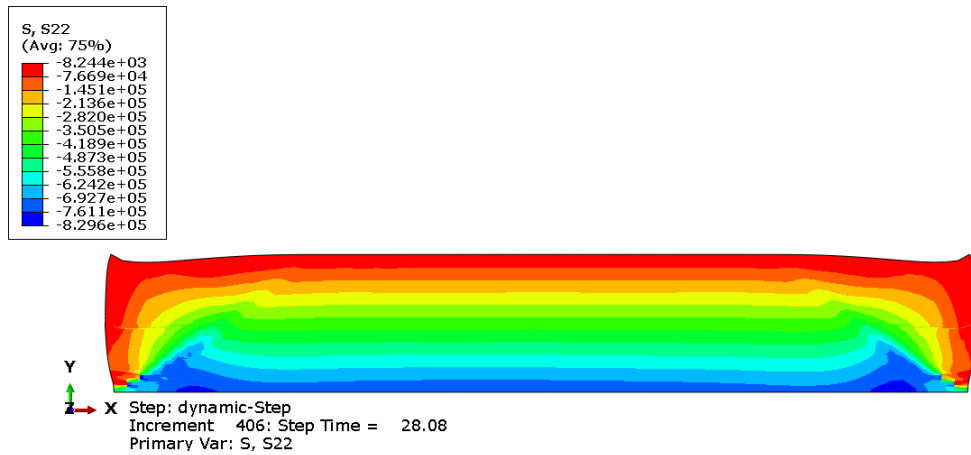
Figure 7-26 Dynamic Step for Case 1 of Sensitive Clay Circumstance (Geostatic, Static, and Dynamic Steps)
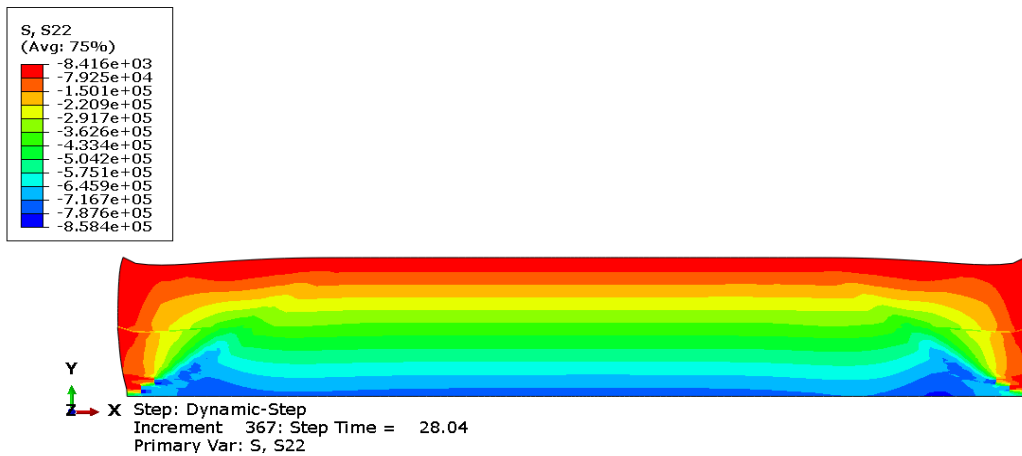
Figure 7-27 Dynamic Step for Case 2 of Sensitive Clay Circumstance
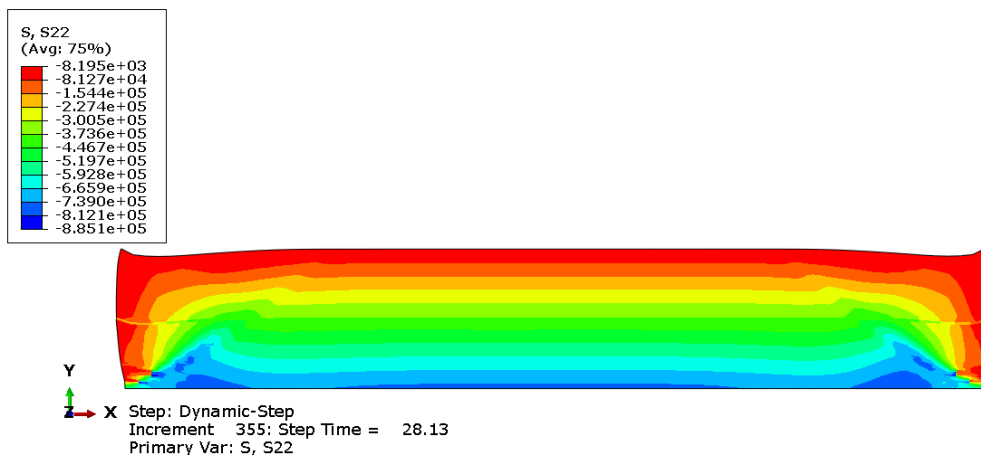
Figure 7-28 Dynamic Step for Case 3 of Sensitive Clay Circumstance
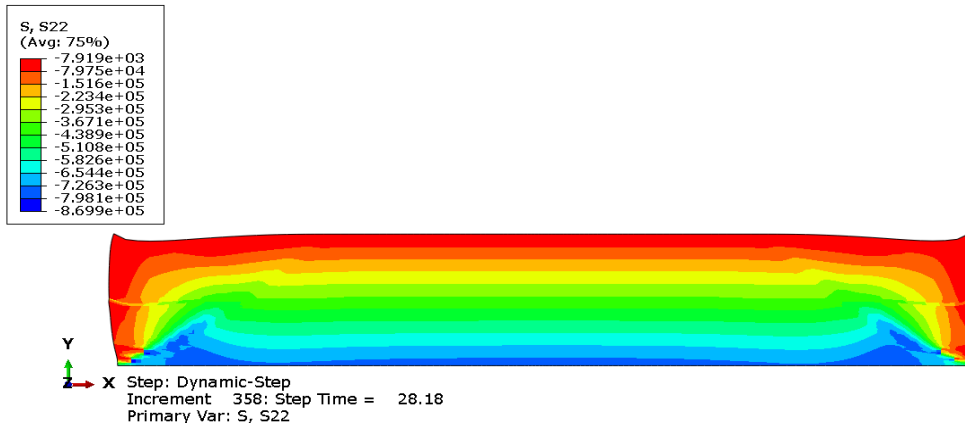
Figure 7-29 Dynamic Step for Case 4 of Sensitive Clay Circumstance
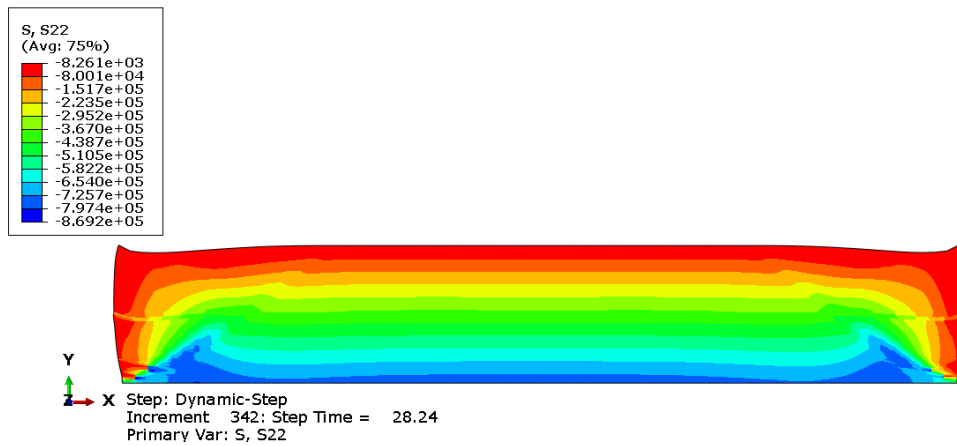
Figure 7-30 Dynamic Step for Case 5 of Sensitive Clay Circumstance
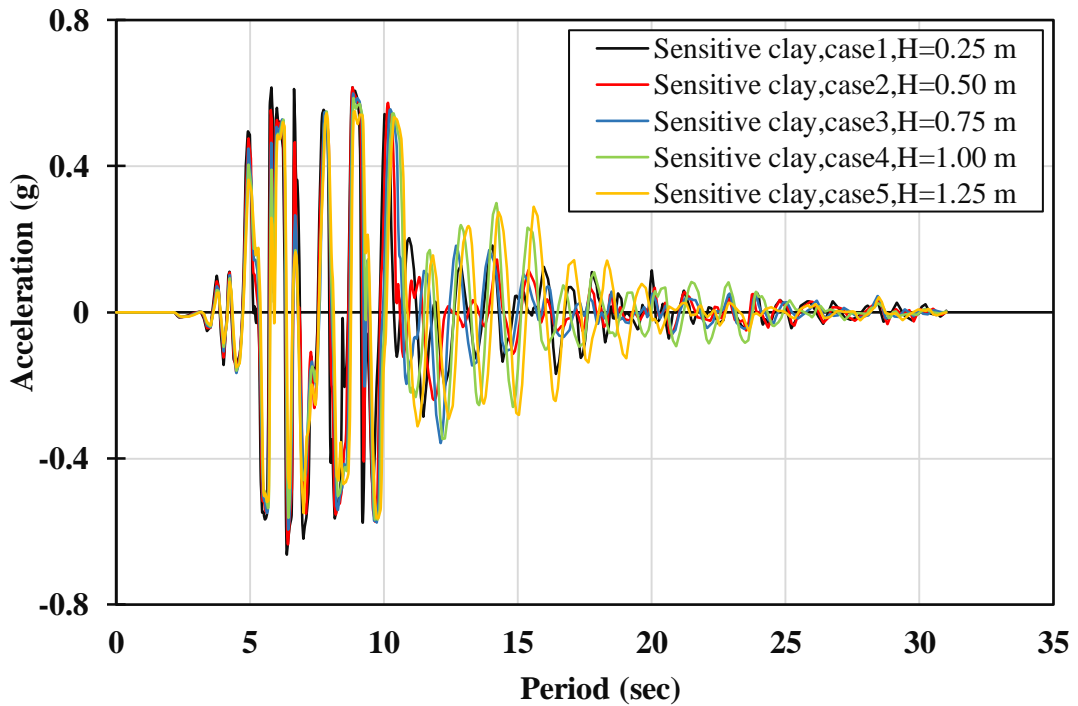
Figure 7-31 Acceleration Time History for the Circumstance of Sensitive Clay for Case 1, Case 2, Case 3, Case 4 and Case 5
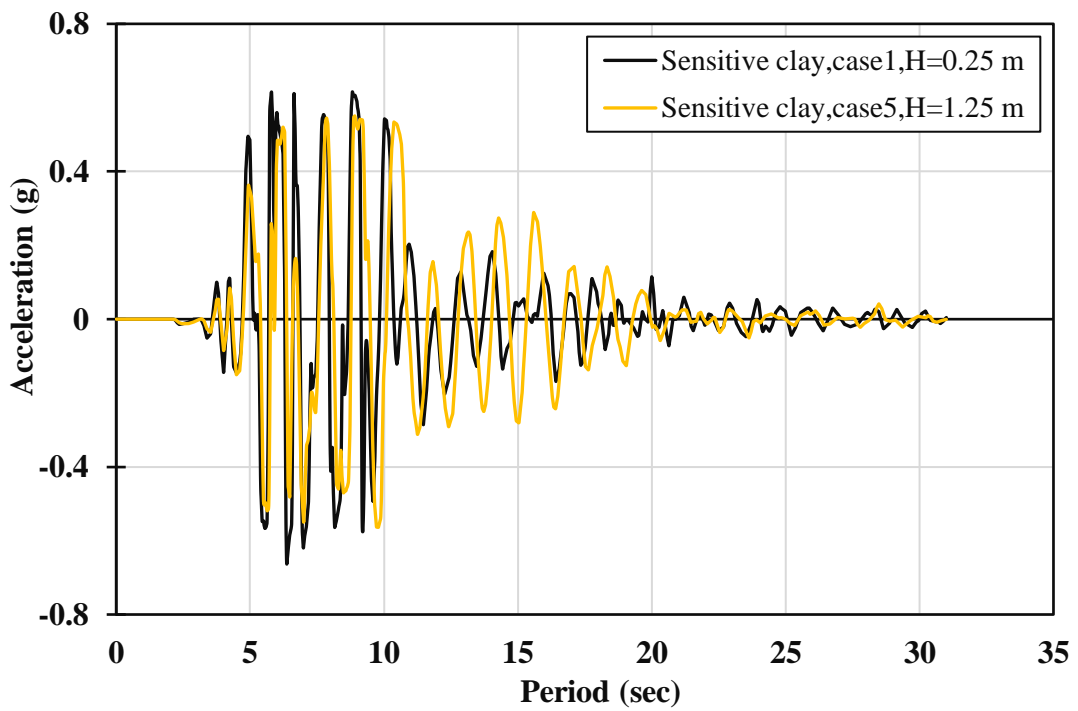
Figure 7-32 Acceleration Time History for The Circumstance of Sensitive Clay for Case 1 and Case 5
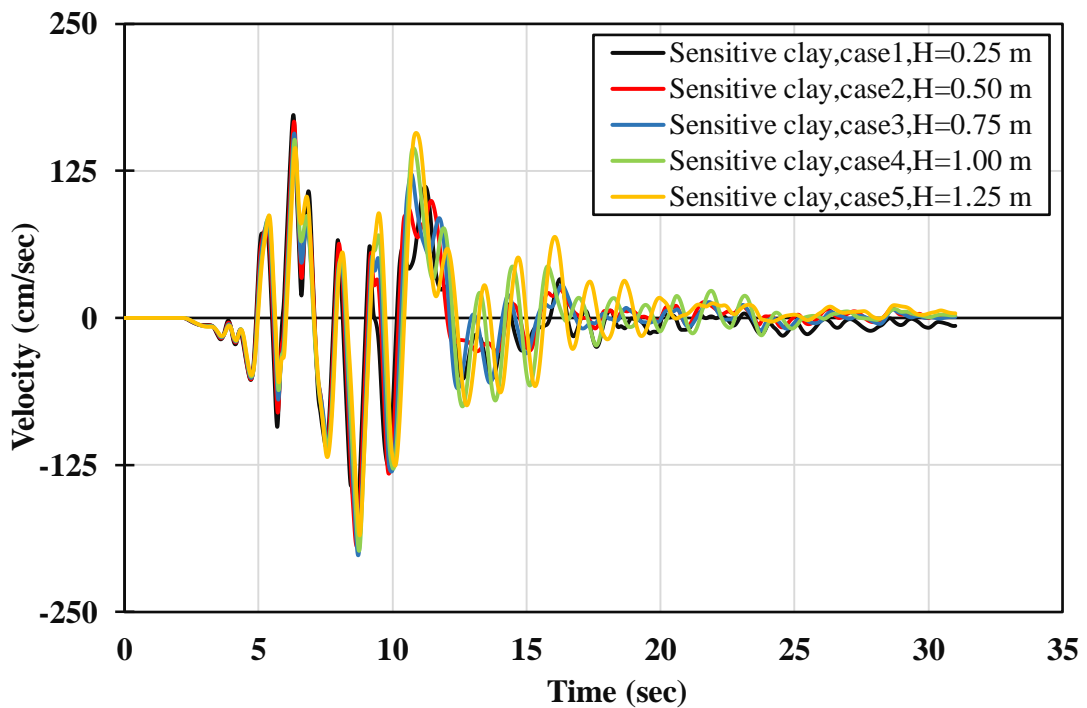
Figure 7-33 Velocity Time History for the Circumstance of Sensitive Clay for Case 1, Case 2, Case 3, Case 4, and Case 5
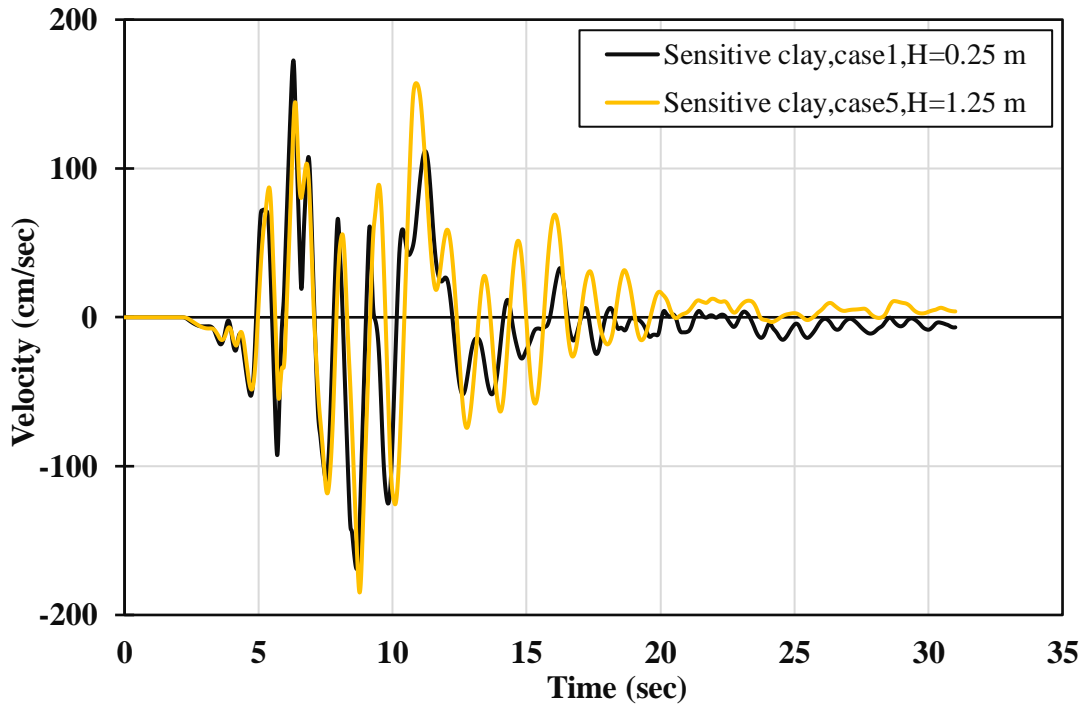
Figure 7-34 Velocity time history for the circumstance of sensitive clay for case 1 and case 5
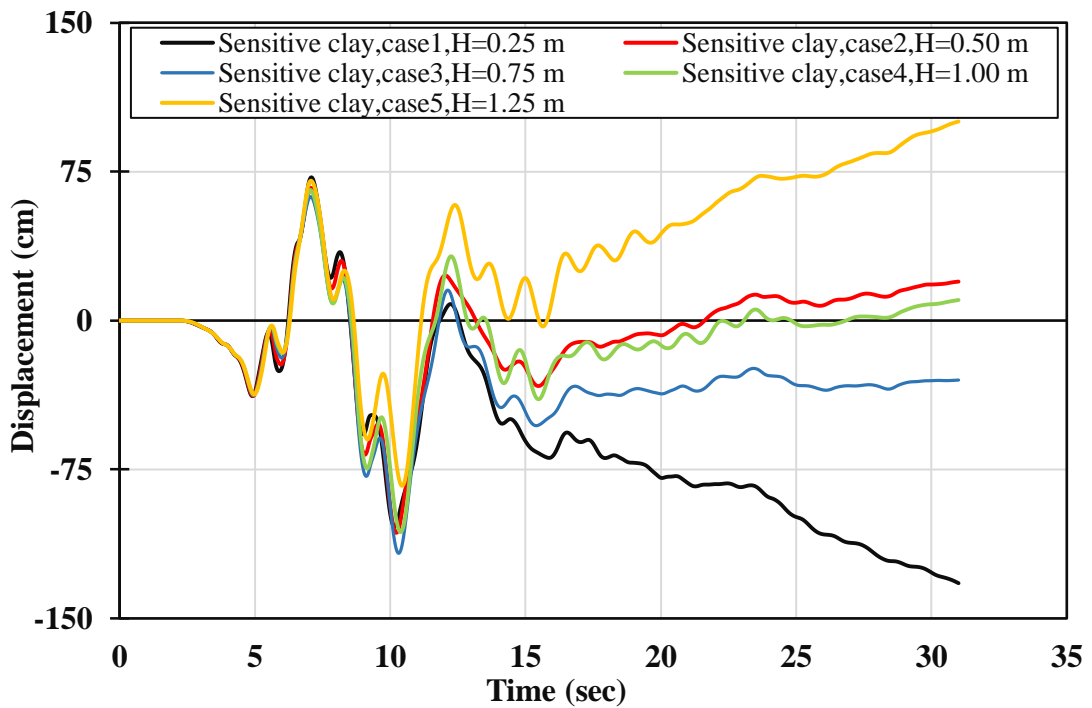
Figure 7-35 Displacement time history for the circumstance of sensitive clay for case 1, case 2, case 3, case 4, and case 5

319
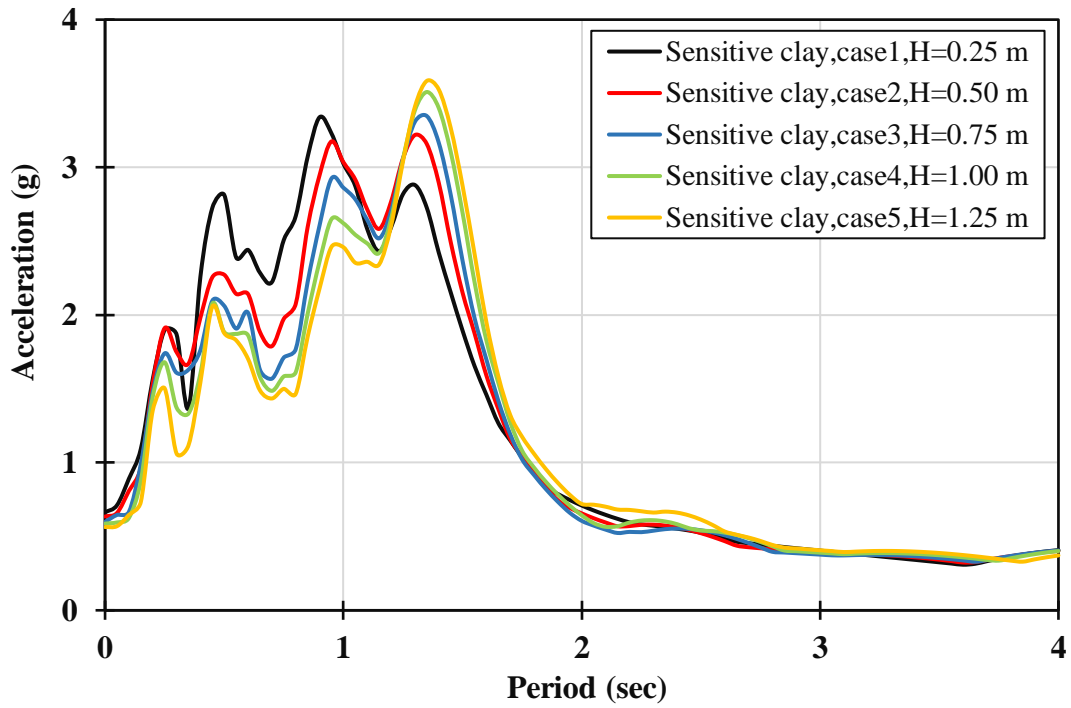
Figure 7-36 Acceleration response spectrum for the circumstance of sensitive clay for case 1, case 2, case 3, case 4, and case 5
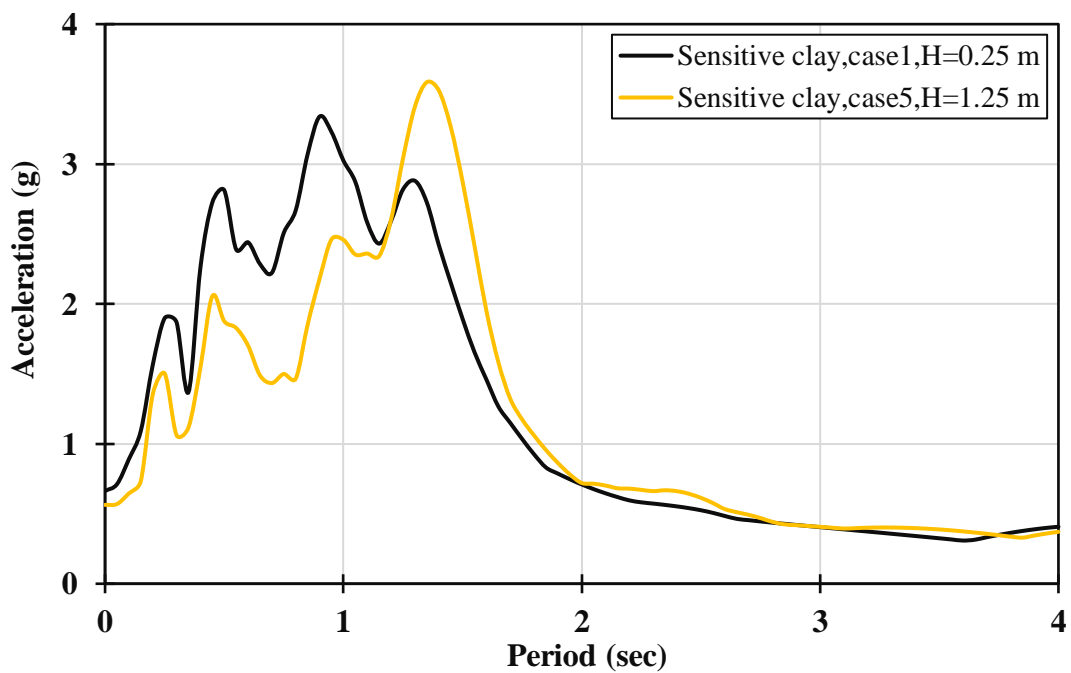
Figure 7-37 Acceleration response spectrum for the circumstance of sensitive clay for case 1 and case 5
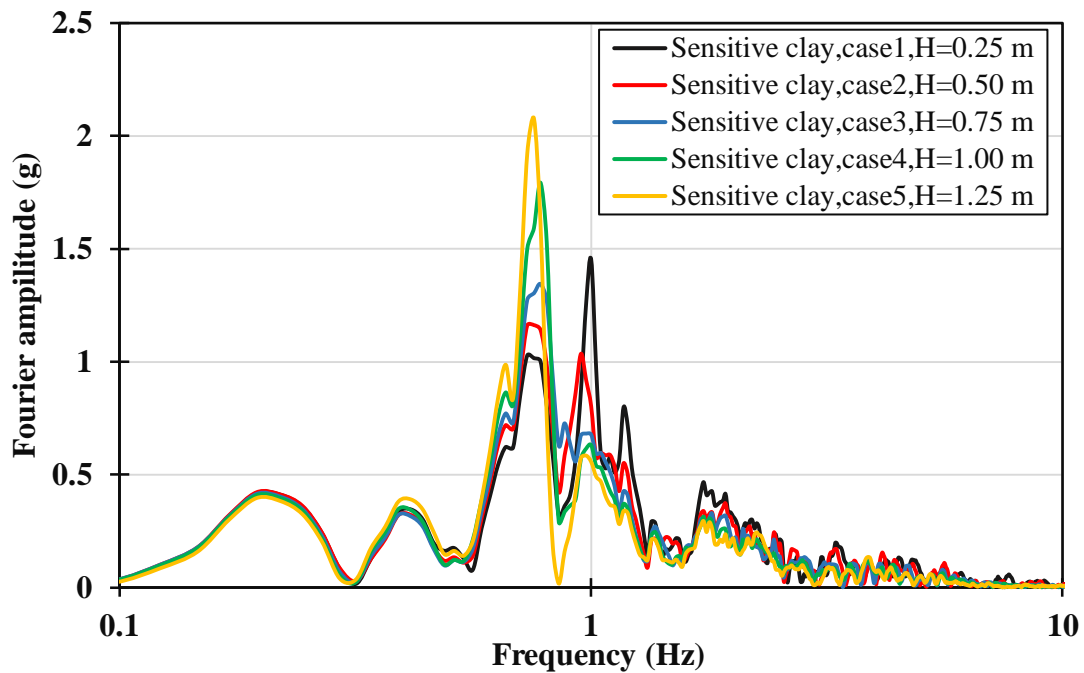
Figure 7-38 FFTs for the circumstance of sensitive clay for case 1, case 2, case 3, case 4, and case 5

7.5.2.3. Cut-off layer

One major theoretical issue that has dominated the field of seismic design and soil classification concept for many years concerns the consideration that site class F needs the soft clay layer to be available continuously with a thickness of ($H \geq 37m$) (Kelly, 2006). A much-debated question by seismic design experts concerning point 4 in Section 20.8.1 in ASCE, is whether the thin layer of sand can cut off the continuity of thick soft clay layer ($H \geq 37m$) so that its behaviour can be no longer considered as soil class F, or that the existence of this sand layer will have no impact and then the accumulative soft clay layer thickness of ($\sum H \geq 37m$) means the soil profile is stuck in class F. The minimum thickness of this active cut-off layer is identified in the present study.

An irrational idea is that cutting this continuity off will definitely address the limitation of classifying class F. Given the dangerous code definition of site class F and the risk of downgrading it to the lesser dangerous site classes, this hazardous issue must be identified clearly in the seismic design codes. To date, no previous study has investigated this crucial issue, and no complete definition has been given for this particular subject of Section 20.8.1. The current study aims to deliver an accurate detailed definition, specifying the minimum thickness of the cut-off sand layer and offering a complete description for this classification issue. Seven models representing seven different cases are performed, with each case consisting of two soft clay layers with a thickness of 20 m

thickness each and one thin sand layer is accommodated at the middle of the analysed models. Seven different thickness of sand layers are used (0.25 m, 0.50 m, 0.75 m, 1.0 m, 1.25 m, 2.0 m and 4.0 m). The sand layer is expanded by 0.25 m gradually for the first five cases, then two larger sand thickness are used for the last two circumstances for the purpose of achieving the objective and applying the conditions of the analysis (see Figure 7-1b). The present study critically assesses the minimum thickness of sand layer that can filter the passing wave and then change the seismic properties of the motion. Maximum acceleration, maximum velocity, maximum displacement, effective design acceleration and predominant period parameters have been compared for the seven case studies. The resultant parameters are selected at three different locations within the model as shown in Figure 7-1 b. Position A is located at the base of the model, position B is located where the motion passes the sand layer, and position C is located at the top surface of the model. All these three positions are located along the centre of the models.
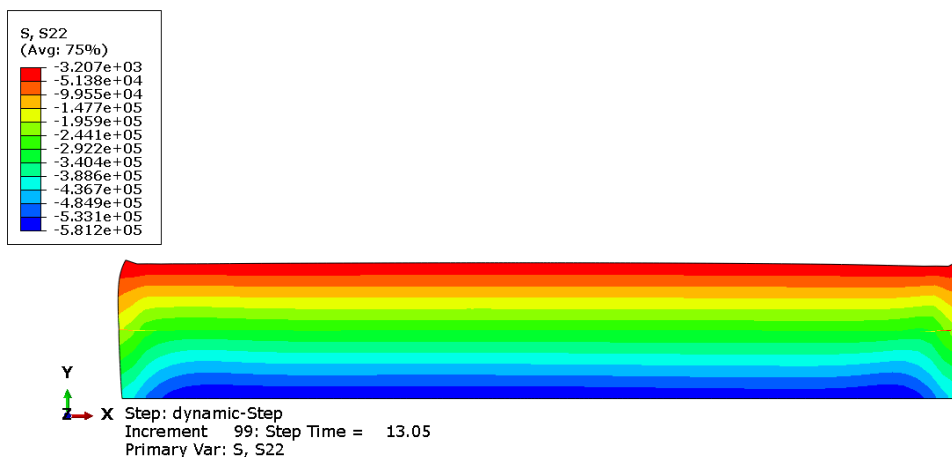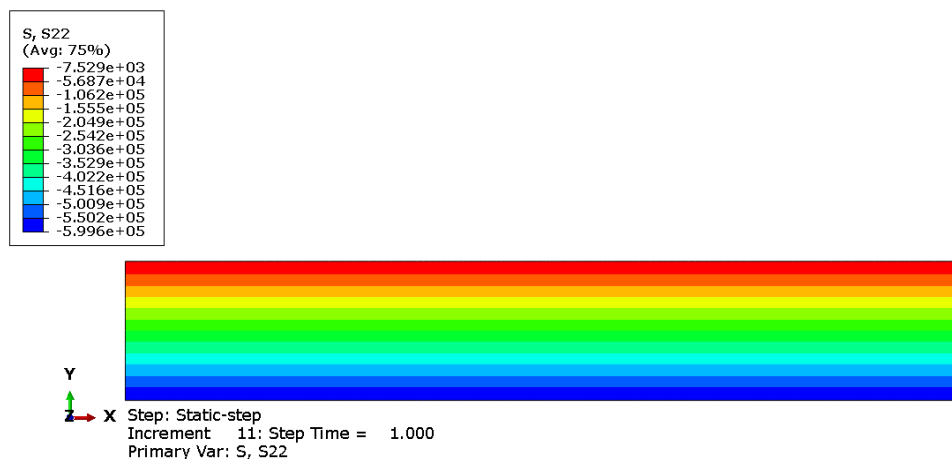
Figure 7-39 illustrates the findings of the geostatic, static and dynamic steps for case 1. Figure 7-40 to Figure 7-45 show the results of the dynamic step for the other six cases (2-7) of circumstance (*ii*). The data in Table 7.6 and Figure 7-46 indicate that the maximum

322

accelerations of first five cases at point B are almost equivalent and range between 0.341 and 0.343 (g). As a result of the above similarity, the existing sand-clay soil profile combination for all five different cases indicate no impact of the availability of sand layer (up to 2.0 m thick) above the soft clay layer, and this combination has no amplified or deamplified acceleration. The maximum accelerations values at point A for case 6 (when the sand layer is expanded to 2.0 m) experiences a slight decrease of 0.6%, suggesting similar behaviour as those of the first five cases).

In case 7, the sand layer is expanded to 4.0 m. An additional analysis is performed under the same condition for the first six cases to confirm the concept that is verified in the first six cases. The maximum acceleration value for case 6 at point A decreases by 5.4%, indicating that the behaviour of the dynamic system in this case starts to behave differently, but not in the way of cutting the thick soft clay layer into two parts. The maximum acceleration values at the top soil surface (point C) are amplified in the range of 1.4%–3%. The maximum acceleration values of case 2, to case 7, however, are almost similar. These findings confirm the conclusion mentioned above regarding the minimal impact of the availability of sand layer on the system behaviour under this combination of soil profile. However, the effective design acceleration at points B and C reveals a similar behaviour for all cases. Amplified or deamplified acceleration does not always indicate the right influences of the soil profile on applied motion.

As previously mentioned, using the weighty relationship between undrained shear strength of the soil and soil shear wave velocity may designate a better indication for system behaviour. The velocity time histories for the seven case studies are compared to find the effect of the different sizes of sand layer on the system behaviour (see Figure 7-47). As shown in Table 7.6, the maximum velocity values at point B have a small difference in values for all of the first five cases (between 151.15 and 158.13 m/sec, $\sim1.5\% - 4.5\%$), indicating the negligible effect of sand layer on the system behaviour. These values are more amplified for case 6 and case 7 (to 161.13 and 162.31 m/sec, ~6.5% and 7.5%) due to the expansion of the sand soil layer to 2.0 and 4.0 m, respectively. These insignificant differences confirm the negligible consequence of sand layer on the system behaviour. The maximum velocity values for all seven cases are centred around the same concept of analysis. The aforementioned results reveal that increasing the cut-off sand layer up to 4.0 m will not demand the system to behave differently, and site class F must be still considered for the accumulative required soft clay thickness ($\sum H \geq 37\ m$).

The critical parameter, however, in the current study is the predominant period values of resultant motion. Figure 7-48, Figure 7-49 and Table 7.6 evidnce that the wave period for the first six case studies are not lengthened or shortened by increasing the thickness of sand layer. The predominant period values at point B for all the first six cases are almost the same (1.36 –1.38 sec), and it is lengthened when it passes the first soft clay and sand layers by 134.5%–138% due to the existing soft clay layer. The predominant periods at top surface of soft clay soil (C) have very close values (1.34–1.36), and they are lengthened by 131%–134.5% due the effect of the dominated soft clay soil profile. The predominant period at point (C) for case 7 tends to behave differently, and it is shortened by 76% to the value of 1.02 sec due to the effects of the combination soil profile of soft clay and sand layers. Despite the significant effect of 4.0 m sand layer on system behaviour but that influence does not rise to be a decisive factor and does not cutting off the continuity of soft clay layers.

As mentioned above, the frequency content of the ground motion plays the main role in identifying the structural damage of a structure that experienced an earthquake. From this perspective, the existence of thin sand layer(s) between two thick soft clay layers does not change the equation, and the accumulative thicknesses of soft soil layers ($\sum H$) must be considered to apply the condition of (H $\geq$37 m). Increasing the cut-off sand layer to be more than 2 m means a new condition, and the average soil properties should be applied to decide the correct soil class according to conditions in Section 20.3.1 of ASCE.

S, S22
(Avg: 75%)
-7.529e+03
-5.687e+04
-1.062e+05
-1.555e+05
-2.049e+05
-2.542e+05
-3.036e+05
-3.529e+05
-4.022e+05
-4.516e+05
-5.009e+05
-5.502e+05
-5.996e+05

Y

X Step: Geostatic-step
Z   Increment   11: Step Time =   1.000
      Primary Var: S, S22

324
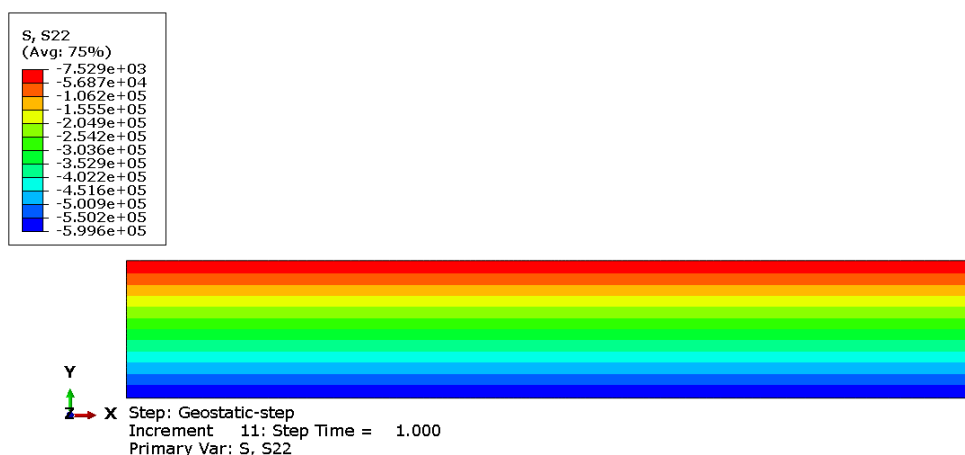
Figure 7-39 Three steps for case 1 of cut-off sand layer circumstance, (geostatic, static, and dynamic steps)
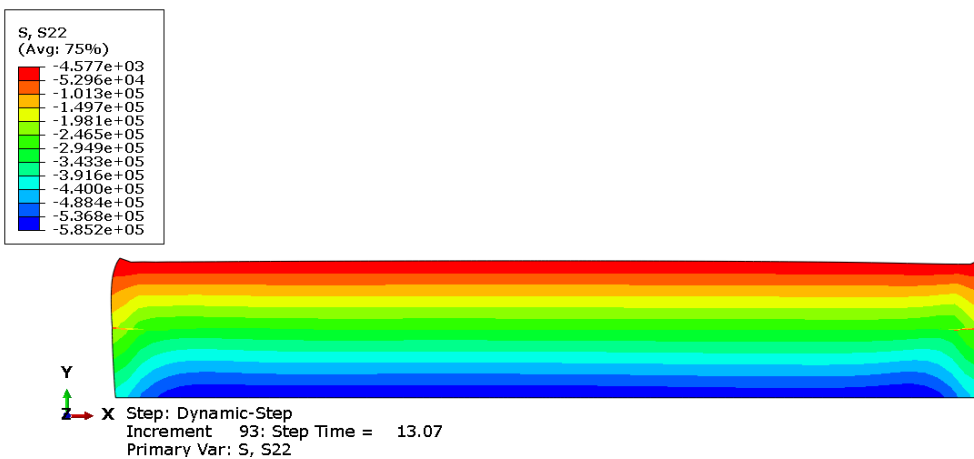
Figure 7-40 Dynamic step for case 2 of cut-off sand layer circumstance
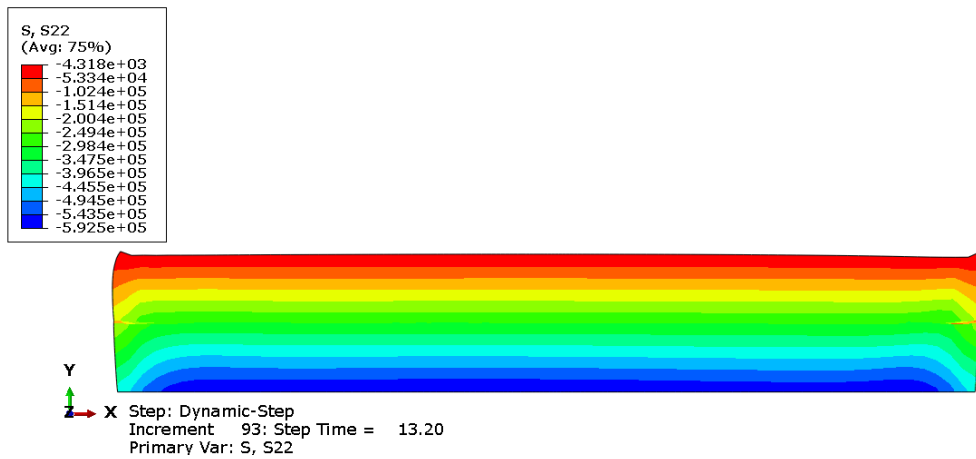
Figure 7-41 Dynamic step for case 3 of cut-off sand layer circumstance
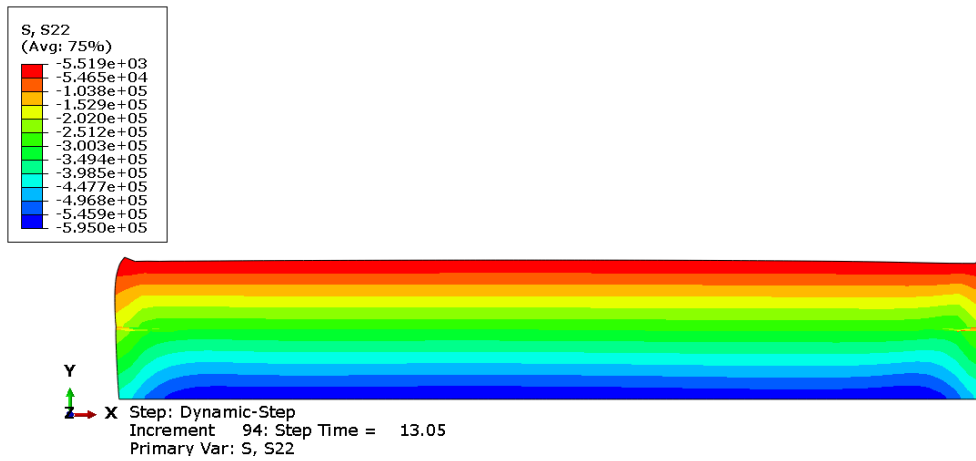
Figure 7-42 Dynamic step for case 4 of cut-off sand circumstance
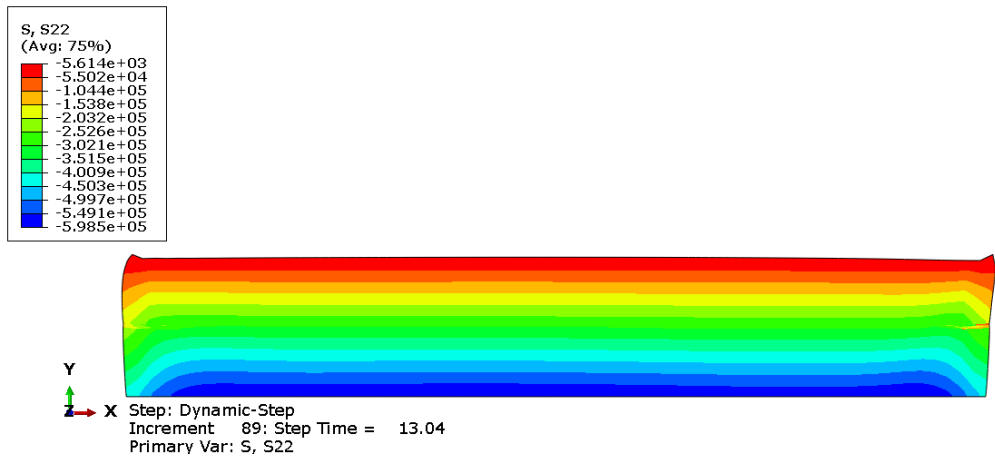
Figure 7-43 Dynamic step for case 5 of cut-off sand layer circumstance
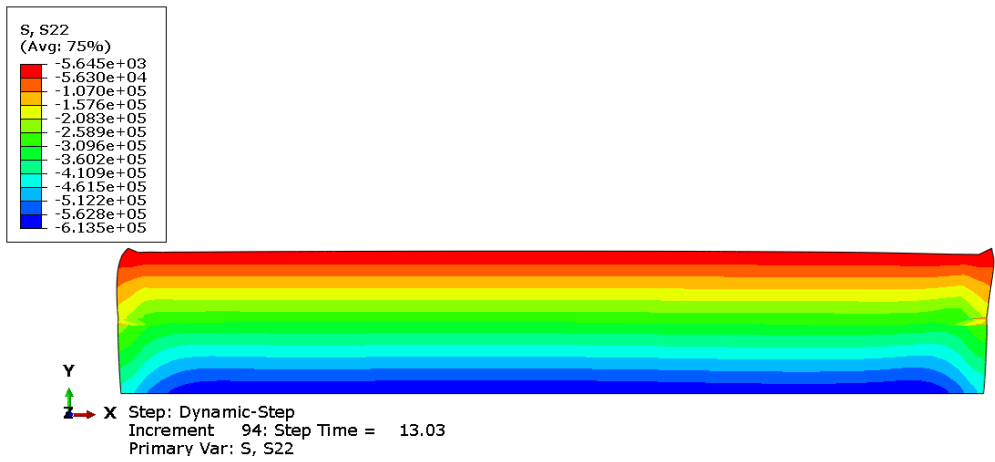
Figure 7-44 Dynamic step for case 6 of cut-off sand layer circumstance
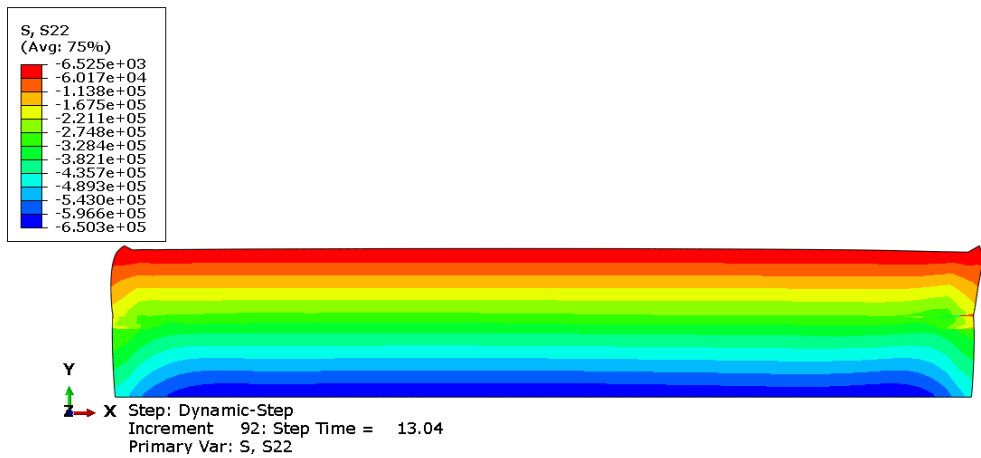
Figure 7-45 Dynamic step for case 7 of cut-off sand layer circumstance
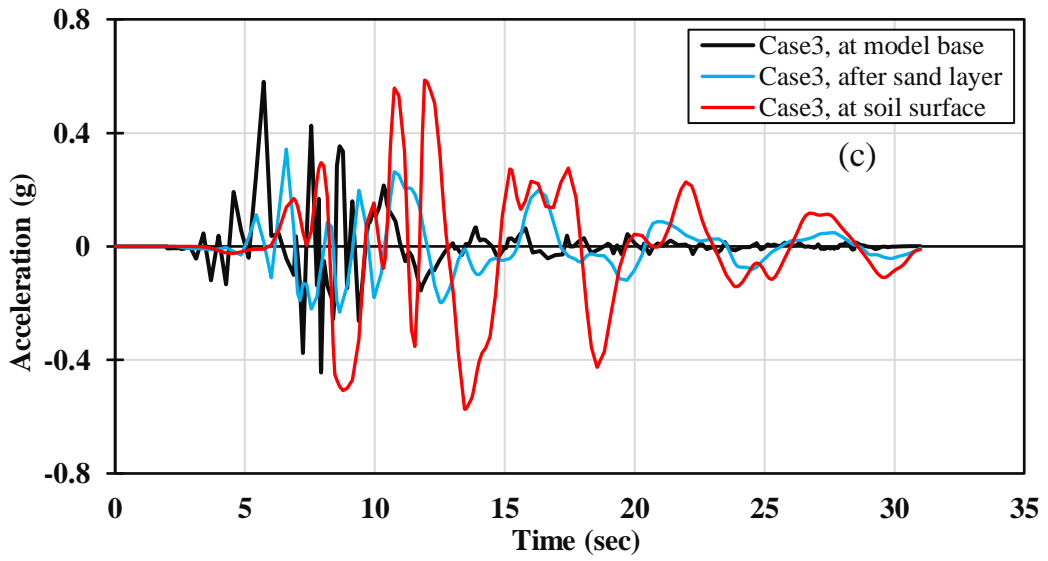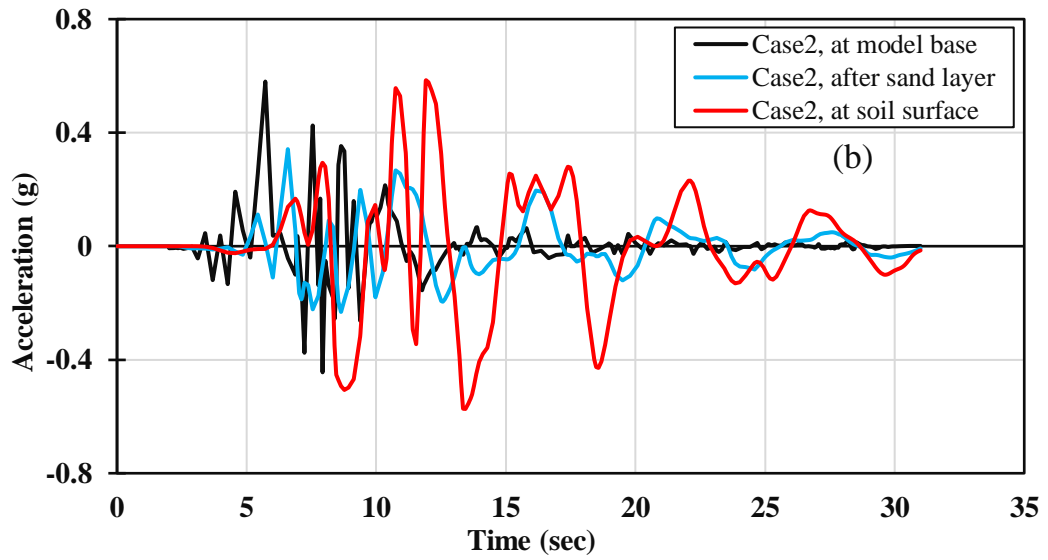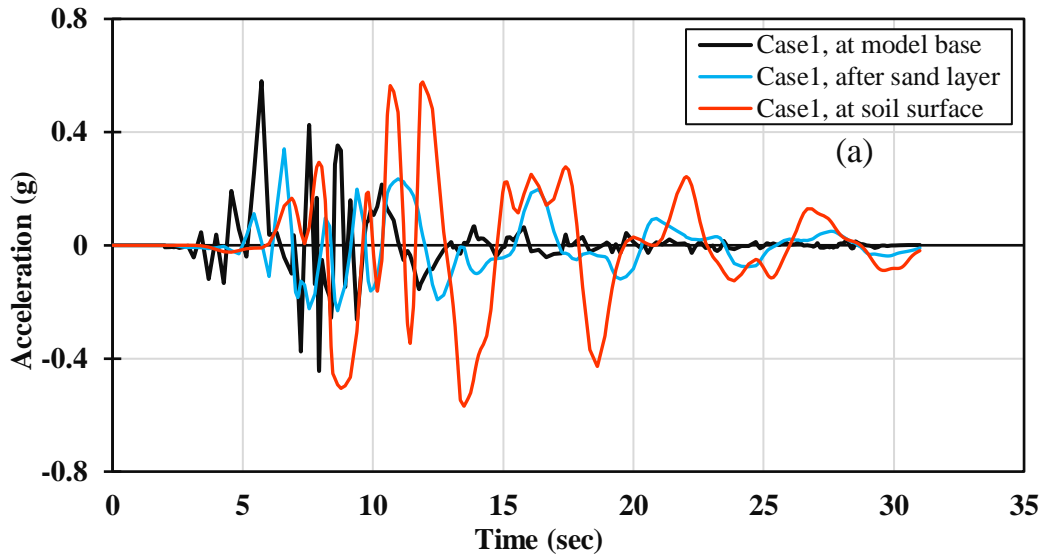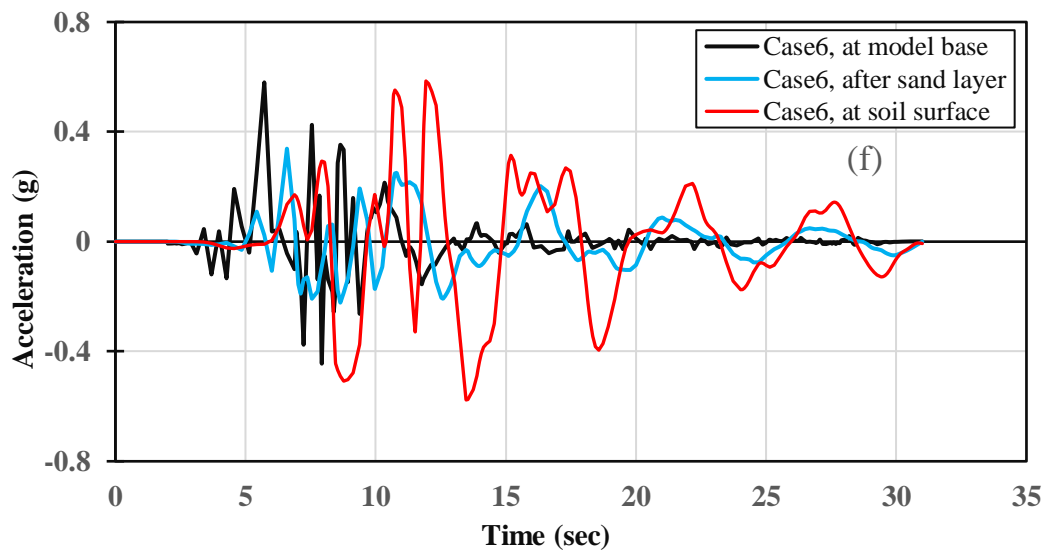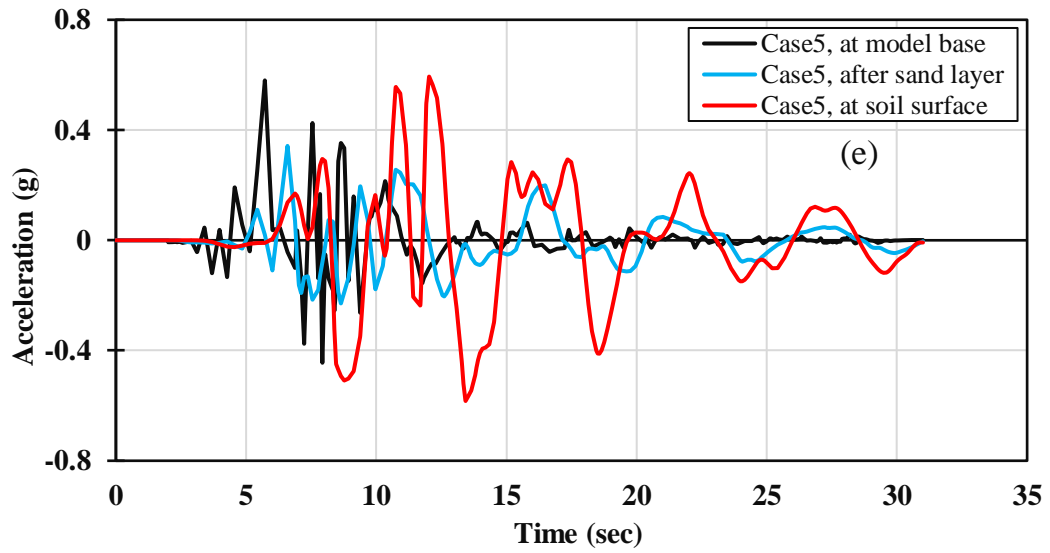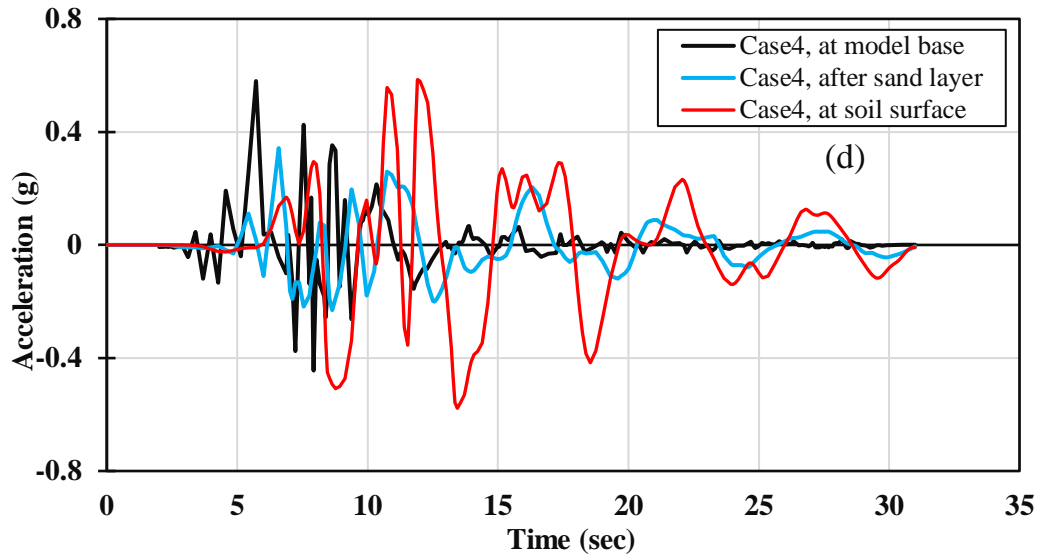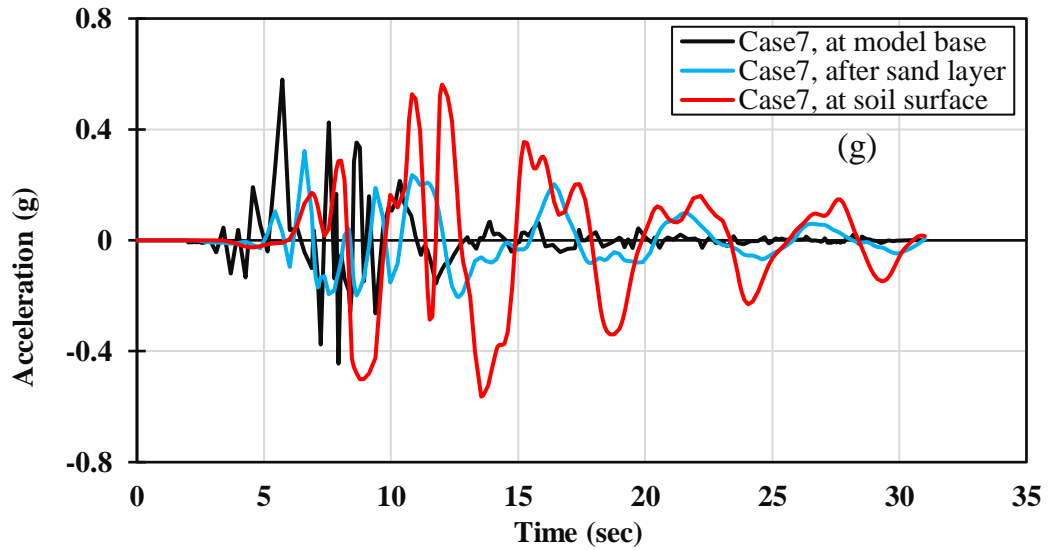
Figure 7-46 Acceleration time history for the circumstance of cut-off sand layer at points A, B and C, (a) Case 1, (b) Case 2, (c) Case 3, (d) Case 4, (e) Case 5, (f) Case 6, (g) Case 7
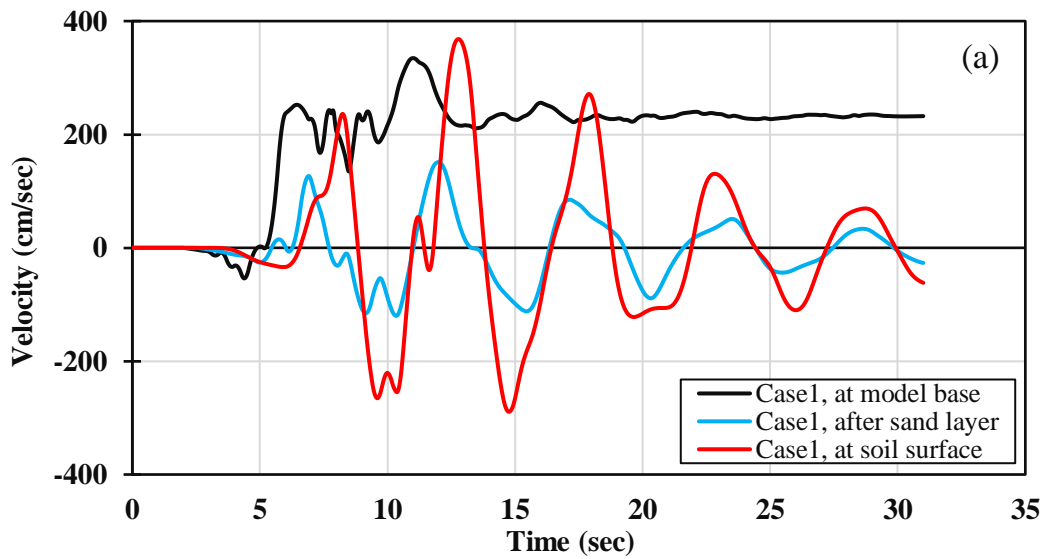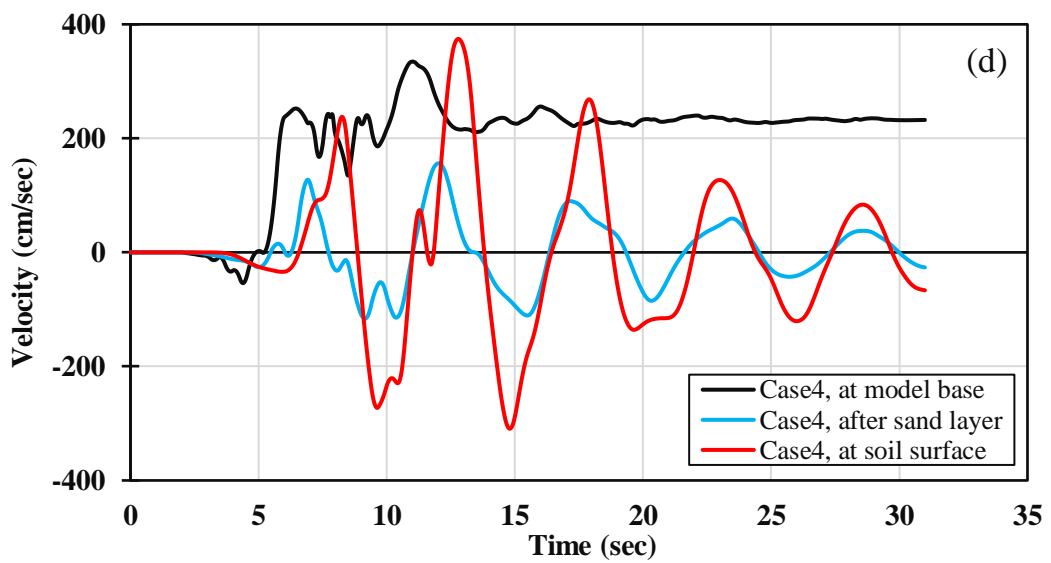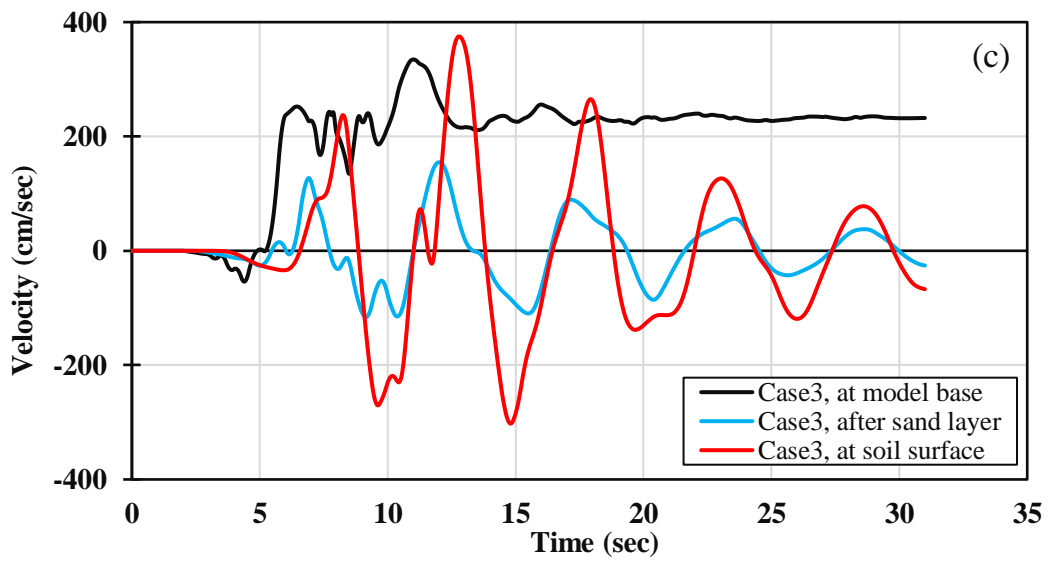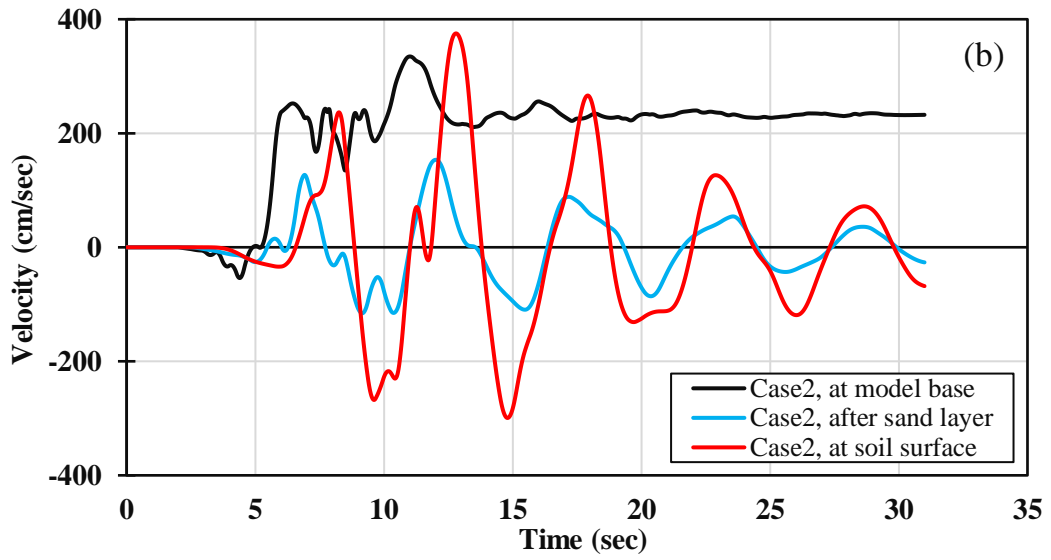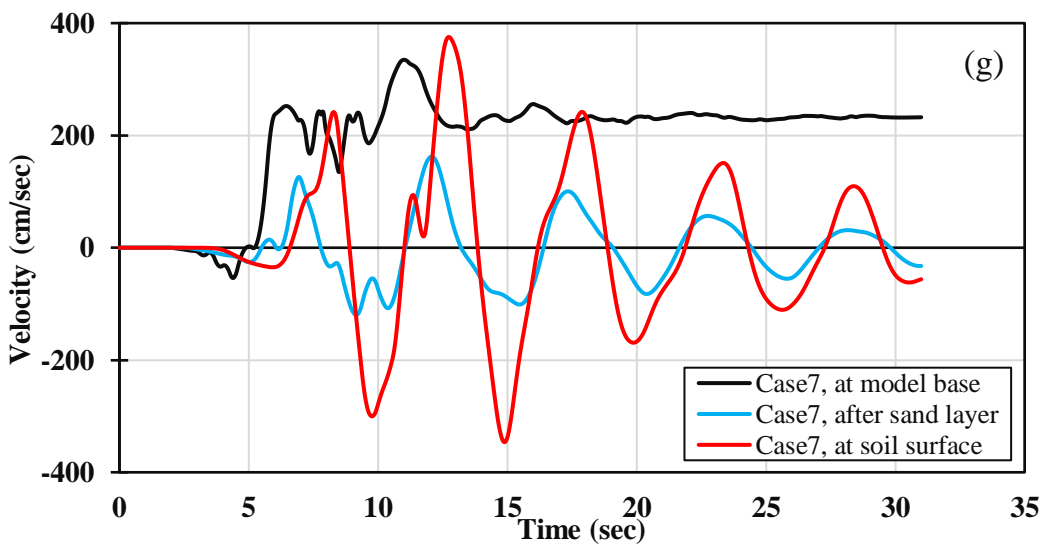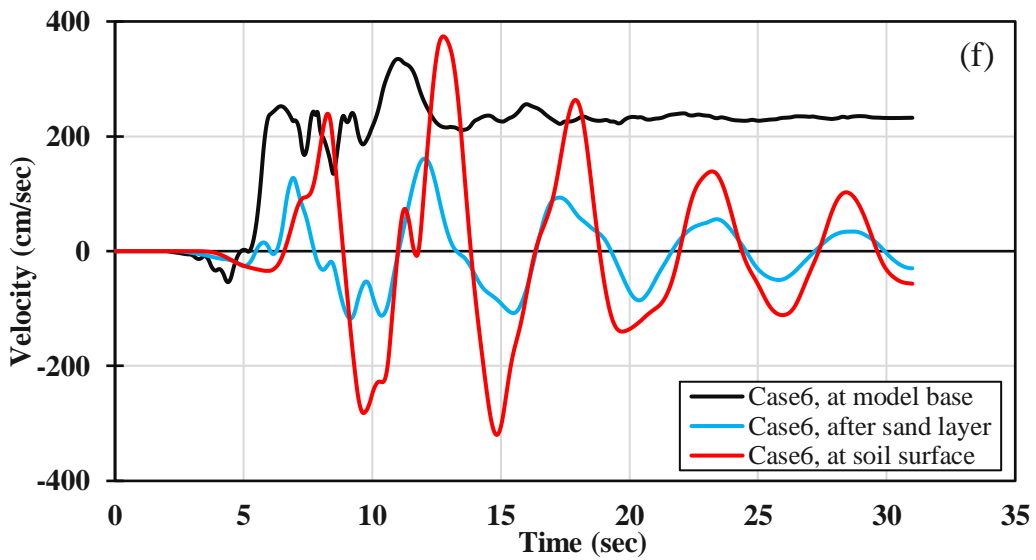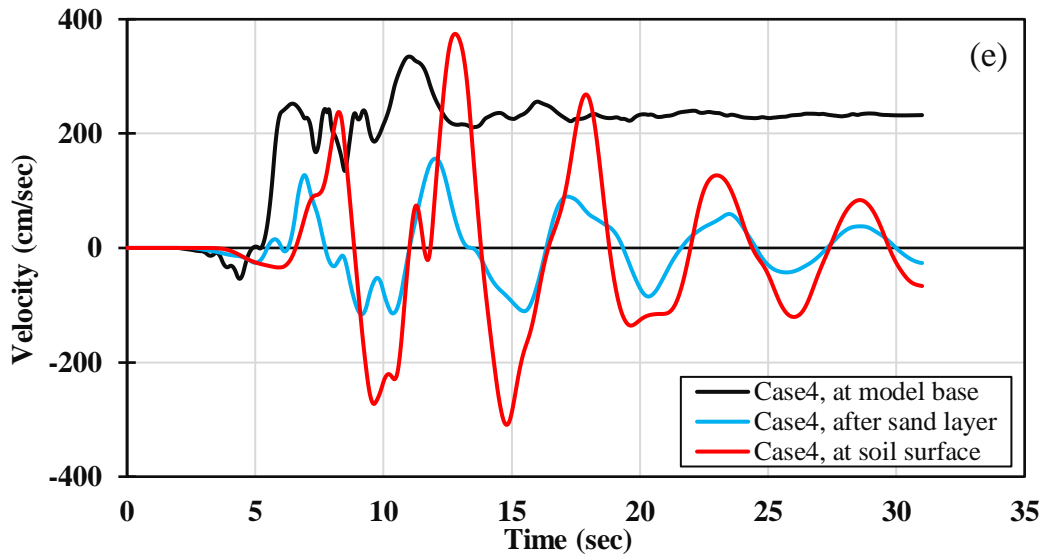
Figure 7-47 Velocity Time History, the Circumstance of Cut-Off Sand Layer at points A, B and C, (a) Case 1, (b) Case 2, (c) Case 3, (d) Case 4, (e) Case 5, (f) Case 6, (g) Case 7

334
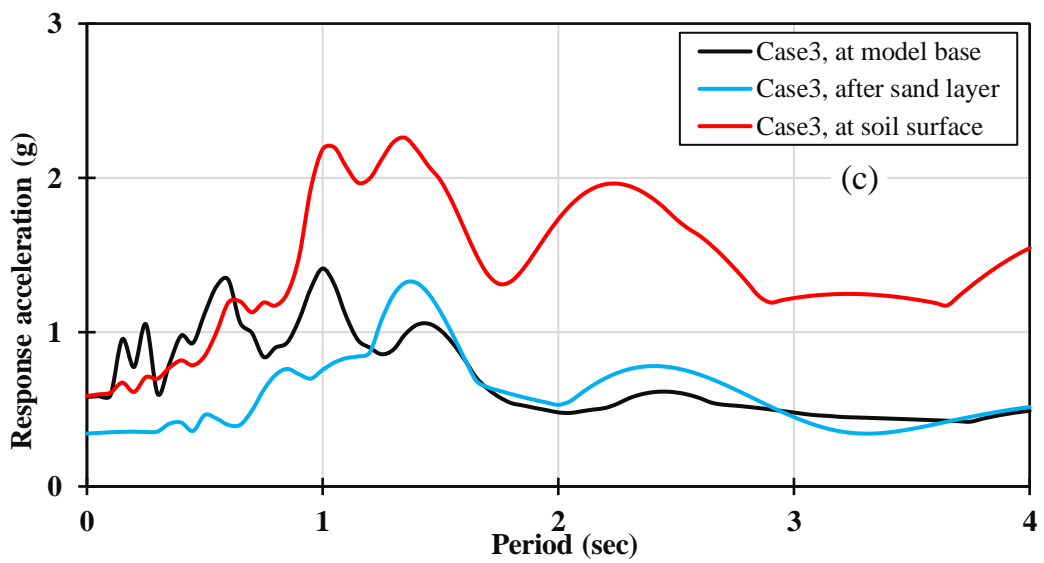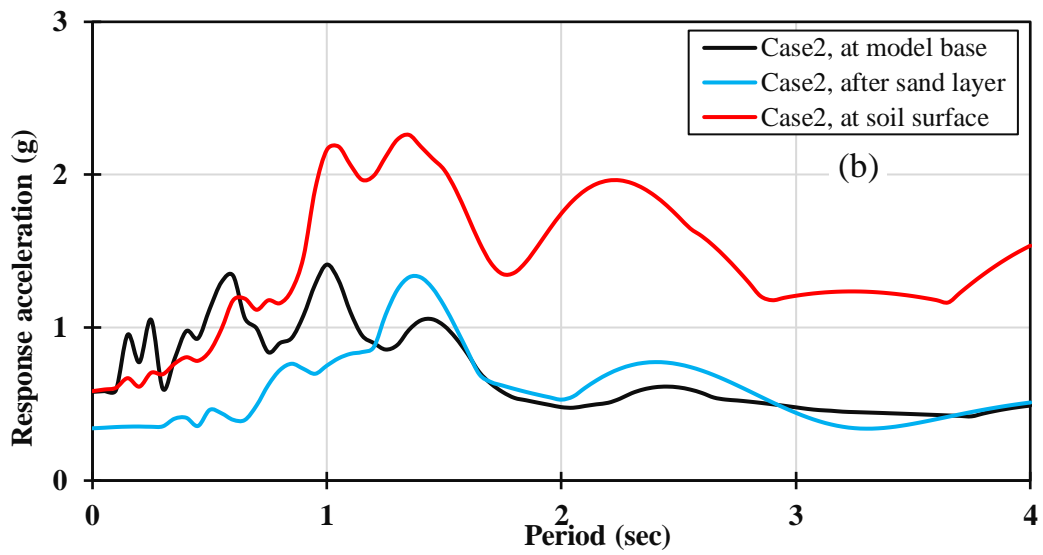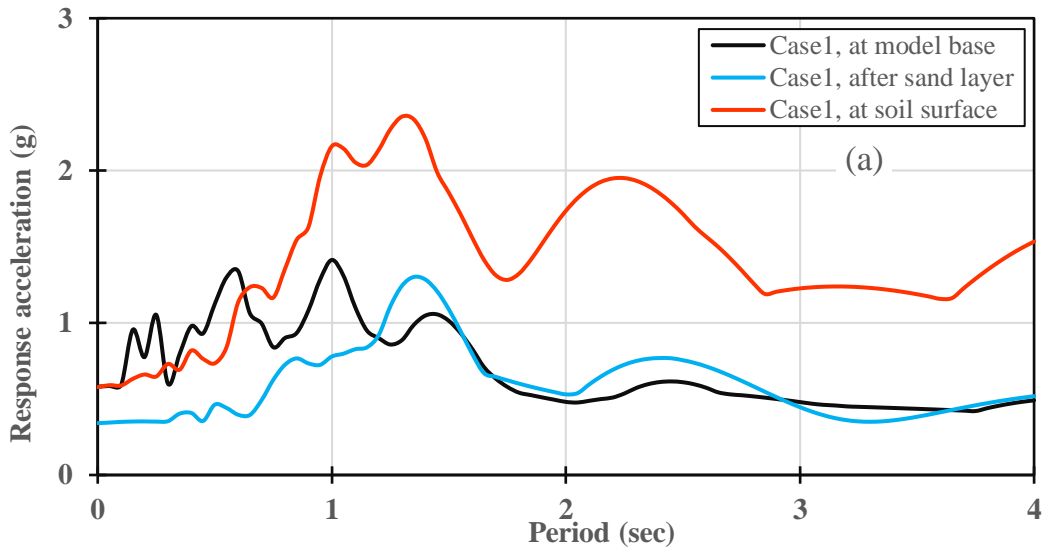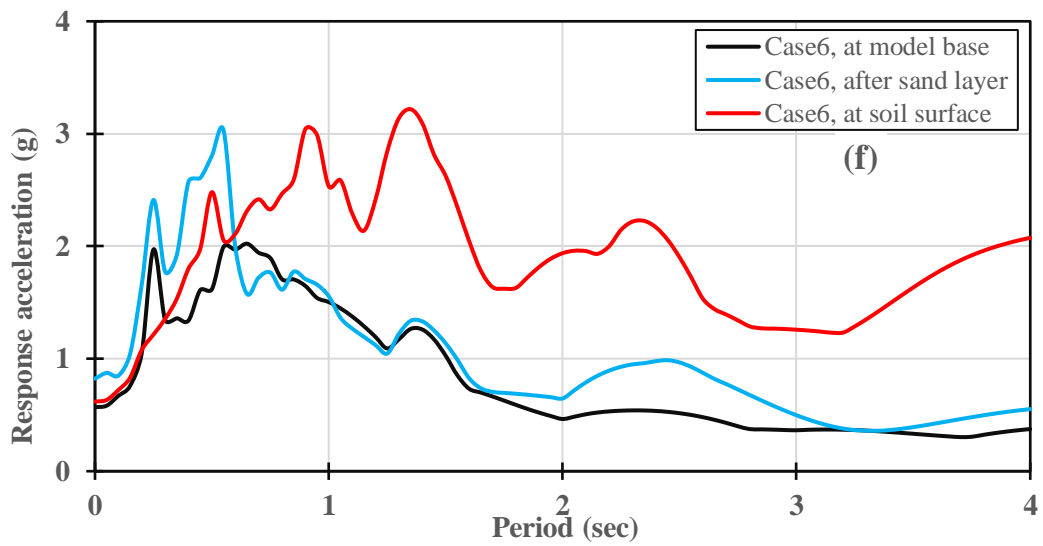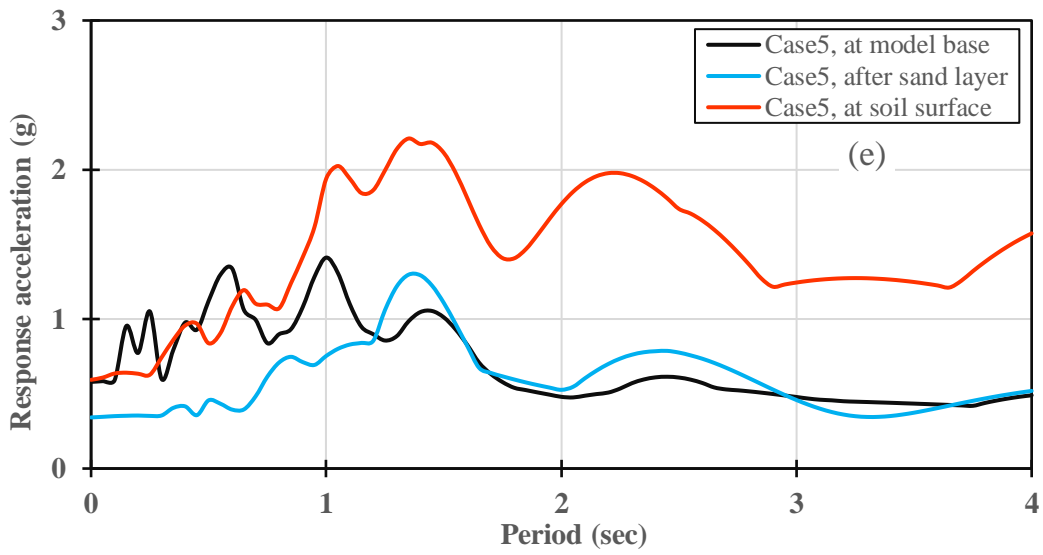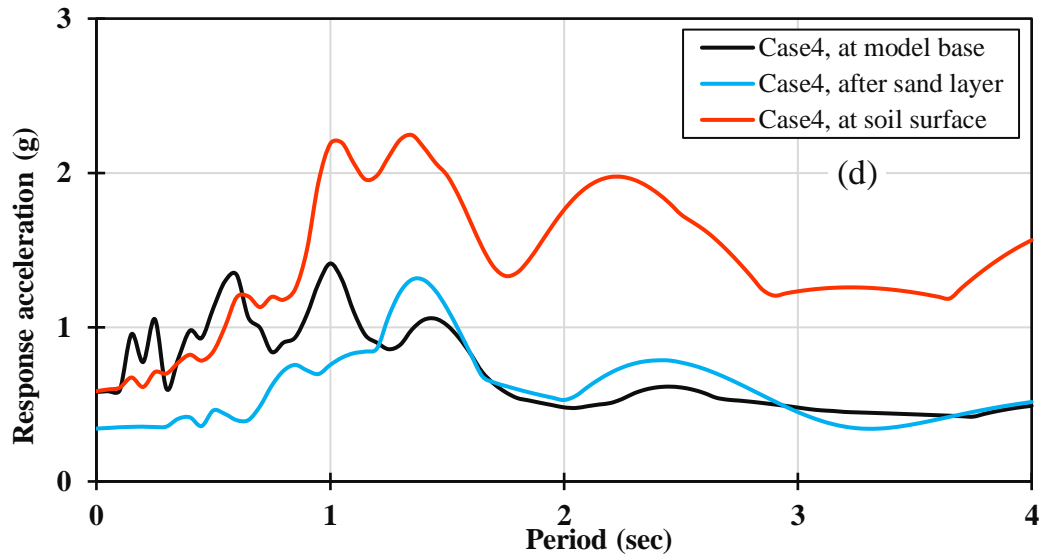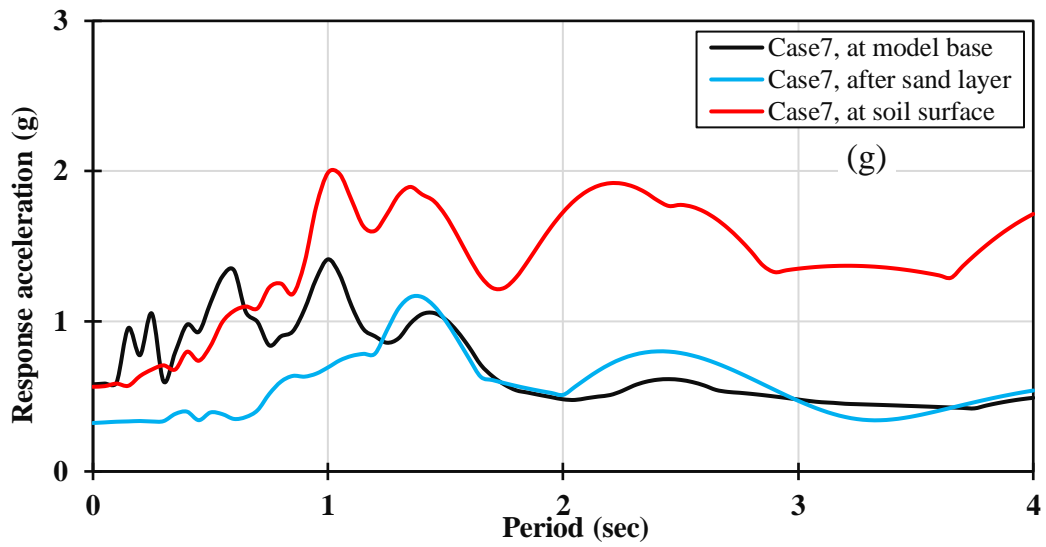
Figure 7-48 Acceleration response spectrum for the circumstance of cut-off sand layer at points A, B and C, (a) Case 1, (b) Case 2, (c) Case 3, (c) Case 4, (d) Case 5, (e) Case 6, (f) Case 7
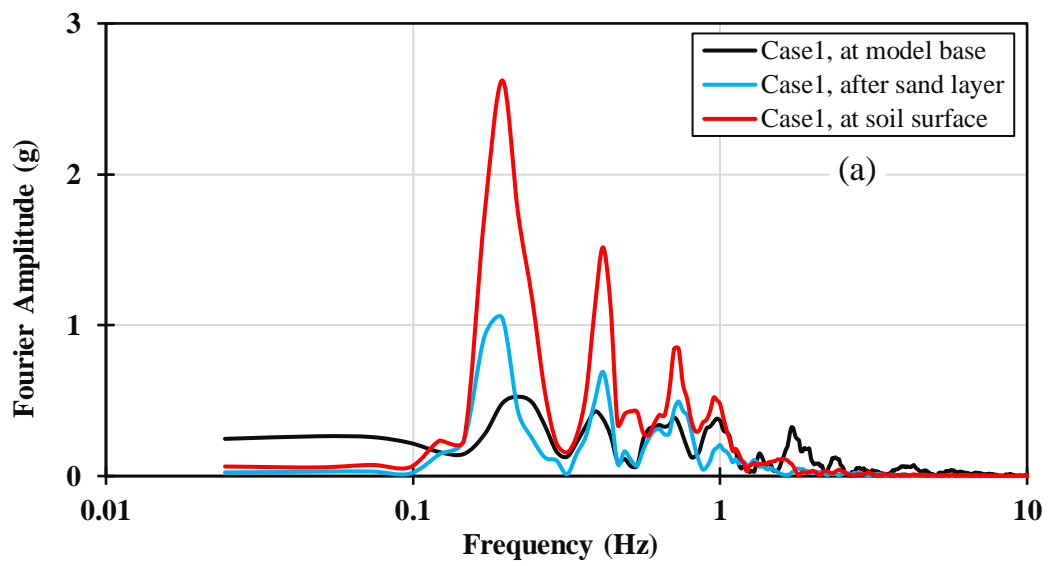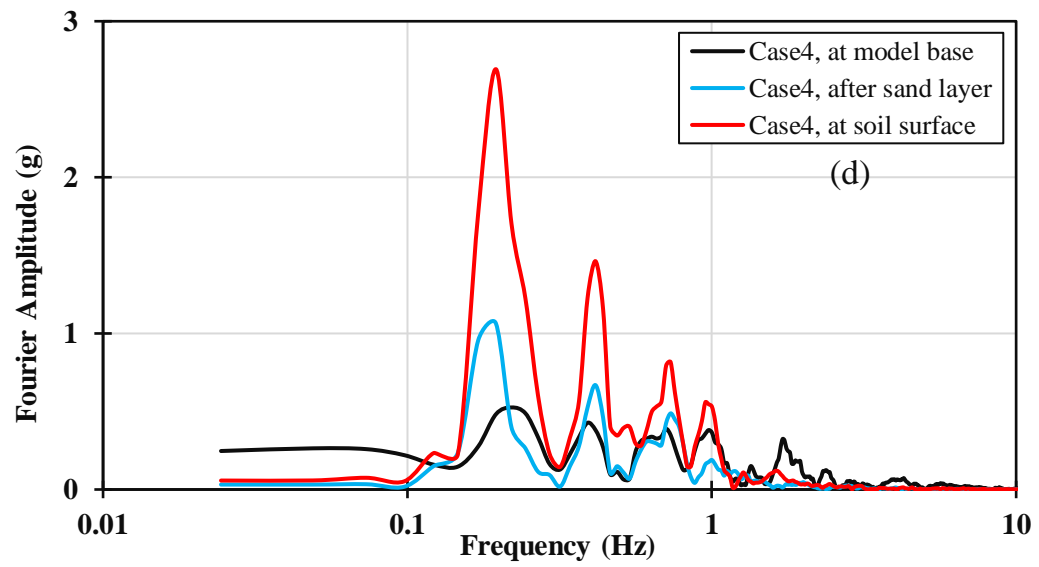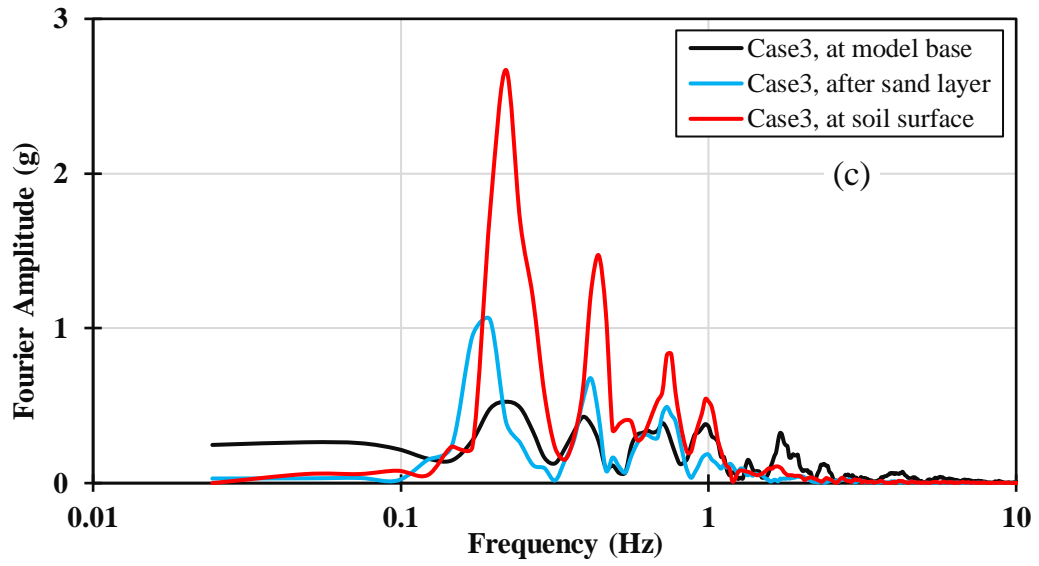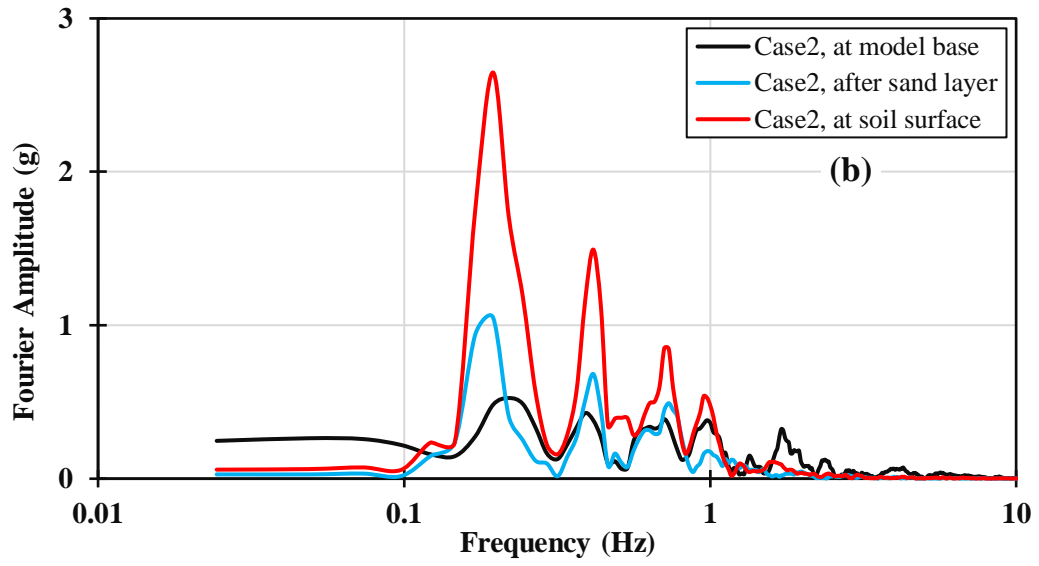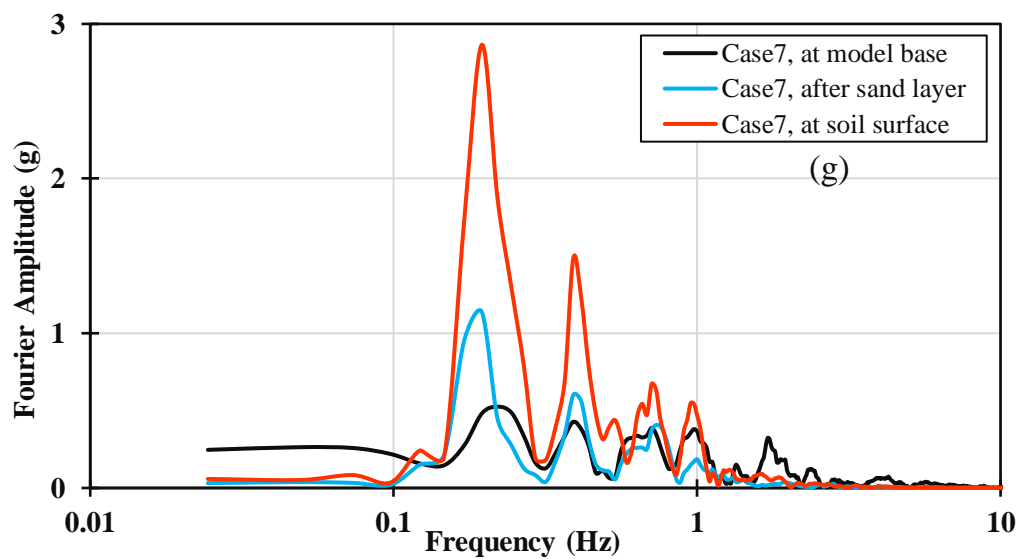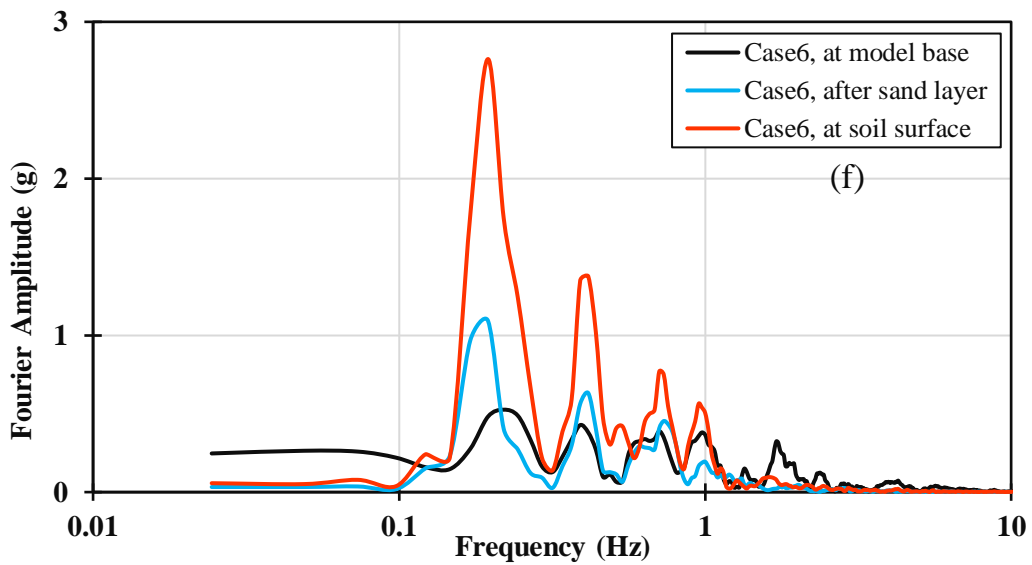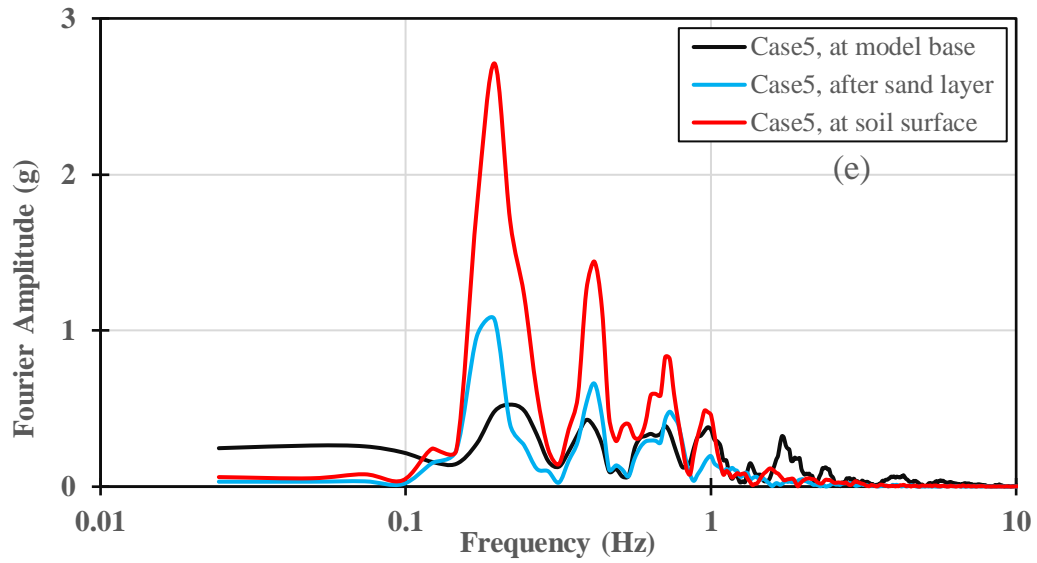
Figure 7-49 FFTs for the circumstance of cut-off sand layer at points A, B and C, (a) Case 1, (b) Case 2, (c) Case 3, (c) Case 4, (d) Case 5, (e) Case 6, (f) Case 7

Table 7.6 Resultant Time Histories Properties of Circumstance (ii)

Parameter	For all	Case1			Case2		Case3		Case4		Case5		Case6		Case7	
		H=0.25 m			H=0. 50 m		H=0.75m		H=1.0m		H=1.25m		H=2.0m		H=4.00m	
		A	B	C	B	C	B	C	B	C	B	C	B	C	B	C
Max. Acceleration (g)		0.58	0.341	0.577	0.342	0.585	0.343	0.586	0.343	0.5854	0.342	0.594	0.339	0.585	0.3225	0.564
Time of Max. Acceleration (sec)		5.72	6.6	11.91	6.59	11.92	6.59	11.92	6.59	11.92	6.59	11.92	6.59	11.93	6.59	13.55
Max. Velocity (cm/sec)		334.68	151.15	368.23	153.40	375.08	154.89	374.87	156.22	374.37	158.13	389.17	161.13	373.96	162.31	375.23
Time of Max. Velocity (sec)		11	12	12.78	12.01	12.8	12.02	12.8	12.02	12.79	12.03	12.79	12.03	12.76	12.07	12.73
Sustained Max. Acceleration (g)		0.425	0.2314	0.5644	0.232	0.557	0.232	0.558	0.231	0.557	0.230	0.556	0.222	0.552	0.21	0.53
Arias Intensity: (m/sec)		3.876	3.811	19.403	3.841	19.46	3.847	19.59	3.86	19.84	3.860	19.82	3.815	19.86	3.64	20.1
Effective Design Acceleration (g)		0.572	0.337	0.577	0.338	0.588	0.339	0.59	0.334	0.589	0.338	0.593	0.335	0.5871	0.32	0.564
Predominant Period (sec)		0.58	1.36	1.32	1.38	1.34	1.38	1.34	1.38	1.34	1.38	1.36	1.36	1.34	1.38	1.02

7.6. Concluding remarks

- The impact and identification of soil class F in EC8 and ASCE follow ambiguous guidelines. The decision of assigning class F or not as a site class for a project mostly depends on the experience and deduction of the personnel concerned.

- To minimise the hazardous consequences of making the wrong decisions and to obtain a clear definition and a consistent solution for researchers, designers, analysers and people who are not specialists in the geotechnical area, the following two identification problems of soil class F are defined accurately:

  (i) The minimum thickness of sensitive clay to be considered to meet code condition for soil class F

  (ii) The minimum thickness of sand layer that cuts off the continuity of soft clay layer (which meets code condition) to be no longer classified as F

- No previous study has investigated this crucial issue, and no complete definition has been provided for this particular subject of Section 20.8.1.

- Given the hazardous code definition of site class F and the risk of downgrading it to the less dangerous site classes, this important issue must be identified clearly in the seismic design codes.

- The findings reveal that the frequency content of the ground motion plays the key role in identifying the system behaviour for circumstances *(i)* and *(ii)*.

- The minimum thickness of sensitive clay layer that makes the system behave under soil class F condition starts from 0.5 m.

- The presence of thin sand layer(s) between two thick soft clay layers does not change anything, and the accumulative thicknesses of soft soil layers ($\sum H$) must be considered to employ the condition of (H $\geq$37 m).

- Expanding the cut-off sand layer to more than 2.0 m means a new behaviour condition, and the average soil properties should be applied to decide the correct soil class according to conditions in Section 20.3.1 of ASCE.
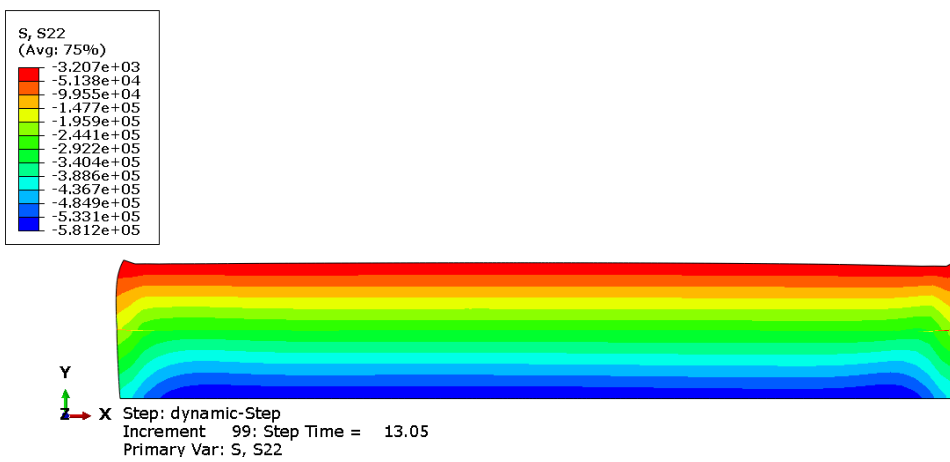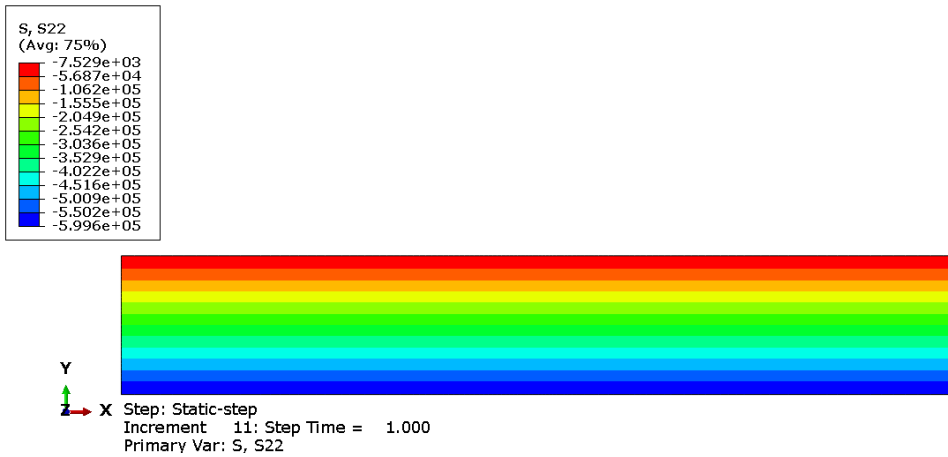
Chapter 8: Multi-Hazard Analysis of Post-Earthquake Fire

8.1. Introduction

Extreme events such as an earthquake, fire or blast have a low likelihood of incidence during a structure's lifecycle but can have tremendous after-effects in terms of the safety of any inhabitants and the integrity of the structure. In addition, there may be a higher risk of a second extreme event occurring, owing to any damage done during the initial event, for example, a fire after an earthquake. In such a case, the structure is exposed to multiple hazards. The current study is concerned with the response of steel framed structures subjected to an earthquake followed by a fire. This particular multi-hazard event is known as a post-earthquake fire (PEF). The soil profile effects have been included in the applied earthquake motion according to the procedure described earlier in chapter 6 section 6.3.2.1.1.

Most structures are required to be designed on the basis of 'life safety' design criteria specified in design codes. These codes guarantee that structures remain stable and continue to carry gravity loads, dead loads and a percentage of live loads during extreme events, thus allowing building occupants to evacuate buildings safely. Based on the function of the structure and its importance, the allowable rate and type of damage which is tolerable during an extreme loading is typically specified during design. The design codes ensure building safety under a variety of load combinations representing various extreme loading scenarios. However, the load combination of an earthquake followed by a fire has yet to be included in the international design standards. The forces and moments which are applied to a structure during a PEF are likely to be much greater than for individual extreme events, as accounted for in design.

Mitigating the effect of PEF on buildings during the design process in order to ensure the safety of occupants and emergency services personnel is a crucial aspect of any PEF safety strategy. The effect of a PEF can be diminished by controlling and determining the status of structural stresses after the first event (the earthquake) and also designing and/or strengthening the building to withstand and survive the fire loading. Eurocode 8 Part 1 (British Standards Institution, 2004) provides a design load combination for a set of different actions (Eq. 8.1). These actions must be combined with those from other loads,

such as permanent loads (*G*), pre-stressing load (*P*), seismic actions ($A_{E,d}$) and a proportion of the variable (live) loads (*Q*). A specific reduction factor ($\Psi_{2,i}$) is given in Eurocode 8 and specifies the recommended values of factors for buildings (British Standards Institution 2011).

Table 8.1 Values of ψ Factors for Buildings, (European Committee for Standardization, 2011)

Action	ψ_0	ψ_1	ψ_2
Imposed loads in buildings, category (see EN 1991-1-1)			
Category A : domestic, residential areas	0,7	0,5	0,3
Category B : office areas	0,7	0,5	0,3
Category C : congregation areas	0,7	0,7	0,6
Category D : shopping areas	0,7	0,7	0,6
Category E : storage areas	1,0	0,9	0,8
Category F : traffic area, vehicle weight ≤ 30kN	0,7	0,7	0,6
Category G : traffic area, vehicle weight ≤ 160kN	0,7	0,5	0,3
Category H : roofs[*]	0	0	0
Snow loads on buildings (see EN 1991-1-3)			
- for sites located at altitude H > 1000 m a.s.l.	0,7	0,5	0,2
- for sites located at altitude H ≤ 1000 m a.s.l.	0,5	0,2	0
Wind loads on buildings (see EN 1991-1-4)	0,6	0,2	0
Temperature (non-fire) in buildings (see EN 1991-1-5)	0,6	0,5	0
[*] See also EN 1991-1-1: Clause 3.3.2 (1)			

$$\sum_{f \geq 1} G_{k,j} + P + A_{E,d} + \sum_{i \geq 1} \Psi_{2,i} \, Q_{k,i} \qquad (8.1)$$

As evident from Eq.(8.1), the wind and temperature loads are not combined with the earthquake excitation (British Standards Institution 2011). There are two important concepts that should be considered while designing a structure to resist different magnitudes of earthquakes and those are frequent earthquakes and design earthquakes. The return period of a frequent earthquake is lower than that of a design or 'maximum considered' earthquake. A design earthquake is defined using a return period R of 475 years which corresponds to a 10% probability of exceedance in 50 years. As shown in Figure 8.1 and Table 8.1 a usual building must be operational in a frequent return period and safe in the zone of a design earthquake. For very important structures, the critical components must remain operational for a 'maximum considered' earthquake.
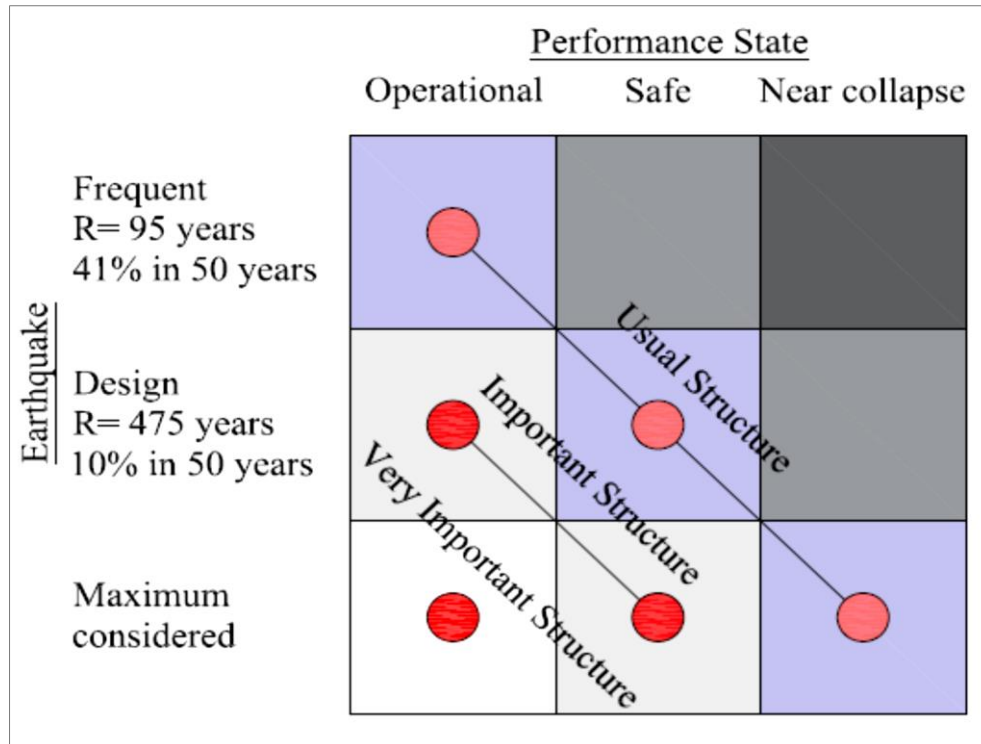
Figure 8-1 Requirements for Structural Performance During Different Types of Earthquake (According to Eurocode 8)

Understanding the structural behaviour of a building is crucial when a fire happens after an earthquake as the event increases the level of complexity. The structural behaviour and material properties of the remaining parts of the structure after the first hazard are used as properties of the structure subjected to fire. Fire-resistance rating is defined as a time period in which the integrity of structural elements subject to fire load is managed to resist applied loads, and this definition is associated with various aspects, such as the type of the structure and material properties (Lansing, 2007). Fire-resistance rating is typically provided in codes such as Eurocode1-9 (Bellova, 2013) and IBC (International Building Code) for a sole event of fire and not for the subsequent occurrence of earthquake and fire. Mousavi, Bagchi and Kodur (2008) presented a review on PEF hazard to a building. Their study indicates that the main factors associated to PEF hazard are the intensity and duration of the applied earthquake, applied fire scenario, protection system and the materials used. In the current study, a multi-hazard analysis approach is developed. The damage caused to the structure during and after an earthquake is included in the sequential thermal analysis. This methodology is developed and employed to study the nonlinear behaviour of a steel-framed structure under a PEF condition. A 3D elastic-plastic model of unprotected steel frame is developed using the Abaqus software. As mentioned in the

342

literature review (Chapter 2), the behaviour of a building during a fire event is not significantly affected owing to the nonlinear geometric effects if the design of the structure complies with serviceability limit state. However, the available research analysis conditions are unreasonable. The nonlinear geometric effects are presumed without considering the effect of structural resonance and frequency effect. Computing inaccurate EC8 design spectrum and then generating an acceleration time history to be applied as motion during the seismic stage of the examined multi-hazard analysis process, according to this loading condition leads to the underestimation of the structural behaviour of the building. According to seismic code provision, the structure should be designed to maintain the spectrum load. The condition mentioned above thus cannot be reliable and assertive to be a basis for assessing PEF consequences.

8.2. Basis of analysis

From the above discussion, it is clear that an accurate evaluation of the response of a structure following an earthquake, which serves as the input data in the fire analysis for a PEF event, is critically important. This response is influenced by many aspects including the level of certainty of the material properties and the mechanical behaviour of the structural components as well as the intensity of the seismic action. These difficulties and uncertainties have led to researchers adopting simplified approaches for assessing the seismic structural behaviour and damage in PEF analyses (Fajfar, 2014). However, simplified methods may not present the actual structural behaviour and the effects seismic loading that lead to stresses redistribution that may be a represent a key factor during the fire analysis of PEF event. The key problem lies in the appraisal of the physical state of the structure following the earthquake, or the 'initial condition' for the subsequent fire action. In most major earthquakes, structures undergo significant levels of plastic deformation. The availability of reliable analysis methods, including sophisticated numerical models, may facilitate a more realistic prediction of the performance and damage of a structure which is subjected to an earthquake. The structural damage can be classified as either geometric, whereby the initial geometry is altered due to plastic deformations that occur during the earthquake, or mechanical, which is the degradation of the mechanical properties of the structural components in the plastic range of deformation during the earthquake. (e.g. (Ziaei, Peyghaleh & Zolfaghari, 2010), (Ronagh & Behnam, 2012), (Behnam & Abolghasemi, 2019))

343

8.2.1. Seismic analysis for PEF

Traditionally, the effect of an earthquake on a structure is studied either using approximate methods, such as a pushover analysis, or a time history analysis. Pushover analysis is a nonlinear static analysis procedure to estimate the strength of a structure beyond its elastic limit, but does not induce actual plastic damage in the structure and does not require a ground motion time history. On the other hand, a time history analysis is a nonlinear dynamic response analysis performed using an actual or artificial earthquake time history to evaluate the response of the system. Time history analysis usually takes significantly longer to complete compared with a pushover analysis and is also more computationally demanding. However, it typically provides a more accurate depiction of the structural response to a seismic event, which is imperative in a PEF assessment. When the damage from the earthquake is underestimated, the structure can be very vulnerable to failure even if it has been thoroughly designed for the fire condition. As described in Chapter 6, earthquake input data must be generated in accordance with the structure frequency modes, geotechnical and geological site properties, and the design response spectrum characteristics. In this context, in the current work, a time history analysis is employed to assess the structural response to the seismic excitation.

8.2.2. Input data

In performance-based design, a structure subjected to a design earthquake should maintain the required design level of performance (EN1998-1, British Standards 2004). Eurocode 8 includes two types of earthquakes, namely Type 1 and Type 2 spectra and also four different importance classifications for buildings, depending on their function. In the current work, it is assumed that the structure being analysed is classified as importance class III (i.e. buildings whose seismic resistance is of importance in view of the consequences associated with a collapse, e.g. schools, assembly halls, cultural institutions, etc.) and is therefore subjected to a Type 2 earthquake. The ground conditions are type E as defined in Eurocode 8, described by various stratigraphic profiles and parameters and the viscous damping is set at 5%. For these conditions, the peak ground acceleration (PGA) that occurs during the earthquake is given as 0.35 g.

The design response spectrum is developed in accordance with Eurocode 8 for selected targeted time histories. The user-selected time histories are subjected to a scaling and matching procedure to derive earthquake input data within the spectrum periods of interest. The spectral scaling method used in the current study employs a computer

algorithm—SeismoSignal and SeismoMatch software (SeismoSoft., 2020)—to modify the real- and artificial-time histories to closely match the target design response spectrum. Using these procedures, data from a real earthquake are modified to a PGA of 0.35 g and frequency content according to the design conditions.

To examine the seismic structural response, two predominate periods are selected for the modified real earthquake, i.e. 0.24 sec and 0.36 sec, in addition to one predominate period of 0.16 sec for the artificial motion. For the latter, a MATLAB algorithm was developed (see the below MATLAB White Nose script) to create the white noise-artificial earthquake to satisfy the Eurocode 8 value of the structural natural period, 0.16 sec (see Table 8.3, Section 8.5). The SeismoSignal and SeismoMatch software (SeismoSoft., 2020) are employed together with data from the U.S. Geological Survey (USGS) peer database (U.S. Geological Survey, 2018) to achieve the spectral design requirement. Figure 8.2 illustrates the Eurocode 8 design response spectrum together with the modified real earthquake spectra with predominant periods of 0.24 sec and 0.36 sec, respectively. On the other hand, Figure 8.3 presents the acceleration time histories corresponding to these spectra. Figure 8.4 and Figure 8.5 present the corresponding data for a spectrum with a predominant period of 0.16 sec, for the artificial motion.

MATLAB White Noise script

```
%Generation of coloured noise in MATLAB
close all;
clear all;
clc;
% % % % % % % % % % % % % % % % % % %
% Time setting and sampling frequency
% % % % % % % % % % % % % % % % % % %
tt=input ('sampling rate (sec)?'); % (1/sampling freq.) =(1/Fs);
take tt=0.02 sec.
ttt=input ('number of time samples?'); %(max time/tt); take 500
to get 10 sec for sampling rate of 0.02sec
tttt=tt*ttt; %maximum time
t = (0:tt: tttt);
Fs = 1/ (t (2)-t (1));
% % % % % % % % % % % % % % % % % % %
% white noise generation (limited in time)
% % % % % % % % % % % % % % % % % % %
white Noise = wgn(length(t),1,1); % generate white noise with
required length
NFFT1 = 2^nextpow2(length (white Noise));
white Noise Spectrum = fft (white Noise, NFFT1)/length (white
Noise);
```

```matlab
f1 = Fs/2*linspace(0,1, NFFT1/2+1);
x=white Noise;
figure (1);
subplot (2,1,1);
plot (t, white Noise);
title ('White Gaussian Noise');
x label ('Time (s)');
y label('acc');
sub plot (2,1,2);
stem (f1,2*abs(white Noise Spectrum(1:NFFT1/2+1)))
title ('Frequency Domain representation of WGN');
x label ('Frequency (Hz)')
y label('|acc|')
% % % % % % % % % % % % % % % % % % % %
%Coloured Noise Generation
% % % % % % % % % % % % % % % % % % % %
max_f=f1(end); % max frequency of input signal
PBf=input ('cut off frequency (Hz)?  '); %LBF cut off frequency
PBf_1=PBf/max_f; % normalized passband frequency
SBf_1=PBf_1 + 0.1; % normalized stopband frequency
LpFilt = design filt('lowpassfir','PassbandFrequency',PBf_1, ...
        'Stop band Frequency', SBf_1,'PassbandRipple',0.5, ...
        'StopbandAttenuation',65,'DesignMethod','kaiserwin');
Fv tool(lpFilt);
Data In=x;
Data Out = filter(lpFilt,dataIn);
coloredNoise2 = dataOut ;
% [coloured Noise Cov,lags] = xcov(coloredNoise2, L);
NFFT3 = 2^nextpow2(length(coloredNoise2));
coloredNoise2Spectrum =
fft(coloredNoise2,NFFT3)/length(coloredNoise2);
f3 = Fs/2*linspace(0,1,NFFT3/2+1);
% % % % % % % % % % % %
figure(3);
subplot(2,1,1);
plot(t,coloredNoise2);
title('coloured Noise');
xlabel('Time (s)');
ylabel('acc');
subplot (2,1,2);
stem (f3,2*abs (coloredNoise2Spectrum(1: NFFT3/2+1)))
title ('Frequency Domain representation of coloured Gaussian
Noise');
xlabel ('Frequency (Hz)')
ylabel('|acc|')
```
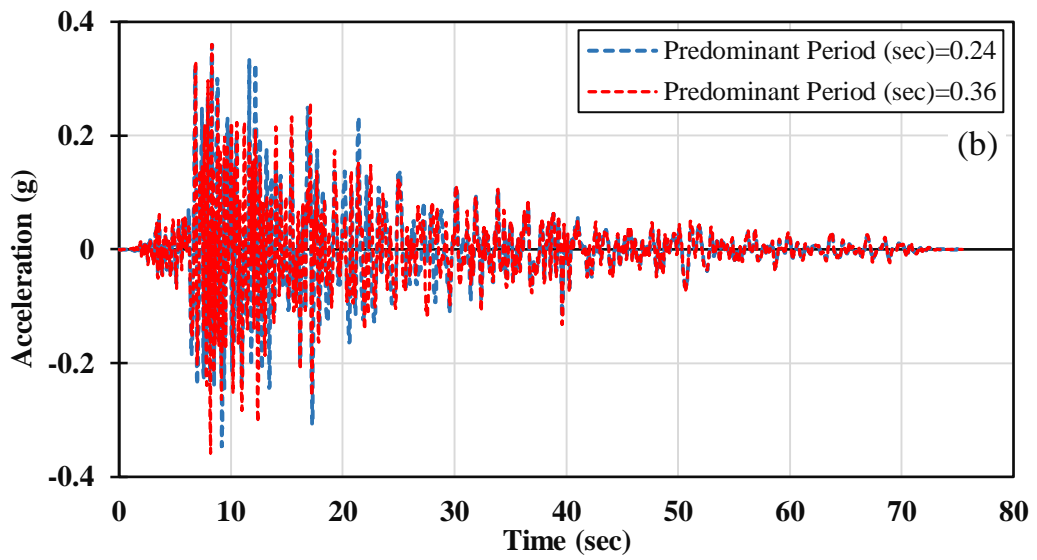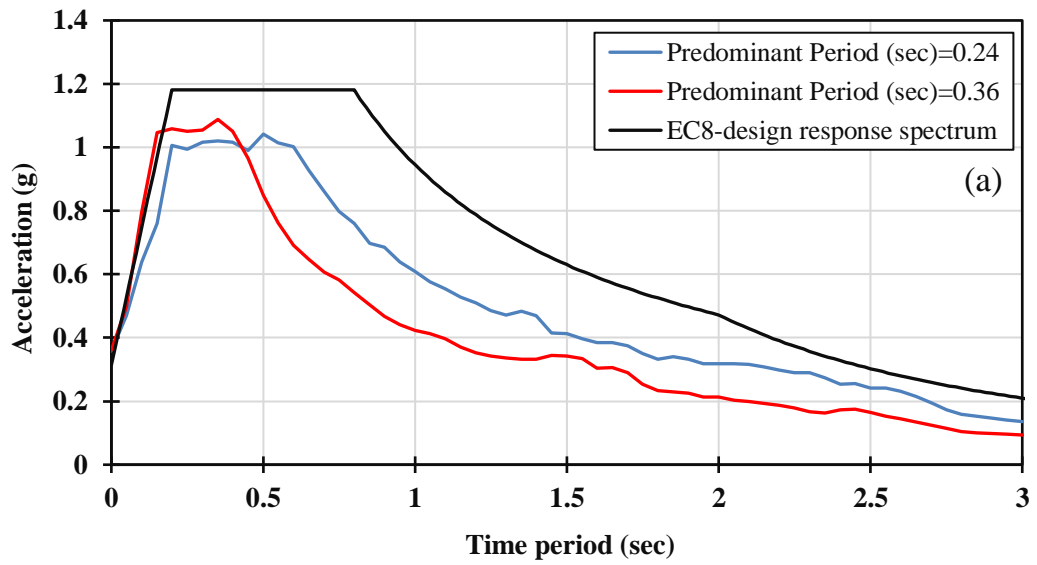
Figure 8-2 Real Earthquake and Eurocode 8, (a) Design Response Spectrum, (b) Acceleration Time Histories
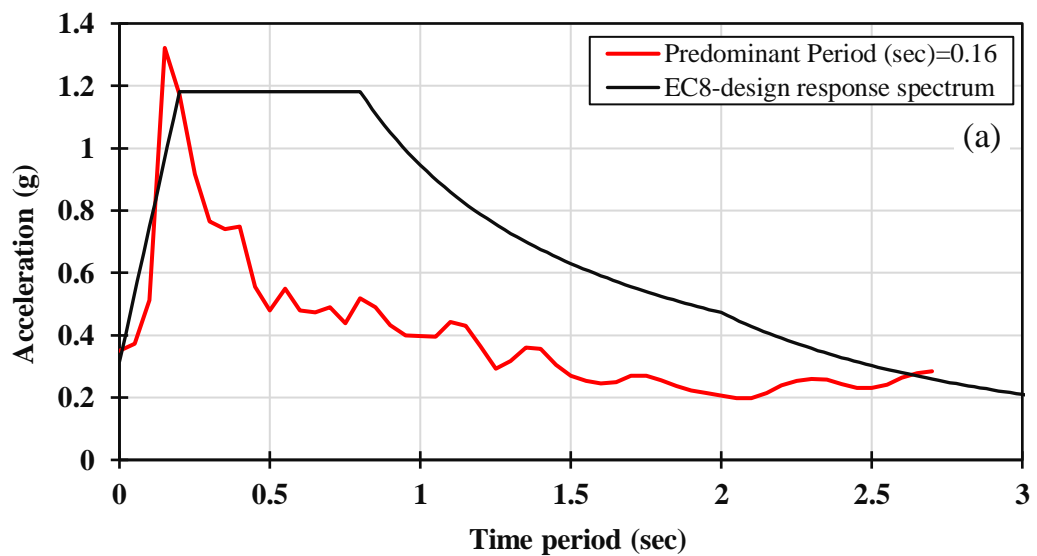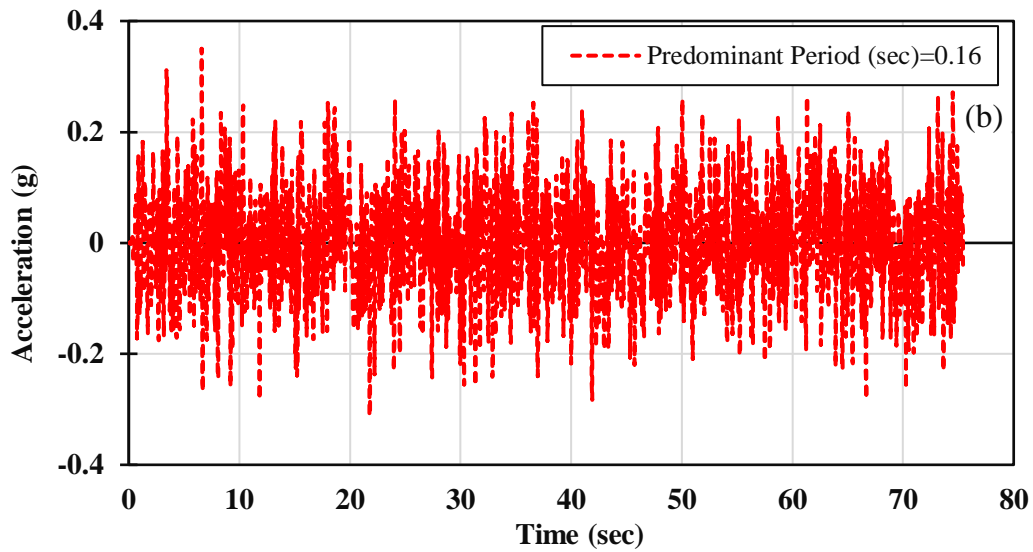
Figure 8-3 Artificial Earthquake and Eurocode 8 (a) Design Response Spectrum (b) Acceleration Time Histories

8.2.3. Thermal stress analysis in PEF analysis

In the post-earthquake fire analysis, the deformed or damaged structural configuration following the earthquake event is employed as the input for the application of the thermal loads. For the fire load, a uniform standard ISO-834 1975 fire exposure is applied to all components of the frame (see Figure 8.4), (Real, 2014).
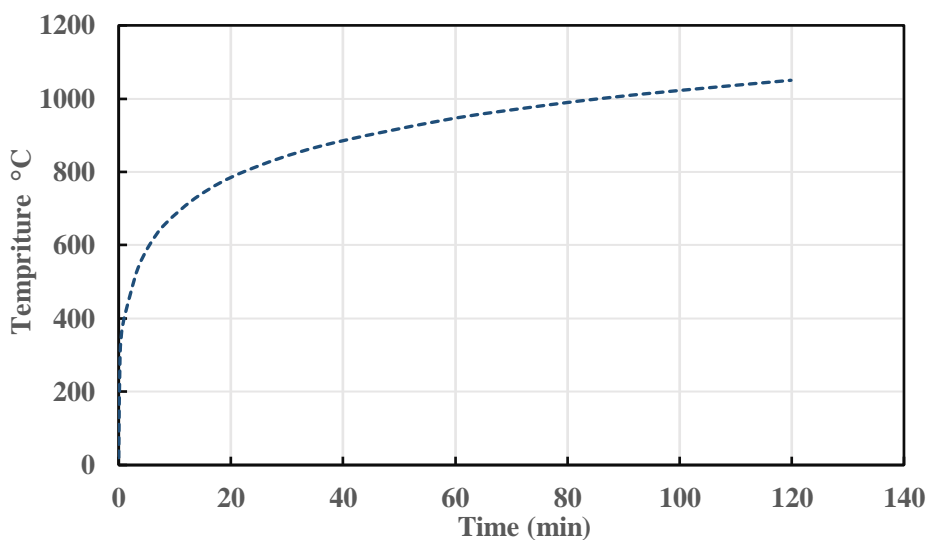
Figure 8-4 Standard Fire Curve ISO-834

The temperature-dependent material properties for steel as given in Eurocode 3 Part 1-2, are employed (British Standards Institution, 2011b). The steel used in the model is mild steel with a yield and ultimate strength at ambient temperature of 385 N/mm^2 and 450
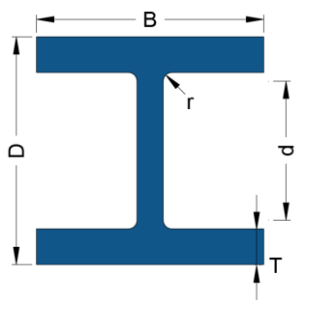
N/mm^2, respectively. The steel has a density of 7850 kg/m^3 and a coefficient of thermal expansion (α_s) of 1.4×10^{-5}.

8.3. Development of the numerical model

8.3.1. General

A three-dimensional geometrically and materially nonlinear model of an unprotected single-storey steel frame is developed using the Abaqus software, to analyse the behaviour during a post-earthquake fire (PEF). The frame is fabricated from beams and columns of the same I-shaped cross-section, which are connected with rigid joints. The cross-section has a depth (D) of 350 mm, flange width (B) of 170 mm, an identical web (t) and flange (T) thickness of 10 mm, a root radius (r) 12 mm and a depth between flange fillets (d) of 306 mm (see Table 8.2). The frame is designed to withstand gravity and seismic loads in accordance with Eurocode 8 Part 1 (British Standards Institution, 2004). Using the concept of structural performance and load combination relationships addressed in EN1990 A.1.2.2 (British Standards Institution 2011), in which structural members are typically designed to meet particular levels of performance and structures are expected to experience minor damages. A description for different live load reduction factor values for different according to the function of the targeted structure are listed in EN 1991 A1.1 (British Standards Institution 2011), the value of 60% is used. Accordingly, the frame is designed for a gravity load combination comprising 100% of the permanent loads and 60% of the live loads capacity during the examination of the current study of extreme events (Behnam & Ronagh, 2014).

Table 8.2 Section Dimensions of the Case Study

	Depth of section (mm)	Width of section (mm)	Thickness		Root radius	Depth between fillets (mm)
			web (mm)	flange (mm)		
	D	B	t	T	r	d
	350	170	10	10	12	306

8.3.2. Elements, meshing and boundary conditions

The steel sections are modelled in the finite element model using general purpose linear brick elements with reduced integration (known as C3D8R in the Abaqus library, (Smith 2018). A mesh sensitivity study was conducted to achieve the optimal combination of

349

accuracy and computational efficiency which resulted in finite elements which are between (10 x 20 and 20 x 20) mm in size at the connections and (10 x100 and 20 x100) mm for the steel sections. The steel is represented using a nonlinear elastoplastic material model which is defined by the yield and ultimate strength, of 385 N/mm^2 and 450 N/mm^2, respectively, and these properties degrade with elevated temperature in accordance with the reduction factors given in Eurocode 3 Part 1-2 for grade S450 carbon steel (British Standards Institution 2011). The beam-column connection is achieved using the tie condition. The base of columns is assumed to rest on a rigid foundation system, so the earthquake boundary condition is applied at the base of all the columns. A roller support is used to constrain the displacement vertically at the bottom of the model. The horizontal boundary conditions permit 'free' horizontal shaking in the direction/directions of the applied seismic load.

8.3.3. Loading and solution procedure

The analysis is performed sequentially comprising of static, dynamic and thermal analysis steps, as illustrated in Figure 8-5. The analysis is carried out in three main multi-hazard analysis steps, as well as an initial sub-step. Accordingly, firstly, a linear perturbation–frequency step is conducted to identify the structural modal analysis (as discussed in more detail later) and frequency content window of the dynamic system. Then, in the first analysis stage, a nonlinear static analysis is conducted, and the gravity loads are applied. The permanent loads are assumed to have a value of 8 kN/m^2 whilst the variable actions equal 2.5 kN/m^2, in accordance with Eurocode 1 (2011). In this step, the full amount of permanent and variable actions are applied. In the second step, the earthquake is simulated through a nonlinear implicit dynamic analysis. The acceleration time history is applied at the base of the structure while the static loads remain constant. The time history is processed, filtering for window frequencies matching the system modes and natural frequency of the structure during an earthquake with a PGA of 0.35 g.
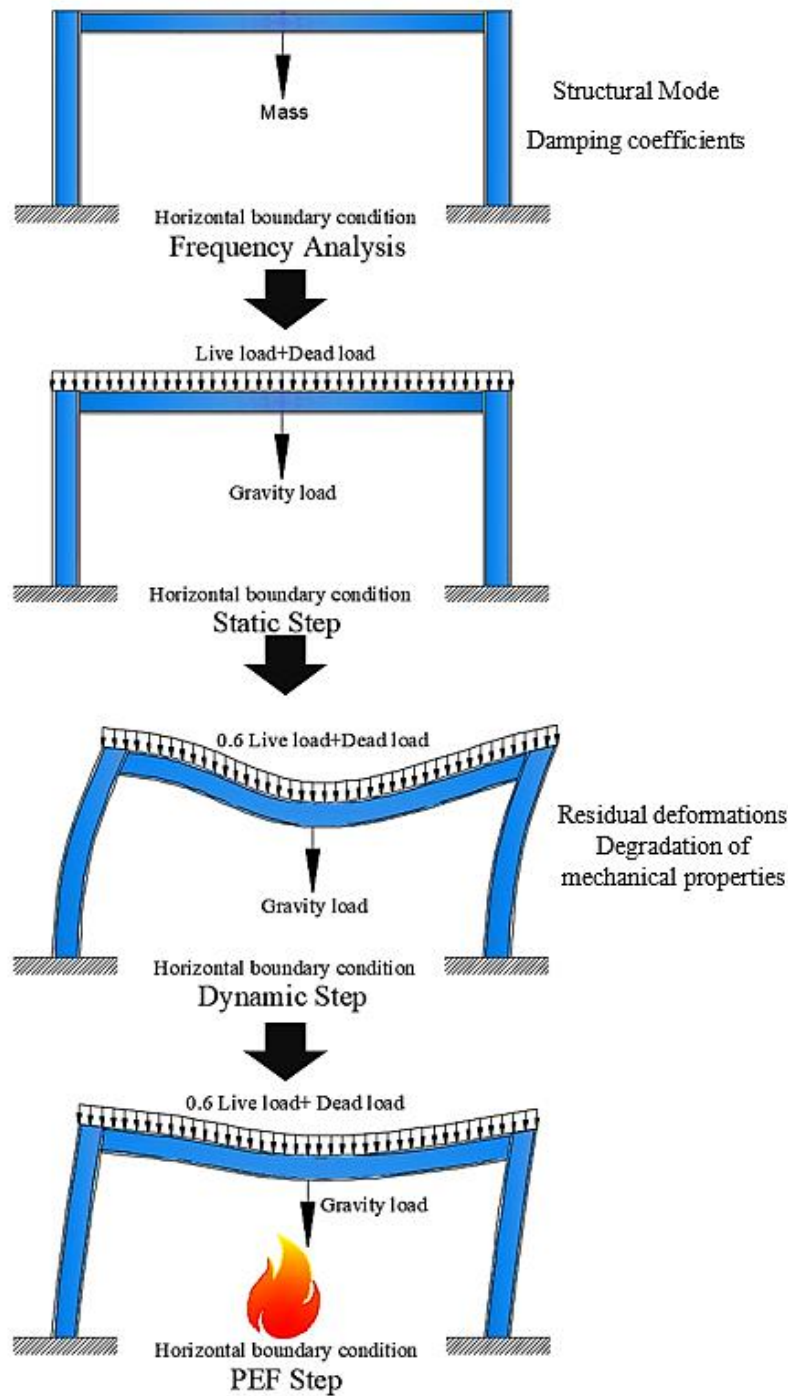
Figure 8-5 Methodology of the Sequential Analysis

In the third analysis stage, the thermal loads are applied to the structure in the form of a time–temperature curve (see section 8.2.3). The thermal temperatures are applied to the deformed structure following the application of the acceleration time history. The load combination in this stage is considered as 100% of the permanent loads acting together with 60% of the variable actions. The complete analysis is performed in a sequence to carry forward the deformations, stresses and damage caused to the structure during one

stage to the next stage of the analysis. The key objective of the current study is to compare between structural behaviour of structures subjected to multi-hazard event with the behaviour of those exposed to an only fire event. Thus, to compare and examine the consequences of applying earthquake on the fire resistance value during PEF analysis, an only fire scenario analysis is also performed as a separate circumstance of analysis.

8.4. Results and analysis

In this section, the results of the finite element analysis using the developed numerical model described previously are presented and analysed. The results are presented first for the frequency analysis, in which a linear perturbation-frequency analysis is developed as a sub-step of analysis, followed by the results from the PEF structural simulations.

8.4.1. Frequency analysis

The natural period of vibration of a dynamic system is an essential factor in the case of the based shear design methodology (Zembaty, Kokot & Kuś, 2018). Where, base shear is the ultimate expected lateral load applied at the base of the structure during seismic activity. The natural period of vibration is a critical parameter in defining the design response spectrum and consequently controlling the value of the base shear force. The hysteretic damping is involved in the restoring force, and viscous damping is considered by Rayleigh damping (proportional damping), (Eq.(6.4) in Chapter6 section 4.). As mentioned in Section 4 of Chapter 6, the damping ratio for the different natural frequencies can be computed from (Eq.(6.5)). According to the orthogonality between system mode and damping matrix and the assumption of 5% damping for the system modes, the corresponding coefficients of Rayleigh damping are calculated by Eq.(6.6) and Eq.(6.7), respectively. Codes provide empirical formulas to estimate the fundamental period of vibration T of the structure. EC8 recommends using the Rayleigh method, which is the expression based on the methods of structural dynamics, to compute the value of the time period (Eq.(8.2)).

$$T = 2\pi \sqrt{\frac{\sum_{i=1}^{n}(m_i \cdot S_i^2)}{\sum_{i=1}^{n}(f_i \cdot S_i)}} \qquad (8.2)$$

Where m_i are storey masses, f_i are horizontal forces, and S_i are displacements of masses caused by horizontal forces. The first six natural vibration periods, damping coefficients, codes of the models are listed in Table 8.3. Figure 8-6 shows the first six structure mode shapes.

Table 8.3 First Six Natural Vibration Periods and Factors of Rayleigh Damping

Model	Natural vibration period (s)							Damping coefficients	
	Model						Codes		
	1	2	3	4	5	6	EC8	α_m	β_k
Natural vibration period (s)	0.36	0.296	0.106	0.101	0.09	0.081	0.16	0.959	0.0026

The data in Figure 8-6, Figure 8-7 and Table 8.3 indicate that the first natural period computed according to EC8 provisions is between the second and the third mode of the simulation estimated values. The estimated natural period values substantially decrease for the first two modes, then gradually slightly decrease for the remaining modes. From this perspective, it can conclude that more modes are attributed and must be considered to the response of the seismic system analysis. Consequently, based on the above this inference, three input motions with three natural vibration periods are created, and they are 0.24, 0.36 and the EC8 value 0.16 sec (see section 8.4.3).

353
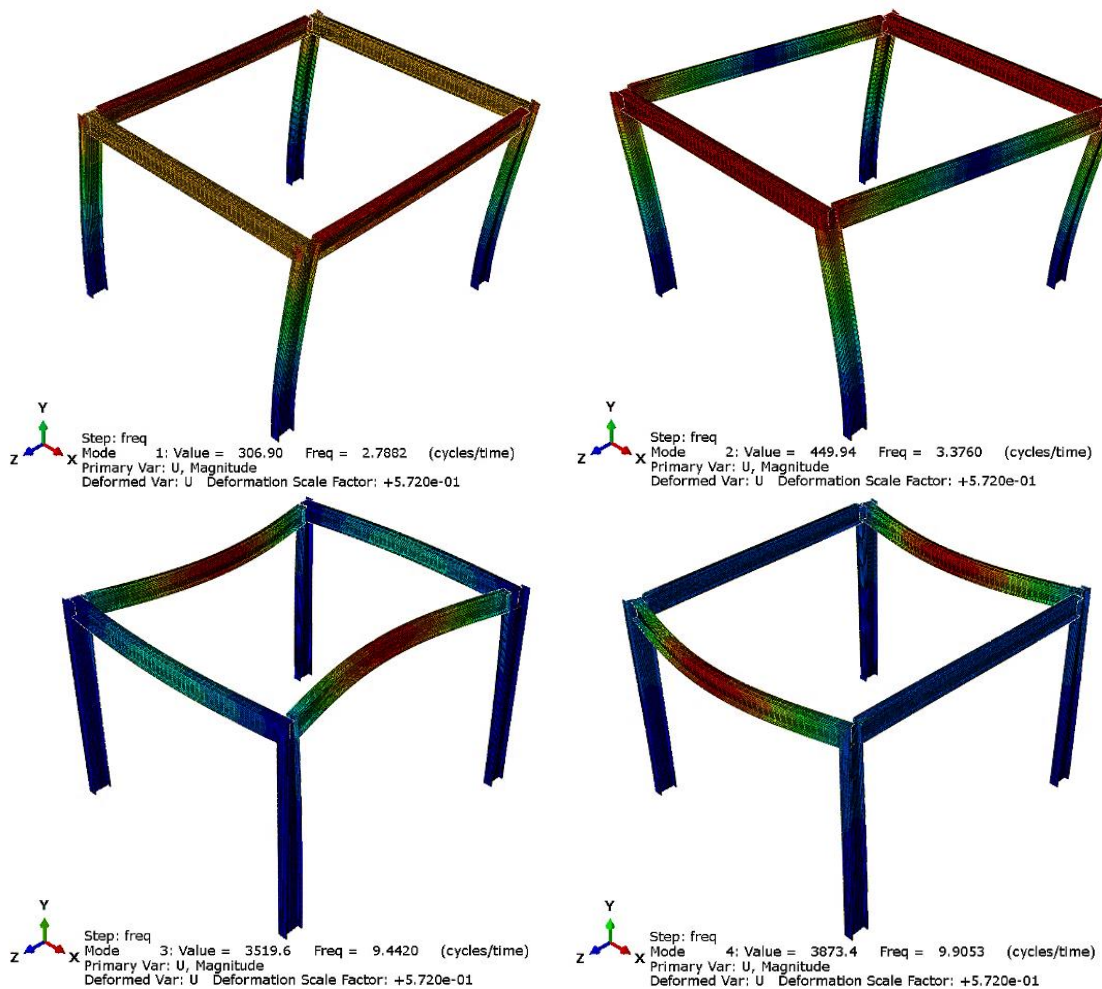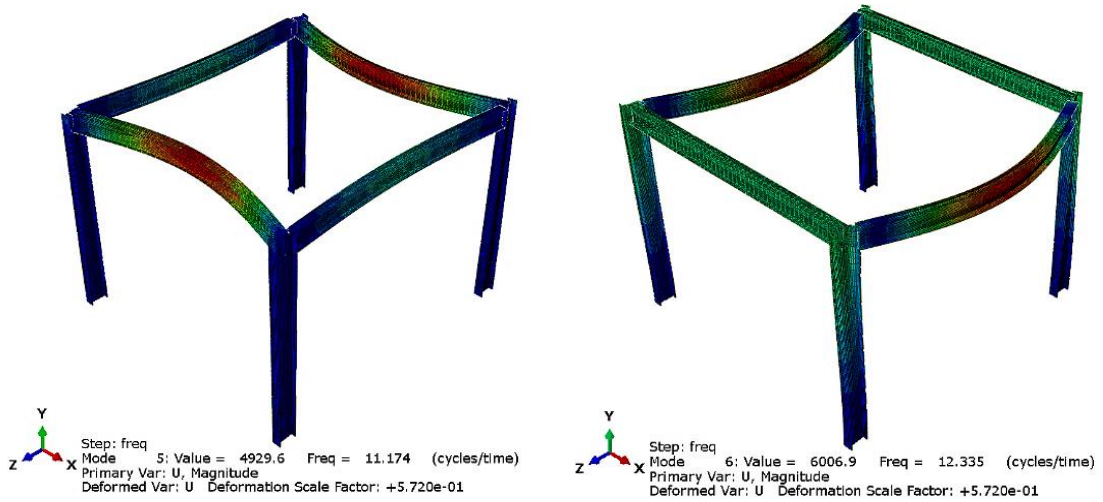
Figure 8-6 First Six Structure Mode Shapes
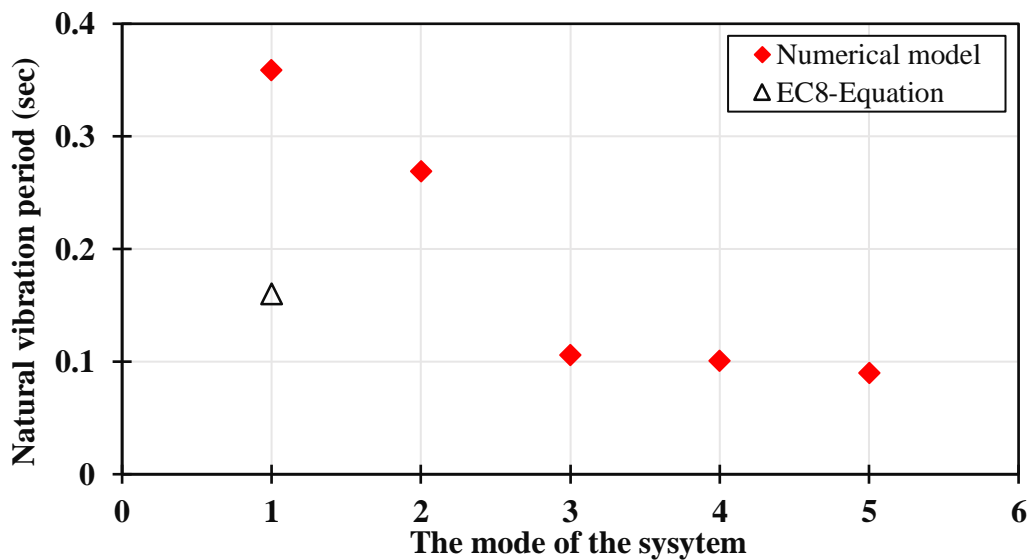
Figure 8-7 EC8 and the Model's First Six Natural Vibration Periods

8.4.2. Results validation

This section is carried out in order to confirm and validate the findings of the current study. As the present study performing a 3D complete structure, with the application of unique approach analysis, it was not easy to find a similar laboratory test to make the validation. Therefore, the validation was achieved through an appropriate approach, including re simulating the system under similar condition using another FE software. The Open System for Earthquake Engineering Simulation (OpenSees) software has been used for that purpose, which was initially developed at the University of California, Berkeley for seismic loading analysis (McKenna, 1997), and was later extended to perform structural fire analysis at the University of Edinburgh (Usmani *et al.*, 2010). Usmani et al. (2012) addressed that an excellent calibration can be received once the

354

model is simulated using both FE software Abaqus and openSees under similitude condition of analysis. Considering all of this evidence, it seems that replicated the simulation using OpenSees software under similar condition is the right approach of validation. Figure 8-8 (a) to (d) shows the displacements recorded, and temperature displacement curves during the analysis of both Abaqus and openSees at the mid-span locations for only fire scenario and PEF analysis, respectively. The results in four figures confirm a very close agreement between the Abaqus data and displacements calculated via OpenSees procedure.
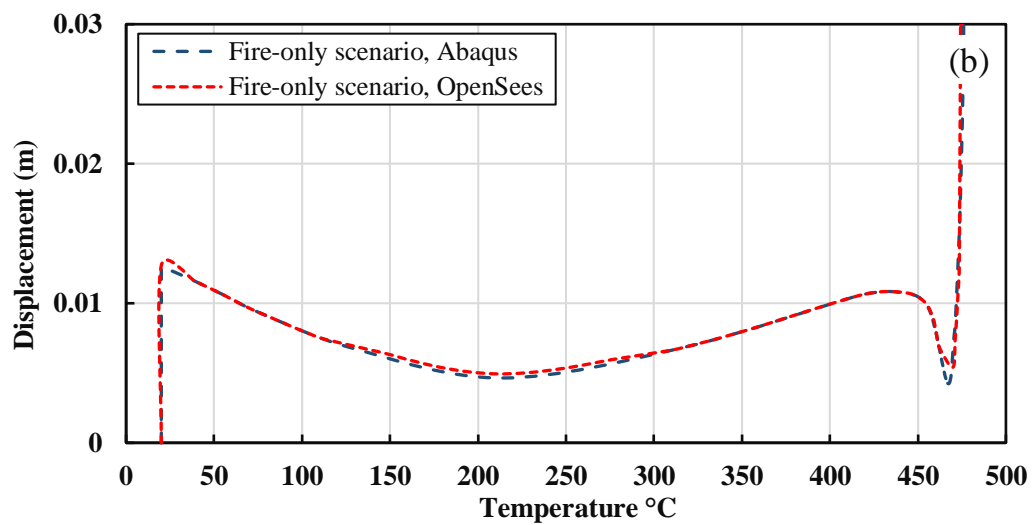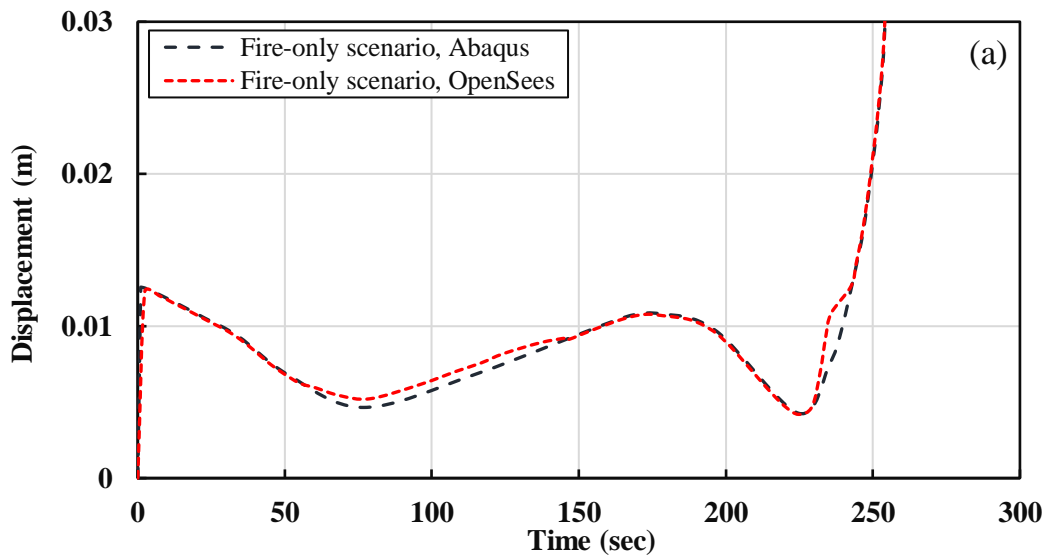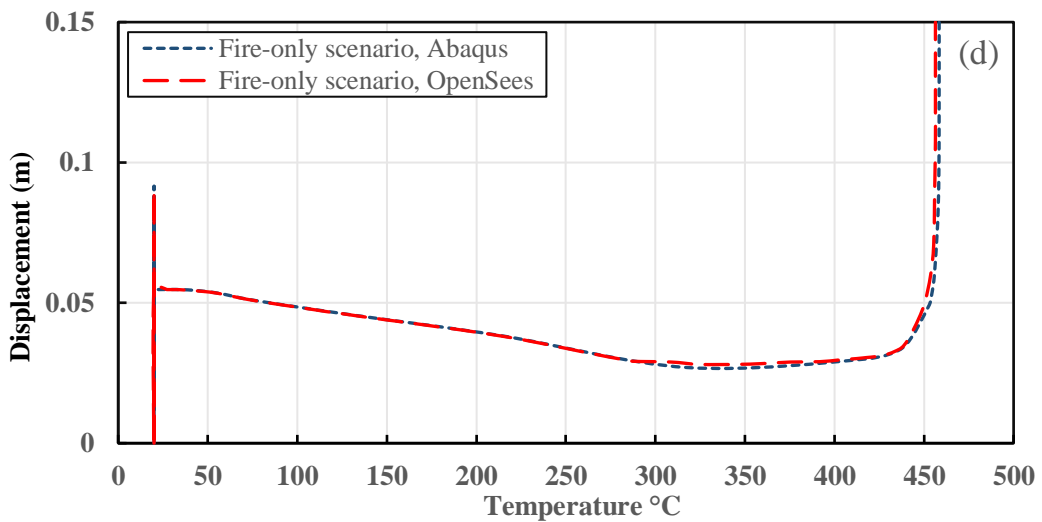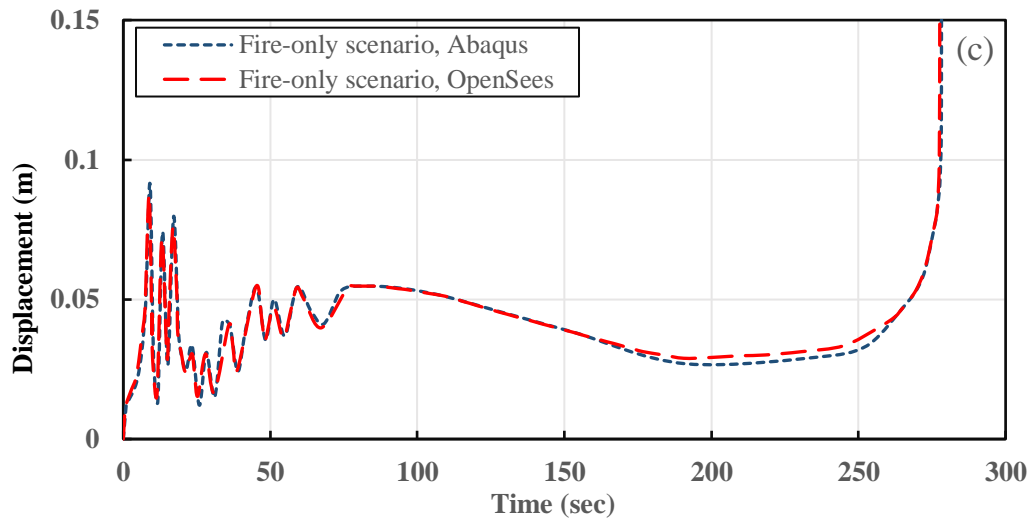
Figure 8-8 Comparison of Abaqus With OpenSees Simulations, (a) Time -Displacement Record for Fire Only Scenario, (b) Temperature-Displacement Record for Fire Only Scenario, (c) Time -Displacement record for PEF scenario, (d) Temperature-Displacement record for PEF scenario

8.4.3. Numerical analysis of post-earthquake fire and only-fire scenarios

In this section, the results of the PEF analysis of the steel framed structure are described and discussed. The sequential analysis developed in this study associates three major nonlinear stages which are the static analysis followed by the time history seismic analysis and then the PEF analysis. A linear frequency analysis is developed as a minor stage to obtain the structural mode and for the computed Rayleigh Damping coefficients to be included in the sequential analysis. In the seismic analysis, the structure is subject to two different real time-history motions which are matched to a particular predominate natural vibration period according to the time period window perceived from the frequency

analysis in addition to the natural period computed according to EC8 guidance. Moreover, to be close to the real earthquake situation, two types of excitation are applied, namely, the unidirectional and bidirectional excitations for using the aforementioned different natural periods. EC8 indicates a performance requirement associated with the limit states. This requirement necessitates the structure to still be operational after a relatively frequent earthquake without significant damage. Damage is only expected in non-structural elements. Accordingly, EC8 states an acceptable degree of reliability and validity contrary to unacceptable damage must be checked during the design stage , (British Standards Institution, 2004). The storey drift criterion is one of the primary stability criteria used in seismic codes as a geometrical stability limitation due to the frequent earthquake (Julián, Hugo & Astrid, 2014). Damage limitation requirement should be corroborated according to the standards supplied by EC8 seismic code. The limit is specified as 1% of the storey height under the ultimate design earthquake which is obtained as 0.03 m in the present study (EN 1993-1-2, 2011). To understand how an earthquake regulates fire resistance, a series of comparisons between only fire analysis scenario and four PEF cases is performed. Figure 8-9 and Figure 8-10 illustrates the collapse mechanism and time displacement and temperature-displacement curves, respectively, of only fire scenario. Local failure with symmetrical shape of failure happens for two opposite beams concurrently. The failure time and temperature degree of fire only scenario are around 260 sec (+ 76 sec for PEF analysis (336 sec)) and 480 °C, and are taken as a scale criterion for the comparison with the other four situations.

S, Mises
(Avg: 75%)
+4.550e+08
+4.172e+08
+3.794e+08
+3.416e+08
+3.039e+08
+2.661e+08
+2.283e+08
+1.905e+08
+1.527e+08
+1.149e+08
+7.714e+07
+3.935e+07
+1.569e+06

Step: fir1
Increment 245: Step Time =   258.5
Primary Var: S, Mises
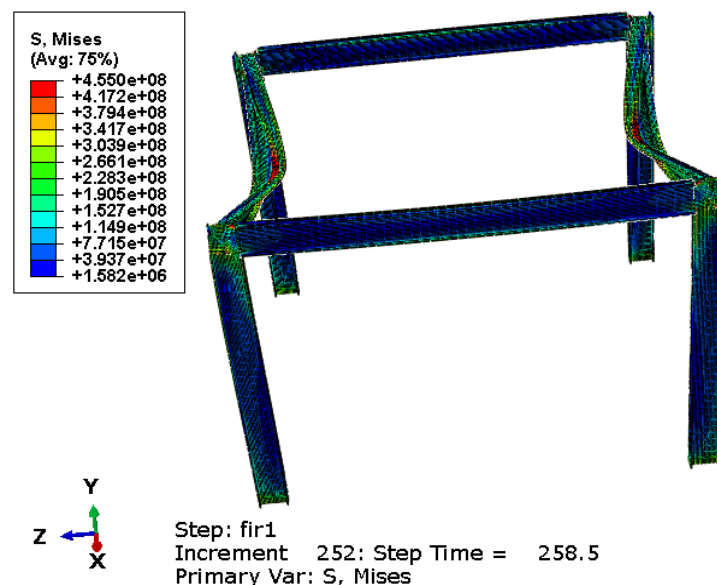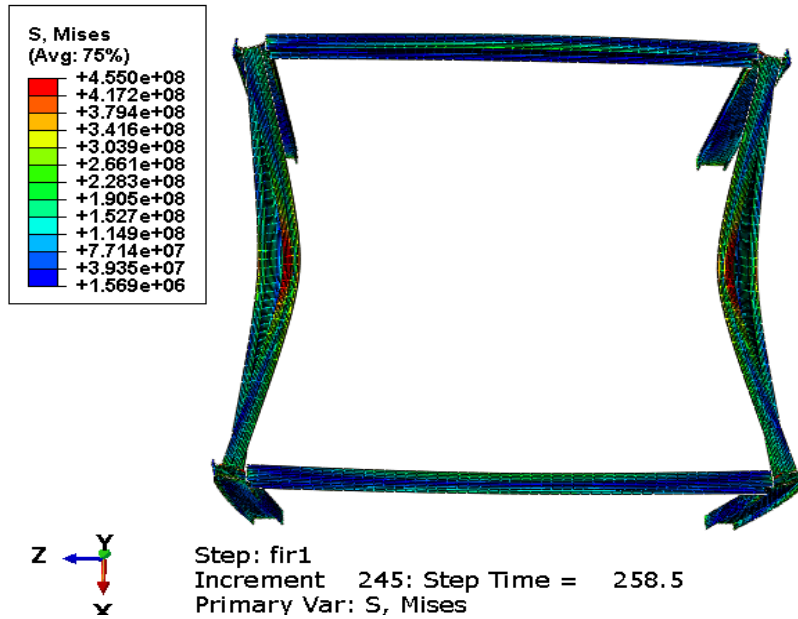
Figure 8-9 Failure Mechanism (Fire- Only Scenario)
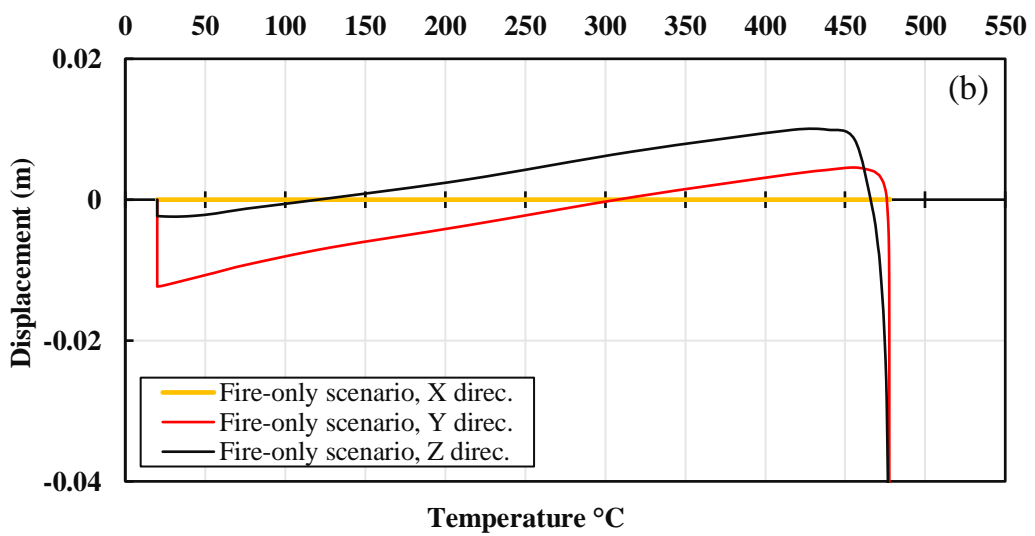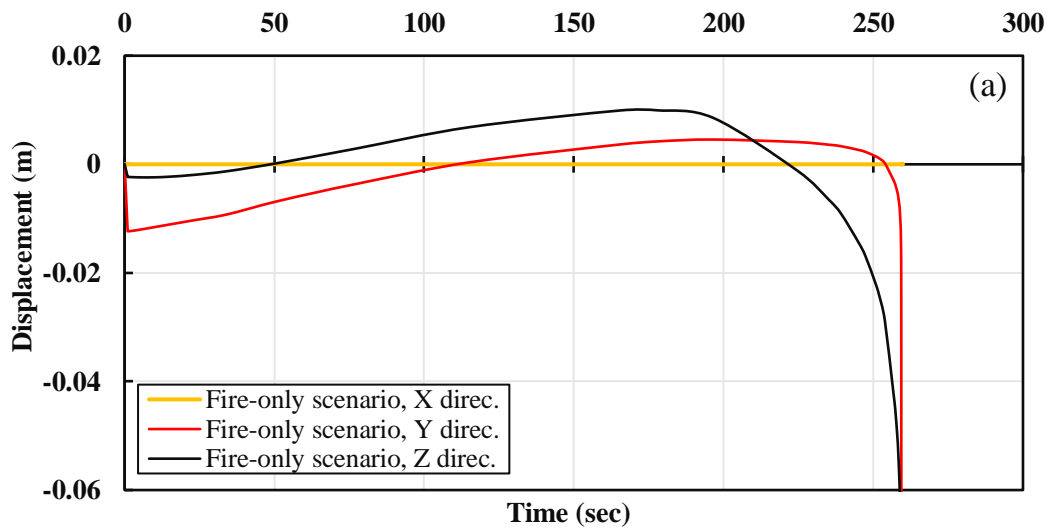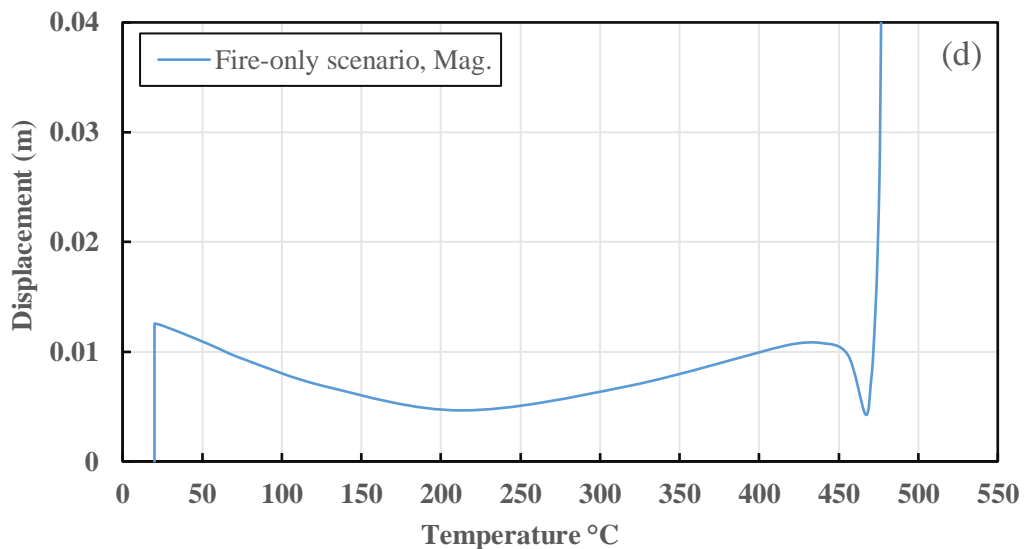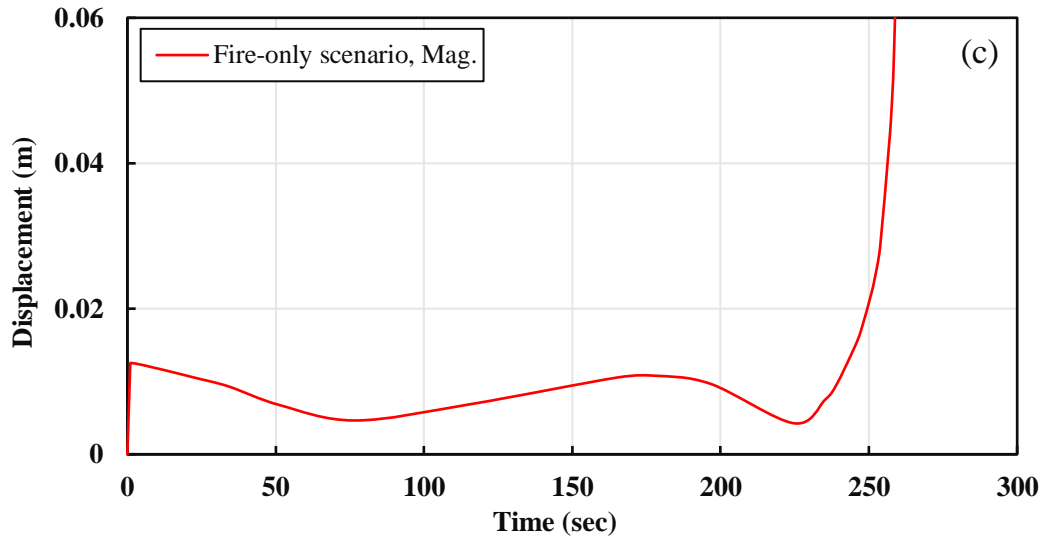
Figure 8-10 Results from the Fire-Only Analysis of the Steel Framed Structure Including (a) The Time-Mid-Span Displacement (b) The Temperature-Mid-Span Displacement (c) the Time-Mid-Span Displacement Data for the Total Displacement, and (d) The Temperature-Mid-Span Displacement Record for the Total Displacement

Figure 8-11and Figure 8-12 display the results obtained from the PEF analysis for case I, which is represented by applying an artificial earthquake with 0.35 g PGA and 0.16 sec predominate natural vibration period exposed to excitation in the Z direction. The results indicate that the structure maintains the earthquake force successfully, experiencing geometrical and mechanical damage within the allowable range of EC8. However, the failure shape of the PEF case is no longer symmetric, and the collapse time is reduced by 19% to 272 sec at a storey drift value of 0.0237 m, and temperature of 455 °C. Figure 8-13 shows the residual deformation of the structure at the end of earthquake event shape

and mechanism of failure after PEF event, respectively, for case II. Figure 8-14 (a to d) compare the structural response of the unidirectional real earthquake (case II) with the properties of 0.35 PGA and 0.36 sec natural period which represent the natural period of the first mode of the system. Unsymmetrical global failure with 277 sec collapse time and temperature of 455 °C are the failure properties, and the time reduction is around 18%. Figure 8-14 (a), (b) and (c) compare the displacements recorded at the mid-span locations for both only fire scenario and PEF analysis in the Z and Y direction and total displacement, respectively.

Figure 8-14 (d) relates the temperature displacement curves for both circumstances of the analysis. Cases I and II reflect the effect of an earthquake on fire strength of the structure during unidirectional excitation. This kind of the excitation does not represent the real situation of earthquake excitation though due to the unidirectional loading. Therefore, more observations are made by examining the structural response to the bidirectional excitation for another two real and artificial motions (Cases III and IV, respectively).
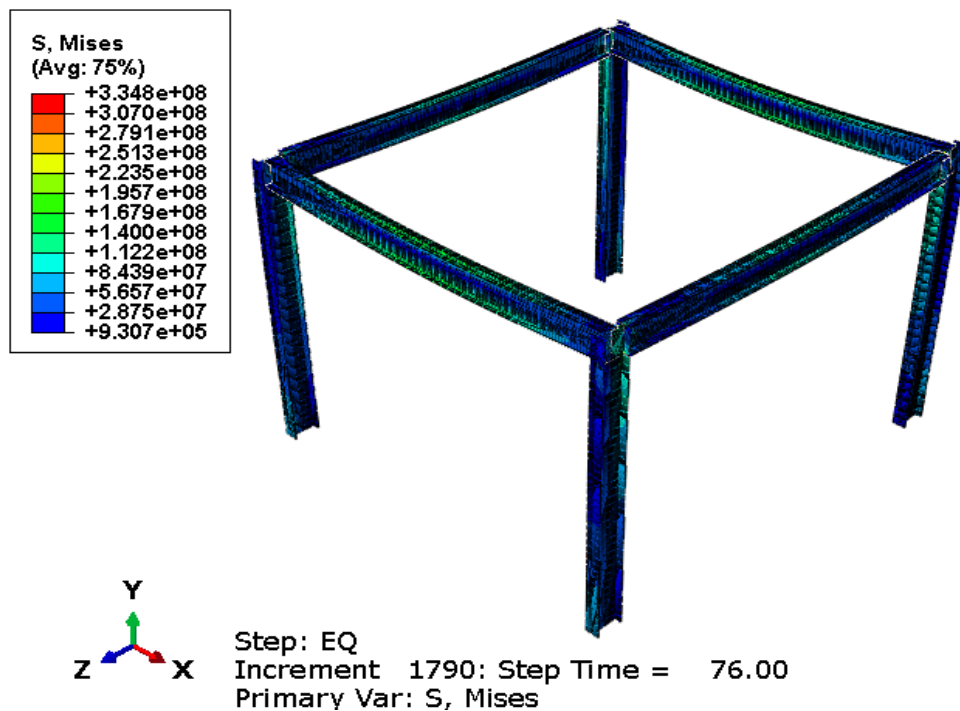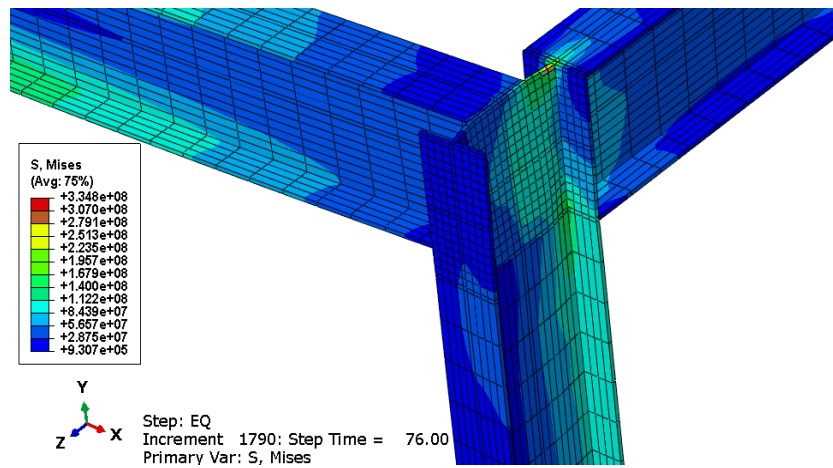
(a)
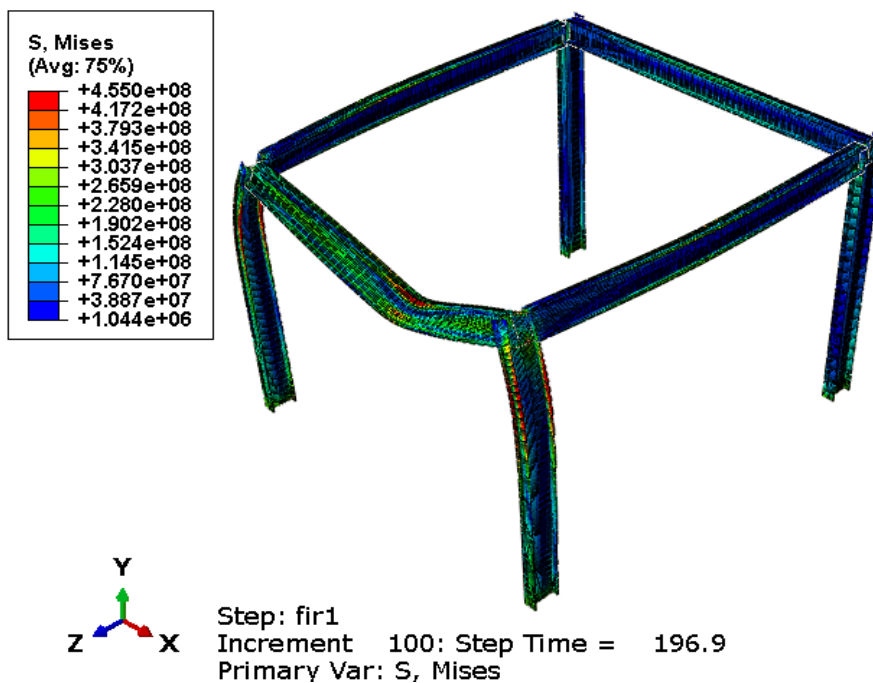
(b)

Figure 8-11 Images from a Case I PEF Analysis with an Artificial Earthquake (PGA = 0.35g, Natural Period = 0.16 sec, One-Directional Excitation in the Z-Direction Including (a) The Residual Deformation of the Structure at the End of Earthquake Event and (b) The Shape and Mechanism of Failure of the Structure after the PEF Event.
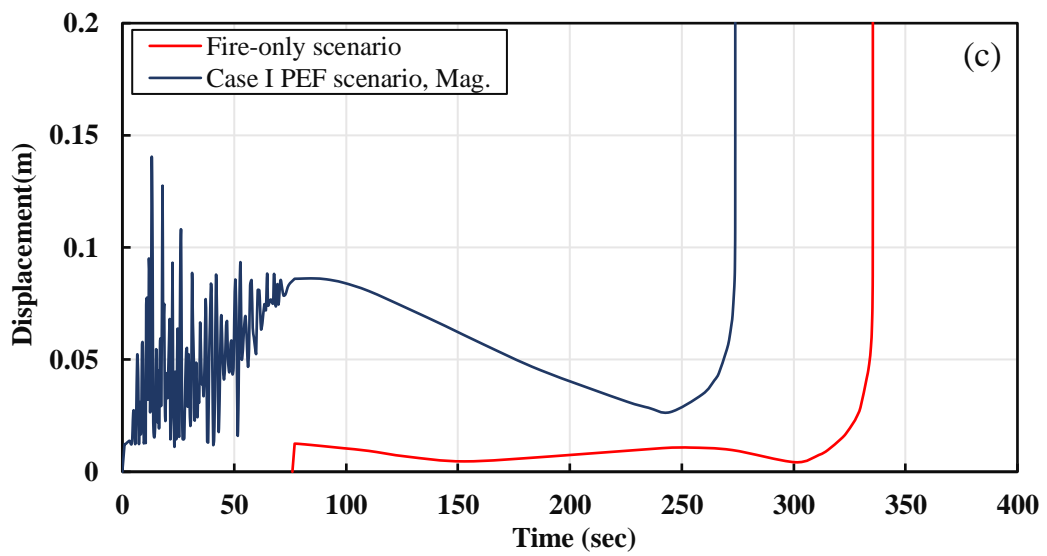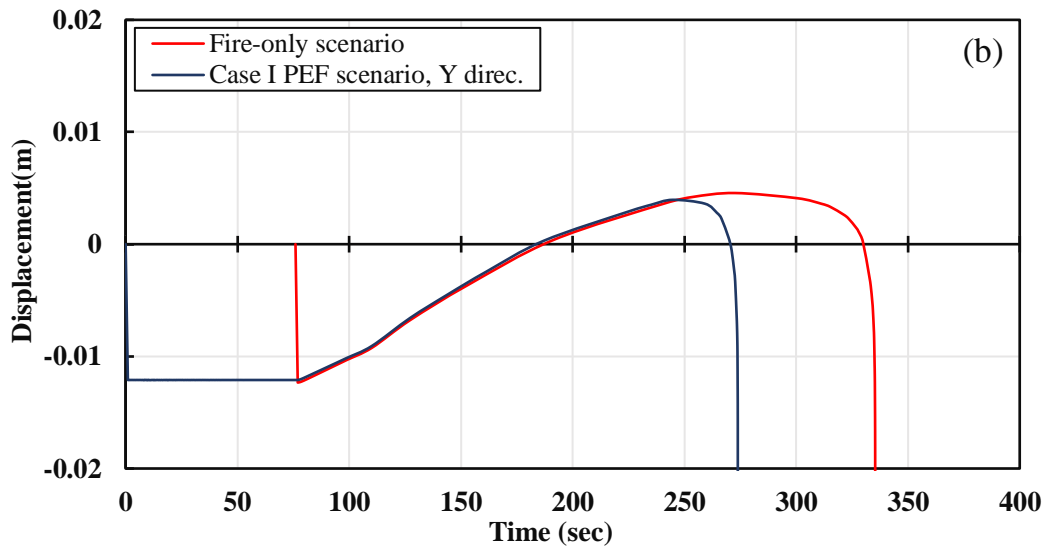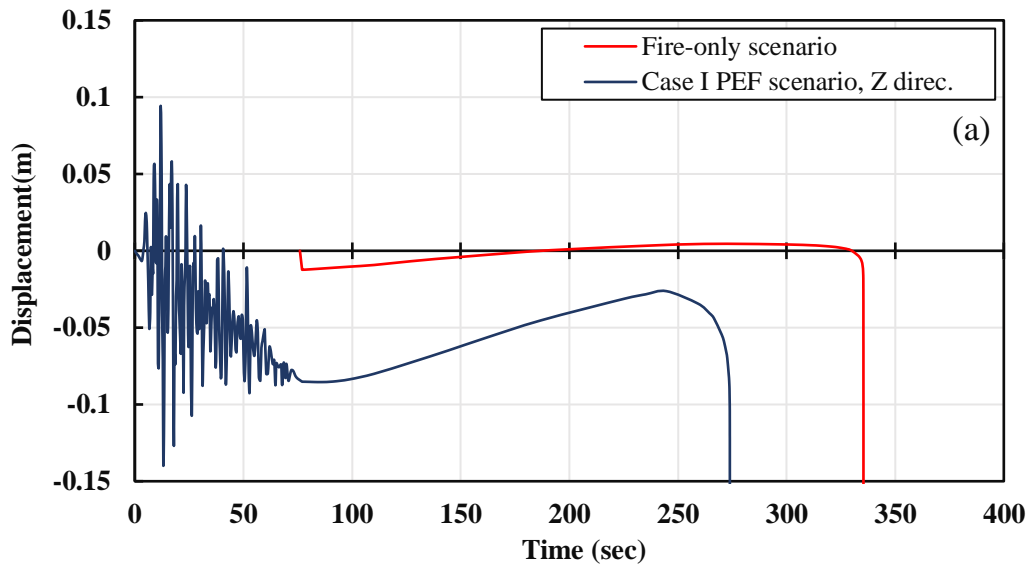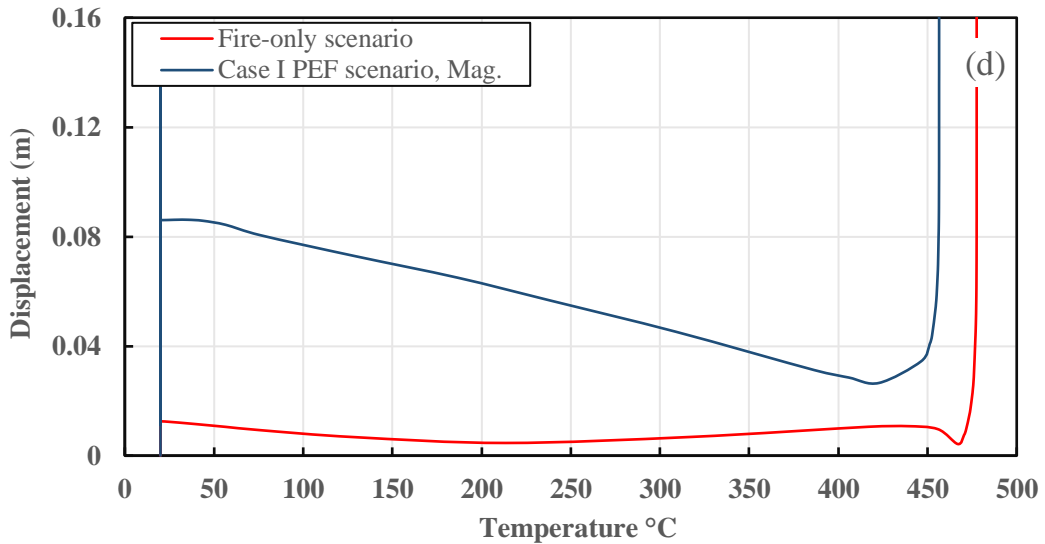
Figure 8-12 Comparison of the Fire-Only Analysis Versus the PEF Analysis for Case I Including (a) The Time-Mid Span Displacement Record in the Z-Direction, (b) The Time-Mid Span Displacement in the Y-Direction, (c) The Time-Mid Span Displacement Record for the Total Displacement and (d) The Temperature-Mid-Span Displacement Record for the Total Displacement
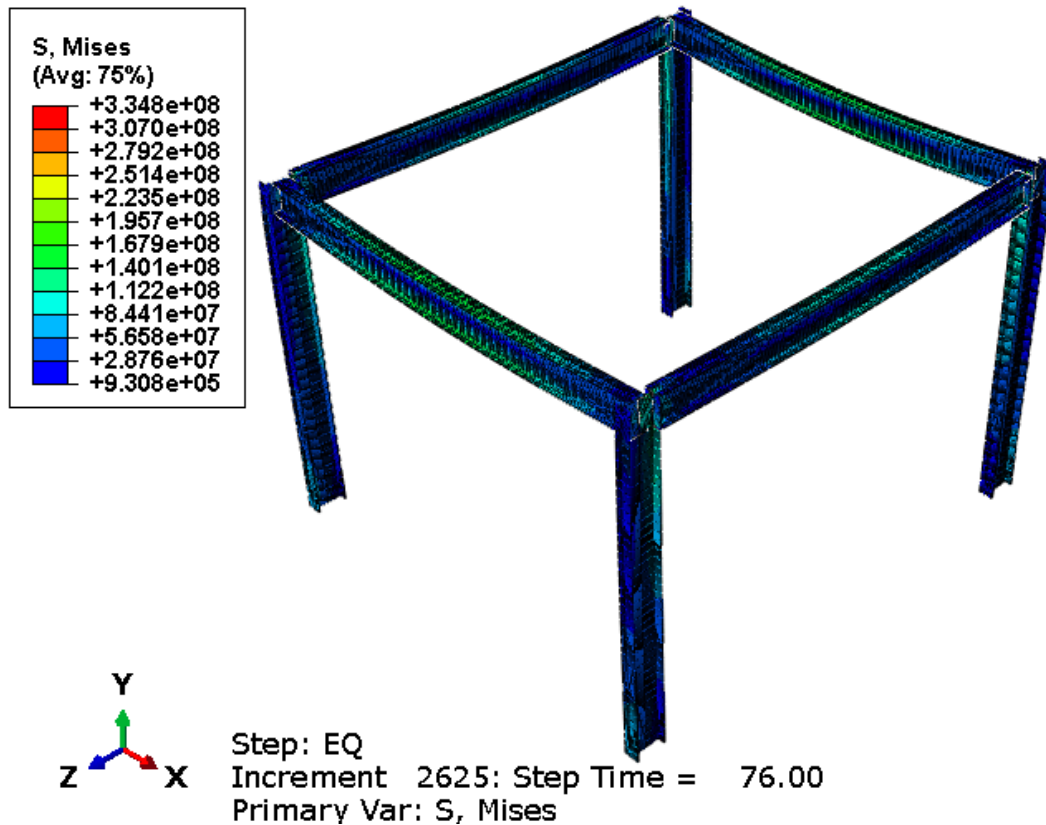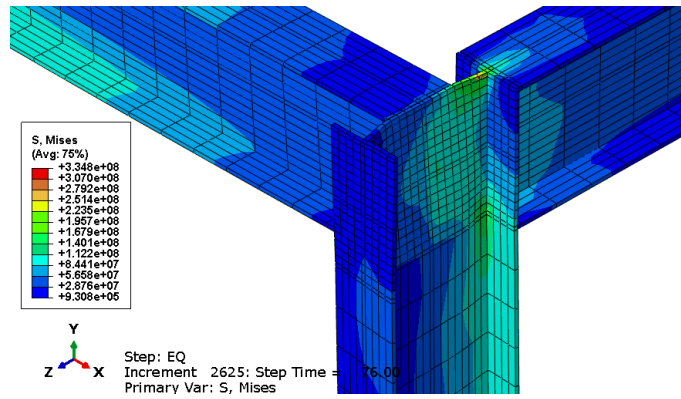
(a)
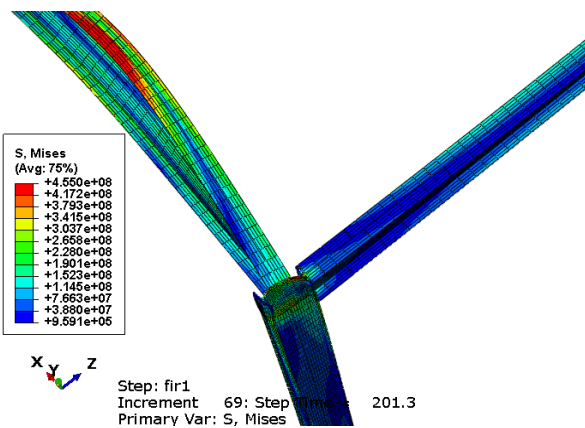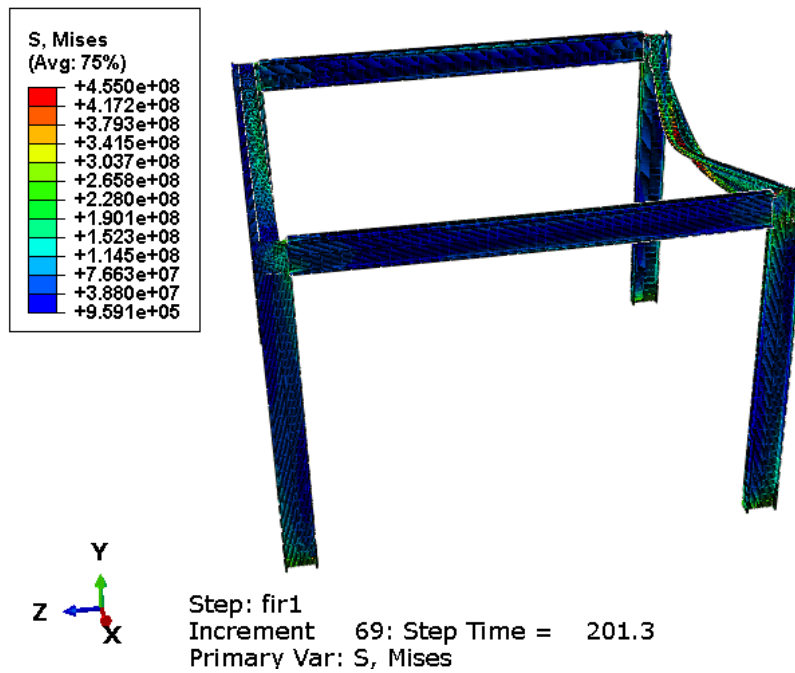
(b)

Figure 8-13 Images from a Case II PEF Analysis with a Real Earthquake (PGA = 0.35g, Natural Period = 0.36 sec, One-Directional Excitation in the Z-Direction Including (a) The Residual Deformation of the Structure at the End of Earthquake Event and (b) The Shape and Mechanism of Failure of the Structure after the PEF Event.
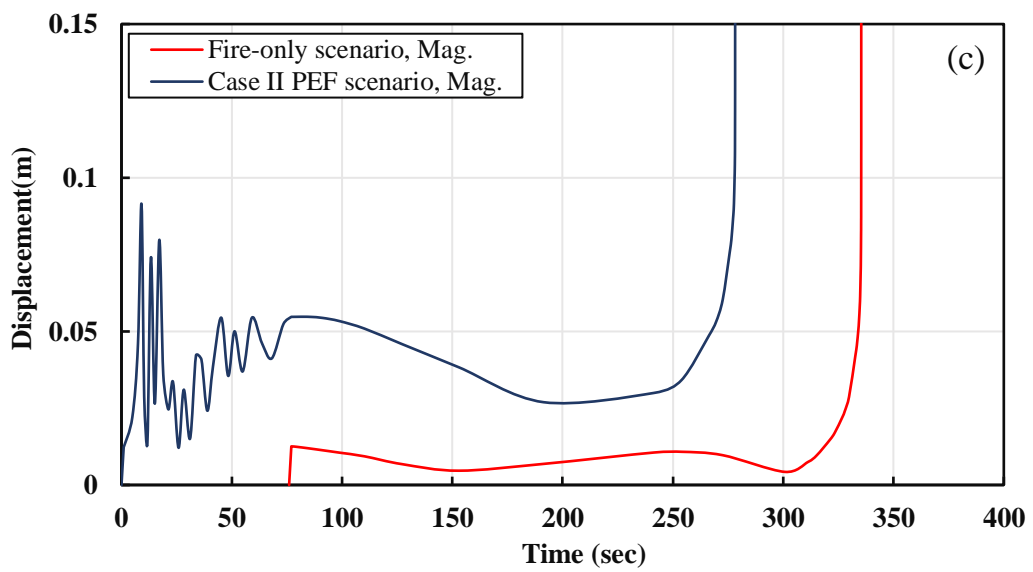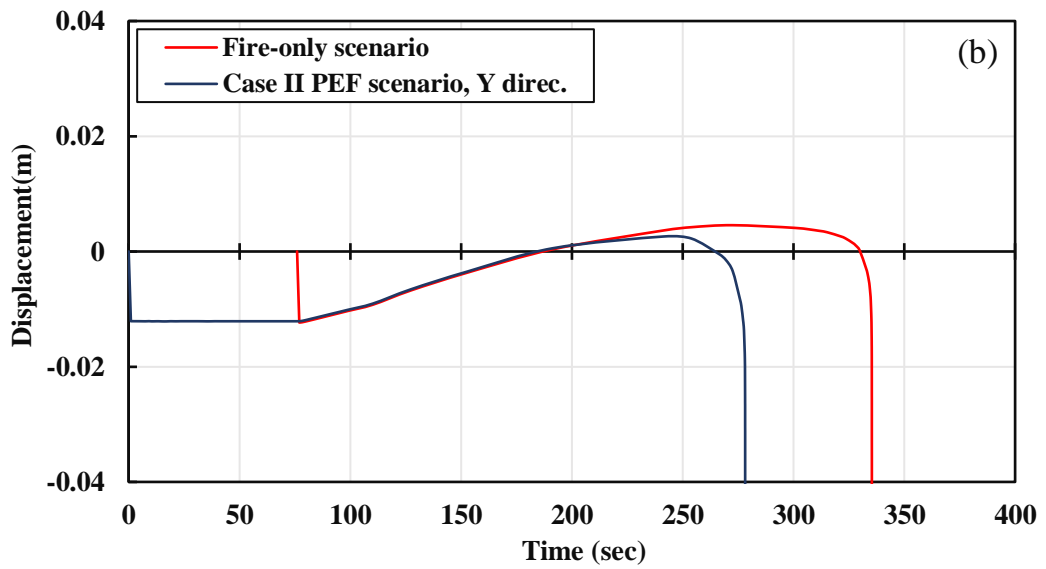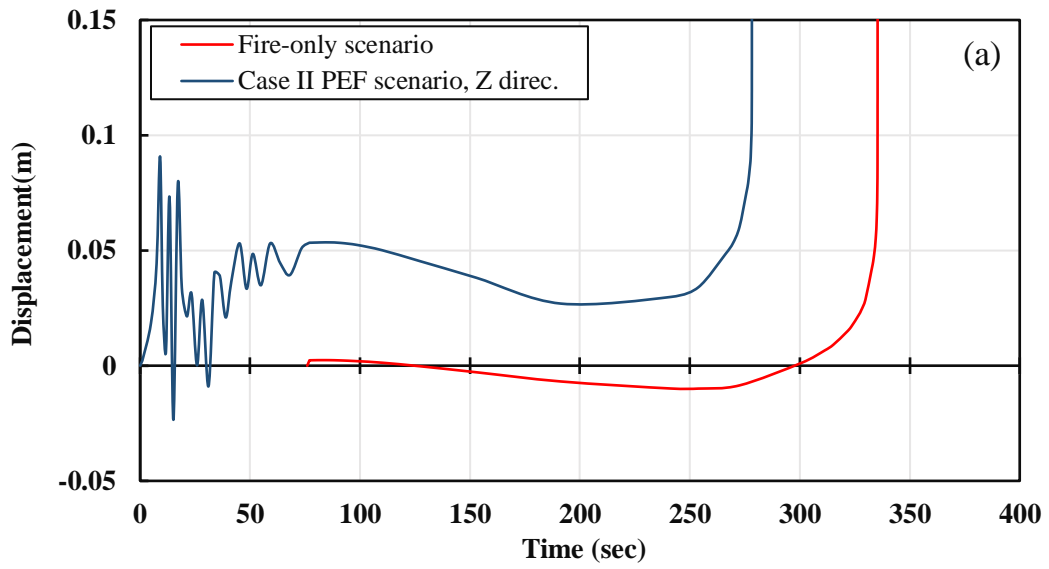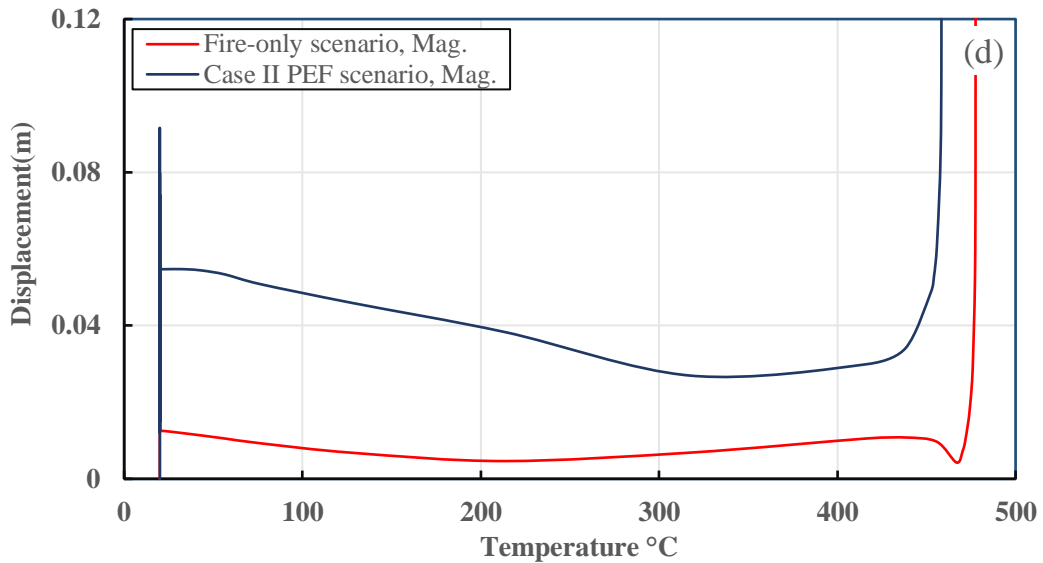
Figure 8-14 Comparison of the Fire-Only Analysis Versus the PEF Analysis for Case II Including (a) The Time-Mid Span Displacement Record in the Z-Direction, (b) The Time-Mid Span Displacement in the Y-Direction, (c) The Time-Mid Span Displacement Record for the Total Displacement and (d) The Temperature-Mid Span Displacement Record for the Total Displacement

Figure 8-15-8-17 present the results from the analysis of a Case I earthquake but with bidirectional excitation in both the x- and z-directions (referred to as Case III); these figures are presented in a similar format as before, for comparison. It is clear that the global failure mechanism is dominant as a result of the combined effect of bidirectional excitation and the PEF event. The columns at one side of the structure completely collapse in this scenario. Thus, the displacement records at the level of 1.4 m along the column length, for both the fire-only and PEF events are compared in Figure 8-17, which presents the time-mid span displacement results at this position in (a) the x-direction, (b) the y-direction and (c) the total displacement, respectively. Figure 8-17 (b) presents the temperature-displacement response at this same point, 1.4 m from the column base. For this case, with bidirectional excitation, failure occurred after just 185 sec and at a temperature of 306 °C, representing a reduction of 45% from the fire-only analysis. The storey drift is 0.118 m, exceeding the allowable value in Eurocode 8.

Similar behaviour and results are observed for Case IV, which has an identical input motion as Case II except with bidirectional excitation in both the x- and z-directions. The corresponding results are given in Figure 8.18-8.20 in a similar format to before. It is clear that there is a significant reduction in failure time for the PEF situation in Case IV of approximately 45% (to 185 sec) as well as a storey drift of 0.115 m, exceeding the

366

allowable Eurocode 8 limiting value by 85%. Significant local and global failure occurs in this case, preventing the structure from withstanding the applied loads.

In summary, the results presented in this section provide valuable insight into the significant effects of a PEF event on a steel framed structure, and also on the importance of choosing a suitable column section in earthquake-prone zones. Furthermore, based on these results, it is proposed that using tubular sections is essential in earthquake zones to provide extra resistance in a PEF scenario, even though other sections may satisfy the seismic design requirements (which do not consider PEF).

(a)

368

(b)
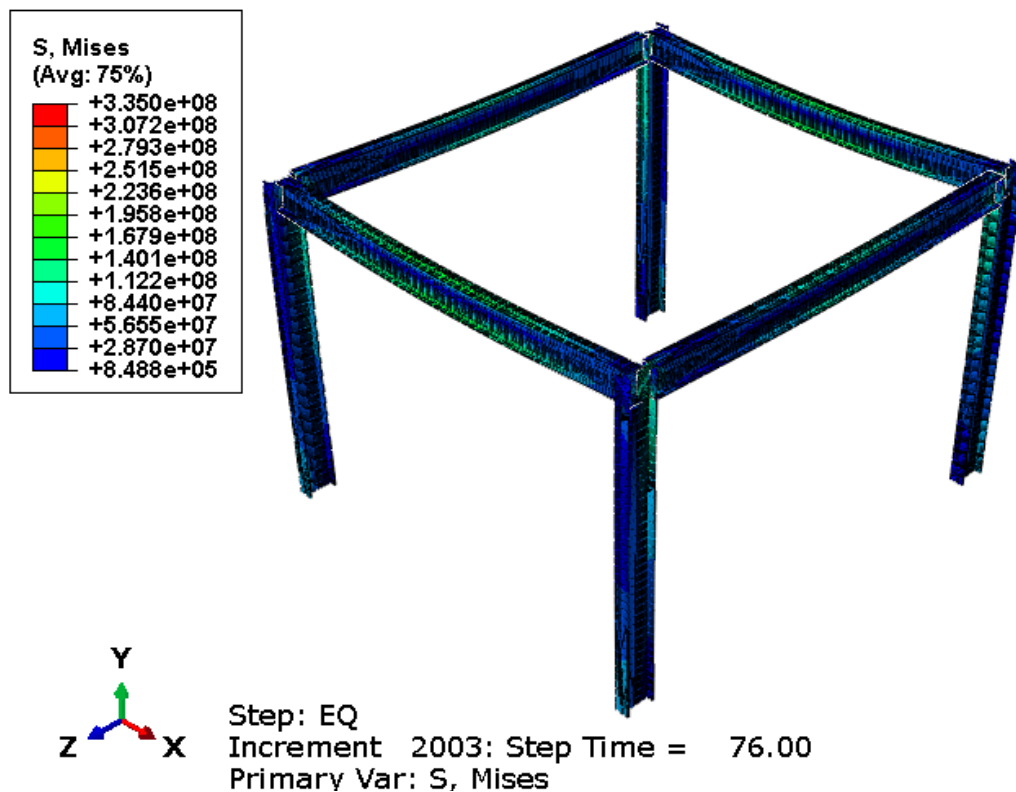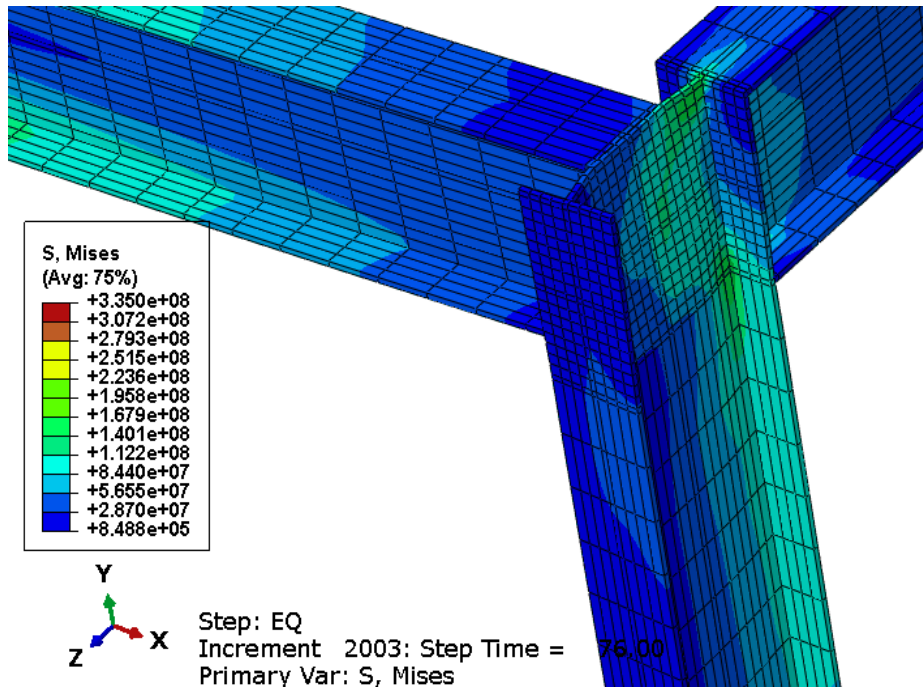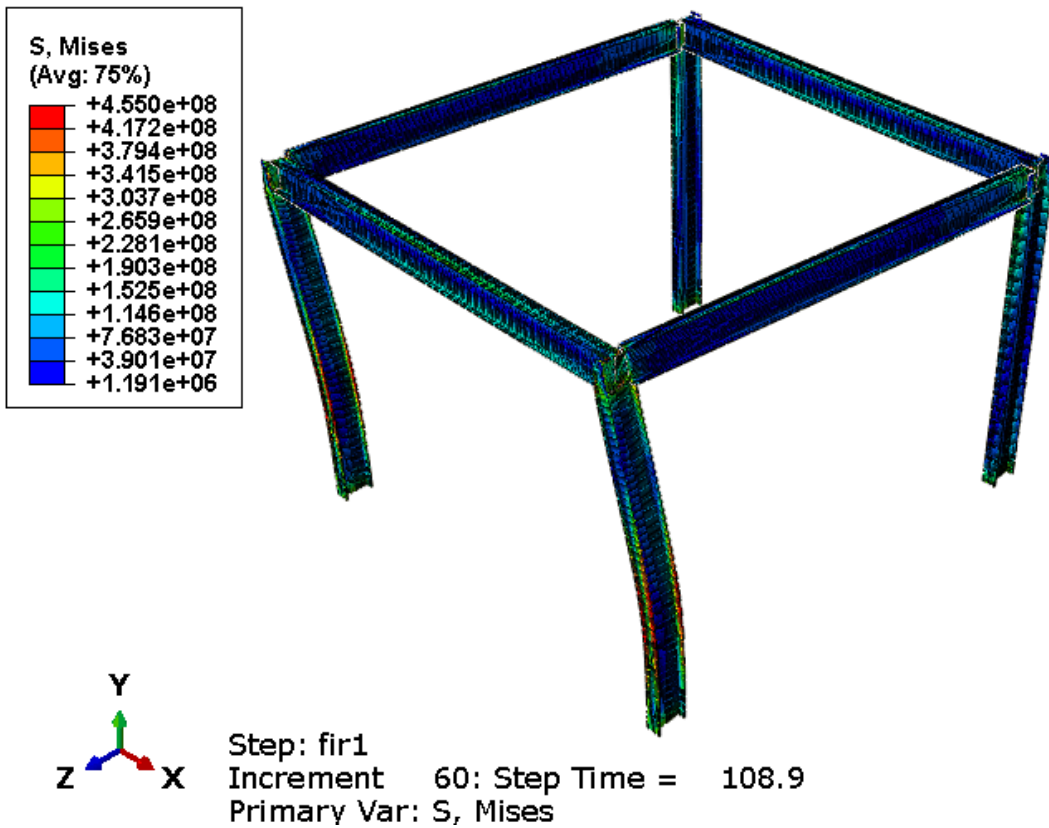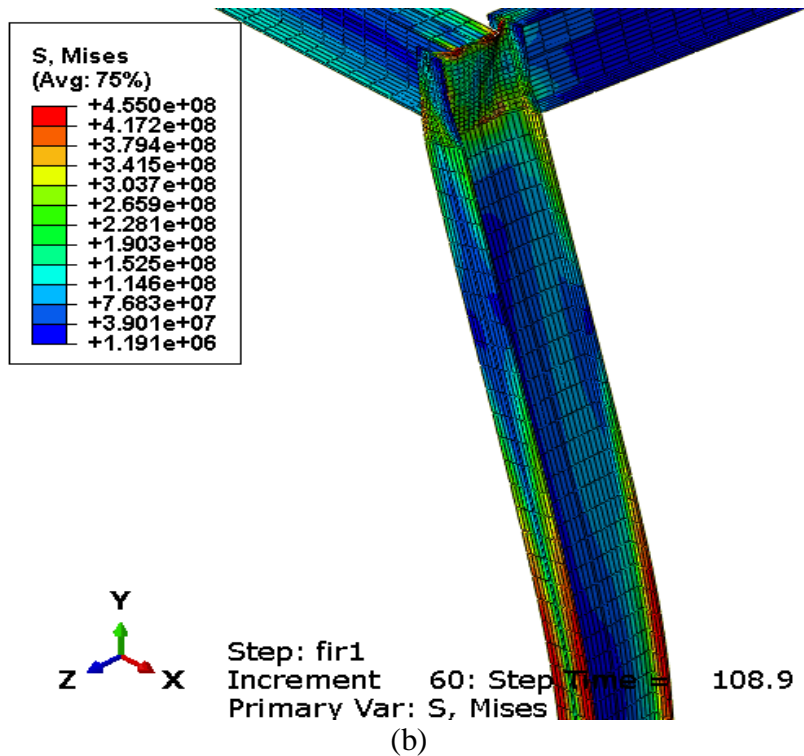
Figure 8-15 Images From a Case III PEF Analysis with a Real Earthquake (PGA = 0.35g, Natural Period = 0.24 sec, Bi-Directional Excitation in the X- and Z-Direction Including (a) The Residual Deformation of the Structure at the End of Earthquake Event and (b) The Shape and Mechanism of Failure of the Structure after the PEF Event.
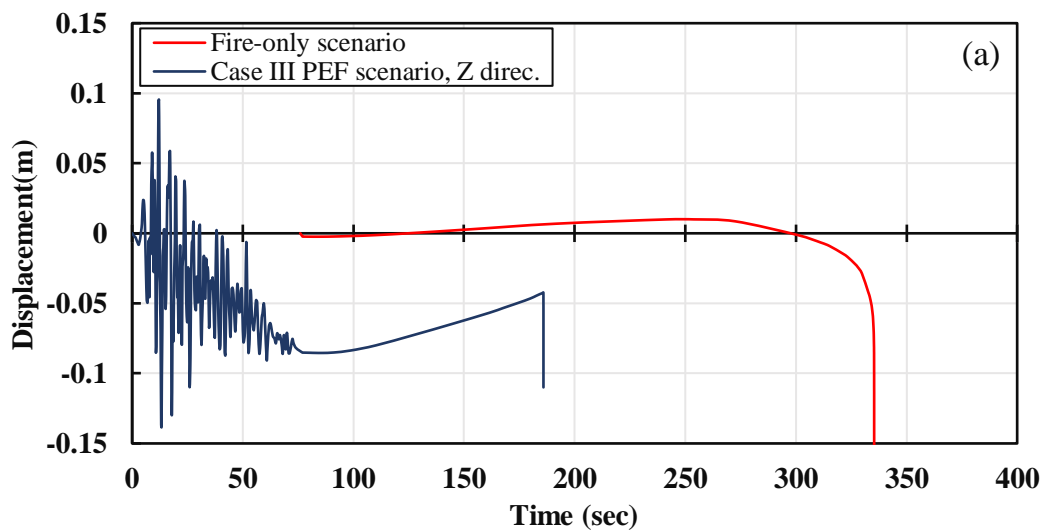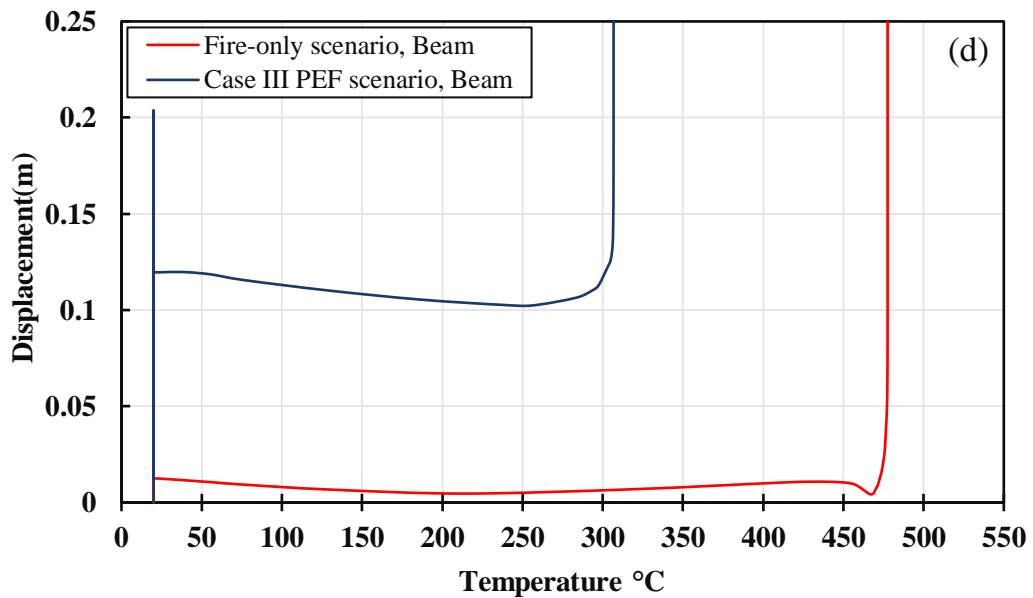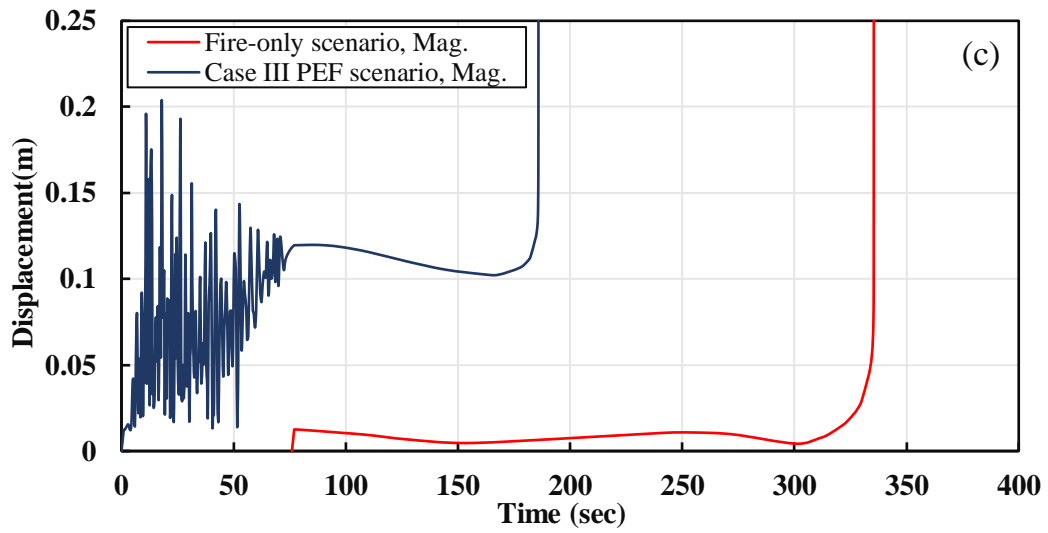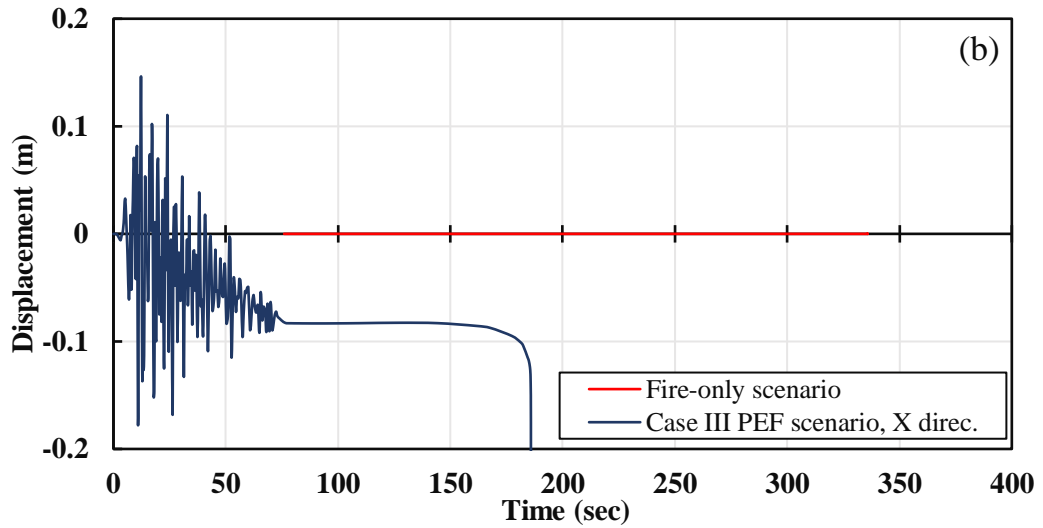
Figure 8-16 Comparison of the Fire-Only Analysis Versus the PEF Analysis for Case III Including (a) The Time-Mid Span Displacement Record in the Z-Direction, (b) The Time-

Mid Span Displacement Record in the X-Direction, (c) The Time-Mid Span Displacement Record for the Total Displacement and (d) The Temperature-Mid Span Displacement Record for the Total Displacement
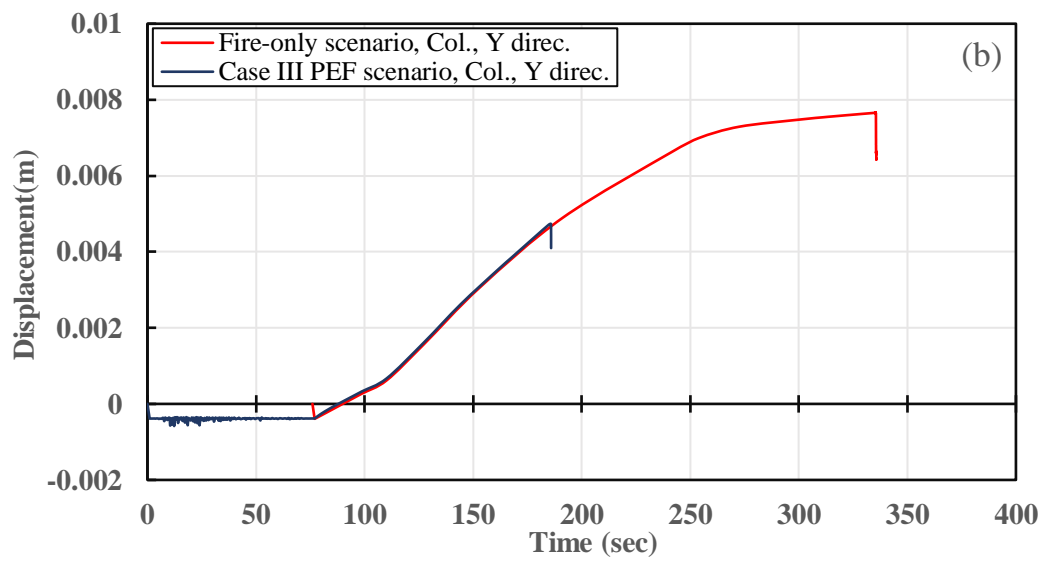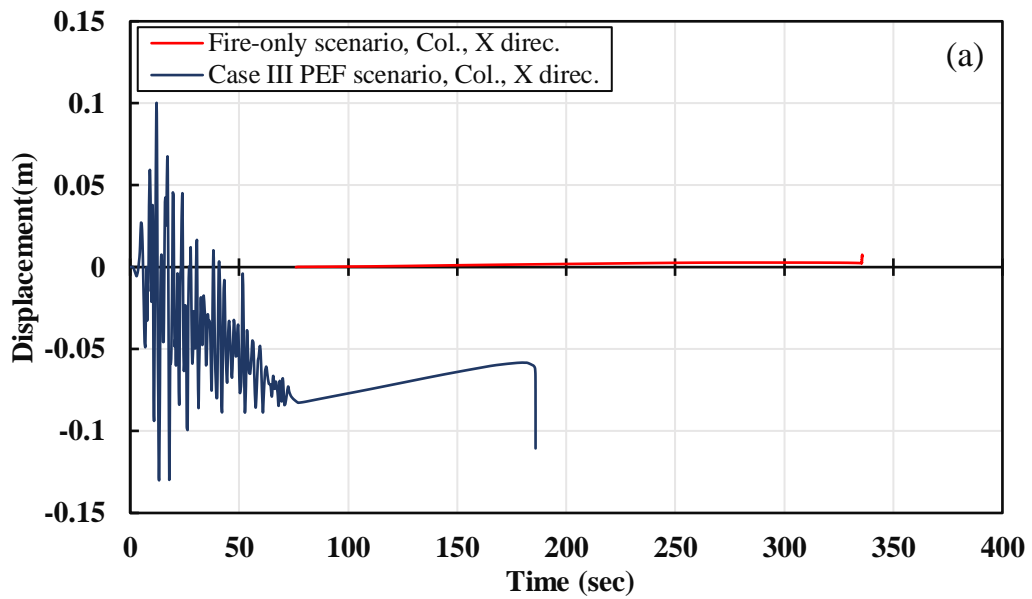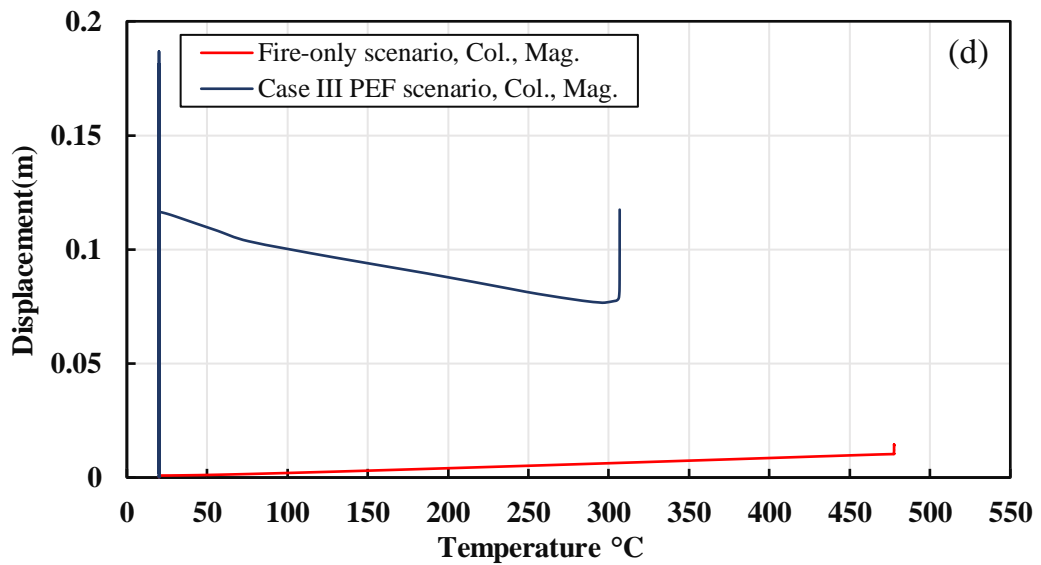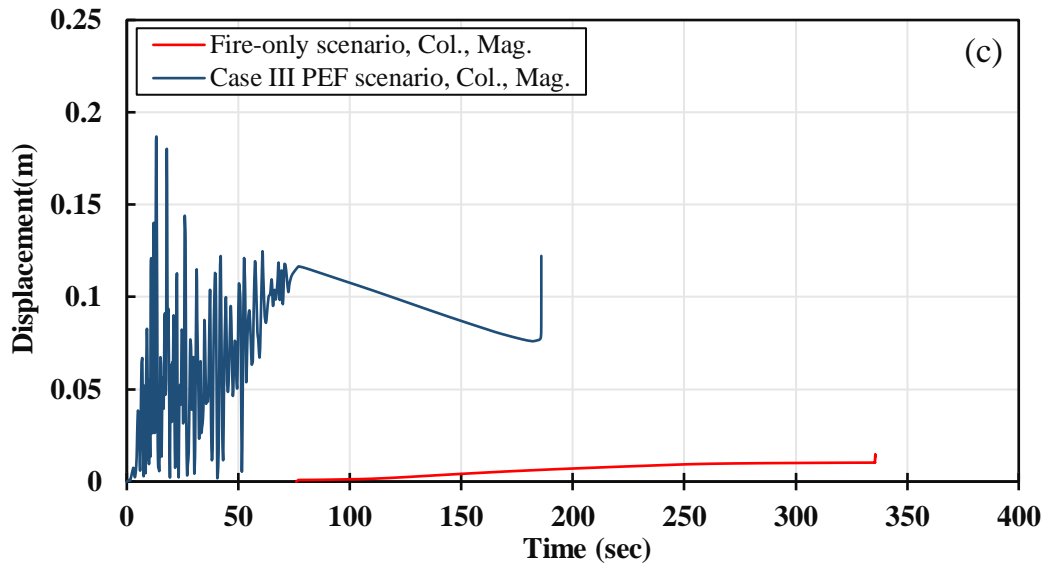
Figure 8-17 Comparison of the Displacement Values at a Point Which Is 1.4 m Along the Column Length for Both the Fire-Only and PEF Events for Case III Including (a) The Time-Displacement Record in the X-Direction, (b) The Time-Displacement Record in the Y-Direction, (c) The Time-Displacement Record for Total Displacement Value and (d) The Temperature-Displacement Record for the Total Displacement Value

S, Mises
(Avg: 75%)
+3.350e+08
+3.072e+08
+2.793e+08
+2.515e+08
+2.236e+08
+1.958e+08
+1.679e+08
+1.401e+08
+1.122e+08
+8.440e+07
+5.655e+07
+2.870e+07
+8.488e+05

Step: EQ
Increment 2003: Step Time = 76.00
Primary Var: S, Mises

(a)

373

S, Mises
(Avg: 75%)
+4.550e+08
+4.172e+08
+3.794e+08
+3.415e+08
+3.037e+08
+2.659e+08
+2.281e+08
+1.903e+08
+1.525e+08
+1.146e+08
+7.683e+07
+3.901e+07
+1.191e+06

Step: fir1
Increment   60: Step Time =   108.9
Primary Var: S, Mises

S, Mises
(Avg: 75%)
+4.550e+08
+4.172e+08
+3.794e+08
+3.415e+08
+3.037e+08
+2.659e+08
+2.281e+08
+1.903e+08
+1.525e+08
+1.146e+08
+7.683e+07
+3.901e+07
+1.191e+06

Step: fir1
Increment   60: Step Time =   108.9
Primary Var: S, Mises

(b)
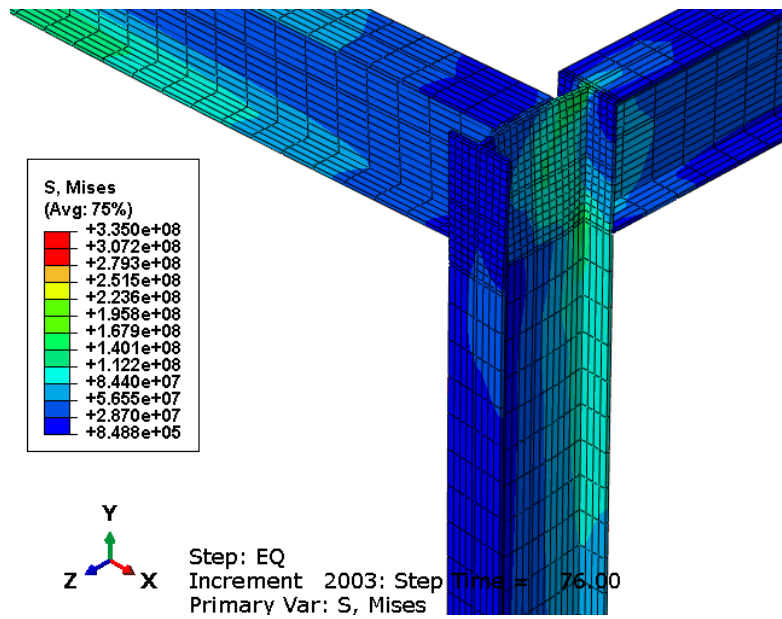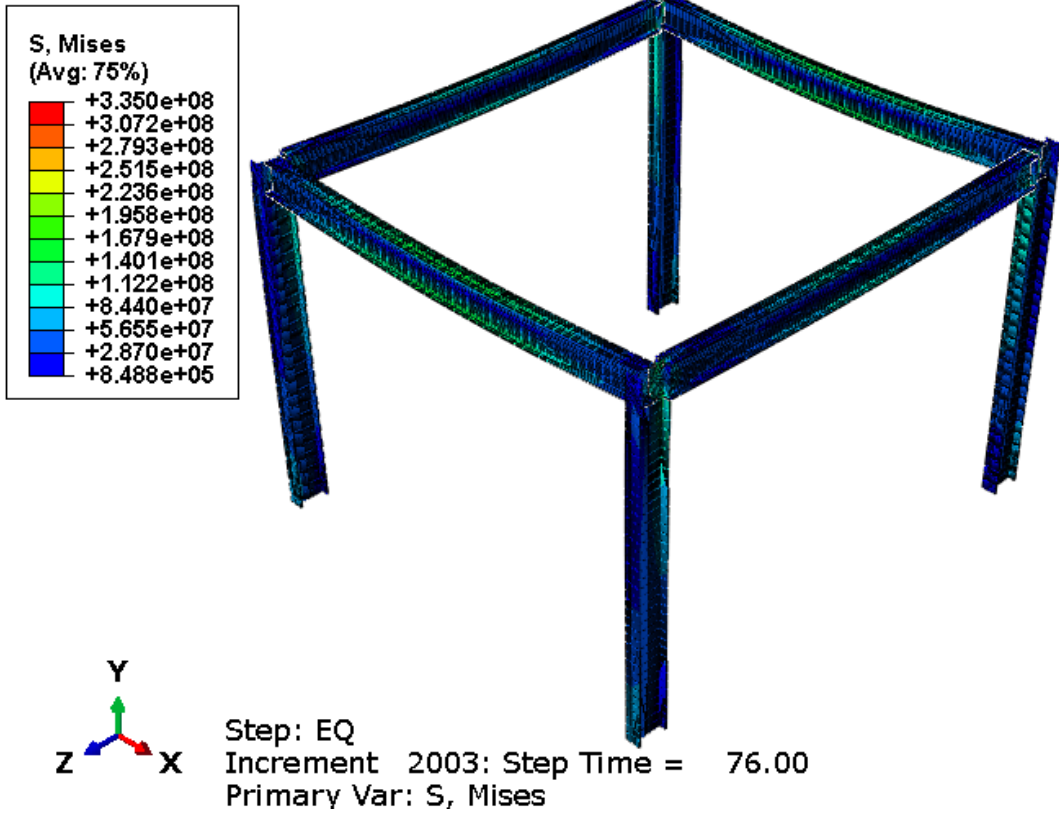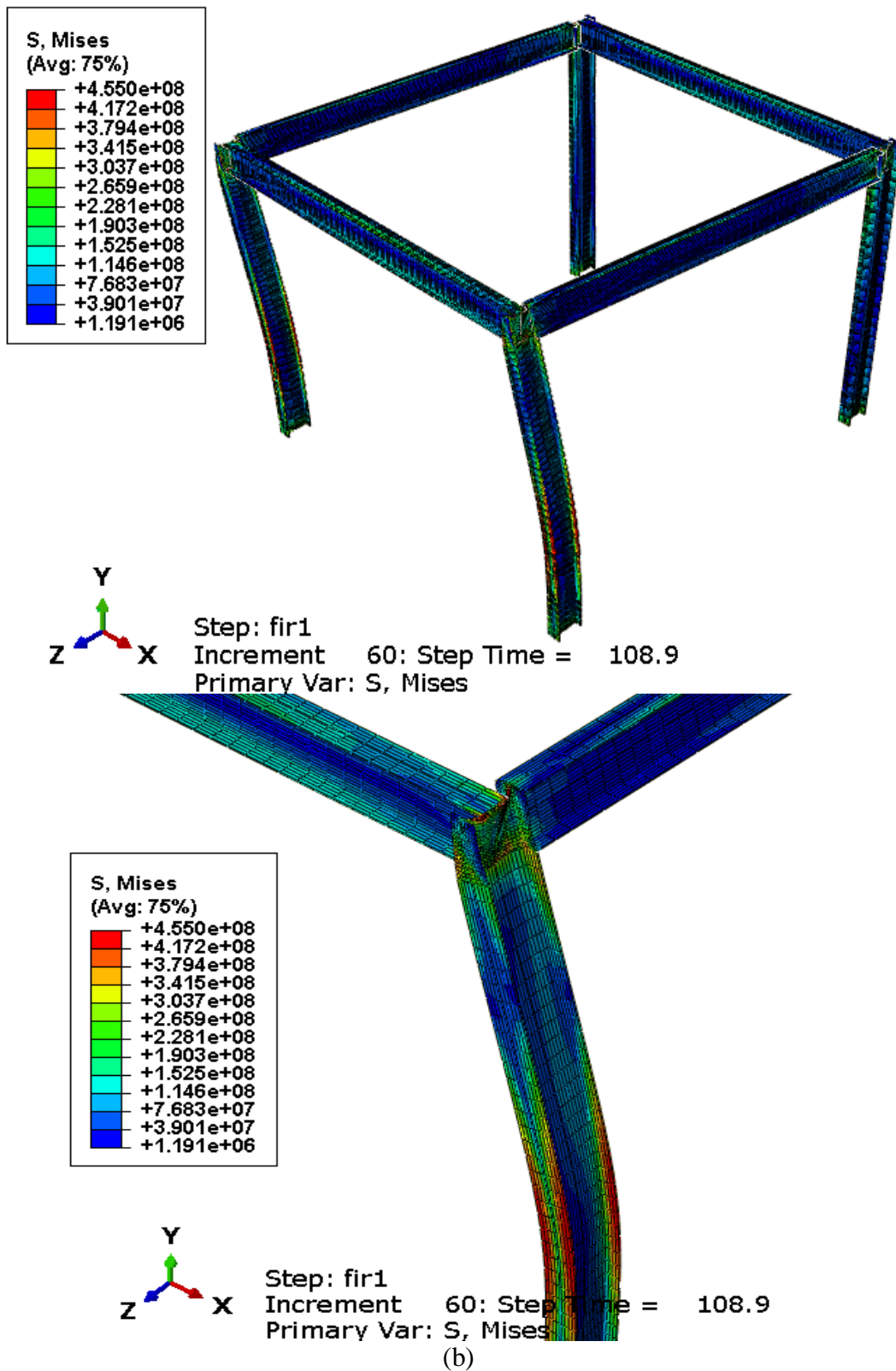
Figure 8-18 Images from a Case IV PEF Analysis with an Artificial Earthquake (PGA = 0.35g, Natural Period = 0.16 sec, Bi-Directional Excitation in the X- and Z-Direction Including (a) The Residual Deformation of the Structure at the End of Earthquake Event and (b) The Shape and Mechanism of Failure of the Structure After the PEF Event.

374
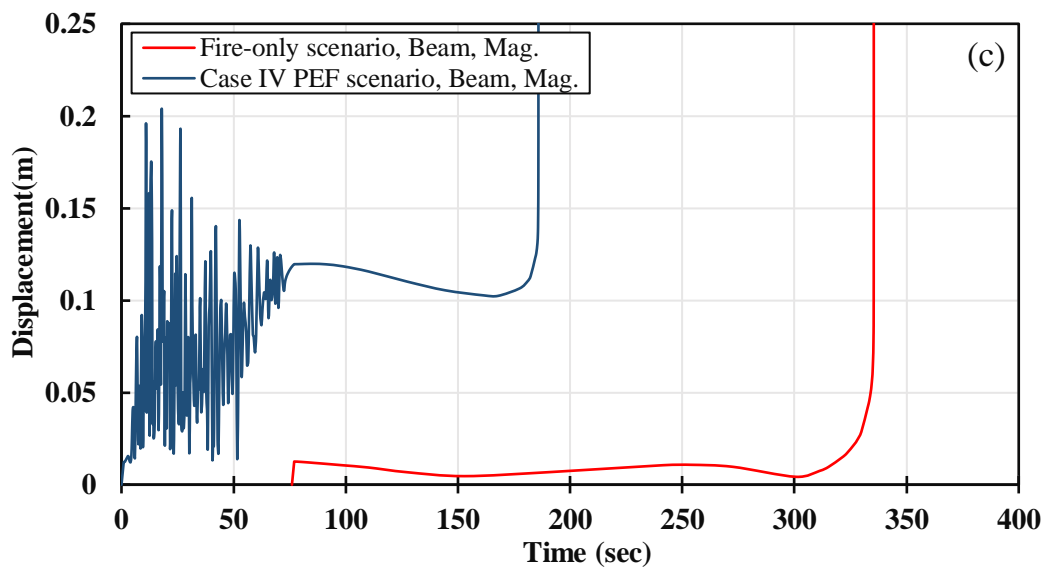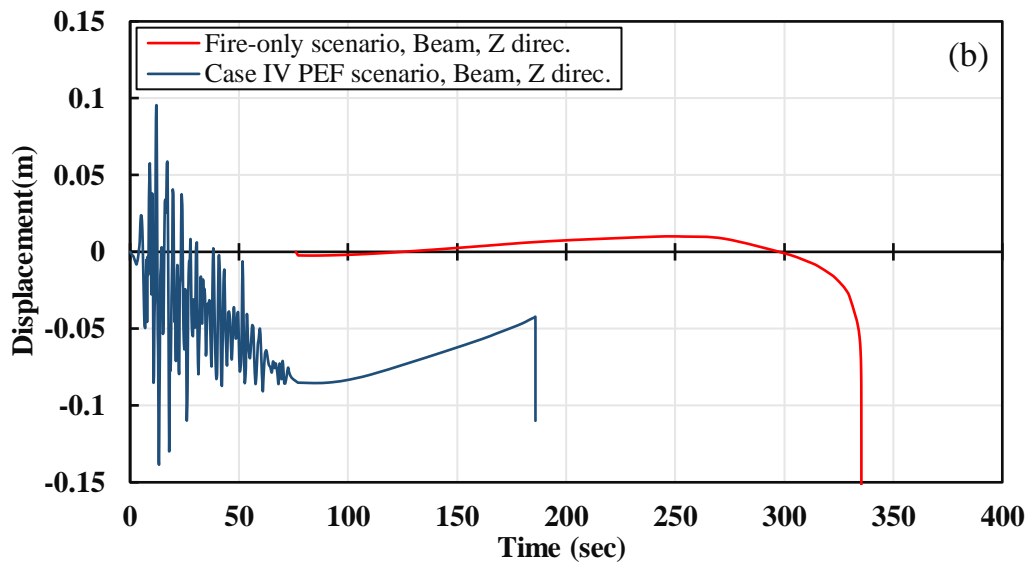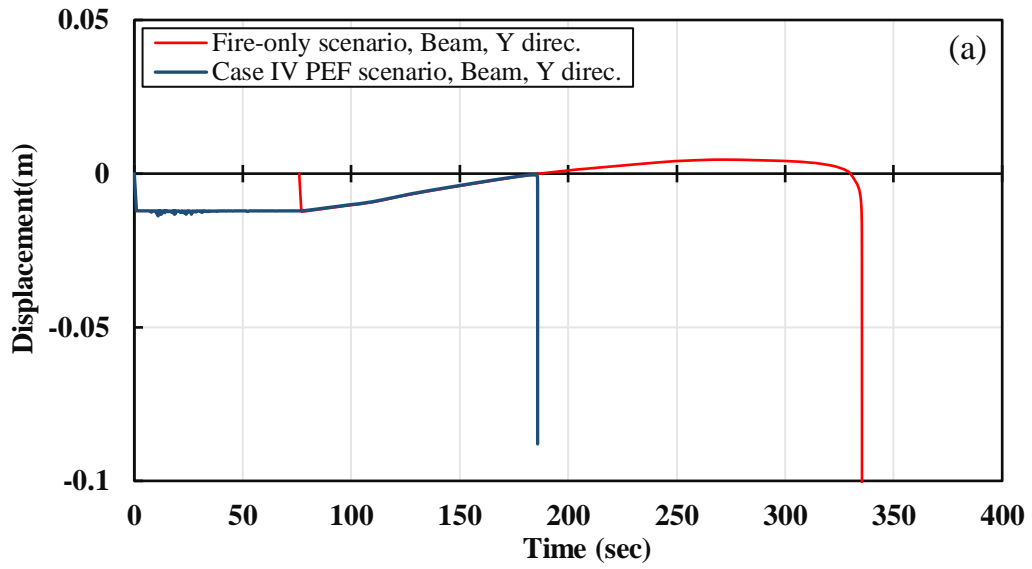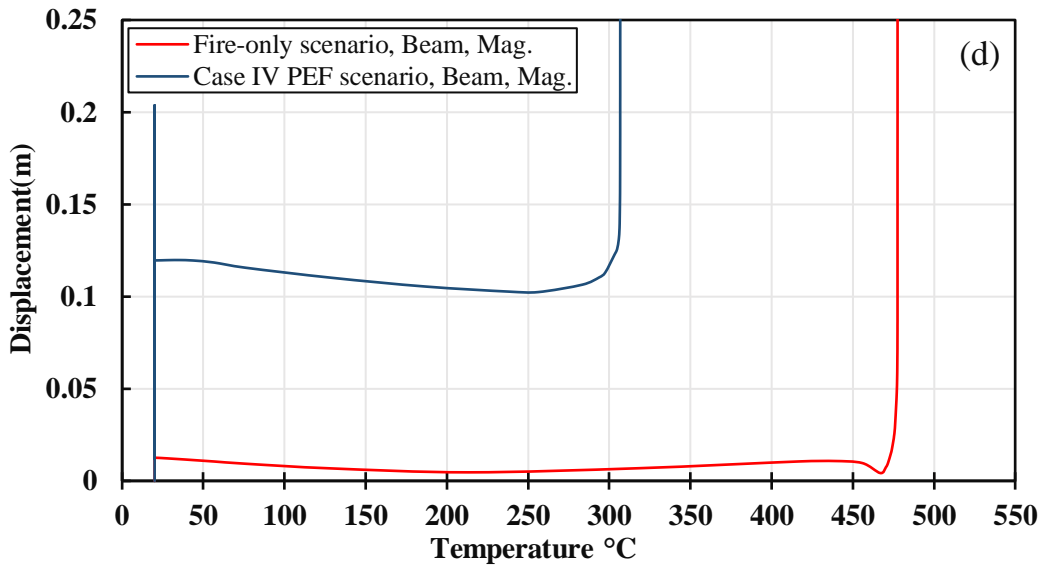
Figure 8-19 Comparison of the Fire-Only Analysis Versus the PEF Analysis for Case IV Including (a) The Time-Mid Span Displacement Record in the Y-Direction, (b) The Time-Mid Span Displacement Record in the Z-Direction, (c) The Time-Mid Span Displacement Record for the Total Displacement and (d) the Temperature-Mid Span Displacement Record for the Total Displacement
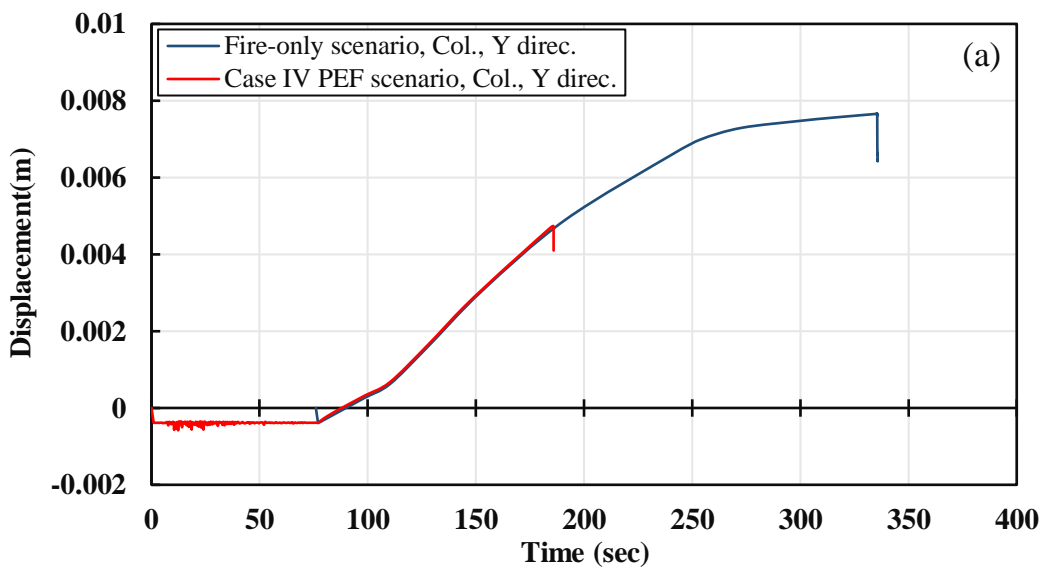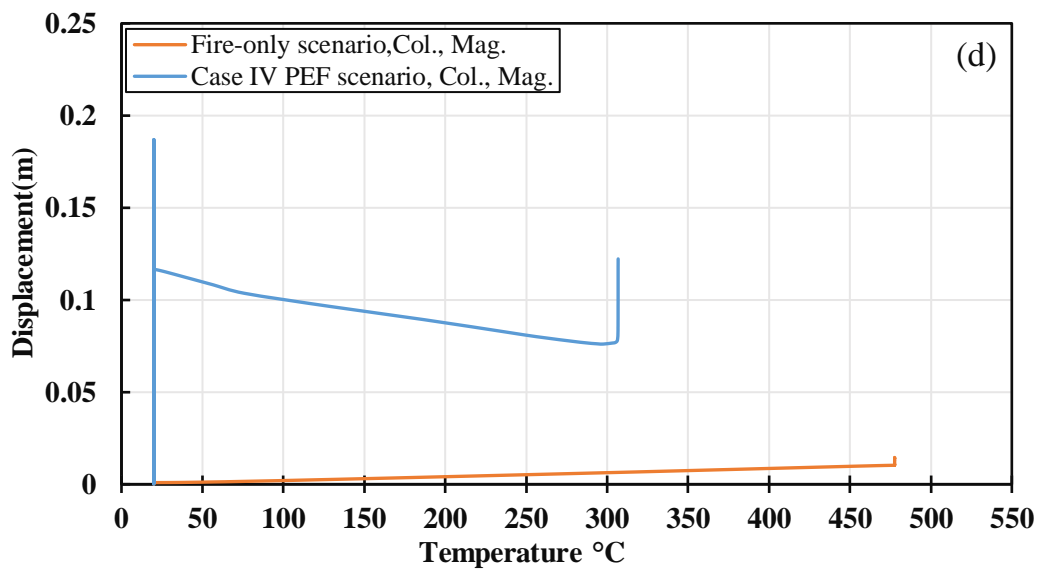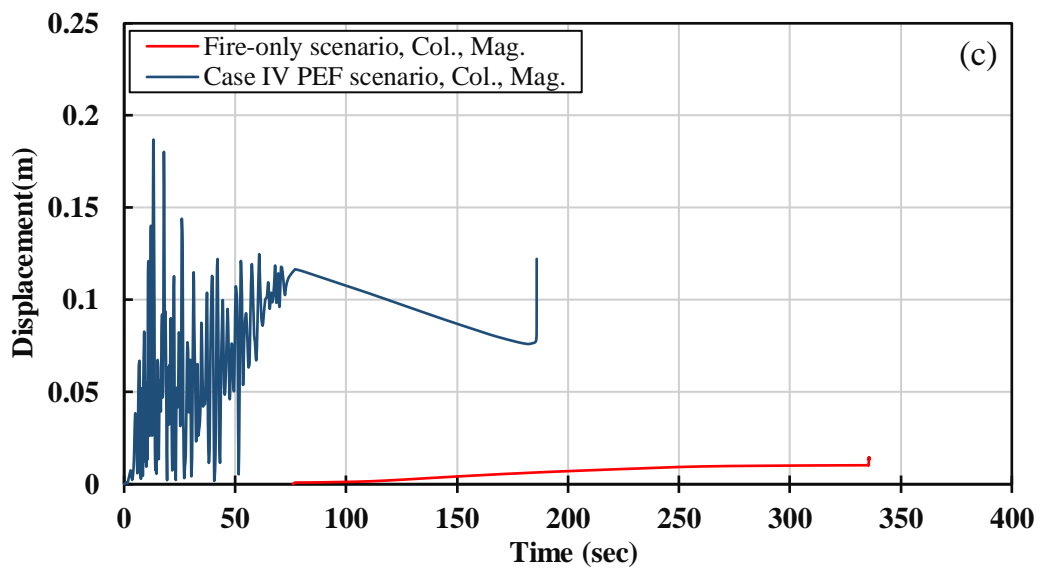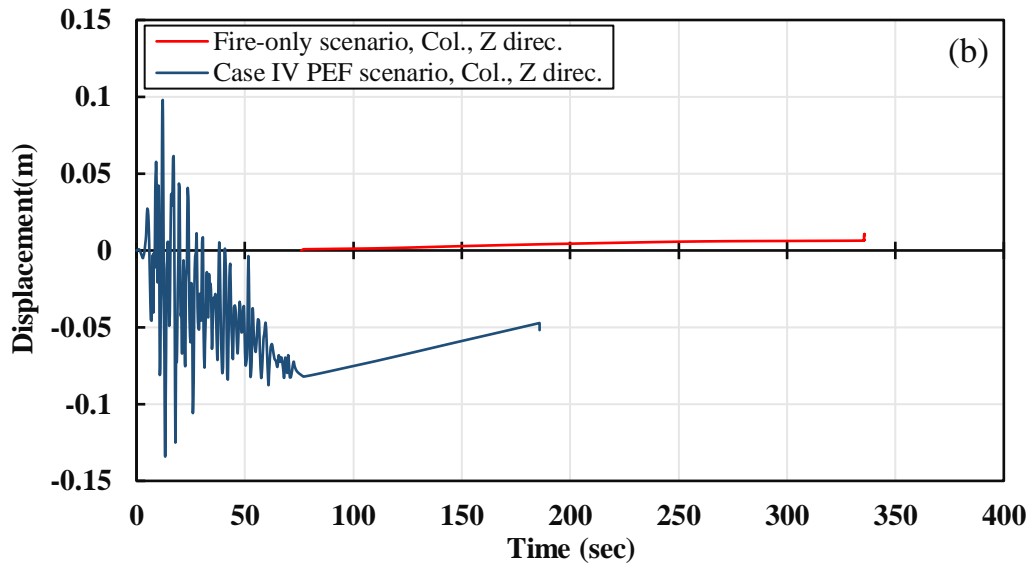
Figure 8-20 Comparison of the Displacement Values at a Point Which is 1.4 m Along the Column Length for Both the Fire-Only and PEF Events for Case IV Including (a) The Time-Displacement Record in the Y-Direction, (b) The Time-Displacement Record in the Y-Direction, (c) The Time-Displacement Record for Total Displacement Value and (d) The Temperature-Displacement Record for the Total Displacement Value

Table 8.4 Results Comparison for all Analysed Circumstances

Case No.	Type of analysis	Type of excitation	Failure		Time failure, compare to fire only results	Type of failure
			Time (sec)	Tem. (°C)		
Case I	Fire-Only	No excitation	336	480	-	Local/Symmetrical
Case II	PEF	Unidirectional	272	455	-19%	Local/Asymmetrical
Case II	PEF	Unidirectional	277	455	-18%	Local/Asymmetrical
Case IV	PEF	Bidirectional	185	306	-45%	Global /Asymmetrical
Case V	PEF	Bidirectional	185	306	-45%	Global /Asymmetrical

8.5. Conclusion

- Considering the grave consequences in terms of occupant and structural safety, an accurate analysis of the response of structures exposed to these events is required at the design stage. Some of the events may occur as a consequence of another hazard, for example, a fire may occur due to the failure of an electrical system following an earthquake. The structure is thus subjected to a multi-hazard loading scenario.

- PEF is one of the major multi-hazard events which are likely to occur.

- PEF has been the subject of relatively little research in the available literature.

- In most design codes, structures exposed to multiple hazards such as earthquake and then fire are analysed and designed separately. Structures subjected to an earthquake experience partial damage, and the subsequent occurrence of a fire may lead to structural collapse. Most available analysis procedures and design codes do not address the association of the two hazards. Thus, the design of structures based on existing standards may develop a high risk of structural failure.

- A suitable method of analysis has been developed to investigate the behaviour of structures exposed to sequential hazards such as PEF.

- PEF is a situation that has not received enough attention in most design codes. Investigating the effects of PEF on structures classified as 'ordinary' in the codes such as educational and residential is significant as these buildings comprise a significant part of urban buildings.

- The design consideration based on performance requires structures to remain within the 'life safety' level of response under the design earthquake and fire separately.

- Two types of failure mechanisms are detected—global and local failure. Local failure happens in the beams, whereas global failure is signified by significant lateral movement in the columns due to bidirectional excitation. Interestingly, the majority of only-fire analysis resulted in local collapse, while all bidirectional excitation PEF analyses resulted in global collapse.

- The tubular column section is more suitable to use in earthquake hazard zones owing to the combined effect of bidirectional excitation and fire.

- The investigations performed here are for a particular class of structures, yet the results confirm the need for the incorporation of PEF during analysis and design stages.

- Further studies must be performed either numerically or experimentally, using complete seismic SSI analysis involving (soil, foundation system and the superstructure), on different structures subject to PEF to develop a better understanding of the issue.

Chapter 9: Conclusion

9.1. Scope of Research

A large number of examples of pile-supported structures that have been damaged due to seismic excitation cases have been examined, but instrumented studies on the response and performance of such structures have been limited. Much of the detected damage was a consequence of soil liquefaction and soil lateral spreading. Cases of seismically induced pile failures in a clay deposit during the Mexico City and Loma Prieta earthquakes were observed.

A comprehensive review of the site and laboratory systems designed to examine seismic soil–structure interaction shows that most attempts have been concentrated on liquefaction problems, overlooking seismic soil–structure interaction in cohesive clay soil. Flexible wall-shaking table tests offer an excellent opportunity to extend the restricted database of seismic SSI in soft clays. These tests can also be employed under various controlled test conditions. A test program is used to simulate the fully coupled behaviour of the soil–pile–superstructure system numerically under the research conditions and objectives. A physical shaking table test performed by Meymand (1998) is adopted as a reference case study. In accordance with the reference case study, soil material properties are obtained and modelled with three different soil constitutive criteria, i.e. Mohr–Coulomb, Drucker–Prager and Cam–Clay models, to achieve and identify the closest behaviour compared with the physical behaviour of shaking table test involving soil simulation related to seismic excitation. To avoid unnecessary free vibration, 5% Rayleigh damping is adopted for all simulations.

The interdependent processes of seismic soil–pile–structure interaction analysis and its components constitute an imperative segment of the scale modelling approach in which the variables involved in the process and the modes of the system are defined. The design of the scale model program is developed to enable the scaled system to capture the behaviour of principal parameters of interest effectively.

A practical modelling methodology involves pinpointing and modelling primary forces and processes within the system effectively whilst suppressing the secondary effects. In this scale modelling approach, the essential modes of the system response are initially identified, and the prototype value is defined for the parameters which contribute to these

modes. The scaling relationships are developed and utilised to determine the parameters of the scale model for the variables of interest. Scale model components are then produced and examined to corroborate their actual behaviour. Subsequently, scaling relationships are applied to determine whether the established model behaviour indicates a reasonable prototype response.

Performing an accurate large-scale laboratory is complicated and expensive and can be impossible depending on the desired degree of complexity and accuracy. These factors present researchers with difficulties on how to validate their studies in the seismic area. Resorting to a scaled testing technique, that is, using shaking tests in the one–g environment, is a viable option and may be the only approach that can resolve this issue. A sophisticated and novel validation approach is developed in the current study to bridge the serious challenge of calibration and validation problem of seismic soil–structure interaction results.

The soil–structure interaction of high-rise buildings is most affected by the essential characteristics of seismic soil–pile–superstructure interactions, including nonlinearity, degradation of resistance, frequency dependence, dynamic load distribution and pile group effects. Moreover, the seismic soil–structure interaction analysis provisions addressed in EC8 and ASCE indicate four significant influences of mode interaction. They are (i) the lengthening of the period, (ii) equivalent damping ratio, (iii) base-shear reduction factor and (iv) inertial and kinematic mode interaction. EC8 and ASCE codes do not specify all these essential factors. Thus, reviewing and upgrading the seismic codes for nonlinear seismic SSI analysis of high-rise buildings is crucial to practically account for the seismic SSI effect. In the present study, the effects of soil–structure interaction in design and analysis procedures and the provisions for pile performance analysis of high-rise building resting on clay soil subjected to seismic loading are examined in accordance with EC8 and ASCE standards. Both codes include simplified approaches to soil–structure interaction analysis. However, they recommend that specific dynamic analysis for structures resting on soft soils subject to intense levels of shaking is essential. On the basis of the site soil properties for the analysis and design purposes, EC8 and ASCE codes have classified sites as site class *A, B, C, D, E* or *F*. Deciding a site class for a particular situation of analysis depends on several soil criteria, such as (i) shear wave velocity $\bar{V}_s$, (ii) average SPT resistance or blow counts $(\bar{N} \, or \, \bar{N}_{cb})$ and (iii) undrained shear strength $\bar{S}_u$ for fine-grained soil. These categories vary from *A* for hard rock soil type to

F for sensitive soft clay. Class *F* soils require particular site response analysis following Section 21.1 in ASCE code or Section 1.2.3 in EC8. The ASCE code specifies conditions to be satisfied to consider the soil as class *F*. Two out of four conditions are incompletely described by seismic codes and need to be defined clearly. These two conditions are the minimum thickness of sensitive clay, and the minimum effective thickness of a sand layer which interrupts the continuity of the sensitive clay layer are specified in the current study.

The probability of extreme events, such as earthquake, fire or blast, occurring during the lifetime of a structure is relatively low, but these events can cause serious damage to the structure and human life. Given the serious consequences in terms of occupant and structural safety, an accurate analysis of the response of structures exposed to these events is required for design. Some events may occur as a consequence of another hazard. For example, a fire may occur due to the failure of the electrical system following an earthquake. In such a scenario, the structure is subjected to a multi-hazard loading scenario.

Although post-earthquake fire is one of the major multi-hazard events which is likely to occur, it is the subject of relatively limited research. In most design codes, structures expected to be exposed to multiple hazards such as earthquake and then fire are analysed and designed separately. Structures subjected to an earthquake experience with partial damage and the subsequent occurrence of a fire may lead to faster structural collapse. Most available analysis procedures and design codes do not address the association of the two hazards. Thus, the design of structures on the basis of existing standards may develop a significant risk of structural failure. A suitable method of analysis is required to investigate the behaviour of structures exposed to sequential hazards, such as post-earthquake fire. In the current study, a multi-hazard analysis approach is developed and it includes the damage caused to the structure during and after an earthquake in the sequential thermal analysis. This methodology is developed and used to study the nonlinear behaviour of a steel framed structure under a PEF condition. A 3D elastic–plastic model of unprotected steel frame is developed using Abaqus software.

9.2. Research Findings, Recommendations and Future Research Directions

Soil–structure interaction includes various mechanisms which represent the association and the interdependence between soil and structural behaviour. These mechanisms are generally categorised under kinematic and inertial modes. Various methods presented in

literature to describe the SSI problem are reviewed in the present study. These approaches can be categorised as continuum versus discrete, linear versus nonlinear, frequency domain versus time domain and direct versus substructure methodologies.

Two major seismic codes, namely, EC8 and ASCE codes, are analysed and contrasted with to their guidelines, standards and provisions of design and analysis of seismic soil–structure interaction problems. This comprehensive analysis and comparison study is developed on the basis of the studies published over the last few years to bridge the significant gaps in the two codes. The study aims to explain the seismic design phenomenon in addition to the limitations in the application of seismic soil–structure interaction of structures resting on soft clay. Considering seismic soil–structure interaction may either be advantageous or disadvantageous to the structural response. This is depending on several aspects, including the contrast between the two contacted material (structure to soil) stiffness, type of soil deposit and geotechnical and geological soil properties. Besides, the method of modifying and selecting the applied earthquake motion can be played a significant role as well.

The dynamic response of a structure resting on a rigid deposit is a function of frequency content of the applied earthquake motion, which (earthquake motion) is matched and filtered according to code provisions and applied at the base of a superstructure. However, this dynamic response tends to rely on the effect of contrition of seismic soil–structure interaction when inelastic nonlinear elastoplastic analysis is considered. In this nonlinear analysis, complete seismic SSI model comprise soil, with pile or without pile foundation system, and the superstructure.

9.2.1. Numerical Analysis of Shaking Table Test

9.2.1.1. Soil Constitutive Models and Soil Model Parameters

The transformation framework of the physical test to a numerical platform from the perspective of using different soil constitutive models is briefly detailed. The dimensional analysis procedure is adopted to determine scale modelling criteria and develop an 'appropriate' scaled model of soil and pile-supported structures. A distinctive approach is developed to achieve a successful model to permit multidirectional simple shear deformation, minimise effects of boundary condition and replicate free-field site response effectively.

The findings demonstrate that the technique is fruitful in using appropriate validation under physical test conditions. A 3D numerical simulation of physical shaking table test

is performed using Abaqus software for three different soil constitutive models, i.e. Mohr–Coulomb, Drucker–Prager and Cam–Clay models. The results prove that using an appropriate soil constitutive model to examine the problem is the key to accomplishing an exceptional correlation to the physical test. The data set developed for the testing program includes the analysis of dynamic pile response. This fully coupled analysis is accomplished accurately by defining the dynamic response of complex soil–pile–superstructure systems with the advantage of solving the seismic soil–pile–structure interaction problem.

Most soil–structure interaction effects, i.e. gap/slap mechanism, consequences of the soil–pile kinematic force, and the superstructure inertial force, can be detected according the adopted approach. The consequences of seismic soil–pile–structure interaction prove that the gap/slap mechanism amplifies the pile head acceleration, lengthens the period of the superstructure and activates the pile free vibration, thereby leading to a reduction in stiffness of the pile. Ignoring the gap/slap mechanism due to simplification of numerical analysis results in misleading stiffness and strength capacity of the analysed piles. The findings clearly indicate that the physical shaking table test with flexible wall barrel container can be simulated successfully by using a sophisticated finite element analysis procedure and the Cam–Clay constitutive model. However, delivering an accurate numerical simulation with high validation level requires defining soil specifications and material properties precisely.

The Mohr–Coulomb model and, in less degree, the Drucker–Prager model are unsuitable for nonmonotonic motion (seismic loading) leading to large deviation from the result of the physical test. This collaboration of numerical results to the physical test data is proof that an accurate numerical model can provide a suitable basis for numerical simulation of the physical shaking test data.

9.2.1.2. Development of Scaling and Validation Methodology

A sophisticated approach of scaling and validating full-scale seismic soil–structure interaction problem is proposed using the association between numerical and physical tests. On the basis of an extensive laboratory test previously conducted by many researchers (see Chapter 5), a dimensional scaling factor $\lambda=8$ is implemented in the current study. An entire approach is built as a step-by-step procedure. The proposed methodology considers the scaling concept of implied prototypes and 'modelling of models' technique which can ensure a satisfactory level of model accuracy.

An advanced 3D finite element modelling using Abaqus software is also developed. The characteristics, properties and results of the physical shaking table test conducted by Meymand (1998) are adopted as a reference case study. The results indicate a good correlation with small deviation between the scaled numerical and physical test when the scaling and validation method is used. The level of accuracy primarily depends on the level of scaling precision, selection of appropriate material that can represent the properties of the prototype materials correctly and the percentage difference between the target and computed values of the primary parameter of the system.

To stimulate the correct prototype flexural stiffness, the proposed scaling and validation technique indicates that the model flexural stiffness must be reduced by a reasonable reduction factor. Consideration of a rational reduction factor is a critical step that warrants further research to provide reasonable guidelines. According to the scaling law, the preparation of clay specimen model is successfully defined for the physical and numerical tests. Therefore, this method of modelling can be adapted to other scale modelling circumstances that require realistic soil behaviour and can validate the results using existing validation methods. Most seismic soil–pile–structure interaction modes, such as the gap/slap mechanism, inertial forces of the superstructure and kinematic soil–pile force, can be modelled correctly.

9.2.2. Soil–structure interaction and Effect of Soil Type: Examination According to Code Provision

9.2.2.1. Analysis of Pile and Structure Performance: According to Seismic Code Provision

This study is designed to determine the effects of incorporating soil–structure interaction on the seismic response of structure and compare the findings with EC8 and ASCE seismic provisions. Seismic design standards according to ASCE and EC8 seismic codes are assumed safe for high-rise structures by considering soil–structure interaction. However, the findings clearly indicate that the structural response may exceed the limitations, making the provisions unsafe. Moreover, the results reveal a significant relationship between the selecting and matching method of input data and the geological and geotechnical site properties, providing accurate results.

The current study raises crucial questions about the nature and reliability of base-shear reduction factor recommended in both codes. Consequently, a small reduction factor should be used as the effects of field nonlinearity, i.e. geometrical and material

nonlinearity, increases the ductility demand of the system. In addition, the effects of soil–structure interaction on different members in divers' position are dissimilar. Thus, different reduction factors must be considered in member seismic design. However, SSI analysis is a very complicated problem, and using pure reduction according to the reduction factor of the current seismic codes may be unsafe. Evidence from the present study suggests that further investigation is needed to determine a rational reduction factor.

The frequency analysis of the SSI system reveals that a number of modes are associated with the dynamic structural response of the system. Given this connection, the SSI effects and number of modes (not only the first mode as it is addressed in seismic codes) should be involved in the analysis. In this respect, the results explain to an extent why the assumption of ASCE and EC8 to base analysis on the fundamental period, which is computed by the code equations, may be illogical and inadequate. Further quantitative research should be undertaken to establish a clear procedure for determining the minimum number of structural modes which should be incorporated in the analysis. This set of analyses reveals the significance of incorporating the piles in the 'complete' seismic SSI analysis. In addition, the findings have important implications for understanding the dynamic pile behaviour and effect of pile group.

9.2.2.2. Effect of Soil Class According to EC8 and ASCE

Site class F pertains to soft clay soils that can strongly amplify long-period ground motions. Codes impose several characteristics and conditions to classify the effect of site class F in the analysis procedure. Section 20.3.1. ASCE or Section 1.2.3 in EC8 classifies soil as class F if one of the four conditions is satisfied. The most two vague and unclear described conditions of these four are successfully characterised in the present study. The findings reveal that the frequency content of the ground motion performs the key role in identifying the system behaviour for both studied circumstances.

Firstly, the minimum thickness of sensitive clay layer that filters the passing ground motions and then satisfies the class F code condition requirement is started from 0.5 m. Secondly, soil with a thick layer of a 37 m of soft, medium or stiff clay and has $S_u < 50$ kPa is considered class F according to (Section 20.3.1) in ASCE. This tricky criterion is due to soil profile arrangement circumstances, such as cutting a tiny layer of sand continuity of the clay layer, which is supposed to satisfy the 37 m thickness condition according to code provisions. The presence of thin sand layer(s) between two thick soft clay layers does not change anything, and the accumulative thicknesses of soft soil layers

$(\sum H)$ must be considered to employ the condition of (H $\geq$37 m). Expanding the cut-off sand layer to more than 2.0 m means a new behaviour condition, and the average soil properties should be applied to decide the correct soil class according to conditions in Section 20.3.1 of ASCE.

9.2.3. Multi-Hazard Analysis

9.2.3.1. Post-Earthquake Fire Multi-Hazard Analysis

In most design codes, structures exposed to multiple hazards such as earthquake and then fire are analysed and designed separately. Structures subjected to an earthquake experience with partial damage and the subsequent occurrence of a fire may lead to faster structural collapse. Most available analysis procedures and design codes do not address the association of the two hazards. Thus, the design of structures based on existing standards may develop a significant risk of structural failure. A suitable method of analysis is required to investigate the behaviour of structures exposed to sequential hazards, such as post–earthquake fire.

Post–earthquake fire has not received sufficient attention in most design codes. Investigating the effects of post–earthquake fire on structures categorised as 'ordinary' in the codes, such as educational and residential, is important because these buildings comprise a large percentage of urban buildings. The design consideration based on performance requires structures to remain within the 'life safety' level of response under the design earthquake and fire separately.

Two types of failure mechanisms are detected, namely, global and local failures. The local failure occurs in the beams, whereas global failure is represented by a significant lateral movement in the columns due to bidirectional excitation. Interestingly, the majority of fire-only analysis result in local collapse, whereas all the design analyses result in global collapse. The tubular column section is more suitable to use in earthquake hazard zones due to the combined effect of bidirectional excitation and fire. Although the investigations performed here are for a particular class of structures, the results confirm the need for incorporating post–earthquake fire in the process of analysis and design. Thus, complete Soil–structure interaction system analysis should be performed numerically or experimentally on different structures subject to post–earthquake fire to develop a better understanding of the issue.

References

(USACE), U.S.A.C. of E. (2007) *Earthquake Design and Evaluation of Concrete Hydraulic Structures*. [Online]. (May). Available from: doi:10.1108/10222529200000006.

AASHTO LRFD Bridge Design (2015) *Design and Construction of Driven Pile Foundation-Volume 1*.

Abadie, C.N. (2015) *Cyclic Lateral Loading of Monopile Foundations in Cohesionless Soils*. University of Oxford.

Abrahamson, N.A. (1992) Non-stationary spectral matching. *Seismological research letters*. 63 (1), 30.

Akia, K., Bary, J.D., Boulanger, R.W. & Christaian, J.T. (1995) *Geotechnical Reconnaissance of the Effects of the January 17, 1995, Hyogoken-Nanbu Earthquake,Japan*.

Akkar, S. & Gülkan, P. (2002) A critical examination of near-field accelerograms from the Sea of Marmara region earthquakes. *Bulletin of the Seismological Society of America*. [Online] 92 (1), 428–447. Available from: doi:10.1785/0120000814.

Al-Isawi, A.T., Collins, P.E.F. & Cashell, K.A. (2019) Fully Non-Linear Numerical Simulation of a Shaking Table Test of Dynamic Soil-Pile-Structure Interactions in Soft Clay Using ABAQUS. *Geotechnical Special Publication*. [Online] 2019-March (GSP 308), 252–265. Available from: doi:10.1061/9780784482100.026.

Alaska, N.R.C.C. on theEarthquake (1968) *The Great Alaska Earthquake of 1964*. 6th edition. National Academies.

Alex, S. (2019) *Numerical modelling of geomaterials at failure Spetz, Alex 2019*. Lund University.

Ali, H.M., Senseny, P.E. & Alpert, R.L. (2004) Lateral displacement and collapse of single-story steel frames in uncontrolled fires. *Engineering Structures*. [Online] 26

(5), 593–607. Available from: doi:10.1016/j.engstruct.2003.12.007.

Anand, V. & Satish Kumar, S.R. (2018) Seismic Soil-structure Interaction: A State-of-the-Art Review. *Structures*. [Online] 16 (June), 317–326. Available from: doi:10.1016/j.istruc.2018.10.009.

ASCE (2013) ASCE 7: Minimum Design Loads for Buildings and Other Structures. *American Society of Civil Engineers*.

ASCE 7-16 (2017) *Minimum Design Loads and Associated Criteria for Buildings and Other Structures (7-16)*.

ASCE7-10 (2010) *Minimum Design Loads for Buildings and Other Structures*. [Online]. Available from: www.pubs.asce.org.

Ashory, M.R. (1999) *High Quality Modal Testing Methods*. Imperial college University London.

ATC (1996) *Seismic evaluation and retrofit of concrete buildings*. California , Berkeley, Senior Advisor.

ATC, 3-06 (1978) *Tentative Provisions for The Development of Seismic Regulations for Buildings*.

Al Atik, L. & Abrahamson, N. (2010) An Improved Method for Nonstationary Spectral Matching. *Eaarthquake Spectra*. [Online] 26 (3), 601–617. Available from: https://doi.org/10.1193/1.3459159.

Aydemir, M.E. & Ekiz, I. (2013a) Soil-structure interaction effects on seismic behaviour of multistorey structures. *European Journal of Environmental and Civil Engineering*. [Online] 17 (8), 635–653. Available from: doi:10.1080/19648189.2013.810177.

Aydemir, M.E. & Ekiz, I. (2013b) *Soil – structure interaction effects on seismic behaviour of multistorey structures*. [Online] 8189. Available from: doi:10.1080/19648189.2013.810177.

Ayough, P., Ali, S., Seiyed, H. & Al., E. (2017) Response of steel moment and braced

frames subjected to near-source pulse-like ground motions by including soil-structure interaction effects. *Soil Dynamics and Earthquake Engineering*. [Online] 3 (1), 53–66. Available from: doi:10.1016/j.soildyn.2017.07.013.

Badry, P. & Satyam, N. (2017) Journal of Asian Earth Sciences Seismic soil structure interaction analysis for asymmetrical buildings supported on piled raft for the 2015 Nepal earthquake. *Journal of Asian Earth Sciences*. [Online] 133, 102–113. Available from: doi:10.1016/j.jseaes.2016.03.014.

Bala, M. (2007) Recommended Practice for Planning , Designing and Constructing Fixed Offshore Platforms — Working Stress Design. *Api Recommended Practice*. [Online] 24-WSD (December 2000), 242. Available from: doi:10.1007/s13398-014-0173-7.2.

Bararnia, M., Hassani, N., Ganjavi, B. & Ghodrati Amiri, G. (2018a) Estimation of inelastic displacement ratios for soil-structure systems with embedded foundation considering kinematic and inertial interaction effects. *Engineering Structures*. [Online] 159 (January), 252–264. Available from: doi:10.1016/j.engstruct.2018.01.002.

Bararnia, M., Hassani, N., Ganjavi, B. & Ghodrati, G. (2018b) Estimation of inelastic displacement ratios for soil-structure systems with embedded foundation considering kinematic and inertial interaction e ff ects. *Engineering Structures*. [Online] 159 (December), 252–264. Available from: doi:10.1016/j.engstruct.2018.01.002.

Bardakis, V.G. & Fardis, M.N. (2011) A displacement-based seismic design procedure for concrete bridges having deck integral with the piers. *Bulletin of Earthquake Engineering*. [Online] 9 (2), 537–560. Available from: doi:10.1007/s10518-010-9215-5.

Basack, S. & Nimbalkar, S. (2017) International Journal of Geomechanics. *International Journal of Geomechanics*. [Online] 17 (8). Available from: doi:10.1061/(ASCE)GM.1943-5622.0000905.

Behnam, B. & Abolghasemi, S. (2019) Post-earthquake Fire Performance of a Generic Fireproofed Steel Moment Resisting Structure. *Journal of Earthquake*

Engineering. [Online] 1–26. Available from: doi:10.1080/13632469.2019.1628128.

Behnam, B. & Ronagh, H.R. (2014) Post-Earthquake Fire performance-based behavior of unprotected moment resisting 2D steel frames. *KSCE Journal of Civil Engineering*. [Online] 19 (1), 274–284. Available from: doi:10.1007/s12205-012-0527-7.

Bellova, M. (2013) Eurocodes: Structural fire design. *Procedia Engineering*. [Online] 65, 382–386. Available from: doi:10.1016/j.proeng.2013.09.059.

Benjamin, J.R. (1988) *A criterion for determining exceedance of the operating basis earthquake*.

Bernal, D. & Youssef, A. (1998) Non-Linear Soil — Structure Interaction. *Earthquake Engineering and Structural Dynamics*. 685 (v), 673–685.

Bezgin, O. (2014) An insight into the influence of the construction Methods on the lateral load capacity of drilled deep foundations. In: *4th ECCOMAS Thematic Conference on Computational Methods in Structural Dynamics and Earthquake Engineering*. [Online]. 2014 Kos Island, Greece. pp. 1–23. Available from: doi:DOI: 10.7712/120113.4821.C1024.

Bigelow, H., Pak, D., Hoffmeister, B., Feldmann, M., et al. (2017) ScienceDirect ScienceDirect Soil-structure interaction at railway bridges with integral abutments. *Procedia Engineering*. [Online] 199, 2318–2323. Available from: doi:10.1016/j.proeng.2017.09.204.

Blaney, G., Kausel, E. & Roesset, J. (1978) Dynamic Stiffness of Piles. In: *Volume II of the Second International Conference on Numerical Methods in Geomechanics*. 1978 Blacksburg. pp. 1001–1012.

Bogard, D. & Matlock, H. (1983) *Simplified Calculation of P-Y Curves for Laterally Loaded Piles in Sands*.

Bolisetti, C., Whittaker, A.S. & Coleman, J.L. (2018) Linear and nonlinear soil-structure interaction analysis of buildings and safety-related nuclear structures. *Soil*

Dynamics and Earthquake Engineering. [Online] 107 (February), 218–233. Available from: doi:10.1016/j.soildyn.2018.01.026.

Bommer, J. & Acevedo, A. (2004) The use of real earthquake accelerograms as input to dynamic analysis. *Journal of Earthquake Engineering*. [Online] 8 (1), 43–91. Available from: doi:10.1080/13632460409350521.

Bommer, J., Borzi, B., Chlimintzas, G., Elnashai, A., et al. (2001) *Definition of displacement response spectra for design. In: Faccioli E, Paolucci R (eds.) Seismic Actions.*

Bommer, J. & Elnashai, A. (1999) Displacement spectra for seismic design. *Journal of Earthquake Engineering*. 3, 1–32.

Bonaparte, R. & Mitchell, J.K. (1979) *The properties of San Francisco Bay mud at Hamilton Air Force Base, California*.

Borcherdt, R.D. (1994) Estimates of Site-Dependent Response Spectra for Design (Methodology and Justification). *Earthquake Spectra*. [Online] 10 (4), 617–653. Available from: doi:10.1193/1.1585791.

Bosch, D.R. & Sotelo, R.R. (2015) Determination of Stratigraphy—Soil Types—Using Cone Penetration Test in Sedimentary Deposits in North-East of Argentina. *Journal of Geoscience and Environment Protection*. [Online] 3 (6), 134–139. Available from: doi:10.4236/gep.2015.36019.

Boulanger, B.R.W., Curras, C.J., Member, S., Kutter, B.L., et al. (1999) Seismic soil-pile-structure interaction experiments and analyses. *Journal of Geotechnical and Geoenvironmental Engineering*. 125 (September), 750–759.

British Standards, I. (2004) Eurocode2: Design of Concrete Structures: Part 1-1: General Rules and Rules for Buildings. *British Standards Institution*. 240.

British Standards Institution (2011a) *Eurocode 1 - Actions on structures Part 1-6: General actions Actions during execution*.

British Standards Institution (2011b) *Eurocode 3: Design of steel structures - Part 1-2: General rules -Structural fire design*. London, British Standards Institution.

British Standards Institution (2004) *Eurocode 8: Design of structures for earthquake resistance - Part 1 : General rules, seismic actions and rules for buildings Eurocode-*. London, British Standards Institution.

Brittsan, D. (1995) *Indicator Pile Test Program for the Seismic Retrofit of the East Approach Structure of the San Francisco-Oakland Bay Bridge*.

Brown, S. (2011) *Copyright - 2007*. [Online] (May), ii–ii. Available from: doi:10.1109/wons.2007.340472.

Bulajic, B., Manic, M. & Ladjinovic, D. (2012) Towards preparation of design spectra for Serbian National Annex to Eurocode 8: Part I: spectral shapes and regional empirical equations for scaling pseudo-acceleration spectra. *Facta universitatis - series: Architecture and Civil Engineering*. [Online] 10 (2), 131–154. Available from: doi:10.2298/fuace1202131b.

Byrne, B.W., McAdam, R.A., Burd, H.J., Beuckelaers, W.J.A.P., et al. (2019) Monotonic laterally loaded pile testing in a stiff glacial clay till at Cowden. *Géotechnique*. [Online] 1–16. Available from: doi:10.1680/jgeot.18.PISA.003.

Cairo, R., Conte, E. & Dente, G. (2005) Interaction Factors for the Analysis of Pile Groups in Layered Soils. *Journal of Geotechnical and Geoenvironmental Engineering*. [Online] 131 (January), 987–1003. Available from: doi:10.1061/(ASCE)1090-0241(2005)131.

Candeias, P.X. (2012) *Physical Modelling , Instrumentation and Testing*. Lisbon, Portugal, Seismic Engineering Research Infrastructures for European Synergies.

Carbonari, S., Morici, M., Dezi, F. & Gara, F. (2017) Soil-Structure Interaction Effects in Single Bridge Piers Founded on Inclined Pile Groups. *Soil Dynamics and Earthquake Engineering*. [Online] 92 (January), 52–67. Available from: doi:10.1016/j.soildyn.2016.10.005.

De Carlo, G., Dolce, M. & Liberatore, D. (2000) Influence of soil-structure interaction on the seismic response of bridge piers. In: *Proceedings of the 12th World Conference on Earthquake Engineering*. 2000 New Zealand Society for Earthquake Engineering Upper Hut, New Zealand. pp. 1–8.

Carvajal-Soto, L.A., Ito, T., Protti, M. & Kimura, H. (2020) Earthquake potential in Costa Rica using three scenarios for the central Costa Rica deformed belt as western boundary of the Panama microplate. *Journal of South American Earth Sciences*. [Online] 97 (July 2019), 102375. Available from: doi:10.1016/j.jsames.2019.102375.

Chatziioannou, K., Katsardi, V., Koukouselis, A. & Mistakidis, E. (2017) The effect of nonlinear wave-structure and soil-structure interactions in the design of an offshore structure. *Marine Structures*. [Online] 52, 126–152. Available from: doi:https://doi.org/10.1016/j.marstruc.2016.11.003.

Chicchi, R. & Varma, A.H. (2018) Research review: Post-earthquake fire assessment of steel buildings in the United States. *Advances in Structural Engineering*. [Online] 21 (1), 138–154. Available from: doi:10.1177/1369433217711617.

Ciampolp, B.M. & Pinto, P.E. (1995) *Effects of soil-structure interaction on inelastic seismic response of bridge piers*. 121 (5), 806–814.

Clough, R.W. & Pirtz, D. (1956) Earthquake Resistance of Rock-Fill Dams. *Journal of the Soil Mechanics and Foundations Division*. 82 (2), 1–26.

Clough, R.W. & Seed, H.B. (1963) Earthquake Resistance of Sloping Core Dams. *Journal of the Soil Mechanics and Foundations Division*. 89 (1), 209–242.

Coleman, J.L., Bolisetti, C. & Whittaker, A.S. (2016) Time-domain soil-structure interaction analysis of nuclear facilities. *Nuclear Engineering and Design*. [Online] 298, 264–270. Available from: doi:10.1016/j.nucengdes.2015.08.015.

Della Corte, G., Landolfo, R. & Mazzolani, F.M. (2003) Post-earthquake fire resistance of moment resisting steel frames. *Fire Safety Journal*. [Online] 38 (7), 593–612. Available from: doi:10.1016/S0379-7112(03)00047-X.

Coutinho, C.P., Baptista, A.J. & Dias Rodrigues, J. (2016) Reduced scale models based on similitude theory: A review up to 2015. *Engineering Structures*. [Online] 119 (July), 81–94. Available from: doi:10.1016/j.engstruct.2016.04.016.

Cruz, C. & Miranda, E. (2017a) buildings subjected to earthquakes. *Soil Dynamics and*

Earthquake Engineering. [Online] 100 (June), 183–195. Available from: doi:10.1016/j.soildyn.2017.05.034.

Cruz, C. & Miranda, E. (2017b) Evaluation of soil-structure interaction effects on the damping ratios of buildings subjected to earthquakes. *Soil Dynamics and Earthquake Engineering*. [Online] 100 (May), 183–195. Available from: doi:10.1016/j.soildyn.2017.05.034.

Darendeli, M.B. (2001) *Development of a new family of normalized modulus reduction and material damping curves*. The University of Texas at Austin.

David, T.K., Krishnamoorthy, R.R. & Mohamed Jais, I.B. (2015) Finite element modelling of soil-structure interaction. *Jurnal Teknologi*. [Online] 76 (8), 59–63. Available from: doi:10.11113/jt.v76.5625.

Dickenson, S.E. (1994) *Dynamic response of soft and deep cohesive soils during the Loma Prieta Earthquake of October 17, 1989*. University of California, Berkeley.

Dickenson, S.E., Barkau, M.G. & Wavra, B.J. (2002) *Assessment and mitigation of liquefaction hazards to bridge approach embankments-final report*. (November).

Dobry, R. (1995) Liquefaction and Deformation of Soils and Foundations Under Seismic Conditions. In: *Third International Conference on Recent Advances in Geotechnical Earthquake Engineering and Soil Dynamics*. 1995 pp. 1465–1490.

Dobry, R., Borcherdt, R.D., Crouse, C.B., Idriss, I.M., et al. (2000) New Site Coefficients and Site Classification System Used in Recent Building Seismic Code Provisions. *Earthquake Spectra*. [Online] 16 (1), 41–67. Available from: doi:10.1193/1.1586082.

Doğangü, A. & Livaoğlu, R. (2006) A comparative study of the design spectra defined by Eurocode 8, UBC, IBC and Turkish Earthquake Code on R/C sample buildings. *Journal of Seismology*. [Online] 10 (3), 335–351. Available from: doi:10.1007/s10950-006-9020-4.

Douglas, J. & Gkimprixis, A. (2017) Using targeted risk in seismic design codes : A summary of the state of the art and outstanding issues. *6th National Conference on*

Earthquake Engineering and 2nd National Conference on Earthquake Engineering and Seismology. (2013).

Dunnavant, T.W. & O'Neill, M.W. (1985) Performance, Analysis, and Interpretation of a Lateral Load Test of a 72-inch-diameter Bored Pile in Overconsolidated Clay. *UHCE*. 84 (7).

Durante, M.G., Angeles, L., Sarno, L. Di, Taylor, C., et al. (2015) Soil-Pile-Structure-Interaction: Experimental Results And Soil-Pile-Structure-Interaction : Experimental. In: *COMPDYN 2015 - 5th ECCOMAS Thematic Conference on Computational Methods in Structural Dynamics and Earthquake Engineering*. [Online]. 2015 Crete Island, Greece. p. Available from: doi:10.7712/120115.3699.2830.

Durante, M.G., Di Sarno, L., Mylonakis, G., Taylor, C.A., et al. (2016) Soil–pile–structure interaction: experimental outcomes from shaking table tests. *Earthquake Engineering & Structural Dynamics*. 45 (7), 1041–1061.

Dutta, S.C. & Roy, R. (2002) *A critical review on idealization and modeling for interaction among soil – foundation – structure system*. 80 (20–21), 1579–1594.

Džakić, D., Kraus, I. & Morić, D. (2012) Direct displacement based design of regular concrete frames in compliance with Eurocode 8. *Tehnicki Vjesnik*. 19 (4), 973–982.

Emadi, A., Shakib, H. & Shadlou, M. (2014) Investigation of beneficial and detrimental effects of soil-foundation-structure interaction on the seismic response of shear buildings. *KSCE Journal of Civil Engineering*. [Online] 18 (1), 253–263. Available from: doi:10.1007/s12205-014-0202-2.

EN 1998-1 (2011) *Eurocode 8: Design of structures for earthquake resistance – Part 1: General rules, seismic actions and rules for buildings*.1 (2005).

EN 1998-5 (2011) *Eurocode 8: Design of structures for earthquake resistance – Part 5: Foundations, retaining structures and geotechnical aspects*.1 (2005).

European Committee for Standardization (2011) *National Annex to Eurocode 0: Basis of Structural Design*.

Faccioli, E., Paolucci, R. & Pessina, V. (2002) Engineering assessment of seismic hazard and long period ground motions at the Bolu viaduct site following the November 1999 earthquake. *Journal of Seismology*. [Online] 6 (3), 307–327. Available from: doi:10.1023/A:1020027207784.

Faccioli, E., Paolucci, R. & Rey, J. (2004) Displacement spectra for long periods Earthq Spectra. *Journal of Earthquake Engineering*. 20, 347–376.

Fajfar, P. (2014) Structural Analysis in Earthquake Engineering – A Breakthrough of Simplified Non-Linear Methods. In: *12th European Conference on Earthquake Engineering*. 2014 p. Paper Reference 843.

Fan, B.K., Gazetas, G., Kaynia, A., Kausel, E., et al. (1992) Kinematic seismic response of single piles. *Journal of Geotechnical Engineering*. [Online] 117 (12), 1860–1879. Available from: https://doi.org/10.1061/(ASCE)0733-9410(1991)117:12(1860).

Far, H. (2019a) Advanced computation methods for soil-structure interaction analysis of structures resting on soft soils. *International Journal of Geotechnical Engineering*. [Online] 13 (4), 352–359. Available from: doi:10.1080/19386362.2017.1354510.

Far, H. (2019b) Advanced computation methods for soil-structure interaction analysis of structures resting on soft soils. *International Journal of Geotechnical Engineering*. [Online] 13 (4), 352–359. Available from: doi:10.1080/19386362.2017.1354510.

Farahani, R. V, Dessalegn, T.M., Vaidya, N.R. & Bazan-zurita, E. (2016) Seismic soil – structure interaction analysis of a nuclear power plant building founded on soil and in degraded concrete stiffness condition. *Nuclear Engineering and Design*. [Online] 297, 320–326. Available from: doi:10.1016/j.nucengdes.2015.12.002.

FEMA P-1050 (2015) NEHRP Recommended seismic provisions for new buildings and other structures. *Building Seismic Safety Council*. [Online]. I. Available from: doi:10.1017/CBO9781107415324.004.

FEMA P-749 (2010) Earthquake-Resistant Design Concepts, An Introduction to the NEHRP Recommended Seismic Provisions for New Buildings and Other

Structures. *Security*. [Online]. (12). Available from: doi:10.4231/D3T727G79.

Fitzgerald, B. & Basu, B. (2016) Structural control of wind turbines with soil structure interaction included. *Engineering Structures*. [Online] 111, 131–151. Available from: doi:10.1016/j.engstruct.2015.12.019.

Fu, F. (2010) 3-D nonlinear dynamic progressive collapse analysis of multi-storey steel composite frame buildings - Parametric study. *Engineering Structures*. [Online] 32 (12), 3974–3980. Available from: doi:10.1016/j.engstruct.2010.09.008.

Fu, F. (2015) *Advanced Modelling Techniques in Structural Design: A Structural Equation Modeling Approach*. [Online]. Wiley Online Library. Available from: doi:10.1002/9781118825440.

Fujii, S., Isemoto, N., Satou, Y., Kaneko, O., et al. (1998) Investigation and Analysis of a Pile Foundation Damaged By Liquefaction During the 1995 Hyogoken-Nambu Earthquake. *Soils and Foundations*. [Online] 38 (Special), 179–192. Available from: doi:10.3208/sandf.38.special_179.

Fukuoka, M. (1966) Damage to Civil Engineering Structures. *Soils and Foundations*. [Online] 6 (2), 45–52. Available from: https://doi.org/10.3208/sandf1960.6.2_45.

G˙ulkan, P. & S¨ozen, M. (1974) Inelastic response of reinforced concrete structures to earthquake motions. *ACI Journal*. 71, 604– 610.

Gajan, S. & Kutter, B.L. (2009) *Contact Interface Model for Shallow Foundations Subjected to Combined Cyclic Loading*. [Online] 135 (March), 407–419. Available from: doi:10.1061/(ASCE)1090-0241(2009)135.

Gajan, S., Raychowdhury, P., Hutchinson, T.C., Kutter, B.L., et al. (2010) Application and validation of practical tools for nonlinear soil-foundation interaction analysis. *Earthquake Spectra*. [Online] 26 (1), 111–129. Available from: doi:10.1193/1.3263242.

Ganjavi, B. & Hao, H. (2013) Optimum lateral load pattern for seismic design of elastic shear-buildings incorporating soil-structure interaction effects. *Earthquake Engineering and Structural Dynamics*. [Online] 42 (6), 913–933. Available from:

doi:10.1002/eqe.2252.

Garevski, M. & Ansal, A. (2010) *Earthquake Engineering in Europe*. [Online]. New York, Springer-Verlag, Berlin Heidelberg New York Tokyo. Available from: doi:10.1007/978-90-48-9544-2.

Gazetas, G. (1992) *FORMULAS AND C H A R T S FOR IMPEDANCES O F*. 117 (9).

Gazetas, G. & Dobry, R. (1984) Horizontal response of piles in layered soils. *Journal of Geotechnical engineering*. [Online] 110 (1), 20–40. Available from: https://doi.org/10.1061/(ASCE)0733-9410(1984)110:1(20).

Gazetas, G. & Mylonakis, G. (1998) Seismic soil-structure interaction: New evidence and emerging issues State of the Art Paper. In: *Geotechnical Earthquake Engineering and Soil Dynamics Geo-Institute ASCE Conference*. 1998 pp. 1119–1174.

Gazetas, G. & Stokoe, K.H. (1992) Free Vibration of Embedded Foundations: Theory Versus Experiment. *Journal of Geotechnical and Geoenvironmental Engineering ASCE*. [Online] 117 (9), 1382–1401. Available from: doi:10.1061/(ASCE)0733-9410(1991)117:9(1382).

Gazetas, G.C. & Mylonakis, G. (2001) Soil-structure interaction effects on elastic and inelastic structures. *4th International Conference on Recent Advances in Geotechnical Earthquake Engineering and Soil Dynamics*. [Online] 1–13. Available from: http://scholarsmine.mst.edu/icrageesd/04icrageesd/session16/3/.

Georgescu, E.S., Georgescu, M.S., Macri, Z., Marino, E.M., et al. (2018) Seismic and energy renovation: A review of the code requirements and solutions in Italy and Romania. *Sustainability (Switzerland)*. [Online] 10 (5), 1–31. Available from: doi:10.3390/su10051561.

Geotechnical Report (2005) *Geotechnical consultants, inc* . (October).

Gerolymos, N., Escoffier, S., Gazetas, G. & Garnier, J. (2009) Numerical modeling of centrifuge cyclic lateral pile load experiments. *Earthquake Engineering and Engineering Vibration*. [Online] 8 (1), 61–76. Available from:

doi:10.1007/s11803-009-9005-8.

Ghalibafian, H., Ventura, C.E. & Foschi, R.O. (2008) Effects of Nonlinear Soil-Structure Interaction on the Inelastic Seismic Demand of Pile-Supported Bridge Piers. *The 14 th World Conference on Earthquake Engineering World Conference on Earthquake Engineering*. (October).

Ghandil, M. & Behnamfar, F. (2017) Ductility demands of MRF structures on soft soils considering soil-structure interaction. *Soil Dynamics and Earthquake Engineering*. [Online] 92 (October 2016), 203–214. Available from: doi:10.1016/j.soildyn.2016.09.051.

Ghiocel, D.M. (2012a) SOME INSIGHTS ON FREQUENCY VS . TIME-DOMAIN APPROACHES FOR SEISMIC SSI ANALYSIS OF NPP STRUCTURES A PERSONAL PERSPECTIVE TECHNICAL NOTE. *Ghiocel Predictive Technologies, Inc. Technical Note GPT-001-201*.

Ghiocel, D.M. (2012b) Some Insights on Frequency Vs Time-Domain Approaches for Seismic SSI Analysis of NPP Structures. In: *Ghiocel Predictive Technologies, Inc. Technical Note GPT-001-201*. 2012 A personal perspective technical note. p. 7.

Ghoreishi, M., Bagchi, A. & Sultan, M.A. (2009) Estimating the response of structural systems to fire exposure: State-of-the-art review. *Conference Proceedings - Fire and Materials 2009, 11th International Conference and Exhibition*. 26 (May 2014), 475–483.

Gibson, A. (1997) *Physical Scale Modeling of Geotechnical Structures at One-G*.

Girault, P. (1986) Analysis of Foundation Failures, in The Mexico Earthquake, 1985 - Factors Involved and Lessons Learned. In: *AMERICAN SOCIETY OF CIVIL ENGINEERS (ASCE)*. 1986 pp. 178-192.

Givens, M.J., Stewart, J.P., Haselton, C.B. & Al., E. (2012) Assessment of Soil-Structure Interaction Modeling Strategies for Response History Analysis of Buildings. In: *15th world conference on earthquake engineering*. 2012 Lisboa,Portugal. p.

Gohl, W.B. (1991) *Response of Pile Foundations to Simulated Earthquake loading: Expermental and Analytical Results*. University of British Columbia.

Goulet, C.A., Watson-Lamprey, J., Baker, J., Haselton, C., et al. (2008) Assessment of ground motion selection and modification (GMSM) methods for non-linear dynamic analyses of structures. *Geotechnical Special Publication*. [Online] 4 (GSP 181 © 2008 ASCE). Available from: doi:10.1061/40975(318)3.

Guin, J. & Banerjee, P.K. (2002) Coupled Soil-Pile-Structure Interaction Analysis under Seismic Excitation. *Journal of Structural Engineering*. [Online] 124 (4), 434–444. Available from: doi:10.1061/(asce)0733-9445(1998)124:4(434).

Hamada, M. (2000) Performances of foundations against liquefaction-induced permanent ground displacements. In: *Proceedings of the 12th World Conference on earthquake engineering, Auckland, New Zealand, paper (no 1754)*. 2000 pp. 1–8.

Hancock, J., Watson-Lamprey, J., Abrahamson, N.A., Bommer, J.J., et al. (2006) An improved method of matching response spectra of recorded earthquake ground motion using wavelets. *Journal of earthquake engineering*. 10 (spec01), 67–89.

Harden, C.W. & Hutchinson, T.C. (2009) Beam-on-nonlinear-winkler-foundation modeling of shallow, rocking-dominated footinǵs. *Earthquake Spectra*. [Online] 25 (2), 277–300. Available from: doi:10.1193/1.3110482.

Harris, H.G. & Sabnis, G. (1999) *Structural Modeling and Experimental Techniques*. Taylor and Francis Group.

Harte, M., Basu, B. & Nielsen, S.R.K. (2012) Dynamic analysis of wind turbines including soil-structure interaction. *Engineering Structures*. [Online] 45, 509–518. Available from: doi:10.1016/j.engstruct.2012.06.041.

Haselton, M.G., Bryant, G.A., Wilke, A., Frederick, D.A., et al. (2009) Adaptive rationality: An evolutionary perspective on cognitive bias. *Social Cognition*. [Online] 27 (5), 733–763. Available from: doi:10.1521/soco.2009.27.5.733.

Hassani, N., Bararnia, M. & Ghodrati, G. (2018) Effect of soil-structure interaction on

inelastic displacement ratios of degrading structures. *Soil Dynamics and Earthquake Engineering*. [Online] 104 (September), 75–87. Available from: doi:10.1016/j.soildyn.2017.10.004.

Hatzigeorgiou, G.D. & Beskos, D.E. (2010) Soil – structure interaction effects on seismic inelastic analysis of 3-D tunnels. *Soil Dynamics and Earthquake Engineering*. [Online] 30 (9), 851–861. Available from: doi:10.1016/j.soildyn.2010.03.010.

Heib, M. Al, Emeriault, F., Caudron, M., Nghiem, L., et al. (2014) Large-scale soil-structure physical model (1g) - assessment of structure damages. *International Journal of Physical Modelling in Geotechnics,*. [Online] 12 (4), 138–152. Available from: http://dx.doi.org/10.1680/ijpmg.13.00007.

Helwany, S. (2007) *Applied Soil Mechanics with ABAQUS Applications*. Hoboken, New Jersey, John Wiley and Sons, Inc.

Helwany, S. (2009) *Applied Soil Mechanics with ABAQUS Applications*. [Online]. Hoboken, New Jersey, John Wiley & Sons; Inc. Available from: doi:10.1002/9780470168097.

Hibbitt, Karlsson, Sorensen & Inc (2012) *ABAQUS. ABAQUS/Standard User's Manual Volumes I–III and ABAQUS CAE Manual*. Pawtucket, USA: Dassault Systèmes.

Hussien, M.N., Tobita, T., Iai, S. & Karray, M. (2016) Soil-pile-structure kinematic and inertial interaction observed in geotechnical centrifuge experiments. *Soil Dynamics and Earthquake Engineering*. [Online] 89 (October), 75–84. Available from: doi:10.1016/j.soildyn.2016.08.002.

Iai, S. (1989) Similitude for Shaking Table Tests on Soil-Structure-Fluid Model in 1-g Gravitational Field. *Soils And Foundations, JSSMFE*. [Online] 29 (1), 105–118. Available from: http://www.mendeley.com/research/geology-volcanic-history-eruptive-style-yakedake-volcano-group-central-japan/.

Idriss, I.M. & Sun, J.I. (1993) *User's manual for SHAKE91 : a computer program for conducting equivalent linear seismic response analyses of horizontally layered soil deposits*. University of California Center for Geotechnical modeling Department of

Civil & Environmental Engineering (ed.). California , Berkeley, University of California, Davis. Center for Geotechnical Modeling.; Building and Fire Research Laboratory (U.S.).Structures Division.

Iervolino, I., Galasso, C. & Cosenza, E. (2010) REXEL: Computer aided record selection for code-based seismic structural analysis. *Bulletin of Earthquake Engineering*. [Online] 8 (2), 339–362. Available from: doi:10.1007/s10518-009-9146-1.

Iervolino, I., Giorgio, M. & Cito, P. (2019) Which earthquakes are expected to exceed the design spectra? *Earthquake Spectra*. [Online] 35 (3), 1465–1483. Available from: doi:10.1193/032318EQS066O.

Jahromi, H.Z., Izzuddin, B.A. & Zdravkovic, L. (2009) A domain decomposition approach for coupled modelling of nonlinear soil-structure interaction. *Computer Methods in Applied Mechanics and Engineering*. [Online] 198 (33–36), 2738–2749. Available from: doi:10.1016/j.cma.2009.03.018.

Jarernprasert, S., Bazan-zurita, E. & Bielak, J. (2013) Seismic soil-structure interaction response of inelastic structures. *Soil Dynamics and Earthquake Engineering*. [Online] 47 (April), 132–143. Available from: doi:10.1016/j.soildyn.2012.08.008.

Jarernprasert, S., Bazan-Zurita, E. & Bielak, J. (2013) Seismic soil-structure interaction response of inelastic structures. *Soil Dynamics and Earthquake Engineering*. [Online] 47 (April), 132–143. Available from: doi:10.1016/j.soildyn.2012.08.008.

Jaya, K.P. & Prasad, A.M. (2001) Dynamic behaviour of embedded and pile foundation in layered soil using cone models. *Géotechnique*. [Online] 54 (6), 399–414. Available from: doi:10.1680/geot.54.6.399.45426.

Jayaram, N., Baker, J.W., Okano, H., Ishida, H., et al. (2011) Correlation of response spectral values in Japanese ground motions. *Earthquake and Structures*. [Online] 2 (4), 357–376. Available from: doi:10.12989/eas.2011.2.4.357.

Jelinek, T., Zania, V. & Giuliani, L. (2017) Post-earthquake fire resistance of steel buildings. *Journal of Constructional Steel Research*. [Online] 138, 774–782. Available from: doi:10.1016/j.jcsr.2017.08.021.

Jennings, P.C. (1971) *Engineering features of the San Fernando earthquake of February 9, 1971*. [Online]. Available from: http://resolver.caltech.edu/CaltechEERL:1971.EERL-71-02.

Jonsson, D. (2014) *Quantities, Dimensions and Dimensional Analysis*. [Online] (August 2014). Available from: http://arxiv.org/abs/1408.5024.

Julián, C., Hugo, H.-B. & Astrid, R.-F. (2014) Analysis of the Earthquake-Resistant Design Approach for Buildings in Mexico. *Ingeniería, Investigación y Tecnología*. [Online] 15 (1), 151–162. Available from: doi:10.1016/s1405-7743(15)30013-5.

Kachadoorian, R. (1968) *Effects on Transportation and Utilities Alaska Highway System*.

Kana, D.D., Boyce, L. & Blaney, G.W. (1986) Development of a scale model for the dynamic interaction of a pile in clay. *Journal of Energy Resources Technology, Transactions of the ASME*. [Online] 108 (3), 254–261. Available from: doi:10.1115/1.3231274.

Karatzetzou, A. & Pitilakis, D. (2018) Reduction factors to evaluate acceleration demand of soil-foundation-structure systems. *Soil Dynamics and Earthquake Engineering*. [Online] 109 (July 2017), 199–208. Available from: doi:10.1016/j.soildyn.2018.03.017.

Karatzia, X. & Mylonakis, G. (2012) Horizontal response of piles in inhomogeneous soil: simple analysis. In: *Second International Conference on Performance-Based, Design in Earthquake Geotechnical Engineering*. 2012 Taormina, Italy. pp. 1–16.

Kausel, E. (2010) Early history of soil – structure interaction. *Soil Dynamics and Earthquake Engineering*. [Online] 30 (9), 822–832. Available from: doi:10.1016/j.soildyn.2009.11.001.

Kaynia, A.M. & Kausel, E. (1991) Dynamics of piles and pile groups in layered soil media. *Soil Dynamics and Earthquake Engineering*. 10 (8), 386–401.

Kelly, D. (2006) Seismic site classification for structural engineers. *Structure Magazine*. 21–24.

Kennedy, R.P. (1980) Ground motion parameter useful in structural design. In: *Evaluation of Regional Seismic Hazards and Risk,Conference*. 1980 Santa Fe, New Mexico. p.

Khalil, L. & Shahrour, I. (2007) Influence of the soil–structure interaction on the fundamental period of buildings. *Earthquake Engineering and Engineering Vibration Structural Dynamics*. [Online] 36 (15), 2445–2453. Available from: doi:10.1002/eqe.738.

Khodair, Y. & Abdel-Mohti, A. (2014) Numerical Analysis of Pile–Soil Interaction under Axial and Lateral Loads. *International Journal of Concrete Structures and Materials*. [Online] 8 (3), 239–249. Available from: doi:10.1007/s40069-014-0075-2.

Khoshnoudian, F., Ahmadi, E. & Kiani, M. (2015) Collapse capacity of soil-structure systems under pulse-like earthquakes. *Earthquake Engineering and Structural Dynamics*. [Online] 44 (October), 481–490. Available from: doi:10.1002/eqe.

Khosravikia, F., Mahsuli, M. & Ghannad, M.A. (2017a) Probabilistic evaluation of 2015 NEHRP soil-structure interaction provisions. *Journal of Engineering Mechanics*. [Online] 143 (9), 1–11. Available from: doi:10.1061/(ASCE)EM.1943-7889.0001274.

Khosravikia, F., Mahsuli, M. & Ghannad, M.A. (2017b) Probabilistic Evaluation of 2015 NEHRP Soil-Structure Interaction Provisions. *Journal of Engineering Mechanics*. [Online] 143 (9), 04017065. Available from: doi:10.1061/(asce)em.1943-7889.0001274.

Kim, N.H. (2015) *Introduction to nonlinear finite element analysis*. [Online]. Available from: doi:10.1007/978-1-4419-1746-1.

Kline, S.J. (1986) *Similitude and Approximation Theory*. Stanford,U.S.A, Springer-Verlag, Berlin Heidelberg New York Tokyo.

Kotronis, P., Tamagnini, C. & Grange, S. (2013) *Soil-Structure Interaction*. [Online]. Available from: http://alerteomaterials.eu.

Krajcinovic, D. & Lemaitre, J. (1987) *Continuum Damage Mechanics Theory and Application*. [Online]. New York, Springer-Verlag, Berlin Heidelberg New York Tokyo. Available from: doi:10.1007/978-3-7091-2806-0.

Kramer, S.L. (2014) Performance-based design methodologies for geotechnical earthquake engineering. *Bulletin of Earthquake Engineering*. 12 (3), 1049–1070.

Küçükarslan, S., Banerjee, P.K., Bildik, N. & Bildik, N. (2003) Inelastic analysis of pile soil structure interaction. *Engineering Structures*. [Online] 25 (9), 1231–1239. Available from: doi:10.1016/S0141-0296(03)00083-X.

kulhawy, F. & Chen, Y. (1995) A Thirty Year Perspective of Broms' Lateral Loading Models, as Applied to Drilled Shafts. In: *Bengt Broms Symposium in Geotechical Enginerring*. 1995 Singapore. pp. 225–240.

Kutanis, M. & Elmas, M. (2001) Non-linear seismic soil-structure interaction analysis based on the substructure method in the time domain. *Turkish Journal of Engineering and Environmental Sciences*. 25 (6), 617–626.

Labuz, J.F. & Zang, A. (2012) *Mohr-Coulomb failure criterion*. [Online]. Available from: doi:10.1007/s00603-012-0281-7.

Lade, P. V. (2005) Overview of constitutive models for soils. *Geotechnical Special Publication*. [Online] 40771 (128), 1–34. Available from: doi:10.1061/40786(165)1.

van Lanen, X. & Mooney, W.D. (2007) Integrated geologic and geophysical studies of North American continental intraplate seismicity. In: Seth Stein & Stéphane Mazzotti (eds.). *Continental Intraplate Earthquakes: Science, Hazard, and Policy Issues*. [Online]. Geological Society of America. p. 0. Available from: doi:10.1130/2007.2425(08).

Langhaar, H. (1951) *Dimensional Analysis And Theory Of Models*. London, John Wiley & Sons; Inc.

Langhaar, H.L. (1980) *Dimensional Analysis Theory Models*. 13th edition. Krieger Pub Company.

Lansing, E. (2007) *Performance-based Fire Safety Design*. [Online] 17 (November). Available from: doi:10.1177/1042391507077198.

Lawson, A.C., Leuschner, A. 0., Gilbert, G.K., Davidson, G., et al. (1990) The California Earthquake of April 18, 1906. *Bulletin of the American Geographical Society*. [Online]. 42 (2). Available from: doi:10.2307/199583.

Lee, J.H. (2018) Nonlinear soil-structure interaction analysis in poroelastic soil using mid-point integrated finite elements and perfectly matched discrete layers. *Soil Dynamics and Earthquake Engineering*. [Online] 108 (January), 160–176. Available from: doi:10.1016/j.soildyn.2018.01.043.

Lew, H.S., Leyendecker, E. V. & Dikkers, R.D. (1971) *Engineering Aspects of the 1971 San Fernando Earthquake*.

Li, S., Zhang, F., Wang, J., Alam, M.S., et al. (2017) Seismic responses of super-span cable-stayed bridges induced by ground motions in di ff erent sites relative to fault rupture considering soil-structure interaction. *Soil Dynamics and Earthquake Engineering*. [Online] 101 (September 2016), 295–310. Available from: doi:10.1016/j.soildyn.2017.07.016.

Lin, Y., Zong, Z., Bi, K., Hao, H., et al. (2020) Experimental and numerical studies of the seismic behavior of a steel-concrete composite rigid-frame bridge subjected to the surface rupture at a thrust fault. *Engineering Structures*. [Online] 205 (July 2019), 110105. Available from: doi:10.1016/j.engstruct.2019.110105.

Martakis, P., Taeseri, D., Chatzi, E. & Laue, J. (2017) *A centrifuge-based experimental veri fi cation of Soil-Structure Interaction e ff ects*. [Online] 103 (September), 1–14. Available from: doi:10.1016/j.soildyn.2017.09.005.

MATLAB (2020) *Version 20 (2020)*. Natick, Massachusetts, The MathWorks Inc.

Matsui, T. & Oda, K. (1996) Foundation damage of structures. *Soils and Foundations*. [Online] (Special), 189–200. Available from: doi:10.3208/sandf.36.special_189.

May, M. & Malhotra, S. (2010) *Seismic Soil-Pile Interaction : Physical Processes and Analytical Models*.

McKenna, F.T. (1997) *Object-oriented finite element programming: Frameworks for analysis, algorithms and parallel computing*. [Online]. University of California,Berkeley. Available from: doi:10.1017/CBO9781107415324.004.

Mekki, M., Elachachi, S.M., Breysse, D. & Zoutat, M. (2016) Seismic behavior of R . C . structures including soil-structure interaction and soil variability effects. *Engineering Structures*. [Online] 126, 15–26. Available from: doi:10.1016/j.engstruct.2016.07.034.

Memari, M., Mahmoud, H. & Ellingwood, B. (2014) Post-earthquake fire performance of moment resisting frames with reduced beam section connections. *Journal of Constructional Steel Research*. [Online] 103, 215–229. Available from: doi:10.1016/j.jcsr.2014.09.008.

Mendoza, M.J. & Auvinet, G. (1988) The Mexico Earthquake of September 19, 1985— Behavior of Building Foundations in Mexico City. *Earthquake Spectra*. [Online] 4 (4), 835–853. Available from: doi:https://doi.org/10.1193/1.1585505.

Menétrey, P. & William, K.J. (1995) Triaxial Failure Criterion for Concrete and its Generalization. *ACI Structural Journal*. 92 (3), 311.

Menglin, L., Huaifeng, W., Xi, C. & Yongmei, Z. (2011) Structure – soil – structure interaction : Literature review. *Soil Dynamics and Earthquake Engineering*. [Online] 31 (12), 1724–1731. Available from: doi:10.1016/j.soildyn.2011.07.008.

Meymand, P.J. (1998a) *Shaking table scale model tests of nonlinear soil-pile-superstructure interaction in soft clay*. [Online]. Available from: http://nisee.berkeley.edu/meymand/files/intro.pdf.

Meymand, P.J. (1998b) *Shaking table scale model tests of nonlinear soil-pile-superstructure interaction in soft clay*. [Online]. University of California, Berkeley. Available from: http://nisee.berkeley.edu/meymand/files/intro.pdf.

Meymand, P.J., Riemer, M.F. & Seed, R.B. (2000) Large scale shaking table tests of seismic soil-pile interaction in soft clay. In: *12th World Conference on Earthquake Engineering*. 2000 p. 2817.

Michel, P., Butenweg, C. & Klinkel, S. (2018) Pile-grid foundations of onshore wind turbines considering soil-structure- interaction under seismic loading. *Soil Dynamics and Earthquake Engineering*. [Online] 109 (March), 299–311. Available from: doi:10.1016/j.soildyn.2018.03.009.

Miguel, L.F.F. & Riera, J.D. (2013) Loads induced on tall structures by thunderstorm winds in temperate Latitudes. *Safety, Reliability, Risk and Life-Cycle Performance of Structures and Infrastructures - Proceedings of the 11th International Conference on Structural Safety and Reliability, ICOSSAR 2013*. [Online] (April 2015), 5579–5584. Available from: doi:10.1201/b16387-811.

Milev, J. (2016) Problems and their solutions in practical application of Eurocodes in seismic design of RC structures. *Gradjevinski materijali i konstrukcije*. [Online] 59 (3), 3–25. Available from: doi:10.5937/grmk1603003m.

Miranda, E. & Bertero, V. V (1994) Evaluation of Strength Reduction Factors for Earthquake-Resistant Design. *Earthquake Spectra*. [Online] 10 (2), 357–379. Available from: doi:10.1193/1.1585778.

Mitropoulou, C.C., Kostopanagiotis, C., Kopanos, M., Ioakim, D., et al. (2016) Influence of soil-structure interaction on fragility assessment of building structures. *Structures*. [Online] 6 (May), 85–98. Available from: doi:10.1016/j.istruc.2016.02.005.

Moncarz, P. & Krawinkler, H. (2006a) *Theory and Application of Experimental Model Analysis in Earthquake Engineering,*. (50).

Moncarz, P.D. & Krawinkler, H. (2006b) *Theory and Application of Expermental Model Ananlysis in Earthquake Engineering*. Stanford ,USA, The John A. Blume Earthquake Engineering Centre.

Mousavi, S., Bagchi, A. & Kodur, V.K.R. (2008) Review of post-earthquake fire hazard to building structures. *Canadian Journal of Civil Engineering*. [Online] 698 (November), 689–698. Available from: doi:10.1139/L08-029.

Murugan, R., V., P.R. & P. R., T. (2013) Establishment of structural similitude for elastic models and validation of scaling laws. *KSCE Journal of Civil Engineering*.

[Online] 17 (January 2013), 139–144. Available from: doi:https://doi.org/10.1007/s12205-013-1216-x.

Mylonakis, G. (2015) *Contributions to Static and Seismic Analysis of Piles and Pile-Supported Bridge Piers*. State University of New York At Buffalo.

Mylonakis, G. & Gazetas, G. (2000a) Seismic soil-structure interaction: beneficial or detrimental? *Journal of Earthquake Engineering*. 4 (3), 277–301.

Mylonakis, G. & Gazetas, G. (2000b) Seismic soil-structure interaction: beneficial or detrimental? *Journal of earthquake engineering*. 4 (3), 277–301.

Mylonakis, G. & Gazetas, G. (2000c) *Seismic soil-structure interaction: beneficial or detrimental?* 4 (3), 277–301.

Mylonakis, G. & Gazetas, G. (2000d) Seismic soil-structure interaction: Beneficial or detrimental? *Journal of Earthquake Engineering*. [Online] 4 (3), 277–301. Available from: doi:10.1080/13632460009350372.

Mylonakis, G., Nikolaou, A. & Gazetas, G. (1997) Soil-pile-bridge seismic interaction: Kinematic and inertial effects. Part I: Soft soil. *Earthquake Engineering and Structural Dynamics*. [Online] 26 (3), 337–359. Available from: doi:10.1002/(SICI)1096-9845(199703)26:3<337::AID-EQE646>3.0.CO;2-D.

Mylonakis, G., Nikolaou, S. & Gazetas, G. (2006a) Footings under seismic loading : Analysis and design issues with emphasis on bridge foundations. *Soil Dynamics and Earthquake Engineering*. [Online] 26 (9), 824–853. Available from: doi:10.1016/j.soildyn.2005.12.005.

Mylonakis, G., Nikolaou, S. & Gazetas, G. (2006b) Footings under seismic loading: Analysis and design issues with emphasis on bridge foundations. *Soil Dynamics and Earthquake Engineering*. 26 (9), 824–853.

Nader, A. (2014) *Engineering Characteristics of Sensitive Marine Clays - Examples of Clays in Eastern Canada*. University Of Ottawa/Faculty of Engineering.

Nakakuki, S. (1986) NII-Electronic Library Service. *Chemical and Pharmaceutical Bulletin*. 34 (1), 430–433.

NEHRP (2012) *Soil-Structure Interaction for Building Structures*. California , Berkeley.

Newmark, N.M. & Hall, W.J. (1972) Seismic Design Criteria for Nuclear Reactor Facilities. *Pressure Vessels Piping Design Anal*.2 pp.1414–1427.

Van Nguyen, Q., Fatahi, B. & Hokmabadi, A.S. (2017) Influence of size and load-bearing mechanism of piles on seismic performance of buildings considering soil–pile–structure interaction. *International Journal of Geomechanics*. 17 (7), 4017007.

Nguyen, Q. Van, Fatahi, B. & Hokmabadi, A.S. (2016) *The effects of foundation size on the seismic performance of buildings considering the soil-foundation-structure interaction*. 58 (6), 1045–1075.

Nikolaou, S., Mylonakis, G., Gazetas, G. & Tazoh, T. (2001) Kinematic pile bending during earthquakes: analysis and field measurements. *Geotechnique*. 51 (5), 425–440.

Nimtaj, A. & Bagheripour, M.H. (2013) Non-linear seismic response analysis of the layered soil deposit using hybrid frequency – time domain (HFTD) approach. *European Journal of Environmental and Civil Engineering*. [Online] 17 (10), 1039–1056. Available from: doi:10.1080/19648189.2013.844205.

Nishizawa, T., Tajiri, S. & Kawamura, S. (1984) Excavation and Response Analysis of a Damaged RC Piles by Liquefaction. *8th World Conf. Earthquake Eng., San Francisco*. 3, 593–600.

Nova, R. & Montrasio, L. (1991) Settlements of shallow foundations on sand. *Géotechnique*. [Online] 41 (2), 243–256. Available from: doi:10.1680/geot.1991.41.2.243.

Novak, M. (1991a) Piles under dynamic loads. In: *Proceedings: Second International Conference on Recent Advances in Geotechnical Earthquake Engineering and Soil Dynamics*. [Online]. 1991 pp. 2433–2456. Available from: https://mospace.umsystem.edu/xmlui/handle/10355/42505.

Novak, M. (1991b) Piles Under Dynamic Loads. In: *2nd International conference on*

Recent Advances in Geotechnical Engineering and Soil Dynamic. 1991 St. Louis. pp. 2433–2456.

Özdemir, H. (1976) *Nonlinear transient dynamic analysis of yielding structures /*. University of California, Berkeley.

Pals, A. & Kausel, E. (1988) Approximate formulas for dynamic stiffnesses of rigid foundations. *Soil Dynamics and Earthquake Engineering*. 7 (4), 213–227.

Pantosti, D., Pucci, S., Palyvos, N., De Martini, P.M., et al. (2008) Paleoearthquakes of the Düzce fault (North Anatolian Fault Zone): Insights for large surface faulting earthquake recurrence. *Journal of Geophysical Research: Solid Earth*. [Online] 113 (1), 1–20. Available from: doi:10.1029/2006JB004679.

Papadopoulos, M., Beeumen, R. Van, François, S., Degrande, G., et al. (2017a) Computing the modal characteristics of structures considering soil-structure interaction effects. *Procedia Engineering*. [Online] 199, 2414–2419. Available from: doi:10.1016/j.proeng.2017.09.296.

Papadopoulos, M., Beeumen, V., Franc, S., Degrande, G., et al. (2017b) Computing the modal characteristics of structures considering soil-structure interaction effects. *Procedia Engineering*. [Online] 199, 2414–2419. Available from: doi:10.1016/j.proeng.2017.09.296.

Phanikanth, V.S., Choudhury, D. & Reddy, G.R. (2013a) Behavior of single pile in liquefied deposits during earthquakes. *International Journal of Geomechanics*. [Online] 13 (4), 454–462. Available from: doi:10.1061/(ASCE)GM.1943-5622.0000224.

Phanikanth, V.S., Choudhury, D. & Reddy, G.R. (2013b) Behavior of Single Pile in Liquefied Deposits during Earthquakes. *International Journal of Geomechanics*. [Online] 13 (4), 454–462. Available from: doi:10.1061/(asce)gm.1943-5622.0000224.

Pitilakis, D., Dietz, M., Wood, D.M., Clouteau, D., et al. (2008) Numerical simulation of dynamic soil-structure interaction in shaking table testing. *Soil Dynamics and Earthquake Engineering*. [Online] 28 (6), 453–467. Available from:

doi:10.1016/j.soildyn.2007.07.011.

Pitilakis, K., Gazepis, C. & Anastasiadis, A. (2004) Design Response Spectra and Soil Classification for Seismic Code Provisions. *13th World Conference on Earthquake Engineering*. (2904), 1–15.

Pontbriand, C. (2014) *The Great Alaska Earthquake of 1964 and Its Legacy*.

Potts, D.M. & Zdravković, L. (2001) *Finite Element Analysis in Geotechnical Engineering: Volume two - Application*. [Online]. London, UK, Thomas Telford Publishing. Available from: doi:doi:10.1680/feaigea.27831.

Poulos, H.G. (1980) An Approach for the Analysis of Offshore Pile Groups. In: *1st International Conference on Numerical Methods in Offshore Piling*. 1980 London. pp. 119–126.

Poulos, H.G. (1971a) Behavior of Laterally Loaded Piles: I-Single Piles. *Journal of the Soil Mechanics and Foundations Division*. 97 (5), 711–731.

Poulos, H.G. (1971b) Behavior of Laterally Loaded Piles: II-Pile Groups. *Journal of the Soil Mechanics and Foundations Division*. 97 (5), 733–751.

Rahmani, A., Taiebat, M., Finn, W.D.L. & Ventura, C.E. (2016) Evaluation of substructuring method for seismic soil-structure interaction analysis of bridges Evaluation of substructuring method for seismic soil-structure interaction analysis of bridges. *Soil Dynamics and Earthquake Engineering*. [Online] 90 (October 2018), 112–127. Available from: doi:10.1016/j.soildyn.2016.08.013.

Rajapakse, R. (2016) *Laterally loaded piles*. [Online]. Available from: doi:10.1016/b978-0-12-804202-1.00017-6.

Ramadan, O.M.O., Mehanny, S.S.F. & Kotb, A.A.M. (2020) Assessment of seismic vulnerability of continuous bridges considering soil-structure interaction and wave passage effects. *Engineering Structures*. [Online] 206 (August 2019), 110161. Available from: doi:10.1016/j.engstruct.2019.110161.

Raoul, J., Sedlacek, G., Tsionis, G., Raoul, J., et al. (2012) *Eurocode 8 : Seismic Design of Buildings Worked examples*. [Online]. Available from: doi:10.2788/91658.

Ravazi, S.A., Fakher, A. & Mirghaderi, S.R. (2007) An insight into the bad reputation of batter piles in seismic performance of wharves. In: *Proceedings of the 4th International Conference on Earthquake Geotechnical Engineering*. 2007 pp. 1–10.

Raychowdhury, P. (2011) Seismic response of low-rise steel moment-resisting frame (SMRF) buildings incorporating nonlinear soil – structure interaction (SSI). *Engineering Structures*. [Online] 33 (3), 958–967. Available from: doi:10.1016/j.engstruct.2010.12.017.

Raychowdhury, P. & Hutchinson, T.C. (2009a) *Performance evaluation of a nonlinear Winkler-based shallow foundation model using centrifuge test results*. [Online] (March), 679–698. Available from: doi:10.1002/eqe.

Raychowdhury, P. & Hutchinson, T.C. (2009b) Performance evaluation of a nonlinear Winkler-based shallow foundation model using centrifuge test results. *Earthquake Engineering and Structural Dynamics*. [Online] March (38), 679–698. Available from: doi:10.1002/eqe.902.

Real, P.V. (2014) *EN 1993-1-2 Resistance of members and connections to fire*. Brussels, European committee for standardization.

Reese, L.C. & Wang, S.T. (1994) Analysis of Piles Under Lateral Loading with Nonlinear Flexural Rigidity. In: *International Conference on Design and Construction of Deep Foundations.* 1994 pp. 842–856.

Reza, H. & Fatahi, B. (2014) Idealisation of soil – structure system to determine inelastic seismic response of mid-rise building frames. *Soil Dynamics and Earthquake Engineering*. [Online] 66, 339–351. Available from: doi:10.1016/j.soildyn.2014.08.007.

Rocha, M. (1953) Similarity conditions in model studies of soil mechanics problems. In: *prepared to be distributed to the members of the 3th International Conference on Soil Mechanics and Foundation Engineering*. 1953 Zurich, Lisboa, Laboratorio Nacional de Engenharia Civil. p.

Rocha, M. (1958) The Possibility of Solving Soil Mechanics Problems by the use of

Models. *Laboratório Nacional De Engenharia Civil*. (77), 6.

Rocscience (2018) *Laterally Loaded Piles*.

Rodrigues, H., Arêde, A., Varum, H. & Costa, A. (2013) Damage evolution in reinforced concrete columns subjected to biaxial loading. *Bulletin of Earthquake Engineering*. [Online] 11 (5), 1517–1540. Available from: doi:10.1007/s10518-013-9439-2.

Roesset, J.M. (1984) Dynamic Stiffness of Pile Groups. In: *Analysis and Design of Pile Foundations*. 1984 Austin, ASCE. pp. 263-286.

Roesset, J.M. (2013) *Soil Structure Interaction The Early Stages*. 16 (1), 1–8.

Roesset, J.M. & Angelides, D. (2015) *Numerical methods in offshore piling, 10. Dynamic stiffness of piles*. London, Published Online: July 07, 2015 ©The Institution of Civil Engineers.

Romo, M.P., Mendoza, M.J. & García, S.R. (2000) Geotechnical factors in seismic design of foundations state-of-the-art report. *Bulletin of the New Zealand Society for Earthquake Engineering*. 33 (3), 347–370.

Ronagh, H.R. & Behnam, B. (2012) Investigating the Effect of Prior Damage on the Post-earthquake Fire Resistance of Reinforced Concrete Portal Frames. *International Journal of Concrete Structures and Materials*. [Online] 6 (4), 209–220. Available from: doi:10.1007/s40069-012-0025-9.

Roscoe, K.H. (1968) Soils and model tests. *Journal of Strain Analysis*. [Online] 3 (1), 57–64. Available from: doi:10.1243/03093247v031057.

Ross, G., Seed, H. & Migliacio, R. (1973) *Performance of Highway Bridge Foundations, in The Great Alaska Earthquake of 1964*.

Sabetta, F. & Bommer, J. (2002) Modification of the spectral shapes and subsoil conditions in Eurocode 8. In: *12th European Conference on Earthquake Engineering*. 1 January 2002 London, UK, Published by Elsevier Science Ltd. p. N° 518.

Sáez, E., Lopez-caballero, F. & Modaressi-farahmand-razavi, A. (2013) Inelastic dynamic soil – structure interaction effects on moment-resisting frame buildings. *Engineering Structures*. [Online] 51, 166–177. Available from: doi:10.1016/j.engstruct.2013.01.020.

Schellart, W.P. & Strak, V. (2016) A review of analogue modelling of geodynamic processes: Approaches, scaling, materials and quantification, with an application to subduction experiments. *Journal of Geodynamics*. [Online] 100, 7–32. Available from: doi:10.1016/j.jog.2016.03.009.

Schmertman, J. (1978) *Guidelines for cone penetration test, performance and design*. [Online]. Available from: https://rosap.ntl.bts.gov/view/dot/958.

Schofield, A.N. (1993) Original Cam-clay. *International Conference on Soft Soil Engineering*.259 (November).

Scott, R.F. (1989) Centrifuge and modeling technology: A survey. *Revue française de géotechnique*. [Online] 48, 15–34. Available from: https://resolver.caltech.edu/CaltechAUTHORS:20140611-132033693.

Seed, H.. & Whitman, R.V. (1970) Design of Earth Retaining Structures for Dynamic Loads. In: *ASCE Specialty Conference, Lateral Stresses in the Ground and Design of Earth Retaining Structures*. 1970 Cornell University., Ithaca, New York. pp. 103–147.

Seed, H.B. & Idriss, I.M. (1967) Analysis of Soil Liquefaction: Niigata Earthquake. *Journal of the Soil Mechanics and Foundations Division*. 93 (3), 83–108.

Seed, R.B., Dickenson, S.E., Riemer, M.F., Bray, J.D., et al. (1990a) *Preliminary Report on the Principal Geotechnical Aspects of the October 17 , 1989 Loma Prieta Earthquake*. (April).

Seed, R.B., Dickenson, S.E., Riemer, M.F., Bray, J.D., et al. (1990b) *Preliminary Report on the Principal Geotechnical Aspects of the October 17 , 1989 Loma Prieta Earthquake*. (April).

SEI/ASCE 7-02 (2013) *ASCE 7: Minimum Design Loads for Buildings and Other*

Structures. Second Edi. Reston, Virginia, Published by the American Society of Civil Engineers.

SEI/ASCE 7-05 (2013) *Minimum Design Loads for Buildings and Other Structures*. [Online]. Reston, Virginia. Available from: doi:10.1061/9780784412916.

SeismoSoft. (2020) Manual and program description of the program SeismoStruct. *Online*.

Siller, H.R.E. (2004) *Non-Linear Modal Analysis Methods For Engineering Structures*.

Simitses, J. (1992) *Structural Similitude And Scaling Laws for Laminated Beam-Plates*.

Smith, M. (2018a) *ABAQUS/Standard User's Manual, Version 2018*. Providence, Rhode Island, United States, dassault systemes simulia corporation.

Smith, M. (2018b) *ABAQUS/Standard User's Manual, Version 2018*.p.1146.

Sokolov, V. & Wenzel, F. (2014) On the modeling of ground-motion field for assessment of multiple-location hazard, damage, and loss: Example of estimation of electric network performance during scenario earthquake. *Natural Hazards*. [Online] 74 (3), 1555–1575. Available from: doi:10.1007/s11069-014-1262-9.

Solberg, J.M., Hossain, Q. & Mseis, G. (2016) Nonlinear time-domain soil – structure interaction analysis of embedded reactor structures subjected to earthquake loads. *Nuclear Engineering and Design*. [Online] 304, 100–124. Available from: doi:10.1016/j.nucengdes.2016.04.026.

Solomos, G., Pinto, A. & Dimova, S. (2008) *A Review of the seismic Hazard Zonation in National Building Codes in the Context of Eurocode 8*. [Online] 82. Available from: moz-extension://9f963504-c2d6-4d80-85be-64863a58ac0c/enhanced-reader.html?openApp&pdf=https%3A%2F%2Feurocodes.jrc.ec.europa.eu%2Fdoc%2FEUR23563EN.pdf.

Sorace, S. (2012) Dissipative Bracing-Based Seismic Retrofit of R/C School Buildings. *The Open Construction and Building Technology Journal*. [Online] 6 (1), 334–345. Available from: doi:10.2174/1874836801206010334.

Stacul, S., Squeglia, N. & Morelli, F. (2017) Laterally loaded single pile response considering the influence of suction and non-linear behaviour of reinforced concrete sections. *Applied Sciences (Switzerland)*. [Online] 7 (12). Available from: doi:10.3390/app7121310.

Stefanidou, S.P., Sextos, A.G., Kotsoglou, A.N., Lesgidis, N., et al. (2017) Soil-structure interaction effects in analysis of seismic fragility of bridges using an intensity-based ground motion selection procedure. *Engineering Structures*. [Online] 151, 366–380. Available from: doi:10.1016/j.engstruct.2017.08.033.

Stone, W.C. & Yokel, F.Y. (1987) *Engineering Aspects of the September 19, 1985 Mexico Earthquake*. (165).

Stromblad, N. (2014) *Modeling of Soil and Structure Interaction Subsea*. Chalmers University of Technology,Sweden.

Šuklje, L. (1969) *Rheological aspects of soil mechanics.* London, Wiley-Interscience,A division of John Wiley & Sons Ltd.

Sun, J.I., Golesorkhi, R. & Seed, H.B. (1990) *Dynamic Moduli And Damping Ratios for Cohesive Soils*.29 (2).

Szücs, E. (1980) *Similitude and Modelling*. Amsterdam-Oxford-New York, Elsevier Scientific Publishing Company.

Tang, L., Ling, X., Xu, P., Gao, X., et al. (2010) Shake table test of soil-pile groups-bridge structure interaction in liquefiable ground. *Earthquake Engineering and Engineering Vibration*. [Online] 9 (1), 39–50. Available from: doi:10.1007/s11803-009-8131-7.

Taranath, B.S. (2016) *Earthquake Effects on Buildings*. [Online]. Available from: doi:10.1201/9781315374468-4.

Thomas, J.M., Gajan, S. & Kutter, B.L. (2005) *Soil-Foundation-Structure Interaction : Shallow Foundations . Centrifuge Data Report for the SSG04 Test Series .* (September).

Tipsunavee, T. & Arangjelovski, G. (2015) *Three Dimensional Analysis of Soil-Pile-*

Structure Interaction Problem in Soft Clay Simulation of Shaking Table Test. In: 2015 pp. 1–6.

Tokimatsu, K. & Asaka, Y. (1998) Effects of Liquefaction-Induced Ground Displacements on Pile Performance in the 1995 Hyogoken-Nambu Earthquake. *Soils and Foundations*. [Online] 38 (Special), 163–177. Available from: doi:10.3208/sandf.38.special_163.

Tokimatsu, K., Mizuno, H. & Kakurai, M. (1996) Building damage associated with geotechnical problems. *Soils and Foundations*. [Online] (Special), 219–234. Available from: doi:10.3208/sandf.36.special_219.

Tokimatsu, K., Oh-oka, H., Satake, K., Shamoto, Y., et al. (1998) Effects of Lateral Ground Movements on Failure Patterns of Piles in the 1995 Hyogoken-Nambu Earthquake. In: *3rd Geotechnical Earthquake Engineering and Soil Dynamics*. 1998 pp. 1175–1186.

Tomeo, R., Bilotta, A., Pitilakis, D. & Nigro, E. (2017) Soil-structure interaction effects on the seismic performances of reinforced concrete moment resisting frames. *Procedia Engineering*. [Online] 199, 230–235. Available from: doi:10.1016/j.proeng.2017.09.006.

Trifunac, M.D. & Brady, A.G. (1976) A study on the duration of strong earthquake ground motion. *International Journal of Rock Mechanics and Mining Sciences & Geomechanics Abstracts*. [Online] 13 (3), 28. Available from: doi:10.1016/0148-9062(76)90487-3.

Turner, B.J., Brandenberg, S.J. & Stewart, J.P. (2017) *Influence of kinematic SSI on foundation input motions for bridges on deep foundations*. California, Berkeley, Pacifi c Earthquake Engineering Research Center.

U.S. Geological Survey (2018) *PEER Ground Motion Database*. [Online]. 2018. Pacific Earthquake Engineering Research Centre. Available from: https://ngawest2.berkeley.edu/.

Ülker-Kaustell, M., Karoumi, R. & Pacoste, C. (2010) Simplified analysis of the dynamic soil-structure interaction of a portal frame railway bridge. *Engineering*

Structures. [Online] 32 (11), 3692–3698. Available from: doi:10.1016/j.engstruct.2010.08.013.

Usmani, A., Zhang, J., Jiang, J., Jiang, Y., et al. (2012) Using opensees for structures in fire. *Journal of Structural Fire Engineering*. [Online] 3 (1), 57–70. Available from: doi:10.1260/2040-2317.3.1.57.

Usmani, A., Zhang, J., Jiang, J., Jiang, Y., et al. (2010) Using OpenSees for structures in fire. *Journal of Structural Fire Engineering*. 3 (1), 919–926.

Varghese, R.M. & Madhavi Latha, G. (2014) Shaking table tests to investigate the influence of various factors on the liquefaction resistance of sands. *Natural Hazards*. [Online] 73 (3), 1337–1351. Available from: doi:10.1007/s11069-014-1142-3.

Venanzi, I., Salciarini, D. & Tamagnini, C. (2014) The effect of soil – foundation – structure interaction on the wind-induced response of tall buildings. *Engineering Structures*. [Online] 79, 117–130. Available from: doi:10.1016/j.engstruct.2014.08.002.

Vucetic, M. & Dobry, R. (1991) Effect of Soil Plasticity on Cyclic Response. *Journal of Geotechnical Engineering*. [Online] 117 (1). Available from: https://doi.org/10.1061/(ASCE)0733-9410(1991)117:1(89).

Waller, R.M. & Stanley, K.W. (1966) Effects of the earthquake of March 27, 1964, in the Homer Area, Alaska. *Geological Survey Professional Paper*. 542-D, 34.

Wang, S.T. & Reese, L.C. (1993) *COM624P: Laterally Loaded Pile Analysis Program for the Microcomputer.* p.510.

Wolf, J. & Hall, W. (1988) Soil-structure-interaction analysis in time domain. *Nuclear Engineering and Design*. [Online] 111 (1989), 381–393. Available from: doi:https://doi.org/10.1016/0029-5493(89)90249-5.

Wolf, J.P. (1991) Classification of Analysis Methods for Dynamic Soil-Structure Interaction. In: *International Conferences on Recent Advances in Geotechnical Earthquake Engineering and Soil Dynamics*. 1991 p.

Wolf, J.P. (1985) *Dynamic soil-structure interaction*.

Wolf, J.P. (1995) Simple Physical Models for Foundation Dynamics. In: *Third international conference on recent advances in geotechnical earthquake engineering & soil dynamics*. 1995 Missouri. pp. 943–984.

Wolf, J.P. & Von Arx, G.A. (1978) Impedance Functions of a Group of Vertical Piles. In: *Volume I of Earthquake Engineering and Soil Dynamics-Proceedings of the ASCE Geotechnical Engineering Division Specialty Conference*. 1978 Pasadena, California, American Society of Civil Engineers. pp. 1024–1041.

Wood, H.O. (1908) *"Distribution of Apparent Intensity in San Francisco," in The California Earthquake of April 18, 1906*. [Online]. Available from: doi:10.3133/pp941A.

Xiong, Y.-C. & Mao, J.-H. (2019) Bearing Behaviour of Single Under Impact and Static Loads. *Journal of Architecture and Civil Engineering*. 36 (2), 116–126.

Yan, G., Shen, Y., Gao, B., Zheng, Q., et al. (2020) Damage evolution of tunnel lining with steel reinforced rubber joints under normal faulting: An experimental and numerical investigation. *Tunnelling and Underground Space Technology*. [Online] 97 (May), 103223. Available from: doi:10.1016/j.tust.2019.103223.

Yang, J., Li, P. & Lu, Z. (2019) Large-scale shaking table test on pile-soil-structure interaction on soft soils. *Structural Design of Tall and Special Buildings*. [Online] 28 (18), 1–19. Available from: doi:10.1002/tal.1679.

Yashinsky, M. (1998) The Loma Prieta, California, earthquake of October 17, 1989: performance of the built environment. Highway systems. *US Geological Survey Professional Paper*. [Online] (1552 B). Available from: doi:10.3133/pp1552b.

Yoshida, N. & Hamada, M. (1990) Damage to Foundation Piles and Deformation Pattern of Ground due to Liquefaction-Induced Permanent Ground Deformations. In: *3rd Japan-U.S. Workshop on Earthquake Resistant Design of Lifeline Facilities and Countermeasures for Soil Liquefaction*. 1990 pp. 147–161.

Yoshida, N., Tazoh, T., Wakamatsu, K., Yasuda, S., et al. (2007) Causes of showa

bridge collapse in the 1964 niigata earthquake based on eyewitness testimony. *Soils and Foundations*. [Online] 47 (6), 1075–1087. Available from: doi:10.3208/sandf.47.1075.

Yue, M.G. & Wang, Y.Y. (2009) Soil-structure interaction of high-rise building resting on soft soil. *Electronic Journal of Geotechnical Engineering*. 14 D (2002).

Zaharia, R. & Pintea, D. (2009) Fire after Earthquake Analysis of Steel Moment Resisting Frames. *International Journal of Steel Structures*. 9 (4), 275–284.

Zangeneh, A., Svedholm, C., Andersson, A. & Pacoste, C. (2018) *Identi fi cation of soil-structure interaction e ff ect in a portal frame railway bridge through full-scale dynamic testing*. [Online] 159 (October), 299–309. Available from: doi:10.1016/j.engstruct.2018.01.014.

Zdravković, L. & Potts, D.M. (2020) Keynote Lecture: Application of Advanced Numerical Analysis in Geotechnical Engineering Design. *Lecture Notes in Civil Engineering*. [Online] 62, 1009–1022. Available from: doi:10.1007/978-981-15-2184-3_132.

Zdravković, L., Taborda, D.M.G., Potts, D.M., Abadias, D., et al. (2019) Finite-element modelling of laterally loaded piles in a stiff glacial clay till at Cowden. *Géotechnique*. [Online] 1–15. Available from: doi:10.1680/jgeot.18.pisa.005.

Zembaty, Z., Kokot, S. & Kuś, J. (2018) Mitigating Rockburst Effects for Civil Engineering Infrastructure and Buildings. In: *Rockburst: Mechanisms, Monitoring, Warning, and Mitigation*. [Online]. pp. 541–548. Available from: doi:10.1016/B978-0-12-805054-5.00017-2.

Zhang, H.. (2006) Study on nonlinear dynamic soil-underground structure interaction and its large-size shaking table test. *Nanjing University of Technology*.

Zhang, Z., Wei, H. & Qin, X. (2017) Experimental study on damping characteristics of soil-structure interaction system based on shaking table test. *Soil Dynamics and Earthquake Engineering*. [Online] 98 (September 2016), 183–190. Available from: doi:10.1016/j.soildyn.2017.04.002.

Zhou, M., Jiang, L., Chen, S., Cardoso, R.P.R., et al. (2020) Remaining fire resistance of steel frames following a moderate earthquake – A case study. *Journal of Constructional Steel Research*. [Online] 164, 105754. Available from: doi:10.1016/j.jcsr.2019.105754.

Ziaei, M., Peyghaleh, E. & Zolfaghari, M.R. (2010) Effects of Fire Following Earthquake on steel moment resisting covered versus uncovered structures. In: *9th US National and 10th Canadian Conference on Earthquake Engineering 2010, Including Papers from the 4th International Tsunami Symposium*. 2010 pp. 4521–4531.

Zuo, H., Bi, K. & Hao, H. (2018) Dynamic analyses of operating o ff shore wind turbines including soil- structure interaction. *Engineering Structures*. [Online] 157 (November 2017), 42–62. Available from: doi:10.1016/j.engstruct.2017.12.001.